

Micro-computed Tomography (micro-CT) in Medicine and Engineering

Kaan Orhan
Editor

Micro-computed Tomography (micro-CT) in Medicine and Engineering

Kaan Orhan
Editor

Micro-computed
Tomography (micro-CT)
in Medicine
and Engineering

 Springer

Editor

Kaan Orhan
Faculty of Dentistry
Department of Dentomaxillofacial
Radiology
Ankara University
Ankara
Turkey

Faculty of Medicine
OMFS IMPATH Research Group
Department of Imaging and Pathology
University of Leuven
Leuven
Belgium

Oral and Maxillofacial Surgery
University Hospitals Leuven
University of Leuven
Leuven
Belgium

ISBN 978-3-030-16640-3 ISBN 978-3-030-16641-0 (eBook)

<https://doi.org/10.1007/978-3-030-16641-0>


© Springer Nature Switzerland AG 2020

This work is subject to copyright. All rights are reserved by the Publisher, whether the whole or part of the material is concerned, specifically the rights of translation, reprinting, reuse of illustrations, recitation, broadcasting, reproduction on microfilms or in any other physical way, and transmission or information storage and retrieval, electronic adaptation, computer software, or by similar or dissimilar methodology now known or hereafter developed.

The use of general descriptive names, registered names, trademarks, service marks, etc. in this publication does not imply, even in the absence of a specific statement, that such names are exempt from the relevant protective laws and regulations and therefore free for general use.

The publisher, the authors, and the editors are safe to assume that the advice and information in this book are believed to be true and accurate at the date of publication. Neither the publisher nor the authors or the editors give a warranty, expressed or implied, with respect to the material contained herein or for any errors or omissions that may have been made. The publisher remains neutral with regard to jurisdictional claims in published maps and institutional affiliations.

This Springer imprint is published by the registered company Springer Nature Switzerland AG. The registered company address is: Gewerbestrasse 11, 6330 Cham, Switzerland

*To the person
who sees diamonds in the blue sky
whom I feel most alive within the worlds that never were
who dreams with me
This is for you—*

Introduction

The discovery of X-rays app. 120 years ago changed dramatically the diagnostic capabilities. Since then, there have been many advances in medicine, which have had more of an impact on modern health care. Radiology offers the best ways of thinking about different diseases of patients and the best methods to understand what is “real” diagnosis: moreover, it gives the opportunity to understand how we see, smell, hear, feel, taste, and touch and more ultimately to see how sick and how healthy we all are. Recently, with the use of Micro-CT, not only medical fields but also a large variety of disciplines can have beneficial effects from this technique in terms of basic sciences, material sciences, engineering, etc.

Research on the use of Micro-CT and 3D printer technologies for medical and industrial prototyping processes are becoming ever widespread throughout the world. Processing of CT or Micro-CT scanning data of a biological structure, and subsequent modelling of its three-dimensional model in the digital environment, creates its own application areas in numerous fields. This growing demand for exploring allows us to jump in another level of research and engineering which needs help on such techniques as Micro-CT.

It should be emphasized that success is measured by the people’s impact on their community. This book is a team effort for creating an understanding of Micro-CT starting from basics to fundamental research. For these reasons and goals, this book should be regarded as a stage in learning and understanding the Micro-CT imaging that will stimulate both engineering and medical professions that seek a more in-depth appreciation of the subject and its contribution to the scientific community.

Kaan Orhan

Faculty of Dentistry, Department of Dentomaxillofacial Radiology,
Ankara University, Ankara, Turkey

Faculty of Medicine, OMFS IMPATH Research Group, Department of Imaging
and Pathology, University of Leuven, Leuven, Belgium

Oral and Maxillofacial Surgery, University Hospitals Leuven,
University of Leuven, Leuven, Belgium

Preface

Experimental and preclinical bone and dental research has employed micro-computed tomography (Micro-CT) increasingly over the last two decades which is currently being utilized in various fields such as biomedical research, materials science, pharmaceutical medicine development and manufacturing, composites, dental research, electronic components, geology, zoology, botany, construction materials, and paper production. From a technical point of view, Micro-CT indeed is a cone beam computed tomography technique which utilizes geometrically cone-shaped beams for reconstruction and back-projection processes, having a voxel size volumetrically almost 1 million times smaller than that of computed tomography (CT). Taking advantage of all these benefits provided by micro-computed tomography, various approaches in medicine and engineering are being conducted on Micro-CT. Throughout this book, all aspects of Micro-CT, including technical details and applications in medicine and engineering, are being discussed.

This book offers a comprehensive, detailed, up-to-date review of our current knowledge in the Micro-CT imaging. The eminently readable text is complemented by numerous and superb illustrations. The authors of the individual chapters were invited to contribute because of their outstanding personal experiences in the Micro-CT imaging and research and their major contributions to the literature on the topic.

Detailed research and Micro-CT findings are given in each chapter to demonstrate the level of detail required for research with insightful “pearls and pitfalls,” all designed to provide novice as well as experienced readers a brief but concise summary of the advantages and limitations of using this technology in the clinical setting.

In this book, the chapters follow two categories: medical approaches and engineering approaches of Micro-CT. The technique and fundamentals of this imaging modality will be discussed in Chaps. 2–4. Chapters 2–3 briefly review the fundamentals of X-radiation and imaging and discuss reconstruction from projections of Micro-CT. Chapter 4 will be reviewing all artifacts for Micro-CT imaging. The rest of the book will focus on medical applications which are covered in Chaps. 5–13, whereas the engineering parts will be covered in Chaps. 14–19.

As a result, this book offers a comprehensive review of the state of the art of Micro-CT imaging. I would like to congratulate the authors most sincerely for their superb efforts which have resulted in this excellent book, which will be of great interest not only for medical but also for engineering fields.

Ankara, Turkey
Leuven, Belgium
2019

Kaan Orhan

Contents

1 Introduction to Micro-CT Imaging	1
Kaan Orhan	
2 X-Ray Imaging: Fundamentals of X-Ray	7
Roberto Molteni	
3 Fundamentals of Micro-CT Imaging	27
Kaan Orhan and Arda Büyüksungur	
4 Artifacts in Micro-CT	35
Kaan Orhan, Karla de Faria Vasconcelos, and Hugo Gaêta-Araujo	
5 Application of Bone Morphometry and Densitometry by X-Ray Micro-CT to Bone Disease Models and Phenotypes	49
Phil Salmon	
6 Analysis of Fracture Callus Mechanical Properties Using Micro-CT	77
Burak Bilecenoğlu and Mert Ocak	
7 Micro-CT in Osteoporosis Research	87
Szandra Körmendi, Bálint Vecsei, Kaan Orhan, and Csaba Dobó-Nagy	
8 Micro-CT in Comparison with Histology in the Qualitative Assessment of Bone and Pathologies	109
Umut Aksoy, Hanife Özkayalar, and Kaan Orhan	
9 Micro-CT in Artificial Tissues	125
Leyla Türker Şener, Gürcan Albeniz, Göker Külişlü, and Işıl Albeniz	
10 Application of Micro-CT in Soft Tissue Specimen Imaging	139
Gina Delia Roque-Torres	
11 Applications of Micro-CT in Cardiovascular Engineering and Bio-inspired Design	171
Bilgesu Çakmak, Erhan Ermek, Muhammad Jamil, Asım Horasan, and Kerem Pekkan	

12 Applications of Micro-CT Technology in Endodontics	183
Marco A. Versiani and Ali Keleş	
13 Micro-Computed Tomography (Micro-CT) Analysis as a New Approach for Characterization of Drug Delivery Systems	213
Müge Kılıçarslan, Miray İlhan, and Kaan Orhan	
14 Challenges in Micro-CT Characterization of Composites	225
Güllü Kızıлтаş, Melih Papila, Bengisu Yılmaz, and Kaan Bilge	
15 Modeling and Mechanical Analysis Considerations of Structures Based on Micro-CT	247
Gökhan Altıntaş	
16 The use of Micro-CT in Materials Science and Aerospace Engineering	267
Sinan Fidan	
17 X-Ray Computed Tomography Technique in Civil Engineering	277
Savaş Erdem and Serap Hanbay	
18 Application of X-Ray Microtomography in Pyroclastic Rocks	289
H. Evren Çubukçu	
19 Detection of Dispersion and Venting Quality in Plastic Composite Granules Using Micro-CT.	303
Orkun Ersoy	



Introduction to Micro-CT Imaging

1

Kaan Orhan

1.1 Introduction

Micro-CT has the ability to create cross-sectional images of a physical object by making use of X-rays. Cross-sectional images created this way are then processed by relevant software in the computer environment, and a three-dimensional model of the scanned object is hence created in the digital environment. Since the pixels forming the 2D cross-sectional images obtained by micro-tomography are in terms of micro (μ) units, scientific and processable information on internal structures and geometries of tiny objects or appropriately sized pieces of larger objects can be attained. Research on the use of Micro-CT and 3D printer technologies for medical and industrial prototyping processes are becoming ever widespread both in our country and throughout the world. Processing of CT or Micro-CT scanning data of a biological structure and subsequent modelling of its three-dimensional model in the digital environment create its own application areas in numerous fields.

Hounsfield created the very first full-body computed tomography device back in 1975, and Hounsfield and Cormack received the Nobel Prize for physiology and medicine with this device in 1979. Main components of the micro-tomography device are the X-ray tube, a computer-driven step motor that intermittently rotates the sample mounted on its body, an image intensifier which focuses the X-rays in the medium onto the camera sensor, a CCD camera which converts X-rays received into image data, an image collector, and a computer that controls all these components. Better spatial resolution is attained by 5–10 μm^3 voxel size scan provided by micro-computed tomography, compared to 1 mm^3 voxel size scan provided by computed tomography. This makes viewing areas 1,000,000 times smaller than that could be viewed by computerized tomography possible, which in turn allows conducting more detailed investigations. This was regarded as a revolutionary development [1, 2].

Micro-CT scanners are mostly utilized in academic and industrial research laboratories. In order to examine specimen such as ceramics, polymers, and biomaterials, different fields of views (FOV) could be selected by Micro-CT devices relevant to the dimensions of the area to be examined, and hence, higher-resolution images can be obtained by working on smaller areas. In vitro and in vivo Micro-CT devices are currently available, and varying FOV ratios

K. Orhan (✉)
Faculty of Dentistry, Department of Dentomaxillofacial
Radiology, Ankara University, Ankara, Turkey

Faculty of Medicine, OMFS IMPATH Research
Group, Department of Imaging and Pathology,
University of Leuven, Leuven, Belgium

Oral and Maxillofacial Surgery, University Hospitals
Leuven, University of Leuven, Leuven, Belgium

applied in these devices determine the area to be examined and the resolution to be attained [3]. Similar to the cone beam computed tomography devices, Micro-CT systems utilize micro focal X-ray sources and high-resolution detectors to create 3D reconstructions of the samples [19]. Main components of the micro-tomography device are the X-ray tube, a computer-driven step motor that intermittently rotates the sample mounted on its body, an image intensifier which focuses the X-rays present in the environment onto the camera sensor, a CCD camera which converts X-rays received into image data, an image collector, and a computer that controls all these components [4].

Figure 1.1 shows analysis of search from www.scopus.com for “Micro-CT” on May 8, 2019. The results show that the papers published are increasing eventually and the works including Micro-CT are increasing. Figure 1.2 shows the distribution of subjects of Micro-CT papers found in Scopus until 2018. The vast majority in medicine scope papers and following engineering.

Interestingly, there are nearly half as many Micro-CT papers on tissue engineering scaffolds as there are in the nonbiology subject areas.

1.2 What Does the Life Sciences Profession Need in Terms of Micro-CT Imaging?

For scientific studies, an objective diagnosis using imaging techniques must be reproducible. Although there are criteria and conventional as well as contemporary evaluation methods in life sciences, there are still an unclear correlation often exists between clinical relevance and symptoms and the imaging findings in diseases.

There is no doubt that this is a maturing technology, but what is perhaps the most exciting aspect of using Micro-CT is that images of internal structures can be obtained without damage to the specimen. The technology provides the opportunity to undertake large-scale studies in a relatively short timescale and use museum collections not normally amenable to conventional anatomical studies [5].

There are various applications for Micro-CT in life sciences. Micro-CT are viable inspection tools for biological applications as they can be used to compliment medical imaging techniques at increased resolution in the absence of dose restrictions. Due to its nondestructive nature, CT samples can be further utilized for other

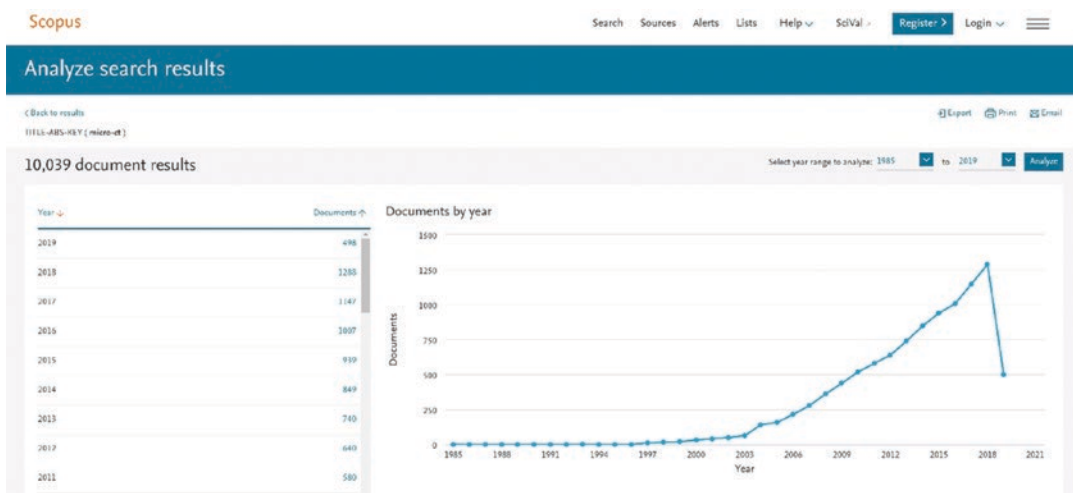


Fig. 1.1 Shows analysis of search from www.scopus.com for “Micro-CT” on May 8, 2019 that reveals the works including Micro-CT are increasing dramatically

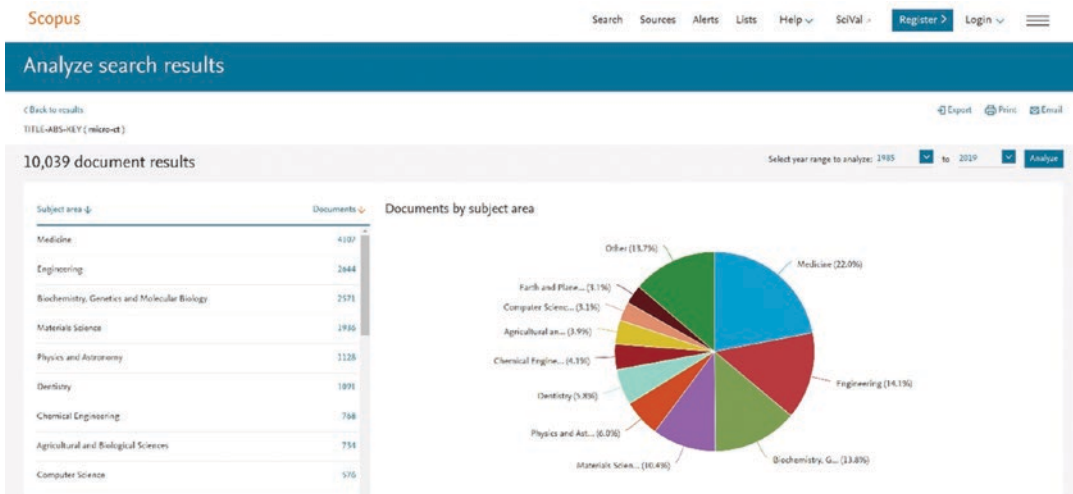


Fig. 1.2 Shows the distribution of subjects of Micro-CT papers found in Scopus until May 8, 2019. The vast majority in medicine scope papers and following engineering

experimental techniques such as mechanical testing and histology [6]. For life sciences histomorphometric analyses are destructive, long term, and costly methods. It is impossible to reuse the same sample for another measurement. Due to these disadvantages, three-dimensional micro-tomography techniques have been put into use as nondestructive, rapid, and reliable methods for analyzing micro-architecture of cortical and trabecular bones [7].

Bone quality evaluation is one of the main applications for Micro-CT in life sciences. The bone is a highly mineralized and multifunctional tissue, which plays roles in mechanical support and protection, mineral homeostasis, and hematopoiesis. The “quality” of bone, as well as its quantity, contributes to the biomechanical performance of the skeleton and encompasses aspects of both macromolecular composition and microarchitectural arrangement [8]. The excellent reproducibility and accuracy of Micro-CT measurements of bone morphology have been established in several studies [9, 10]. The accuracy of Micro-CT morphology measurements has been evaluated by comparing them with traditional measures from 2D histomorphometry both in animal and in human specimens [9, 11, 12]. These studies

show that 2D and 3D morphologic measurements by Micro-CT generally are highly correlated with those from 2D histomorphometry. The most important part for these kinds of evaluations is gathering as much information to the Micro-CT technologists which allows to have a proper analysis in a realistic way.

1.3 What Does the Material Sciences Profession Need in Terms of Micro-CT Imaging?

The appearance of new digital scanning systems with numerous features in addition to the mentioned advantages above is changing the evaluation of the materials in engineering as well.

Previously, the material science was stuck for evaluation in 2D. However, 2D have several drawbacks, including errors that are classified as “errors of projection” and “errors of identification.” Errors of projection are due to the two-dimensional (2D) which causes a shadow of the three-dimensional (3D) object. As a result of the various evaluations, modalities may lead to errors of identification and reduced measurement accuracy.

New technological advances in material science especially Micro-CT imaging have resolved these errors and are becoming increasingly popular for evaluations for the materials, and this area is rapidly growing (Fig. 1.2). Mainly Micro-CT imaging can use not only hard characteristic materials like geological samples but also the materials such as composites to understand the mechanical behaviors. In particular, Micro-CT is a nondestructive technique that visualizes interior features within specimens with 3D imaging. This effective characterization method can alter the focus size from micro to macro to obtain reliable image data [13].

In materials science it is often necessary to make correlations between the properties of materials and their microstructure. In the case of metallic materials, the microstructure is usually correlated to defects defined as perturbations in comparison with the perfect single crystal and to the presence of alloying elements. These defects are thus vacancies, dislocations, grain boundaries, pores, and cracks, and in the case of alloys, one can find foreign atoms in solid solutions [14]. There are several evaluations that can be made by Micro-CT such as phase volume fractions and phase connectivity to more complex measurements such as spatial distributions, orientations, alignment, and connectivity of microstructural features. These various microstructural features can form during elaboration, shaping, and use of the materials all along their life time [15, 16]. Throughout this book, detailed applications of Micro-CT will be discussed in detail.

The chapters that follow fall into two categories: medical approaches and engineering approaches and use of Micro-CT. The technique and fundamentals of this imaging modality will be discussed in Chaps. 2–4. Chapters 2–3 briefly review the fundamentals of X-radiation and imaging and discuss reconstruction from projections of Micro-CT. Chapter 4 will be reviewing all artifacts for Micro-CT imaging. The rest of the book will focus on medical applications which are covered in Chaps. 5–13, whereas the engineering parts will be covered in Chaps. 14–19.

Acknowledgments Some of the researches in this book were supported by Ankara University Scientific Research Projects Coordination Unit (Grant number: 17A0234001).

References

1. Feldkamp LA, Goldstein SA, Parfitt AM, Jesion G, Kleerekoper M. The direct examination of three-dimensional bone architecture in vitro by computed tomography. *J Bone Miner Res.* 1989;4(1):3–11.
2. Kuhn J, Goldstein S, Feldkamp L, Goulet R, Jesion G. Evaluation of a microcomputed tomography system to study trabecular bone structure. *J Orthop Res.* 1990;8(6):833–42.
3. Guldberg RE, Lin AS, Coleman R, Robertson G, Duvall C. Microcomputed tomography imaging of skeletal development and growth. *Birth Defects Res C Embryo Today.* 2004;72(3):250–9.
4. Rhodes JS, Ford TR, Lynch JA, Liepins PJ, Curtis RV. Micro-computed tomography: a new tool for experimental endodontology. *Int Endod J.* 1999;32(3):165–70.
5. Paterson GLJ, Sykes D, Faulwetter S, Merk R, Ahmed F, Hawkins LE, Dinley D, Ball AD, Arvanitidis C. The pros and cons of using micro-computed tomography in gross and microanatomical assessments of polychaetous annelids. *Mem Mus Victoria.* 2014;71:237–46.
6. Faillace ME, Rudolph RA, Brunke O. Micro-CT and Nano-CT as a valuable complimentary tool for life sciences. *Microsc Microanal.* 2013;19:636–7.
7. Parfitt AM. Bone histomorphometry: proposed system for standardization of nomenclature, symbols, and units. *Calcif Tissue Int.* 1988;42:284–6.
8. Aaron JE, Shore PA. Bone Histomorphometry. In: *Handbook of histology methods for bone and cartilage.* Totowa, NJ: Humana Press; 2003. p. 331–51.
9. Bouxsein ML, Boyd SK, Christiansen BA, Guldberg RE, Jepsen KJ, Müller R. Guidelines for assessment of bone microstructure in rodents using micro-computed tomography. *J Bone Miner Res.* 2010;25(7):1468–86.
10. Chappard D, Retailleau-Gaborit N, Legrand E, Baslé MF, Audran M. Comparison insight bone measurements by histomorphometry and μ CT. *J Bone Miner Res.* 2005;20(7):1177–84.
11. Bonnet N, Laroche N, Vico L, Dolleans E, Courteix D, Benhamou CL. Assessment of trabecular bone microarchitecture by two different X-ray microcomputed tomographs: a comparative study of the rat distal tibia using Skyscan and Scanco devices. *Med Phys.* 2009;36(4):1286–97.
12. Müller R, Van Campenhout H, Van Damme B, Van Der Perre G, Dequeker J, Hildebrand T, Rüeeggesser P. Morphometric analysis of human bone biopsies: a quantitative structural comparison of histological sections and micro-computed tomography. *Bone.* 1998;23(1):59–66.

13. Bayraktar E, Antolovich SD, Bathias C. New developments in non-destructive controls of the composite materials and applications in manufacturing engineering. *J Mater Process Technol.* 2008;206(1–3):30–44.
14. Salvo L, Michel S, Marmottant A, Limodin N, Bernard D. 3D imaging in material science: application of X-ray tomography. *C R Physique.* 2010;10:641–9.
15. Landis EN, Keane DT. X-ray microtomography. *Mater Charact.* 2010;61(12):1305–16.
16. Guldberg RE, Ballock RT, Boyan BD, Duvall CL, Lin AS, Nagaraja S, Oest M, Phillips J, Porter BD, Robertson G, Taylor WR. Analyzing bone, blood vessels, and biomaterials with microcomputed tomography. *IEEE Eng Med Biol Mag.* 2003;22(5):77–83.



X-Ray Imaging: Fundamentals of X-Ray

2

Roberto Molteni

2.1 X-Rays and Their Interaction with Matter

X-rays are electromagnetic radiation with wavelength (λ) in the 10^{+1} to 10^{-3} nanometers range. Since the frequency (ν) of an electromagnetic radiation equals to the speed of light (c) divided by its wavelength, i.e., $\nu = c/\lambda$, this corresponds to a frequency range of approximately 10^{16} to 10^{20} Hz. The energy of a single photon (E) equals to ν multiplied by the Planck constant h (6.626×10^{-34} J s), so the energy range of a single X-ray photon falls between 2×10^{-17} and 6×10^{-14} joule, corresponding to 100 eV (very “soft”) to 1 MeV (very “hard”), where 1 eV (electron volt) is the energy acquired by one electron when accelerated by an electric field of 1 V (the energy of subatomic particles is usually expressed in eV and multiples thereof, 1 eV corresponding to 1.602×10^{-19} J).

Electromagnetic radiation in this energy range is called γ (gamma)-rays or X-rays depending on the process that generated it: a nuclear transition for the former, a phenomenon outside the atomic nucleus for the latter. However, a γ -ray beam is composed of photons all having essentially the same energy (monochromatic or monoenergetic radiation), because of the nature of the generation

process, whereas an X-ray beam is generally composed of photons having a multitude of different energies, i.e., a continuous spectrum of energies (polychromatic radiation). Moreover, usually γ -rays have higher energies (are “harder”) than the typical energy of X-rays, although some overlapping exists.

X-rays (and γ -rays alike) have the desirable property of interacting with matter only moderately, which is why they are so convenient for imaging the interior of solid bodies, that they penetrate to various depths before being stopped through absorption or scattering. Practically speaking and unlike visible light, an X-ray beam cannot be reflected, refracted, or focused (except minimally and under special conditions).

The interaction with matter of electromagnetic photons in the range of energy of our interest mostly occurs via two processes: photoelectric absorption and Compton scattering. Other two less-intense interaction phenomena can happen: production of an electron-positron pair and coherent scattering. The former start occurring when the photon’s energy is above 1022 keV (rest energy of the electron-positron pair); the latter is relevant just at very low photon energies. Both of them are outside the energy range of our interest here and will not be discussed further.

Photoelectric absorption occurs when a photon fully transfers its energy to the electronic shell of an atom and is thus absorbed. It predominates at photon energies up to approximately 30 kV.

R. Molteni (✉)
American Academy of Oral and Maxillofacial
Radiology, Lombard, IL, USA

American Association of Physicists for Medicine,
Alexandria, VA, USA

Compton scattering (or Compton effect) occurs when a photon interacts with an atom by yielding only part of its energy. As a consequence, its trajectory is randomly deviated, or scattered. The Compton scattering is rather undesirable (albeit unavoidable) from the radiologic imaging standpoint since it causes a component of randomly directed, non-information-bearing photons to overlap the information-bearing component of the X-ray beam, fogging the resulting radiographic image.

The interaction of photons, electrons, and atoms is governed by random statistics since they are quantic objects. Indeed, for an individual photon, one cannot predict with certainty what thickness (or distance travelled) of a given material it will traverse before an interaction occurs. Only the probability that such interaction occurs for a certain thickness of a given material can be defined. Such probability, and the penetration capacity of an X-ray beam, can be expressed as a “Mean Free Path” and depends upon the photon energy and the material. The Mean Free Path is the mean distance travelled by a photon before an interaction occurs. It is also—by the law of Gaussian statistics—the thickness of material that causes a reduction in intensity (i.e., in the number of photons) of a monochromatic beam to 0.368 (the inverse of the Napier’s constant 2.718). The inverse of the Mean Free Path is used more frequently, called the “Linear Attenuation

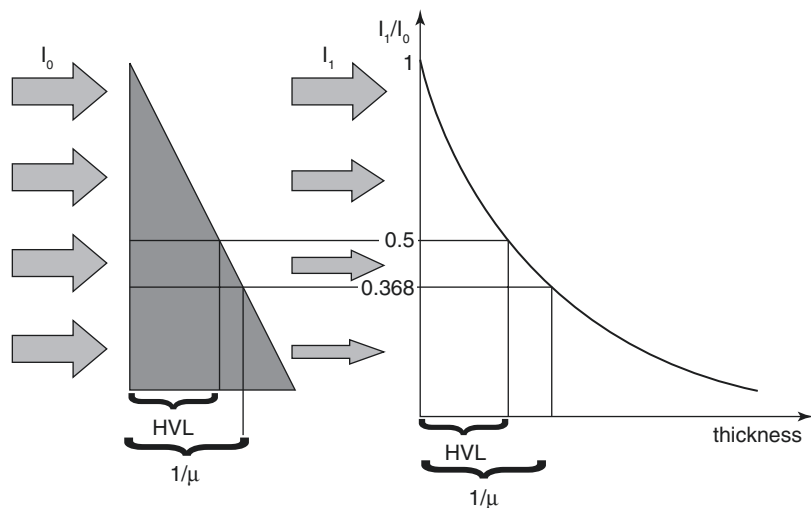
Coefficient” (μ). Another pertinent quantity is the “mass attenuation coefficient,” which is the Linear Attenuation Coefficient divided by the density (ρ) of the material. In the practical technical arena, another related quantity—essentially equivalent to the Mean Free Path—is much more frequently used, that is, the “Half-Value Layer” (HVL), namely, the thickness (usually in mm) of a given material that attenuates by half the intensity of a monochromatic X-ray beam of given energy. It corresponds to $0.693/\mu$ or 0.693 times the Mean Free Path. So, an X-ray beam with HVL of, e.g., 2.5 mm Al_{equiv} means that two and half millimeter of pure aluminum, or of a substance of stopping power equivalent to aluminum, are needed to attenuate it by half. Aluminum (Al), for lower beam energies, or copper (Cu), for higher beam energies, is the material generally used to indicate the HVL for the range of interest in radiology (Fig. 2.1).

These numerical coefficients, and the formula that entails them, can be derived with merely theoretical mathematical considerations from the normal (or Laplace-Gauss) statistical nature of the interaction of photons with matter, which leads to the Beer-Lambert Law:

$$A = I_1 / I_0 = \exp(-\mu t)$$

where A is the attenuation of beam intensity, I_0 is the beam intensity at the entrance of the absorbing material, I_1 is the beam intensity after

Fig. 2.1 Attenuation of a monochromatic X-ray beam through an increasing thickness of material, according to the Beer-Lambert Law, as shown with a wedge-shaped object of uniform radiologic density. HVL is the Half-Value Layer, and the Mean Free Path is $1/\mu$ (the inverse of the Linear Attenuation Coefficient μ)



transiting through the absorbing material, t is the thickness of the material, and μ is the Linear Attenuation Coefficient.

For the component of X-ray absorption due to photoelectric effect, the mass attenuation coefficient (μ/ρ) depends—very steeply, namely, to the third power—on the (effective) atomic number (Z) of the material. This is why elements with high atomic number (like lead, $Z = 82$; bismuth, $Z = 83$; barium, $Z = 56$) are very effective at shielding (= stopping) X-rays. Mass attenuation coefficients and density of all the natural elements and of many substances and compounds, for the whole range of photon energies of interest, can be found tabulated at the website established and maintained by the NIST—National Institute of Standards and Technology (USA): www.nist.gov/pml/x-ray-mass-attenuation-coefficients.

The Beer-Lambert Law is very useful and straightforward for γ -rays, which are essentially monochromatic. Unfortunately, X-ray beams generally are polychromatic; hence each component of their continuous energy spectrum involves a different value of μ . The attenuation is the result of an integral of all the differential beam intensities and values of μ through the energy spectrum.

The Linear Attenuation Coefficient decreases markedly as the energy increases, in other words X-rays with higher energy are more penetrant, or “harder.” Therefore, the different components of the spectrum are variously attenuated when the polychromatic X-ray beam passes through a layer of material, the lower-energy portion being attenuated more than the higher-energy portion. As a consequence after the attenuation, or “filtering,” the spectrum of the X-ray beam is skewed toward higher energies, that is, “hardened” with respect to the original spectrum. Again, this is obtained by absorbing portions of the spectrum in a differential manner—more at low energies, less at higher energies—not by shifting the spectrum, whose value of maximum energy bin remains unaffected by the filtering. By selectively attenu-

ating the softer parts of the spectrum more than the harder part, filtering causes the beam to become slightly less polychromatic—but just slightly. There is a common misconception that more filtering always results into improved quality of the X-ray images, since the beam becomes harder (more penetrating) and less polychromatic. This is generally true for the minimal filtering recommended by the standards for a given application, which removes a large portion of very soft radiation ineffectual for imaging but that adds unnecessary skin dose to a live patient. Beyond that, the primary consequence of filtering is attenuation of the radiative flux that was laboriously obtained via the best application of technology, with the hardening as a modest side effect. Anyway, there is an optimal radiation hardness for every radiological process and increasing it further is not beneficial.

Since hardness, or penetration capacity, of a polychromatic X-ray beam increases with filtration, its HVL after a first filtration is increased. Let us suppose that an X-ray beam is made to traverse a layer of material corresponding to its Half-Value Layer; at the exit the beam intensity is half than at the entrance, and the beam is harder. If the beam then traverses a second layer of equal thickness of the same material, the attenuation will be less than before because of the beam’s increased hardness; therefore the beam intensity at the second exit will be more than half of the intensity at the second entrance. In order to attenuate to half, the thickness of the second layer has to be increased with respect to the (1st) Half-Value Layer; this new thickness is called the 2nd Half-Value Layer; and so on with any further attenuating layers or filters (Fig. 2.2). Of course, this “beam hardening” phenomenon is solely due to the polychromatic nature of the beam. The spectrum of a hypothetical monochromatic X-ray beam would be just a line (as with γ -ray); therefore there could not be reshaping of the spectrum, hence no hardening. Thus, the only effect of filters and of traversed materials would be attenuation of the intensity.

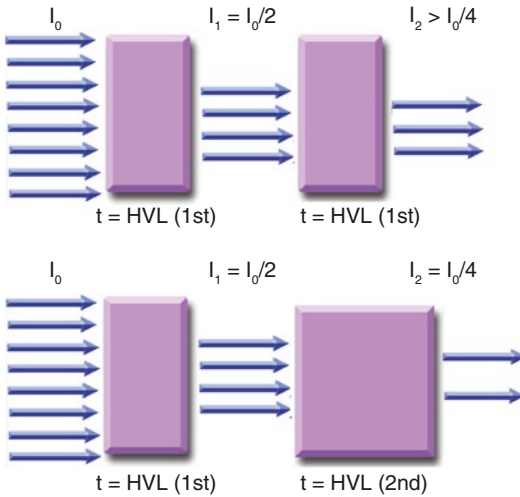


Fig. 2.2 Half-Value Layer attenuation of a polychromatic X-ray beam

2.2 The Radiographic Process

The radiographic process basically consists of four elements:

1. The X-ray source
2. The object to be radiographed (in medical radiology, a bodily part)
3. The image detector
4. The software for image processing and the device for its visualization

Together with the projection geometry, these four elements fully determine the outcome of the radiographic process.

A radiograph is produced when an X-ray beam from the source crosses the object to be radiographed, being thus variously absorbed and attenuated in the different parts of the object—depending on its density and extent—and casts an X-ray shadow onto the radiographic image detector, namely, a negative image of the object. Thus, the signal is at full scale where there is no attenuation (= void), while it is zero where the attenuation is complete (no X-rays passing through).

To optimize the radiographic result as a whole, it is necessary to balance and compro-

mise the optimization of each element's settings. For instance, maximizing spatial resolution may require increasing the examination time, the imparted radiation dose, the size and/or the cost of the system, etc. This holds true also in micro CT, where, however, one goal is sought above all others, that is, the maximization of spatial resolution for the visualization of small details, whereas, e.g., irradiation time and imparted dose are of secondary or no concern.

X-rays are generated when electric charges (electrons) are abruptly decelerated or as a result of transitions between the atomic orbitals (or statuses) of electrons. Two devices are used to artificially generate X-rays: synchrotrons and X-ray tubes.

A synchrotron consists of a very large ring-shaped vacuum pipe along which numerous properly synchronized electromagnets veer the path of a beam of electrons travelling at relativistic velocity. At suitable locations along the ring, a swift deceleration of the electrons causes the emission of “synchrotron radiation,” i.e., X-rays.

There is no doubt that synchrotron-generated X-rays vastly exceed in quality and features those produced from X-ray tubes (which will be addressed immediately after). Flux and spectral brightness is orders of magnitude greater; they can be quasi-monochromatic, tightly collimated, coherent, and even polarized, which makes possible applications unachievable with X-ray tubes.

However, synchrotrons require very large and very expensive facilities that are also expensive to operate. Furthermore, the range of X-ray energies attainable falls somewhat below of what is required in many micro-CT applications. There are only a few dozens of them in the whole world; therefore they are impractical for routine applications and are used mostly for research.

Compact (even tabletop) synchrotron systems have been speculated and described, but mostly they are the object of experimental researches, and their industrial production and commercial availability are still away in the future.

2.3 X-Ray Tubes

X-ray tubes constitute the vastly overwhelming majority of X-ray sources in any radiological imaging application, whether medical, industrial NDC (nondestructive controls), security (e.g., baggage scanning), or scientific.

The simplest (and possibly the most common) type of X-ray tube is the stationary anode X-ray tube (Fig. 2.3), a direct evolution of the design initially developed by William Coolidge in 1913. As in any electric vacuum tube, there are two main electrodes: the cathode and the anode, sealed in a gas-tight enclosure in a high-vacuum environment (10^{-4} Pa, or better). In operation, a very large difference of electrical potential is applied between cathode (at negative potential) and anode (at positive potential), in the order of several tens, or even hundreds, of kilovolts, causing a flow of electrons inside the X-ray tube and the circulation of an electric current in its circuit, called the anodic current (or just tube current). By universal convention and standards, such current is referred to as the “mA” (milliampere) and the maximum instantaneous difference of electric potential (or high voltage) as the “kVp” (kilovolt peak—although the qualifier “peak” nowadays is rather unnecessary and obsolete in view of the current technology). The high voltage kV, the anodic current mA, the exposure time s (seconds), and the product of anodic current by exposure time mAs are called the technique factors.

The X-ray tube can (be designed to) operate in either:

- “Bipolar” mode, where the high voltage is equally split between cathode and anode,



Fig. 2.3 An X-ray tube, stationary anode type

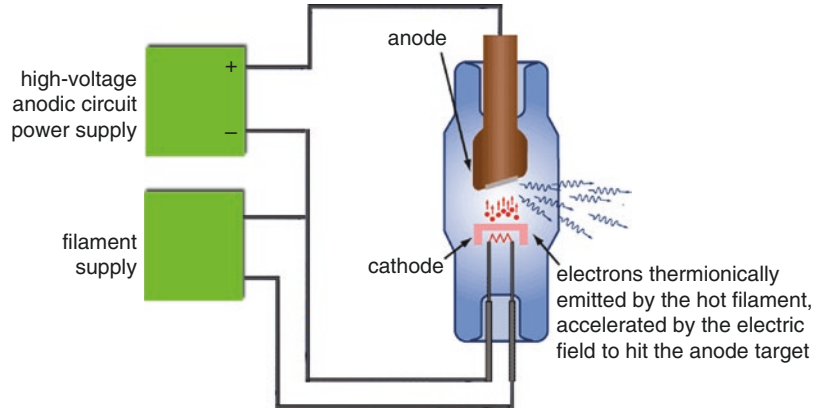
namely, a negative high voltage equal to half of the difference of potential is applied to the cathode and a positive high voltage equal to the balance (the other half) is applied to the anode. This is advantageous in terms of reduced stress to the X-ray tube and because of less stringent insulation requirements.

- “Grounded anode” mode, where the anode is electrically connected to ground and all the difference of potential consists of a negative high voltage at the cathode (potentially advantageous for dissipating the thermal load of the anode, but with more severe insulation requirement at the cathode side).
- “Grounded cathode” mode, where the cathode (i.e., one side of the cathodic filament) is electrically connected to ground and all the difference of potential consists of a positive high voltage at the anode (with the benefit of simplifying the circuitry needed to supply and drive the cathodic filament, see below).

The cathode consists of a filament wire, which in operation is heated to glowing temperature by an electrical current, hence emitting a cloud of electrons by thermionic effect. Because of the large difference of electric potential applied between cathode and anode, the electrons are swept away and accelerated by the electric field to hit the anode. Here they are abruptly decelerated by the interaction with solid matter, thus releasing the energy, which they had acquired from the electric field, as high-energy electromagnetic photons, i.e., the X-rays (Fig. 2.4).

The filament is usually made of a tungsten wire (W) or alloys thereof, and is wound in a tight helicoid, similarly to that of the now-obsolete glowing filament light bulb. The helicoidal shape is mandated by the need to expose as much surface as feasible in order to boost the quantity of electrons thermionically emitted from a source of compact area. Generally, the greater the required electron flow (= the current), the larger the filament. In most cases it is, say, approximately 10 mm of length \times 2 mm of diameter, or slightly bigger. However, when the current intensity to be achieving is not a major consideration (as is the case for certain micro-CT

Fig. 2.4 Principle electrical schematic of an X-ray tube circuit



systems), the filament could also be a straight wire or even just the tip or the corner of an angle-bent wire.

The geometrical design of the X-ray tube is such to converge and focus the flow of electrons, by properly shaping the electric field onto a defined small area of the anode, called the “focal spot” or simply the “focus.” Often such goal is also assisted by the presence of a suitably shaped third electrode, called the grid, situated in close proximity of the cathode. The grid is at a more negative potential than the cathode itself and can be used to converge the electrons beam in a more stable and controlled way. Alternatively, a grid, if properly close to the emitting cathode, can also be used to suppress the electrons beam right at its thermionic emission, repelling the electrons into the cathode, hence controlling the turn on and off of the anodic current or its intensity.

The thermionic filament is an inconvenient emitter of electrons. It is energetically inefficient: in order to emit a relatively small number of electrons, it generally requires several watts of power, most of which is lost and dissipated as heat. It requires a control and drive circuit (potentially of significant sophistication) that in most circumstances must drive the filament in electrical isolation from other system’s circuitry, namely, floating at many tens of thousands kV, therefore requiring substantial insulation. Worst of all, since the slow thermal response of the filament mediates the transfer function from power imparted to the filament to anodic current, the response time of the latter is

slower than what would be desirable for many applications, being anything in the range 0.1–1 s.

A possible alternative to the thermionic filament is the cold emission cathode, where extraction of the electrons is directly achieved by an electric field. It utilizes the phenomena that at sharp edges and point-like features of conductors the strength of the electric field is boosted (the smaller the feature, the more the boosting), potentially to exceed the electron extraction force of the material. For instance, the surfaces of material of suitably low extraction potential, such as diamond or ZnO, can be nano-shaped into, e.g., a pattern of tiny pyramids with sharp vertices. More commonly, carbon nanotubes (CNT) are used, where the open tip of the nanotubes is down in size to molecular scale. From these quasi-singularities, a flow of electrons can be emitted under the action of an electric field of reasonably-moderate force (say, a few kV/mm). Potentially, cold cathode X-ray tubes offer many advantages over traditional thermionic cathode X-ray tubes:

1. Instantaneous response, making possible to switch the emission on-off at a frequency of many kHz, if needed.
2. Little or no circuitry appended to the cathode.
3. Energetic efficiency, since there is no power dispersed in heating the filament.
4. Ease to produce very small point-like sources, which, as we shall see in the subsequent

chapters, is of paramount importance for micro CT.

Many regard cold cathode as the necessary evolution of X-ray tubes for the future. However, the technology and the manufacturing process for CNT cathodes, and X-ray tubes based upon them, is not yet mature. Indeed, there are still open questions about their long-time reliability and the applicability for large anodic current, notwithstanding the scientific/technical investigations conducted in the past 20 years. Consequently, their adoption for industrially made devices has been quite slow; nevertheless they are now used in a number of commercially available products but typically outside the realm of mainstream medical radiology.

As said, the beam of electrons accelerated by the cathode-anode high-voltage electric field is focused onto the “target” portion of the anode, hitting the small area called the focal spot. At any given time, all hitting electrons have precisely the same energy, equal in eV to the accelerating voltage at that moment. If the cathode-anode difference of potential is, say, 80 kV, then all electrons hitting the anodic target have an energy of 80 keV. The electrons cede their energy to the anode’s target, mostly in form of heat. The majority of the X-rays are generated by the abrupt deceleration of the electrons over a path several micrometers deep into the target, through a mechanism called “bremsstrahlung,” which produces a continuous spectrum of energy. The maximum photon energy thus possible corresponds to the (peak) high voltage, which occurs when the electron yields all its energy in a single event generating just one photon having the entire energy that was carried by the electron; however, this is a vanishingly rare event since usually the hitting electrons interact multiple times with those in the atoms of the target, yielding a fraction of their energy at each interaction. The continuous X-ray spectrum originated from bremsstrahlung, unfiltered, has its maximum intensity in the lowest energies bins and slopes down to zero at the maximum energy corresponding to the accelerating difference of potential.

There is a second process by which X-ray is generated: the “characteristic radiation” (of the target’s material). It happens when an orbital electron of the innermost atomic shell (the K shell) gets knocked off its orbital (or energy status) and another free electron (or an electron from an outer lower-energy orbital) refills the temporarily empty orbital, thus emitting a photon having an energy corresponding to the (negative) potential of that orbital. This ensues in quasi-monochromatic lines or peaks, superimposed to the continuous spectrum caused by bremsstrahlung, with energies corresponding to the (negative) potential of the K orbital of the target’s material. Energy lines corresponding to transitions into other orbitals (notably the L) are also possible but of scarce practical relevance. Usually (but not always) characteristic radiation accounts for only a small portion of the total X-ray flux.

Part of the generated X-rays is reabsorbed before it leaves the target into empty space, preferentially so for the very low-energy photons, which modifies the spectrum to a bell shape, with empty bins at very low energies (Fig. 2.5).

The X-ray generation mechanism just described is very inefficient, since only a small

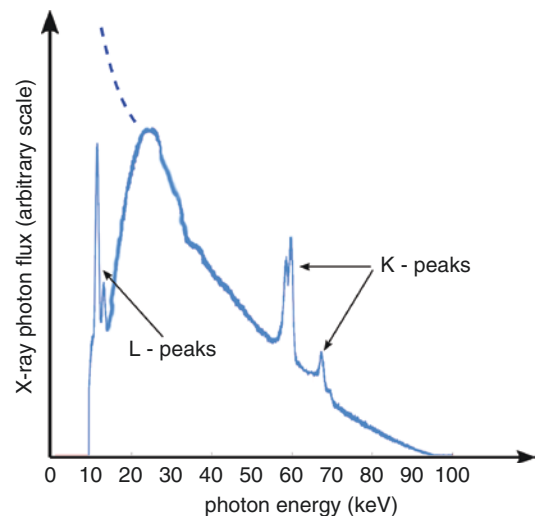


Fig. 2.5 X-ray spectrum from a tungsten anode X-ray tube operated at 100 kV, with bremsstrahlung and peaks of characteristic radiation (after inherent filtration). The dashed lines indicate what the low-energy spectrum would be in the hypothetical case of zero inherent filtration (including no self-filtration by the target)

portion (about 1%, or less) of the energy carried by the cathode-to-anode electrons beam results into X-rays, the remainder is wasted as heat. Managing the dissipation of such heat is one of the crucial points in the design of X-ray tubes and of their operation too.

The energy load per unit time (= per second) carried by the electrons' beam, i.e., the thermally dissipated power (in watts), is simply calculated by the product of anodic current time cathode-anode difference of potential, i.e., $\text{mA} \times \text{kV}$. Such power is imparted entirely to the anodic target, from where the ensuing heat has to be removed in the fastest and most efficient manner possible.

Only a limited number of metallic materials are practically suitable for the target. Tungsten (W) is the one used in the vast majority of cases (sometime alloyed or coated with rhodium) because of a combination of desirable properties:

- Extremely high melting temperature (3422 °C) and boiling temperature (5930 °C, the highest of all elements).
- Good thermal conductivity.
- Very good mechanical properties (hardness).
- Very high atomic number ($Z = 74$) and density (19.3), hence very short electron Mean Free Path so the X-ray generation occurs within a short depth from the surface.
- Characteristic radiation (K-line) at 59 keV, which is around the center of the energy spectrum suitable for many radiographic applications.

Another material used as target is molybdenum (Mo), which also has good thermal and mechanical properties, high density, and characteristic radiation at about 18 and 20 keV which makes it suitable for applications with relatively soft X-rays, such as in particular mammography. Rhenium, silver, or copper are also occasionally used for special applications.

In stationary anode tubes, the anodic target practically consists of a small disk of tungsten (say, approximately 10×20 mm in diameter and 2 mm thick) embedded in a much more massive anodic bulk made out of copper, which is the best

heat-conductive material practically available. The temperature of the focal spot in the target must not exceed 2600 °C with tungsten, 1800 °C with molybdenum, above which the metal begins to evaporate and blister. Such thermal load must be dissipated radiatively and/or conductively, the latter being the prevailing mechanism in the stationary anode case. The heat flows to the tungsten-copper junction, where the temperature must already drop to less than 900 °C (copper melts at 1085 °C), and then through the body of the anode to outside the tube where it is dissipated, often with the assistance of a heat sink. The immediate outside environment is frequently dielectric oil which, in addition to conveying away the heat, is also required for high-voltage electrical insulation. Sometime the heat dissipation is assisted by recirculation of coolant liquid inside the anode itself.

Therefore, power management is a two-stage process in X-ray tubes: one relates to the maximum instantaneous power that the target can sustain, defined by the combination of kV and mA on short-time loads, and the other to the maximum energy (in joule) resulting into a thermal load, which the bulk of the anode and its eventual heat sink can take and slowly dissipate into the surrounding environment, up to a steady-state equilibrium. They are expressed by characteristic diagrams (Fig. 2.6a–c).

From the imaging geometry standpoint—in micro CT, in particular, and also in general radiology—it is intuitive that the smaller the focal spot, the better, all the rest being the same; but the rest cannot be the same! So it is desirable that the focal spot is as tiny as possible, but if a given current and power per unit surface is exceeded, the anode would promptly deteriorate. Such value is very approximately in the order of 200 W/mm². Of course, it depends upon the total exposure time and duty cycle of the anodic current flow.

The remedy to increase the achievable anodic current while retaining an effectively small focal spot is the so-called Line Focus Principle. It is based on the optical illusion that a segment of line on a sloping plane is effectively seen as shorter than its actual length when observed at a

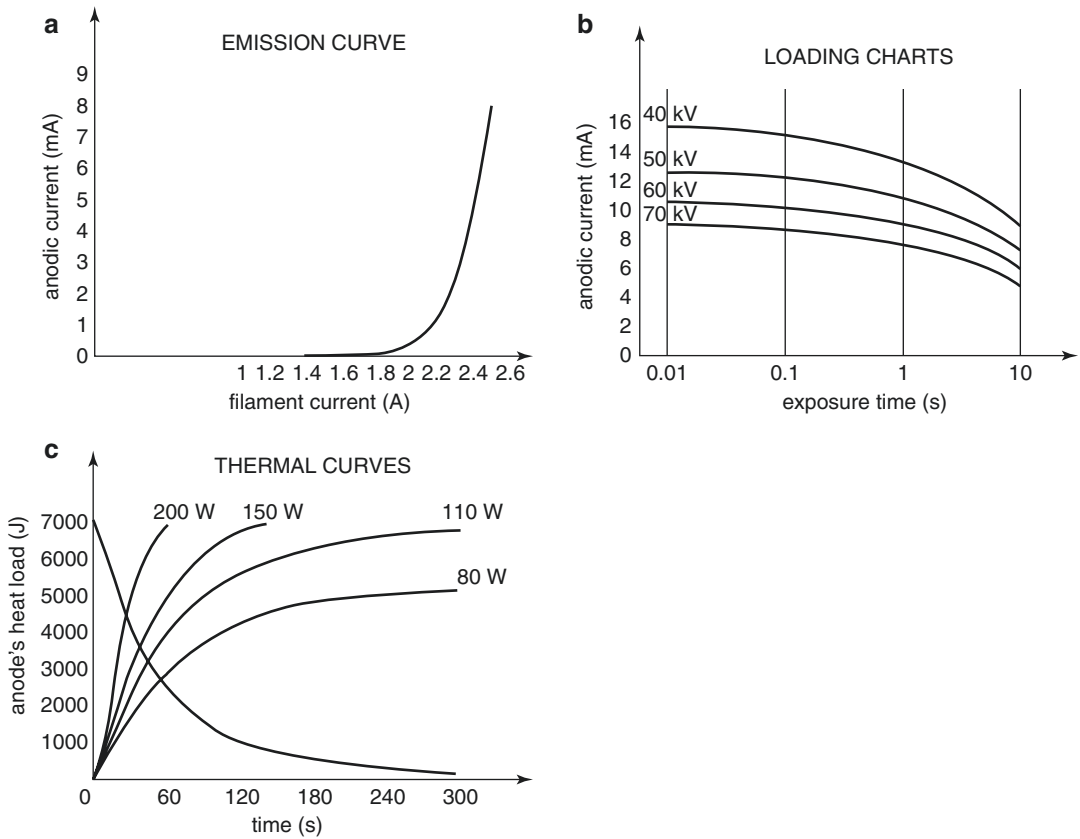


Fig. 2.6 Main characterization charts for a small stationary anode X-ray tube, typically for dental intraoral application, with focal spot 0.4 per IEC 60336 (derived from original technical data by Skan-X/C.E.I., San Lazzaro di Savena BO, Italy): (a) Emission curve. The flow of anodic current (and the consequent X-rays) starts rather abruptly and steeply at a value of filament current called the “knee,” at which the temperature of the filament is high enough to cause significant thermionic emission. (b) Loading charts. The curves indicate, for each given value of anodic high-

voltage potential (kV), the limit combination of anodic current (mA) and exposure time (s) that must not be exceeded to prevent thermal damage of the anode. The abscissa is in logarithmic scale. (c) Thermal curves. The curves represent the thermal energy (in joules) accumulated by the anode under different conditions of continuous power load (in watts). The descending curve shows the dissipation over time of the thermal energy, after suspension of the load

small angle from the plane, namely, reduced by a factor equal to the sinus of that angle. The anode surface facing the anode and holding the target, therefore, is slanted at a small angle from orthogonality to the main axis of the X-ray tube, called the anodic angle, and the “focal spot” produced by the hitting electrons beam is actually a “focal stripe” spread over a much larger surface, and consequently with less power to dissipate per unit area, at a given anodic current. The nominal X-ray beam axis, i.e., the central axis of the beam, is normally defined as one perpendicular

to the X-ray tube axis. When observed from the nominal beam axis (and only at that angle), the focal stripe appears shortened in length, but not in width, typically to an approximate square aspect (Fig. 2.7).

As the direction of view changes, so does the apparent shape and size of the focal spot: if the line of view moves toward the cathode side, the apparent length increases, while it decreases toward the anode side. In an X-ray tube, therefore, the nominal size of the effective focal spot is defined and specified explicitly along the line-

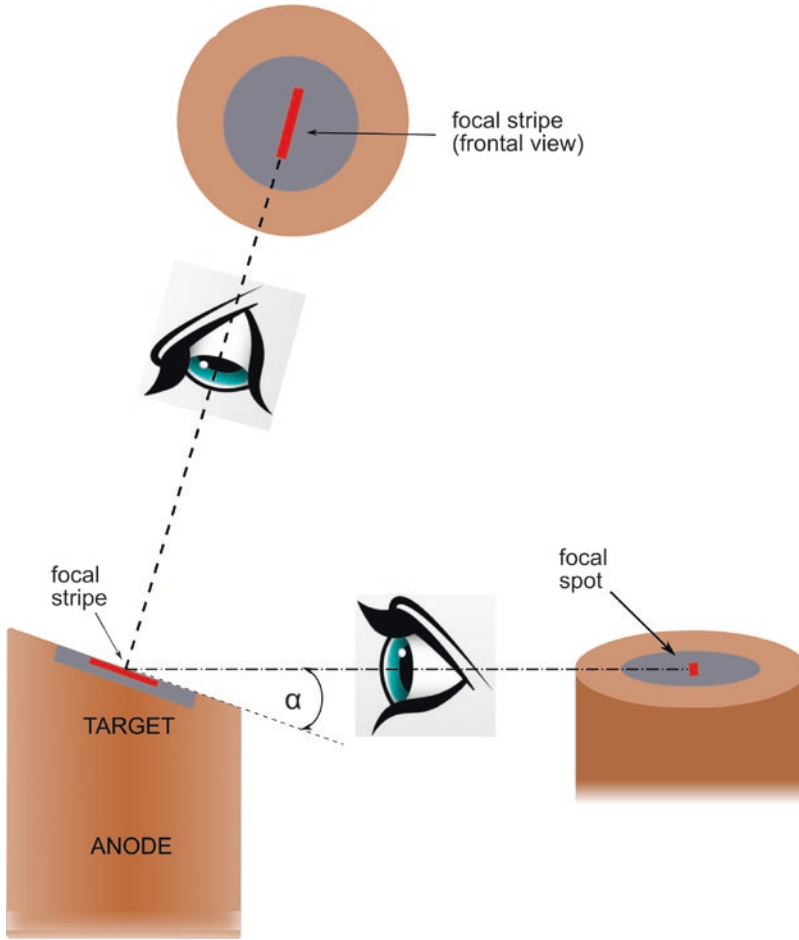


Fig. 2.7 Line Focus Principle. The X-ray emission area (shown in red) of the target is actually a stripe (or a quasi-line). When observed along the nominal X-ray output axis of the tube, the stripe appears effectively shortened (by a

factor $\sin \alpha$) into a quasi-spot (the focal spot). The angle α between the flat surface of the target and the nominal X-ray output axis is called the anodic angle

of-view corresponding to the nominal central axis of the X-ray beam. Such specification entails the detailed definition of the methodology by which it is measured—not a trivial matter especially for tiny physical dimensions, as is the case of the so-called microfocal X-ray tubes. Such methodology (or methodologies, actually, as there are more than one) and the classification of the focal spot sizes are addressed by the standard IEC 60336 for the range of focal spot sizes of interest in medical radiology—from 0.1 upward—and by EC 12543-2 for the microfocal X-ray tubes. Note that the figure classifying the focal spot size is not (contrarily to a widespread

misconception) the dimension of its square side in mm but just a conventional reference that only approximates it, by defect. For instance, a 0.5 focal spot (a fairly common figure) per IEC 60336 is anything with width and length in the range 0.60–0.75 mm and 0.85–1.10 mm, respectively.

X-ray tubes with very small focal spot are called microfocal, and micro CT is one of the main applications and technologies in which they are required. A microfocal X-ray tube is generally considered one with focal spot dimensions not exceeding 50 μm (0.05 mm), down to a few microns.

X-rays generated at the target are emitted in all directions, in principle over the half of the whole solid angle, however not with the same flux at all angles. In particular, as the direction of the outgoing X-ray beam departs from orthogonality to the target surface, they are subject to more and more filtration as the length travelled in the target's material increases, with a slight decrease in intensity and a slight increase in hardness; this phenomenon is called the heel effect and becomes especially relevant for very small grazing angles (a few degrees). Note that the mentioned 1% efficiency in converting the energy imparted to the tube into X-rays refers to the whole X-ray flux over half the solid angle; the portion collimated and utilized for radiographic imaging is a further small percentage of that, say typically another hundredth!

The Line Focus Principle can only be exploited up to a certain extent. The smaller the angle and the greater the shortening of the focal strip length, the narrower is the possible aperture of the beam. In fact, the absolute maximum at the anode side corresponds to the anodic angle, even if the edge effect caused by the self-reabsorption of the X-rays in the target at very small grazing angle were to be neglected (Fig. 2.8).

Most of X-ray tubes have anodic angle between 12° and 20° , typically suitable for general medical radiology applications. In some case smaller angles are used, e.g., when the dimensions of the detector to be covered are small with respect to the SDD (source detector distance) as it is often the case in micro CT or 5° for applications with fan-shaped X-ray beam such as maxillofacial panoramic radiology.

The case is not infrequent of X-ray tubes with two separate filaments, which can be alternately powered in order to generate two distinct shapes and sizes of focal spot for different application requirements, i.e., a smaller focal spot with lower maximum anodic current and a larger focal spot with higher maximum anodic current.

Within the stationary anode type, another sub-type exists, which is of particular importance in micro CT in view of its suitability for achieving tiny focal spots: the transmission-anode (or transmission-target) X-ray tube. Here the target is

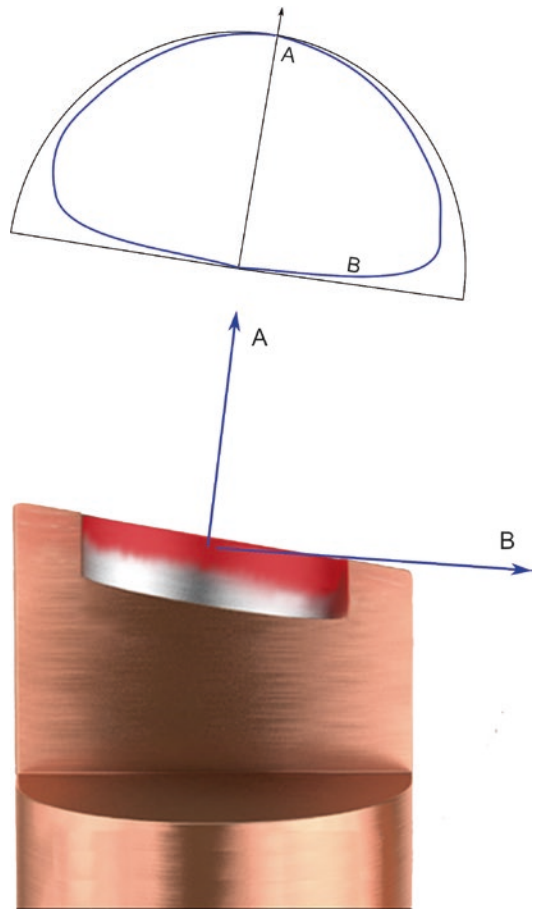


Fig. 2.8 Heel effect. Part of the X-rays are generated at some depth (albeit shallow) in the body of the target, namely, not precisely at its surface. Those (A) that happen to have a direction roughly orthogonal to the surface of the target and the anode exit into the free space without transiting much thickness of the target material and are not subject to much absorption by it. However, those (B) that happen to be produced at a direction close to the plane of the anode do transit through a significant thickness of (highly filtering) target material and are in part reabsorbed and attenuated by the target (and anode) itself. Consequently, the X-ray intensity is maximum at a direction perpendicular to the plane of the anodic face and gradually decreases at other angles, dropping almost to zero for X-rays grazing the anode surface, as qualitatively shown in the polar diagram of intensity in the figure. This is called the heel effect and limits the minimum anodic angle attainable

a very thin lamina or foil of metal (say, a few tens of μm at most), hit by the anodic electrons beam on the face internal to the tube. The target is thin enough that a substantial portion of the produced

X-rays escapes it from the opposite face, into the exterior. The target must also act as a sealant for the high vacuum inside the tube. Generally speaking, only rather small loads can be sustained by this design, but the advantages of this design include a very compact construction and the possibility to emit soft X-rays that are unfiltered by anything but the target's own self-filtration, with a fairly uniform angular distribution.

An important element in the X-ray tube design is also its physical enclosure, or body, that ensures the internal high-vacuum conditions essential for prolonged operation. In addition to that, the enclosure must also provide the electric insulation for the very high difference of potential between the electrodes for cathode and anode. Most frequently this is accomplished with a tubular body of borosilicate glass, with the electrodes brazed at the opposite ends through the intermediation of kovar (a Fe-Ni-Cu alloy) or silver. Such metal parts need to have thermal expansion coefficient similar to that of the glass, to prevent cracks and loss of vacuum sealing when the anode gets hot. Although the finished X-ray tube may look like a small and simple object, its glass-blowing fabrication and the concurring thermal and electrical conditioning processes are a delicate and critical affair. Alternatively, the enclosure of an X-ray tube can also be made out of a combination of ceramics and metal.

The glass wall usually has a thickness of about 0.8 mm. Since the Mean Free Path of X-rays in borosilicate glass is similar to that in aluminum, then the glass wall contributes significantly to the minimum filtration required by the standard. However, such inherent filtration can be excessive when soft X-rays are required—which is the case, e.g., in mammography, but also in micro CT where the broad variety of possible radiographic objects require the range of kV to extend to relatively low values. In these cases, the output window of the X-ray tube is provided with a filter of beryllium, flanged to the glass. Beryllium ($Z = 4$) is the structural metal with the lowest density and as such its filtration of even very soft X-rays is quite modest.

Generally, the X-ray tube is shielded against leakage or emission of unwanted radiation with layers of lead or other high-filtration materials, in almost all directions but at an output window.

Another major type of X-ray tube is the rotating anode X-ray tube. Indeed, rotating anode X-ray tubes are predominant in major medical radiology applications where the radiographic source must be able to sustain very large power loads, such as in medical CT, radiographic examination tables and U-arm, fluoroscopic C-arms for cardiac and chest applications, and more—to the point that rotating anode tubes are sometimes the only type really familiar to many medical radiologists and addressed in detail in general medical radiology textbooks!

In rotating anode tubes, the idea behind the Line Focus Principle is pushed one step forward. The anode consists of a thick disk, or circular plate, slightly conical to implement the anodic angle, made to rotate at very high speed (say 5000 to 15,000 rpm) during the X-ray emission. Therefore, the focal stripe is continuously and very rapidly swept through the surface of the anode target, and the momentary thermal load is uniformly spread all over the surface facing the cathode thus increasing the maximum sustainable load up to one or even two orders of magnitude compared to stationary anode X-ray tubes.

The rotating anode is generally made out of solid tungsten (or molybdenum) or thick tungsten clad to a copper back. Since the anode must be contained within the high-vacuum interior of the tube, rotation is imparted by induction with a stator wrapped outside the posterior part of the tube body. Electrical connection between the anode and the external circuitry must pass through bearings with, e.g., silver-coated balls. So rotating anode X-ray tubes imply using a (rather-demanding) induction motor drive (Fig. 2.9).

It is evident that rotating anode is more complicated and expensive (up to tenfold) than stationary anode X-ray tubes. Their superiority in terms of maximum attainable power (for the same focal spot size) is also evident. However, they also have shortcomings other than the greater cost:

- While their maximum instantaneous load is much larger, not so is the long-term continuous load. In fact, in stationary anode X-ray tubes, the thermal load of the anode can be dissipated conductively, especially with the

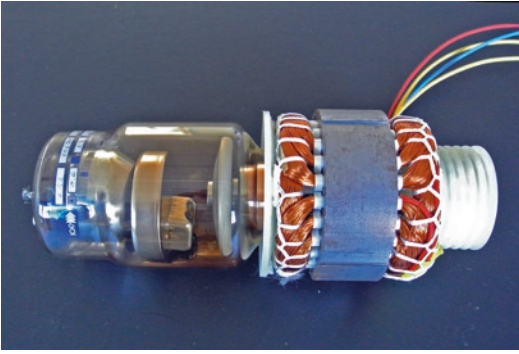


Fig. 2.9 A rotating anode X-ray tube. The stator for the rotation drive is wrapped around the anodic rotor part at the right side

help of heat sinkers and/or forced fluid circulation; but in rotating anode X-ray tubes, there can be only very little thermal conduction from the anode to the exterior (through the ball bearings), so all heat dissipation is left to irradiation. Thus, long-term thermal load capacity is left only to the large thermal mass of the anode, with little contribution from thermal dissipation to the exterior. This does not bode well in applications where the X-ray source must emit continuously, such as, e.g., baggage security scanning, certain nondestructive inspections, and in fact micro CT.

- The useful operating life of rotating anode X-ray tubes is generally shorter than that of stationary anode ones, and in situations of heavy utilization, they may need to be replaced, e.g., once a year.
- It is difficult, if not impossible, to achieve microfocus with rotating anodes (say, much smaller than 0.3 mm), which rules them out for applications in micro CT, where anyway their large instantaneous load capacity is not of interest.

2.4 Power Generators

The X-ray tube is the actual fount of radiation, but there is another element of fundamental importance for the X-ray source system: the electrical power high-voltage generator.

In the past, high-voltage generation to supply the anode-cathode circuit was simply achieved with a very high-turns ratio transformer with elevation factor of hundreds of times. The transformer would elevate the low-frequency mains electric power (230 V–50 Hz or 115 V–60 Hz) to the high voltage required for the anodic circuit. The alternate current often was rectified directly by the X-ray tube itself. This is a relatively simple, robust, and inexpensive design but has several shortcomings, notably the difficulty (or impossibility) to accurately control fluctuations of kV (for instance, caused by transients of the mains power), the difficulty (or nearly impossibility) to impart very short emissions of accurately controlled duration, significant ripple, bulkiness, and weight. Consequently, this kind of design, called “AC generator” (AC for alternate current), is nowadays obsolete and abandoned except for low-cost applications.

All newly designed high-voltage generators are now of the so-called DC type (DC for direct current) or also “high frequency” (improperly, because the frequencies involved are medium frequency, not high frequency). In this case the mains electrical power is first rectified to direct current, converted to a stabilized square wave at medium frequency (range 5–200 kHz) with an electronic power inverter/converter, and elevated to the required high voltage via a “high-frequency” transformer that utilizes a ferrite magnetic circuit and is therefore much more compact and lightweight than a conventional low-frequency transformer with iron magnetic circuit. After the transformer, the voltage is rectified and/or further elevated typically with a Cockcroft-Walton multiplier circuit and delivered to the X-ray tube as a highly stabilized DC voltage with small ripple and accurately controlled duration, which can be very short.

2.5 Image Detectors

It should be made clear that micro CT is not conventional computed tomography (CT), but rather cone beam computed tomography (CBCT), since the beam is cone-shaped divergent (or actually

pyramidal-shaped, in most cases), not fan shaped, and the detector is an area detector, not a linear one.

In the past, the now long-obsolete chemical-processed X-ray film (“analog” radiographic systems, or “direct detectors” in the peculiar parlance of IEC), combined in one and the same element the image detector and the display, and no controllable image post-processing was possible. All new radiographic systems use electronic digital detectors, and the image processing, display, and storage functions are assigned to different sub-systems, which will be addressed later in this book.

In fact, the most basic and fundamental mechanism that determines and limits the performance in radiographic image detectors is ..., well, ... the detection! By detection it is here meant the conversion of the individual electromagnetic X-rays into another form of energy, namely, electric charges, either directly or via the intermediate of visible light, viz., lower-energy photons by a layer of scintillator. The electric charges are generated locally at the surface of a sensor with a matrixial structure of pixels (a pixel being the primary image element), which collects and subsequently transfers them out as an electronic image.

In this chapter, the semiconductor matrix, or regular array, of charge-generating pixels, which compose the digital image, is called the sensor. The device as a whole, i.e., including the X-ray detection material (scintillator or direct conver-

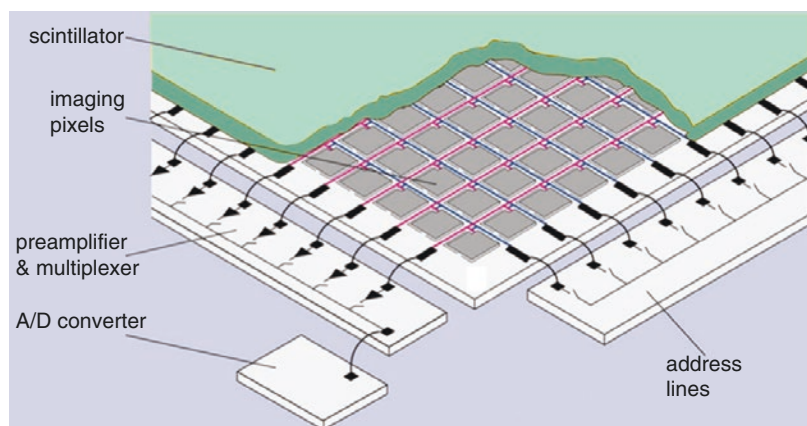
sion), the driving electronics, the software drivers, and all accouterments required to produce the electronic image and transmit to the receiving circuitry, is called the detector (Fig. 2.10).

Efficient detection requires a high statistical likelihood that X-ray photons are converted over a very short span of detecting material (i.e., high stopping power), so that the punctual information associated with the details of the radiographic image stays localized. Otherwise, if the X-ray stopping power of the detecting material is scarce, then a point-like radiographic detail generally would smear out, due to the diffusion of the charges or of the secondary photons of visible light in case of indirect detection. Optimally, the effective thickness of the detection material (= the detection depth) should be comparable and balanced with the size of the pixel.

The efficiency in converting X-rays into information-bearing charges is expressed by a physical quantity called detector quantum efficiency (DQE) (or spectral detection quantum efficiency, if differentiated over specific energy bins), which (roughly speaking) expresses the ratio between the information-bearing charges produced in the detector and the number of hitting X-ray photons. A more formal definition as a complete treatment of the concepts involved is outside the scope of this book, and the reader is directed to specialized literature.

If the thickness of detection layer were increased indefinitely (and many other factors

Fig. 2.10 Structure of an X-ray imaging detector



were speculatively ideal), the DQE could very theoretically increase asymptotically toward the ideal unity, but this would occur at the expense of unlimited degradation of spatial resolving power. Practically speaking, the DQE of commercial X-ray image detectors nowadays ranges between approximately 0.5 and 0.8. With all matters considered, this is a very remarkable feat!

The image sharpness or spatial resolution (or spatial resolving power) is expressed by the modulation transfer function (MTF), a diagram that correlates the contrast (usually in percent) with the spatial frequency, which is the inverse of the pitch of a periodic pattern (usually expressed in line pairs per mm—lp/mm), also related to the minimum size of a discernable detail feature. In case of a square matrix sensor where the spatial resolution limit is determined by the pixelation of the image caused by the finite dimension of the pixel (which is practically the case with optical = photographic sensors), the MTF can be predicted from merely mathematical considerations, resulting into the formula $\text{contrast} = \text{sinc } f = \frac{\sin(\pi f)}{(\pi f)}$, where f is the spatial frequency. This is the “theoretical” or “geometrical” MTF (Fig. 2.11).

So, the contrast is always 100% at zero spatial frequency (i.e., for features of very large dimensions) and drops to zero at a value of spatial frequency called the “Nyquist limit,” which corresponds to the inverse of twice the pixel pitch (this is a particular application of a more general theory of information and communication, called the Nyquist-Shannon Sampling Theorem).

In a real radiographic detector, the situation is more complicate, because the blurring, i.e., reduction in spatial resolution, caused by the finite-thickness detection layer, comes into play. The overall actual MTF is the product of the square of the theoretical MTF with the square of the MTF curve attributable to the detection layer and obviously is always lower than either of the two.

For simplicity, the MTF is often summarized by a single value (rather than with a complete diagram), i.e., the spatial frequency at which the contrast has dropped to 50% (MTF50) or to 10% (MTF10), the latter rather arbitrarily regarded as the minimum contrast discernible by the human eye.

It has to be noted that often the vendors of digital image X-ray detectors declare only the

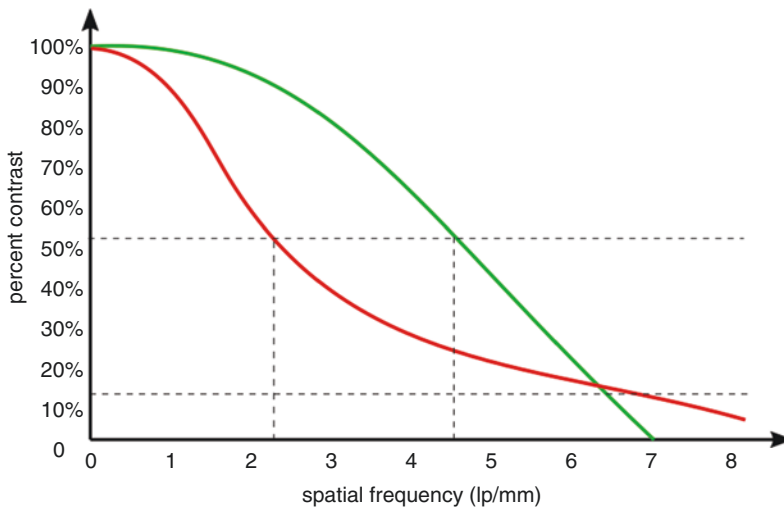


Fig. 2.11 Modulation transfer function (MTF) of a digital detector, comparing the maximum “theoretical” (or “geometrical”) curve (green line), solely determined by the pixelation of the sensor (70 μm), with the experimental curve (red line) also affected by the scintillator thick-

ness. The curve is interrupted at the Nyquist spatial frequency of 7.1 lp/mm. Evidently, the spatial frequencies for 50% contrast are very different between the “theoretical” and the actual MTF

“theoretical” or “geometrical” maximum spatial resolution of their devices and confuse it with the actual maximum resolution, of which the former is just an unreachable upper limit.

There are indeed not many substances in nature that satisfactorily offer all the feature necessary for good detection of X-rays. Let’s address first those practically suitable for direct conversion of X-rays into electrical charges.

At first glance, silicon may appear as a superb candidate for X-ray detection, since it is the one of which all microelectronic structures are currently made of. There is a tremendous technological-manufacturing know-how available and stupendous mass production efficiency. Indeed, silicon matrix sensors (CCD or CMOS, as we shall see shortly) can be, and sometime are, made for X-ray direct detection, which means conversion of X-ray photons to electric charges in the pixels themselves. However, the atomic number of silicon is only 14; hence the free mean path of photons at the energies generally of interest in radiology is relatively long, in the order of a few mm. For instance, $HVL = 2.3$ mm at 40 keV; hence its stopping power is rather modest. Now and then, attempts are made to develop direct X-ray detection in a silicon matrix of pixels, but that has proved possible only for very special applications, where DQE is not a major consideration. However, micro CT could potentially be one of those.

Selenium has been used for direct X-ray detection for several years; however it is generally deemed to be poorly suitable for fast sequences of rapid detection due to slow release of the electric charges. Furthermore, its atomic number 34 is rather low for applications with hard X-rays.

A very promising material for direct conversion of X-rays into electrical charges is CdTe (cadmium telluride, or variations thereof). It has rather high effective atomic number, hence good X-ray stopping power and good charges mobility for them to be carried to the collecting electrodes (in the pixels) before recombination. It offers the potential of high spatial resolution, very good DQE, and—consequently—high signal-to-noise ratio, even at fast readout speed. However, the detector needs to be a single crystal, whose

growth process is challenging; the coupling to the underlying matrix sensor is also technologically demanding and expensive and is mastered only at a few places in the world. Due to the single-crystal nature of the detector, the maximum area attainable is currently just a few cm^2 , which makes it potentially suitable for applications like scientific, nondestructive testing, dental, and—in fact—micro CR, but hardly for general-purpose human radiology.

The large majority of digital X-ray image detectors are based upon indirect detection, where X-rays are converted into visible light (thousands of light photons per X-ray photon) in a medium called the scintillator, and such light is then detected and converted into electric charges by the underlying matrix sensor (Fig. 2.12). Many factors determine the suitability of a material as scintillator: high stopping power to X-rays, efficiency in converting the X-ray photon into visible-light photons, short latency, wavelength of the produced visible light well-tuned with the detection range of the associated sensor (namely, that of silicon), transparency and low self-absorption of the produced light, suitable mechanical properties and chemical stability, and much more. In fact, only two substances are currently used in most cases: gadolinium oxysulfide ($\text{Gd}_2\text{O}_2\text{S}$, also called Gadox) and thallium-activated cesium iodide (CsI:Tl) or variations thereof. Both offer good physical/spectral/optical characteristics for the range of X-ray energy of interest in radiology.

Gadox is simple to process: it is chemically inert and stable and is easily applied after blending with a proper binder (it could simply be spray-painted!)

CsI is quite more difficult to process: it is highly hygroscopic, becomes chemically aggressive to metals in presence of electric potentials typical of sensors, and needs to be coated through technologically demanding deposition and growth in vacuum. However, it can be grown as parallel-aligned tiny crystals, which act as light guides for the light photons generated by the scintillations, thus countering to some extent, even with rather thick layers, the isotropic diffusion that causes blurring (Fig. 2.13). For the reasons mentioned above, frequently CsI

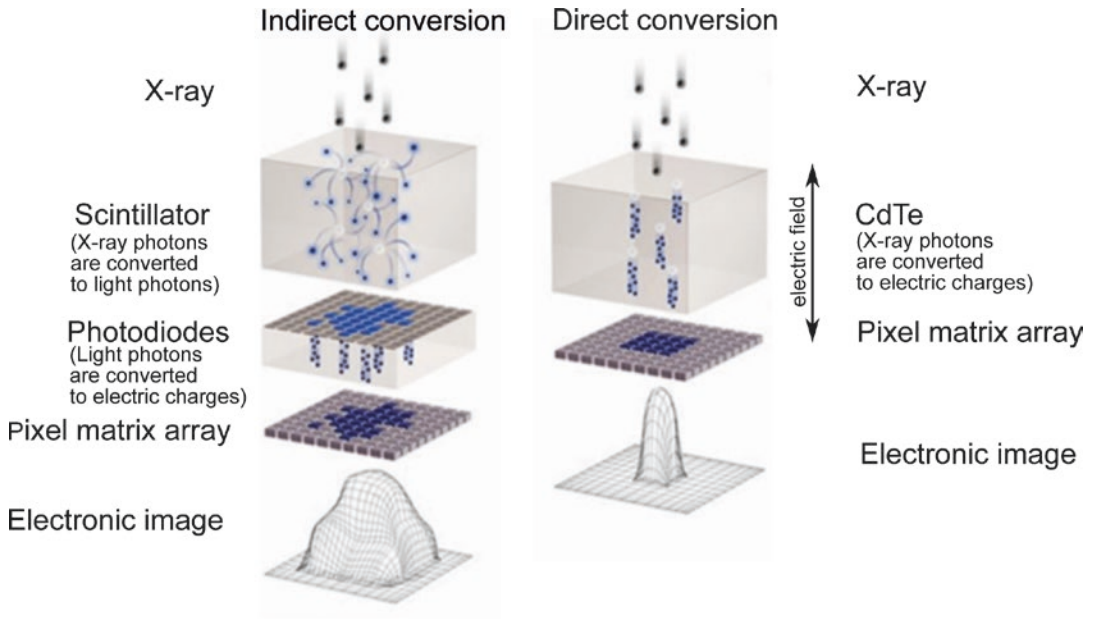


Fig. 2.12 Principle operation of indirect (with scintillator) and direct (with CdTe) detectors. Illustration courtesy of Direct Conversion AB, Stockholm, Sweden

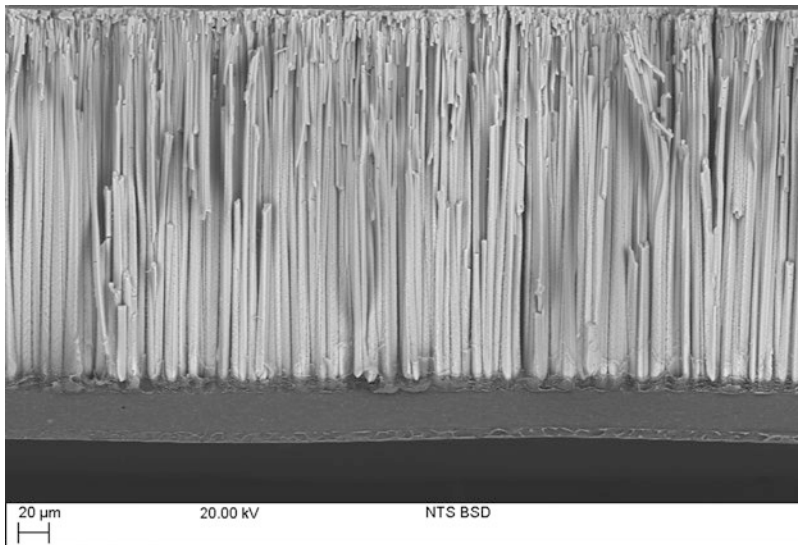


Fig. 2.13 Microphotography, in lateral section, of a CsI:Tl scintillator, with structured crystal needles approximately 5 μm wide and 220 μm long. The bottom one is the side that would face the X-ray source, capped with an optical-reflective layer and a sealant. The upper side

would normally be attached (= grown over) to a fiber optics plate or directly to the surface of the sensor, but for this microphotography, it has been stripped bare. Image courtesy of Scintacor Ltd., Cambridge, UK

scintillators rather than being deposited directly on the sensor are coated, and sealed, over a thin fiber optics plate, having dimension of the optical fibers significantly smaller than the pixel size, and the fiber optics plus scintillator layer rela-

tively robust assembly is coupled (glued) to the sensor.

The more expensive CsI scintillator is generally regarded as offering superior image quality in respect to Gadox; however this may depend on

several circumstances, and the difference in certain cases may be marginal if any.

At this time, there are essentially three types of practically available electronic (digital) image sensors suitable for quasi-instantaneous image capture (“digital radiography”—DR), and for fluoroscopic/cinescopic/radioscopic operation where long sequences of images are acquired at short intervals each other (as the case is also in computed tomography): CCD cameras and flat panel, these being either TFT or CMOS.

Quite some confusion has been made and continues to be made (also in specialized professional literature) in comparing the presumed advantages and limitations among these technologies, whereas various other specific aspects and confounding factors, that affect the overall performance and image quality of specific detectors, are often neglected and not considered.

Currently, the most frequently used type of digital image detector is the thin-film transistor (TFT) flat panel. It consists of a glass substrate upon which an array of thin transistors and diodes is lithographically deposited. Basically, it is the same technology as for the common and universally used flat-screen display, except that the surface photodiodes are used as sensors instead of light emitter. In principle they can be produced to any size; in fact nowadays the most common format in radiology is also the largest standard one, 43×43 cm. However, designing them for dynamic operation, as needed in micro CT, is technically challenging, and only recently

dynamic TFT flat panels have become commercially available from a multiplicity of vendors.

The complementary metal-oxide semiconductor (CMOS) sensor is a semiconductor array epitaxially grown in a wafer of crystalline silicon. Each pixel consists of a photodiode associated with a charge storage cell and buffering preamplifier that can be addressed (read and reset) as a random access memory (RAM). The CMOS sensor exhibits excellent signal-to-noise and dynamic performances, and very small pixels are doable. However, its manufacturing is still inherently more expensive than TFT, and the maximum size attainable is generally limited by the diameter of silicon wafer practically available, currently 8 in., constraining the maximum side of a square CMOS sensor to no more than about 140 mm—which is anyway more than sufficient for micro CT (Fig. 2.14). Detectors with larger sensitive area can be achieved by tiling together multiple sensors.

The charge-coupled device (CCD) was the first type of semiconductor-based electronic image sensor to be developed and is gradually being supplanted by flat panels in new design; however it is still used in certain special applications and in low-cost systems. It is a matrixial sensor that has to be read (and reset) in sequential manner, as a video camera. Fabricating CCD sensors with very large sensitive area is very demanding and impractical (if at all possible); hence they can be used in head-on 1:1 imaging only with sizes up to few cm^2 , e.g., for dental



Fig. 2.14 A medium-sized CMOS image sensor, 150×100 mm with $100 \mu\text{m}$ square pixel size. Note that it can be tiled, on three sides out of four, with other like sen-

sors to compose a larger area detector. Image courtesy of ISDI Ltd., London, UK

intraoral radiographic detectors. In all other cases, the CCD camera is used in combination with an image intensifier (II) where the full-scale image formed at the entrance photocathode is intensified by electron multiplication and reformed at the smaller output “phosphor” screen. The ensuing visible-light image is focal-

ized through a conventional optics onto the (small) CCD sensor. In some cases (including certain micro-CT systems), the optics of the CCD sensor focuses directly onto a scintillator screen (or “phosphor”) without the intermediation of an image intensifier to enhance the brightness.

Fundamentals of Micro-CT Imaging

3

Kaan Orhan and Arda Büyüksungur

3.1 X-Ray

3.1.1 Introduction

In 1979, Allan Cormack and Godfrey Hounsfield were awarded for the development of computer-assisted tomography with the Nobel Prize in Physiology or Medicine.

X-ray computed tomography (CT) is used for revealing the inner structure of the samples by obtaining two-dimensional projections (radiographs) from different angles. The projections are used to reconstruct the sample for the analysis and imaging of the inner structure of the specimen. X-ray tomography is a noninvasive and nondestructive visualization method that reveals the inner structure of the material and gives the opportunity to analyze the inner parameters. Sample preparation, slicing, and staining are not required to obtain the shadow projections.

K. Orhan (✉)
Faculty of Dentistry, Department of Dentomaxillofacial Radiology, Ankara University, Ankara, Turkey

Faculty of Medicine, OMFS IMPATH Research Group, Department of Imaging and Pathology, University of Leuven, Leuven, Belgium

Oral and Maxillofacial Surgery, University Hospitals Leuven, University of Leuven, Leuven, Belgium

A. Büyüksungur
BIOMATEN, Center of Excellence in Biomaterials and Tissue Engineering, METU, Biotechnology Research Unit, Ankara, Turkey

Generally, micro-CT use polychromatic X-ray source, a cone beam. The resolution is the key to the difference for micro-computed tomography (micro-CT or μ CT) from the CT of the hospitals. μ CT has a very high resolution in comparison with the CT. The resolution micro-CT ranges from \sim 400 nm to 70 μ m. The resolution actually refers to isotropic voxel size, which is used in 3D images, but in 2D it refers to pixel size.

Polychromatic X-ray sources produce a broad spectrum of X-ray. The attenuation means the transmitted energy from the material and it depends on the energy used. The soft “low-energy” X-rays are more easily absorbed by the material or scattered, and the hard “high-energy” X-rays can reach the detector; this process leads to hardening of the beam and is called “beam hardening.” Figure 3.1 shows the beam-hardening process.

Figure 3.1 shows that the X-ray has a broad spectrum at the beginning of the process, but the X-rays that leave the object have the higher-energy level and are less intense. The beam hardening is explained in other chapters in this book.

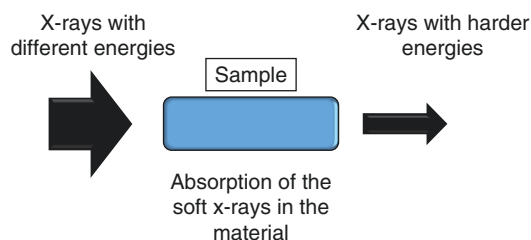
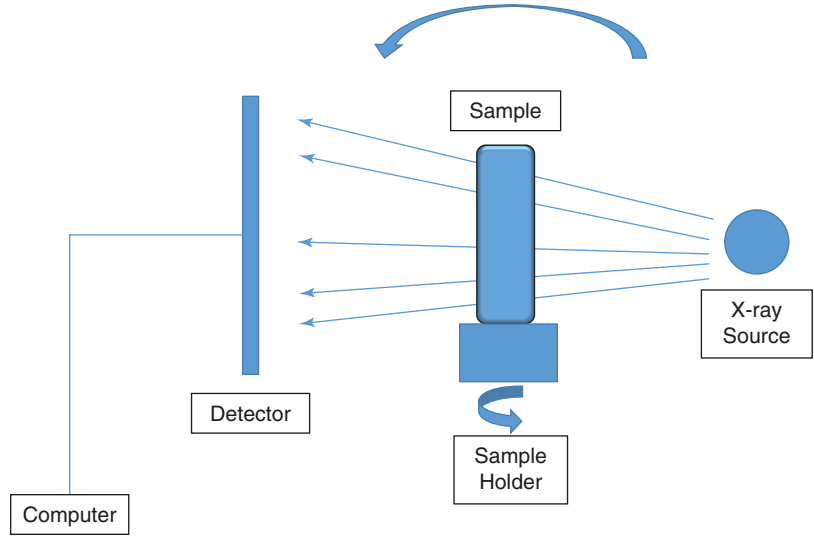


Fig. 3.1 Beam hardening

Fig. 3.2 Basic elements of the micro-CT



In 1984, Lee Feldkamp used a cone-beam X-ray source and 2D detector to visualize the rotating sample and found the cone-beam algorithm for reconstruction of the 3D structure of the object [1].

3.1.2 Principles of Micro-Computed Tomography

The parts of micro-CT and their functions are described in Chap. 2, but basically, micro-CT is composed of an X-ray generator (X-ray tube) emitting X-rays, sample holder, detector and CCD camera, and filter. Generated X-rays fly through the sample and create shadow projections on the detector/CCD camera. The CCD cameras cannot detect the X-rays, but the scintillator converts the X-rays to visible light so that the CCD cameras detect the projections. Either the sample or the detector/the X-ray source rotates to obtain another projection. The rotation can be in 180° or 360° to produce the complete 3D structure of the object. The basic principle of the micro-CT is the detection of the X-ray passed through the sample. The X-rays attenuated while passing the object, and this attenuation can be explained by the following equation:

$$I_x = I_0 e^{-\mu x}$$

where I_0 is the intensity of the beam, x is the distance, I_x is the intensity of the beam at distance x from the source, and μ is the linear attenuation coefficient. The attenuation depends on the material and the energy and can be used to quantify the density of the material that is imaged. Figure 3.2 shows the basic elements of micro-CT.

Figure 3.2 shows that in micro-CT systems either the sample or the detector and X-ray source rotates.

If the angular steps are small enough, the attenuation value for every voxel can be found. For the reconstruction from the 2D to 3D structure, back-projection algorithm is used [2]. The smaller angular steps mean the addition of the new data for the detection of the areas inside the object. The new and the more data increases the accuracy of the shape of the areas inside the object. Figure 3.3 explains the increase in the shape accuracy when more projections are introduced.

The angular step used in the scanning process allows better localization and better absorption detection of the objects inside the sample. In the case of many angular positionings and applied back projections, the object inside the sample has a blur area around itself. The filtered back projection is used to obtain an accurate signal from the object. It actually erases the false absorption data

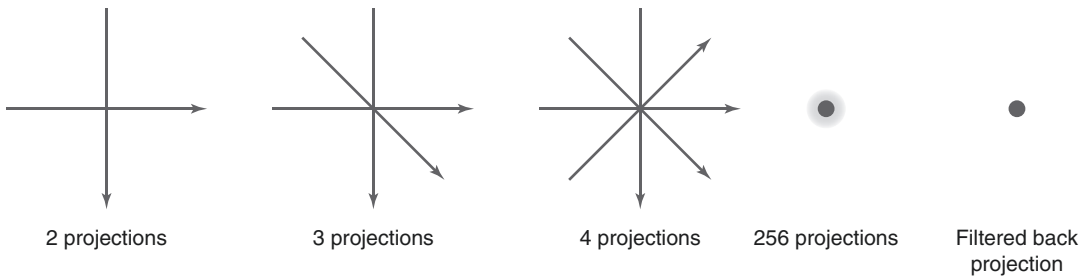


Fig. 3.3 Effect of projections number and processing

by filtering the obtained data by introducing negative absorption to the absorption spectra of the object. The negative absorption leads to a uniform signal from the object and the removal of the blur area. The filtered back-projection algorithm is the most common algorithm in the reconstruction process for micro-CT.

The synchrotron is a monochromatic X-ray source and produces a specific X-ray energy. Furthermore, synchrotrons produce X-rays that are almost parallel which leads to better resolution and less signal to noise ratios. Synchrotrons use magnetic fields to produce parallel X-rays. Figure 3.4 shows the difference between the synchrotron and the cone-beam X-ray sources.

Figure 3.4 shows the differences between the cone-beam geometry and the synchrotron beam geometry. Because of the parallel beams and the monochromatic feature, the beam hardening is almost not detected in the synchrotrons.

3.1.3 Reconstruction to Image

3.1.3.1 Acquisition

Acquisition is the number of projections acquired in 2D by the detector, which obtain the data. The detector obtains the data in 2D, and obtained projections present a grayscale image. The grayscale actually shows the X-rays that reached the detector after absorption by the sample [3].

Projections are related to the rotation step. After acquisition at a point, the sample is rotated and new projection is obtained. The rotation can be 180° or 360° , and if the rotation step is 0.4° for 360° scanning, there will be 900 projections.

Generally, more projections lead to better results and more accurate 3D structure. After obtaining a stack of projections, the 3D image can be established [4].

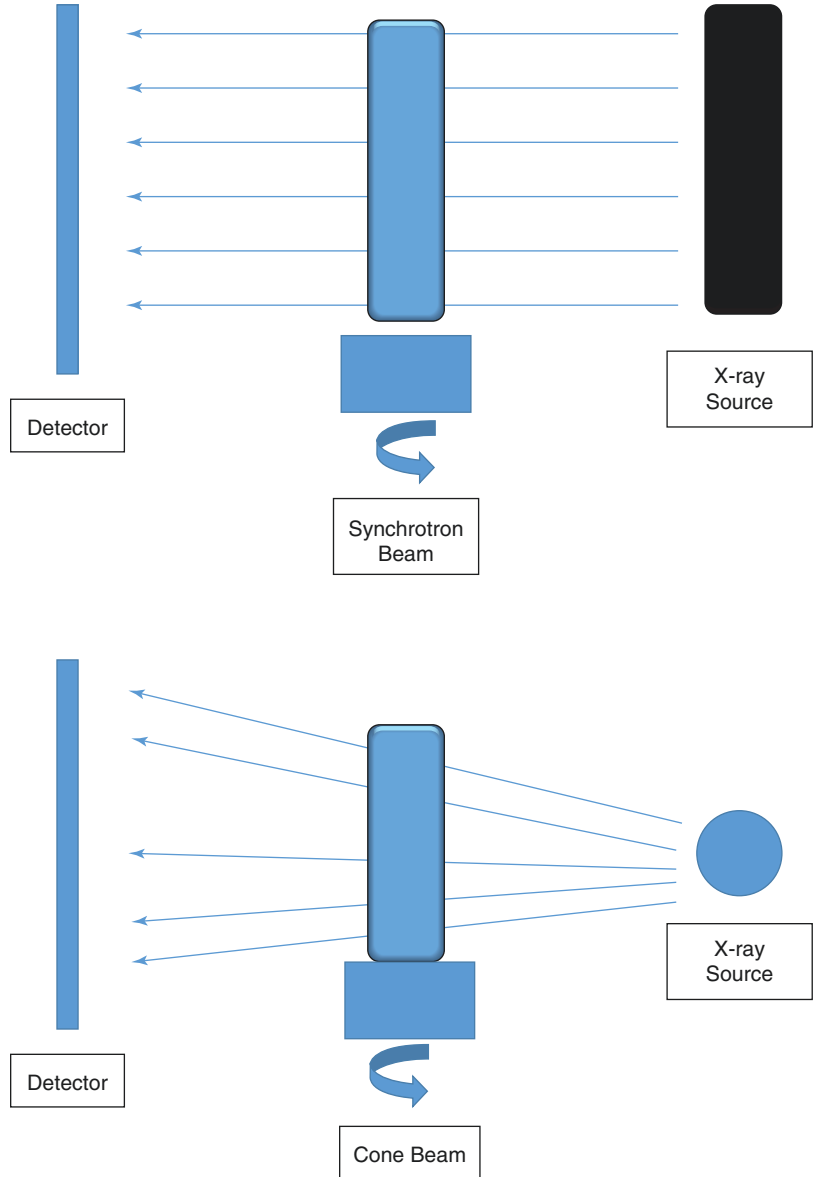
3.1.3.2 Reconstruction: 3D Image

The projection images (radiographs) represent the intensity of the object of that particular angle. The obtained images are generally 16-bit radiographs, and these can be reconstructed in 16-bit or 8-bit formats. In 16-bit formats, image has 65,536 gray value, and in 8-bit formats, image has 256 gray value. The reconstruction can be in 16-bit or 8-bit format. If the scanned sample has a broad range of materials inside, then the 16-bit reconstruction can be used, but if the sample has very limited materials inside, then the 8-bit format can be used. The densities inside the sample are directly related to the X-ray absorptions. The different densities are represented differently in gray values.

There are several reconstruction methods available such as Fourier theorem, filtered back-projection, and algebraic methods. These and the other methods are explained very detailedly in [3]. The filtered back-projection method is the most common method used in the reconstruction.

Reconstruction algorithm, which is Feldkamp algorithm, is used to obtain the point matrix for calculating the absorption data by the object. This makes the matrix representing the pixels inside a cross section. Actually, reconstruction is the mathematical procedure that helps to create a 3D object from the 2D images. In 3D image, pixels are named as voxels, the volume of thickness

Fig. 3.4 Cone beam and synchrotron beam differences



[2]. 3D image is presented from the stack of 2D slices by reconstruction. The distance between two slices depends on the pixel size used in the scanning process.

3.1.3.3 Obtaining Image

Generally, 8-bit images are used for generating images. This leads to analyze the images in 256 grayscale. The gray value image is generated from the floating matrix, and the values of gray

scale are displayed halftone. The halftone image serves as a tool that allows the calculation from the cross sections [5]. The images after reconstruction are the cross-section images of the sample. These can be visualized by rendering software and also analyzed because these images have the attenuation data in 2D and they represent the whole sample in 3D and also represent the attenuations of an object inside a sample in the 3D.

3.1.4 Micro-CT Components

3.1.4.1 X-Ray Sources

In the previous section, X-ray sources and their working principles are explained very detailedly. In this part mostly used X-ray sources are explained, and their working principles will be defined briefly.

Generally, tube-based X-ray sources are used in the micro-CT systems. Generally, tube-based systems are polychromatic X-ray sources, meaning tubes produce different energy levels of X-ray to the upper limit. In these systems, the tube potential and the tube current can be adjusted to change the sample absorption [3]. The change in the voltage (kV) is used to optimize the contrast by changing the X-ray spectrum. Increase in the kV leads to produce higher-energy X-ray and less absorption from the less dense materials. Decreasing the voltage leads to the enhanced contrast between low absorption phases [3]. The change in the current does not change the X-ray energies but changes the intensity of the X-ray [1]. Increase in the current leads to spread in the focal spot of the X-ray and decreases the resolution. The tube-based systems generally use cone-beam X-ray sources. Due to its geometry, X-rays begin to spread after being released from the source.

The micro-focus fixed tungsten anode tubes are the mostly used X-ray sources for micro-CT. These operate in continuous mode with voltages in the range of 20–100 kV and anode currents in the range of 50–1000 μA [6].

Synchrotron-based micro-CTs are monochromatic X-ray sources. The produced X-rays have the same energy level, and the X-rays are almost parallel to each other. This leads to better resolution and higher image brilliance for the scanned specimen food [3].

3.1.4.2 Detectors

The X-ray detectors generally use one- or two-dimensional detector arrays. The detectors are designed to not detect the X-rays directly, but with the help of a scintillator, X-rays turned into photons, and the camera systems detect the visi-

ble light. The detection can be with a lens system or a fiber-optic channel plate.

The energy-integrating and the energy-discriminating detectors are the two categories for the micro-CT detectors. Generally, energy-integrating detectors are used in the micro-CT systems [7]. Charged-coupled devices (CCDs) combined with scintillator screens are most widely used detectors with the micro-CT systems.

Complementary metal-oxide semiconductor (CMOS) detectors are being used recently for their large area and high frame rates.

Photon-counting X-ray detectors (PCXD) are in the second category of the detector type, the energy-discriminating detectors. Silicon (Si), gallium arsenide (GaAs), and cadmium telluride (CdTe) are used as sensor materials in these detectors, and the detector has the advantage of elimination of the noise below the signal [6].

The detector captures the images with the field of view (FOV). Sometimes the FOV is smaller than the specimen scanned; then the FOV can be doubled with a displacement of the detector “offset detector” [8]. The offset detector captures asymmetric projection from the specimen, and this situation should be covered in the reconstruction process. Figure 3.5 shows the offset detector movement.

Figure 3.5 explains the movement of the detector when the specimen is bigger than the FOV. Detector travels horizontally to capture the whole image, and then by the reconstruction algorithm, the whole image is captured.

3.1.4.3 X-Ray Fluorescence Computed Tomography (XFCT)

Boisseau proposed the X-ray fluorescence computed tomography (XFCT) with synchrotron radiation in 1986 [9]. This technique is generally used to measure trace element distribution within the specimen.

XFCT imaging is a combination of CT and quantitative fluorescence imaging systems. X-ray fluorescence imaging is basically detection of X-ray emissions after X-ray excitation [10].

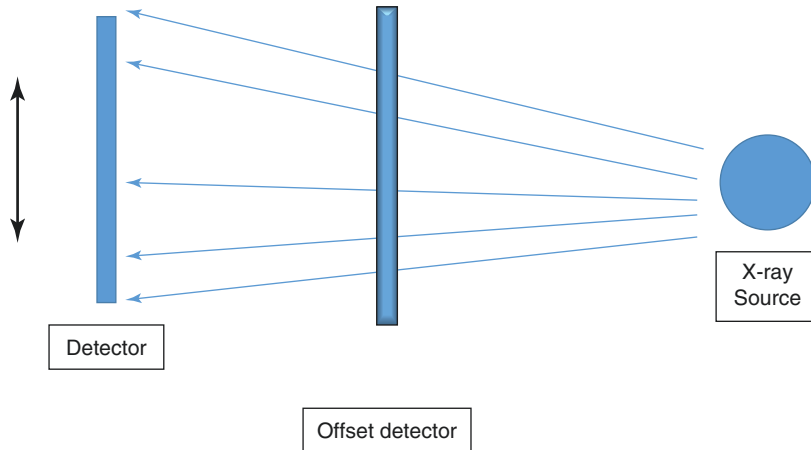


Fig. 3.5 The offset detector movement

XFCT collects the X-ray photons emitted by the specimen and because of the high sensitivity enables quantitative element identification [11].

X-ray fluorescence is applied X-rays produce secondary X-ray emission in a target material. X-ray with the photoelectric effect ejects an inner shell electron, and the vacancy created is filled by a second electron from outer electron shells and the energy difference emitted in the form of a characteristic X-ray [12]. The first X-ray excitation leads to the production of second X-ray emission; therefore, this process is called X-ray fluorescence which is actually analogous to optical fluorescence.

Synchrotrons are used for XFCT because of their monochromatic and brilliant results. It can be used for detection of the trace elements in the living body and has many applications [11]. Small-animal molecular imaging is carried out for cerebral perfusion by using XFCT [13]. These studies led to single cross-sectional images because of the long measurement time. Sasaya in 2017 showed fast imaging of the $15 \times 15 \times 5 \text{ mm}^3$ with high quantifiability, a spatial resolution of less than 0.35 mm.

3.1.4.4 Phase-Contrast Micro-CT

The phase shift of the X-rays passing through the specimen is used to create images, while normally images are created by usage of X-ray attenuation [14, 15]. Because of this factor, soft

biological tissues are imaged with higher-contrast than absorption-based X-ray imaging without the use of external contrast agents.

There are three different techniques for the synchrotron-based systems: propagation-based, analyzer-based, and crystal interferometer-based phase contrast.

Propagation-based phase-contrast imaging relies on the change in the distance between the detector and the specimen. The X-ray refracted within the specimen can be detected with the changing distance, and with the help of algorithms higher contrast for low-absorbing tissues can be obtained.

Analyzer-based imaging consists of a stable sample and the detector, but there is a crystal in front of the specimen. The analyzer crystal positioned in Bragg diffraction and X-ray exiting sample create a rocking curve. The data obtained is used to obtain the projections [6].

Grating interferometer-based phase-contrast methods use X-ray grating to obtain three modalities: attenuation signal, the differential phase shift, and the scattering.

3.1.4.5 Small-Angle X-Ray Scattering

X-rays can also be scattered by internal structures of the specimen. X-ray scattered from the inner structure forms patterns in detector, and 1D or 2D data can be obtained. Figure 3.6 explains the principle of the SAXS.

Fig. 3.6 Schematic representation of a SAXS technique, polyoxometalates (POMs). Image from Li et al. 2018

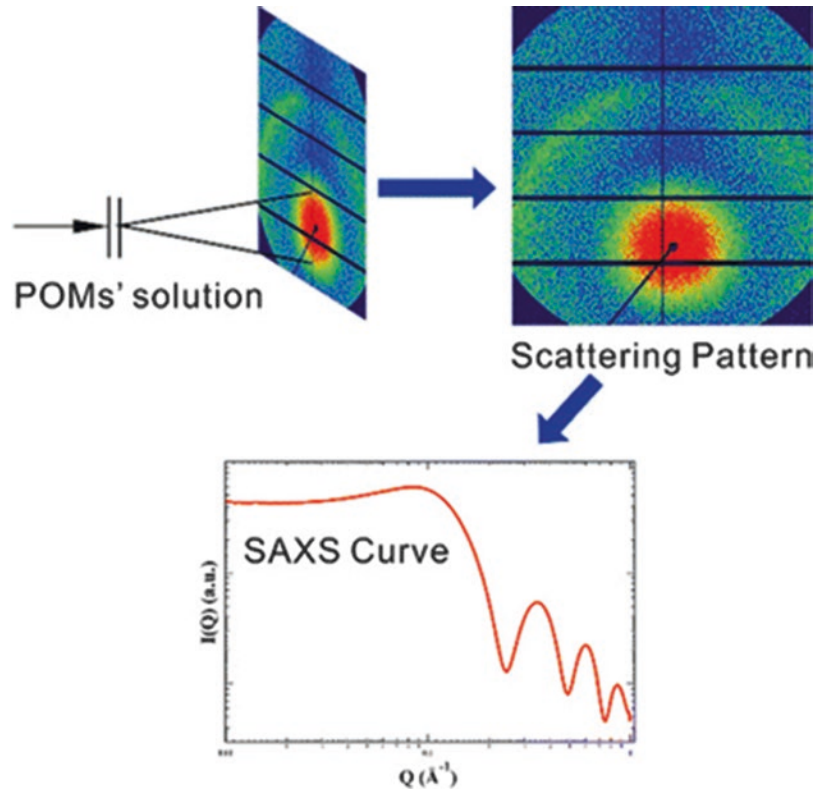


Figure 3.6 shows the SAXS curve which contains information about the structure.

References

- Feldkamp LA, et al. Practical cone-beam algorithm. *J Opt Soc Am A*. 1984;1(6):612–9.
- Barigou M, Douaire M. X-ray micro-computed tomography for resolving food microstructures. In: *Food microstructures*. Cambridge: Woodhead Publishing; 2013. p. 246–72.
- Stock SR. *Microcomputed tomography: methodology and applications*. Boca Raton, FL: CRC Press; 2008.
- Iglauer S, Lebedev M. High pressure-elevated temperature X-ray micro-computed tomography for subsurface applications. *Adv Colloid Interf Sci*. 2018;256:393–410.
- SkyScan NV. *SkyScan 1172 desktop X-ray microtomography instruction manual*. 2005
- Badea CT. Small animal X-ray computed tomography. In: *Handbook of X-ray imaging: physics and technology*. Boca Raton, FL: CRC Press; 2018.
- Iglauer S, Lebedev M. High pressure-elevated temperature X-ray micro-computed tomography for subsurface applications. *Adv Colloid Interf Sci*. 2018;256:393–410.
- Sharma KS, et al. Interior micro-CT with an offset detector. *Med Phys*. 2014;41(6):061915.
- Boisseau P. Determination of three-dimensional trace element distributions by the use of monochromatic X-ray microbeams, Ph.D. Dissertation, MIT Cambridge, 1986.
- Ahmad M, Bazalova-Carter M, Fahrig R, Xing L. Optimized detector angular configuration increases the sensitivity of X-ray fluorescence computed tomography (XFCT). *IEEE Trans Med Imaging*. 2015;34(5):1140–7.
- Sasaya T, Sunaguchi N, Hyodo K, Zeniya T, Yuasa T. Multi-pinhole fluorescent X-ray computed tomography for molecular imaging. *Sci Rep*. 2017;7(1):5742.
- Ahmad M, Pratz G, Bazalova M, Xing L. X-ray luminescence and X-ray fluorescence computed tomography: new molecular imaging modalities. *IEEE Access*. 2014;2:1051–61.
- Takeda T, et al. X-ray fluorescent CT imaging of cerebral uptake of stable-iodine perfusion agent iodoamphetamine analog IMP in mice. *J Synchrotron Radiat*. 2009;16:57–62.
- Hetterich H, et al. Phase-contrast CT: qualitative and quantitative evaluation of atherosclerotic carotid artery plaque. *Radiology*. 2014;271(3):870–8.
- Li M, et al. The applications of small-angle X-ray scattering in studying nano-scaled polyoxometalate clusters in solutions. *J Nanopart Res*. 2018;20(5):124.



Kaan Orhan, Karla de Faria Vasconcelos,
and Hugo Gaêta-Araujo

4.1 Introduction

Micro-computed tomography (micro-CT) is a nondestructive three-dimensional imaging modality, which can provide images from small samples with high resolution. There are two types of micro-CT systems, the ones with parallel and monochromatic X-ray beam (synchrotron systems) and those with cone-shaped beam and polychromatic energy.

Synchrotron systems provide an accurate quantification of linear attenuation coefficients as a parallel and monochromatic beam is emitted by high-speed electrons in a magnetic field of a par-

ticle accelerator [1], thereby avoiding density calibration and additional corrections. However, this technology has limited access [2]. Differently, in polychromatic systems, the beam is composed of individual photons with a range of energies. In this way, the relationship between attenuation and material thickness is nonlinear, leading to errors in the measurement of attenuation coefficients. Nevertheless, this technology has been applied to quantitative studies of mineralized tissue [3, 4]. The great challenge of the polychromatic systems is related to the physical principles, which have a major impact on image quality due to artifact generation.

Artifacts are image reconstruction errors that appear in the volume, but it does not belong to the scanned object. The presence of artifacts can compromise the micro-CT image analysis and, consequently, generates over- or underestimated results. However, facing the limitations of this technology, some artifact reduction techniques have been developed. Nowadays, it is possible to minimize (or eliminate) artifacts by selecting appropriate scanning parameters and/or using some artifact reduction tools available in the image reconstruction step. This chapter approaches the main types and causes of micro-CT artifacts, how they appear in the images, and a brief discussion about available tools to correct or reduce their presence.

K. Orhan

Faculty of Dentistry, Department of Dentomaxillofacial Radiology, Ankara University, Ankara, Turkey

Faculty of Medicine, OMFS IMPATH Research Group, Department of Imaging and Pathology, University of Leuven, Leuven, Belgium

Oral and Maxillofacial Surgery, University Hospitals Leuven, University of Leuven, Leuven, Belgium

K. de Faria Vasconcelos (✉)

Faculty of Medicine, OMFS IMPATH Research Group, Department of Imaging and Pathology, University of Leuven, Ankara, Turkey

H. Gaêta-Araujo

Department of Oral Diagnosis, Area of Oral Radiology, Piracicaba Dental School, University of Campinas, Piracicaba, Sao Paulo, Brazil

4.2 Main Causes of Artifacts in Micro-CT Image

4.2.1 Related to the Source

4.2.1.1 Beam Hardening (Cupping and Streak)

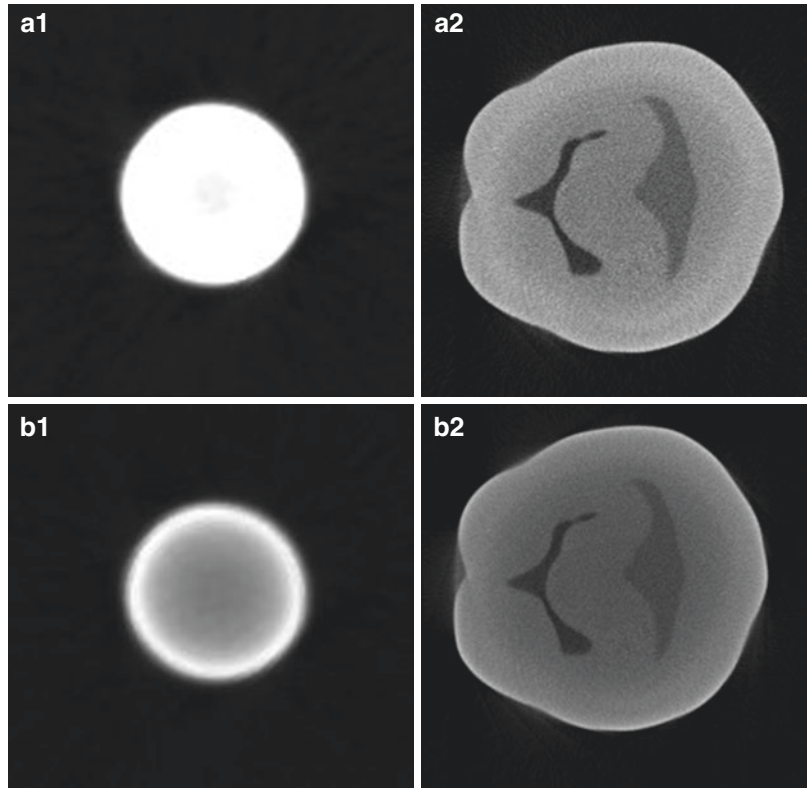
When polychromatic X-ray systems are used, the beam-hardening phenomenon is the major challenge [5], since it is inherent to the physical principles of the image acquisition. As previously mentioned, in this kind of systems, a wide spectrum of X-ray energies is used. The beam hardening occurs because the low-energy photons are more absorbed from the beam than the higher-energy photons. Due to the low-energy depletion, the average photon energy increases along the beam path. Consequently, the beam becomes “harder” or more penetrating, after it passes through the object [6, 7].

The harder a beam, the less it is further attenuated, and less beam-hardening effect is expected

and vice versa. However, all beams passing through a particular pixel follow different paths and consequently introduce a different degree of beam hardening. Hence, they perceive different attenuation values in each pixel, which contribute to gray-level nonuniformity in micro-CT images and can lead to different artifacts within the reconstructed image, as the cupping artifact and the appearance of streaks or hypodense bands [8].

The cupping artifact is resulted by the underestimation of the true density of the object. This effect can be clearly demonstrated when a homogeneous cylindrical object is imaged (Fig. 4.1a1, b2). In this situation, a same gray level (pixel value intensity) is expected for the entire object. However, the gray levels decrease in value in the center of the homogeneous cylinder (Fig. 4.1b2) owing to the increase in transmitted intensity to the detector from the presence of beam hardening and scatter radiation [8]. Thus, a homogeneous object with same pixel value intensity appears with dis-

Fig. 4.1 Micro-CT images of a homogeneous metal cylinder (**a1/b1**) and a dental crown of a human molar (**a2/b2**). Figures **a1** and **a2** show the ideal conditions, without cupping artifact, while **b1** and **b2** show the presence of cupping artifact with distinct gray values in the periphery and the center of the objects (Courtesy of Dr. Gustavo Santaella, School of Dentistry of Piracicaba, University of Campinas, Piracicaba Dental School, Piracicaba, Sao Paulo, Brazil)



tinct gray values in the periphery and the center. As clinical applications, Fig. 4.1a2 and b2 shows the cupping effect in an image of a dental crown of a human molar, while Fig. 4.2 shows a coronal reconstruction of Mucograft sample stained in Phosphomolybdic acid solution inside the trephine. It is possible to observe in three different profiles the depression on the curve that remaining higher-energy photons are not attenuated as easily due to the metal material of the trephine around the sample which caused the artifact also observed in the middle of the axial section of the same sample. Therefore, the resultant attenuation profile differs from the ideal profile and displays a characteristic cupped shape artifact (Fig. 4.2).

The streak artifacts or hypodense bands appear between dense objects present on the scanned volume by the combination of the beam-hardening phenomenon and scattered radiation [9]. In the presence of high-thickness materials or

those with high atomic number (e.g., gold, amalgam, barium, and bismuth), the X-ray beam is completely absorbed, and photon starvation occurs [10]. In this situation, a combination of hypo- and hyperdense streaks is observed (Fig. 4.3). The streak artifacts are common in computed tomography images due to the principles of image generation, and the streaks gradually diminish from the metallic region toward the periphery.

4.2.1.2 Noise

Low photon counts cause random bright and dark streaks, especially in the direction of higher attenuation, that are known as noise artifact [11]. Another source of noise is scattered radiation. Scattered radiation arises from interactions of the primary radiation beam with the atoms in the object being imaged. The occurrence of this kind of artifact results in degradation of image quality

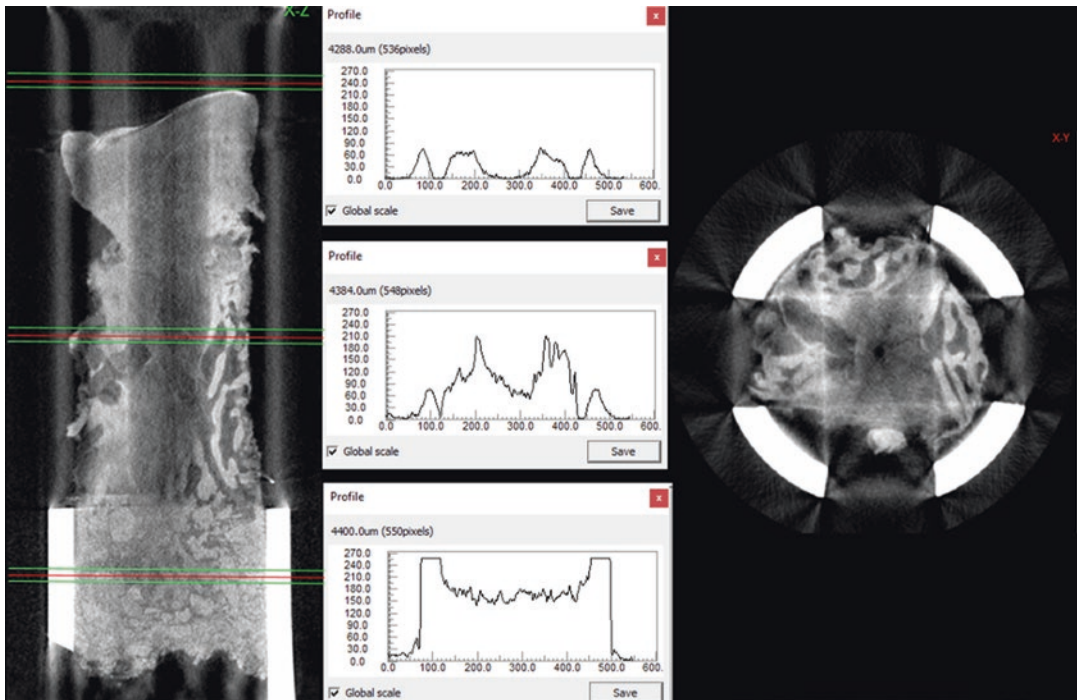


Fig. 4.2 The coronal reconstruction shows a Mucograft sample stained in Phosphomolybdic acid solution and scanned inside the trephine. Three different profiles show the depression on the curve in different positions of the scan. The remaining higher-energy photons are not easily attenu-

ated due to the metal material of trephine around the sample which caused the artifact, also observed in the middle of the axial section of the same sample (Courtesy of Dr. Alan Herford and Dr. Gina Roque-Torres, Loma Linda University, Center of Dental Research, CA, USA)

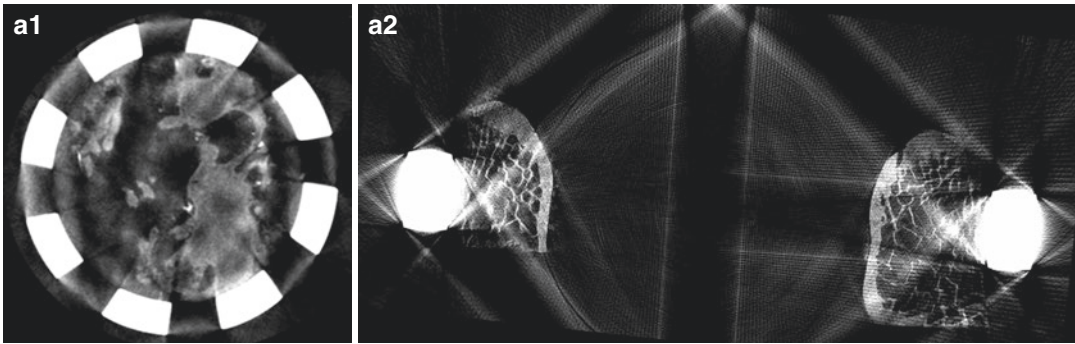


Fig. 4.3 The axial reconstruction **a1** shows a Mucograft sample stained in Phosphomolybdic acid solution and inside the trephine. The trephine was used to extract the sample from the patient but also caused artifact due to metal. Moreover, **a2** shows an osteoporotic human vertebra sample with titanium fixation which generated signifi-

cant artifacts caused by the metal objects; in both images, we can observe considerable hypodense and hyperdense streaks typical of photon starvation (Courtesy of Dr. Alan Herford and Dr. Gina Roque-Torres, Loma Linda University, Center of Dental Research, CA, USA)

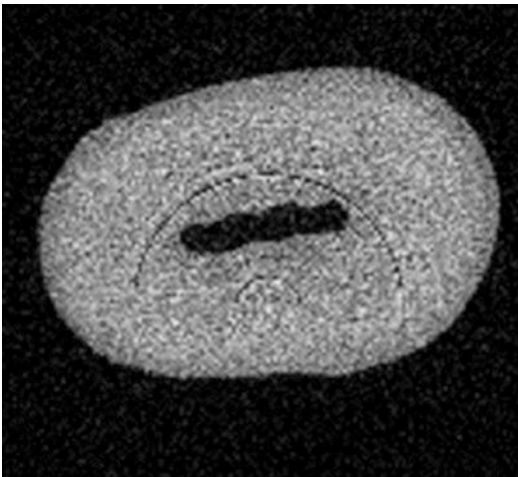


Fig. 4.4 Noise reducing image contrast. (Courtesy of Dr. Hugo Gaêta-Araujo, University of Campinas, Piracicaba Dental School, Piracicaba, Sao Paulo, Brazil)

and poor contrast resolution (Fig. 4.4) [12]. The tube current applied for acquisition is related to image noise, in which higher tube current produces less noise [11].

This artifact certainly has an impact on micro-CT image processing, quantitative and qualitative analysis, segmentation, and 3D rendering; thus some denoising methods have been proposed based on smoothing such as Gaussian and median filtering [12]. Smoothing filters blur the image to reduce unwanted noise, but the major challenge is to keep image diagnostic valuable information, such as texture, contour, and fine details [12].

Recently, Shahmoradi et al. [12] proposed two methods for image denoise: total variation and block-matching and 3D (BM3D), which both presented good results in reducing noise while maintaining image information depending on type of image and analysis. However, the smoothing tool will be better described later on in this chapter.

4.2.2 Related to the Detector

4.2.2.1 Ring Artifact

The ring artifact formation is related to the flat-field detectors used in tomographic scans, caused by failures in its elements [13]. These malfunctioning pixels can produce white, black, or over-/underestimated pixel values that are not representative of the original value for the object, and it is classified into two types: type I, result of defective detector elements and damaged scintillator screens and type II, generated because of miscalibration of the detector elements [14]. A ring format of this artifact is caused by the backprojection lines of the defective detector element due to the circular scanning geometric relation between the X-ray source and the detector [15]. In the images, the ring artifacts present as concentric rings seen in the axial views (Fig. 4.5) (original images) and as stripes or lines in the coronal and sagittal views [13]. The ring artifact correction can be applied in two moments: before

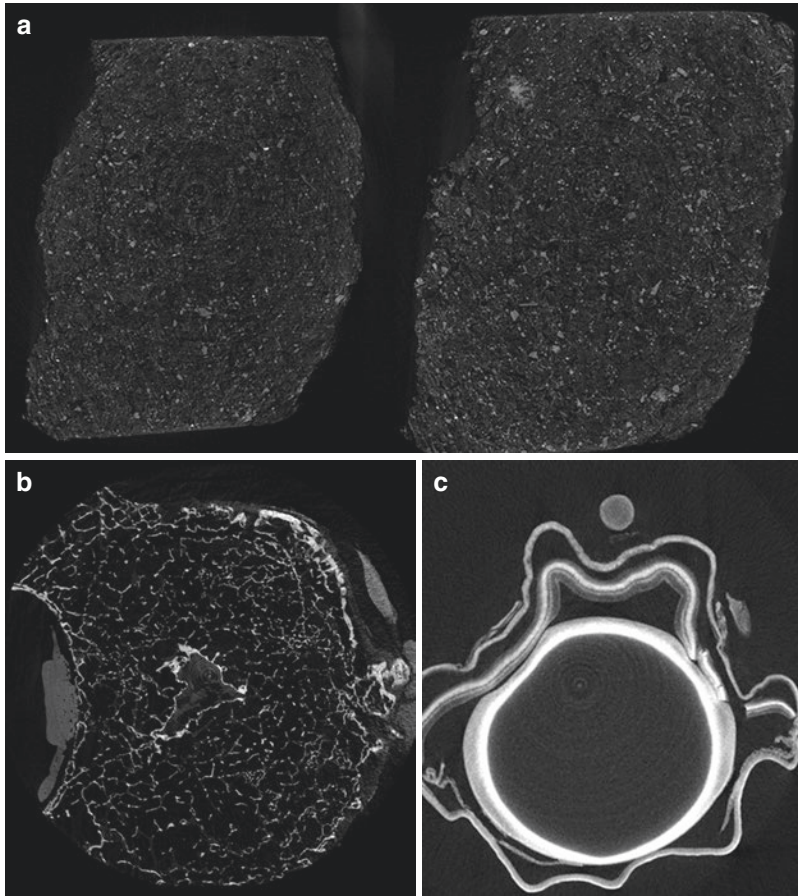


Fig. 4.5 Images acquired for different applications showing the rings on the center of the rotation, typical of ring artifact. **(a)** Axial reconstructions from a rock used to evaluate the porosity (Courtesy of Dr. Varner Leggit and Dr. Gina Roque-Torres, Loma Linda University, Center of Dental Research, CA, USA). **(b)** Axial reconstruction of a human vertebra at the end plate level that was scanned for the assessment of bone microarchitecture (Courtesy of Dr.

Serkan Inceoglu and Dr. Gina Roque-Torres, Loma Linda University, Center of Dental Research, CA, USA) and **(c)** axial reconstruction of the mice eye sample stained in PMA that was used to evaluate the retinal injury in mice eyes (Courtesy of Dr. Xiao Mao and Dr. Gina Roque-Torres, Loma Linda University, Center of Dental Research, CA, USA)

reconstruction (preprocessing) or directly at the CT images (post-processing) [15]. Algorithms applied before image reconstruction work on image sinogram to eliminate or reduce outliers' pixels representative of ring artifacts [14].

4.2.3 Related to the Reconstruction Step

4.2.3.1 Aliasing (Undersampling)

Aliasing artifact is caused by an insufficiency of data that may occur either through unders-

ampling of projection data or because not enough projections are recorded. This results as a consequence of the dixel's size within the detector, the spatial location of the image projection in relation to the X-ray source and detector (due to X-ray divergency), a large interval between projections (i.e., number of basis images) (Fig. 4.6), and the mathematical algorithms used for reconstruction ([16, 17]; Makins 2014). In the reconstructed volume, aliasing artifacts appear as fine wavy lines (moire patterns) toward the periphery of the image.

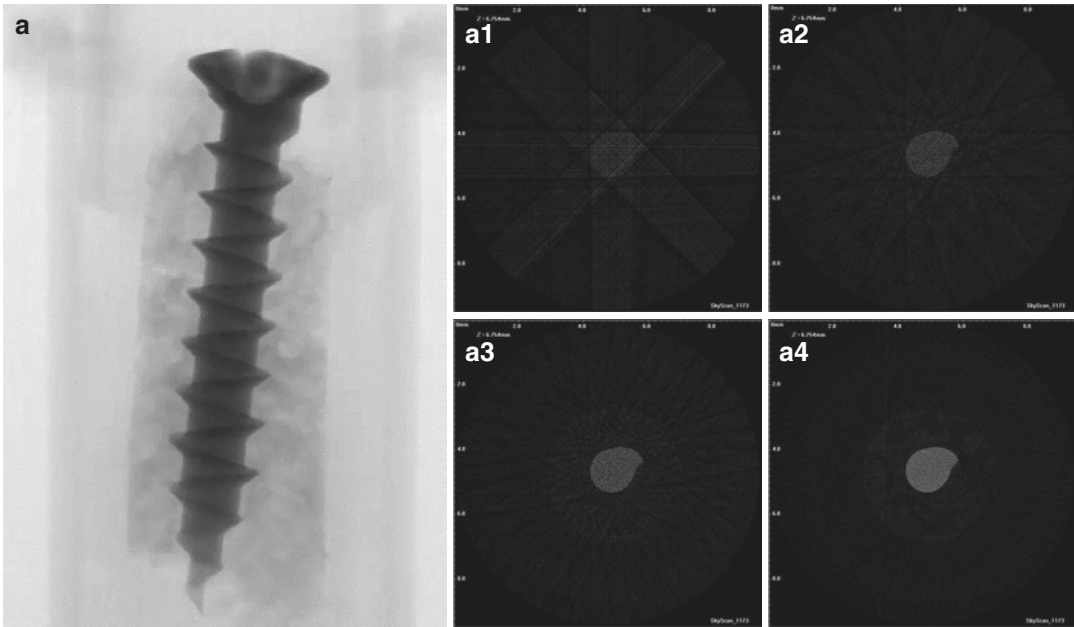


Fig. 4.6 (a) shows a micro-CT image projection of fixation screw surrounded by the bone. Figure **a1/a2/a3/a4** is axial reconstructions illustrating the aliasing artifact (moiré patterns) related to the number of basis images or interval between projections that were 4/10/20 and 900

projections, respectively (Courtesy of Dr. Karla de Faria Vasconcelos, KU Leuven, Omfs Impath research group, Leuven, Belgium and Dr. Gustavo Santaella, School of Dentistry of Piracicaba, University of Campinas, Piracicaba Dental School, Piracicaba, Sao Paulo, Brazil)

4.3 Steps and Approaches to Reduce Artifacts in Micro-CT Images

The artifacts are an important disadvantage of micro-CT images, once it degrades the image and may impair its quantitative and qualitative analysis. For that, several researches are focusing on elimination or minimization of the artifacts. As previously mentioned, artifacts arise from different sources. Therefore, approaches in different steps of micro-CT imaging can influence on artifacts' magnitude.

4.3.1 Acquisition

4.3.1.1 Filter

The X-ray spectrum is arguably the most important variable to control in order to minimize beam-hardening artifacts. In this sense, several approaches to minimize inaccuracies arising from this phenomenon have been developed. Some of them can be applied during the image acquisition such as the beam filtration [18, 19].

Filtration is typically used to pre-harden the X-ray spectrum by removing low-energy X-rays from the beam in order to reduce artifacts. Currently, several materials with different thickness are available for beam filtration, each of them resulting in different X-ray spectra. Therefore, the filtration effectiveness, along with the impact that it has on the image noise and contrast, needs to be investigated. With this propose, Meganck et al. [19] compared filters of 0.254 mm of Al, 0.254 mm of Cu, and 1.016 mm of Al, in conjunction with the beam flattening, and they found significant differences among them, a marked reduction in contrast and increase in noise, which can be explained by the fact that the number of photons at the lower energy levels decreases as filtration increases. However, it is important to highlight that one single energy number as the “effective” energy does not fully describe all the properties of the spectral composition of the beam; the instability and wear of the source further alter the estimation of an accurate effective energy level [20].

As mentioned before, since attenuation coefficients are very dependent on X-ray energy, the

altered energies of a polychromatic beam lead to different attenuations of the same material [2] known as cupping artifact. In order to show the effectiveness of filtration on this condition, Hamba et al. [6] scanned 15 tooth samples using different protocols (100 kVp in a combination with 50 μ A + 0.5 mm Al filter, 165 μ A + 0.5 mm Al/0.3 mm Cu, and 200 μ A + 0.5 mm Al/0.4 mm Cu), all of them with and without beam-hardening correction (BHC) applied during the post-processing step. Afterward, they compared the micro-CT measurements for the enamel lesions against a reference image of transverse microradiography. They found that micro-CT measurements were well correlated with transverse microradiography under all conditions, except for 0.5 mm Al without BHC ($p > 0.05$). The results also showed that even without posterior BHC, the combined Al/Cu filters successfully reduced the artifacts.

As a general conclusion, cupping artifacts can be reduced by filtration. Nevertheless, the filtration should be used with caution because it decreases image contrast and increases noise.

4.3.1.2 Detector Correction

There are two possibilities for detector error correction: flat-field correction and detector shifting. The flat-field correction works as a calibration for the detector prior to image acquisition to identify flawed detector elements. For this, a scan for air is made, so it is possible to verify the inhomogeneous elements of the detector [15]. However, as the detector elements do not present a linear response, mostly it is not sufficient to overcome the ring artifact formation, and in fact it can introduce new artifacts [13, 15]. Another possibility is detector shifting. This method shifts the array of the detector during the scanning and calculates an average data to reduce the ring artifacts, but heavy artifacts caused by defects in scintillator and CCD may not be overcome by this method [15].

4.3.1.3 Scan Degree/Rotation Step/ Frame Average

Some setups for micro-CT image acquisition influence on image data size. These are scan degree, frame average, and rotation step. Scan

degree sets if the scan rotation will be 180° or 360°, and a 360° scan has bigger image data; rotation step determines how many degrees the sample/gantry will rotate to acquire each projection, and therefore lower rotation step increases image data; and the frame average represents how many images (i.e., projections) will be taken at each rotation step, so, the more frames by rotation step, the greater the image data. Image data size is related to the appearance of aliasing and noise artifacts. In this sense, bigger image data means more information to volume reconstruction, minimizing the artifacts related to this (Fig. 4.7). However, image acquisition time and storage requirement are also increased. It is important to overthink image requirements needed for the proposed evaluation, to have acceptable quality images but save time and hardware storage.

4.3.2 Reconstruction

Subsequently the micro-CT acquisition, cross-section images are generated by reconstruction of the full set of projections, and they are called “reconstructed cross-section” images. At this step, some approaches are recommended in order to improve the image quality, among them: beam-hardening correction, ring artifact reduction, and smoothing [21].

4.3.2.1 Beam-Hardening Correction

When the same object is scanned in a polychromatic and monochromatic system, the main difference between the final images appears due to the beam-hardening phenomenon. To address this difference, by correcting the beam hardening, a linearization method with a second-order polynomial fit algorithm has been used [5]. After some simulations using this correction method, Kovács et al. [7] revealed that there remain only a few small differences between the monochromatic and polychromatic images. Additionally, they showed that the relative error can be reduced to an acceptance level of approximately 1% with the correction of the post-processing tool.

With similar purpose, other studies used linearization procedures based on step wedge calibration or polynomial-based approaches to

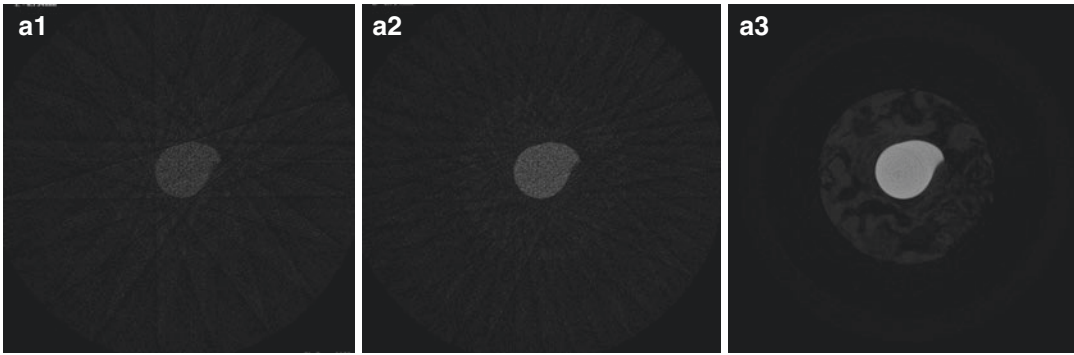


Fig. 4.7 More image data means more information to volume reconstruction, minimizing the aliasing and noise artifacts. In **a1**, the image was reconstructed using 10 projections, **a2** image reconstructed using 20 projections, and **a3** image reconstructed using 900 projections (Courtesy

of Dr. Karla de Faria Vasconcelos, KU Leuven, Omfs Impath research group, Leuven, Belgium and Dr. Gustavo Santaella, School of Dentistry of Piracicaba, SP, Brazil)

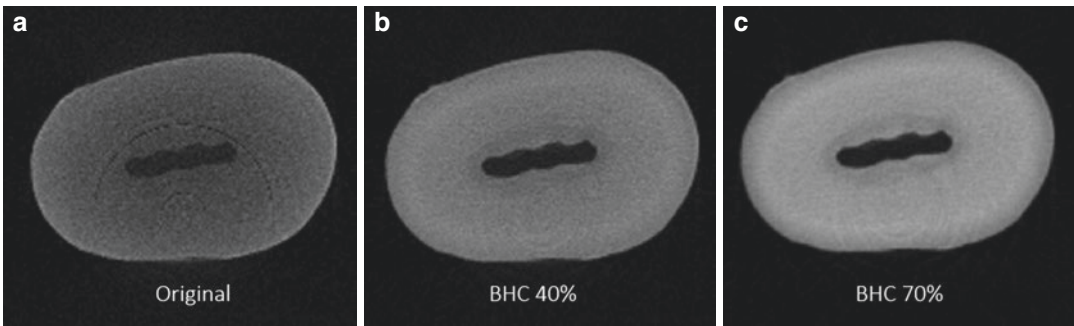


Fig. 4.8 Axial micro-CT images illustrating the beam-hardening correction tool available on the reconstruction software package (NRecon, Bruker, Kontich, Belgium). Original image of a single-root tooth (a). After beam-

hardening correction 40% (b) and after beam-hardening correction 70% (c). (Courtesy of Dr. Hugo Gaêta-Araujo, University of Campinas, Piracicaba Dental School, Piracicaba, Sao Paulo, Brazil)

correct beam-hardening artifacts [22, 23]. In a commercially available reconstruction software package (NRecon, Bruker, Kontich, Belgium), beam-hardening correction (Fig. 4.8) utilizes a second-order relationship: $\epsilon v = A2[\ln(I_0/I_{\text{meas}})]^2$. The options in the program allow the operator to select the $A2$ level from 0% to 100% [5].

4.3.2.2 Ring Artifact Correction

First of all, it is important to regularly update the flat-field correction for the scan mode that you use in order to minimize ring artifacts. However, even with the right scan settings, and an up-to-date flat-field correction, some ring artifacts will often appear in the image. So, the ring artifact

correction can be also applied to the micro-CT images during the post-processing step [15]. Algorithms applied after image reconstruction are based on the median filter [13] and need coordinate (polar and Cartesian) transformations, but the correct identification of the artifact in the image is not accurate resulting in incomplete removal [15].

The ring artifact reduction tool available in NRecon software, has varying strength from 0 to 20. The number in the slider refers to the pixel diameter of the operation. It is important to pay attention to higher-density particles when setting ring reduction since a value of ring reduction that is too high will cause a new, “secondary” ring artifact around the particle [24]. Figure 4.9 shows

an image after ring artifact correction using the tool available on the reconstruction software package.

4.3.2.3 Smoothing

Smoothing or “blurring” is suggested to reduce the noise in the reconstructed image (Fig. 4.10). This correction, which can also be called a filter,

works averaging voxel’s grayscale with neighboring voxels. There are two parameters related to the smooth filtering: sigma and support. Sigma represents the standard deviation (i.e., variation) of the voxel grayscale averaging, while support is the width in pixels or voxels that the smoothing is applied. The NRecon software allows the user to choose from three specific types of smoothing

Fig. 4.9 Axial and sagittal micro-CT images illustrating the ring artifact correction tool available on reconstruction software package (NRecon, Bruker, Kontich, Belgium). The original images of a tooth crown (a) of the rat’s jaw (c) and of the tooth root with hypercementose (e). And after applying the ring artifact correction (b; d and f) (Courtesy of Dr. Karla Rovaris da Silva, Federal University of Piauí, PI, Brazil)

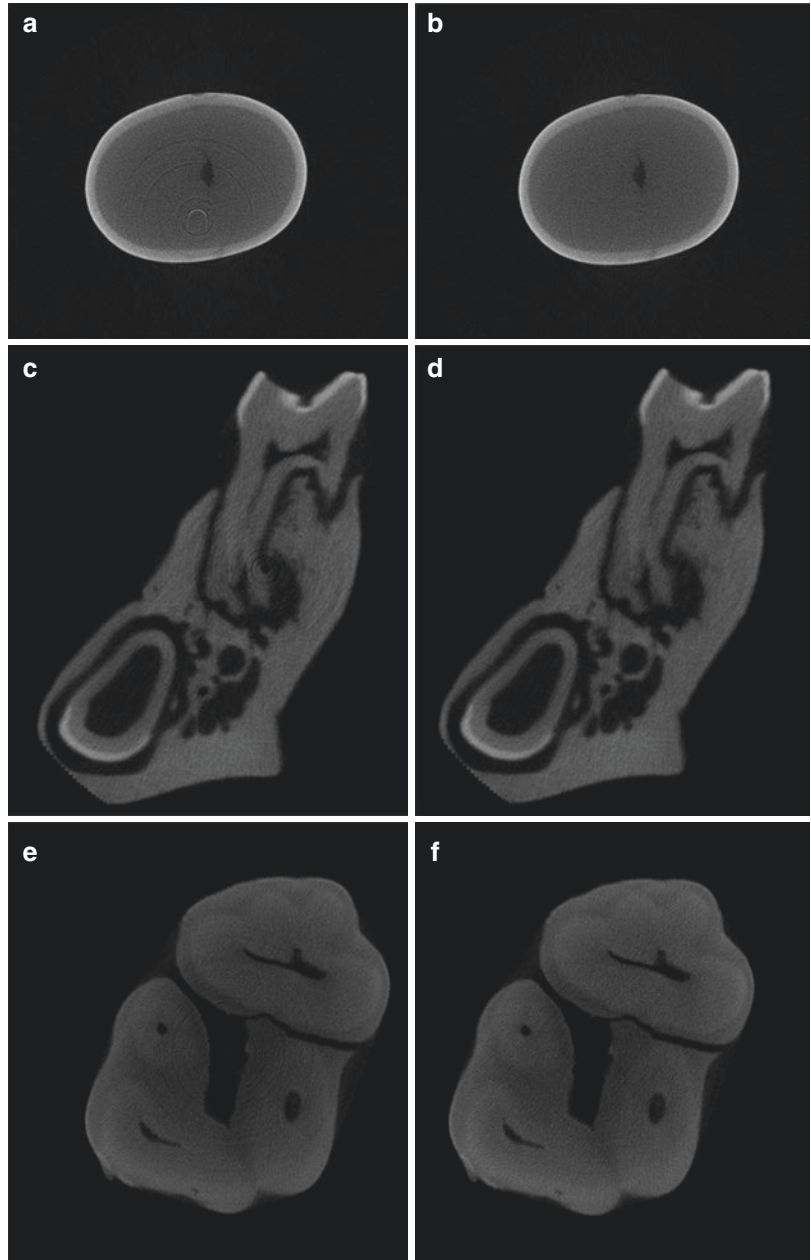


Fig. 4.10 Axial micro-CT images showing the smoothing correction (4) for caries lesion diagnosis propose (Courtesy of Dr. Karla Rovaris da Silva, Federal University of Piaui, PI, Brazil)

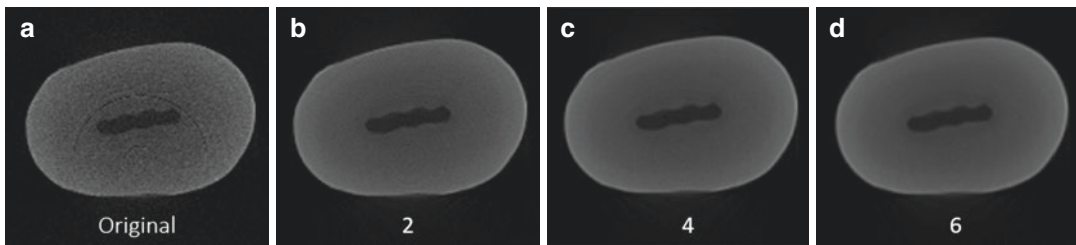
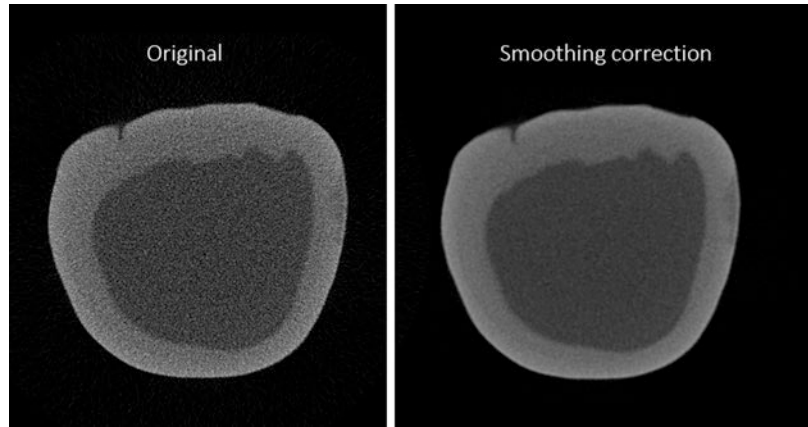


Fig. 4.11 Axial micro-CT images illustrating the smoothing correction tool available on the NRecon reconstruction software package. The original image (a) and after applying the smoothing correction 2 (b), smoothing

correction 4 (c), and smoothing correction 6 (d). (Courtesy of Dr. Hugo Gaêta-Araujo, University of Campinas, Piracicaba Dental School, Piracicaba, Sao Paulo, Brazil)

kernel: box asymmetric, box symmetric, and Gaussian. Generally, the Gaussian kernel is recommended. All these smoothing filters work by averaging a voxel's grayscale with that of some neighboring pixels. In Gaussian filtering the voxels are weighted in the averaging, the central voxel getting the maximum weighting and the surrounding voxels receiving decreasing weighting with distance from the central smoothed voxel according to the Gaussian function (which is also related to the normal distribution) (Bruker brochure MN071). In the NRecon software, the smoothing is set as a value on a scale from 0 to 10, and the operator can judge visually the appropriate amount of smoothing that is applicable for each sample (Fig. 4.11).

The final reconstructed image should be a result of a combination of all appropriated select parameter scanning with all the post-processing corrections in order to obtain an ideal image for the analysis purpose. Figure 4.12 shows the original image and a combination of all the cor-

rections related to the respective parameters selected.

4.3.2.4 Misalignment

In micro-CT imaging, the quality of the reconstructed images depends highly on the precision of the geometric parameters of the system. Image quality would be severely degraded by misalignment parameters, such as more obvious artifacts, lower resolution, and more blurred images [25]. Therefore, high-precision methods for estimating CT system parameters are necessary, and misalignment during acquisition is an important one. If a scan has wrong alignment compensation, it would cause tails, doubling, or blurring in the reconstructed image (Fig. 4.13) and may differ slightly from one dataset to another on some scanners. The misalignment artifact can be solved with post-alignment corrections. A scan affected by this problem of a top-bottom difference can be “saved” at reconstruction phases. von Smekal et al. [26] presented a high-precision method to

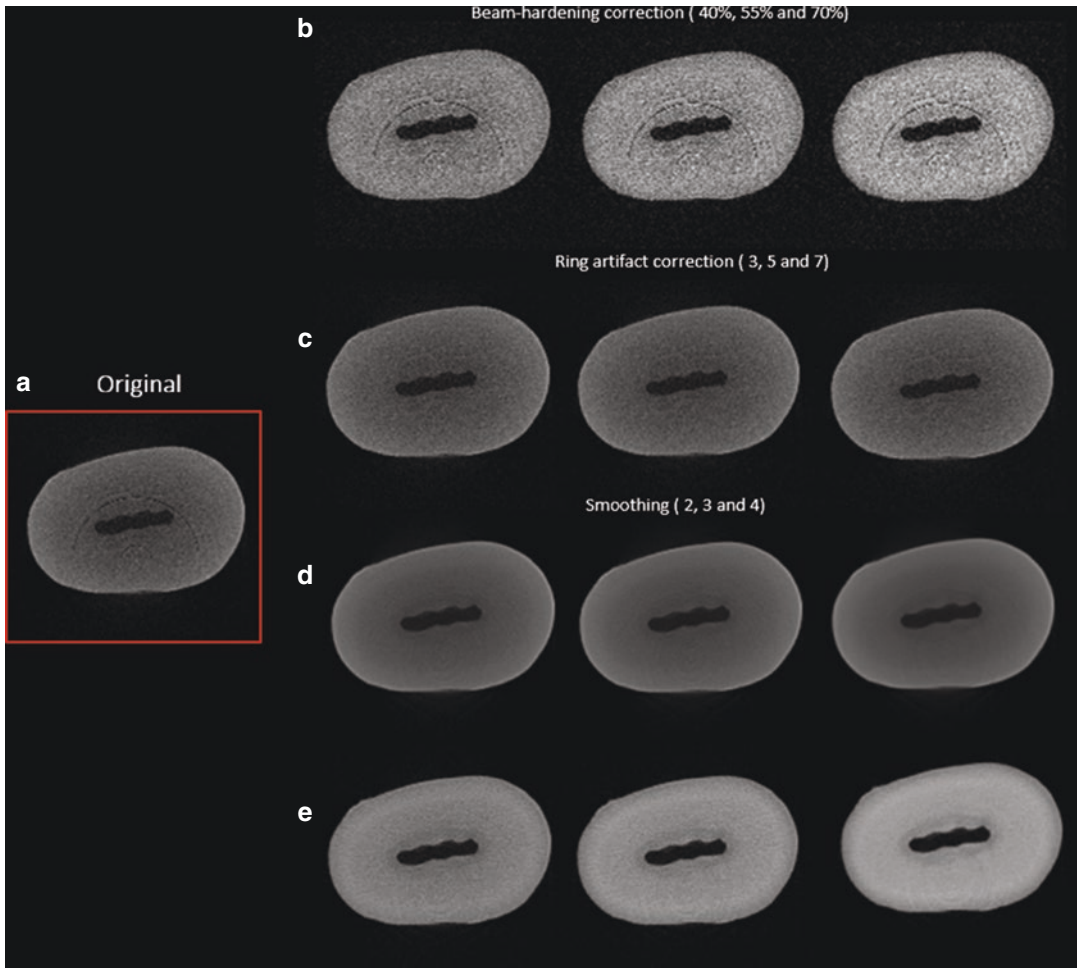


Fig. 4.12 Axial micro-CT images of a single-root tooth and reconstruction tool for artifacts reduction in NRecon software. In the first column, there is the original image (a). The line (b) beam-hardening correction tool was used with 40%, 55%, and 70%, respectively. In line (c), ring artifact correction tool was applied with 3, 5, and 7 values,

respectively. For line (d) smoothing tool was applied with values of 2, 3, and 4, respectively. And the last line, (e), shows a combination on the respective row parameters (Courtesy of Dr. Hugo Gaêta-Araujo, University of Campinas, Piracicaba Dental School, Piracicaba, Sao Paulo, Brazil)

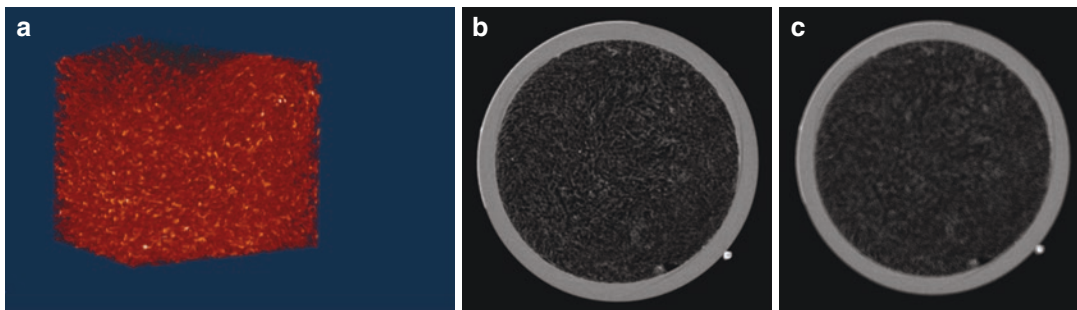


Fig. 4.13 Scanned sample and the middle slice of the volume data. (a) sample; (b) the middle slice after system adjustment; (c) the middle slice before system adjustment

Table 4.1 Recommendations for scan settings and reconstruction parameters according to different samples [24]

Scan category	Scan resolution level	Smoothing	Beam-hardening correction	Ring artifact reduction
<i>No filter</i>				
Paper, etc., low density, low volume	High	0	15	7–13
Insect, plant material, organic non-calcified, low-density tablet	Medium-high	0–2	25	7–13
Larger volume of biological tissue (brain, kidney, muscle, tissue biopsy, etc.) or of other low-density material	Medium	3–5	25	7–25
<i>0.25 mm Al filter</i>				
Mixed density biomaterial, e.g., porous calcium phosphate, tablet (medium density)	Medium-high	1–3	40–50	5–11
Soft biological tissue with partial calcification, e.g., late embryo	Medium-high	2–4	40–50	5–11
Larger volumes of low-density material, e.g., wood, plastic	Low-medium	2–4	40–50	3–13
Very small medium-density materials, e.g., bone, ceramic, rock, polymer	Medium-high	0–2	40–50	5–13
<i>0.5 mm Al filter</i>				
Mouse bone	Medium-high	0–2	45	4–9
Mouse hind limb in vivo (high resolution/high dose)	High	1–3	30	4–9
Mouse body in vivo (high contrast/high dose)	Low-medium	3–5	30	2–5
Small rock, mineral, ceramic sample, very small tooth	Medium-high	2–4	40–70	4–9
Large volume—low density, e.g., wood, plastic, water, bio-tissue	Low-medium	3–5	30	2–7
<i>1 mm Al filter</i>				
Rat, rabbit bone	Medium	1–2	35	5–11
Small tooth	Medium	1–3	35–50	5–11
Mouse hind limb in vivo (low dose)	High	0–2	30	4–9
Rat hind limb in vivo	Medium	0–2	30	2–5
Mouse body in vivo	Low	3–5	30	2–5
Rat (small) body in vivo	Low	4–6	30	3–7
Rock, ceramic, glass	Low-medium	1–3	30–50	4–9
Biomaterial, medium density	Medium-high	1–3	30–50	5–11
<i>40 micron Cu + 0.5 mm Al (equivalent to ~2 mm Al)</i>				
Large tooth, large bone	Medium	2–4	25–35	5–13
Metal-containing sample	Low-medium	2–6	50–100	1–4
Rat (large) body in vivo	Low	3–7	25–30	3–7
High-low-density combination, e.g., metal implant in bone	Low-medium	2–4	30–50	1–5
Rock, ceramic, other materials with high absorption	Low-medium	2–4	35–50	5–11
<i>0.11 mm Cu and higher filter</i>				
Metal sample	Low-medium	2–4	30–60	2–7
Rock, ceramic, other materials with high absorption	Low-medium	2–4	25–50	2–7
High-low-density combination, e.g., metal implant in bone	Low-medium	2–4	25–50	1–5
Very large rat in vivo	Low	4–7	20	2–7

Table 4.1 (continued)

Summary
<p><i>Beam hardening</i></p> <ul style="list-style-type: none"> Occurs because the low-energy photons are more absorbed from the beam than the higher-energy photons. Appears in the image as cupping or streak artifacts. X-ray source energy, effective filtration, and beam-hardening correction tools try to minimize its effect
<p><i>Ring artifact</i></p> <ul style="list-style-type: none"> Is a consequence of detector error and appears in the image as concentric rings; flat-field correction, detector shifting, and ring artifact correction tool can fix it
<p><i>Aliasing</i></p> <ul style="list-style-type: none"> Is caused by undersampling of the structures. Appears as fine wavy lines (moire patterns) toward to the periphery of the image. Increase in basis image has a positive effect on this kind of artifact
<p><i>Noise</i></p> <ul style="list-style-type: none"> Low photon counts cause noise in images. Appears as random bright and dark streaks. Smoothing filters are commonly applied to reduce its impact on micro-CT images

determine the complete misalignment parameters based on Fourier analysis through multiple projection images. Yang et al. [27] proposed an analytic method for deriving five system parameters assuming that the detector does not have serve out-of-plane rotation ($<2^\circ$) by using multiple projection images and angle information. It should be kept in mind that all the methods mentioned above could estimate some or all the geometric parameters by using analytic or iteration equations in the range of acceptable accuracy. However, a potential weakness is that they rely on multi-projections at different angles. This means that the precision of calibration would be affected by the errors of the rotation, such as radial or axial errors whose effect would be obvious in micro-CT. Recently, methods such as iterative methodology were used to estimate geometric parameters of micro-CT. This method can estimate all the parameters by acquiring only one projection [25].

Table 4.1 brings some recommendations for scan settings and reconstruction parameters according to different samples. These suggestions are of a general nature and should be interpreted with flexibility [24].

References

- Lewis R. Medical applications of synchrotron radiation x-rays. *Phys Med Biol.* 1997;42(7):1213–43.
- Elliott JC, Wong FS, Anderson P, Davis GR, Dowker SE. Determination of mineral concentration in dental enamel from X-ray attenuation measurements. *Connect Tissue Res.* 1998;38(1–4):61–72.
- Willmott NS, Wong FS, Davis GR. An X-ray microtomography study on the mineral concentration of carious dentine removed during cavity preparation in deciduous molars. *Caries Res.* 2007;41(2):129–34.
- Wong FS, Anderson P, Fan H, Davis GR. X-ray microtomographic study of mineral concentration distribution in deciduous enamel. *Arch Oral Biol.* 2004;49(11):937–44.
- Zou W, Hunter N, Swain MV. Application of polychromatic μ CT for mineral density determination. *J Dent Res.* 2011;90(1):18–30.
- Hamba H, Nikaido T, Sadr A, Nakashima S, Tagami J. Enamel lesion parameter correlations between polychromatic microCT and TMR. *J Dent Res.* 2012;91(6):586–91.
- Kovács M, Danyi R, Erdélyi M, Fejérdy P, Dobó-Nagy C. Distortional effect of beam-hardening artifact on microCT: a simulation study based on an in vitro caries model. *Oral Surg Oral Med Oral Pathol Oral Radiol Endod.* 2009;108(4):591–9.
- Hunter AK, McDavid WD. Characterization and correction of cupping effect artifact in cone beam CT. *Dentomaxillofac Radiol.* 2012;41(3):217–23.
- Schulze R, Heil U, Gross D, Bruellmann DD, Dranschnikow E, Schwanecke U, Schoemer E. Artifact in CBCT: a review. *Dentomaxillofac Radiol.* 2011;40(5):265–73.
- Nardi C, Borri C, Regini F, Calistri L, Castellani A, Lorini C, Colagrande S. Metal and motion artifacts by cone beam computed tomography (CBCT) in dental and maxillofacial study. *Radiol Med.* 2015;120(7):618–26.
- Boas FE, Fleischmann D. CT artifacts: causes and reduction techniques. *Imaging Med.* 2012;4(2):229–40.
- Shahmoradi M, Lashgari M, Rabbani H, Qin J, Swain M. A comparative study of new and current methods for dental micro-CT image denoising. *Dentomaxillofac Radiol.* 2016;45:20150302.

13. Kyriakou Y, Prell D, Kalender WA. Ring artifact correction for high-resolution micro CT. *Phys Med Biol*. 2009;54(17):N385–91. <https://doi.org/10.1088/0031-9155/54/17/N02>.
14. Anas EM, Lee SY, Hasan K. Classification of ring artifacts for their effective removal using type adaptive correction schemes. *Comput Biol Med*. 2011;41(6):390–401. <https://doi.org/10.1016/j.combiomed.2011.03.018>.
15. Zhu Y, Zhao M, Li H, Zhang P. Micro-CT artifacts reduction based on detector random shifting and fast data inpainting. *Med Phys*. 2013;40(3):031114. <https://doi.org/10.1118/1.4790697>.
16. Barrett JF, Keat N. Artifacts in CT: recognition and avoidance. *Radiographics*. 2004;24(6):1679–91.
17. Makins SR. Artifacts interfering with interpretation of cone beam computed tomography images. *Dent Clin North Am*. 2014;58(3):485–95. <https://doi.org/10.1016/j.cden.2014.04.007>. Review.
18. Jennings RJ. A method for comparing beam-hardening filter materials for diagnostic radiology. *Med Phys*. 1988;15(4):588–99.
19. Meganck JA, Kozloff KM, Thornton MM, Broski SM, Goldstein SA. Beam hardening artifacts in micro-computed tomography scanning can be reduced by X-ray beam filtration and the resulting images can be used to accurately measure BMD. *Bone*. 2009;45(6):1104–16.
20. Nuzzo S, Peyrin F, Cloetens P, Baruchel J, Boivin G. Quantification of the degree of mineralization of bone in three dimensions using synchrotron radiation microtomography. *Med Phys*. 2002;29(11):2672–81.
21. Queiroz PM, Rovaris K, Gaêta-Araujo H, Marzola de Souza Bueno S, Freitas DQ, Groppo FC, Haiter-Neto F. Influence of artifact reduction tools in micro-computed tomography images for endodontic research. *J Endod*. 2017;43(12):2108–11. <https://doi.org/10.1016/j.joen.2017.07.024>.
22. Burghardt AJ, Kazakia GJ, Laib A, Majumdar S. Quantitative assessment of bone tissue mineralization with polychromatic micro-computed tomography. *Calcif Tissue Int*. 2008;83(2):129–38.
23. Mulder L, Koolstra JH, Van Eijden TM. Accuracy of microCT in the quantitative determination of the degree and distribution of mineralization in developing bone. *Acta Radiol*. 2004;45(7):769–77.
24. Bruker Method Note. An overview of NRecon: reconstructing the best images from your microCT scan.
25. Zhao J, Hu X, Zou J, Hu X. Geometric parameters estimation and calibration in cone-beam micro-CT. *Sensors (Basel)*. 2015;15(9):22811–25.
26. Von Smekal L, Kachelrieß M, Stepina E, Kalender WA. Geometric misalignment and calibration in cone-beam tomography. *Med Phys*. 2004;31:3242–66. <https://doi.org/10.1118/1.1803792>.
27. Yang K, Kwan ALC, Miller DWF, Boone JM. A geometric calibration method for cone beam CT systems. *Med Phys*. 2006;33:1695–706.



Application of Bone Morphometry and Densitometry by X-Ray Micro-CT to Bone Disease Models and Phenotypes

5

Phil Salmon

5.1 Introduction

Microcomputed tomography, or micro-CT, is being employed widely for bone and dental research. Bone biologists were enthusiastic early adopters of laboratory micro-CT systems since the 3D morphometric capability it introduced met very well the requirements of this research field for 3D analysis of the architecture and mechanical competence of trabecular and cortical bone, in both clinical biopsy samples and animal disease models—foremost among these being osteoporosis. The dentists followed closely behind—soon recognising the strong potential of micro-tomographic data in dental research investigation, again both with clinical dental samples and animal models.

This article will touch only briefly on the physical essentials of micro-CT. The focus will be a practical one of using the technique to obtain results—mostly quantitative ones—that can deliver quantitative 3D image-based data on outcomes of preclinical disease models.

5.1.1 Tomography and Micro-CT

“Tomography” comes from the Greek “tomos” for slice and implies obtaining the cross-sectional image nondestructively, without physically cutting the slice. (Thus other imaging-at-depth methods not involving rotating geometry are also called “tomography”.) “Computed” does not have the trivial meaning of just using a computer (!) but “compute” implies synthesis of data from multiple images. “Computed tomography” is thus taking X-ray projection images of an object from many angles and mathematically converting this set of images into a stack of cross-sectional image slices, which collectively represents a three-dimensional image or “dataset”. These projection images are taken incrementally over a total rotation of either 180° or 360°.

The essential data of X-ray CT is a negative or inverse signal—that of attenuation (which means “to weaken or diminish”). If there is no object in the scanner, the projection image is uniform and bright background only. Objects present decrease the X-ray signal giving darker patches on the image, by absorbing X-rays, so they attenuate the signal. The reduction of measured intensity at a camera pixel shows that attenuation has happened along the line from the X-ray source emission spot to that camera pixel. But from a single projection only, you don’t know where along the line that attenuation has happened.

P. Salmon (✉)
Bruker-micro CT, Kontich, Belgium
e-mail: Phil.Salmon@bruker.com

The essentials of micro-CT are explained more fully in earlier chapters in this book. The mathematics of CT, based on a procedure called the “Radon transform” and involving “back-projection”, allow you with a set of projection images from multiple angles to improve your knowledge about where exactly in space X-ray attenuation has happened. Instead of along a line, we can reconstruct what attenuation has happened within a specific discrete volume element within the scanned volume. The scanned volume in CT is a cylinder. The cubic volume elements we call voxels. CT—or micro-CT—is thus the 3D voxelised mapping of X-ray attenuation (Fig. 5.1).

Reconstructing this 3D data from images from large-area X-ray cameras is called “cone-beam” reconstruction since the volume defined by the X-ray point source and the rectangular camera is like a cone (actually a pyramid), in contrast to “fan beam” reconstruction along a thin line from very narrow X-ray detectors. Most conventional cone-beam reconstruction today is based on the algorithm of Feldkamp et al. [1]. Medical CT scanners have been an important part of hospital medicine since the invention of the technique by Godfrey Hounsfield in 1972 [2]. Micro-CT is CT of small objects in specialised laboratory scanners which have a very high spatial resolution [3]. A simple schematic of this process, with examples of projection and reconstructed images, is shown in Fig. 5.1.

In bone biomedical research, the forerunner of micro-CT bone morphometry was bone histomorphometry using light microscope histology. This started with the creation of histological

methods for the embedding and sectioning of calcified tissue without prior decalcification [4]. These developments were accompanied by new staining methods (e.g. Von Kossa, Goldner’s Trichrome, dynamic fluorochrome labelling) which enhanced the histological study of bone, allowing the distinguishing of mineralised bone from unmineralised newly formed osteoid and measurement of the dynamics of bone formation [e.g. 5, 6]. This in turn was accompanied by progress in microscope image analysis technology such as video cameras and partial automation of analysis, plus the rapid development of personal desktop computers. All this together allowed the growth of bone histomorphometry, the quantitative study of mineralised bone tissues.

Histomorphometry attempts to convert measurements made in two dimensions (2D) on single or multiple microscope sections through a volume of bone to estimates of three-dimensional parameters [7, 8]. Thus bone perimeter measurements could be converted to an estimate of surface area and cross-sectional area converted to a bone volume estimate. Measured perimeter to area ratio provided the basis for estimates of bone thickness. These mathematical conversions deriving 3D bone structural parameters from 2D cross-sectional have significant error associated with them. A major source of error in measurements is the need to assume an architectural model for the structures being studied. For example, one can apply a “plate” model and assume that the (trabecular) bone studied is composed only of parallel flat plates, or a “rod” model, assuming the sample is a regular parallel array of cylinders. Real objects of interest such as

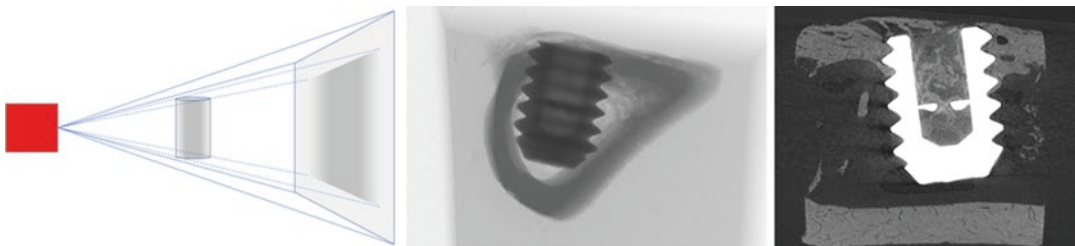


Fig. 5.1 The projection image is the raw data of tomography. Every pixel records X-ray absorption on the path from the point source to that camera pixel. Darker pixel

greyscale means more absorption along that path; brighter greyscale means less. Cone-beam reconstruction maps X-ray attenuation in a 3D volume dataset

trabecular bone depart greatly from such idealised structures.

What micro-CT brings to bone research—and indeed to any research field—is the ability non-destructively and directly to obtain a three-dimensional image of a scanned object. The word “direct” here is important, implying the imaging method is 3D in a true and fundamental sense, providing a 3D model of an object based directly on imaging measurements. The great advantage of this for bone morphometry is the chance to “side-step” all the mathematics of 2D–3D conversions and model-based estimates and to make direct measurements on a 3D image model using true 3D algorithms such as surface rendering [9] and the distance transform [10]. So this represents a simplification as well as a significant improvement in the capability to obtain information about the 3D architecture of structures such as bone. Furthermore, having a 3D image model makes possible some wholly new architectural parameter measurements that are completely inaccessible to analysis based on 2D image slices.

5.2 The Use of Micro-CT 3D Data in Bone Disease Models

5.2.1 A Universal “Pipeline” of Micro-CT Analysis Methodology for All Bone Research Models

There are a wide range of animal models of bone disease that can be imaged and analysed by micro-CT. These include (but not limited to) osteoporosis, arthritis, bone tumour and osteogenesis imperfecta, as well as models of nutritional, metabolism and obesity studies. Furthermore, transgenic mice can be imaged for phenotypes of bone architecture and mineralisation resulting from genetic modification. There are also orthopaedic models of fracture callus healing and of osteointegration of implanted metal screws or osteogenic biomaterials.

While these model systems and the relevant bone sites associated with each are diverse, there is a universal approach that can be applied to the

micro-CT analysis in all cases. There are universal features in 3D micro-CT quantitative analysis, and they are always encountered whatever the experimental model. This fact helps to simplify the development of a micro-CT analysis protocol for a bone disease model. A single software package can be used for most or all models, without the purchase of and training in expensive additional software modules or programmes for each and every model used. The programme that will be used in this article is Bruker (originally “SkyScan”) CT-analyser, although others are available with similar functionality and flexible adaptiveness such as the IPL environment in Scanco Medical systems or platform-independent software packages such as VG Studio Max. There does not have to be a new learning process and software environment for different models. Once one has grasped the “pipeline” approach, it is possible to adapt it to create new and effective analysis protocols to new experimental model systems.

Table 5.1 indicates the four general stages of the micro-CT “analysis pipeline”. These are scan-reconstruction, 3D orientation, volume of interest and segmentation-analysis. They will be discussed in turn, before we move on to look at the implementation of this four-step pipeline in a range of bone disease models.

5.2.1.1 The Scan and Reconstruction

First comes the scan—the micro-CT imaging for a preclinical bone model must image the appropriate bone site. The right filter and voltage combination will give optimal absorption contrast in the sample while reducing beam hardening, which otherwise would compromise measurements of bone mineral density (BMD). All bone scans should use some filter, to keep down beam hardening. As a general rule, start with the filter that will minimise beam hardening for the bone in question. Then, for that filter, set the lowest voltage possible that will give a minimum transmission in the projection images (at the darkest part of the image) of about 15–25% relative to saturation. Going to higher voltages than this will increase noise, beam hardening and ring artefacts. For in vivo scanning of the hindlimb of

Table 5.1 The “universal analysis pipeline”

Stage	Description
1. Scan-reconstruction	<ul style="list-style-type: none"> • The correct site must be included in all scans • Sample/animal mounting: stability, hydration • Resolution: how much is actually needed? • Contrast agent? Can be necessary for cartilage or blood vessels • X-ray spectrum shaping—best filter and voltage to enhance contrast, reduce beam hardening • In vivo—short scans for low X-ray dose • Reconstruction: check stability and alignment, smooth for best clarity of structures, minimise artefacts such as beam hardening
2. Orientation in 3D	<ul style="list-style-type: none"> • Rotate in DataViewer for standardised 3D orientation for VOI selection • Save images from rotated volume
3. Volume of interest	<ul style="list-style-type: none"> • Anatomical landmarks • Fixed size or flexible depending on structure • Simple or complex • Hand-drawn or automatic (CTAn custom processing)
4. Segmentation-analysis	<ul style="list-style-type: none"> • Segmentation (binarisation) • Morphometry (volume, thickness, porosity, etc.) • Densitometry (BMD, HU) • Visual interpretation in 3D

Analysis of complex asymmetric biological structures such as bone sites requires careful definition of the volume to be analysed in order to measure a morphometric signal relating to the biological or disease process and then a practical method to select and delineate such a volume consistently between different animals and samples. Standardisation of alignment is a good place to start for this

both mouse and rat, with a view to reducing radiation dose, a 1 mm filter is suitable.

For a mouse the voltage would be 40–50 kV, for a rat 60–80 kV. Ex vivo, radiation dose is less of an issue and for mouse and other similar-sized bones, and a 0.25 mm Al filter will give the best contrasted images (40–50 kV), although 0.5 mm Al filter (40–50 kV) will reduce beam hardening and be preferable if substantial surrounding tissue is present. For rat bone 1 mm Al filter (60–70 kV) is best, as well as for smaller rabbit bones. For larger animal bones such as of sheep and human, the stronger copper filters and voltages up to 100 kV can be required. One should select a voltage and filter that optimise dynamic contrast in the X-ray projection image.

Mounting bones for scanning ex vivo should meet the normal requirements for micro-CT—that of stability (no movement) and also maintaining hydration to prevent drying. Placing bones in vertically held plastic tubes, wrapped in either plastic film or paper tissue (moistened with water or saline), achieves both these objectives while also allowing high-throughput batch scanning.

For in vivo scanning of rodent bone under anaesthesia, the most common site is the hindlimb, providing convenient sites for trabecular and cortical analysis at the femur or tibia metaphysis. Other studied sites include the tail (caudal vertebrae), lower back (lumbar vertebrae), thorax, head or whole body for bone mineral content and density of the entire skeleton. When mounting the hindlimb for scanning, a single scanned limb should be positioned in a tube of low-density foam (polypropylene or polystyrene) as shown in Fig. 5.2. In combination with tape and soft dental wax, the hindlimb can be held securely for scanning while allowing gentle handling of the limb without undue pressure applied. Scanning a limb singly and centrally positioned in the bed by means of a tube improves image quality substantially compared to scanning paired hindlimbs in a rodent’s unmodified supine position.

Reconstruction parameters need to be optimised for each scanner, noting that appropriate parameters can differ significantly between scanner models. Therefore *do not copy reconstruction parameters verbatim from other published work*

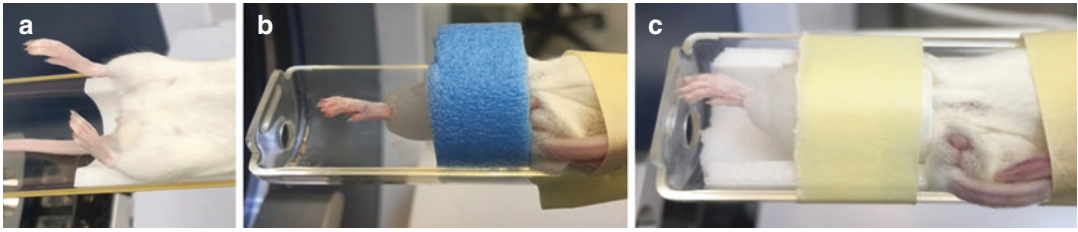


Fig. 5.2 For micro-CT imaging of the rodent hindlimb, do not perform the scan with the legs in the natural prone position (a)—this will irradiate an unnecessarily large amount of abdominal and pelvic tissue, increasing noise in the image and the limbs will be positioned away from the scan midline, compromising image quality. Instead the

hindlimb should be held in a tube as shown of polypropylene (b) or polystyrene (c) foam. Soft dental wax is used to hold the protruding foot in place without injury to the foot or ankle. (Such is the X-ray transparency of wax that this setup also allows scanning of the foot and ankle, e.g. for arthritis studies)

unless the scanner model in the publication is exactly the same as the one you are using. (The same applies to scan parameters also.) For example, amount of beam hardening and thus the amount of beam hardening correction that are needed are strongly dependent on the thickness of the scintillator (the X-ray-sensitive outer layer) in the X-ray camera. This thickness varies a lot between scanner models. A thinner scintillator layer, in scanners optimised for very high spatial resolution, results in more beam hardening since the camera's detection efficiency falls off sharply with increasing X-ray energy. Generally speaking, X-ray cameras based on a CCD detector have a much thinner scintillator than cameras based on a large-area “flat panel” CMOS detector. Thus more beam hardening correction is needed in the CCD-based than in the flat panel-based systems. To give an example from Bruker-SkyScan systems, mouse bone scans in the SkyScan 1172 and 1272 CCD-based models, with 0.5 mm Al filter, require about 40% [11] beam hardening correction in NRecon software, while the same mouse bone scanned also with 0.5 mm Al filter in the flat panel-based SkyScan 1275 requires about 10% beam hardening correction.

Always check scan alignment for each scan even if multiple scans are imaged and reconstructed with the same parameters for comparative quantitative analysis. The alignment correction that is always necessary in high-resolution tomography differs slightly between

scans, so each scan needs to have the alignment (“post-alignment”) checked individually, even where the reconstruction software makes an estimate of this parameter automatically. A check of alignment also constitutes a quality check of the scan, to ensure, for instance, that no movement artefact is present.

Concerning other reconstruction parameters, smoothing should be applied to optimise the visual clarity of the structures of most interest—such as trabecular bones. It is wrong to exclude any smoothing on the assumption that image data will be lost. Scattering artefacts and stochastic limitation in detected photon number cause an artificial sharpening and noisiness in images, and real improvement can be made by simple Gaussian or box kernel smoothing. Visual appearance is always a reliable guide in micro-CT—if it looks better, it is better. Artefact corrections in reconstruction should be used with caution since they can themselves cause secondary artefacts if applied too strongly. Therefore for correction of ring artefacts and beam hardening, one should use the minimum values that are necessary or that make a noticeable improvement.

As for contrast limits or the intensity window, set the low limit to zero attenuation (or to a small negative value to enhance contrast of low-density material) and the high limit to 10–20% above the highest attenuation value corresponding to the material of interest such as bone. This maximum attenuation can be seen in the histogram of attenuation shown in the reconstruction software.

5.2.1.2 Orientation in 3D

All bone samples analysed in 3D in an experiment should have the same spatial orientation. Long bones (e.g. femur, tibia) should have their central axis aligned with the z-axis, or depth axis, of the dataset. It is not always possible—and not necessary—to scan bones in exactly the same orientation each time. In vivo scans of a rodent hindlimb in particular are likely to be done with the femur and tibia at significant departure from orthogonal alignment. Software such as SkyScan DataViewer allows rotation of a dataset in all three orthogonal axes (coronal, transaxial, sagittal) allowing 3D rotation to any spherical angle (Fig. 5.3). As well as the long axis being aligned, it is a good idea to apply consistent angular position in the cross-sectional plane as well—such that the femoral or tibia condyles are pointing either upwards or downwards in all bone scans. Such consistency in dataset alignment in three dimensions will result in greater consistency in volumes of interest (VOIs) especially where these involve manually drawn shapes.

The 3D orientation that is applied to the scans depends on the goal of the study. For example, when bones are scanned containing metal screw implants, with the objective of analysing the sta-

tus of bone at or near the implant surface, then it is appropriate to standardise the alignment of all experimental scan dataset such that it is the central axis of the screw implant, not the bone, that is aligned parallel with the depth z-axis of the dataset. With this orthogonal alignment of the implant, the cross-sectional images will be at right angles to the implant long axis, not at some oblique angle. Since in this case the distance in an orthogonal (normal) direction away from the implant surface needs to be defined accurately in order to assess peri-implant bone status in a consistent way, such orthogonal alignment of the cross-sectional plane with respect to the screw implant axis is essential. In short, the cross section of a cylindrical implant should be circular, not oval shaped.

5.2.1.3 Volume of Interest

The volume of interest (VOI) is of central importance to any kind of quantitative micro-CT analysis in 3D. Developing a method and workflow to analyse any given disease model by micro-CT will always, inescapably, have to address the question “what VOI is needed and how do I make it?” The 3D parameters that you measure have their meaning defined by the volume of interest.

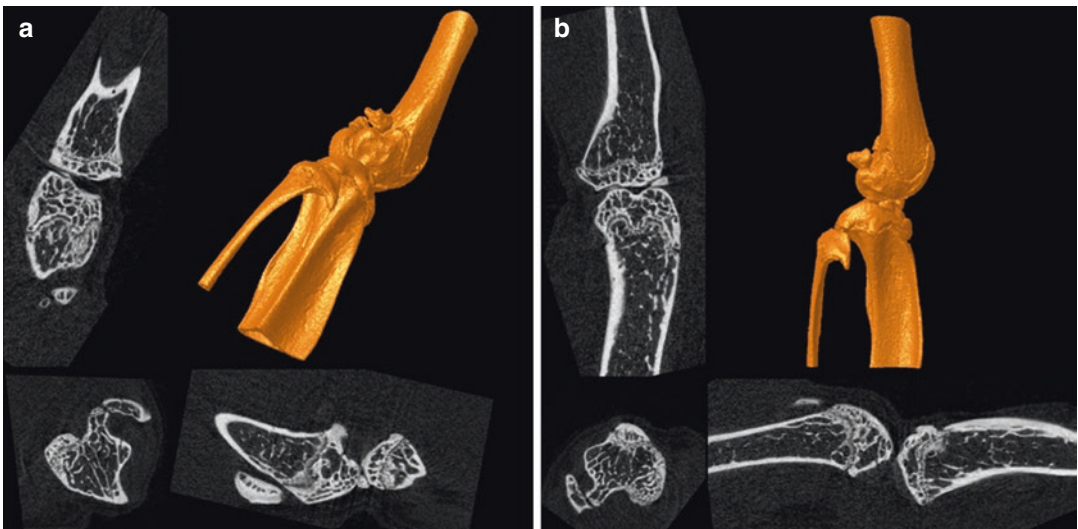


Fig. 5.3 An in vivo scan of a mouse knee, before (a) and after (b) realignment in DataViewer software. DataViewer and similar software allow rotation of a dataset in all three

orthogonal axes (coronal, transaxial, sagittal) allowing 3D rotation to any spherical angle

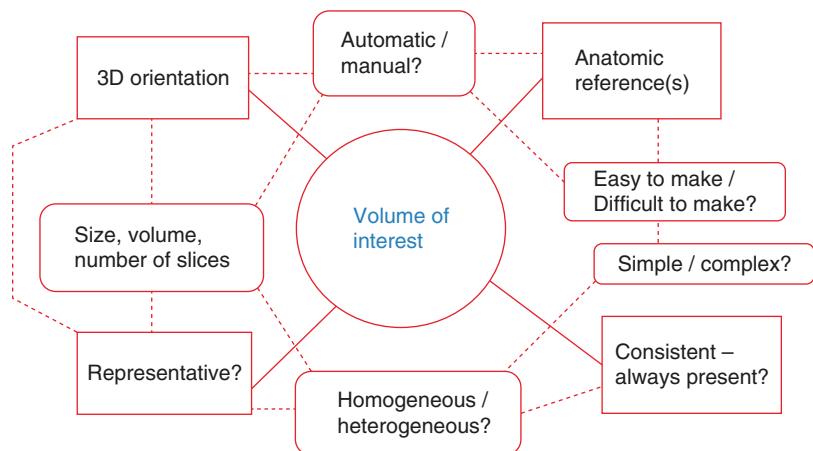
To give a simple example, software such as SkyScan CT-analyser (“CTAn”) measures thickness of an object in 3D (independent of object orientation). What makes the measured thickness become trabecular thickness is to set a trabecular bone VOI. Likewise for a cortical bone VOI, note that one can use advanced software functions to automatically delineate trabecular from cortical bone and set VOIs for each. But automation does not change this fact—the definition of what you measure depends on the VOI that you set.

VOIs and the methods by which they are set or delineated can be either simple or complex. In a uniform material such as a sample of manufactured biomaterial scaffold, a simple cylinder will suffice as VOI, delineated by a single circle and a range of cross-sectional slices. However when bones or other biological organs, tissues or organisms are the subject of micro-CT analysis, then VOIs will be complex and asymmetrical. Uniform volumes and regular geometric shapes are rare in living organisms. Trabecular and cortical bone VOIs can be made as complex 3D shapes with software interpolation between a limited number of freehand-drawn shapes, in analysis software such as CTAn. Another important category of methods for setting a VOI is to start with a binarised object of a bone or tissue site and manipulate it by—for example—erosion, dilation and the filling of spaces, to generate semi-automatically a VOI that accurately delineates

the site to be studied. Examples of these methods will be described in more detail in the section below on micro-CT analysis methods for individual disease models.

Some of the factors to consider when setting a VOI are shown diagrammatically in Fig. 5.4. A VOI sometimes uses an anatomic reference, such as the growth plate in the femur and tibia. The process of creating the VOI should not be too laborious or difficult. It should select structures and features that are always present in the scanned samples. Depending on the homogeneity or (more likely in biological structures) heterogeneity of the analysed volume, the VOI should meet the required size for statistical representativeness. A useful concept in considering the size of a volume of interest is the REV—“representative elemental volume”. This is the minimum volume within a structure that is representative of its morphometry—so that the value measured within the sub-volume would be similar to the value measured over the entire object volume. There is a helpful discussion of the REV by Srivastava et al. applied to the study of the 3D architecture of snow [12] which turns out to be remarkably similar to the study of trabecular bone—both are cancellous labyrinthine matrix structures whose mechanical performance is important (for avoiding snow avalanches and bone fractures, respectively) and closely linked to the 3D architecture.

Fig. 5.4 A network of factors to consider when setting the VOI for bone analysis in 3D, in micro-CT analysis of a preclinical disease model, bone or otherwise



5.2.1.4 Segmentation-Analysis

Segmentation

Following directly after the normalisation of alignment of the dataset, and the selection of the VOI, the selected sub-volume of the dataset is segmented and analysed. Segmentation is also called thresholding or binarisation. The most common form of segmentation is global thresholding, where a high range of greyscales in the reconstructed image are segmented to white (solid) and all pixels with lower greyscale are segmented to black. Global thresholding is a good and sufficient thresholding method providing the resolution and quality (e.g. signal to noise ratio) of micro-CT bone images is high. However in some cases such as in vivo scanning where scan times and radiation dose are kept low, image resolution is reduced, and global segmentation results in significant loss of bone detail due to greyscale biasing (Fig. 5.5). In this

case more advanced forms of segmentation, such as local adaptive thresholding, can improve the results of thresholding with less loss of detail.

A general rule is that, for a given experimental study, the thresholding values should be kept the same for all bones that are analysed. This applies equally to a global threshold range as to the low and high pre-threshold values employed in local adaptive thresholding. Occasionally a study unavoidably analyses micro-CT images from samples of widely differing size and density. In this case, the differing tomography conditions (combined with beam hardening and resultant context sensitivity) make it not possible to apply the same threshold values to all samples. In this case, a solution can sometimes be provided by algorithms that automatically find a global threshold. A commonly used example is the Otsu thresholding algorithm [13], another one being the Ridler-Calvard algorithm.

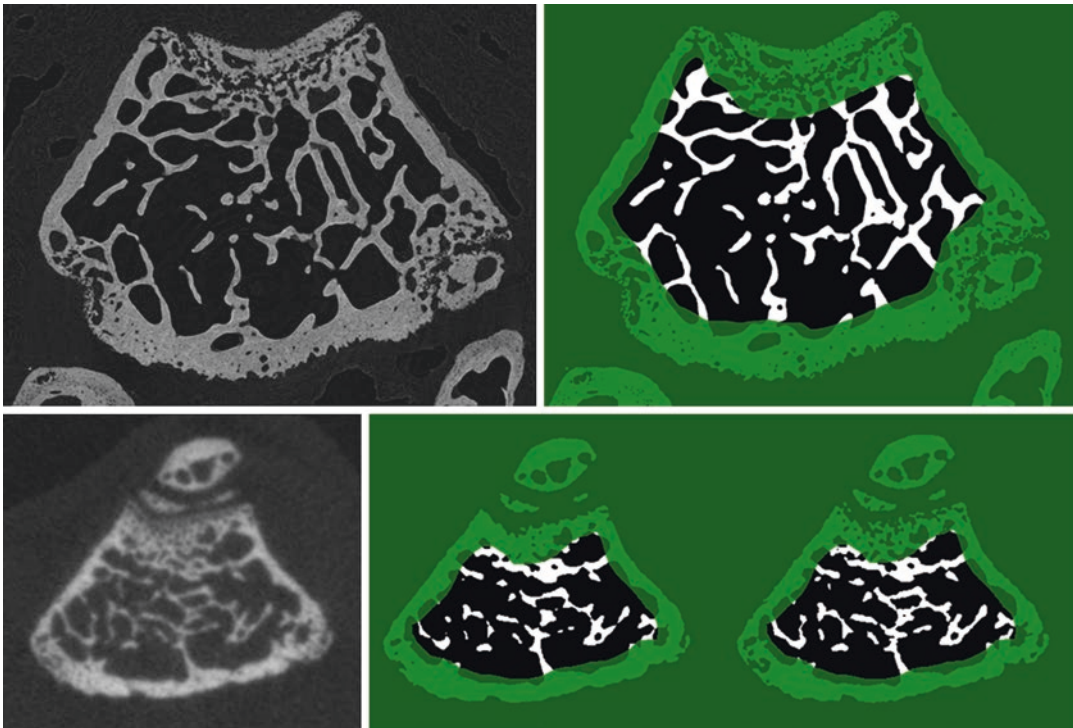


Fig. 5.5 Upper: high-resolution micro-CT images of murine trabecular bone (left) can be adequately segmented by global thresholding (right). Lower: lower-resolution fast (low-dose) in vivo scans produce images

(left) where some trabecular detail is lost during global thresholding (middle); this loss of detail is reduced by using adaptive local thresholding (right)

Analysis

Once the VOI is delineated and the segmentation (thresholding to binary) performed, 3D and 2D morphometric parameters can be calculated for the trabecular and cortical (determined by which VOI is set). True 3D analysis implies that a rendered 3D model is created (though not necessarily displayed) and analysis is performed in 3D space, which can be computationally intensive with large datasets. By contrast what can be called “pseudo-3D” analysis is where 2D image measurements are performed on individual cross sections delivering results in terms of perimeters and areas in 2D only but then integrated across multiple cross-sectional slices to give 3D parameters.

Noise objects if present in the binarised image can be removed by a “despeckle” (object labelling and size-related selection) and/or open and close morphological operations. Morphometric parameters in 3D are commonly based on analysis of a marching cubes [6] type model with a rendered surface. Calculations of all 2D areas and perimeters are based on either whole pixel-based calculations or a 2D-interpolated surface derived, for instance, by the 2D Pratt [14] algorithm of subpixel perimeter interpolation.

Morphometric parameters measured by Bruker-SkyScan CT-analyser have been validated on both virtual objects and aluminium foil and wire phantoms [15]. Structure thickness in 3D is generally calculated using the local thickness or “sphere-fitting” (double distance transform) method [6, 16, 17], and structure model index (SMI, an indicator of the relative prevalence of plates and rods) is measured according to the method of Hildebrand and Rueggsegger [18]. Degree of anisotropy can be calculated in a number of ways such as star lengths and volumes [19], the mean intercept method (MIL) [20] and local analysis of structure orientation by either triangular facet orientations from binary surface rendering or tensor analysis at the unbinarised greyscale level to find local anisotropy and orientation [21]. Euler connectivity can be calculated either by the 2D-based “Conneulor” method [22] or true 3D algorithms, e.g. [23]. Fractal dimension is often calculated in 3D by the Kolmogorov

(or Richardson) box counting method [24]. The definitions, symbols and units for bone morphometric parameters should follow the ASBMR standardised nomenclature [25]. A listing and brief description of the morphometric parameters applied to bone analysis is given in Table 5.2.

Recently the parameter SMI has been shown to be biased by porosity especially at high percent volumes [26] so that it departs from indicating ideal plate and rod structure (and can give confusing negative values due to concave surfaces). However if its limitations are understood, it can still be an informative parameter. It correlates closely with trabecular bone pattern factor, a parameter similarly calculated on the basis of the ratio of convex to concave surface curvature, but without the structure model assumptions of SMI [27].

An Alternative to SMI: The Un-rod Index

The shortcoming of the SMI parameter is that although the minimum SMI should be zero corresponding to a flat plate, in practice negative values can be measured due to concave surfaces arising from porosity [19]. Concave surfaces are not envisioned in the ideal “plate” and “rod” 3D shapes. An alternative parameter indicating departure from an ideal plate morphology is available which avoids this problem of out-of-range values. It can be called the “un-plate index” (uRi) and is calculated as the ratio of the structure’s thickness measured in direct 3D to the thickness derived by a 2D-based structure model. In 2D histomorphometry, thickness is estimated from surface and volume based on a formula assuming that the trabecular structures are either parallel plates or parallel rods [18]. Thickness assuming the plate model, Th_{plate} , is given:

$$Th_{plate} = \frac{2 \times BV}{BS}$$

where BS and BV are bone surface and volume, respectively. To estimate thickness assuming a parallel rod morphology, the 2 is simply substituted by 4, so that:

$$Th_{rod} = \frac{4 \times BV}{BS}$$

Table 5.2 The morphometric parameters quantifying the structure and architecture of trabecular and cortical bone, as imaged by micro-CT

Parameter name	Parameter symbol (ASBMR nomenclature)	Comment
Bone volume	BV	The total volume of trabecular bone within your VOI
Tissue volume	TV	The total volume of the medullary VOI. As well as being the referent for % volume, TV is a meaningful parameter in its own right, indicating endosteal expansion
Percent bone volume	BV/TV	Occupancy of trabecular bone in the medullary VOI
Bone surface to volume ratio	BS/BV	This is inversely proportional to thickness and indicates general complexity also
Trabecular thickness	Tb.Th	Average thickness
Trabecular separation	Tb.Sp	Average separation
Trabecular number	Tb.N	Spatial density—mean number of trabeculae crossed per mm of a transect through the VOI
Trabecular bone pattern factor	Tb.Pf	This is also called “surface convexity index”. It measures the ratio of convex to concave surface curvature. High connectivity between trabeculae causes more concave surface and thus lower (or more negative) values
Fractal dimension	FD	An index of overall complexity of architecture and surface topography
Degree of anisotropy	DA	The degree of preferential orientation of all structures in one 3D direction (stereo-angle). Use with caution for mouse trabecular bone since the small number of metaphyseal trabecular structures, especially in older mice, reduces the meaningfulness of this parameter
Connectivity density	Conn.D	The number of independent connections within a complex structure. It is a Euler parameter (Betti number β_1). Deterioration of trabecular architecture due to OVX, for example, can sharply reduce the number of connections

Now the “un-plate index” uPi is simply the thickness measured by micro-CT in direct 3D (Th) divided by the thickness estimate based on surface, volume and the parallel plate model, so that:

$$\text{un-Plate index } uPi = \frac{\text{Th} \times \text{BS}}{2 \times \text{BV}}$$

Likewise the “un-rod index” or uRi would be given:

$$\text{un-Rod index } uRi = \frac{\text{Th} \times \text{BS}}{4 \times \text{BV}}$$

To complete the full set of structure models, substituting 6 for 2 or 4 gives what might be called the “un-sphere index”, or uSi , degree of departure from sphere morphometry, such that:

$$\text{un-Sphere index } uSi = \frac{\text{Th} \times \text{BS}}{6 \times \text{BV}}$$

The un-plate index is also the ratio of surface areas between the real measured object and an “equivalent plate” with the same values of both volume and mean thickness. Likewise for rod or sphere. These un-shape indices, the un-plate, un-rod and un-sphere index, can be used beyond the morphometry of trabecular bone for analysis of any structure for departure from any one of these ideal shapes. The index is dimensionless.

5.3 Example 1: Trabecular and Cortical Bone Analysis for Osteoporosis and Bone Phenotyping

The metaphyseal trabecular bone in the femur or tibia of the rat or mouse is the most commonly used site for morphometric analysis of bone in preclinical rodent models. This applies both to

microscope histomorphometry and micro-CT morphometry. Here we will describe the method for first selecting an appropriate volume of interest (VOI) for trabecular bone in the metaphysis, including the method for standardising this VOI relative to the growth plate, and then the subsequent binarisation and 3D morphometric analysis of the trabecular bone.

5.3.1 Scan-Reconstruction

During reconstruction, beam hardening correction is perhaps the most important parameter to get right for reconstruction of bone scans. This will improve the accuracy of bone mineral densitometry based on X-ray attenuation. Having said that, the software beam hardening correction is approximate and imperfect, as mathematically it assumes the scanned object is a cylinder of a uniform single material. So an approximate beam hardening correction is the best one can do. Note that if bones are scanned with a thick layer of plastic or liquid or other medium (such as animal tissue or embedding resin) around them, you may have to add a further 10–20% to the beam hardening value since surrounding medium decreases the effectiveness of beam hardening correction [28]. This means that if accurate densitometry is an objective of your study, then scanning bones immersed in liquid, even alcohol, is not recommended as this will prevent effective software correction of beam hardening.

5.3.2 3D Orientation

The method of selection of the region of interest for trabecular bone includes setting distance along the bone in terms of number of cross-sectional slices. For this to be consistent between bone scans, it is necessary that the long axis of the bone is approximately aligned to the z -axis of the dataset, so that the cross sections in the XY plane are truly orthogonal to the bone axis—as shown in the image below.

Of course this has to be an approximate assessment, since long bones are not straight rods (very

few biological structures contain straight lines!). Instead they are significantly curved. You should establish for yourself a way of assessing if the bone's z -axis is orthogonal to the cross-sectional plane. If the bone is approximately aligned, then no reorientation is needed, and you can go on directly with the morphometric analysis. However if there is a departure from straight alignment, then it is necessary first to reorient the bone in the tri-axis view and then save a new copy of the dataset in the adjusted orientation. This process is illustrated above in Fig. 5.3 and can be done in software such as SkyScan DataViewer.

5.3.3 Volume of Interest

5.3.3.1 The Growth Plate Reference Level

In microscope-based bone histomorphometry and also in micro-CT morphometry, it is customary to use the growth plate as an anatomical reference in the setting of both trabecular and cortical volumes of interest. This makes sense biologically, since the growth plate is the location from which growing bone expands and extends longitudinally. The growth plate is the site of origin and extension of growing long bones and is the natural choice of an anatomical reference for trabecular and cortical regions of interest in long bones such as the femur and tibia of the mouse or rat.

So the method of micro-CT morphometry begins with the designation of a growth plate reference cross-sectional level. However, the growth plate is a convoluted structure (Fig. 5.6). How then does one identify a single cross section to be a reference of the growth plate?

To address that question, we can first look at cross-sectional images at four locations, showing the transition from below to above the growth plate cross-sectional plane, in Fig. 5.7. In these numbered images, number 1 is below the growth plate; the robust bony bridge in the centre is part of the epiphysis. Image 2 is the highest image in the dataset in which there is a continuous “bridge” of low-density growth plate (chondrocyte) seam,

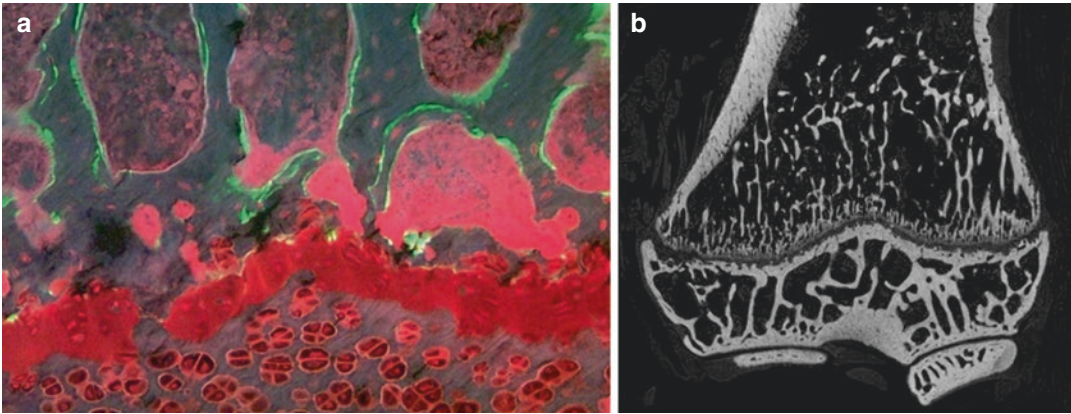


Fig. 5.6 The growth plate of a mouse tibia (a) viewed by microscope with epifluorescence after Villanueva staining which visualises both dynamic double labels (here both calcein) and also osteoid and marrow cells and (b) a rat

tibia micro-CT coronal image showing the growth plate. Both images show the convoluted shape of the growth plate

separating regions of trabecular bone right and left. If we go a little higher, this seam is broken by connections of bone, until the chondrocyte seam disappears from the cross section as in image 3. The bone in cross section 3 includes very fine “primary spongiosa” trabecular structures in the centre. If we now move higher “downstream” above the growth plate, we reach eventually a cross section where the fine-textured primary spongiosa disappears and all the trabecular bone is of the mature “secondary spongiosa” type, as shown in image 4.

Image 2 in Fig. 5.7 shows the first—or last—connection of the low-density chondrocyte seam, depending on from which side you approach the growth plate; this is the level we use where possible as the growth plate reference level.

Note that the growth plate in cross section has different structure in the rodent tibia and femur. In the tibia it appears as two “islands” separated by chondrocyte seams, while in the femur there are four such islands (Fig. 5.8). However the principle of setting the reference level as the highest level (in the direction towards the mid-shaft), where there is an intact bridge of chondrocyte seam, works equally in both tibia and femur. If however the rodent is old and the chondrocyte seam in the growth plate is almost absent, then a reference level can be obtained alternatively from

the bony bridge that is lower than (on the epiphyseal side of) the original chondrocyte seams of the original growth plate. This is shown in Fig. 5.7 (image 1) and in Fig. 5.8b.

The cross-sectional level where the fine-textured primary spongiosal trabecular bone has disappeared and only more robust remodelled secondary trabecular bone is present (Fig. 5.7, image 4) corresponds to the level above which we would analyse the morphometry of trabecular bone. Here is the level where our trabecular volume of interest would begin. By contrast, image 3 contains in the centre regions of fine-textured primary spongiosal trabecular bone and should not be included in the volume of interest for morphometric analysis of trabecular bone.

So in summary, a reference cross-sectional level at the growth plate should be selected based on a visibly identifiable criterion such as the appearance of a bridge of either unmineralised chondrocyte seam (young growing rodent) or an epiphyseal bony bridge (aged rodent). This way of choosing a reference level works both in the femur and the tibia, of both the rat and mouse. In old rodents the chondrocyte growth plate is almost gone. Here the corresponding bony bridge a little further in the epiphyseal direction provides an alternative location criterion for the growth plate reference.

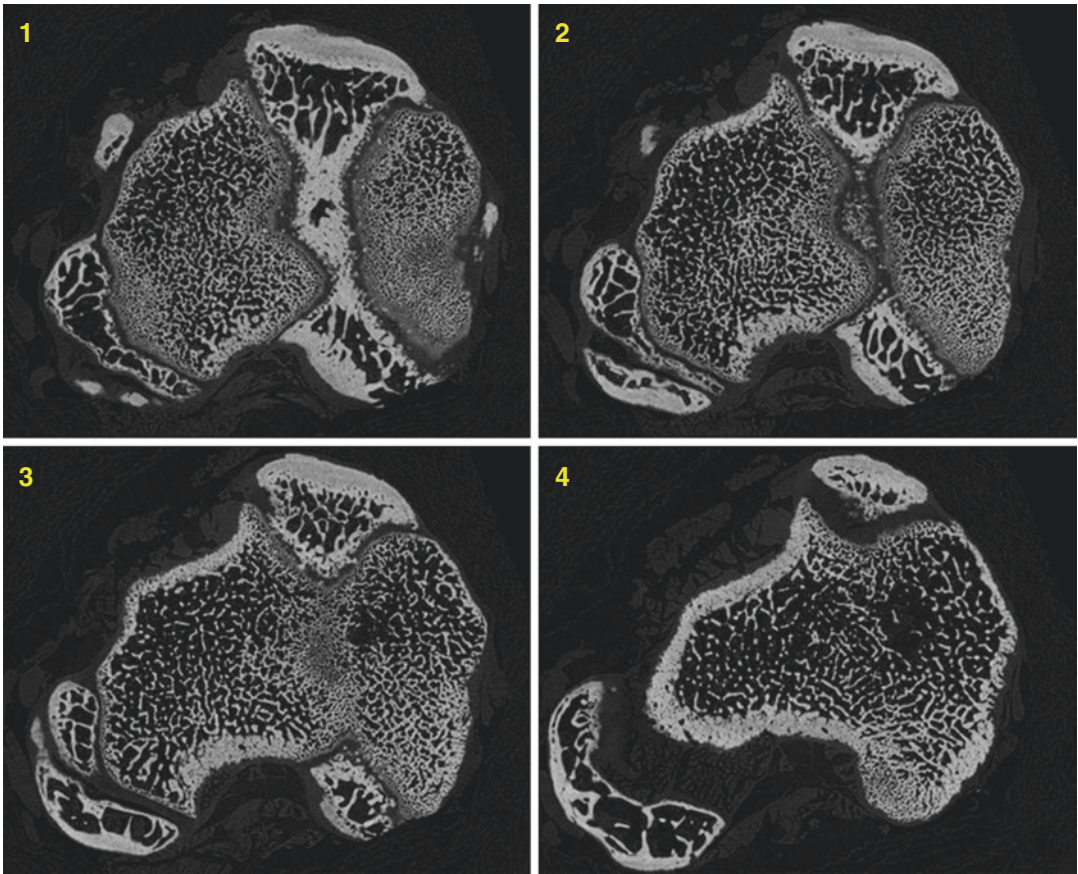


Fig. 5.7 Cross-sectional images across the growth plate, starting below the growth plate in the epiphysis (1); the highest level showing a low-density chondrocyte seam “bridge” across the cross-section, used as the growth plate reference level (2); a higher level just above the growth

plate showing fine-textured primary spongiosal trabecular bone (3); and finally, higher still, beyond the primary and into the secondary, thicker and remodelled trabecular bone (4) which is where morphometric analysis is carried out

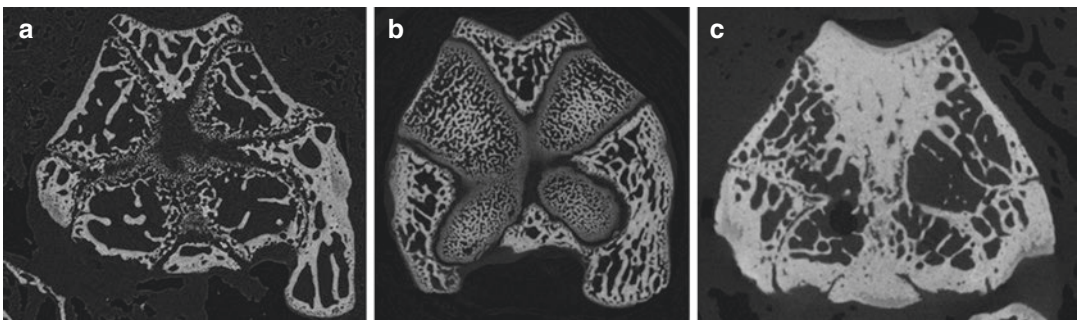


Fig. 5.8 The growth plate in cross section of the femur, in the mouse (a) and rat (b), shows four “islands” surrounded by growth plate structures, in contrast to the tibia where there are two such islands (Fig. 5.7). The bridge of chondrocytes demarks the reference level in both femur and tibia. In old rodents, especially mice (c) the growth

plate is vestigial without chondrocyte seams; in such cases a bridge of bone just below (on the epiphyseal side of) the growth plate can be used as an alternative structure to define the growth plate reference level for morphometric analysis

5.3.3.2 The Offset and the Height

Once the growth plate reference level is selected, then the range of cross-sectional slices to be analysed for trabecular and cortical bone can be defined relative to this level. Both the trabecular and the cortical volumes of interest begin a certain distance on the metaphyseal side of the growth plate reference level. If we are analysing the micro-CT scan in the cross-sectional plane, then this distance is defined as a number of cross-sectional slices that we move in the z direction, before commencing the analysis of trabecular or cortical bone. This number of slices is referred to as the “offset”. It is illustrated in Fig. 5.9. For trabecular bone the offset is around 0.2–0.4 mm for mice and about 0.4–1.5 mm for rats. The analyst should select the offset distance as the distance needed to move clear of most of the fine-textured primary spongiosal structures near the growth plate into a metaphyseal region dominated by more mature (and remodelled) secondary trabecular structures. For cortical bone, a longer offset of several millimetres is needed to move into a region where the metaphysis merges into the diaphysis (mid-shaft) and the cortical bone is thick and intact. Note this can be within a few mm of the growth plate and it does not need to be at the actual mid-shaft of the bone. Cortical bone near the metaphysis-diaphysis boundary is more metabolically active than that at the mid-shaft, so analysis in this region will show effects of the experimental treatment or genetic modification more sensitively than at the mid-shaft.

Also shown in Fig. 5.9 is the “height”—the length along the bone’s long axis of the volume of interest to be analysed. The offset and height are defined both as a number of cross-sectional slices and as the corresponding distance in mm. The height of the trabecular VOI should be enough to encompass the majority (not necessarily all) of the metaphyseal mature secondary spongiosal trabecular bone. If one is scanning with a pixel size around 5 microns, this is typically 200–400 cross-sectional slices. Note however that in some experiments including ones involving ovariectomy, the distance that trabecular bone extends along the metaphysis towards the diaphysis (mid-shaft) can vary significantly.

This extent will be shorter by as much as half in ovariectomised mice and (especially) rats, compared to sham operated or intact controls. In such cases, the height should be determined by reference to the sham or intact controls—to correspond to the maximum extent of trabecular bone along the metaphysis (in other words—the length of the metaphysis itself). This will give a more sensitive detection of difference in the amount and architecture of the trabecular bone. It will however result in the VOI for analysis of ovariectomised (OVX) rodents consisting of a significant amount of empty space. This fact should be kept in mind when interpreting the experimental results. For instance, when reporting trabecular thickness and separation (Tb.Th, Tb.Sp), it is useful to also report the measured standard deviations of both these parameters, to give an idea of the homogeneity or heterogeneity of the thickness and separation. These Tb.Th and Tb.Sp SD values are reported together with those parameters in SkyScan CT-analyser.

5.3.3.3 How to Adjust the Offset and Height for Different Age, Strain, Gender and Phenotype?

A question that follows from the discussion of offset and height is: how do you find the correct value—in distance, mm, and in number of cross-sectional slices—of the offset and height in mice of different age, gender, strain and genetic type? As mentioned above, visual inspection can allow determination of the offset needed to “skip” the growth plate-related primary spongiosa structures and the height needed to encompass the majority of the metaphyseal trabecular bone. Within a single study comparing similar animals, a single value of offset and height can be chosen that is suitable for all the studied animals, even if “compromise” values are needed to allow for some variation in bone size and shape.

However in some studies, the variation in size and architecture of the bone is too great to allow a single value of offset and height to be used for all animals. The differences are too large for a compromise value to work. An example is studies of mice or rats at different ages or lifespan studies, where the femurs and tibias of neonatal and

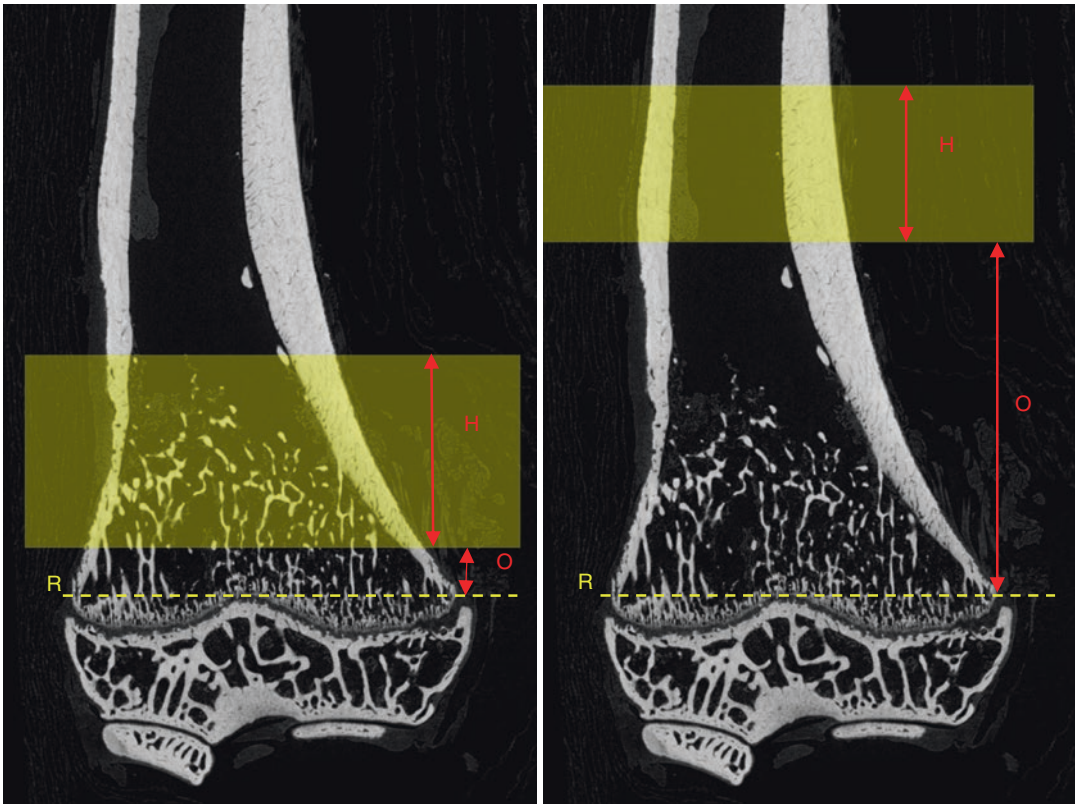


Fig. 5.9 The selection of the volume of interest of trabecular (left) and cortical (right) bone. The example shown is a rat femur, but the principle applies to the mouse also. R, reference level (growth plate); O, the offset,

required to move clear of fine primary spongiosal trabecular bone, defined as distance and number of cross sections; H, the height of the VOI to be analysed, also defined in distance and number of cross sections

juvenile animals are much shorter than those of adults—but bones of both are to be studied and compared morphometrically. In the case of such a study starting with neonates and continuing to old age, how would offset and height be determined?

One solution that has sometimes been proposed in this situation is to scale the offset and height with the length of the femur or tibia, thus with small values for young animal and larger distances for adults. However this simple scaling to length is wrong. It does not result in an equivalent adjustment. The size that is important here is not the size of the whole bone but the size of the growth plate. One must bear in mind that the growth plate is the central reference for metaphyseal bone morphometry, both as a structure and with regard to its role in causing the growth,

shape and architecture of the bone. As the animal grows to adulthood and then progresses to old age, the size of the whole bone and the size of the growth plate move in opposite directions. The bone gets longer, but the growth plate gets smaller and narrower. The size of the growth plate is correlated to the *rate* of bone longitudinal growth at that moment in time (not the size or length of the bone). Growth rate diminishes in growing mammals; thus the growth plate is thickest (has its greatest length in the direction of the bone's long axis) in infancy and becomes thinner with growth and increasing age. Once old age is reached—about a year—the growth plate in mice can be almost non-existent. Rat growth continues further into old age than that of mice. But in both rodents, the thickness of the growth plate's central columnar layer of bone-forming chondrocytes,

and of the downstream primary spongiosa, decreases with age as the growth rate decreases.

Therefore with increasing age and size in both rat and mouse bones, the value of the offset needs to become less, not more. Recent unpublished work (Behzad Jahaveri and Andy Pitsillides, Royal Veterinary College, London, UK) has shown that for morphometry at the mouse tibia (BL6-based mice) from ages of juvenile (2 months) till about 6 months, the offset found by visual inspection to clear the primary spongiosal layer has a fairly fixed value of 0.3–0.35 mm (or 60–70 cross-sectional slices at a typical 5 micron pixel size in micro-CT imaging). By 12 months all the way to end of life at around 20 months, the effective offset distance was found to hold steady at the lower value of about 0.2 mm (40 cross-sectional slices at the same 5 micron pixel).

5.3.4 Segmentation and Analysis

Most or all of the parameters described above in Table 5.2 can be analysed for descriptive morphometry of the metaphyseal trabecular bone in

the tibia and femur. A study that nicely illustrates the application of 3D trabecular morphometry in a preclinical bone biology study is the demonstration in ovariectomised rats of an additive effect of the steroid sex hormones oestrogen and testosterone [29]. Here Tivesten et al. showed that while both oestrogen and testosterone have a protective effect minimising ovariectomy-associated osteopenia (oestrogen having the stronger effect of the two), the combined administration of both sex steroids resulted in a bone volume-enhancing effect bigger than either sex steroid, apparently additive. The effect of the sex steroids on the rat trabecular bone volume is shown in Fig. 5.10a. In Fig. 5.10b, the structure model index (SMI) parameter values from this same study are shown. The problem of SMI manifests itself in the high bone volume group where both sex steroids are administered—here the average SMI is negative. By contrast, in Fig. 5.10c where the parameter un-plate index, uPi, described above is calculated, the same restoration of plate-like architecture is indicated but without the problem of out-of-range values. Thus in this case the un-plate index uPi serves the objective of indicating departure from plate-like

Fig. 5.10a From Tivesten et al. (2004) [29]: oestradiol (e2) has a stronger protective effect on OVX than dihydroxytestosterone (dht), while both steroids together exert an additive effect. *Different from the OVX + V (vehicle) group with $p < 0.05$; ** different from the OVX + V group with $p < 0.005$. (Reproduced with permission)

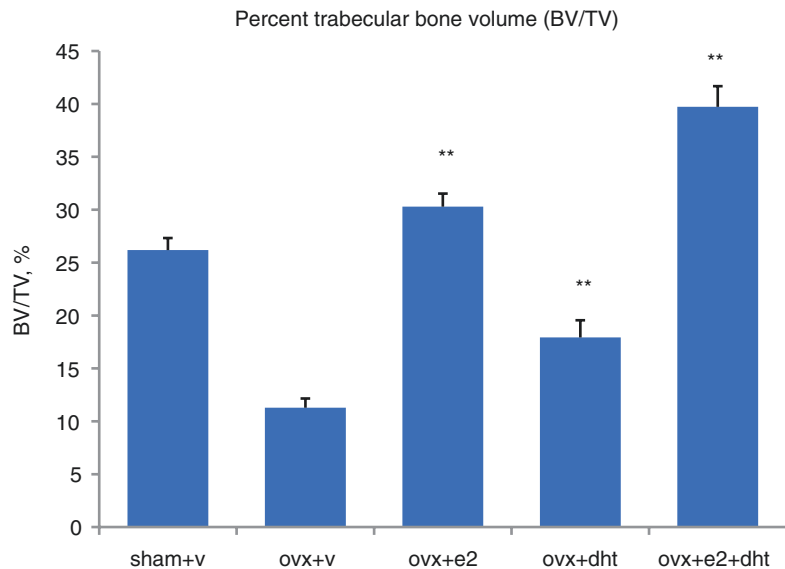


Fig. 5.10b The SMI values from the rat OVX study by Tivesten et al. [29] illustrate the problem with the SMI parameter at high percent volumes. The enhanced bone volume from the additive protection of oestradiol and testosterone results in a negative SMI value. *Different from the OVX + V (vehicle) group with $p < 0.05$; ** different from the OVX + V group with $p < 0.005$. (Reproduced with permission)

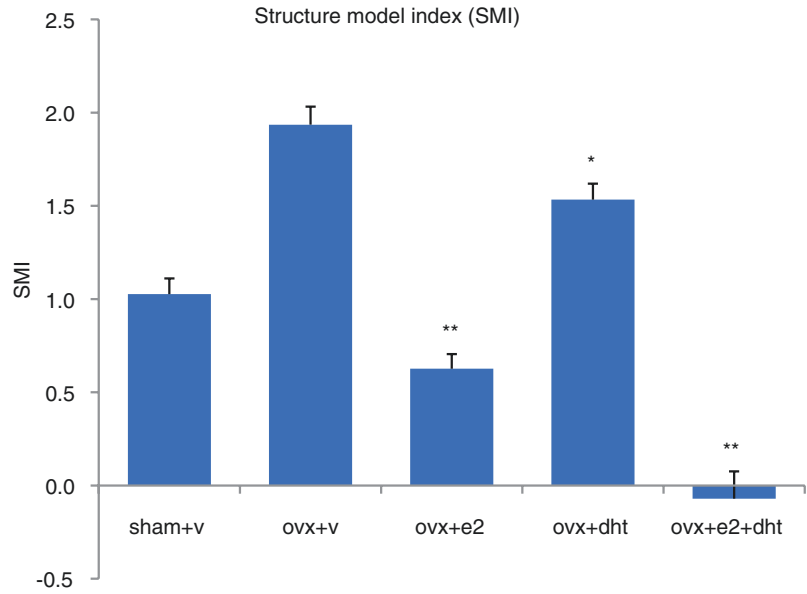
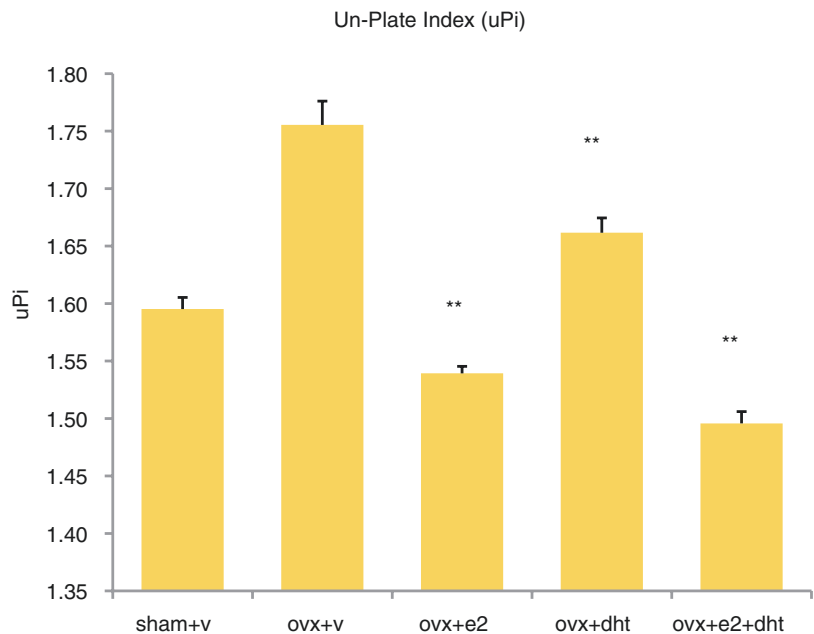


Fig. 5.10c The un-plate index uPi applied to the Tivesten rat OVX study avoids the “out-of-range” problem of the SMI parameter, indicating different degrees of restoration of plate-like structure from oestrogen, testosterone treatment or both combined. *Different from the OVX + V (vehicle) group with $p < 0.05$; ** different from the OVX + V group with $p < 0.005$. (Reproduced with permission)



architecture without the problem associated with the SMI parameter of being confounded by porosity at high percent volumes. uPi would appear to be an acceptable alternative to SMI in such studies of trabecular morphometry in rela-

tion to osteoporosis. (Since uPi is calculated as a simple formula of thickness, surface area and volume, it can be calculated retrospectively for most micro-CT studies where these values will have been measured.)

5.4 Example 2: Collagen-Induced Arthritis (CIA) at the Mouse Ankle—Bone Damage

It must be emphasised that micro-CT bone morphometry can be applied much more widely than just to the study of osteoporosis in ovariectomy or orchidectomy—or indeed beyond standard trabecular and cortical phenotype characterisation at the long bone metaphysis and diaphysis. Another preclinical disease model that has been successfully characterised by micro-CT morphometry is the collagen-induced arthritis (CIA) model in the mouse ankle. The analysed site is different here—the protruding heel bone or calcaneus—so a different methodology is needed. However the “pipeline” approach of scan—align—volume of interest—analyse is again a sufficient basis for the analysis method. It is described for the CIA model in Table 5.3.

CIA results in generalised disruption to the foot and ankle of the mouse, including pathological periosteal structures (fine, trabecular-like) which are referred to alternatively as “periosteal reaction” or “roughage”. These are illustrated in Fig. 5.11. The ankle is a complex bone site with many bones in close contact. The calcaneus is fully involved in the changes resulting from CIA but has the advantage that the distal part of it is

sticking out, separate from surrounding bones, and thus being easier to select within a VOI. Where possible, a VOI should be chosen that is easier, rather than more difficult, to delineate. Studies by Seeuws et al. [30] and Quan et al. 2016 [31] employed micro-CT analysis of the distal part of the calcaneus to quantify arthritic changes in murine models of collagen-induced arthritis.

5.5 Example 3: Bone Tumour Metastasis Damage in the Tibial Metaphysis

Bone tumour metastatic damage can include both osteolysis (destruction of bone) and pathological reaction structures similar to those seen in the CIA arthritis model described just above. Since it is the metaphysis, one might think that a region could be selected by reference to the growth plate, as described above (example 1) for osteoporosis morphometry of the tibia or femur. However tumour damage is sometimes so extensive that part or all of the growth plate is missing. Therefore a simpler reference protocol is needed that can be just counting cross-sectional slices from the end of the tibia (condyles) articulating with the femur. This allows a standardised region of metaphysis to be analysed for tumour-related

Table 5.3 The micro-CT morphometry pipeline for the assessment of bone damage in the murine CIA model of arthritis applied at the calcaneus (heel) bone

Stage	Description
1. Scan-reconstruction	<ul style="list-style-type: none"> Standard scan and reconstruction method and parameters for mouse bone If in vivo, the leg is supported in a tube as shown in Fig. 5.2, but the foot and ankle are scanned, not the knee. (Soft dental wax used to hold the foot secure is sufficiently X-ray transparent so as not to interfere with scanning)
2. Orientation in 3D	<ul style="list-style-type: none"> Rotate in DataViewer with respect to the calcaneus, so that the calcaneus long axis aligns with the dataset z depth axis
3. Volume of interest	<ul style="list-style-type: none"> Select a fixed number of cross-sectional slices, starting from the protruding tip of the calcaneus and stopping before the calcaneus comes into apposition with surrounding ankle bones such as the tarsus. Use an auto-wrap function such as “shrink-wrap” in SkyScan CTAn to delineate the boundary, stretching over holes as necessary over irregular peripheral structures with a distance transform or convex hull function
4. Segmentation-analysis	<ul style="list-style-type: none"> Segmentation (binarisation) and morphometry (adaptive local thresholding can be helpful) Calcaneus bone disruption by arthritis may be reflected in a change to the following parameters: surface to volume ratio, thickness, trabecular pattern factor, un-plate index, fractal dimension, connectivity Visualisation by volume or surface rendering assists in illustrating disease or treated state

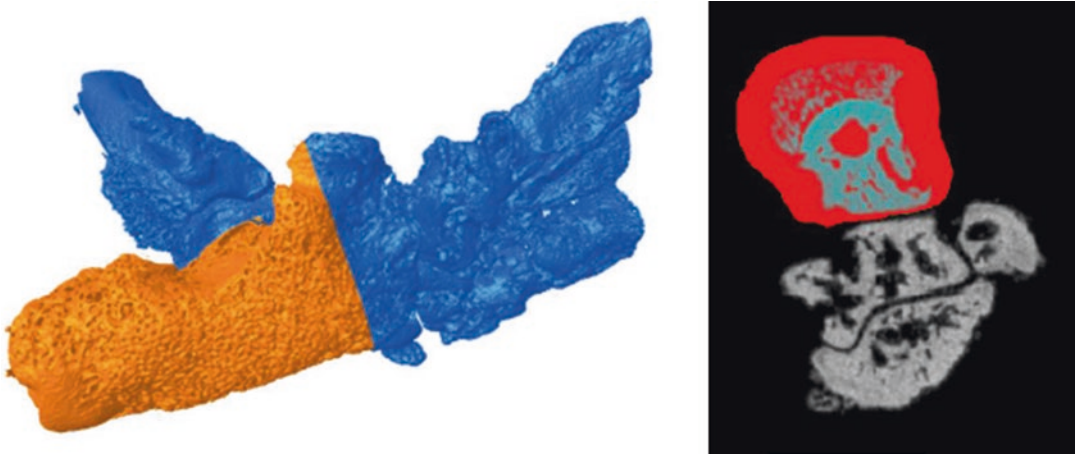


Fig. 5.11 The selected distal portion of the calcaneus is illustrated in the rendered image on the left; the volume of interest selection in the cross-sectional plane of the aligned calcaneus is shown to the right

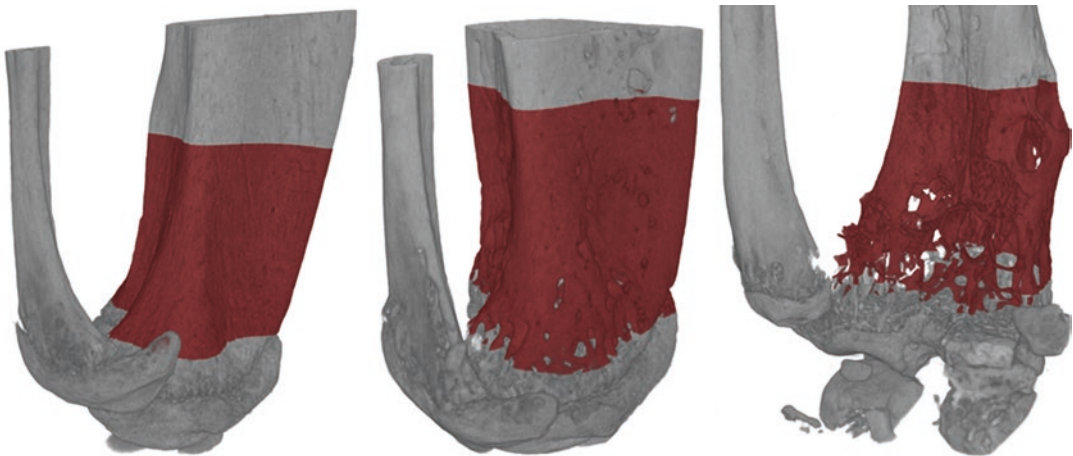


Fig. 5.12 Mouse tibial metaphyseal damage caused by tumour metastasis: a normal (left), slightly affected (centre) and severely affected case (right). The red highlighted region is the VOI, selected relative to an end-of-bone ref-

erence such as the first appearance of tibial bone in a cross-section. Or the first joining of the two condyles in a cross section

bone disruption in all animals in an experiment. The “pipeline” table for morphometry of a mouse tibial bone tumour metastasis model is given below in Table 5.4. Studies illustrating the use of micro-CT morphometry to characterise tumour damage to the tibia in a mouse model include Chantry et al. (2010) [32] Cox et al. (2015) [33] and Kassen et al. (2016) [34].

The parameters of bone morphometry that can be informative for bone tumour damage are

more or less the same as those for arthritis bone disruption and the fracture callus. Indices of complexity and connectivity can be indicative of tumour damage. For cortical bone, the parameter Euler connectivity corresponds almost entirely to porosity since fully intact cortical bone has connectivity of 1. The number of Euler connections almost equals the number of pores or perforations. Note—however—if you use connectivity to indicate number of perforations, it is essential

Table 5.4 The micro-CT morphometry pipeline for a murine bone tumour metastasis model of arthritis applied at the calcaneus (heel) bone

Stage	Description
1. Scan-reconstruction	<ul style="list-style-type: none"> Standard scan and reconstruction method and parameters for mouse bone If in vivo, the knee is scanned the same as for osteoporosis
2. Orientation in 3D	<ul style="list-style-type: none"> Rotate in DataViewer so that the tibial long axis aligns with the dataset z depth axis
3. Volume of interest	<ul style="list-style-type: none"> Using the condylar end of the tibia, select a fixed number of cross-sectional slices to delineate the entire metaphyseal region where tumour damage is typically prevalent (see Fig. 5.12). Use an auto-wrap function such as “shrink-wrap” in SkyScan CTAn to delineate the boundary, stretching over holes as necessary over irregular peripheral structures with a distance transform or convex hull function
4. Segmentation-analysis	<ul style="list-style-type: none"> Segmentation (binarisation) and morphometry Tumour bone disruption by metastasis may be reflected in a change to the following parameters: surface to volume ratio, thickness, trabecular pattern factor, un-plate index, fractal dimension, connectivity Visualisation by volume or surface rendering assists in illustrating disease or treated state

to run a prior despeckle operation to remove both black and white small noise dots from the image, which would otherwise contribute a noise signal to the measurement of perforation number.

5.6 Example 4: Cartilage Status in an Arthritis Rodent Model

The micro-CT morphometric pipeline approach is not limited to bone. It can be applied to the measurement of cartilage thickness in a rodent knee. Visualisation of cartilage requires staining with a contrast agent such as phosphotungstic acid (PTA). A PTA-stained mouse knee is shown in Fig. 5.13, also indicating regions of medial cartilage at both the femur and tibia condyles that are selected as VOIs for analysis. How are these VOIs chosen? The pipeline approach works again for this. First the scanned knee joint is aligned. Again, as in above examples, we look for regions of cartilage that are if possible easier to delineate. Scrolling through coronal sections, one finds the coronal level where the medial articular cartilage layers on the tibia and femur separate from being in contact. About 50 cross-sectional slices away from this separation (5 micron pixel), the two articular cartilage layers are well separated and straightforward to delineate as VOIs, as shown in Fig. 5.13. The pipeline analysis workflow for this articular cartilage analysis is given in Table 5.5.

5.7 Example 5: The Fracture Callus and Fracture Healing

Following experimentally induced fracture at a site such as the long bone mid-shaft, a callus forms which is then gradually remodelled as the fracture heals. The early fracture callus is a low-mineralised and fine-textured structure which is morphometrically very distinct from the cortical bone out of which it arises. The fracture region itself is often a complex mix of intact cortical bone, dissociated cortical bone fragments and callus at different stages of remodelling. The morphometric analysis of callus and its progression is similar in some respects to the above examples 2 and 3, that is, bone damage and pathological reactive growth caused by arthritis and bone tumour, respectively. Both of these bone disease models as well as the fracture callus can be considered as models of bone disruption requiring the morphometric measurement of this disruption.

5.7.1 The Fracture Midplane

For a mid-shaft long bone fracture such as of the guillotine type, it is possible to identify a midline—or more correctly a midplane—orthogonal to the axis of the long bone and representing the plane of the fracture. Of course, fractures are rarely orthogonal precisely to the long axis. The fracture plane can be at an oblique, and indeed

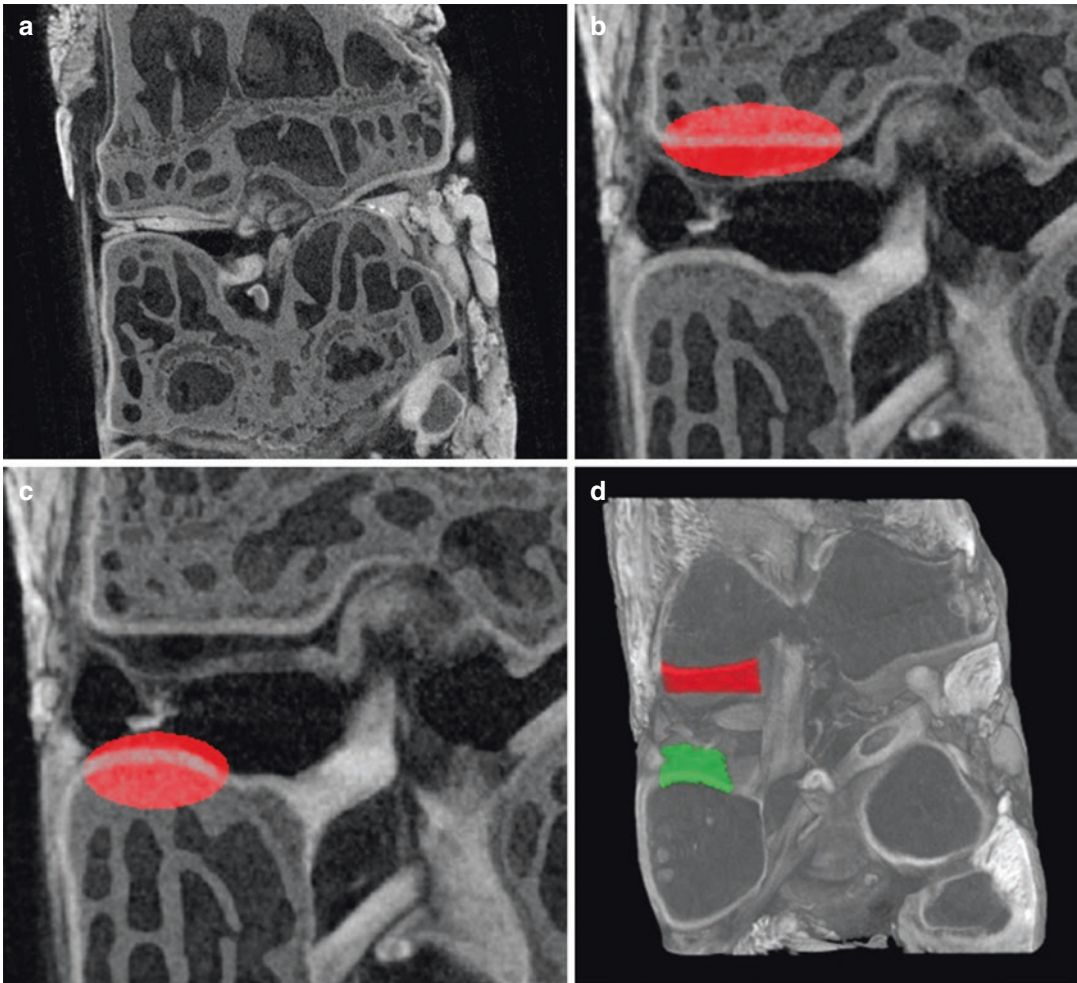


Fig. 5.13 (a) The mouse knee PTA-stained shows articular cartilage in contact at the medial condyles. (b) The femoral and (c) the tibial articular cartilage 50 cross sections displaced from the level of last apposition (a); and (d) a volume rendered model of the VOI-selected cartilage regions

Table 5.5 The micro-CT morphometry pipeline for murine knee articular cartilage thickness and roughness measurement from PTA-stained micro-CT imaging

Stage	Description
1. Scan-reconstruction	<ul style="list-style-type: none"> Standard scan and reconstruction method and parameters for mouse bone, possibly with increased filter or voltage to allow for extra X-ray opacity from the PTA staining
2. Orientation in 3D	<ul style="list-style-type: none"> Rotate in DataViewer so that the knee long axis aligns with the dataset z depth axis
3. Volume of interest	<ul style="list-style-type: none"> In a coronal view, find the slice moving top to bottom where the condylar cartilage at the medial side separates from contact. A fixed number of slices from this level, select a volume of cartilage defined by a number of cross-sectional slices and a fixed VOI shape such as an oval or rectangle (see Fig. 5.13)
4. Segmentation-analysis	<ul style="list-style-type: none"> Segmentation (binarisation) and morphometry Measure thickness of the cartilage Measure roughness of cartilage as SD of thickness, FD or Tb.Pf.

there can be multiple and branching fracture planes. Thus some visual approximation is needed to assign a cross-sectional plane to serve as a mid-fracture reference. Viewing 3D-like visual models of the fracture region using techniques, such as volume rendering or maximum intensity projection, can help to identify the fracture midplane (see the method given in Table 5.6).

Note that, as always with morphometric analysis of a long bone, the analysis should start with checking that the cross-sectional micro-CT reconstructed dataset has its cross-sectional plane orthogonal to the bone's long axis. If the long axis is not orthogonal but oblique to the cross-sectional plane (such that the bone cross section is seen to move position as one scrolls through the micro-CT scan slice by slice), then the realignment procedure described above should be performed, before commencing the analysis with setting the volume of interest.

Table 5.6 The micro-CT morphometry pipeline for a model of bone fracture callus remodelling and fracture healing

Stage	Description
1. Scan-reconstruction	<ul style="list-style-type: none"> Standard scan and reconstruction method and parameters for rodent or large animal bone (if no metal parts are present) If implants or fixators made of metal are present, then the micro-CT scan will require strong X-ray filtration such as with a copper-containing filter and a high applied voltage. Analysis can be challenged by artefacts caused by metal objects adjacent to bone
2. Orientation in 3D	<ul style="list-style-type: none"> Rotate in DataViewer so that the long axis of the bone with fracture aligns with the dataset z depth axis
3. Volume of interest	<ul style="list-style-type: none"> First identify the fracture "midline"
4. Segmentation-analysis	<ul style="list-style-type: none"> Segmentation (binarisation) and morphometry Fracture status and degree of callus remodelling may be reflected in a change to the following parameters: surface to volume ratio, thickness, trabecular pattern factor, un-plate index, fractal dimension, connectivity, degree of anisotropy Visualisation by volume or surface rendering assists in illustrating disease or treated state

Once a cross-sectional slice is assigned as the reference, corresponding to the midplane of the fracture, then the setting of the range of cross-sectional slices to serve as the VOI (volume of interest) can be as simple as selecting a fixed number of cross sections both above and below this reference plane. This is illustrated in Fig. 5.14.

Delineation of the VOI requires defining the periphery of the callus in the cross-sectional plane, as well as defining the number of slices. The perimeter of a complex and porous structure can be delineated using automatic wrapping methods such as the distance transform-based "shrink-wrap" in SkyScan CTAn and as described above in the analysis of bone disrupted by arthritis and tumour (examples 2 and 3, respectively).

Once the callus VOI is defined, the next stage, segmentation, can be particularly challenging in fracture callus images. This is because thick cor-

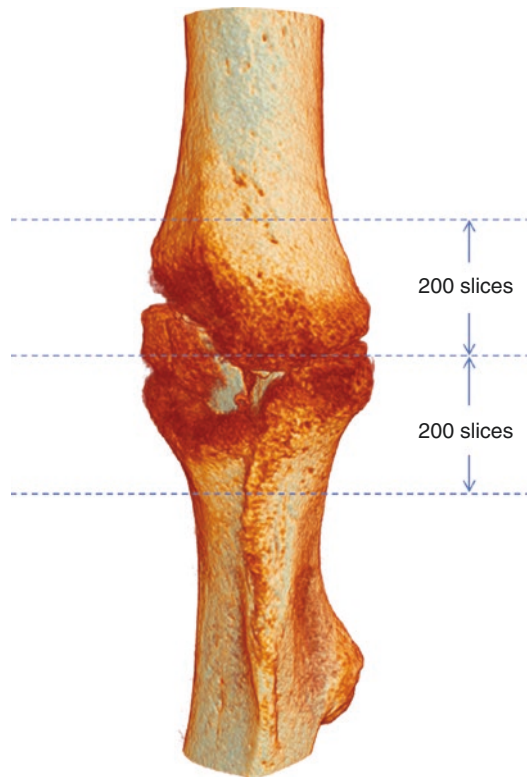


Fig. 5.14 Analysis of fracture of a long bone (orthogonally aligned) can employ a VOI defined as a fixed number of slices (here 200) on both sides of a cross-sectional slice corresponding by visual inspection to the average fracture midplane

tical bone and thin callus structures are closely associated. When fine-textured structures such as callus are close to the resolution limit, their attenuation and thus image greyscale are reduced artificially due to surface gradients. Therefore if looking for a simple global threshold, different thresholds are needed for the thin and thick structures. This problem is illustrated in Fig. 5.15. A global threshold suitable for the trabecular-like callus structures is too low for the cortical structures, causing expansion of the binary image and loss of porous voids. Conversely, a threshold suitable for the thick cortical structures will fail to binarise the thinnest callus structures whose resolution-affected greyscale falls below this threshold. (This problem was also discussed above in under “Segmentation and Analysis” and in Fig. 5.5.) A solution to this problem is also shown in Fig. 5.15 by the use of local adaptive

thresholding, where the thresholds applied to dataset voxels are adapted dependent on voxel greyscales in the spherical vicinity of the voxel in question. This has the effect of reducing thresholds near to thin structures and increasing it near to thick structures. Figure 5.15 shows that the adaptive thresholding—in this case the “mean of minimum and maximum” variant in SkyScan CTAn—effectively thresholds both thin callus bone structures and the porous structures within much thicker cortical bone. Improved thresholding of both the fractured cortical bone and the reactive callus will improve the accuracy of the morphometric analysis of the fracture callus as a whole.

Morphometric analysis of the segmented fracture callus does not necessarily require region separation of the callus from the cortical bone. This can be complex and time-consuming. One

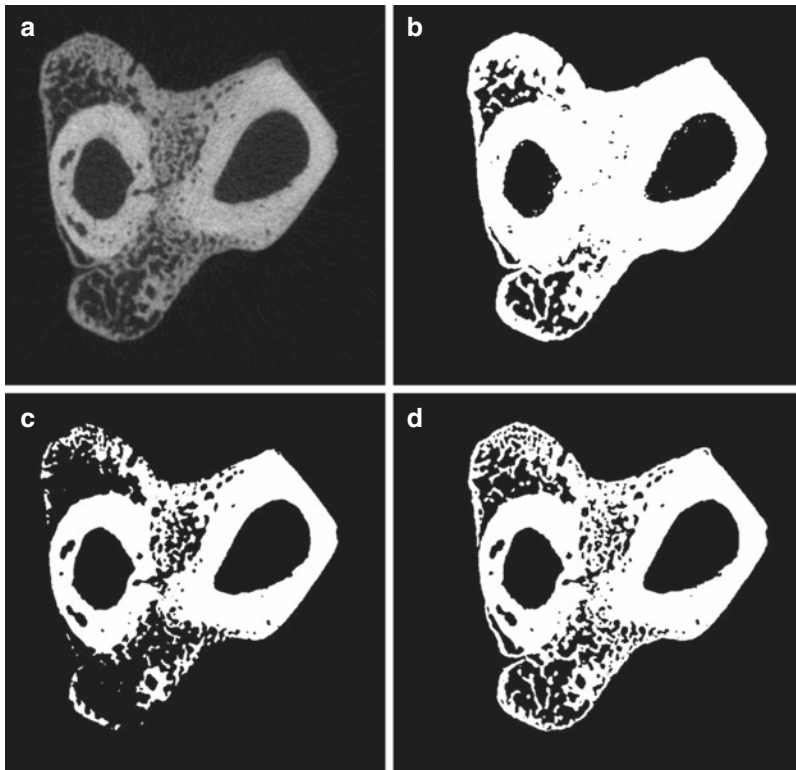


Fig. 5.15 Fracture callus at the rabbit forearm (radius and ulna), greyscale reconstructed cross section (a). Segmenting both thin callus and thick cortical structures presents a challenge; a low global threshold set to segment the thin callus structures (b) obliterates porosity detail in the thicker bone regions such as between radius and ulna.

Conversely, a high threshold set to correctly segment porosity at regions of higher percent bone volume and thickness (c) results in substantial loss of thin callus structures from the binary image. Local adaptive thresholding (d) solves this problem by accurately segmenting both thin and thick structures in the same image

can take advantage of the massive difference in morphological texture between callus and cortical bone. Callus structures are thinner and form a complex labyrinthine lattice with much higher values of parameters relating to complexity and connectivity, such as fractal dimension, trabecular bone pattern factor and Euler connectivity. In the analysis of a VOI containing a mixture of cortical bone and callus, these complexity-related parameters can be considered as a “morphometric signature” of the presence of callus. They will sensitively indicate the prevalence of callus without the need to separate regions of callus and pure cortical bone.

Studies employing micro-CT morphometry of rodent fracture callus models include McDonald et al. (2008) [35] and Jeyabalan et al. (2013) [36].

5.8 Concluding Comments

In the foregoing we have seen that the micro-CT 3D morphometric analysis of a wide range of bone disease model experimental outcomes can be reduced to a common series of steps. These are described as an analysis “pipeline” for pre-clinical quantitative assessment of bone models by micro-CT. First the scan should be done following normal principles for optimising image quality and, in the case of *in vivo* scanning, minimising radiation dose. Next comes “straightening out” the dataset, that is, adjusting 3D orientation in space so all datasets have standardised spatial direction.

After this is the all-important step of setting the volume of interest (VOI). The VOI defines the meaning of the measured parameter—for instance, if the bone is trabecular or cortical, or calvarial, or vertebral, etc. The complexity and asymmetry of biological structures mean that VOIs need to be delineated by careful reference to an anatomical reference location, such as the growth plate in long bones and the end plates of vertebrae. The accuracy, consistency and appropriate selection of the VOI will have at least as much impact on the quality of a study’s morphometric data, as the resolution and quality of the micro-CT images on which the analysis is per-

formed. Thus it is important that sufficient attention is paid to the VOI delineation process in all preclinical studies. (The question “what VOI will we use” should arise in initial planning of a study involving micro-CT morphometry.) In practical terms, it is also the stage that will take the analyst—whether a principal investigator or a technician—the most time to carry out of all the steps in the analysis process (with the possible exception of the micro-CT scan itself).

The final step of the process is the measurement of 3D (and 2D) morphometric parameters. This step can be largely automated and requires little operator time. Although there is a long list of morphometric parameters available, not all need to be employed in any particular study. The meaning and utility of most generally used morphometric parameters are discussed above.

There has been a tendency in the published literature on preclinical bone research for micro-CT morphometric analysis to be confined to the simple parameters of bone volume and thickness and possibly surface area. Relatively few studies include parameters of complexity, surface curvature and connectivity. This represents potentially an underutilisation of the value of 3D structural image data obtained by micro-CT imaging of bone disease models, as there are many more architectural parameters that can be informative. Part of the reason for this use of the basic parameters only is an argument that has been advanced in the bone micro-CT research community that in analysis of trabecular bone, many of the more apparently esoteric parameters (anisotropy, SMI, trabecular pattern factor, connectivity, fractal dimension, etc.) are strongly and linearly dependent on percent bone volume. Thus the argument has been made that these parameters—while interesting aspects of 3D morphology and topology—add little to the analytical power of the study.

This argument might have some truth in the analysis of long bone metaphyseal or vertebral trabecular bone for assessing osteopenia. But even here it is questionable—for instance, percent trabecular volume can change with or without changes to average trabecular thickness, depending on the bone site and biochemical cau-

sation of the change. For example, Movérare et al. [37] found, in a study of sex hormone protection against trabecular osteopenia, that trabecular enhancement via the oestrogen receptor (ER α) elevated both thickness and number density of trabeculae, while enhancement via the androgen receptor (AR) elevated trabecula number density only, leaving thickness unaffected.

However micro-CT analysis in bone preclinical research is about much more than osteoporosis only. There are several preclinical models of pathologies of bone disruption such as arthritis, tumour and fracture, as well as some transgenic models, where bone volume alone falls short as a parameter to indicate the disruption. To give a simple example, in bone tumour and tumour metastasis, some bone is lost due to osteolysis, while new pathological periosteal reaction bone structures are gained due to osteoblastic tumour cells. The net result, even in a bone significantly affected by tumour, can sometimes be little or no volume change, since some bone is lost and some added. However the tumour disruption has a profound effect on the complexity and texture of the bone, since pathological structures are often much more finely textured, complex and highly interconnected or porous than intact bone. Thus parameters of complexity and connectivity can be orders of magnitude higher in tumour affected than control bones, where there is little or no difference in total bone volume. The same can be true of the pathological periosteal reaction in arthritis models and the callus in fracture models. In all these models of disruption, parameters indicating complexity and connectivity can serve as a “morphometric signature” of the disease process and have much greater sensitivity to the prevalence of the disease process than volume or thickness alone.

In studies of human biopsied or autopsied trabecular bone, anisotropy- and MIL (mean intercept length) tensor-related data [38] indicating spherical angle 3D orientation of structures, as well as spatial inhomogeneity (trabecular separation and its variation) [39], have been long known to improve prediction of mechanical properties of bone. However in a rodent, especially a mouse, the small volumes of trabecular bone reduce the

analytical possibilities for parameters such as anisotropy—with one or two interesting exceptions. For instance, in fracture callus, the parameter degree of anisotropy can be a useful indicator of the degree of callus remodelling and fracture healing. A non-fractured or a healed bone is a simple tube with a high anisotropy since it is an oriented structure. However, introduce a fracture and a callus, and the degree of anisotropy falls significantly due to the more disordered structure of the fracture and callus. The same is true of long bone diaphysis disrupted by bone tumour. In both these cases, degree of anisotropy can serve as a morphometric signature of the status of a healing fracture or of the severity of tumour damage.

In summary, micro-CT imaging and quantitative 3D image analysis put in the hands of the bone researcher a powerful and flexible tool for visualising and quantifying the status of a disease model or transgenic animal. There are a great many disease models and a practically infinite number of potential transgenic models available for research. But there does not need to be a correspondingly bewildering array of analysis and software solutions for these models—a specific solution (and commercial package or add-on) for each research model. What this article has shown is that there is a unifying “pipeline” methodology that allows the researcher themselves to develop effective solutions, with a single imaging and software environment, for every in vivo research model. Scientifically based creativity and imagination can release the full power of micro-CT analysis for every bone research laboratory, whose specific research methods and needs are always unique.

References

1. Feldkamp LA, Davis LC, Kress JW. Practical cone-beam algorithm. *JOSA A*. 1984;1(6):612–9.
2. Hounsfield GN. Computerized transverse axial scanning (tomography): part 1. Description of system. *Br J Radiol*. 1973;46:1016–22.
3. Sasov AY. Desktop x-ray micro-CT. DGZiP proceedings BB 67-CD. Computerised tomography for industrial applications and image processing in radiology. March 15-17, 1999, Berlin, Germany, pp. 165–168, 1999.

4. Frost HM. Preparation of thin undecalcified bone sections by rapid manual method. *Stain Technol.* 1958;33(6):273–7.
5. Frost HM. Tetracycline-based histological analysis of bone remodelling. *Calcif Tissue Res.* 1969;3:211–37.
6. Villanueva AR, Hattner RS, Frost HM. A tetrachrome stain for fresh, mineralized bone sections, useful in the diagnosis of bone diseases. *Stain Technol.* 1964;39:87–94.
7. Recker RR. *Histomorphometry B. techniques and interpretation.* Boca Raton, FL: CRC Press, Inc.; 1983.
8. Parfitt AM, Drezner MK, Glorieux FH, Kanis JA, Malluche H, Meunier PJ, Ott SM, Recker RR. Bone Histomorphometry: standardization of nomenclature, symbols and units. *J Bone Miner Res.* 1987;2(6):595–610.
9. Lorensen WE, Cline HE. Marching cubes: a high resolution 3d surface construction algorithm. *Comput Graph.* 1987;21(4):163–9.
10. Borgefors G. On digital distance transforms in three dimensions. *Comput Vis Image Underst.* 1996;64(3):368–76.
11. Salmon PL, Liu X. MicroCT bone densitometry: context sensitivity, beam hardening correction and the effect of surrounding media. *Open Access J Sci Technol.* 2014;2:101142. <https://doi.org/10.11131/2014/101142>.
12. Srivastava PK, Mahajan P, Satyawali PK, Kumar V. Observation of temperature gradient metamorphism in snow by X-ray computed microtomography: measurement of microstructure parameters and simulation of linear elastic properties. *Ann Glaciol.* 2010;50(54):73–82.
13. Otsu N. A threshold selection method from gray-level histograms. *IEEE Trans Sys Man Cyber.* 1979;9(1):62–6. <https://doi.org/10.1109/TSMC.1979.4310076>.
14. Pratt WK. *Digital image processing.* 2nd ed. New York: Wiley; 1991. Chapter 16.
15. Salmon PL, Buelens E, Sasov AY. Performance of in vivo micro-CT analysis of mouse lumbar vertebral and knee trabecular bone architecture. *J Bone Miner Res.* 2003;18(Suppl 2):S256.
16. Hildebrand T, Ruegsegger P. A new method for the model independent assessment of thickness in three dimensional images. *J Microsc.* 1997;185:67–75.
17. Remy E, Thiel E. Medial axis for chamfer distances: computing look-up tables and neighbourhoods in 2D or 3D. *Pattern Recogn Lett.* 2002;23:649–61.
18. Hildebrand T, Ruegsegger P. Quantification of bone microarchitecture with the structure model index. *Comp Meth Biomech Biomed Eng.* 1997;1:15–23.
19. Smit TH, Schneider E, Odgaard A. Star length distribution: a volume-based concept for the characterization of structural anisotropy. *J Microsc.* 1998;191(3):249–57.
20. Harrigan TP, Mann RW. Characterisation of microstructural anisotropy in orthotropic materials using a second rank tensor. *J Mater Sci.* 1984;19:761–7.
21. Straumit I, Lomov SV, Verpoest I, Wevers M. Determination of local fibers orientation in composite material from micro-CT data. In: *Proceedings of the 11th International Conference on Textile Composites (TexComp-11)* 2013 Sep 19.
22. Gunderson HJG, Boyce RW, Nyengaard JR, Odgaard A. The Connellor: unbiased estimation of connectivity using physical dissectors under projection. *Bone.* 1993;14:217–22.
23. Toriwaki J, Yonekura T. Euler number and connectivity indexes of a three dimensional digital picture. *Forma Tokyo.* 2002;17(3):183–209.
24. Theiler J. Estimating fractal dimension. *J Opt Soc Am.* 1990;7(6):A1055–73.
25. Dempster DW, Compston JE, Drezner MK, Glorieux FH, Kanis JA, Malluche H, Meunier PJ, Ott SM, Recker RR, Parfitt AM. Standardized nomenclature, symbols, and units for bone histomorphometry: a 2012 update of the report of the ASBMR histomorphometry nomenclature committee. *J Bone Miner Res.* 2013;28(1):1–16.
26. Salmon PL, Ohlsson C, Shefelbine SJ, Doube M. Structure model index does not measure rods and plates in trabecular bone. *Front Endocrinol.* 2015;6:162.
27. Hahn M, Vogel M, Pompesius-Kempa M, Delling G. Trabecular bone pattern factor—a new parameter for simple quantification of bone microarchitecture. *Bone.* 1992;13(4):327–30.
28. Salmon PL, Liu X. MicroCT bone densitometry: context sensitivity, beam hardening correction and the effect of surrounding media. *Open Access J Sci Technol.* 2014;2:ID 101142. <https://doi.org/10.11131/2014/101142>.
29. Tivesten Å, Movérare-Skrtic S, Chagin A, Venken K, Salmon P, Vanderschueren D, Säwendahl L, Holmäng A, Ohlsson C. Additive protective effects of estrogen and androgen treatment on trabecular bone in ovariectomized rats. *J Bone Miner Res.* 2004;19(11):1833–9.
30. Seeuws S, Jacques P, Van Praet J, Drennan M, Coudenys J, Decruy T, Deschepper E, Lepescheux L, Pujuguet P, Oste L, Vandeghinste N. A multiparameter approach to monitor disease activity in collagen-induced arthritis. *Arthritis Res Ther.* 2010;12(4):R160.
31. Quan L, Zhang Y, Dusad A, Ren K, Purdue PE, Goldring SR, Wang D. The evaluation of the therapeutic efficacy and side effects of a macromolecular dexamethasone prodrug in the collagen-induced arthritis mouse model. *Pharm Res.* 2016;33(1):186–93.
32. Chantry AD, Heath D, Mulivor AW, Pearsall S, Baud'huin M, Coulton L, Evans H, Abdul N, Werner ED, Boussein ML, Key ML. Inhibiting activin-A signaling stimulates bone formation and prevents cancer-induced bone destruction in vivo. *J Bone Miner Res.* 2010;25(12):2633–46.
33. Cox TR, Rumney RM, Schoof EM, Perryman L, Høye AM, Agrawal A, Bird D, Ab Latif N, Forrest H, Evans HR, Huggins ID. The hypoxic cancer secretome induces pre-metastatic bone lesions through lysyl oxidase. *Nature.* 2015;522(7554):106.

34. Kassen D, Lath D, Lach A, Evans H, Chantry A, Rabin N, Croucher P, Yong KL. Myeloma impairs mature osteoblast function but causes early expansion of osteo-progenitors: temporal changes in bone physiology and gene expression in the KMS12BM model. *Br J Haematol*. 2016;172(1):64–79.
35. McDonald MM, Dulai S, Godfrey C, Amanat N, Szynda T, Little DG. Bolus or weekly zoledronic acid administration does not delay endochondral fracture repair but weekly dosing enhances delays in hard callus remodeling. *Bone*. 2008;43(4):653–62.
36. Jeyabalan J, Viollet B, Smitham P, Ellis SA, Zaman G, Bardin C, Goodship A, Roux JP, Pierre M, Chenu C. The anti-diabetic drug metformin does not affect bone mass in vivo or fracture healing. *Osteoporos Int*. 2013;24(10):2659–70.
37. Movérare S, Venken K, Eriksson AL, Andersson N, Skrtic S, Wergedal J, Mohan S, Salmon P, Bouillon R, Gustafsson JÅ, Vanderschueren D. Differential effects on bone of estrogen receptor α and androgen receptor activation in orchidectomized adult male mice. *Proc Natl Acad Sci*. 2003;100(23):13573–8.
38. Ulrich D, Van Rietbergen B, Laib A, Ruegsegger P. The ability of three-dimensional structural indices to reflect mechanical aspects of trabecular bone. *Bone*. 1999;25(1):55–60.
39. Tassani S, Öhman C, Baleani M, Baruffaldi F, Viceconti M. Anisotropy and inhomogeneity of the trabecular structure can describe the mechanical strength of osteoarthritic cancellous bone. *J Biomech*. 2010;43(6):1160–6.



Analysis of Fracture Callus Mechanical Properties Using Micro-CT

Burak Bilecenoglu and Mert Ocak

6.1 Bone Tissue

The human body is composed of 74 bones forming the axial skeleton, 26 of which are located in the spine, 22 of which are in the head skeleton, 25 of which are in chest wall which form the ribs and sternum, and 1 of which is the hyoid bone. Sixty-four pieces of upper extremity bones and 62 pieces of lower extremity bones which consist of 126 pieces of bones compose the appendicular skeleton. When six pieces of ear bones (*ossicula auditoria*) are added to these, a total of 206 bones form the human skeleton. The bones, which are the most rigid structure of the body after the teeth, weight approximately 15% of an adult human body, and the total weight of it is around approximately 5–6 kg [1].

Bone tissue is made of two main substances: organic substances (30–40%) which give flexibility to the structure of it and inorganic salts (60–70%) which give rigidity to the structure. The inorganic portion of the bone forms calcium phosphate (CaPO_4) (85%), calcium carbonate (CaCO_3) (10%), magnesium phosphate (MgPO_4) (1.5%), calcium fluoride (CaF_4), calcium chloride

(CaCl), and alkali salts. Ninety-nine percent of body calcium is found in the bones, and this acts as a reservoir for metabolic calcium metabolism, whereas the phosphate content in bone structure is under the control of hormones and cytokines [1, 2].

Osteoblasts develop from mesoderm-derived stem cells and are found in bone marrow and some other connective tissues. Osteoblasts are responsible for the synthesis and mineralization of bone matrix; which then differentiate into osteocytes. The osteocytes are the essential structures that form the bone tissue, and they are dispersed within the bone matrix and are connected to each other by extensions to form a meshwork appearance. A bone volume of 1 mm^3 contains approximately 700–900 osteocytes which are the most important cells that provide bone viability. The death of these cells trigger the bone resorption as osteoclastic activity. Osteoclasts are responsible for the bone destruction during growth and formation [1, 2].

Bone tissue usually consists of bone substance (*substantia ossea*) and bone marrow (*medulla ossea*). The bone membrane (*periosteum*), which provides the feeding and repair of the bone, surrounds all the faces of the bones except for the parts of the bones participating in articular surfaces. Arteries that supply the bone (nutrient arteries) enter the bone from the periosteum, and then the periosteal arteries supply the cortical bone by entering the bone from many points. For

B. Bilecenoglu (✉)
Faculty of Dentistry, Department of Anatomy,
Ankara University, Ankara, Turkey

M. Ocak (✉)
Vocational School of Health, Ankara University,
Ankara, Turkey

this reason, if the periosteum is damaged the bone loses its supply and ability to repair. The ligaments, the tendons, and the muscles that connect bones to each other attached to the bones via the periosteum. Another task of periosteum is to enable the transverse growth of the bone [2].

The inner side of the bones are covered with a membrane called *endosteum*. The nutrient artery, which generally in the middle of the shaft enters from different points of each bone, and passes through the cortical bone obliquely that supplies the trabecular portion and bone marrow. *Metaphyseal* and *epiphyseal arteries* supply the ends of each bone. The veins accompany to the arteries, but the veins are numerous than the arteries within the red bone marrow. In periosteum, there are many receptors that are responsible for nerve impulse which receive sense from periosteum following the vessels. Periosteum consists of two layers; an outer fibrous layer (*stratum fibrosum*) and inner osteogenic layer (*stratum osteogenicum*). The fibrous layer of the periosteum continues with the fibrous layer of the articular capsule at the articular surfaces. The osteogenic layer of the periosteum is rather rich than vessels and enables the transverse growth of the bone. The periosteum, as it contains too many receptors, is very sensitive to trauma [3].

6.2 Types of Bone Tissue

There are two types of bone tissue according to their mechanical and biological characteristics: primary (immature) coarse fibrous bone and secondary (mature) lamellar bone [4]. Immature bone creates an embryological skeleton, and it continuously replaces with mature bone during the development. During the repair process of fractures, the immature bone forms the premature fracture repair tissue similar procedure how happens during the development process. The impaction and resorption process in the immature bone are faster, fibrils in the matrix that is collagen-structured exhibit an irregular sequence, and mineralization of the matrix

forms an irregular shape when it is compared to the mature bone. The formation of the immature bone is being irregular that allows fracture callus to be distinguished from the mature bone tissue by creating an irregular image. The immature bone is softer and more easily deformed than the mature bone due to the irregularity and weakness of the sequence in the collagen fibers, depending on the high water content and irregular mineralization [4]. There are two types of tissue in the mature bone. A tight (cortical, compact) bone on the outer surface, and cancellous (trabecular, spongy) bone part is located on the inner surface. Compact bone forms the outer layer that provides a connection with the Havers channels and Volkmann channels that contain vascular structures that extend inwardly. The blood in the Havers channels supplies the osteocyte cells through numerous small canals. The osteon structure of the long bones is aligned in a manner coherent with the long axis of the bone. The structure that tightly connects to the periosteum is the Sharpey's fibers. The cancellous bone in the inner layer is similar to the structurally tight bone and has a trabecular structure. Matured osteon units are only present in thickened trabeculae. The facing inward layer of the trabecules is covered with resting osteoblast cells [3, 5].

The term *bone quality* is frequently used in the literature to describe the structural properties of the bone. Bone quality is often associated with the trabecular bone structure [6]. Trabecular bone is the primary anatomic and functional structure of the cancellous bone. Bone quality is particularly important for implants placed on the bone. Besides, the amount of the cortical bone affects the primary stabilization of the implant; the role of trabecular bone in implant success is very important because the vast majority of an implant placed in the bone remains inside of the cancellous bone and is in direct contact with the implant. Bone contact and osseointegration can be measured by histomorphometric analysis. The histomorphometric analysis is a long-lasting and expensive method that can damage the analyzed

sample and not allow to use the same sample for another evaluation. Due to these disadvantages, three-dimensional microtomography techniques have been put into use as nondestructive, rapid, and reliable methods with the aim of analyzing the microarchitecture of cortical and trabecular bones [6–9].

6.3 Ossification (Osteogenesis)

Osteogenesis may occur in two different ways.

The first one is; undifferentiated mesenchymal cells which merge in the form of layers and turn into osteoblasts with “intramembranous ossification” that develops by mineralizing and forming organic matrix. There is no cartilage model in this type of ossification. Flat bone formation, healing fractures with stable distraction methods, and long bone healing in children are examples of this type of ossification. The first point where the ossification begins in the mesenchymal tissue concentration is called the primary ossification center.

The second type of ossification is; “endochondral ossification.” Long and short bones are ossified through this way. In this type of ossification, initially small bone models of hyaline cartilage is being form during the development of bone. The cartilage model is replaced by bone tissue over time with endochondral ossification. Unstable fractures heal in this way.

6.4 Healing of Bone Tissue

The deterioration of the anatomical integrity of the bone as a result of mechanical forces coming from outside or inside of the body is called a fracture. The most remarkable feature of the fracture healing is that the repair tissue formed during the healing is in good quality bone tissue without developing the scar tissue when it is compared with the healing of the other tissues. Therefore, when defining the process of fracture healing, it can be called regeneration instead of restoration

or repair [10]. The fracture developed in the bone leads to inflammation, repair, and remodeling process. Immediately after the development of the fracture, the inflammation process begins and the repair starts subsequently. Damaged cells and bone matrix in the process of repair will be recovered after that remodeling phase that is more long-lasting in comparison with the other two processes begins. The cells grow rapidly and the matrix synthesis constitutes the repair process in the area where the fracture fragments meet [11]. Inflammatory cytokines such as lymphocytes and macrophages are immigrating to the fracture site. The cytokines secreted by the inflammatory cells provide the formation of new vessels [11]. As inflammation decreases, necrotic dead tissues are removed, and fibroblasts appear in the region and begin to produce callus that is a new bone matrix and fracture union tissue. The fracture is a hematoma that initiates the progression of all these stages, allows the release of the cytokines, and emerges by the development of fracture, and there are scientific studies showing that the healing process has been disrupted by the loss of fracture’s hematoma [12, 13]. There are studies about the mineral density that indicated the low density in an extremity where fracture develops even after a well fracture union [14, 15]. The fracture healing is divided into two types in terms of the method; direct fracture healing and indirect fracture healing. Direct fracture healing is a type of fracture healing that is anatomically a reduced healing in the event that the tight detection is applied. Indirect fracture healing is a type that is seen more common than direct fracture healing. It is seen after the fractures that aren’t or can’t be reduced anatomically without being performed tightly [16]. The stages of fracture healing are histomorphologically divided into sections as *inflammation*, *soft callus*, *hard callus*, and *remodelation*. These four phases of fracture healing are intertwined; however, it should be stated that this staging is based on clinical and microscopic observations of fractures with soft tissue cover and with relatively low-energy mechanisms [10].

6.5 Use of Micro-CT in Bone Researches

Imaging methods have been used for scientific purposes as well as for diagnostic purposes as technology evolves, in recent years. The voxel range of micro-CT is almost one million times smaller than normal tomography. It obtains the 3D image of the object with detectors that have a high-resolution. In addition, micro-CT allows the visualization of the three-dimensional structures of anatomical structures and the necessary measurements can be made without using the histological sample preparation steps. The integrity of the samples is not impaired and is not subjected to any chemical effect on the specimen (Fig. 6.1).

Several parameters such as bone trabecular thickness (Tb.Th), trabecular number (Tb.N), trabecular separation (Tb.Sp), bone volume (BV),

total tissue volume (TV), trabecular bone ratio (BV/TV), structural model index that shows numeric characteristics of trabecular as three-dimensional (SMI), trabecular bone connections, number of trabecular nodes in each tissue volume (N.Nd/TV), and bone density that can be determined depending on hydroxyapatite amount can be calculated quickly and reliably by high-resolution 3D micro-CT.

In the literature, the use of micro-CT has become widespread in the studies that are done in order to evaluate implants and assessment of implant-bone circumference. Many researchers have used three-dimensional microtomography in order to assess implant and the bone surrounding the implant (union between the implant surface and bone osseointegration) and obtain approximately the same results. Although some analyses can be made regarding the implant and

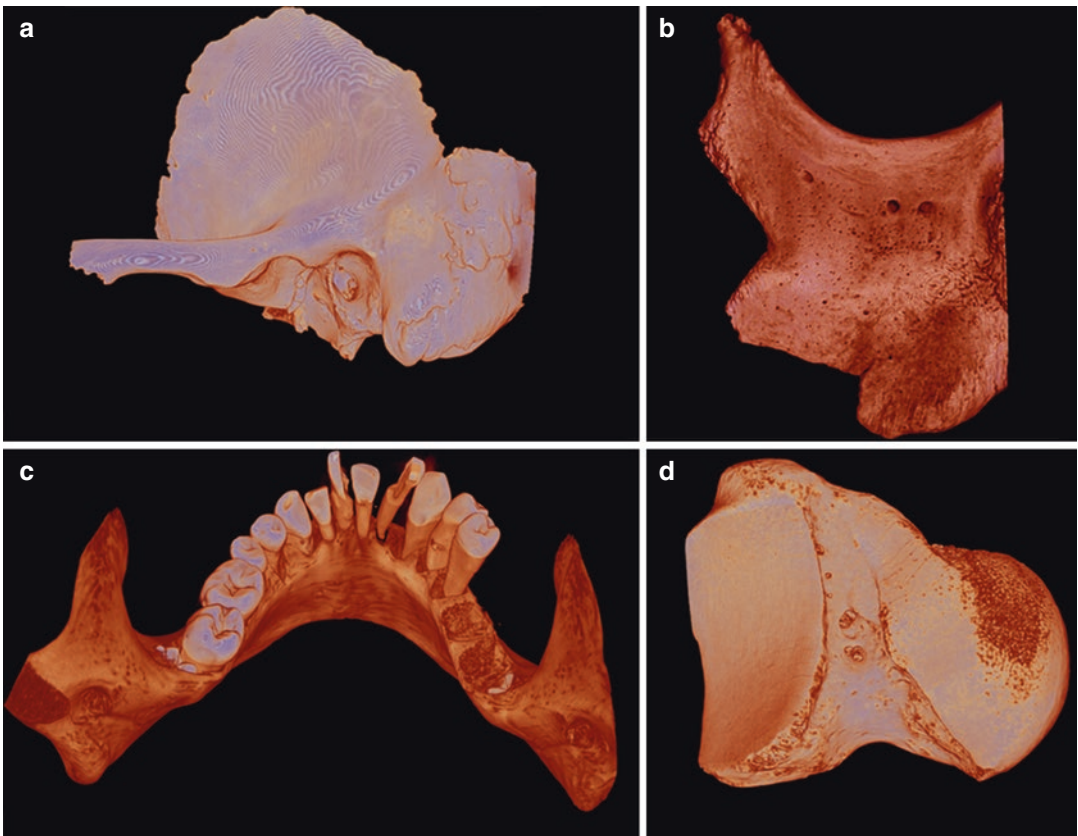


Fig. 6.1 Three-dimensional reconstruction of bones using micro-CT (human; (a) temporal bone, (b) zygomatic bone, (c) mandible, (d) talus)

surrounding bone by 3D micro-computed tomographies, these analyses can also be affected negatively by metal artifacts and, miscalculation of bone density that is caused by titanium implant absorbing more X-rays than the bone and scatters it to the surrounding tissue [17–20]. Moreover, it is also possible to evaluate the stress of the implant on the trabecular and cortical bone by performing finite element analysis with digital data obtained by micro-CTs [20].

Mulder et al. used the micro-CT method in order to examine the structure of pig condyle, the mineralization, and the trabecular bone development. According to their study, the remodeling on the anterior and posterior aspect of the mandible condyle was different from each other and that the remodeling of the posterior aspect of the condyle was larger. The study showed that trabecular bone volume and thickness is more in the body of the mandible and the quantity of mineralization in the anterior and posterior side of the condyle is the same, but more mineralization in the body of the mandible [19].

Tissue engineering is a multidisciplinary approach that forms a lost tissue or organ again which aims them to function. The use of micro-computed tomography in tissue engineering has become popular in recent years in order to investigate the materials forming the tissue skeleton. Micro-CT is mainly widely used in examining the material structure that constitutes the skeleton of the tissue and the amount of bone growth in materials such as polymeric and calcium phosphate in evaluation as *in vitro* [21]. Three-dimensional data presents more effective information compared to the two-dimensional inspection. Micro-computed tomography allows getting information about the material of lost tissue skeleton as well as investigation of the acquired tissue [22].

Dharan et al. [23] compared the effect of porous titanium granules on sinus augmentation by using different graft materials and using micro-computed tomography. For this, they made comparisons by using the parameters such as bone volume (BV), total tissue volume (TV), trabecular bone ratio (BV/TV), trabecular number (Tb.N), trabecular separation (Tb.Sp), trabecular

thickness (Tb.Th), structural model index that shows numeric characteristics of trabecular as 3-dimension (SMI), trabecular bone connections, the number of trabecular nodes (N.Nd/TV), and bone density in each tissue volume. They emphasized that porous titanium granules provide space for the new bone formation and this may be effective in long-term success [23].

6.6 Use of Micro-CT in the Research of Bone Healings

Bone samples can be scanned in micro-CT with dry or distilled water in the tube. Dry scanning is a classic and fast method for micro-CT, and it is widely used for samples that are not affected by heat. The sample can be fixed to the center of the stage with a radiolucent substance, following the scan operation is performed. The wet screening is recommended if samples are wanted not to be affected by heat or if the samples are to be subjected to histopathological analysis after the micro-CT procedure. Additionally, wet scanning absolutely must be made in a tube in order to be able to make an analysis of the bone mineral density (g/mm^3).

Generally, aluminum or copper filters are used in order to review the bone samples and to minimize radiologic artifacts during scanning. The samples are being scanned at 360° rotation, and high-resolution scans $33\ \mu\text{m}$ or the smaller cross section are recommended for resulting the analysis correctly. The resulting images automatically are converted to 8-bit gray axial images by the software. Bone components are determined on axial images, and upper and lower limits are determined for analysis. ROIs (regions of interest) are selected by determining bone regions in axial images that lie within these limits. The white and black pixel ranges in the ROI are determined by setting histogram as semiautomatic, and global thresholding process is performed between these reference ranges for the automatic analyses in the next stage. If it needs to be expressed more clearly, the gray image of the ROIs in the respective range is pixelated as black and white dots. Total tissue volume, total bone

volume, bone surface area, and the percentage rate of bone tissue further can be measured, and analysis of trabeculae structure mentioned earlier can be performed (Fig. 6.2). Please see chapter 5.

A robust old and mature bone can easily be distinguished from the healing tissue in the newly formed cartilage or immature callus during the global thresholding procedure. Similarly, the outer cortical bone can be differentiated easily trabeculae of bone located inside by selecting the correct field during the process of ROI. All these

bone tissues can be analyzed together or separately (Fig. 6.3).

Several studies were made according to fracture calculus. Shefelbine evaluated fractures by using micro-computed tomography and images with the finite element analysis method. In this study, a torsional fracture in the mouse femurs was made and, following scans were performed from fracture calluses to determine three-dimensional geometry and material properties for finite element models in the third and fourth weeks following recovery. The area, stiffness, and mineral density of these calluses were calculated [24].

Bosemark also examined the anabolic use with autograft treatment in bone fractures using micro-CT. He performed the same type of autograft implementation by creating the same type of fracture indifferent mice groups using an anabolic substance or physiological salt water [25].

Reynolds et al. also compared the treatments with autograft and allograft in a similar study on mice using micro-CT. They made a volumetric analysis of the callus tissue and estimated biomechanical predictions [26].

Ezirganli et al. investigated the different types of bone graft effect of the healing on New Zealand rabbits. They analyzed the amount of new ossification with the micro-CT method and supported their studies with histomorphological tests. They declared that there were no statistical

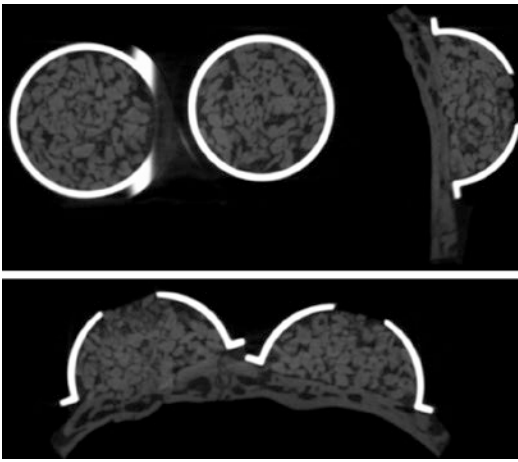


Fig. 6.2 Demonstration of the newly formed bone tissue, bounded by titanium barrier, in two-dimensional, respectively, coronal, sagittal, and axial sections (rabbit calvaria)

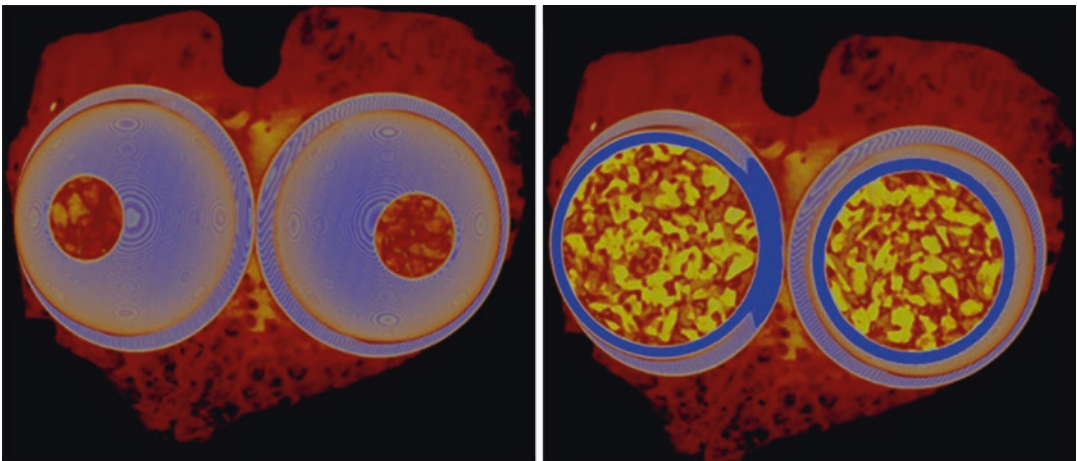


Fig. 6.3 3D reconstruction of the newly formed bone tissue bounded by titanium barrier (rabbit calvaria)

differences between the two methods during their studies [27].

Morgan et al. suggested that quantitative data from the newly formed callus to be obtained using micro-CT are more reliable than other methods. They followed different experimental conditions that changed postfracture recovery with micro-CT imaging and torsion test. In their research, total tissue volume (TV), bone volume (BV), trabecular bone ratio (BV/TV), bone mineral content (BMC), tissue mineral density (TMD), standard deviation (σ TMD), active mineral density polar moment of inertia (Jeff), torsional strength, and torsional rigidity were calculated [28].

Yang et al. analyzed the callus tissue characteristics by micro-CT and Fourier transform by infrared imaging spectroscopy (FT-IRIS) in their research. Tissue mineral density (TMD) and bone volume fraction (BVF) analysis were performed in their research and stated both techniques are comparable [29].

Nyman et al. evaluated the quantitative measurements of the rat femoral fracture repair on micro-CT images as well. They analyzed the callus formation at three separate points in the same long bones. They specified these three points separately by the ROI operation, and among them, they calculated the volume of total callus (TVcallus), the volume of mineralized callus (BVcallus), and the volume of total callus (BVcallus/TVcallus) in mineralized tissue fraction and callus (mBMDcallus) containing the mineralized tap volumetric BMD (g/cm^3) [30].

Studies with human samples in the literature are also available. Thomsen et al. compared the stereological measurements of the trabecular bone structure with three-dimensional micro-CT images and two-dimensional histological sections in human proximal tibial bone biopsies. The study revealed high correlations between data that gained from conventional 2D cross section and 3D micro-CT and measurements of the

bone structure. 3D micro-CT showed that bone structural evaluations can be used instead of conventional histological sections [31].

Figures 6.4 and 6.5 are related with callus formation in the healing process of long bone fractures and newly formed bone tissue with graft treatment (Figs. 6.4 and 6.5).

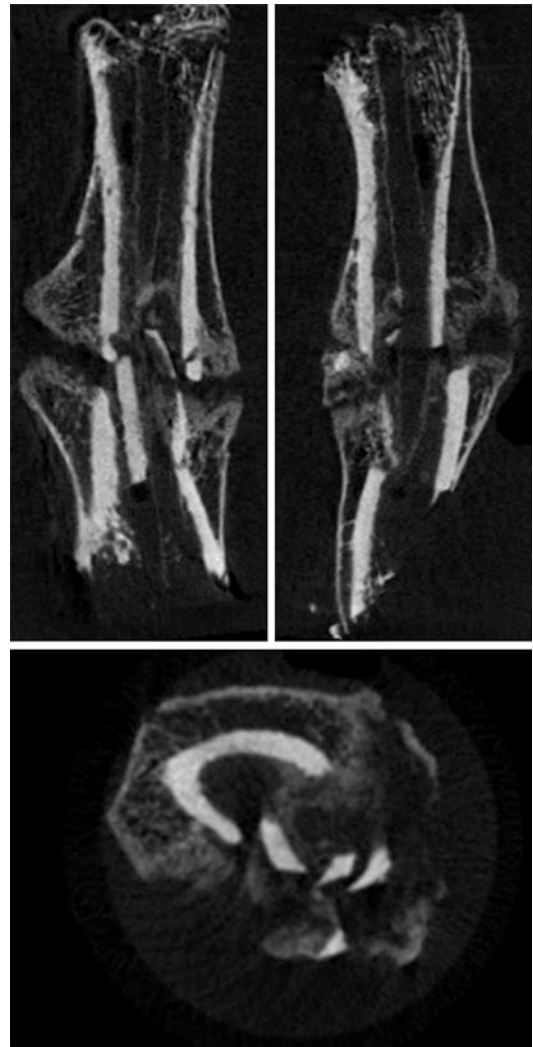


Fig. 6.4 Callus formation in the healing process of long bone fractures (rat femur)

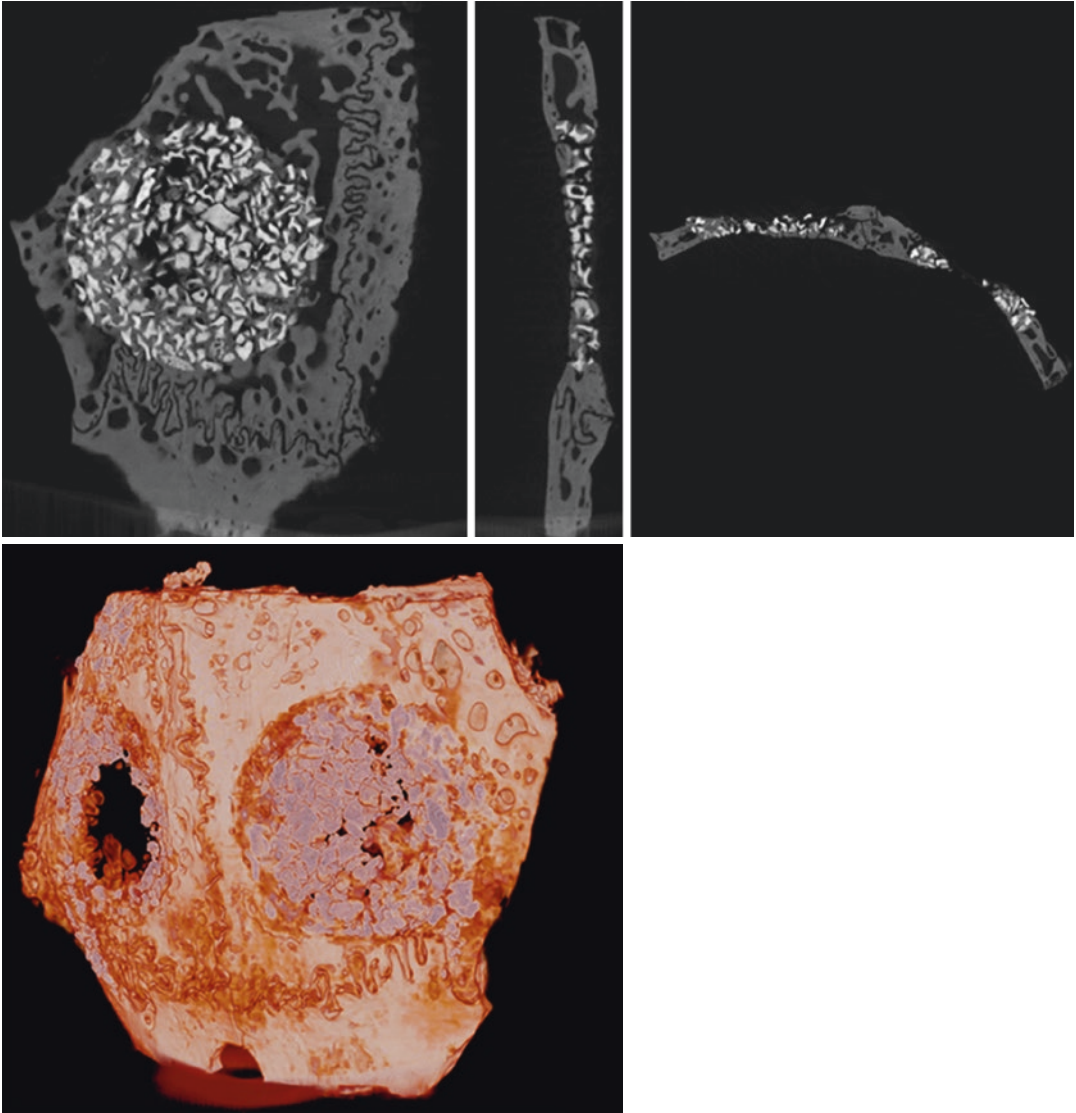


Fig. 6.5 The newly formed bone tissue with graft treatment in two-dimensional, respectively, coronal, sagittal, and axial sections and 3D reconstruction (rat calvaria)

Acknowledgment All figures in this chapter were scanned and reconstructed with Skyscan 1275 (Skyscan, Kontich, Belgium) in Ankara University, Faculty of Dentistry, Micro-CT Laboratory which was founded by Ankara University Research Fund (Project No:17A0234001) and belongs to the courtesy of Orhan, K., Bilecenoğlu B., and Ocak. M.

References

1. Moore KL, Dalley AF, Agur AM. Clinically oriented anatomy. Philadelphia, PA: Lippincott Williams & Wilkins; 2013.
2. Standring S. Gray's anatomy E-book: the anatomical basis of clinical practice. Philadelphia, PA: Elsevier Health Sciences; 2015.
3. Buckwalter JA, Glimcher MJ, Cooper RR, Recker R. Bone biology. I: structure, blood supply, cells, matrix, and mineralization. *Instr Course Lect.* 1996;45:371–86.
4. Buckwalter JA, Einhorn TA, Marsh J. Bone and joint healing. *Rockwood and Green's fractures in adults.* Philadelphia, PA: Lippincott, Williams, and Wilkins; 2001. p. 245–71.
5. Buckwalter JA, Glimcher MJ, Cooper RR, Recker R. Bone biology. II: formation, form, modeling, remodeling, and regulation of cell function. *Instr Course Lect.* 1996;45:387–99.

6. Fyhrie DP. Summary—measuring “bone quality”. *J Musculoskelet Neuronal Interact.* 2005;5(4): 318–20.
7. Sakka S, Coulthard P. Bone quality: a reality for the process of osseointegration. *Implant Dent.* 2009;18(6):480–5. <https://doi.org/10.1097/ID.0b013e3181bb840d>.
8. Fanuscu MI, Chang TL. Three-dimensional morphometric analysis of human cadaver bone: microstructural data from maxilla and mandible. *Clin Oral Implants Res.* 2004;15(2):213–8.
9. Muller R, Van Campenhout H, Van Damme B, Van Der Perre G, Dequeker J, Hildebrand T, et al. Morphometric analysis of human bone biopsies: a quantitative structural comparison of histological sections and micro-computed tomography. *Bone.* 1998;23(1):59–66.
10. Marsh DR, Li G. The biology of fracture healing: optimising outcome. *Br Med Bull.* 1999;55(4):856–69.
11. Mark H, Penington A, Nannmark U, Morrison W, Messina A. Microvascular invasion during endochondral ossification in experimental fractures in rats. *Bone.* 2004;35(2):535–42.
12. Grundnes O, Reikeras O. The importance of the hematoma for fracture healing in rats. *Acta Orthop Scand.* 1993;64(3):340–2. <https://doi.org/10.3109/17453679308993640>.
13. Grundnes O, Reikeras O. The role of hematoma and periosteal sealing for fracture healing in rats. *Acta Orthop Scand.* 1993;64(1):47–9.
14. Van der Wiel HE, Lips P, Nauta J, Patka P, Haarman HJ, Teule GJ. Loss of bone in the proximal part of the femur following unstable fractures of the leg. *J Bone Joint Surg Am.* 1994;76(2):230–6.
15. Karlsson MK, Nilsson BE, Obrant KJ. Bone mineral loss after lower extremity trauma. 62 cases followed for 15–38 years. *Acta Orthop Scand.* 1993;64(3):362–4.
16. Mattox DE. Bone healing and grafting. *Ear Nose Throat J.* 1983;62(8):409–11.
17. Butz F, Ogawa T, Chang T-L, Nishimura I. Three-dimensional bone-implant integration profiling using micro-computed tomography. *Int J Oral Maxillofac Implants.* 2006;21(5):687–95.
18. Morinaga K, Kido H, Sato A, Watazu A, Matsuura M. Chronological changes in the ultrastructure of titanium-bone interfaces: analysis by light microscopy, transmission electron microscopy, and micro-computed tomography. *Clin Implant Dent Relat Res.* 2009;11(1):59–68.
19. Mulder L, Koolstra JH, de Jonge HW, van Eijden TM. Architecture and mineralization of developing cortical and trabecular bone of the mandible. *Anat Embryol (Berl).* 2006;211(1):71–8. <https://doi.org/10.1007/s00429-005-0054-0>.
20. Van Oosterwyck H, Duyck J, Sloten JV, Perre GV, Jansen J, Wevers M, et al. The use of microfocus computerized tomography as a new technique for characterizing bone tissue around oral implants. *J Oral Implantol.* 2000;26(1):5–12.
21. Cartmell S, Huynh K, Lin A, Nagaraja S, Guldberg R. Quantitative microcomputed tomography analysis of mineralization within three-dimensional scaffolds in vitro. *J Biomed Mater Res A.* 2004;69(1):97–104.
22. Hollister SJ, Lin C, Saito E, Lin C, Schek R, Taboas J, et al. Engineering craniofacial scaffolds. *Orthod Craniofac Res.* 2005;8(3):162–73.
23. Dursun E, Dursun CK, Eratalay K, Orhan K, Celik HH, Tözüm TF. Do porous titanium granule grafts affect bone microarchitecture at augmented maxillary sinus sites? A pilot split-mouth human study. *Implant Dent.* 2015;24(4):427–33.
24. Shefelbine SJ, Simon U, Claes L, Gold A, Gabet Y, Bab I, et al. Prediction of fracture callus mechanical properties using micro-CT images and voxel-based finite element analysis. *Bone.* 2005;36(3):480–8.
25. Bosemark P, Isaksson H, McDonald MM, Little DG, Tägil M. Augmentation of autologous bone graft by a combination of bone morphogenic protein and bisphosphonate increased both callus volume and strength. *Acta Orthop.* 2013;84(1):106–11.
26. Reynolds DG, Hock C, Shaikh S, Jacobson J, Zhang X, Rubery PT, et al. Micro-computed tomography prediction of biomechanical strength in murine structural bone grafts. *J Biomech.* 2007;40(14):3178–86.
27. Ezirganli S, Polat S, Baris E, Tatar I, Celik HH. Comparative investigation of the effects of different materials used with a titanium barrier on new bone formation. *Clin Oral Implants Res.* 2013;24(3):312–9. <https://doi.org/10.1111/j.1600-0501.2011.02323.x>.
28. Morgan EF, Mason ZD, Chien KB, Pfeiffer AJ, Barnes GL, Einhorn TA, et al. Micro-computed tomography assessment of fracture healing: relationships among callus structure, composition, and mechanical function. *Bone.* 2009;44(2):335–44.
29. Yang X, Ricciardi BF, Hernandez-Soria A, Shi Y, Camacho NP, Bostrom MP. Callus mineralization and maturation are delayed during fracture healing in interleukin-6 knockout mice. *Bone.* 2007;41(6):928–36.
30. Nyman JS, Munoz S, Jadhav S, Mansour A, Yoshii T, Mundy GR, et al. Quantitative measures of femoral fracture repair in rats derived by micro-computed tomography. *J Biomech.* 2009;42(7):891–7.
31. Thomsen JS, Laib A, Koller B, Prohaska S, Mosekilde L, Gowin W. Stereological measures of trabecular bone structure: comparison of 3D micro-computed tomography with 2D histological sections in human proximal tibial bone biopsies. *J Microsc.* 2005;218(2):171–9.



Micro-CT in Osteoporosis Research

7

Szandra Körmendi, Bálint Vecsei, Kaan Orhan,
and Csaba Dobó-Nagy

Abbreviations

BALP	Bone-specific alkaline phosphatase	Ca.V/TV	Canal porosity
BMC	Bone mineral content	CKD	Chronic kidney disease
BMD	Bone mineral density	Conn.D	Connectivity density
BRONJ	Bisphosphonate-related osteonecrosis of the jaw	Cr. BMD	Cortical bone mineral density
BS/BV	Bone surface/bone volume ratio	CS	Canal surface
BV	Bone volume	Ct.Po	Cortical porosity
BV/TV	Percentage of bone volume	Ct.Th	Cortical thickness
Ca.Dm	Canal diameter	CTX	C-terminal telopeptide fragment of type I collagen
Ca.Sp	Canal separation	DA	Degree of anisotropy
Ca.V	Canal volume	DEXA, DXA	Dual energy X-ray absorptiometry
		DPD	Deoxypyridinoline
		FEA	Finite element analysis
		L1–L4	Lumbar 1–4 vertebra
		Lc.N/TV	Lacunar density
		Lc.V/TV	Lacunar porosity
		NTX	Type I collagen cross-linked N-telopeptide
		OC	Osteocalcin
		OPG	Osteoprotegerin
		OVX	Ovariectomized
		PINP	Procollagen type 1 amino-terminal propeptide
		PTH	Parathyroid hormone
		ROI	Region of interest
		SAMP6	Senescence-accelerated mouse P6
		SHAM	Sham-operated
		SMI	Structural model index
		Tb.N	Trabecular number
		Tb.Pf	Trabecular pattern factor

S. Körmendi (✉) · B. Vecsei
Faculty of Dentistry, Department of Prosthodontics,
Semmelweis University, Budapest, Hungary
e-mail: kormendi.szandra@dent.semmelweis-univ.hu;
vecsei.balint@dent.semmelweis-univ.hu

K. Orhan
Faculty of Dentistry, Department of Dentomaxillofacial
Radiology, Ankara University, Ankara, Turkey

Faculty of Medicine, OMFS IMPATH Research
Group, Department of Imaging and Pathology,
University of Leuven, Leuven, Belgium

Oral and Maxillofacial Surgery, University Hospitals
Leuven, University of Leuven, Leuven, Belgium
e-mail: knorhan@dentistry.ankara.edu.tr;
kaan.orhan@uzleuven.be

C. Dobó-Nagy
Faculty of Dentistry, Department of Oral Diagnostics,
Semmelweis University, Budapest, Hungary
e-mail: dobo-nagy.csaba@dent.semmelweis-univ.hu

Tb.Sp	Trabecular separation
Tb.Th	Trabecular thickness
TMD	Tissue mineral density
TRACP-5b	Tartrate-resistant acid phosphatase 5b
TV	Tissue volume
VOI	Volume of interest

building and bone degeneration, we differentiate low, normal and high turnover osteoporosis; secondary and primary types can also be differentiated depending on the fact if the osteoporosis is a result of another primary disease or it is a separate clinical picture; also there is Type I (postmenopausal) and Type II (senile) classifications.

7.1 Introduction: Osteoporosis

Osteoporosis is a systemic bone disease that occurs along with low bone density, loss of bone and the lesion of the microarchitecture of bone tissue, resulting in an increase in bone fragility.

Around 200 million people are affected in civilized societies worldwide, and a significant surge in this number can be expected in the future. An even more alarming data is that only a low percentage of patients will be getting treated. This number is around 10%, although we know that the average lifespan of a woman with osteoporosis is 4 years less than of someone not having this disease. Two thirds, according to some other data three quarters of all patients are women which can derive from various presumed reasons. Firstly, the initially thinner and lower-weight bone structure [1] can be mentioned; secondly, women due to postmenopausal oestrogen deficiency are more prone to bone loss; and thirdly, in almost all populations, women live longer than men so their proportion with the progression of age grows at the expense of men [2]. All these data along with the fact that following cardiovascular diseases, musculoskeletal disorders impose the greatest burden on the economy and on the society contributed to the fact that the World Health Organization initiated by Swedish orthopaedists announced the Bone and Joint Decade first between 2000 and 2010 and then the second time between 2011 and 2020. The initiative joins together 65 countries, and it is supported by 750 associations. Its aim is to reduce the economic and social burden caused by musculoskeletal diseases by improving prevention, diagnosis and treatment of these diseases.

Types of osteoporosis can be classified in different ways: based on the dynamics of bone

7.2 Role of Micro-CT in Osteoporosis Research

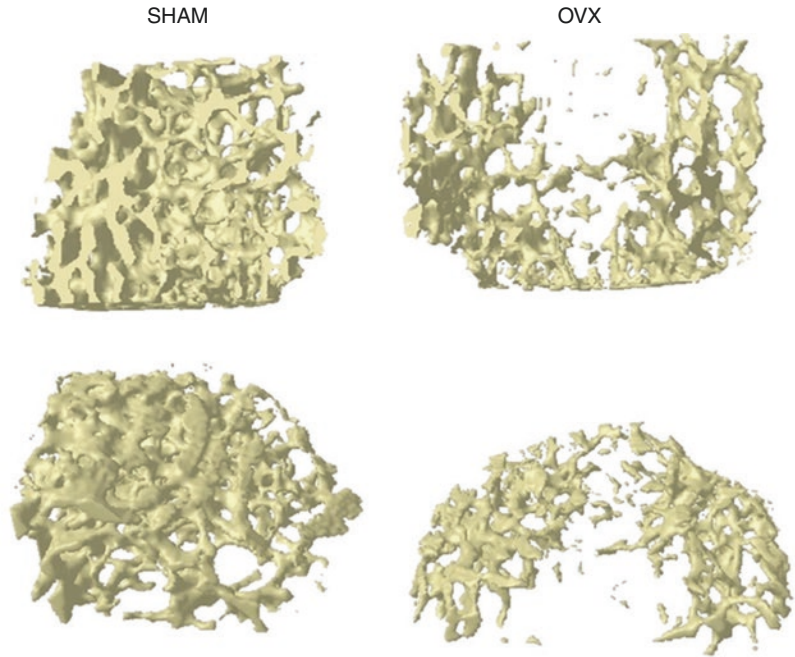
Micro-CT is a widespread tool used for observing the changes in the microarchitecture of the bone tissue; thus the pathology of osteoporosis and the effects of treatments can be well examined by it. It is primarily used in *in vitro* examinations, but there is opportunity for *in vivo* experiments too. The sample used for the examination can be of human as well as of animal origin (Fig. 7.1).

7.2.1 Human Researches

In micro-CT studies, due to the size of the sample, mainly in the case of *in vivo* studies, they are mostly animal-derived, but we can also find many human studies. The importance of selecting the location of sampling is shown by the research of Eckstein and his colleagues. One hundred sixty-five samples taken from human cadavers were processed using micro-CT. The locations of the sampling were the distal radius, the femoral neck and trochanter, iliac crest, calcaneus and second vertebral body, where in each case the volume of interest (VOI) was a 6-mm-diameter and 6-mm-long cylinder examined with a 26 μm voxel. At the distal radius and at the femoral neck, the trabecular bone had a more plate-like structure, thicker trabeculae, higher trabecular number (Tb.N), smaller trabecular separation (Tb.Sp), higher connectivity and higher degree of anisotropy (DA) by men than by women. The trochanter shows more plate-like and thicker trabeculae by men. The calcaneus, the iliac crest and the lumbar 2 (L2) vertebra show no difference between the two genders [3].

In 2003, Dufresne et al. examined the effect of risedronate in placebo-controlled test on the

Fig. 7.1 Representative samples from mice femur in the case of ovariectomy or sham operation



samples taken from the hip bone. After 1 year of treatment, it was found that the percentage of bone volume (BV/TV) decreased by 20%, the Tb.N decreased by 14% and Tb.Sp increased by 13% compared to the baseline in the group taking placebo, while by the ones taking risedronate, it did not appear to have significant differences compared to baseline values. However, during this time, the bone mineral density (BMD) measured with dual energy X-ray absorptiometry (DEXA) in the lumbar spine section decreased only by 3.3% among placebo users [4].

Arlot et al. treated postmenopausal patients with strontium ranelate or with placebo in a 3-year follow-up study. With the help of micro-CT, they analysed transiliac bone biopsy at the end of the research, and it was found that compared to the placebo group by the strontium ranelate consumers, structural model index (SMI) significantly improved and Tb.Sp significantly decreased, while cortical thickness (Ct.Th) and Tb.N increased [5].

The effectiveness of treatment with human parathyroid hormone (PTH) was also tested in placebo-controlled research; in a micro-CT analysis of the sample obtained with hip biopsy, there

it was found that BV/TV was 44%, Tb.N 12%, and trabecular thickness (Tb.Th) 16% higher compared to the values of the placebo group at the end of the 18-month-long treatment [6].

Yamashita-Mikami et al. examined the bone structure of the alveolar spongiosa taken from the site of implants to be implanted in place of the molars or premolars of the lower jaw among pre-, post- and late postmenopausal women with micro-CT. Besides that, they also examined bone turnover markers (type I collagen cross-linked N-telopeptide (NTX), bone-specific alkaline phosphatase (BALP), osteocalcin (OC), deoxypyridinoline (DPD)). The BV/TV was significantly smaller, the trabeculae were more separated and more rod-like at the postmenopausal group than in the premenopausal and all bone parameters showed correlation with at least one bone turnover marker [7].

7.2.2 Rat Studies

Because none of the animal models are fully suitable for modelling osteoporosis, since 1994 FDA requires any potential new therapy to be verified

in experiments conducted on at least two different animal species before proceeding further [8]. Osteoporosis models can be created medically (e.g. dosage of oestrogen receptor antagonist [9], gonadotropin release hormone agonist [10]) or surgically. However, besides these, an immobilization model (created surgically, e.g. with neurectomy [11] or with tenotomy [12], or in a conservative way, e.g. with hindlimb [13]), or a model created by interfering in their nutrition (e.g. a low-calcium diet [14]), can also be found in the literature [15]. The ovariectomized rat model was used even before 1973, and then in 1992 it was confirmed that it might be useful in modelling postmenopausal osteoporosis [16]. This model, along with its known errors, represents the gold standard even today. Surgical techniques can also be of several types: both ventral or dorsal approaches are possible [17] (Fig. 7.2). Techniques can also be combined (e.g. simultaneous application of ovariectomy and low doses of calcium intake [18]).

Caution should be taken however when choosing the age of the animals, since with age the modelling changes into the remodelling in cases of both spongiosa and cortical in the rats' skeletal system [19]. Studies show that the examination of remodelling is possible in rats after 12 months of age in cases of the lumbar vertebrae and the

tibia proximal metaphysis, because by this time this is the dominant activity in the case of the spongiosa and the cortical [20]. As long as modelling dominates, areas adjacent to proximal tibia epiphysis nearby the growth plate cannot be used for densitometry, tomography or histomorphometry, since length growth can still be experienced in the bones. In female rats this process ends in the case of tibia by the age of 15 months and in the case of lumbar vertebrae by the age of 21 months [20]. Bone loss does not develop at the same pace at different test locations in the spongiosa: 14 days after ovariectomy by the tibia proximal metaphysis; 30 days after by the femoral neck; and 60 days after by the body of lumbar vertebrae, a significant change can be seen. On the contrary after the ovariectomy, the thickness of the cortical bone decreases significantly, in 180 days in the case of the tibia and 90 days in the case of the femur [20]. The rate of bone loss in respect of the whole organism is also of altering dynamics: rapid bone loss is experienced in the first 100 days. This is followed by an intermediate period where, at an osteopenia level, a relative stabilization occurs in the spongiosa and then after 270 days a slower bone loss is experienced [21]. When analysing the cortical bone, the fact that for a long time Havers remodelling could not be demonstrated in rodents posed a problem. It can be experienced that the cortical increases from the periosteum's side and gets thinner from the endosteum side [22]. Further studies have confirmed that Havers system can be found also in the rats' cortical: they are large, highly interconnected and irregular in the endosteal region, while the canals in the periosteal region are straight and small [23].

Micro-CT is suitable for both in vivo and in vitro examinations in the case of animals this size, as well as several types of sampling places can be used: may this be in the area of the tibia, femur, vertebrae, and mandible.

It was an in vivo examination of Brouwers et al., when they were examining the parathyroid hormone (PTH) treatment's effects in an ovariectomized (OVX) rat model. Immediately after the surgery and then on the 8th, 10th, 12th and 14th week, micro-CT examinations were conducted

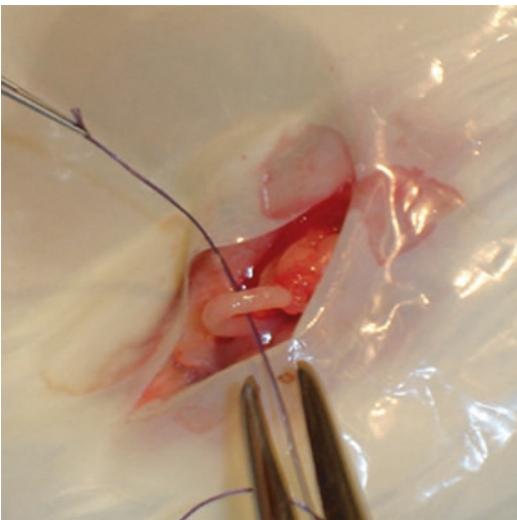


Fig. 7.2 The dorsal ovariectomy technique

under general anaesthetic, in order to cross-reference the proximal tibia meta- and its epiphysis's microstructure. At both areas the growth of the Tb.Th was found as an effect of the therapy. Tb.N grew only in the epiphysis during the time of the longitudinal examination. It was found, therefore, that the two areas react differently to the therapy and firstly bone is to be formed where due to the increased force it is most necessary and only after that at all other surfaces. During the PTH treatment, the cortical bone mass was continuously increasing [24], in accordance with other studies [25].

Dai et al. studied the changes of the alveolar bone in the area of the maxilla in the ovariectomized rat model in vitro. Twelve weeks after the ovariectomy and the sham-surgery (SHAM), the animals were examined, and their maxilla was removed; in order to examine the alveolar bone between the roots of the upper first molar by using micro-CT, a histological examination was also performed. Compared to the BMD, BV/TV and Tb.Th values of the sham-operated group, significantly smaller values were measured at the ovariectomized group. Based on their results, it can be concluded that changes created during ovariectomy can be observed in the maxilla spongiosa the same way like in other bones [26].

Ovariectomized rat models are not only used in micromorphological investigations, but most of the time, biomarkers are also examined along with the aforementioned. This is how it happened in Yoon et al.'s in vitro research, where OC and BALP levels were examined in the serum, which are the sensitive indicators of bone formation, and C-telopeptide of type I collagen (CTX), which is the marker molecule of bone degradation. They found that in the OVX group compared to the SHAM group, a 75.4% higher level of osteocalcin and a 72.5% higher level of CTX level were detected. The increased values of resorption markers indicate the activation of bone resorption in postmenopause, which can be explained by oestrogen deficiency. Bone formation increases due to the elevated number of bone building, starting in the bone lacuna. The osteoporotic bone develops because the balance among these processes shifts. As a result of all these

changes, an osteoporotic bone was found, in this case, while the L4 vertebra was examined and mechanical testing was done. In the case of the spongiosa, there was a significant difference between the groups in respect of the Tb.Th, BV/TV and the Tb.Sp, as well as in the case of the cortical bone mineral density (Cr.BMD) [27].

Besides studying the spongiosa, examining the cortical bone keeps gaining greater and greater importance. By using the ovariectomized rat model, Sharma et al. have also studied the spongiosa and the cortical bone structures on the tibia proximal meta- and epiphysis. In line with most of studies, they found that the BV/TV, Tb.Th and Tb.N significantly decreased in the OVX group in respect of the spongiosa, while Tb.Sp and SMI significantly increase. In respect of the cortical, they found that vascular canal porosity (Ca.V/TV) and canal diameter (Ca.Dm) in both the anterior and the posterior region increase in the OVX group, which may contribute to the increased fragility of the osteoporotic bones. In contrast, lacunar porosity (Lc.V/TV) and lacunar density (Lc.N/TV) did not show significant differences between the groups [28].

Bone lesions developed due to oestrogen deficiency were studied in rats' mandible by Ames et al. They found that in the OVX group in the alveolar bone, the variability of the value of tissue mineral density (TMD) is greater than in the control region, which was designated to represent the bone part of the mandible, which is not an alveolar bone, and neither the internal nor the external borders. Oestrogen deficiency increases the level of bone remodelling, and consequently, the variability of TMD also increases. The variability in the alveolar bone increased even more compared to this, presumably due to the chewing, what makes bone remodelling here quite active anyway [29].

The cortical of the mandible in the ovariectomized rats was found significantly thinner by Yang and his colleagues compared to the sham-operated animals. However, 12 months were required for this change [30].

Mavropoulos et al. compared the microarchitecture and bone mineral density (BMD) of the mandible and the proximal tibia. The rats were

ovariectomized or sham-operated and were paired isocaloric diets containing either 15% or 2.5% casein. The animals were given 100 IU/kg body weight vitamin D in peanut oil every day. Seventeen weeks after the surgery, blood was sampled to determine the IGF 1 and OC levels, and they were exterminated. They worked with a 16 μm voxel size in the case of both bones. The mandible VOI was drawn between the roots of the molars and the root of the incisor. The following differences were found: in the members of the SHAM group by a low protein intake, the mandible BV/TV decreased with 17.3%, and the tibia BV/TV decreased with 84.6%. By normal protein intake in the OVX group, the decrease of the mandible BV/TV was 4.9%, as opposed to the 82% decrease of the tibia ($p < 0.001$). A possible explanation of the deviation may be that the mandible's alveolar bone structure is stimulated the continuous chewing, with this protecting the microstructure of this area [31].

Kozai et al. were investigating the impact of the glucocorticoids on the bone structure on the mandible and femur. BMD values were measured by pQCT in both bones. They were also analysing the structure of the spongiosa (voxel size 32 μm) from the first molar root through 100 slices by micro-CT. They found a strong correlation between the mandibular and femoral cortical bone mineral content (BMC): steroid treatment significantly reduces the value of the BMC and the thickness of the cortical in the mandible and the diaphysis of the femur. At the same time, in the trabecular structure of the mandible, no significant changes were observed. The microstructure of the femur was not investigated [32].

Blazsek et al. created an interesting rat model where implants were placed in tail vertebra and treated with aminobisphosphonate. They published a surprising result that the rat tail vertebra was poor in the bone marrow parenchyma but rich in bone forming and resorbing cells. This means that rat tail vertebra is an ideal microenvironment in preclinical investigation where drug affecting bone metabolism can be examined without drug interactions with bone marrow cells just like in the mandible [33].

In light of the above-mentioned researches, it can be seen that within even a single bone, the change of the bone structure can be differing, in osteoporosis models created in different ways.

7.2.3 Mice Studies

Among all animal models, the mouse model is the second most common in osteoporosis research. But while in most rat studies, we meet examinations of the micromorphological changes caused by ovariectomy and consequential oestrogen deficiency, genetically modified mice experimental researches are carried out more frequently among mice. Experiments are usually done on young, 8-week-old mice. Mice do not develop menopause, but as they grow older, they eventually become acyclic. Due to their extremely diverse genetic properties by each mice species, slightly different bone physiological characteristics can be seen.

The bone structure of mice responds similarly to ovariectomy as rats: for example, the stock loss of spongiosa in the proximal metaphysis of tibia is 50% in 5 weeks at Swiss-Webster mice [34]. C57BL/6J is another commonly used mice type. The increase of the femur ends in the 6th–7th month. However, the increase of the intramedullary and the deceleration of bone building are already common at 12-week-old mice (corresponding 40 human years), and these processes result in thinner cortex [35]. Glatt et al. also call attention to the fact that in this tribe the BV/TV value reaches its maximum in the metaphysis of bones when the animals are in 6–8 weeks of age. From that point there is a slow but continuous decrease during their aging even without any bone metabolism influencing factors [36]. However, the cortical bone mass of BALB/c mice does not start to decrease until they reach the age of 20 months [37]. Senescence-accelerated mouse P6 (SAMP6) is used for the modelling of senile osteoporosis. This is the species that attracts attention because microscopic changes in the trabecular bone structure of vertebrae can be observed earlier than in the spongiosa of tibia and femur, but the bone changes of the cortical are

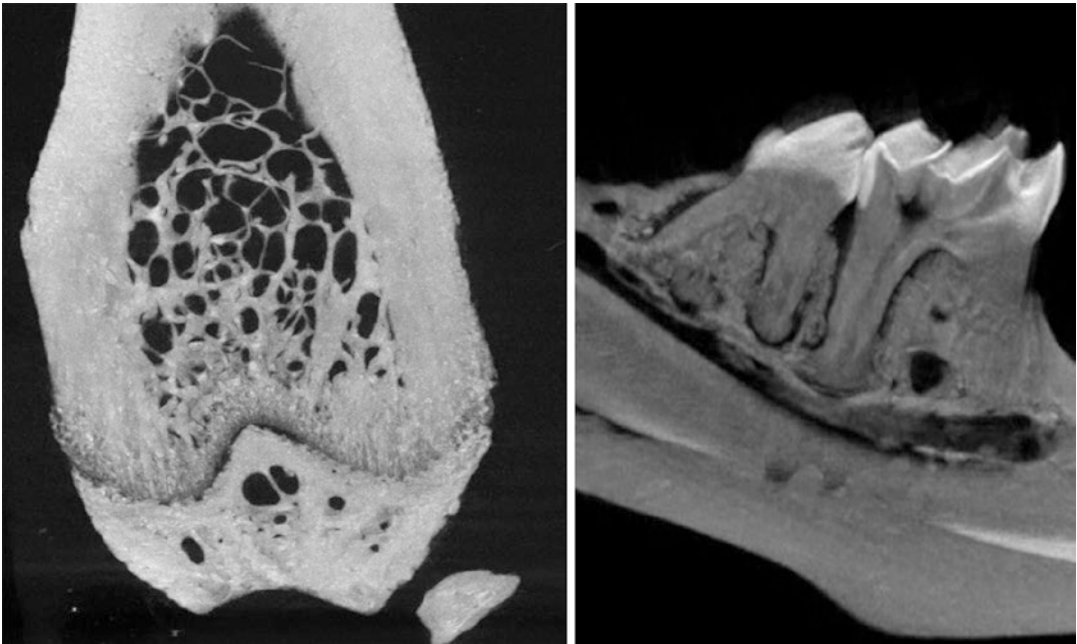


Fig. 7.3 Several types of sampling place (e.g. mouse femur and mandible)

not significant compared to SAMR1 mice of the same age [38].

The femur [39], tibia [38], lumbar vertebra [40] and less often the mandible [41] are the most commonly investigated areas in the case of spongiosa in mice as well (Fig. 7.3).

Sheng et al. examined the effect of zoledronate on osteoprotegerin-deficient mice. Mice received zoledronate or the medium for 4 weeks. BALP and tartrate-resistant acid phosphatase 5b (TRACP-5b) levels were determined from serum with ELISA, and after that the animals were exterminated and the mandible and tibia were removed. Values of BALP and TRACP-5b of KO mice were significantly higher than the ones of the wild type or ones that had received zoledronate. As an effect of zoledronate treatment, high values of BALP and TRACP-5b decreased among KO mice. Both bones were examined using 7- μ m-wide voxel size. VOI expanded from the mesial edge of first molar until the distal edge of third molar during the examination of mandible spongiosa, except the teeth and the cortical. A 1.5-mm- X 1.5-mm-wide area was marked out between the lower

and the upper barrier on the buccal side of the mandible body during the examination of the cortical. In the case of the KO mice in the mandible, the BV/TV by 31%, Tb.Th by 60%, connectivity density (Conn.D) by 66% and Tb.N by 21% became lower, while the bone surface/bone volume ratio (BS/BV) by 61%, Tb.Sp by 37% and SMI by 114% became higher than in the wild type. In the case of the tibia in KO mice, BV/TV by 93%, Conn.D by 87% and Tb.N by 88% became lower, while SMI became higher by 82% than in wild type. Porosity grew dramatically in the mandible cortical region of KO mice. Lower involvement of the mandible spongiosa in the alveolar area was seen compared to long bones [42].

Six weeks after the ovariectomy and sham surgery of C57BL/6 mice, a 0.8-mm-diameter-wide cortical bone defect was created into the middle diaphysis of the right femur of those mice that were not exterminated. Its changes then were examined in vivo on the 0, 3, 7, 10, 14 and 21 days after the surgery. When these animals were exterminated as well, procollagen type 1 amino-terminal propeptide (PINP) and CTX with

ELISA were determined, and several expressions of more genes were also investigated (i.e. type I collagen, OC). In vivo micro-CT analysis gave the result that bone volume fraction was significantly lower in the defect and intramedullary areas in the OVX group between day 10 and 20. It seems that intramembranous ossification was damaged in the osteoporosis caused by the OVX [43].

7.2.4 Other Animal Models in Osteoporosis Research

Most commonly used postmenopausal animal models were elaborated on rodents which usually means the ovariectomization of the animals. However, these models are often criticized in respect of what kind of significant differences there are between rodents' and humans' bone metabolisms. Critics firstly emphasize the fact that rodents don't have menopause, so it is artificially created for the experiment, and they also differ in their remodelling. That is why, less often though, there are a few researches done on other mammals too. The execution of these is more complicated, and their process time is longer than by rodent models.

Not surprisingly, primates are very similar to humans in respect of hormonal and bone structural changes. These animal species have similar menstruation cycles to humans, and they can reach menopause, only at a much later age [44]. The ovariectomized or sham-operated cynomolgus apes were selected as subjects of the experiment by Binte Anwar et al. Seventy-six weeks after the surgeries, the mandibles and L2–L4 vertebrae were scanned, and the microarchitecture of the area between the second molar and of vertebrae was compared. SMI growth was found in the alveolar bone of the OVX group, and an increasing number of pores were found towards the top of alveolus. A positive correlation between the damage in the structure of the alveolar bone and the microarchitectural condition of the vertebrae was also detected, which observation is of great significance from a parodontological aspect [45].

Effects of drugs used in osteoporosis are being tested on ovariectomized models of cynomolgus apes, for example, the romosozumab by Ominsky et al. [46]. The developed OVX model was applied on rhesus apes [47] and on baboons [48], especially for the micro-CT investigation of lumbar and thoracalis vertebrae's micromorphology. During the test done on baboons, tight correlation was observed between the histological and micromorphological changes of vertebra T12; however, histology was determined as a more sensitive process than micro-CT, at least when the number of cases is low [48]. It must be taken into account that these models require animals aged 8–22 years, and the duration of experiments is 12–24 months.

Minipigs have been used for a long time in various ways in the research of osteoporosis [49] or bisphosphonate-related osteonecrosis of the jaw (BRONJ) [50] research. The advantage of the pig model is they have a well-developed Havers canal system and their oestrous cycle duration is approx. 20 days, but a disadvantage is the relatively low amount of data available of the ovariectomized model [44]. Attention is being drawn in the case of model OVX that while with cynomolgus apes the animals should be older than 9 years, when the operation takes place, minipigs can be operated when they are only 10–18 months old. When testing different medicines, it should be taken into account that a 16 months' dosage at minipigs and cynomolgus apes equals 4 years in the case of human testing [51].

Bone resorption and formation markers raise significantly in 3–4 months at sheep [52]; these animals have Havers canal system, and their oestrous cycle duration is 14–21 days. However, it can be a problem that they are able to spontaneously lose bone volume during the winter because of the decreased bone formation [44]. In the case of a combined model, microstructural bone changes develop over 6 months, as it happened in the case of Lill et al. while they were working with sheep aged 7–9 years. Animals were divided into four groups according to the treatment they had gone through (simulated surgery/ovariectomization/calcium/vitamin D/methylprednisolone). Their BMD was determined every

2 months; then 6 months after the surgeries, the animals were exterminated; and the central located biopsy—taken from vertebrae L3 and L4—was analysed with micro-CT. Results showed that at this species the combined procedure is the most expedient as well, because the ovariectomized, calcium- and vitamin D-withdrawn but methylprednisolone-injected group had the largest BMD, Tb.Th and Tb.N decrease [53].

Neither is the rabbit model common, but Baofeng et al. worked with this model in 2010. Actually, this experiment is very similar to the model of Castaneda et al. [54]. It is a combined model too: osteoporosis was created with the simultaneous ovariectomy and glucocorticoid dosage. BMD *in vivo* was measured three times, animals were exterminated 10 weeks after the first surgery and the microarchitecture of vertebrae L3 and L4 were examined, as well as mechanical test was run on them. Their outcomes proved that this model is advantageous from many aspects: active Havers remodelling takes place in the bones of the rabbit, this species reaches bone maturity quickly (7–8 months) and besides the time scale of this model is relatively fast (10 weeks) [55].

The advantages of examinations done on dogs are that dogs have Havers canal systems and their intracortical remodelling is the same as the one found in the human's bone system. There are disadvantages to be found as well; judgements of microstructural changes occurring after ovariectomy can vary because dogs only have one oestrous cycle per year [44]. Even so the ovariectomized dog model is useful [56]. Effects of bisphosphates on lumbar vertebra's (L1) spongiosa's microarchitecture and on its changes were tested on female beagles aged 1–2 years. The control group did not receive anything, while the second group received risedronate and the third received alendronate for a year in high concentrate. Micro-CT examinations gave the outcome that microstructure moved towards the plate-like model as a consequence of the treatment and the bone structure became denser compared to the control [57].

Siu et al. worked with a goat model. Averagely aged 3.4-year-old Chinese mountain goats were ovariectomized and then kept on low-calcium diet for 6 months. Important selection criteria were the growth zone's completion of the distal femoralis and the proximal tibia. Both the micro-CT testing and the BMD determination were done on a biopsy of iliac crest at the beginning and then 6 months later. BMD decreased by 16.3% in the 6th month, while BV/TV decreased by 8.34%, Tb.N by 8.51%, Conn.D by 18.52% and Tb.Sp increased by 8.26%. Straightforward positive correlation was determined between BMD and BV/TV, while negative correlation was determined between BMD, Tb.Sp and SMI [58]. Yu et al. did a long-term experiment on Chinese mountain goats. Serum oestrogen levels and the BMD on the vertebrae L1–L4, on the femoral neck and on the diaphysis of femur and tibia were measured at the beginning and 24 months after the ovariectomy and sham surgeries; moreover cyclic mechanic testing was executed on the vertebra, femoral head and femoral neck. Micro-CT examination took place on the vertebra, femoral head and femoral neck only after the extermination. A decrease of the BMD value was found along with a significant decrease of the Tb.N, Tb.Th and BV/TV in the OVX group compared to group SHAM. At the same time, cortical bone porosity was significantly higher at group OVX in the aspect of femoral neck and vertebrae [59].

Osteoporosis experiments conducted on guinea pigs [60] and micropigs might be the rarest [61].

7.3 Micromorphological Changes of Bones in Osteoporosis

Most of the time, it is the first fracture that draws the attention to the fact that someone has osteoporosis. For a long time, the illness lacks any symptoms. However, the broken bones and microfractures accompanied by symptoms are not predominantly derived from the lessened state of the bone tissue; the underlying cause is also the significant change in the microarchitecture

of the bones. These changes occur in the time and the way of appearance bone by bone. Deviations within a certain bone can be found too. For some time besides the changes of the trabecular bone structure, researchers attach increasing importance to the cortical bone loss in the pathogenesis of osteoporosis, especially with patients above the age of 60. Unfortunately, nowadays most anti-osteoporotic drugs used clinically have less effect on cortical bone than trabecular bone, since these two types of bone tissue differ not only in their structure but in their mechanical characteristics and metabolic activity too [62].

When choosing the size of the voxel, we have to consider that a too high resolution expands the time of scanning and makes it harder to manage the file. The voxel number at the same time must be high enough in order to manage to catch the complex structure of the bone. It seems that it is enough if six voxels form one trabecula along the thickness direction to analyse the structure, and for the acceptable accurateness of the finite element analysis (FEA) model, it is also appropriate if six elements create a trabecula [63].

When setting the value of the threshold, we create a binary picture from a complex picture. It is a qualitative definition, if a calibrated expert compares the original greyscale images to the picture of the segmented trabecular bone. It is quantitative, if it is determined based on a histogram what counts as bone tissue and what does not. In the case of the global threshold, there is a set threshold for the whole data set, while by the local threshold, there is a different threshold value assigned to each and every pixel, based on the greyscale information of the adjacent pixels [64].

In the research done by Isaksson et al., the standardized sampling was taken from alive subjects' iliac crest area, cadavers, femur and the tibia's condylus medialis or the medialis plateau. The donors were males and females, alive and cadaver, who were divided into groups: osteoporotic and ones with normal bones based on DXA, clinical diagnosis and quantitative histomorphometrics. The size of the voxel was 14 μm at the iliac samples and 18 μm by the femur and the tibia. Two different threshold techniques were used in every case, global threshold independently from the size of the voxel and local threshold used

with a technique demonstrated by Waarsing [65]. Taken everything into consideration, they found that the algorithm using local thresholds is less applicable, when we want to show the difference between the highlighted parameters (BV/TV, Tb.Th, Tb.Sp, DA, SMI), and that the value of BV/TV does not change significantly in normal bone structure over 150 micron voxel size, but by osteoporotic samples deviation can be seen, even in the case of a smaller voxel size [66].

Longo et al.'s experiment draws special attention to choosing the right voxel size. They analysed the rat tibias, using micro-CT on an ovariectomized model, with an in vivo 18 μm and ex vivo 9 and 18 μm resolution. There was no difference by 18 micron voxel size between the in vivo and ex vivo scanning in the analysed bone parameters. However when comparing the values obtained using 9 micron voxel size to the ones obtained using 18 micron voxel size, Conn.D is significantly lower, and Tb.Th and the Ct.Th are significantly higher at 18 micron resolution both by OVX and SHAM groups, although most of the parameters are correlated with the parameters obtained using 9 micron ex vivo scan settings [67].

In a research conducted on a vertebra belonging to a mouse, the pixel size was varied between 6 and 30 micron, and the threshold values were defined both quantitatively and qualitatively. They found that certain parameters are highly depending on the voxel size, for example, CD and Tb.Th, but with other parameters like Tb.N and Tb.Sp, there was no significant difference either by small or bigger voxel size. By small voxel size, the two threshold techniques concluded in similar results, but when increasing the voxel size, the differences were increasing. The qualitative segmenting technique was more effective for measuring BV/TV and Tb.Th besides varying voxel sizes, while the quantitative technique seemed to be more effective in the case of Tb.N, Tb.Sp and SMI [68].

Milovanovic et al. found in his research that when examining the femoral neck cortical of both healthy women and women with osteoporosis and contralateral hip fracture, the fragile bone demonstrated lower pore volume at the measured scales. The investigated pore size was between 7.5 and 1500 nm. In the healthy bone 200 to

1500 nm pores were present in a higher rate. The osteoporotic bone is known for increased porosity at macroscopic level and level of tens or hundreds of microns, but this study with a unique assessment range of nano- to micron-sized pores reveals that osteoporosis does not imply increased porosity at all length scales [69].

7.3.1 Micromorphological Changes in Vertebra

The prevalence of broken vertebra is higher in younger generations than any osteoporotic fractures, i.e. hip fractures. The annual occurrence of osteopathic vertebrae fractions can be hardly determined, because a substantial proportion of the fractures remains unrecognized in clinical practice. But whether they cause complaints or not, a broken vertebra causes increased morbidity and mortality [70]. When testing on humans [71], rats [27], mice [38] and on other species [48, 53] inside the vertebral body, we usually see the following changes while performing micro-CT analysis: the trabeculae are getting thinner, they are mostly rod forms, the distance between them is increasing and the BV/TV connectivity decreases [71].

7.3.2 Micromorphological Changes in the Femur and Tibia

The distal femur and proximal tibia are the most investigated fields of the osteoporosis research done by micro-CT, usually in animal testing. A well-defined and assessable-sized region of interest (ROI) can be marked out even in the case of the mouse. Marking out the ROI in the case of meta- and diaphysis spongiosa and cortical research can be conducted easily by keeping a certain distance from the growth plate. Femoral neck is a rarely investigated area with micro-CT [69], although it is used in more models conducting mechanical tests [72]. While examining humans in this area in the spongiosa, even aging results in a 20% decrease in BV/TV and Tb. Th, Conn.D and Tb.N also decrease in both genders [73]. It was observed on more occasions that osteoporotic microstructure changes can be detected earlier in the trabecular bone structure of the vertebra than in the spongiosa of the femur and the tibia [20, 38]. In osteoporosis by these bones, mainly BMD decrease was observed along with a decrease in BV/TV, Tb.Th and Tb.N and rod-form trabeculae [39, 74] (Fig. 7.4).

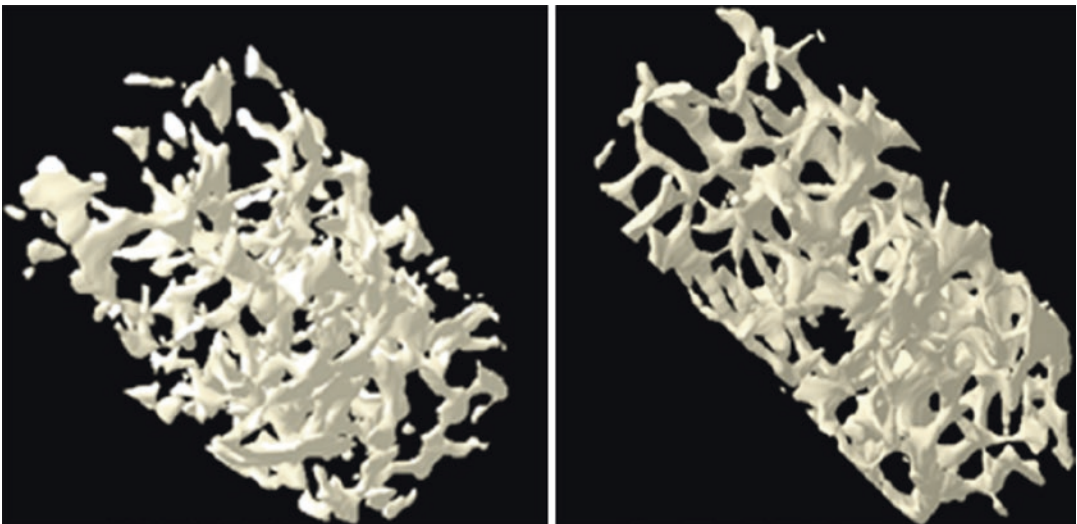


Fig. 7.4 OVX and SHAM trabecular bone from mouse tibia

7.3.3 Micromorphological Changes in the Mandible and Maxilla

In a systematic review, published in 2015, attention is drawn to the fact that the examination areas of the rodents' jaw microstructure are rather heterogenic and standardization would be required [75]. Most frequently on the maxilla, the alveolar bone around the first molars, the interdental septum is examined. On the mandible, the alveolar bone around the molars, the area between the molars and the incisor and the base of the mandible are determined differently by each author, and the condylus are investigated [75]. Defining the ROI is a more difficult task in this case, harder than with the other bones, mainly because of the small size of the sample (Fig. 7.5).

The examination of alveolar bone structure in osteoporosis shows a different result: in some cases, no significant changes were found in these areas [32], or at least slower-evolving and less significant changes were found in the bone structure [45], but in other cases, damage of the bone tissue similar to those found in other bones was found, correlated with the bone marker molecules [7].

In the condylus of the mandible, two regions, the anterior and posterior, were examined on an ovariectomized rat model by Tanaka et al. The anterior and the posterior regions

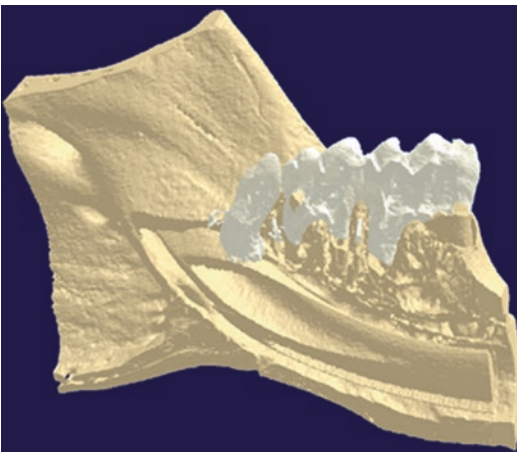


Fig. 7.5 The most commonly used ROIs on mandible are between the roots of molars

showed different bone dynamics. In the OVX group, the bone volume (BV) decreased significantly in the posterior area, though there was no change in the anterior. At the same time in the anterior region, BV was increasing while aging in the SHAM group, and there was no change found in the posterior area. An explanation for this deviation might be that the mechanical stress caused by occlusion affects the two regions differently. The tendency of decreasing bone mass caused by oestrogen deficiency was to be seen in both regions, with time passing by [76].

7.3.4 Future Trends in Analysis of Micromorphological Changes of Cancellous Bone in Osteoporosis

As can be seen from the above, micro-CT is a widespread method for the analysis of the microstructure of the spongiosa, in the case of samples of both human and of animal origin. Data derived this way, or data calculated from these, describe the current state of the trabecular bone structure well. For analysing bone stiffness and locating the potential area, where a bone fracture might occur, a numerical method is used, called finite element analysis (FEA)[77], which has been more and more widely used in biomechanics since 1972 [78]. There is an increasing number of algorithms based on the data of the micro-CT to simulate bone remodeling [79]. Wu et al. tried to find an approach based on micro-CT data to evaluate the changes in bone structure and determine the bone stiffness as quickly as possible especially in the case of longitudinal in vivo examinations [63]. A new field of usage is the mechanical testing of the 3D printed trabecular bone structure, created from micro-CT data. In Barak et al.'s research in the case of the chimpanzee third metacarpal head, they found that an 8% BT/TV decrease results in a 17% structural stiffness and a 24% structural strength decrease [80]. The key step of this analysis is to choose a threshold method and a resolution correctly.

7.3.5 Micromorphological Changes of Cortical Bone in Osteoporosis

When examining the structure of the corticalis, for quite some time, the histological examination was the gold standard. Therefore they wished to compare micro-CT and histological results on human tibia and femur samples. They used two threshold values during the segmentation: one higher than that scanned from the air and the other lower than the sample embedded into the PMMA. Cortical porosity (Ct.Po), canal separation (Ca.Sp) and canal diameter (Ca.Dm) data measured on both histological and micro-CT showed good correspondence and good correlation. It was also revealed that if the threshold value is adequate, then the medium surrounding the sample has no influence on the results [81] (Fig. 7.6).

The cortical of bones gets thinner while aging, even without the presence of osteoporosis. Tiede-Lewis et al. examined the changes in the cortical bone on a mouse model. In their experiment they compared the femur of 5-month-old and 22-month-old C57BL/6 mice. The analysis of the microstructure with the help of micro-CT was conducted on both male and female mice, they analysed the microstructure with micro-CT and they found that in the area of the distal femur, the cortical BV/TV decreased by 6.3% in female mice, while in males it decreased only by 19%.

By these significant changes, not only there is a decreasing number of dendrite in the osteocytes, but the cell density is reduced too. The decrease in dendricity precedes the decrease in the number of osteocytes, giving the impression that the prior is a trigger of the reduced vitality of the osteocytes. However, the osteocytes have a key role of maintaining bone volume [82].

While examining the cortical in the case of a rabbit's femur by Pazzaglia et al., micro-CT pictures were used to calculate tissue volume (TV), canal volume (CaV), Ct.Po and canal surface (CS). Subperiosteally higher canal number was found then subendosteally [83]. In the case of rats, Kim JN et al., in an aforementioned research, found wider diameter and higher connectivity Havers canals near the endosteal area, than subperiosteally [23].

Cortical canals can be visualized on the rat tibia on micro-CT slices and can also be used to examine percent porosity and mean canal diameter with global thresholding [84].

7.4 Materials and Methods of Our Mice Study

While the negative effects of osteoporosis on the quality of the bone and the increased risk of fracture in the vertebrae and long bones are well known and frequently tested in experiments,

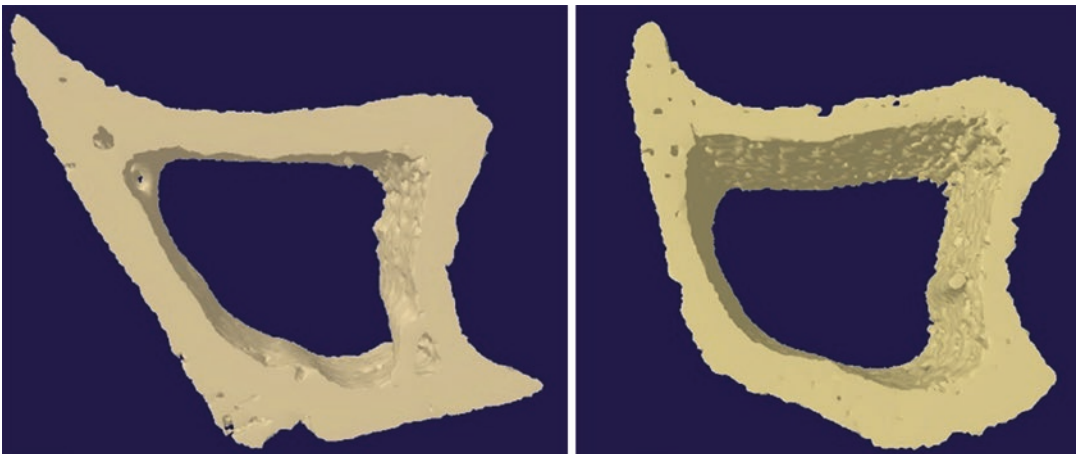


Fig. 7.6 SHAM and OVX cortical bone from mouse tibia

changes in the jaw are less clear. The structure of the mandible and maxilla due to their function and unlike other bones and, uniquely, because of the teeth that are fixed in them, is even more complex. Experiments have shown that postmenopausal osteoporosis can play a role in the progression of periodontal disease and consequent tooth loss [85, 86] but also in later alveolar wound healing [87]. Still, the involvement of the jaw bone in osteoporosis, perhaps because of the different sampling sites, is disputed. Our aim was to investigate the changes in the trabecular and cortical bone structure of the mandible and the femur together while adding vitamin D on the OVX mouse model.

7.4.1 Examination of Femur and Mandible

We divided 30 6-week 22 g CRL:OF1 (Charles River Laboratories) mice into three groups. Ten members of the D3 group after ovariectomy had received vitamin D each day for 6 weeks (4 ng/day, Alpha D3-TEVA 0.25 µg), while ten members of the OVX group after the operation, and ten members of the SHAM group after the sham operation during the period of examination received peanut oil as a vehicle. Following the extermination of the animals, the left hemimandibulas and the left femur were removed and stored in phosphate-buffered saline containing 0.02% sodium aside at 4 degrees Celsius. Scanning was done by Skyscan 1172 (Bruker, Kontich, Belgium). For femur the scanning protocol was set at X-ray energy settings of 50 kV and 198 µA, and the voxel size was 5.02 µm. The settings for the mandible were 70 kV, 114 µA and 7.1 µm. In both cases 0.5 mm Al-filter and 0.5 degree rotation degree were used. The reconstruction was performed with the NRECON (Skyscan, Burker) software; the analysis of the microarchitecture of the mandible and the femur was implemented with the CT Analyzer 1.7.0.0 (Skyscan, Burker) software. During the segmentation global manual threshold technique was applied. For the examination

of the parameters of the mandibula spongiosa, we used the area between the roots of the first molar tooth. The attributes of the mandibula corticalis were examined at the base of the mandible starting from the distal surface of the root of the third molar through 250 mesial slices (Fig. 7.7).

Femurine ROI was determined from the growth plate at the distal epiphysis. From here, the parameters of the trabecular bone were analysed in 400 slices (1.807 mm) from the height of 50 slices measured in the direction of diaphysis. We specified the examination of the cortical bone between the 500. and 600. slices counted from the growth plate (Fig. 7.8).

Statistical analysis was performed using SPSS 24.0 (SPSS, Chicago, IL, USA) software. Kruskal-Wallis test was applied. Significance was set at $p < 0.05$. Then Tukey's post hoc test was used.

7.4.2 Results

In the cortical bone of the femur, Ct.Th was significantly lower in the OVX group than in SHAM or D3 ($p < 0.005$) (Fig. 7.9). There were no significant changes in mandibular cortical bone in the examined parameters.

In the trabecular bone of the femur, BV/TV was significantly lower in the OVX group than in SHAM ($p < 0.001$), Tb.Th was significantly lower in the OVX group compared to SHAM and D3 ($p < 0.05$), and Tb.Pf in the OVX group was significantly higher than in the SHAM group ($p < 0.005$). BS/BV was higher in the OVX group compared to D3 and SHAM ($p = 0.064$). In this case, an increase in the number of elements would be required to confirm any significance (Fig. 7.10).

In trabecular bone of the mandible in the OVX group, BV/TV was significantly lower than in the SHAM or D3 group ($p < 0.05$), BS/BV in the OVX group was significantly higher than in the SHAM group ($p < 0.05$) and Tb.Th in the OVX group was significantly lower than in SHAM or D3 ($p < 0.005$) (Fig. 7.11).

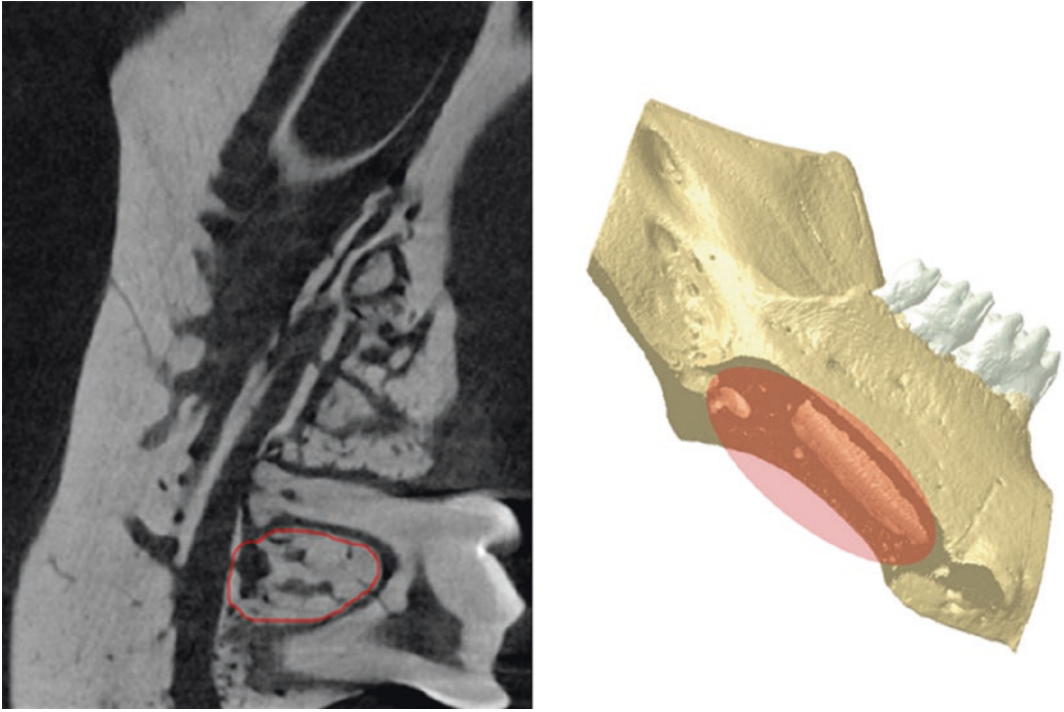


Fig. 7.7 Mandibular ROIs

Fig. 7.8 ROIs from femur

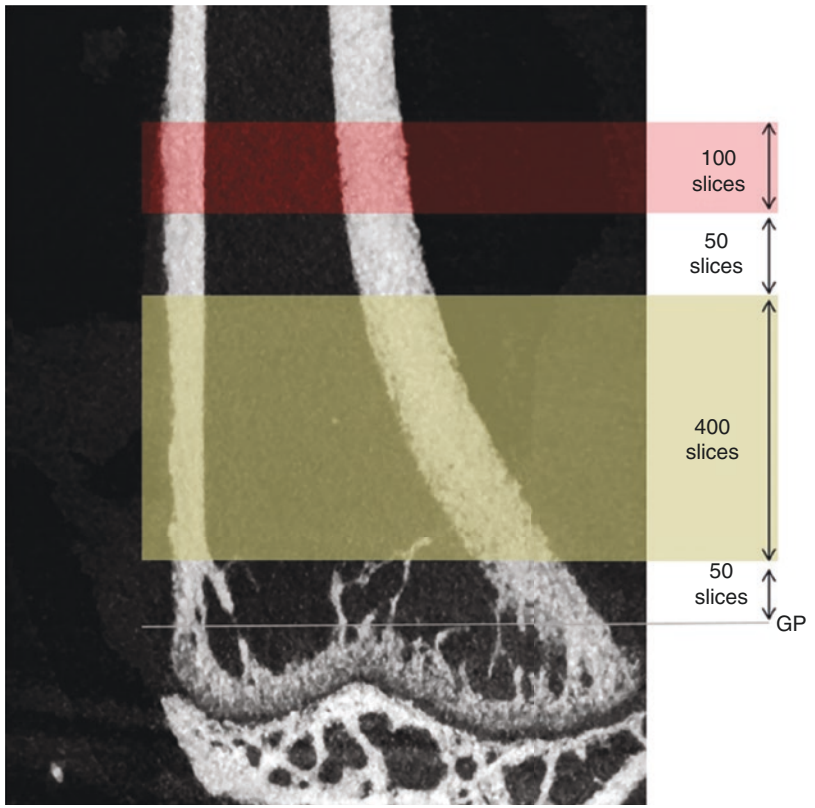
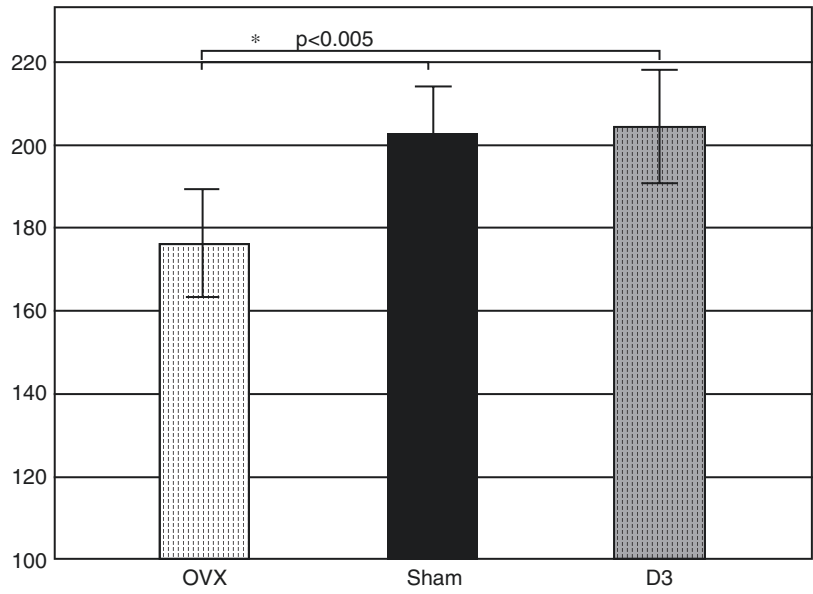
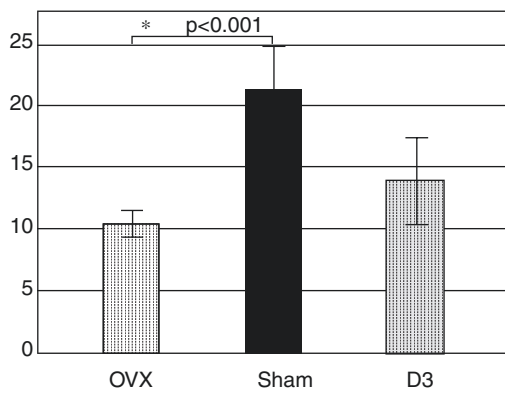


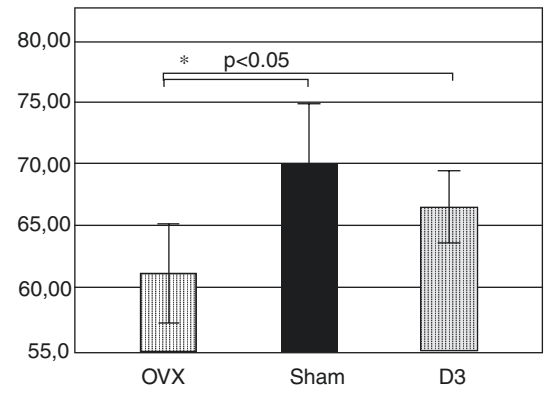
Fig. 7.9 The cortical thickness in femur ($n = 10$)



a



b



c

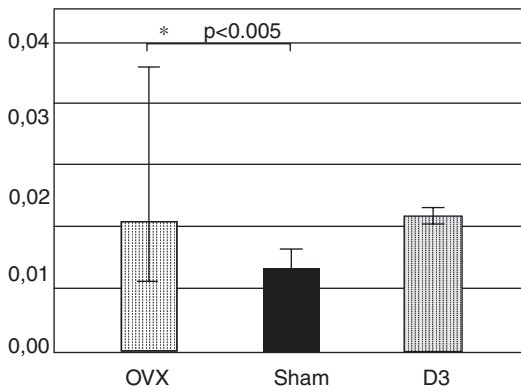


Fig. 7.10 Micromorphological results in trabecular bone of the femur. (a) BV/TV; (b) Tb.Th; (c) Tb.Pf ($n = 10$)

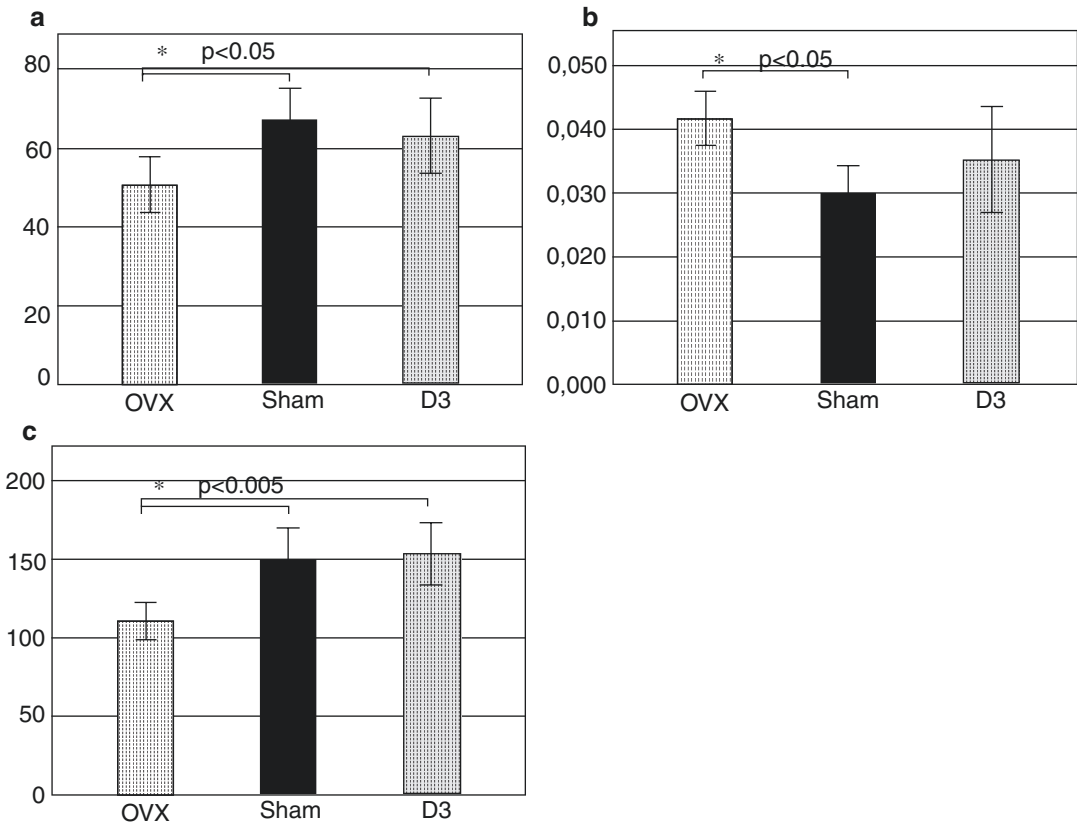


Fig. 7.11 Micromorphological results in trabecular bone of the mandible. (a) BV/TV; (b) BS/BV (c) Tb.Th ($n = 10$)

7.4.3 Discussion

In the cortical examination, the results showed that in the OVX group, femoral cortical bone tends to become thinner due to oestrogen deficiency, and this negative change could be eliminated by the administration of vitamin D3. In contrast, there was no significant change in the cortical mandible. Considering the tendency of the data, this may be due to the need for more time to change the cortical thickness of the mandible than for long bones. Lee et al. investigated the development of renal osteodystrophy on mouse mandible, and at the end of week 15, the cortical was significantly thinner [88]. In a surgical model of postmenopausal osteoporosis in chronic kidney disease (CKD), in the case of mouse, 12 weeks after ovariectomy, mandibular cortical thickness was significantly lower in OVX

and OVX + CDK groups compared to SHAM in Guo et al.'s study [89].

The bone parameter determinations in trabecular bone both in the case of femur and mandible also resulted in significantly lower BV/TV values in the OVX group compared to SHAM and D3 groups. Likewise, BV/TV was also lower in both study areas in the OVX group for SHAM and for mandible in relation to D3. The increase in BS/BV values in the OVX group, consistent with the previous parameters, shows a weakened microarchitecture in both bones in the OVX group. Based on the results of the D3 group, it can be said that in both designated test areas, microstructural damage to bone tissue was reduced. The assessment of alveolar bone involvement in osteoporosis is controversial in the literature. Sheng et al. found that the bone structure of the mandibula was less responsive to the osteoprotegerin (OPG)

gene deprivation than the tibia [42]. In the study of Bouvard et al., the BV/TV value of alveolar bone decreased significantly in 28 days [41]. Ejiri et al. examining the alveolar bone structure on OVX rat model found that serious bone loss was caused by high bone resorptive activity, which was accelerated immediately after ovariectomy, followed by a milder, but longer-lasting, resorptive activity. During this time, trabeculae are separated into smaller fragments, while their number decreases, so their recovery is very cumbersome [87]. In their examinations, it was concluded that occlusal hypofunction could significantly increase the fragility of the bone structure around the teeth [87]. The cause of the mentioned controversy may be different ROI. Johnston et al. call attention in that the alveolar bone ROI should be limited to the interradicular septum of the first molar, because it is the most well-characterized site and appears to respond positively to the established bone-sparing effect of oestrogen [90].

7.5 Summary

In our study the microstructure of mandibular and femoral trabecular bone changed in the same way under the influence of ovariectomy in 6 weeks, and the protective effects of vitamin D were also shown in the two test sites. To observe the changes of cortical bone in the case of the mandible, 6 weeks were not enough, unlike in the case of the femur.

References

- Nieves JW, Formica C, Ruffing J, Zion M, Garrett P, Lindsay R, Cosman F. Males have larger skeletal size and bone mass than females, despite comparable body size. *J Bone Miner Res.* 2005;20:529–35.
- Barling PM. Osteoporosis - an increasingly important issue for both young and aging citizens of Malaysia. *leJSME.* 2013;7(1):1–3.
- Eckstein F, Matsuura M, Kuhn V, Priemel M, Müller R, Link TM, Lochmüller EM. Sex differences of human trabecular bone microstructure in aging are site-dependent. *J Bone Miner Res.* 2007;22:817–24.
- Dufresne TE, Chmielewski PA, Manhart MD, Johnson TD, Borah B. Risedronate preserves bone architecture in early postmenopausal women in 1 year as measured by three-dimensional microcomputed tomography. *Calcif Tissue Int.* 2003;73:423–32.
- Arlot ME, Jiang Y, Geneant HK. Histomorphometric and microCT analysis of bone biopsy from postmenopausal osteoporotic women treated with strontium ranelate. *J Bone Miner Res.* 2008;23:215–22.
- Fox J, Miller MA, Recker RR, Sp B, Smith SY, Moreau I. Treatment of postmenopausal osteoporotic women with parathyroid hormone 1-84 for 18 months increases cancellous bone formation and improves cancellous architecture: a study of iliac crest biopsy using histomorphometry and micro computed tomography. *J Musculoskelet Neuronal Interact.* 2005;5:356–7.
- Yamashita-Mikami E, Tanaka M, Sakurai N, Arai Y, Matsuo A, Ohshima H, Nomura S, Ejiri S. Correlation between alveolar bone microstructure and bone turnover marker sin pre- and post-menopausal women. *Oral Maxillofac Surg.* 2013;115:12–9.
- Thompson DD, Simmons HA, Pirie CM, Ke HZ. FDA guidelines and animal models for osteoporosis. *Bone.* 1995;17(4 Suppl):125–33.
- Gallagher A, Chambers TJ, Tobias JH. The estrogen antagonist ICI 182,780 reduces cancellous bone volume in female rats. *Endocrinology.* 1993;133:2787–91.
- Goulding A, Gold E. A new way to induce oestrogen-deficiency osteopaenia in the rat: comparison of the effects of surgical ovariectomy and administration of the LHRH agonist buserelin on bone resorption and composition. *J Endocrinol.* 1989;121:293–8.
- Zeng QQ, Jee WS, Bigornia AE, King JG Jr, D'Souza SM, Li XJ, Ma YF, Wechter WJ. Time responses of cancellous and cortical bones to sciatic neurectomy in growing female rats. *Bone.* 1996;19:13–21.
- Thompson DD, Rodan GA. Indomethacin inhibition of tenotomy-induced bone resorption in rats. *J Bone Miner Res.* 1988;3:409–14.
- Tian XY, Jee WS, Li X, Paszty C, Ke HZ. Sclerostin antibody increases bone mass by stimulating bone formation and inhibiting bone resorption in a hindlimb-immobilization rat model. *Bone.* 2011; 48(2):197–201.
- Kim C, Park D. The effect of restriction of dietary calcium on trabecular and cortical bone mineral density in the rats. *J Exerc Nutr Biochem.* 2013;17(4):123–31.
- Lelovas PP, Xanthos TT, Thoma SE, Lyritis GP, Dontas IA. The laboratory rat as an animal model for osteoporosis research. *Comp Med.* 2008;58:425–30.
- Frost HM, Jee WSS. On the rat model of human osteopenias and osteoporoses. *Bone Miner.* 1992;18:227–36.
- Khajuria DK, Razdan R, Mahapatra DR. Description of a new method of ovariectomy in female rats. *Rev Bras Reumatol.* 2012;52(3):462–70.
- Gao X, Ma W, Dong H, Yong Z, Su R. Establishing a rapid animal model of osteoporosis with ovariectomy plus low calcium diet in rats. *Int J Clin Exp Pathol.* 2014;7(8):5123–8.

19. Dennison E, Cole Z, Cooper C. Diagnosis and epidemiology of osteoporosis. *Curr Opin Rheumatol*. 2005;17:456–61.
20. Jee WS, Yao W. Overview: animal models of osteopenia and osteoporosis. *J Musculoskelet Neuronal Interact*. 2001;1(3):193–207.
21. Egermann M, Goldhahn J, Schneider E. Animal models for fracture treatment in osteoporosis. *Osteoporos Int*. 2005;16:129–38.
22. Turner RT, Maran A, Lotinun S, Hefferan T, Evans GL, Zhang M, Sibonga JD. Animal models for osteoporosis. *Rev Endocr Metab Disord*. 2001;2:117–27.
23. Kim JN, Lee JY, Shin KJ, Gil YC, Koh KS, Song WC. Haversian system of compact bone and comparison between endosteal and periosteal sides using three-dimensional reconstruction in rat. *Anat Cell Biol*. 2015;48(4):258–61.
24. Brouwers JEM, van Rietbergen B, Huiskes R, Ito K. Effects of PTH treatment on tibia bone of ovariectomized rats assessed by in vivo micro-CT. *Osteoporos Int*. 2009;20(11):1823–35.
25. Iwaniec UT, Moore K, Rivera MF, Myers SE, Vanegas SM, Wronski TJ. A comparative study of the bone-restorative efficacy of anabolic agents in aged ovariectomized rats. *Osteoporos Int*. 2007;18(3):351–62.
26. Dai QG, Zhang P, Wu YQ, Ma XH, Pang J, Jiang LY, Fang B. Ovariectomy induced osteoporosis in the maxillary alveolar bone: an in vivo micro-CT and histomorphometric analysis in rats. *Oral Dis*. 2014;20(5):514–20.
27. Yoon KH, Cho DC, Yu SH, Kim KT, Jeon Y, Sung JK. The change of bone metabolism in ovariectomized rats: analyses of microCT scan and biochemical markers of bone turnover. *J Korean Neurosurg Soc*. 2012;51(6):323–7.
28. Sharma D, Larierra AI, Palcio-Mancheno PE, Gatti V, Fritton JC, Bromage TG, Cardoso L, Doty SB, Fritton SP. The effects of estrogen deficiency on cortical bone microporosity and mineralization. *Bone*. 2018;110:1–10.
29. Ames MS, Hong S, Lee HR, Fields HW, Johnston WM, Kim DG. Estrogen deficiency increases variability of tissue mineral density of alveolar bone surrounding teeth. *Arch Oral Biol*. 2010;55(8):599–605.
30. Yang J, Farnell D, Devlin H, Horner K, Graham J. The effect of ovariectomy on mandibular cortical thickness in the rat. *J Dent*. 2005;33(2):123–9.
31. Mavropoulos A, Rizzoli R, Ammann P. Different responsiveness of alveolar and tibial bone to bone loss stimuli. *J Bone Miner Res*. 2007;22(3):403–10.
32. Kozai Y, Kawamata R, Sakurai T, Kanno M, Kashima I. Influence of prednisolone-induced osteoporosis on bone mass and bone quality of the mandible in rats. *Dentomaxillofacial Radiol*. 2009;38(1):34–41.
33. Blazsek J, Dobó-Nagy CS, Blazsek I, Varga R, Vecsei B, Fejérdy P, Varga G. Aminobisphosphonate stimulates bone regeneration and enforces consolidation of titanium implant into a new rat caudal vertebra model. *Pathol Oncol Res*. 2009;15:567–77.
34. Bain SD, Bailey SC, Celino DL, Lantry MM, Edwards MW. High-dose estrogen inhibits bone resorption and stimulates bone formation in the ovariectomized mouse. *J Bone Miner Res*. 1993;8:435–42.
35. Ferguson VL, Ayers RA, Bateman TA, Simske SJ. Bone development and age-related bone loss in male C57BL/6J mice. *Bone*. 2003;33:387–98.
36. Glatt V, Canalis E, Stadmeier L, Bouxsein ML. Age-related changes in trabecular architecture differ in female and male C57BL/6J mice. *J Bone Miner Res*. 2007;8:1197–207.
37. Willingham MD, Brodt MD, Lee KL, Stephens AL, Ye J, Silva MJ. Age-related changes in bone structure and strength in female and male BALB/c mice. *Calcif Tissue Int*. 2010;86(6):470–83.
38. Chen H, Zhou X, Emura S, Shoumura S. Site-specific bone loss in senescence-accelerated mouse (SAMP6): a murine model for senile osteoporosis. *Exp Gerontol*. 2009;44(12):792–8.
39. Cano A, Dapía S, Noguera I, Pineda B, Hermenegildo C, del Var R, Caeiro JR, García-Pérez MA. Comparative effects of 17 B-estradiol, raloxifene and genistein on bone 3D microarchitecture and volumetric bone mineral density in the ovariectomized mice. *Osteoporos Int*. 2008;19(6):793–800.
40. Willey JS, Livingston EW, Robbins ME, Bourland JD, Tirado-Lee L, Smith-Sielicki H, Bateman TA. Risedronate prevents early radiation-induced osteoporosis in mice at multiple skeletal location. *Bone*. 2010;46(1):101–11.
41. Bouvard B, Gallois Y, Legrand E, Audran M, Chappard D. Glucocorticoids reduce alveolar and trabecular bone in mice. *Joint Bone Spine*. 2013;80(1):77–81.
42. Sheng ZF, Xu K, Ma YL, Liu JH, Dai RC, Zhang YH, Jiang YB, Liao EY. Zoledronate reverses mandibular bone loss in osteoprotegerin-deficient mice. *Osteoporos Int*. 2009;20(1):151–9.
43. He XY, Zhang G, Pan XH, Liu Z, Zheng LZ, Chan CW, Lee KM, Cao YP, Li G, Wei L, Hung LK, Leung KS, Qin L. Impaired bone healing pattern in mice with ovariectomy-induced osteoporosis: a drill-hole defect model. *Bone*. 2011;48(6):1388–400.
44. Bonucci E, Ballanti P. Osteoporosis-bone remodeling and animal models. *Toxicol Pathol*. 2014;42(6):957–69.
45. Binte Anwar R, Tanaka M, Kohno S, Ikegame M, Watanabe N, Nowazesh Ali M, Ejiri S. Relationship between porotic changes in alveolar bone and spinal osteoporosis. *J Dent Res*. 2007;86:52–7.
46. Ominsky MS, Boyd SK, Varela A, Jolette J, Felx M, Doyle N, Mellal N, Smith SY, Locher K, Buntich S, Pyrah I, Boyce RW. Romosozumab improves bone mass and strength while maintaining bone quality in ovariectomized cynomolgus monkeys. *J Bone Miner Res*. 2017;32(4):788–801.
47. Cabal A, Williams DS, Jayakar RY, Zhang J, Sardesai S, Doung LT. Long-term treatment with odanacatib maintains normal trabecular biomechanical properties in ovariectomized adult monkeys as demonstrated by

- micro-CT based finite element analysis. *Bone Rep.* 2017;6:26–33.
48. Hordon LD, Itoda M, Shore PA, Heald M, Brown M, Kanis JA, Rodan GA, Aaron JE. Preservation of thoracic spine microarchitecture by alendronate: comparison of histology and microCT. *Bone.* 2006;38:444–9.
 49. Borah B, Dufresne TE, Cockman MD, Gross GJ, Sod EW, Myers WR, Combs KS, Higgins RE, Pierce SA, Stevens ML. Evaluation of changes in trabecular bone architecture and mechanical properties of minipig vertebrae by three-dimensional magnetic resonance microimaging and finite element modeling. *J Bone Miner Res.* 2000;15(9):1786–97.
 50. Pautke C, Kreutzer K, Weitz J, Knödler M, Münzel D, Wexel G, Otto S, Hapfelmeier A, Stürzenbaum S, Tischer T. Bisphosphonate related osteonecrosis of the jaw: a minipig large animal model. *Bone.* 2012;51(3):592–9.
 51. Tsutsumi H, Ikeda S, Nkamura T. Osteoporosis model in minipigs. In: McAnulty PA, Dayan AD, Ganderup NC, Hastings KL, editors. *The minipig in biomedical research.* Boca Raton, FL: CRC Press; 2012. p. 517–25.
 52. Chavassieux P, Garnero P, Duboeuf F, Vergnaud P, Brunner-Ferber F, Delmas PD, Meunier P. Effects of a new selective estrogen receptor modulator (MDL 103,323) on cancellous and cortical bone in ovariectomized ewes: a biochemical, histomorphometric, and densitometric study. *J Bone Miner Res.* 2001;16(1):89–96.
 53. Lill CA, Fluegel AK, Schneider E. Effect of ovariectomy, malnutrition and glucocorticoid application on bone properties in sheep: a pilot study. *Osteoporos Int.* 2002;13(6):480–6.
 54. Castaneda S, Calvo E, Largo R, Gonzalez-Gonzalez R, de La Piedre C, Diaz-Curiel M, Herrero-Beaumont G. Characterization of a new experimental model of osteoporosis in rabbits. *J Bone Miner Metab.* 2008;26(1):53–9.
 55. Baofeng L, Zhi Y, Bei C, Guolin M, Quingshui Y, Jian L. Characterization of a rabbit osteoporosis model induced by ovariectomy and glucocorticoid. *Acta Orthop.* 2010;81(3):396–401.
 56. Wilson AK, Bhattacharyya MH, Miller S, Mani A, Sacco-Gibson N. Ovariectomy-induced changes in aged beagles: histomorphometry of rib cortical bone. *Calcif Tissue Int.* 1998;62(3):237–43.
 57. Ding M, Day JS, Burr DB, Mashiba T, Hirano T, Weinans H, Sumner DR, Hvid I. Canine cancellous bone microarchitecture after one year of high-dose bisphosphonates. *Calcif Tissue Int.* 2003;72(6):737–44.
 58. Siu WS, Qin L, Cheung WH, Leung KS. A study of trabecular bones in ovariectomized goats with micro-computed tomography and peripheral quantitative computed tomography. *Bone.* 2004;35(1):21–6.
 59. Yu Z, Wang G, Tang T, Fu L, Yu X, Zhu Z, Dai K. Long-term effects of ovariectomy on the properties of bone in goats. *Exp Ther Med.* 2015;9(5):1967–73.
 60. Ding M, Danielsen CC, Hvid I. The effects of bone remodeling inhibition by alendronate on three-dimensional microarchitecture of subchondral bone tissues in guinea pig primary osteoarthritis. *Calcif Tissue Int.* 2008;82(1):77–86.
 61. Kim SW, Kim KS, Solis CD, Lee MS, Hyun BH. Development of osteoporosis animal model using micropigs. *Lab Anim Res.* 2013;29(3):174–7.
 62. Li J, Bao Q, Chen S, Liu H, Feng J, Qin H, Liu D, Shen Y, Zhao Y, Zong Z. Different bone remodeling levels of trabecular and cortical bone in response to changes in Wnt/B-catenin signaling in mice. *J Orthop Res.* 2017;35(4):812–9.
 63. Wu Y, Adeeb S, Doschak MR. Using micro-CT derived bone microarchitecture to analyze bone stiffness—a case study on osteoporosis rat bone. *Front Endocrinol.* 2015;6:1–7.
 64. Firdousi R, Parveen S. Local threshold techniques in image binarization. *Int J Engin Comput Sci.* 2014;3(3):4062–5.
 65. Waarsing JH, Day JS, Weinans H. An improved segmentation method for in vivo microCT imaging. *J Bone Miner Res.* 2004;19(10):1640–50.
 66. Isaksson H, Töyräs J, Hakulinen M, Aula AS, Tamminen I, Julkunen P, Kröger H, Jurvelin JS. Structural parameters of normal and osteoporotic human trabecular bone are affected differently by microCT images resolution. *Osteoporos Int.* 2011;22(1):167–77.
 67. Longo AB, Salomon PL, Ward WE. Comparison of ex vivo and in vivo micro-computed tomography of rat tibia at different scanning settings. *J Orthop Res.* 2017;35(8):1690–8.
 68. Christiansen BA. Effect of micro-computed tomography voxel size and segmentation method on trabecular bone microstructure measures in mice. *Bone Rep.* 2016;5:136–40.
 69. Milovanovic P, Vukovic Z, Antonijevic DD, Zivkovic V, Nikolic S, Djuric M. Porotic paradoxon: distribution of cortical bone sizes at nano- and micro-levels in healthy vs. fragile human bone. *J Mater Sci Mater Med.* 2017;28(5):71–7.
 70. Oszteoporotikus csigolyatörések I. rész 2007 *Oszteológiai Közlemények* 3:137–146.
 71. Cesar R, Boffa RS, Fachine LT, LeviasTP SAMH, Pereira CAM, Reiff RBM, Rollo JMDA. Evaluation of trabecular microarchitecture of normal osteoporotic and osteopenic human vertebrae. *Proc Engineer.* 2013;59:6–15.
 72. Mackay DL, Kean TJ, Bernardi KG, Haerberle HS, Ambrose CG, Lin F, Dennis JE. Reduced bone loss in a murine model of postmenopausal osteoporosis lacking complement component 3. *J Orthop Res.* 2018;36(1):118–28.
 73. Chen H, Zhou S, Shoumura S, Emura S, Bunai Y. Age- and gender-dependent changes in three-dimensional microstructure of cortical and trabecular bone at the human femoral neck. *Osteoporos Int.* 2010;21(4):627–36.

74. Kang KY, Kang Y, Kim M, Kim Y, Yi H, Kim J, Jung HR, Park SH, Kim HY, Ju JH, Hong YS. The effects of antihypertensive drugs on bone mineral density in ovariectomized mice. *J Korean Med Sci.* 2013;28(8):1139–44.
75. Faot F, Chatterjee M, de Camargos GV, Duyck J, Vandamme K. Micro-CT analysis of rodent jaw bone micro-architecture: a systematic review. *Bone Rep.* 2015;2:14–24.
76. Tanaka M, Ejiri S, Kohno S, Ozawa H. Region-specific bone mass changes in rat mandibular condyle following ovariectomy. *J Dent Res.* 2000;79:1907–13.
77. Rhee Y, Hur JH, Won YY, Lim SK, Beak MH, Cui WQ, Kim KG, Kim YE. Assessment of bone quality using finite element analysis based upon micro-CT images. *Clin Orthop Surg.* 2009;1(1):40–7.
78. Parashar SK, Sharma JK. A review on application of finite element modelling in bone biomechanics. *Perspect Sci.* 2016;8:696–8.
79. Christen P, Schulte FA, Zwahlen A, van Rietberger B, Boutroy S, Melton LJ III, Amin S, Khosla S, Goldhahn J, Müller R. Voxel size dependency, reproducibility and sensitivity of an in vivo bone loading estimation algorithm. *J R Soc Interface.* 2015;13:1–8.
80. Barak MM, Black MA. A novel use of 3D printing model demonstrates the effects of deteriorated trabecular bone structure on bone stiffness and strength. *J Mech Behav Biomed Mater.* 2018;78:455–64.
81. Particelli F, Mecozzi L, Beraudi A, Montesi M, Baruffaldi F, Viceconti M. A comparison between micro-CT and histology for evaluation of cortical bone: effect of polymethylmethacrylate embedding on structural parameters. *J Microsc.* 2011;245(3):302–10.
82. Tiede-Lewis LM, Xie Y, Hulbert MA, Campos R, Dallas MR, Dusevich V, Bonewald LF, Dallas SL. Degeneration of the osteocyte network in the C57BL/6 mouse model of aging. *Aging.* 2017;9(10):2190–208.
83. Pazzaglia UE, Zarattini G, Giacomini D, Rodella L, Menti AM, Feltrin G. Morphometric analysis of the canal system of cortical bone: an experimental study in the rabbit femur carried out with standard histology and micro-CT. *Anat Histol Embryol.* 2010;39(1):17–26.
84. Britz HM, Jokihara J, Leppanen OV, Jarvinen T, Cooper DML. 3D visualisation and quantification of rat cortical bone porosity using a desktop micro-CT system: a case study in tibia. *J Microsc.* 2010;240:32–7.
85. Gur A, Nas K, Kayan O, Atay MB, Akyuz G, Sindal D, Adam M. The relation between tooth loss and bone mass in postmenopausal osteoporotic women in Turkey: a multicenter study. *J Bone Miner Metab.* 2003;21(1):43–7.
86. Jeffcoat M. The association between osteoporosis and oral bone loss. *J Periodontol.* 2005;76:2125–32.
87. Ejiri S, Tanaka M, Watanabe N, Anwar RB, Yamashita E, Yamada K. Estrogen deficiency and its effect on the jaw bones. *J Bone Miner Metab.* 2008;26(5):409–15.
88. Lee MM, Chu EY, El-Abbadi MM, Foster BL, Tompkins KA, Giachelli CM, Somerman MJ. Characterization of mandibular bone in a mouse model of chronic kidney disease. *J Periodontol.* 2010;81:300–9.
89. Guo Y, Sun N, Duan X, Xu X, Zheng L, Seriwatanachai D, Wang Y, Yuan Q. Estrogen deficiency leads to further bone loss in the mandible of CDK mice. *PLoS One.* 2016;11(2):e0148804. <https://doi.org/10.1371/journal.pone.0148804>.
90. Johnston BD, Ward WE. The ovariectomized rat as a model for studying alveolar bone loss in postmenopausal women. *Biomed Res Int.* 2015;2015:635023. <https://doi.org/10.1155/2015/635023>.

Micro-CT in Comparison with Histology in the Qualitative Assessment of Bone and Pathologies

Umut Aksoy, Hanife Özkayalar, and Kaan Orhan

Bone tissue along with cartilage, fibrous tissue, fat, blood vessels, nerves, and hematopoietic elements forms individual bones. Bone is highly mineralized and multifunctional tissue, which plays roles in mechanical support and protection, mineral homeostasis, and hematopoiesis. In recent years, it has become clear that bone also serves an essential endocrine function. To achieve these functional goals, bone is organized hierarchically, from nanometer- to millimeter-sized structures. This contributes not only to its mechanical role in support and movement of the body but also to its other functions. At the nanostructural level, bone is composed of organic and mineral components, mainly consisting of a matrix of cross-linked type I collagen mineralized with

nanocrystalline, carbonated apatite. Due to its high mineral content, bone tissue is extremely resilient, but its organic part also provides a certain degree of flexibility and elasticity improving its behavior under mechanical forces [1, 2].

The “quality” of bone, as well as its quantity, contributes to the biomechanical performance of the skeleton and encompasses aspects of both macromolecular composition and microarchitectural arrangement [3]. Different analysis techniques to qualify and quantify the bone have been developed.

8.1 Tissue Processing

Fixation: Fixation is the chemical or physical process that allows tissue sections to be viewed in a close approximation to the living tissue. It is the single most important factor in achieving a well-prepared section for microscopic analysis [3]. Fixation processes should be standardized so that subtle changes in microanatomy may be detected by comparing similarly fixed sections. The fixative must also protect the tissue during the embedding and sectioning process [4].

There are different types of fixative and fixation method. Neutral buffered formalin (NBF) is the method of choice. The term “formalin” is often incorrectly interchanged with “formaldehyde.” Ten percent NBF is suitable for standard paraffin processing with a hematoxylin and eosin (H&E) staining [5, 6].

U. Aksoy (✉)
Faculty of Dentistry, Departments of Endodontics,
Near East University, Nicosia, Mersin, Turkey
e-mail: umut.aksoy@neu.edu.tr

H. Özkayalar
Faculty of Medicine, Department of Pathology,
Near East University, Nicosia, Mersin, Turkey
e-mail: hanife.ozkayalar@neu.edu.tr

K. Orhan
Faculty of Dentistry, Department of Dentomaxillofacial
Radiology, Ankara University, Ankara, Turkey

Faculty of Medicine, OMFS IMPATH Research
Group, Department of Imaging and Pathology,
University of Leuven, Leuven, Belgium

Oral and Maxillofacial Surgery, University Hospitals
Leuven, University of Leuven, Leuven, Belgium

- Alcohols such as methanol and ethanol are protein denaturants and are not used routinely for tissues because they cause excessive brittleness and hardness. However, they are very good for small specimens. Ethanol is preferred for low cost and low toxicity. These fixatives may be used when studying enzymatic activity, such as acid and alkaline phosphatases and when specimens of small dimension are to be investigated.
- Glutaraldehyde binds with phospholipids and with DNA and is mainly used for transmission electron microscopy (TEM). Glutaraldehyde causes deformation of the alpha-helix structure in proteins and thus is not a good choice for immunoperoxidase staining. It penetrates very poorly yet fixes very quickly, providing the best overall cytoplasmic and nuclear detail.
- Bouin's solution has a high-penetrating capability and can be used also for larger specimens that must be immersed in the solution for 12–24 h. It is a popular fixative for embryonic tissues and the skin, because of its excellent preservation of nuclei and chromosomes. Bouin's is very compatible with the trichrome stain. It is used for the fixation of small, calcified specimens.
- Chemical fixation may be enhanced by the use of physical fixation, such as heat and vacuum. Heat fixation is used to precipitate proteins, rendering them less soluble in water. Heat is generally used to accelerate fixation and not as a stand-alone method. The diffusion of molecules increases with increasing temperature, so penetration of a tissue by a fixative is increased with temperature. Heat causes pro-

tein coagulation, and thus, it also causes undesirable distortions. Microwave fixation is also used to enhance chemical fixation, reducing fixation time. Freeze-drying is used to fix highly soluble materials.

Concentrations of fixatives are also very important [6]. This will be determined by the cost, the solubility, and the necessity. Osmolality or ionic concentration will also influence fixation. Hypertonic solutions will lead to shrinkage, while hypotonic solutions will lead to swelling [3, 4].

Undecalcified bone specimens normally are sectioned transversely or longitudinally using a ground section technique to achieve 150–250 μm thick sections [7–12]. For three-dimensional reconstruction purposes, specimens are sectioned longitudinally with a sledge macrotome to obtain thin serial 10–25 μm sections [13, 14] (Figs. 8.1, 8.2, 8.3, 8.4 and 8.5).

Decalcification: Classic and current texts describe decalcification as the removal of the inorganic components from the hard tissue. The end point of decalcification is the moment when all inorganic material is removed from the tissue. Post-end-point decalcified tissue, consisting of the cellular components and organic matrix, should theoretically be soft enough for paraffin processing by routine means and sectioning with standard equipment [15, 16].

- Acids are nominally categorized as either strong or weak. Strong acids commonly used for decalcifiers are hydrochloric acid and nitric acid, usually employed in aqueous

Fig. 8.1 Cassette





Fig. 8.2 Tissue processing device



Fig. 8.3 Embedding machine

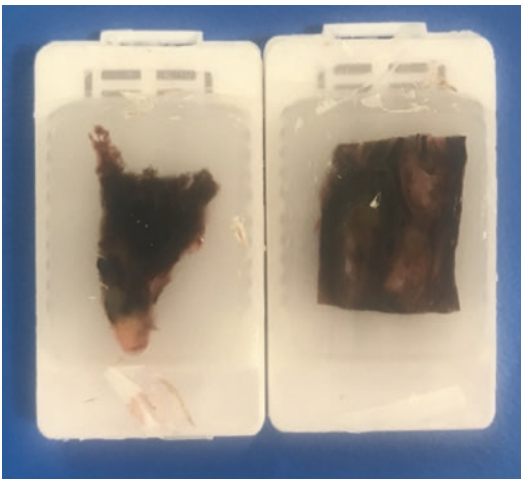


Fig. 8.4 Paraffin block



Fig. 8.5 Microtome

solutions of concentrations ranging from 5 to 10%. Decalcifying weak acids are formic acid, picric acid, and acetic acid. Formic acid is the one used principally as a stand-alone reagent or in consort with a buffer (usually sodium citrate) in aqueous solutions from 5 to 15%. Acetic acid in aqueous solutions of 5–10% was once a popular choice.

- A chelator is an organic chemical that bonds with and removes free metal ions from solutions. Ethylenediaminetetraacetic acid (EDTA) is a chelating agent that reacts with calcium. It is the most widely used chelator for decalcification in concentrations of up to 14%.

Embedding: Before embedding, the specimens require a lengthy time for fixation, decalcification (for hard tissue), dehydration, clearing, and impregnation or infiltration. Each step is interdependent, and failure in one of these will directly affect both the ease of sectioning and the quality of the sections [3].

After trimming, fixation, and decalcification, the specimens should be completely dehydrated for further processing, including clearing, infiltration, and embedding in paraffin, celloidin, plastics, or resins. Alcohol (ethanol) is the most common reagent used for dehydration. Through a graduated series of increasing alcohol concentrations, usually ranging from 70% through 95% to absolute, all the water in the specimen can be removed. Other dehydration agents such as acetone and dioxane (diethylene dioxide) can also be used.

Clearing is the process in which the dehydration fluid in the specimen is replaced with a substance that is miscible with alcohol and the embedding medium. There are many clearing reagents available, but most routine laboratories rely on only a few, such as xylene, toluene, or benzene. Each one has its advantages and disadvantages. Toluene and benzene cause less hardening of tissue than xylene. Xylene is the most commonly used reagent in most laboratories, but one should bear in mind that xylene tends to make most tissue brittle, a fact that is compounded when used with already harder decalcified bone.



Fig. 8.6 Sectioning

Paraffin is most suitable for embedding soft tissues and decalcified hard tissues for thin sections of 3–6 μm and is the most widely used embedding method. Celloidin is a better option when working with large, harder, and more fragile tissues. Depending on the size of the specimen, sections of 3–12 μm can be cut. Hard embedding materials such as glycol methacrylate, methyl methacrylate (MMA), or Spurr's resin are chosen for undecalcified hard tissue embedding suitable for heavy-duty sectioning or ground sectioning. Sections from the latter method are relatively thick, ranging from 50 to 200 μm (Figs. 8.6 and 8.7) [3, 17–19].

Staining: Trichrome stains, hematoxylin and eosin, toluidine blue, safranin O, and fast green, and other stains have been adapted for studying decalcified bone and cartilage in paraffin-embedded sections [20]. The most commonly used staining techniques include H&E, safranin O/fast green, and Goldner's trichrome [21].

Hematoxylin is the most commonly used dye in the pathology laboratory [3]. In combination with eosin, this dye is almost indispensable for



Fig. 8.7 Paraffin block and slide

routine morphological visualization of tissue to every histopathologist (Figs. 8.8 and 8.9). Hematoxylin is a good nuclear stain, and it stains the nuclei bluish black. However, the dye also stains collagenous material, minerals, and myelin fibers. Methylene blue/basic fuchsin and other metachromatic stains can be used to view entire long bones with epiphysis, physis, and metaphysis present in one specimen with good distinction of growth plates [22]. Enzyme histochemistry has played an important role in the identification and study of osteoblasts and osteoclasts. Two phosphohydrolases have special relevance: alkaline phosphatase, an ectoenzyme present in the osteoblast and in matrix vesicle membranes, and tartrate-resistant acid phosphatase (TRAP), a lysosomal enzyme whose localization provides a sensitive method of osteoclast identification [23, 24]. Inorganic calcium is the important constituents of bone and teeth. Calcium deposition can be demonstrated by Von Kossa. Typical histochemical stains for the identification of collagen fibers are

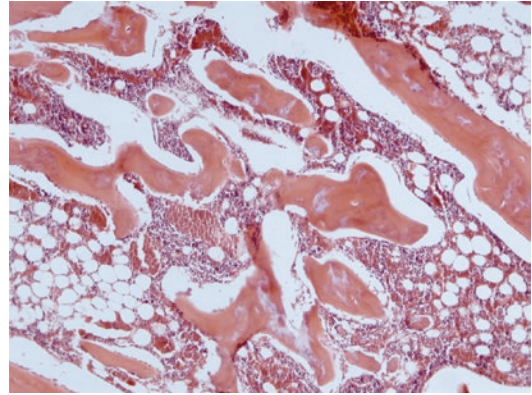


Fig. 8.8 Bone marrow and bone fragments

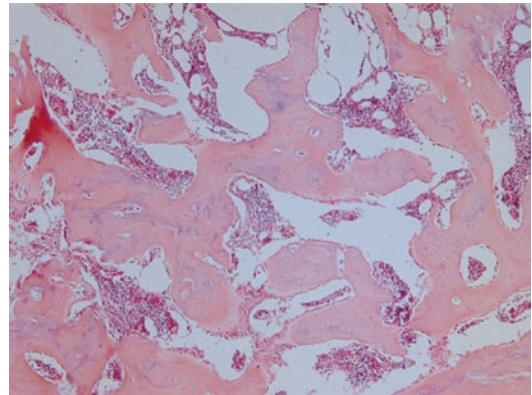


Fig. 8.9 Osteomyelitis

the van Gieson's and Masson's trichrome stains. In the van Gieson's stain, collagen fibers are strongly stained red, and in the Masson's trichrome stain, they are green or blue, depending on the chromogen used [25, 26]. Toluidine blue staining is very easy to perform and can be carried out in about 15 min. It stains nucleic acids blue and polysaccharides purple [3]. In human tissue, osteocalcin (OC) immunolocalization was highly specific for osteoblasts, as was expected since OC is the most bone-specific of the noncollagenous bone matrix proteins. Osteocalcin is expressed by osteoblasts late in the differentiation process and is not expressed by osteoblast-precursor cells or adipocytes [27]. It has been reported that osteocytes produce high levels of OC, even higher than osteoblasts and that this may be linked to an attempt by the osteocytes to prevent the mineralization of the

osteoid tissue immediately surrounding them to allow increased diffusion of nutrients and waste products to and from the cell [28]. OC is now also used as an osteocyte-specific in vitro marker [29]. Osteonectin (ON) is expressed by many cells other than osteoblasts.

Young, healthy bone has been found to present higher preserved osteocyte-lacunar characteristics, in contrast to aged and osteoporotic bone [30]. Aging has also been found to diminish the canaliculi per lacuna and interosteon connections, leading to decreased mechanosensitivity of the osteocytes [31]. Despite long-term negative effects, antiresorptive treatment may improve the vitality of cortical bone osteocytes as well as the number of osteocyte lacunae [32, 33]. On the other hand, as the ability of cortical bone to resist fracture deteriorates with increased age, the age-associated changes of the cortical structure may explain susceptibility to fractures [34]. In particular, in the human femur, the osteocyte distribution may be associated with age- and anatomical region-dependent cortical microarchitecture. Limited studies on this issue have been published [35–38].

8.2 Bone Diseases

8.2.1 Developmental Abnormalities

Developmental abnormalities of the skeleton are frequently genetically based; they first become manifest during the earliest stages of bone formation. But, acquired group diseases are usually detected in adulthood. Developmental anomalies result from localized problems in the migration of the mesenchymal cells [39]. Table 8.1 shows a classification of developmental abnormalities of the bone based on the nature of the genetic abnormality [40, 41].

8.2.2 Fractures

Fractures are divided into two basic groups: traumatic and nontraumatic fractures. And, they are some of the most common pathologic conditions affecting bone. Fractures are classified as:

- Complete or incomplete
- Closed (simple) when the overlying tissue is intact
- Compound when the fracture site communicates with the skin surface
- Comminuted when the bone is splintered
- Displaced when the ends of the bone at the fracture site are not aligned

If the break occurs in bone already altered by a disease process, it is described as a *pathologic fracture*. A *stress fracture* is a slowly developing fracture that follows a period of increased physical activity in which the bone is subjected to new repetitive loads.

Rapidly, after fracture, rupture of blood vessels results in a hematoma, which fills the fracture gap and surrounds the area of bone injury. The clotted blood makes a fibrin mesh, which helps seal off the fracture site and at the same time creates a framework for the influx of inflammatory cells and ingrowth of fibroblasts and new capillary vessels. Simultaneously, these cells secrete some growth factors (PDGF, TGF- β , FGF, and interleukins). These factors activate the osteoprogenitor cells in the periosteum, medullary cavity, and surrounding soft tissues and stimulate osteoclastic and osteoblastic activity [39, 45]. At the end of the first week, the hematoma is organizing, the adjacent tissue is being modulated for future matrix production, and the fractured ends of the bones are being remodeled. This fusiform and predominantly uncalcified tissue is called *soft-tissue callus or procallus*.

The activated mesenchymal cells in the soft tissues and bone surrounding the fracture line also differentiate into chondroblasts that make fibrocartilage and hyaline cartilage. The newly formed cartilage along the fracture line undergoes enchondral ossification. The fractured ends are bridged by a *bony callus* [46].

8.2.3 Osteonecrosis (Avascular Necrosis)

Infarction of bone and marrow is a relatively common event that can occur in the medullary cavity of the metaphysis or diaphysis and the subchondral region of the epiphysis [47].

Table 8.1 Defects in transcription factors producing abnormalities in mesenchymal condensation and related cell differentiation

Disorder	Gene mutation	Affected molecule	Phenotype
Synpolydactyly	<i>HOXD13</i>	Transcription factor	Extra digit with fusion
Waardenburg syndrome	<i>PAX3</i>	Transcription factor	Hearing loss, abnormal pigmentation, craniofacial abnormalities
Greig syndrome	<i>GLI3</i>	Transcription factor	Synpolydactyly, craniofacial abnormalities
Campomelic dysplasia	<i>SOX9</i>	Transcription factor	Sex reversal, abnormal skeletal development
Oligodontia	<i>PAX9</i>	Transcription factor	Congenital absence of teeth
Nail-patella syndrome	<i>LMX1B</i>	Transcription factor	Hypoplastic nails, hypoplastic or aplastic patellas, dislocated radial head, progressive nephropathy
Holt-Oram syndrome	<i>TBX5</i>	Transcription factor	Congenital abnormalities, forelimb anomalies
Ulnar-mammary syndrome	<i>TBX3</i>	Transcription factor	Hypoplasia or absent ulna, third to fifth digits, breast, and teeth, delayed puberty
Cleidocranial dysplasia	<i>CBFA1</i>	Transcription factor	Abnormal clavicles, Wormian bones, supernumerary teeth
<i>Defects in extracellular structural proteins</i>			
Osteogenesis imperfecta types I-IV	<i>COL1A1</i> , <i>COL1A2</i>	Type 1 collagen	Bone fragility, hearing loss, blue sclera, dentinogenesis imperfecta
Achondrogenesis II	<i>COL2A1</i>	Type 2 collagen	Short trunk, severely shortened extremities, relatively enlarged cranium, flattened face
Hypochondrogenesis	<i>COL2A1</i>	Type 2 collagen	Short trunk, shortened extremities, relatively enlarged, cranium, flattened face
Stickler syndrome	<i>COL2A1</i>	Type 2 collagen	Myopia, retinal detachment, hearing loss, flattened face, premature osteoarthritis
Multiple epiphyseal dysplasia	<i>COL9A2</i>	Type 9 collagen	Short or normal stature, small epiphyses, early-onset osteoarthritis
Schmid metaphyseal chondrodysplasia	<i>COL10A1</i>	Type 10 collagen	Mildly short stature, bowing of lower extremities, coxa vara, metaphyseal flaring
<i>Defects in hormones and signal transduction mechanisms producing abnormal proliferation or maturation of chondrocytes and osteoblasts</i>			
Brachydactyly type C	<i>CDMP1</i>	Signaling molecule	Shortened metacarpals and phalanges
Jansen metaphyseal chondrodysplasia	<i>PTHrp receptor</i>	Receptor	Short bowed limbs, clinodactyly, facial abnormalities, hypercalcemia, hypophosphatemia
Achondroplasia	<i>FGFR3</i>	Receptor	Short stature, rhizomelic shortening of limbs, frontal bossing, midface deficiency
Hypochondroplasia	<i>FGFR3</i>	Receptor	Disproportionately short stature, micromelia, relative macrocephaly
Thanatophoric dwarfism	<i>FGFR3</i>	Receptor	Severe limb shortening and bowing, frontal bossing, depressed nasal bridge
Crouzon syndrome	<i>FGFR2</i>	Receptor	Craniosynostosis
Osteoporosis-pseudoglioma syndrome	<i>LRP5</i>	Receptor	Congenital or infant-onset loss of vision, skeletal fragility

[39] (Modified from [42-44])

Reason for osteonecrosis:

- Trauma
- Corticosteroid drug use
- Infection
- Radiation therapy
- Connective tissue disorders
- Gaucher disease
- Pregnancy
- Sickle cell and other anemias
- Alcohol abuse

The cortex is usually not affected because of its collateral blood flow. In subchondral infarcts, a triangular or wedge-shaped segment of tissue undergoes necrosis. In the healing response, osteoclasts resorb the necrotic trabeculae [39].

8.2.4 Osteomyelitis

Osteomyelitis denotes inflammation of bone and marrow. Osteomyelitis may be a complication of any systemic infection but frequently manifests as a primary solitary focus of disease. All types of organisms, including viruses, parasites, fungi, and bacteria, can produce osteomyelitis, but infections caused by certain pyogenic bacteria and mycobacteria are the most common [48, 49].

Pyogenic osteomyelitis is almost always caused by bacteria. Organisms may reach the bone by:

- (a) Hematogenous spread
- (b) Extension from a contiguous site
- (c) Direct implantation

Staphylococcus aureus is responsible for 80–90% of the cases of pyogenic osteomyelitis. In the neonatal period, *Haemophilus influenzae* and group B streptococci are frequent pathogens. Tuberculous osteomyelitis is seen in developed countries.

8.2.5 Tumors

• Osteoma

Osteomas are benign, slow-growing, round-to-oval sessile tumors that project from the sub-

periosteal surface of the cortex. They most often arise on or inside the skull and facial bones. They are usually solitary and are detected in middle age [39].

• Osteoid Osteoma and Osteoblastoma

Osteoid osteoma and osteoblastoma are benign bone tumors that have identical histologic features but differ in size, sites of origin, and symptoms. Osteoid osteomas are by definition less than 2 cm in greatest dimension and usually occur in the teens and 20s. They can arise in any bone but have a predilection for the appendicular skeleton and posterior elements of the spine. Osteoid osteomas produce severe nocturnal pain that is relieved by aspirin [50]. Osteoblastoma is larger than 2 cm and involves the spine more frequently; the pain is dull, aching, and unresponsive to salicylates, and the tumor usually does not induce a marked bony reaction.

Histopathological: Osteoid osteoma and osteoblastoma are well circumscribed and composed of randomly interconnecting trabeculae of woven bone that are prominently rimmed by osteoblasts.

• Osteosarcoma

Osteosarcoma is a malignant mesenchymal tumor in which the cancerous cells produce bone matrix. It is the most common primary malignant tumor of bone. Osteosarcoma occurs in all age groups but has a bimodal age distribution; 75% occur in persons younger than 20 years of age [51]. The smaller second peak occurs in the elderly. Men are more commonly affected than women (1.6:1). The tumors usually arise in the metaphyseal region of the long bones of the extremities, and almost 50% occur about the knee [39].

Macroscopically, osteosarcomas are big bulky tumors. The tumors frequently destroy the surrounding cortices and produce soft-tissue masses. Microscopically, the tumor cells vary in size and shape and frequently have large hyperchromatic nuclei. Bizarre tumor giant cells are common. The formation of bone by the tumor cells is characteristic. These aggressive neoplasms spread hematogenously, and at the time of diagnosis

approximately 10–20% of affected patients have demonstrable pulmonary metastases.

- **Osteochondroma (Exostosis)**

Osteochondroma is a benign cartilage-capped tumor that is attached to the underlying skeleton by a bony stalk. It is the most common benign bone tumor. Men are affected three times more often than women. They develop from bones of the pelvis, scapula, and ribs. Rarely, they involve the short tubular bones of the hands and feet [39].

Histopathology: The cap is composed of benign hyaline cartilage varying in thickness and is covered peripherally by perichondrium.

- **Chondroma (Enchondroma)**

Chondromas are benign tumors of hyaline cartilage. They can arise within the medullary cavity. Enchondromas are the most common of the intraosseous cartilage tumors. The most common localizations are the short tubular bones of the hands and feet. Histopathologically, they are composed of well-circumscribed nodules of cytologically benign hyaline cartilage.

- **Chondroblastoma**

Chondroblastoma is a rare benign tumor that accounts for less than 1% of primary bone tumors. It usually occurs in young patients. Most arise about the knee. This tumor is painful [52].

- **Chondromyxoid Fibroma**

Chondromyxoid fibroma is the rarest of cartilage tumors and because of its varied morphology can be mistaken for sarcoma. Microscopically, there are nodules of poorly formed hyaline cartilage and myxoid tissue delineated by fibrous septae. The tumor cells show varying degrees of cytologic atypia, including the presence of large hyperchromatic nuclei [39].

- **Chondrosarcoma**

Chondrosarcoma is the second most common malignant matrix-producing tumor of bone.

Patients are usually in their 40s or older. The tumor affects men twice as frequently as women. It commonly arises in the central portions of the skeleton, including the pelvis, shoulder, and ribs. Tumor is composed of malignant hyaline and myxoid cartilage. The malignant cartilage infiltrates the marrow space and surrounds pre-existing bony trabeculae. The tumors vary in degree of cellularity, cytologic atypia, and mitotic activity [53].

- **Fibrous Cortical Defect and Non-ossifying Fibroma**

Fibrous cortical defects are extremely common, being found in 30–50% of children older than 2 years. It commonly arises eccentrically in the metaphysis of the distal femur and proximal tibia. Often they are small, about 0.5 cm in diameter. If they grow to 5 or 6 cm in size, they develop into *non-ossifying fibromas*, which are usually not detected until adolescence. Fibrous cortical defects are asymptomatic and are usually detected on radiography as an incidentally. Both fibrous cortical defects and non-ossifying fibromas consist of gray to yellow-brown cellular lesions containing fibroblasts and macrophages [39].

- **Fibrous Dysplasia**

Fibrous dysplasia is a benign tumor. All of the components of normal bone are present, but they do not differentiate into their mature structures. It is diagnosed by radiology [54]. The lesion of fibrous dysplasia is composed of curvilinear trabeculae of woven bone surrounded by a moderately cellular fibroblastic proliferation. The shapes of the trabeculae mimic Chinese letters, and the bone lacks prominent osteoblastic rimming.

8.3 Histomorphometry

Histomorphometry is one of the most commonly used methods to qualify bone morphology and architecture and to quantify bone ongrowth. Bone histomorphometric analysis has commonly been used to study the changes in bone remodeling and

bone structure, and it is an essential tool for understanding tissue-level mechanisms of bone physiology, assessing the mechanisms by which bone diseases occur, the mechanisms by which therapeutic agents affect the skeleton, and the skeletal safety of therapeutic agents. It is the gold standard for tissue-level bone activity. It can yield a wealth of information about the bone structure, bone formation, bone resorption, bone mineralization, as well as bone modeling and remodeling activity [55].

Histomorphometric studies in healthy subjects have focused almost exclusively on cancellous bone. Its volume can be measured on histologic sections. A more detailed evaluation of trabecular architecture, such as thickness, number, and separation, can be calculated from the primary measures of bone area and surface. Cortical geometry, such as bone area and periosteal and endosteal perimeters, can be directly measured [1].

Discriminating between woven and lamellar bone tissue can be valuable for determining whether the bone formation is occurring in a normal fashion. Evaluating lamellar and woven bone is accomplished using polarized light microscopy on unstained sections, although some stains allow collagen orientation to be visualized. In pathologic conditions such as Paget disease of bone, the presence of woven bone provides key diagnostic criteria. Lamellar bone, viewed under polarized light, can be assessed in more detail to elucidate features such as the number of lamellae within a given basic multicellular unit (BMU), the thickness of lamellae, or the type of lamellar organization (alternating or homogeneous) [1].

Using stains for osteoid, the examination of mineralized versus nonmineralized bone can provide information about changes in the mineralization process. Analysis of osteoid involves measuring the extent of the bone surface covered by osteoid (and then normalizing it by the total bone surface examined) and either the width or volume of osteoid. Although called osteoid volume in the literature, this is actually an area (given that it is a 2D assessment). If osteoid width is normal, increased osteoid surface is indicative of higher bone formation. Increased

width of osteoid is indicative of a mineralization defect [1].

The extent of surfaces covered with osteoblasts and osteoclasts provides a primary index of how bone formation and/or resorption are altered under various conditions. Osteoblasts can be identified using morphological characteristics on sections stained with Goldner's trichrome, Von Kossa and McNeal's, or even hematoxylin and eosin. Their metabolic state is closely related to their morphology; they are spindle-shaped when quiescent and large and polyhedral when rapidly producing bone. Primary outcomes related to osteoblasts include osteoblast surface and their number, both typically normalized to bone surface. The most commonly employed technique for assessing activity of resorption is to measure eroded (or resorption) surfaces or erosion depth. A variable related to erosion depth from previous remodeling activity is average wall width (W. Wi), a measure of the amount of bone formed at a given BMU. The balance between W. Wi and erosion depth determines BMU balance [1].

Although osteoblast function can be inferred through measures of osteoid, the most commonly used method is the assessment of fluorochrome labels (dynamic histomorphometry), because it allows the calculation of rates of modeling and remodeling. Mineralizing surface is reported per unit bone surface (MS/BS; %) by dividing the mineralizing surface by the total bone surface measured. MS/BS is often considered an index of osteoblast activity such that interventions that impact osteoblast proliferation and/or differentiation would be expected to change MS/BS [1].

The mineral apposition rate (MAR) is a commonly used parameter for the characterization of bone formation and is often determined to test for experimental effects on cortical bone.

During histomorphometric analysis different staining methods can be used which highlight certain features. Toluidine blue is used to identify cavities under polarized light by looking at the presence of cutoff collagen fibers (disruption of the lamellar system) at the edge of the cavity. The polarized light allows visualization of the orien-

tation of collagen lamellae along the mineralized bone surface. The identification of scalloped surfaces can, however, be subjective. Tartrate-resistant acid phosphatase can be used to mark active osteoclasts and thus “active” cavities. Von Kossa/van Gieson staining allows to discriminate osteoid from mineralized bone [1, 3].

Before histomorphometric analyses take place, study specimens are subjected to a complex preparation protocol, from sample collection to microscopical observation of the prepared slide: sample collection, decalcification, fixation and dehydration, infiltration and embedding, orientation/plane of section, and staining.

Using the histologic sections for quantification, the paraffin-embedded sections can distort and shrink up to 15%. This can make a big difference in histologic measurements and potentially obscure real differences between groups. Another limitation of paraffin embedding is that decalcification is usually incomplete. Thus, tissue sectioning is very challenging, resulting in suboptimal sections for analysis. Also, measurement variance associated with bone histomorphometry arises from some factors including intraobserver, interobserver, intermethod, and sample variation. Observer variation is mainly due to the subjective criteria used for identification of features such as osteoid seams, bone structural units, and resorption cavities. The protocol complexity, costs, required time, and high level of expertise and training are limitations of bone histomorphometry. It is also a two-dimensional and invasive technique [1, 3, 56, 57].

More recently micro-computed tomography appeared. It is capable of forming both 2D and 3D images with applications in bone formation quantification, as well as in bone modeling in bone grafts. It is also fast and allows nondestructive analysis without a specific preparation protocol.

The excellent reproducibility and accuracy of micro-CT measurements of bone morphology have been established in several studies [58, 59]. The accuracy of micro-CT morphology measurements has been evaluated by comparing them with traditional measures from 2D histomor-

phometry both in animal and in human specimens [58, 60, 61]. These studies show that 2D and 3D morphologic measurements by micro-CT generally are highly correlated with those from 2D histomorphometry.

Ex vivo micro-CT scanners typically produce scans with pixel sizes in the range of 1–30 μm . This provides sufficient resolution to accurately detect individual trabecular structures in small rodents, such as rats and mice, as well as in larger species. Higher-resolution scans, on a nanometer scale, can be obtained with nano-CT and synchrotron-CT machines [1].

There are numerous advantages to using micro-CT for assessment of bone mass and morphology in excised specimens: (1) it allows for direct 3D measurement of trabecular morphology, such as trabecular thickness and separation, rather than inferring these values based on 2D stereologic models, as is done with standard histologic evaluations; (2) compared with 2D histology, a significantly larger volume of interest is analyzed; (3) measurements can be performed with a much faster throughput than typical histologic analyses of histomorphometric parameters using undecalcified bone specimens; and (4) assessment of bone morphology by micro-CT scanning is nondestructive; thus, samples can be used subsequently for other assays, such as histology or mechanical testing [59].

Micro-CT presents advantages over histomorphometry, but only the latter one can make cellular level observation. The additional value of micro-CT imaging is that it allows to provide details on the morphology of the cancellous network (avoiding assumptions of trabecular morphology) and more detailed data on cortical bone geometry. It is, therefore, beneficial to use a combination of both histomorphometry and micro-CT to increase the obtained information. For this reason, several authors have studied the bone tissue along with histomorphometric and micro-CT parameters in their research.

In studies which were evaluated, the new bone formation, the number of osteoblasts/bone surface, bone formation rate per bone surface,

mineral apposition rate (MAR), and the number of osteoclasts/bone surface were assessed by histomorphometry. Other information which included the bone volume over total volume percentage, trabecular thickness, trabecular number, trabecular separation, and trabecular bone pattern factor were able to obtain by micro-CT analysis [62, 63].

In case that the area of interest of the studies includes the strength of bone tissue, parameters such as the cross-sectional moment of inertia, volumetric cancellous bone mineral density, volumetric cortical bone mineral density, and bone strength index can also be measured by micro-CT [63, 64]. The classical way of measuring the moment of inertia of the bone involves histomorphometry on 2D histological sections. These techniques can only measure the cross-sectional area and perimeters at the endo- and periosteal envelopes in a 2D plane and are unable to measure the true bone volume. Micro-CT involves a three-dimensional reconstruction of the bone region of interest, reduces the sample site alteration, and allows the true calculation of the bone volume. Geometric analysis of the bone by micro-CT correlates well with ultimate strength data obtained by mechanical testing, and therefore, it provides an important noninvasive method to study the effect of various therapies on cortical bone metabolism, geometry, and strength [63, 65].

Micro-CT is a strong tool for evaluation of the periapical lesions measurement in the field of dentistry [66–68]. In addition, it has some other applications in dental research, such as peri-implant bone healing, implant osseointegration [69], bone morphology [70], evaluation of shrinkage of composites [71], and inspection of caries excavation [72]. Histomorphometry is a preferable technique for the observation and evaluation of cell and tissue morphology as well as to the count of inflammatory infiltrate in dentistry [66]. The combination of both procedures allows a better evaluation and interpretation of data in researches in the dental field, which can widely contribute to clinical studies.

8.4 Registration of Histopathology and Micro-CT

The development of novel technologies plays an important role in dental studies. Micro-CT analyses, as one of the novel three-dimensional (3D) methods, have substantially improved perspectives of dental researches [73]. Combining different measurement methods and integrating their results into a 3D frame is nowadays a common task to answer specific research questions. The techniques that allow us to integrate 2D information into a 3D micro-CT volume to evaluate and quantify bony lesions were investigated in the literature [66]. A semiautomatic registration tool allowing quantification and comparison of registration quality for periapical lesions in a rat model was defined for this purpose. The periapical lesions can be evaluated by the registration result and compare the quality among the different samples.

8.4.1 Method

The pulps of the mandibular first molars were surgically exposed with a-size round steel bur in high-speed rotation under constant irrigation. Pulp were left open to the oral cavity for 21 days to allow establishment of periapical lesion. After 21 days of periapical lesion induction, the animals were sacrificed by decapitation. The mandibles were then surgically removed, dissected, and fixed in 10% neutral buffered formalin solution. The samples were demineralized with 5% nitric acid (pH 7.4), which was renewed every 2 days. Paraffin blocks containing the mandibles were serially sectioned with average thickness of 4 μm in a mesiodistal plane. Sections were stained with hematoxylin–eosin and examined under light microscopy (2009 magnification). Two histologic slides (four fields in each) were evaluated for every tooth, which included the root dentin, the apical foramen, and the periapical tissues.

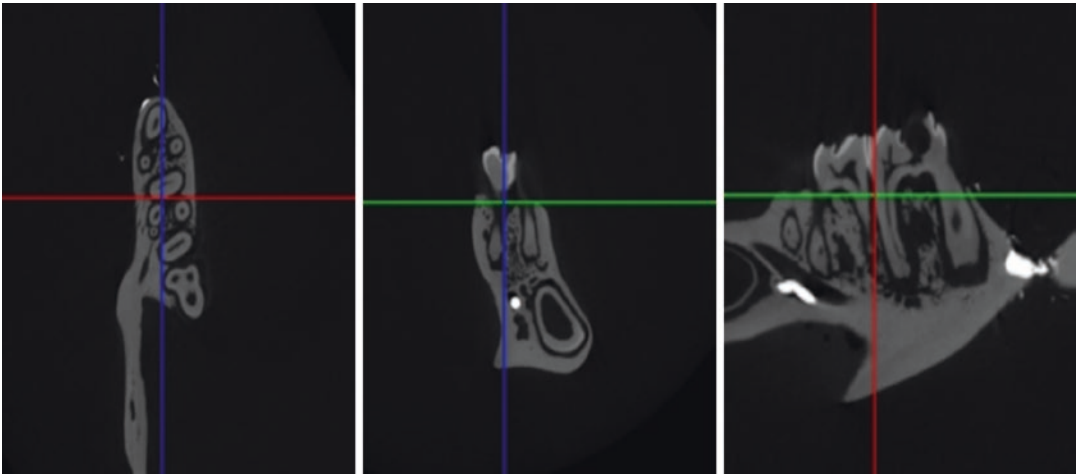


Fig. 8.10 Axial, sagittal, and coronal sections of rat mandible

8.4.2 Micro-CT Acquisition

All rat mandibles were scanned with a high-resolution micro-CT system (Bruker Skyscan 1275, Kontich, Belgium). The scanning parameters were set at 100 kVp, 100 mA, 0.5 mm of Cu filter, 10 μ m of pixel size, and 0.5 degree of rotation step. To minimize the ring artifacts, air calibration of the detector was carried out prior to each scanning. Each sample was rotated 360 within an integration time of 5 min. The mean time of scanning was around 4 h. Other settings included beam-hardening correction, and optimal contrast limits adjustments were done, during the reconstruction step, according to the manufacturer's instructions, using the NRecon software (version 1.6.7.2, SkyScan, Kontich, Belgium). In the reconstruction step, the ring artifact correction and smoothing were fixed at zero, and the beam artifact correction was set at 40% (Fig. 8.10).

8.4.3 Micro-CT Imaging Analysis

For the 3D volumes, the original grayscale images were processed with a Gaussian low-pass filter for noise reduction, and an automatic segmentation threshold was applied using CTAn (ver. 1.16.1.0, SkyScan). A thresholding (bina-

rization) process was used, which entails processing the range of gray levels to obtain an imposed image of black/white pixels only. Then, separately for each slice, a region of interest was chosen to contain a single object entirely to allow the registration on histopathology using a 3D software (3D Synapse, Fujifilm, Japan). Each slice was detected perpendicular to rotation axis and then register match the 3D volume and 2D slice. After registration the loss of bone and density measurements was made from histopathology, micro-CT images, and fused image.

To register a 2D histopathology image into a 3D micro-CT dataset, a semiautomatic approach was used. A grayscale-based approach was used to transform the 2D image. The fine structures both in bone and also the teeth such as cement/dentin-cement junction were used for fixed standardized points to use the registration method. The initial registrations obtained by applying the thresholds were then improved using a standard image registration method. The whole registration was performed using CTAn (ver. 1.16.1.0, SkyScan) and 3D software (3D Synapse, Fujifilm, Japan). The whole registration process was visually guided. Once the datasets loaded, the registration was made semiautomatically or manually. If the orientation of the bone was already roughly the same

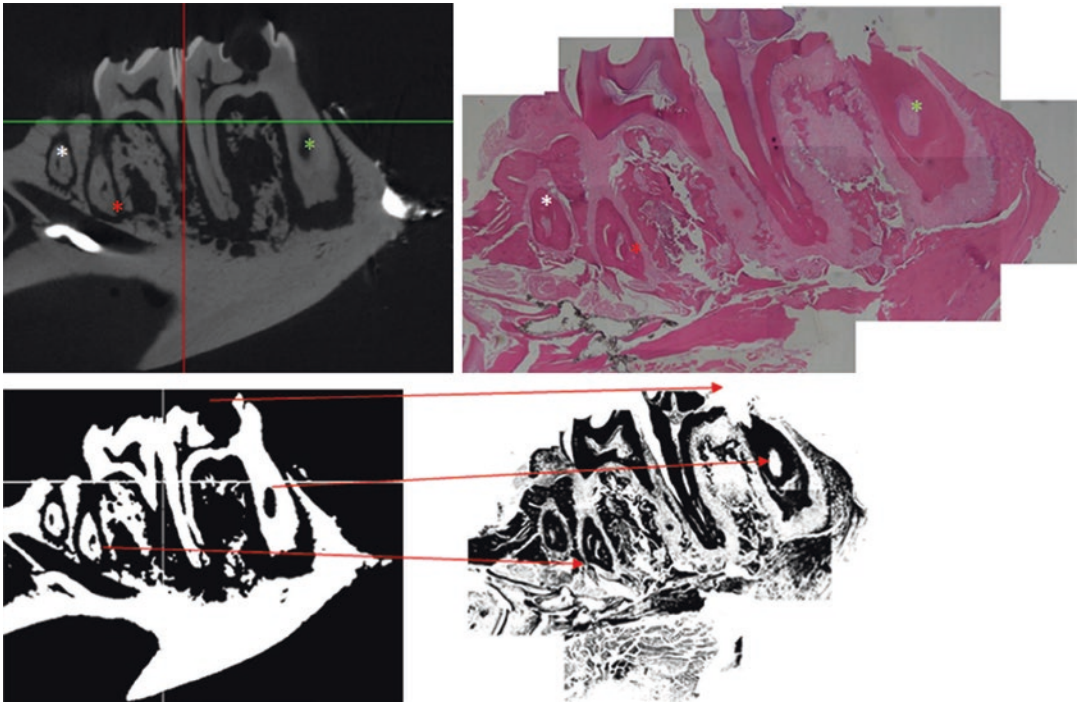


Fig. 8.11 Registration of histopathology and micro-CT slices

images, a semiautomatic registration tool allowing quantification and comparison of registration quality for periapical lesions in a rat model was defined (Fig. 8.11).

Acknowledgment The specimen in this study were scanned and reconstructed with Skyscan 1275 (Skyscan, Kontich, Belgium) in Ankara University, Faculty of Dentistry, Micro CT Laboratory which was founded by Ankara University Research Fund (Project No: 17A0234001).

References

- Allen MR, Burr DB. Techniques in histomorphometry. In: Basic and applied bone biology; 2014. p. 131–48.
- Clarke B. Normal bone anatomy and physiology. *Clin J Am Soc Nephrol.* 2008;3(Suppl 3):S131–9.
- An YH, Martin KL. Handbook of histology methods for bone and cartilage. Totowa, NJ: Humana Press; 2003.
- Eltoum I, Fredenburgh J, Myers RB, Grizzle WE. Introduction to the theory and practice of fixation of tissues. *J Histotechnol.* 2001;24:173–90.
- Jones ML. To fix, to harden, to preserve—fixation: a brief history. *J Histotechnol.* 2001;24:155–62.
- Fox CH, Johnson FB, Whiting J, Roller PP. Formaldehyde fixation. *J Histochem Cytochem.* 1985;33(8):845–53.
- Frost HM. Preparation of thin undecalcified bone sections by rapid manual method. *Stain Technol.* 1958;33:273–7.
- Schaffler MB, Radin EL, Burr DB. Mechanical and morphological effects of strain rate on fatigue of compact bone. *Bone.* 1989;10:207–14.
- Burr DB, Martin RB. Calculating the probability that microcracks initiate resorption spaces. *J Biomech.* 1993;26:613–6.
- Lee TC, Myers ER, Hayes WC. Fluorescence-aided detection of microdamage in compact bone. *J Anat.* 1998;193:179–84.
- O'Brien FJ, Taylor D, Lee TC. An improved labelling technique for monitoring microcrack growth in the compact bone. *J Biomech.* 2002;35:523–6.
- O'Brien FJ, Hardiman DA, Hazenberg JG, Mercy MV, Mohsin S, Taylor D, Lee TC. The behaviour of microcracks in compact bone. *Eur J Morphol.* 2005;42:71–9.
- O'Brien FJ, Taylor D, Dickson GR, Lee TC. Visualisation of three-dimensional microcracks in compact bone. *J Anat.* 2000;197:413–20.
- Mohsin S, Taylor D, Lee TC. Three-dimensional reconstruction of Haversian system in ovine compact bone. *Eur J Morphol.* 2002;40:309–15.

15. Shibata Y, Fujita S, Takahashi H, Yamaguchi A, Koji T. Assessment of decalcifying protocols for detection of specific RNA by non-radioactive in situ hybridization in calcified tissues. *Histochem Cell Biol*. 2000;11:153–9.
16. Cunningham CD, Schulte BA, Bianchi LM, Weber PC, Schmiedt BN. Microwave decalcification of human temporal bones. *Laryngoscope*. 2001;111(2):278–82.
17. Buijs R, Dogterom AA. An improved method for embedding hard tissue in polymethyl methacrylate. *Stain Technol*. 1983;58:135–41.
18. Sanderson C. Entering the realm of mineralized bone processing: a review of the literature and techniques. *J Histotechnol*. 1997;20:259–66.
19. Sanderson C, Emmanuel J, Campbell P. A historical review of paraffin and its development as an embedding medium. *J Histotechnol*. 1988;11:61–3.
20. Skinner RA, Hickmon SG, Lumpkin CK, Aronson J, Nicholas RW. Decalcified bone: twenty years of successful specimen management. *J Histotechnol*. 1997;20:267–77.
21. Kahveci Z, Minbay FZ, Cavusoglu L. Safranin O staining using a microwave oven. *Biotech Histochem*. 2000;75:264–8.
22. Derckx P, Birkenhäger-Frenkel DH. A thionin stain for visualizing bone cells, mineralizing fronts and cement lines in undecalcified bone sections. *Biotech Histochem*. 1995;70:70–4.
23. Gruber HE, Marshall GJ, Nolasco LM, Kirchen ME, Rimoin DL. Alkaline and acid phosphatase demonstration in human bone and cartilage: effects of fixation intervals and methacrylate embedments. *Stain Technol*. 1988;63:299–306.
24. Taylor CR, Shi SR, Chen C, Young L, Yang C, Cote RJ. Comparative study of antigen retrieval heating methods: microwave, microwave and pressure cooker, autoclave, and steamer. *Biotech Histochem*. 1996;71:263–70.
25. Garvey W. Modified elastic tissue-Masson trichrome stain. *Stain Technol*. 1984;59(4):213–6.
26. Lebeau A, Muthmann H, Sendelhofert A, Diebold J, Löhns U. Histochemistry and immunohistochemistry on bone marrow biopsies. A rapid procedure for methyl methacrylate embedding. *Pathol Res Pract*. 1995;191:121–9.
27. Hughes FJ, Aubin JE. Culture of cells of the osteoblast lineage. In: Arnett TRHB, editor. *Methods in bone biology*. London: Chapman and Hall; 1998. p. 1–39.
28. Mikuni-Takagaki Y, Kakai Y, Satohoshi M, Kawano E, Suzuki Y, Kawase T, Saito S. Matrix mineralisation and the differentiation of osteocyte-like cells in culture. *J Bone Miner Res*. 1995;10:231–42.
29. Kato Y, Windle JJ, Koop BA, Mundy GR, Bonewald LF. Establishment of an osteocyte-like cell line, MLO-Y4. *J Bone Miner Res*. 1997;12:2014–23.
30. Carpentier VT, Wong J, Yeap Y, Gan C, Sutton-Smith P, Badiei A, Fazzalari NL, Kuliwaba JS. Increased proportion of hypermineralized osteocyte lacunae in osteoporotic and osteoarthritic human trabecular bone: implications for bone remodeling. *Bone*. 2012;50:688–94.
31. Milovanovic P, Zimmermann EA, Hahn M, Djonic D, Püschel K, Djuric M, Amling M, Busse B. Osteocytic canalicular networks: morphological implications for altered mechanosensitivity. *ACS Nano*. 2013;7:7542–51.
32. Bernhard A, Milovanovic P, Zimmermann EA, Hahn M, Djonic D, Krause M, Breer S, Püschel K, Djuric M, Amling M, Busse B. Micro-morphological properties of osteons reveal changes in cortical bone stability during aging, osteoporosis, and bisphosphonate treatment in women. *Osteoporos Int*. 2013;24:2671–80.
33. Plotkin LI, Lezcano V, Thostenson J, Weinstein RS, Manolagas SC, Bellido T. Connexin 43 is required for the anti-apoptotic effect of bisphosphonates on osteocytes and osteoblasts *in vivo*. *J Bone Miner Res*. 2008;23:1712–21.
34. Chen H, Zhou X, Fujita H, Onozuka M, Kubo KY. Age-related changes in trabecular and cortical bone microstructure. *Int J Endocrinol*. 2013;2013:213234.
35. Vashishth D, Verborgt O, Divine G, Schaffler MB, Fyhrie DP. Decline in osteocyte lacunar density in human cortical bone is associated with accumulation of microcracks with age. *Bone*. 2000;26:375–80.
36. Power J, Noble BS, Loveridge N, Bell KL, Rushton N, Reeve J. Osteocyte lacunar occupancy in the femoral neck cortex: an association with cortical remodeling in hip fracture cases and controls. *Calcif Tissue Int*. 2001;69:13–9.
37. Busse B, Djonic D, Milovanovic P, Hahn M, Püschel K, Ritchie RO, Djuric M, Amling M. Decrease in the osteocyte lacunar density accompanied by hypermineralized lacunar occlusion reveals failure and delay of remodeling in aged human bone. *Aging Cell*. 2010;9:1065–75.
38. Carter Y, Suchorab JL, Thomas CD, Clement JG, Cooper DM. Normal variation in cortical osteocyte lacunar parameters in healthy young males. *J Anat*. 2014;225:328–36.
39. Kumar V, Abbas AK, Aster JC. *Robbins and cotran pathologic basis of disease*. 8th ed. Philadelphia, PA: Saunders Elsevier; 2010.
40. Hartmann C. Skeletal development—Wnts are in control. *Mol Cell*. 2007;24:177–84.
41. Alman BA. Skeletal dysplasias and the growth plate. *Clin Genet*. 2008;73:24–30.
42. Mundlos S, Olsen BR. (a). Heritable diseases of the skeleton. Part I: molecular insights into skeletal development-transcription factors and signaling pathways. *FASEB J*. 1997;11:125–32.
43. Mundlos S, Olsen BR. (b). Heritable diseases of the skeleton. Part II: molecular insights into skeletal development-matrix components and their homeostasis. *FASEB J*. 1997;11:227–33.
44. Superti-Furga A, Bonafé L, Rimoin DL. Molecular-pathogenetic classification of genetic disorders of the skeleton. *Am J Med Genet*. 2001;106(4):282–93.

45. Styrkarsdottir U, Halldorsson BV, Gretarsdottir S, Gudbjartsson DF, Walters GB, Ingvarsson T, Jonsdottir T, Saemundsdottir J, Center JR, Nguyen TV, Bagger Y, Gulcher JR, Eisman JA, Christiansen C, Sigurdsson G, Kong A, Thorsteinsdottir U, Stefansson K. Multiple genetic loci for bone mineral density and fractures. *N Engl J Med*. 2008;358:2355–65.
46. Giannoudis PV, Einhorn TA, Marsh D. Fracture healing: the diamond concept. *Injury*. 2007;38:S3–6.
47. Lafforgue P. Pathophysiology and natural history of avascular necrosis of bone. *Joint Bone Spine*. 2006;73:500–7.
48. Kaplan SL. Osteomyelitis in children. *Infect Dis Clin N Am*. 2005;19(4):787–97.
49. Calhoun JH, Manring MM. Adult osteomyelitis. *Infect Dis Clin N Am*. 2005;19:765–86.
50. Lee EH, Shafi M, Hui JH. Osteoid osteoma: a current review. *J Pediatr Orthop*. 2006;26:695–700.
51. Klein MJ, Siegal GP. Osteosarcoma: anatomic and histologic variants. *Am J Clin Pathol*. 2006;125:555–81.
52. Ramappa AJ, Lee FY, Tang P, Carlson JR, Gebhardt MC, Mankin HJ. Chondroblastoma of bone. *J Bone Joint Surg Am*. 2000;82:1140–5.
53. Chow WA. Update on chondrosarcomas. *Curr Opin Oncol*. 2007;19:371–6.
54. Weinstein LS. G(s)alpha mutations in fibrous dysplasia and McCune-Albright syndrome. *J Bone Miner Res*. 2006;21:120–4.
55. Erben RG, Glösmann M. Histomorphometry in rodents. In: *Bone research protocols*. Totowa, NJ: Humana Press; 2012. p. 279–303.
56. Vedi S, Compston J. Bone histomorphometry. In: *Bone research protocols*: Humana Press; 2003. p. 283–98.
57. Vandeweghe S, Coelho PG, Vanhove C, Wennerberg A, Jimbo R. Utilizing micro-computed tomography to evaluate bone structure surrounding dental implants: a comparison with histomorphometry. *J Biomed Mater Res B Appl Biomater*. 2013;101:1259–66.
58. Boussein ML, Boyd SK, Christiansen BA, Goldberg RE, Jepsen KJ, Müller R. Guidelines for assessment of bone microstructure in rodents using micro-computed tomography. *J Bone Miner Res*. 2010;25:1468–86.
59. Chappard D, Retailliau-Gaborit N, Legrand E, Baslé MF, Audran M. Comparison insight bone measurements by histomorphometry and microCT. *J Bone Miner Res*. 2005;20:1177–84.
60. Bonnet N, Laroche N, Vico L, Dolleans E, Courteix D, Benhamou CL. Assessment of trabecular bone microarchitecture by two different x-ray micro-computed tomographs: a comparative study of the rat distal tibia using Skyscan and Scanco devices. *Med Phys*. 2009;36:1286–97.
61. Müller R, Van Campenhout H, Van Damme B, Van Der Perre G, Dequeker J, Hildebrand T, Rügsegger P. Morphometric analysis of human bone biopsies: a quantitative structural comparison of histological sections and micro-computed tomography. *Bone*. 1998;23:59–66.
62. Kuroyanagi G, Adapala NS, Yamaguchi R, Kamiya N, Deng Z, Aruwajoye O, Kutschke M, Chen E, Jo C, Ren Y, Kim HKW. Interleukin-6 deletion stimulates revascularization and new bone formation following ischemic osteonecrosis in a murine model. *Bone*. 2018;116:221–31.
63. Zhao B, Zhao W, Wang Y, Zhao Z, Zhao C, Wang S, Gao C. Prior administration of vitamin K2 improves the therapeutic effects of zoledronic acid in ovariectomized rats by antagonizing zoledronic acid-induced inhibition of osteoblasts proliferation and mineralization. *PLoS One*. 2018;13:e0202269.
64. Hsu JT, Wang SP, Huang HL, Chen YJ, Wu J, Tsai MT. The assessment of trabecular bone parameters and cortical bone strength: a comparison of micro-CT and dental cone-beam CT. *J Biomech*. 2013;46:2611–8.
65. Bagi CM, Hanson N, Andresen C, Pero R, Lariviere R, Turner CH, Laib A. The use of micro-CT to evaluate cortical bone geometry and strength in nude rats: correlation with mechanical testing, pQCT and DXA. *Bone*. 2006;38(1):136–44.
66. de Oliveira KM, da Silva RA, Küchler EC, de Queiroz AM, Nelson Filho P, da Silva LA. Correlation between histomorphometric and micro-computed tomography analysis of periapical lesions in mice model. *Ultrastruct Pathol*. 2015;39(3):187–91.
67. Balto K, Müller R, Carrington DC, Dobeck J, Stashenko P. Quantification of periapical bone destruction in mice by micro-computed tomography. *J Dent Res*. 2000;79:35–40.
68. Wan C, Yuan G, Yang J, Sun Q, Zhang L, Zhang J, Zhang L, Chen Z. MMP9 deficiency increased the size of experimentally induced apical periodontitis. *J Endod*. 2014;40:658–64.
69. Wang S, Ogawa T, Zheng S, Miyashita M, Tenkumo T, Gu Z, Lian W, Sasaki K. The effect of low-magnitude high-frequency loading on peri-implant bone healing and implant osseointegration in beagle dogs. *J Prosthodont Res*. 2018;
70. Sakagami N, Kobayashi T, Nozawa-Inoue K, Oda K, Kojima T, Maeda T, Saito C. A histologic study of deformation of the mandibular condyle caused by distraction in a rat model. *Oral Surg Oral Med Oral Pathol Oral Radiol*. 2014;118:284–94.
71. Hirata R, Clozza E, Giannini M, Farrokhanesh E, Janal M, Tovar N, Bonfante EA, Coelho PG. Shrinkage assessment of low shrinkage composites using micro-computed tomography. *J Biomed Mater Res B Appl Biomater*. 2015;103:798–806.
72. Lai G, Kaisarly D, Xu X, Kunzelmann KH. MicroCT-based comparison between fluorescence-aided caries excavation and conventional excavation. *Am J Dent*. 2014;27:12–6.
73. Guerrero ME, Jacobs R, Loubele M, Schutyser F, Suetens P, van Steenberghe D. State-of-the-art on cone beam CT imaging for preoperative planning of implant placement. *Clin Oral Investig*. 2006;10:1–7.



Micro-CT in Artificial Tissues

9

Leyla Türker Şener, Gürcan Albeniz, Göker Külüşlü,
and Işıl Albeniz

9.1 Micro-CT in Artificial Tissues

9.1.1 Introduction

The computed tomography (CT) technology, whose theoretical basis goes back to 1917, started after an Australian mathematician Johan Radon proved that the reconstruction of an (N) dimensional object might be obtained from the (N-1) dimensional projections of the same object. As the general structure, the micro-CT (microcomputed tomography) is similar to computed tomography. Computed tomography was invented in 1972 by engineer Godfrey Hounsfield and physician Allan Cormack. Hounsfield invented the first whole-body computed tomography device in 1975. Hounsfield and Allan McLeod *Cormack* were awarded with a Nobel Prize in 1979 for their studies on X-ray-based computed tomography and diagnostic techniques.

L. T. Şener (✉) · I. Albeniz
Istanbul Faculty of Medicine, Department
of Biophysics, Istanbul University, Istanbul, Turkey
e-mail: leylasen@istanbul.edu.tr;
ialbeniz@istanbul.edu.tr

G. Albeniz
Cerrahpaşa Faculty of Medicine, Department
of General Surgery, Istanbul University Cerrahpaşa,
Istanbul, Turkey

G. Külüşlü
Istanbul Faculty of Medicine, 3B Medical
and Industrial Design Laboratory, Istanbul University,
Istanbul, Turkey

The imaging phase is one of the important steps for artificial tissues. These technologies include the most frequently used noninvasive imaging methods of computed tomography and magnetic resonance imaging. The tomography results may be used in obtaining the scaffolds. Computer-assisted design and computer-assisted manufacturing tools and mathematical modellings are used to collect the complex tomographic, architectural information of the tissues and transfer the information to the digital environment. The information about the complex structures to be used in the computer-assisted design (CAD) and mathematical modelling of the biological print is obtained using the medical imaging devices.

9.1.2 Basic Principles of Microcomputed Tomography

The technology enabling the noninvasive observation of the inner structure of the body with the discovery of X-rays by Röntgen in 1895 started a new era in diagnostic medicine. In conventional radiography, X-ray passes through the observed object, and the transmitted energy is recorded as a two-dimensional image. The three-dimensional (3D) structure information of the sample may be obtained using computer algorithms if the imaging of the sample from different directions is performed, which is described as tomographic reconstruction [1].

Typically, the clinical CT scanners produce images consisted of voxels with a volume of 1 mm^3 ; X-rayed microcomputed tomography (μCT) systems, which were developed in the beginning of the 1980s which produce voxels between 5 and $50 \mu\text{m}$ intervals, have more better spatial resolution [2]. The system gets several X-ray shadow transition images of the object in different angles while the object turns on a high accuracy bed. The reconstruction of sequence images is recorded using these shadow images with a modified Feldkamp conic ray algorithm, and a complete 3D representation of the inner microstructure and density selected in the height interval of the transition images is created. The best micro-CT images are obtained from the objects where the sample content materials of the microstructure overlap with the X-ray absorption contrast. The inner morphological parameters may be measured using the reconstruction.

The X-rays which are included in the electromagnetic spectrum are in the energy intervals between 0.125 and 125 keV. However, they involve electromagnetic waves or photon bunch between the wavelength interval of 10–0.01 nm. The X-rays with small wavelengths and with higher penetration degrees are described as “sharp X-ray”; however, X-rays with higher wavelengths and with smaller penetration degrees are described as “soft X-ray”. The X-rays at $0.5\text{--}2.5 \text{ \AA}$ (soft) wavelength are used in crystallography; however, X-rays at $0.5\text{--}1 \text{ \AA}$ (sharp) wavelength are used in radiology. The frequency of X-rays is approximately 1000 times higher than the frequency of visible light, and the X-ray photon has a higher energy than the photon of the rays in the visible region. Therefore, the main features of these rays are short wavelength and having a higher energy.

X-rays emerge as the products of events occurring in the level of electrons, not inside the nucleus. Radiation emission is initiated as photons from the anode as a consequence of two different atomic processes with the acceleration of electrons under high voltage are separated from the heated cathode through thermionic pathway with the crash with the anode. These are bremsstrahlung and the characteristic photon radiation. Bremsstrahlung radiation is generated with acceleration with the deviation from the pathway

due to the affinity force of the nucleus when passing close to a nucleus of an electron with high speed. The accelerated load makes an electromagnetic radiation, releases a photon, and causes a continuous X-ray spectrum (Fig. 9.1).

The characteristic X-rays emerge with the breaking off an electron from the orbit where the high-speed electron crashed from the target object. Another electron coming from a higher orbit fills the space of the broken electron and generates a radiation as much as the energy difference between these two orbits. Each element has a unique characteristic emission wavelength (Fig. 9.2).

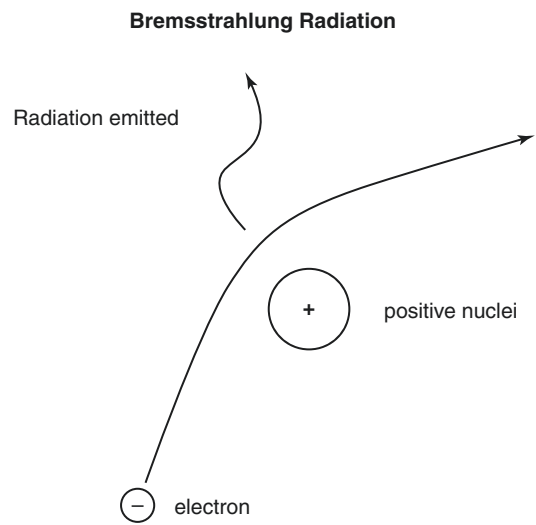


Fig. 9.1 Bremsstrahlung X-ray shape

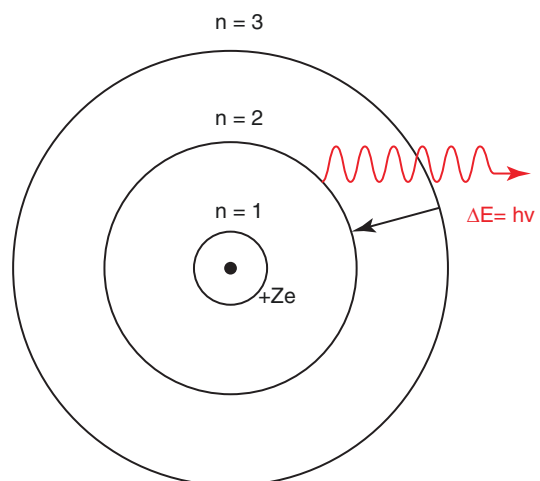
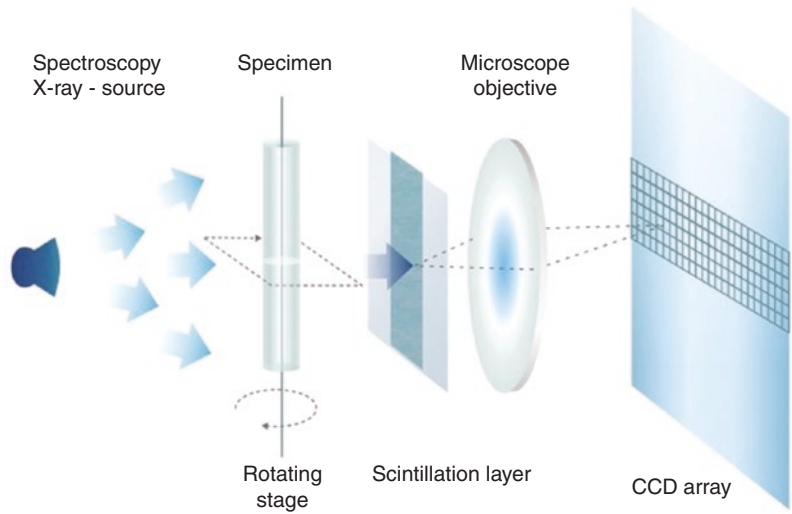


Fig. 9.2 Characteristic X-ray

Fig. 9.3 Basic configuration of micro-CT scanner



The main components of a micro-CT device consist of an X-ray tube, computer-controlled stepper motor which periodically rotates the sample, an image intensifier which intensifies the X-ray in the environment onto the camera sensor, a CCD camera which converts the reflecting X-rays to digital image data, image collector, and a computer controlling all these devices [3] (Fig. 9.3).

Three-dimensional models may be created with the sections taken from the object using X-rays with giving no harm to the object. Microtomography has frequently been used in medical studies and providing significant data in screening and analysis of porous structures in the objects (or materials) such as composites, polymers, and biologic materials (bone, tooth, cartilage tissue). The three-dimensional structures of shadow projection images obtained by micro-CT may be generated using various computer programs (3D reconstruction).

The main components of a micro-CT scanner consist of an X-ray tube, a computer-controlled stepper motor that rotates the sample that is fixed on the device at specified intervals, image intensifier which intensifies the X-ray of the environment to the camera sensor, a CCD camera which converts the X-rays on itself to a digital image data, image collector, and a computer that controls all these devices.

The μ CT systems create images which have good spatial resolution by generating voxels between 5 and 50 μm intervals. The sample in the μ CT device is scanned by rotating around the vertical axis in a system involving a fixed X-ray

source and X-ray imaging series. The vibration decreases, and the resolution increases. The inner characteristics of the sample may be examined for several times since the imaging does not cause any harm for the sample. The obtained data may be recorded as three-dimensional or two-dimensional images and may be used for qualitative and quantitative analyses [4].

9.1.3 Artificial Tissues

Significant developments were observed in medicine since the last three centuries when the diagnosis and treatments were organized in accordance with assumptions and predictions. The world has entered into a new era after engineers started to use the problem-solving techniques in medicine. This series of developments has reached to the artificial organs which are the prospects in ameliorating and extending the human life.

The first successful organ transplant was performed by Joseph Murray in 1954 with kidney transplantation. However, there are various problems about organ transplant such that the recipients have to use lifelong immunosuppressive drugs, and the adequate number of organs required for organ transplant cannot be obtained. Although the number of patients awaiting for organ transplant has rapidly been increasing worldwide, the number of organ donation is small. Thus, the patients awaiting for organ

transplant may die before organ transplant, or they cannot undergo surgery due to deteriorations in general health. Therefore, scientists who are working on organ transplant searched for new remedies and developed the artificial organs by working in cooperation with bioengineers.

Producing an artificial organ is creating of three-dimensional organ-like structures which will substitute the function of an organ using the stem cells collected from human blood. Bio-production of the organs or organ-like structures, which will substitute the function of various organs that lose their function due to various reasons and will fulfil the most significant function of the organ and which may be transplanted into the location of the organ or may be transplanted into the different parts of the body, is called organ production. Artificial organ production and the recent successful studies performed on stem cells demonstrated that three-dimensional organ productions are possible. Although fully functional organs have not yet been produced and transplanted to patients, the importance of this groundbreaking topic has been increasing in science. Owing to the artificial organs that will be produced using a 3D bio-scanner with the use of patients' own cells or stem cells, the problems such that of tissue rejections will be cleared out.

The aim of the studies that were initiated around 2 years ago was to produce some parts of tissue or organs using the living cells on a 3D bio-scanner.

The prototyping of living cells prioritized from stem cells with the 3D rapid prototyping technique in recent years, and reaching to functional competence after tissue bonding, is the main component of the organ production. The produced organ must be preserved in the bioreactor for a particular period for the cellular and tissue bonding after organ prototyping; otherwise, the produced soft structure cannot be integrated and will start to collapse. The collapse developing in the structure creates mechanical load on the cells and results in cell death. Bioreactor is a mechanism which has an envi-

ronment similar to a human body and accelerates the cellular division and tissue bonding. The organ is reserved in the bioreactor for a particular period after organ prototyping in accordance with particular criteria. The reservation period varies in accordance with many factors. The 3D rapid prototyping technique and its use in biomedical area have frequently become popular in the biomedical area due to its unique advantages. 3D rapid prototyping is a production technique which enables to obtain physical models directly from the three-dimensional designs in the electronic environment. In this model, the physical models are generated with the overlapping of surfaces starting from the base. Each printed layer forms the basis for the subsequent layer [5].

In conventional methods, each component needs to be produced and assembled separately to create a model with multiple components; however, the model can be produced as a complete single model in one single time and as functional in this method. One other important fact in organ production is the heterogeneous structure observed in native organs. Multiple varieties of cell types and their distribution and connections within the organ that are required for creating the heterogeneous structure make the production of a functional complete organ impossible at present. Though, if the required functioning of the organ could be enabled with only one or several cell types, the requirement for a complex structuring might be decreased. Another important factor in organ production is the scientific developments observed in the area of stem cells. As it is known, stem cells are the main cells generating the tissues and organs in the body. The cells which have not yet been differentiated have the ability of unlimited division and renewal and the ability to transform to organ and tissues. However, the stem cells which have been transformed to the cells of the related organ may not be compatible with the patients' tissue. The incompatibility between the produced organ and patients' tissue may mean that all these studies were futile attempts [6].

In this respect, the studies conducted on stem cells have a significant role. Another critical factor is the vessel and vessel-like structures to be located within the produced organ. These structures have the roles of carrying the oxygen and nutrition and removing the waste of metabolism from the cell for the cell growth, division, and bonding in the remaining part of the organ. Otherwise the cells confined within the produced structure cannot maintain their vital functions. The other important factor is the preservation of the produced organ structure in the bioreactor. The reactor has to pump oxygen and nutrition required for the cells. If the organ is produced in a different environment rather than in the bioreactor environment, the collapses occurring in the transportation process of the produced structure into the bioreactor create mechanical load on the cells, and this mechanical load destroys the viability of the cells. This problem may be resolved by the insertion of 3D organ prototyping device into the bioreactor by minimizing the human factor. One last factor is the geometrical complexity of the produced organ structure. Organs with hollows such as the heart and lung require temporary supporting structures in the production phase. The type, geometrics, durability, and the dissolution by the time of the biomaterial required for these supporting structures are the main parameters to be considered [7].

9.2 Process for Producing an Artificial Tissue

9.2.1 Scaffolds and Micro-CT

Tissue engineering is an interdisciplinary branch of science that aims to develop artificial systems using the engineering and life sciences for tissue renewal which takes the attraction of many scientists. Tissue engineering is based on the idea of reproducing artificial tissue scaffolds using the biosignal molecules of specific cells obtained from the patients and implantation to the deteriorated region in the body.

Tissue scaffolds are one of the most important factors which enable the adhesion and reproduction of the cells by providing a temporary extracellular matrix for the cells in tissue engineering approach [8].

The physical, mechanical, and biological features of the tissue scaffolds must be designed as to be compatible with the features of the tissue which is targeted to be repaired. Tissue scaffolds are the three-dimensional structures which are required to have porous structure that will enable the diffusion of the food/waste material, surface features that will enable cell reproduction/differentiation in addition to adequate degradation speed, adequate mechanical endurance, reproduction, and migration of cells. The materials used in the reproduction of tissue scaffold must be biocompatible as to avoid undesirable tissue reactions after insertion into the body and must have nontoxic features [9].

Hybrid systems may be generated with the combining of the cells which have the functionality to generate the required tissue with the tissue scaffolds prepared with proper material in tissue engineering. Tissue scaffold provides the required support in transformation of cells to organized functional tissue. The ability to control the position and functions of the cells in tissue scaffolds is the critical point in the success of the prepared structure. The nanotechnological approaches are becoming important in developing the material in preparation of tissue scaffolds and in designing the structures with the required geometrical, topographical, and functional characteristics [10, 11].

The biomaterials used in the production of tissue scaffolds are grouped as the polymers, ceramics, metals, and composite materials. The tissue scaffolds that will generate the soft tissue may be obtained from natural or synthetic polymers; however, the tissue scaffolds that will generate the hard tissue are composed of ceramic, polymer, or composites because the similarity of the biomaterial with the tissue aimed to be repaired has a significant importance [11].

An efficient tissue scaffold must have a porous structure attached to one another that will allow the adjustment of the speeds of controllable degradation and reabsorption with its rates of cell division, transfer of food and waste, and tissue renewal. In addition, the microstructure with proper surface chemical and tissue scaffold is one of the factors which affect the addition, reproduction, and differentiation of the cells [12].

The conventional methods used in the production of tissue scaffold are the fibre binding, solvent casting, particle leak technique, membrane lamination, dilution moulding, and gas foaming. However, these methods have some disadvantages such as the use of toxic solvents in high rates, longer production times, inability to adequately remove the residual particles from the polymer matrix, disordered porous structures, and inadequate connection between the structures. In addition to all these disadvantages, there are limitations in the control of the shape in most of these methods. It is dependent to the shape of the cast mould and porosity, and the dimension of pore cannot be adequately controlled [13, 14].

The rapid prototyping that emerged with the developing technology is the method of generating three-dimensional objects with the overlapping accumulation of material layers and processing using computer-controlled equipment. The computer-assisted design model of the generated object is based on the two-dimensional cross-sectional data obtained after slicing. The main three-dimensional systems that have currently been used are stereolithography, selective laser sintering (SLS), laminated object manufacturing (LOM), and the fused deposition modelling (FDM). The tissue scaffold generated with this technology enables the generating of three-dimensional connection, and structure, and is a highly repeatable procedure owing to the computer-controlled production [15]. Three-dimensional printers were started to be used in the design and production of tissue scaffold after all these developments in technology [16].

The design of the tissue scaffold may significantly affect the mechanical features and cellular behaviours.

Tissue scaffold must have three important features:

- Tissue scaffold must be biodegradable and may be biologically fragmented.
- Must have appropriate material and structure for 3D modelling.
- Must allow the growth, interaction, and physiological functioning of the cells.

Designing of each layer by dividing into units, ability to easily control, and fine adjustment method in production of scaffold have become attractive since the production proceeds layer by layer in three-dimensional printing technologies. Artificial cellular skeleton may be generated using different printing techniques with computed microtomography devices based on the screened cell tissues. It is possible to obtain successful results using different methods with cellular skeletons which have the required characteristics [16] (Figs. 9.4 and 9.5).

A sample of practice steps of our studies using micro-CT (Sky Scan 1174) and three-dimensional printing technology is given below:

- (a) The opening of data set, which is restructured after screening, with the CTAn, and identification of the related areas (ROI) in the structure are presented in Figs. 9.6 and 9.7.
- (b) The screening of three-dimensional model that is generated by CTAn using CTVol and then reducing the high number of polygons are presented in Figs. 9.8 and 9.9.
- (c) Results of the 3D printing of the model that was obtained after micro-CT screening are presented in Fig. 9.10.

9.2.2 3D Bioprinting

Three-dimensional printers utilize various different technologies. The differences between the technologies are generally related with how the layers have been generated. Some of the 3D printer technologies used in three-dimensional printers may be counted as selective laser sinter-

Fig. 9.4 Types of scaffold

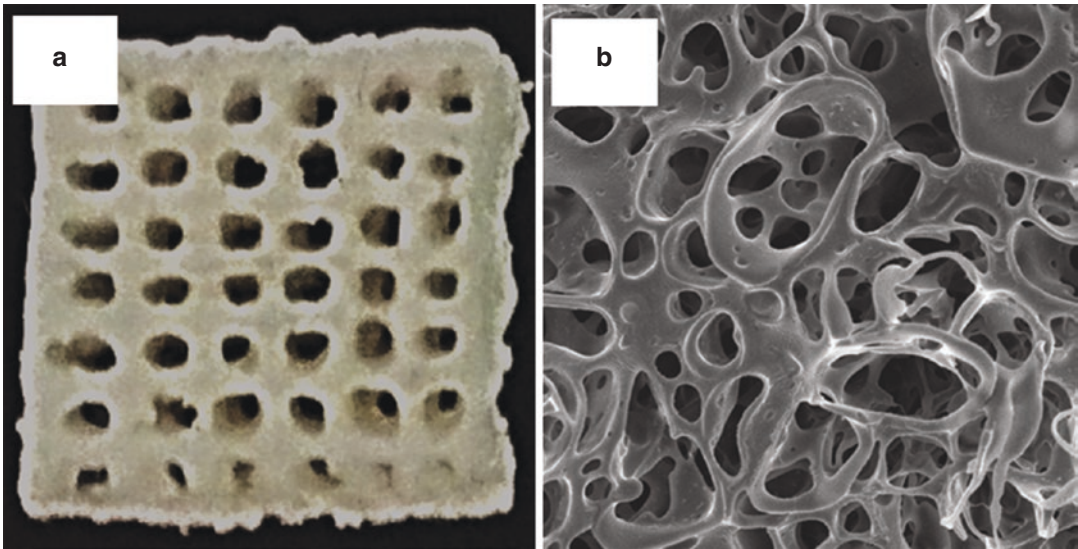
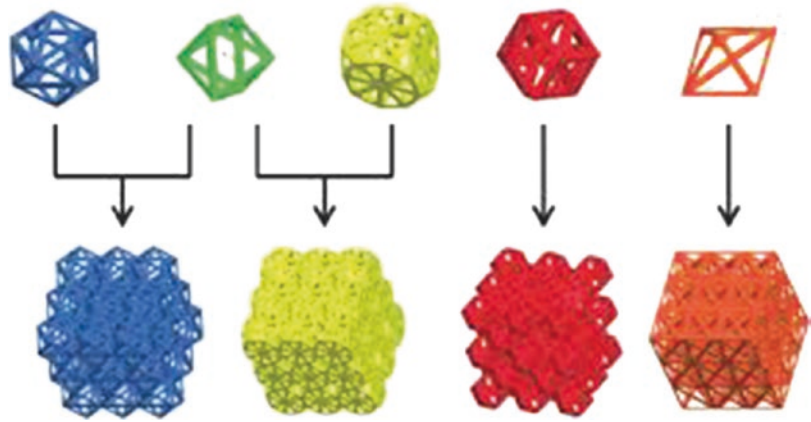


Fig. 9.5 The cellular skeleton generated using a three-dimensional printer. (a) Microscope image. (b) The image of the nanopores taken by SEM [17]

ing (SLS), fused deposition modelling (FDM), and stereolithography. The most frequently used method is FDM, which starts with a software process and the software groups the STL format models to mathematical layers and sends these layers to a triaxial CNC controlled device to obtain overlapped layers. Generally thermoplastic materials are used. Thermoplastic materials

are relatively more proper materials compared with the thermoset materials because they can be melted multiple times and can be liquefied in a specified heat interval.

Thermoplastic material has to pass through a nozzle which is heated up to the melting heat for proper production. The nozzle is controlled by a computer and is moved to simulate the part

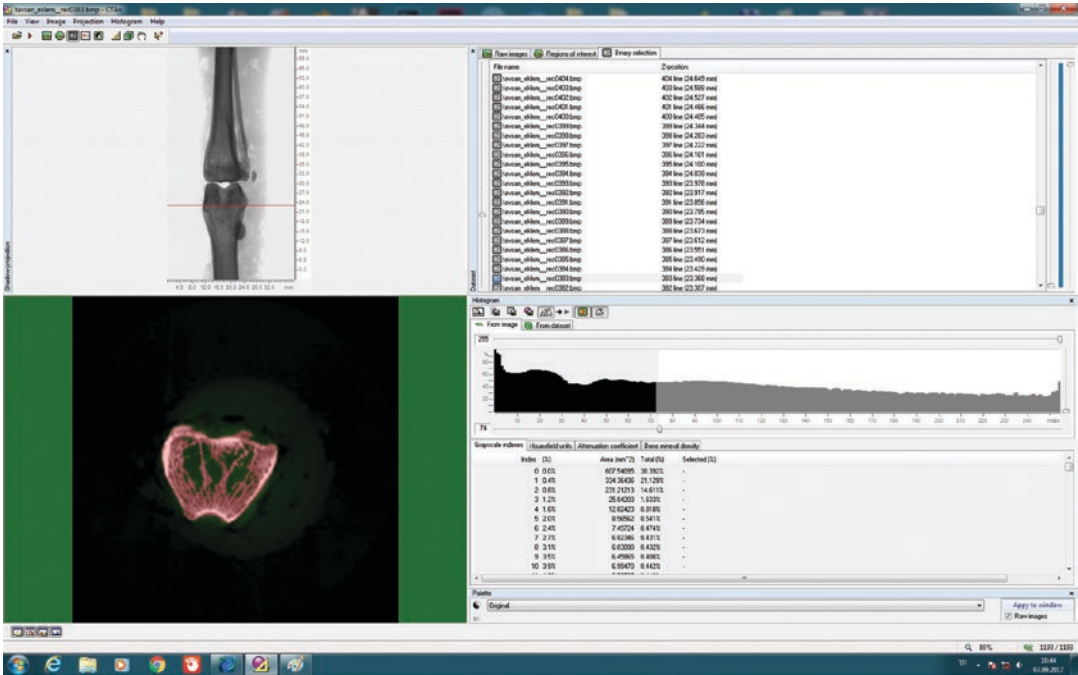


Fig. 9.6 Identification of the appropriate ROI

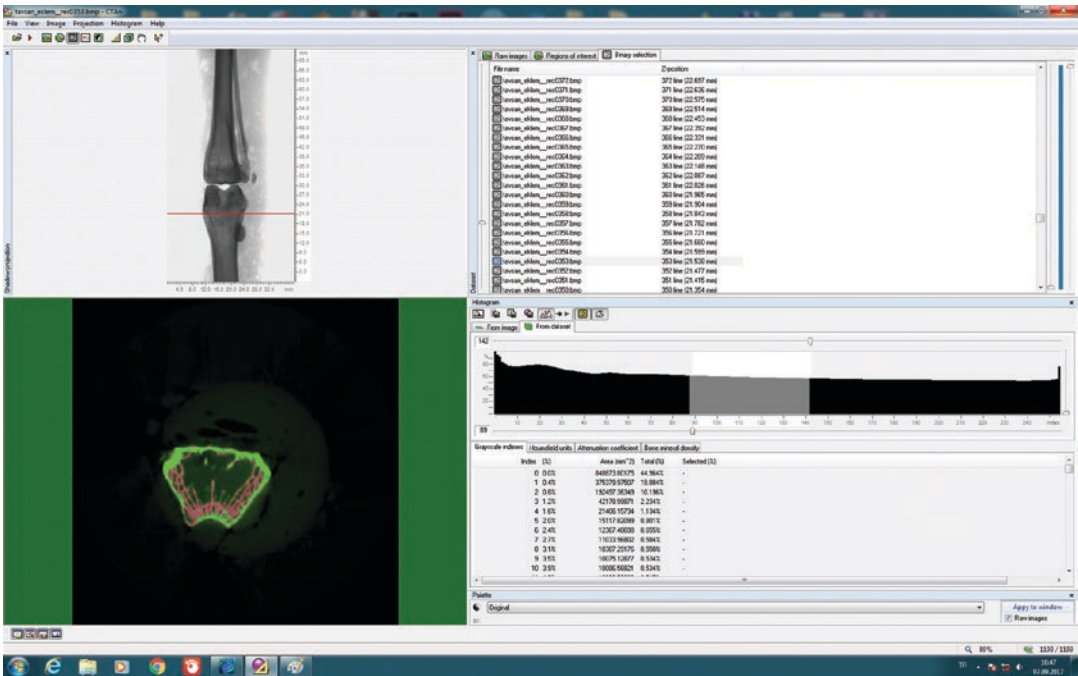


Fig. 9.7 Identification of the appropriate threshold

geometry. The part is accumulated on the table in two-dimensional layers with the accumulation of the thermoplastic material and will be produced. This process has currently been used in the areas of rapid prototyping and 3D printing, which are

also known as 3D printing, three-dimensional production, or 3D printer.

The cells are filled in cartridges after the cells are reproduced until they reach the adequate number of cells in the culture environment. Cellular

Fig. 9.8 Reducing the number of polygons of the model

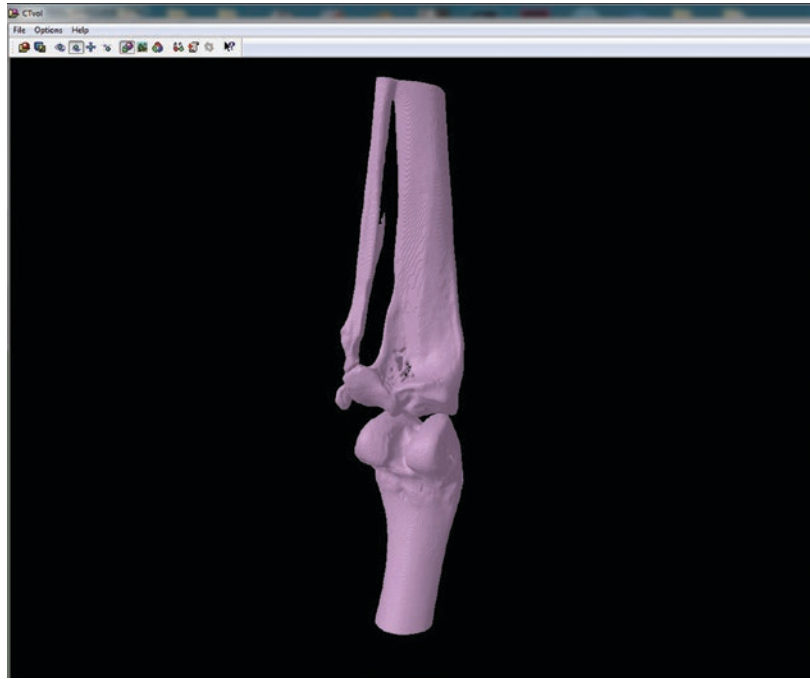
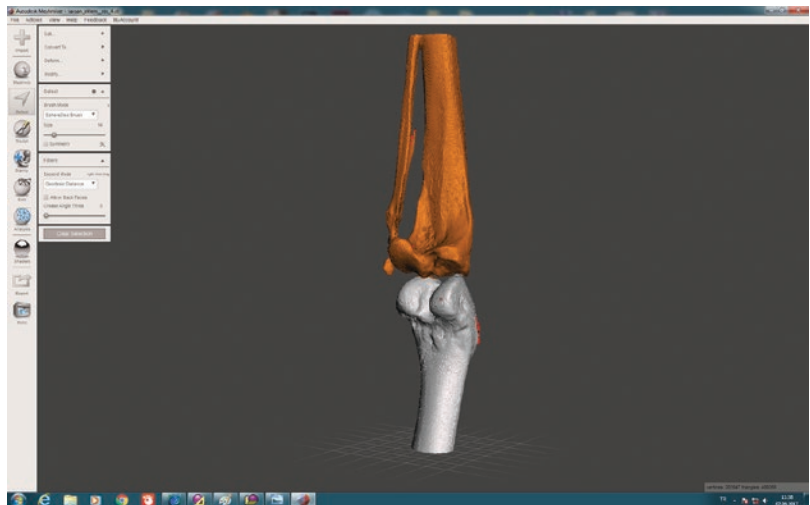


Fig. 9.9 Preparing the model ready for printing



matrix molecules in fluid gel viscosity, which have higher water content and known as the intercellular substance, are included in the cells in the cartridge. This substance with polysaccharide and protein structure enables the intercellular transfer of nutrients and oxygen. The viability of the cells has to be preserved when the cell is released out from the injection nozzle on the printer head.

Therefore, a supporting hydrogel fluid (nutritional and diluent) composed of water, protein, and nutritional is used in the bioprinter (as a second substance different than the cells) to nurture the cells, prevent them from drying, and help to form the tissues with their combination. Two separate cartridges each including cell and hydrogen printing substance are placed side by side on the nuzzling



Fig. 9.10 The 3D printing of the obtained model after micro-CT screening

unit of the bioprinter. Each cartridge is connected to a fine thin injection nozzle. The cell is released out of the needle of the nuzzling injection as drops. The printer head starts to accumulate the cells layer by layer by moving from right to left, downward and upward, and from front to the back. Each drop contains 10,000–50,000 cells. The cells are produced appropriate with the tissue or organ model designed on computer owing to simultaneous nozzleed hydrogel from another injector. The cells preserve their viability, connect with one another, and transform to tissue parts owing to the porous hydrogel which supports the cells as a mould by surrounding the cells, spreading between the cells that were overly applied and accumu-

lated. Hydrogel is completely removed from the environment or disappears by fragmentation by the time cell maturation and transformation to tissues are completed. Thus, tissue samples are obtained for only medical investigation purposes using the three-dimensional printing technology. The significance of hydrogels is that they block the fusion and mediate in contacting and assembling of biometric material to the 3D structures.

3D printer is a supportive tool for the reproduction of the proper organs for transplantation in regenerative medicine. Three-dimensional bioprinter has additional complexities such as cell types and growth, differentiating factors, and technical difficulties such as the sensitivity of living cells and production of tissues compared with the nonbiological printing. This requires the integration of the technologies of engineering, biomaterial science, cellular biology, and physics.

Three-dimensional bioprinters can perform spatial positioning, living cell planting of layer-by-layer biological material, and placement of biochemical and functional parts, and three-dimensional structures may be produced.

Several approaches are required in generating the biological structures for preserving the viability of the cells during the procedure:

- Biomimicry
- Autonomous conjunction
- Mini tissue structure blocks

Biomimicry aims to produce the biological structures which have similar features with the native biological structure by investigating the nature and functionality of the cells.

Autonomous conjunction aims to provide the same structural features, cell localisation, and tissue functionality with the native biological structure by investigating the interactions of the cells with one another.

The term of mini tissue describes the obtained tissue or organs with the combining of small functional structure blocks associated with two strategies above.

First, the imaging of the model to be printed is performed in preparation of the structural scaffold. The imaging phase is one of the important steps. These technologies include the most frequently

used noninvasive imaging methods of computed tomography and magnetic resonance imaging (MRI). The tomography results may be used in obtaining the scaffolds. Computer-assisted design and computer-assisted manufacturing (CAD/CAM) tools and mathematical modellings are used to collect the complex tomographic and architectural information of the tissues and transfer the information to the digital environment. The information about the complex structures to be used in the computer-assisted design and mathematical modelling of the biological print is obtained using the medical imaging devices [18]. The raw data obtained through screening using the imaging devices are converted to three-dimensional digital drawings using the computer-assisted software. The results obtained in the imaging may be used for the tissue to be manufactured; and printing may be performed after the required appropriate design changes and tissue-specific scaffold material and cell selection are completed [19].

Synthetic and natural polymers and extracellular matrix are generally preferred as the scaffold material. The source of stem cell may be allogenic or autologous. The cells are loaded to the device after the cells are purified. The cells which are loaded on inkjet, microextrusion, or laser-assisted bioprinters are planted on the target tissue-specific scaffold, and the manufacturing of the living target tissue is obtained through the tissue-specific differentiation factors after the cells proliferative wrap around the skeleton [20].

The cells may be added to the scaffold structure as follows in artificial tissue technology:

- As rolls
- With injection
- By planting

Organ printing technology consists of three main steps:

- I. Preprocessing (CAD, plannings, preconditioning)
- II. Processing (genuine printing, solidification)
- III. Post-processing (perfusion, postcondition, accelerated tissue maturation)

1. **In designing step** (CAD, plannings, preconditioning), the appropriate design approach is identified for the target tissue planned to be manufactured. The processed 3D digital drawings in accordance with the design approaches are prepared for the bioprinting procedure and are sliced into two-dimensional consecutive layers in the determined thickness.
2. **In processing step** (genuine printing, solidification), the appropriate material and cell resource are selected for the shape and functioning of the target tissue. Synthetic and natural polymers and extracellular matrix are commonly used in material selection. The source of cell may be allogenic or autologous in selection of the cell. These components are integrated to inkjet, microextrusion, or laser-assisted printer.
3. **In post-processing step**, the stem cells which will differentiate to new cells are planted on the skeleton after the scaffold for the organ is generated using the three-dimensional bioprinter. Proteins and stimulants are added for the forming of the organ shape. Maturation period may be required for various tissues in the bioreactor before transplantation. These tissues may be alternatively used in vitro (laboratory environment) studies. The tissues completing the maturation period are analysed, and the compatibility to the target tissue is identified [18].

9.3 Future Work/Future Projection

The studies investigating the use of micro-CT and three-dimensional printing technologies in the processes of medical and industrial prototyping have gradually become prevalent in Turkey and worldwide. The processing of CT or micro-CT screening data and generating the three-dimensional model of a biological structure in digital environment take place in various areas. Innovative development has been accomplished, and more productive results have been obtained in the area of health owing to the ability to generate (print) the structures such as skull models,

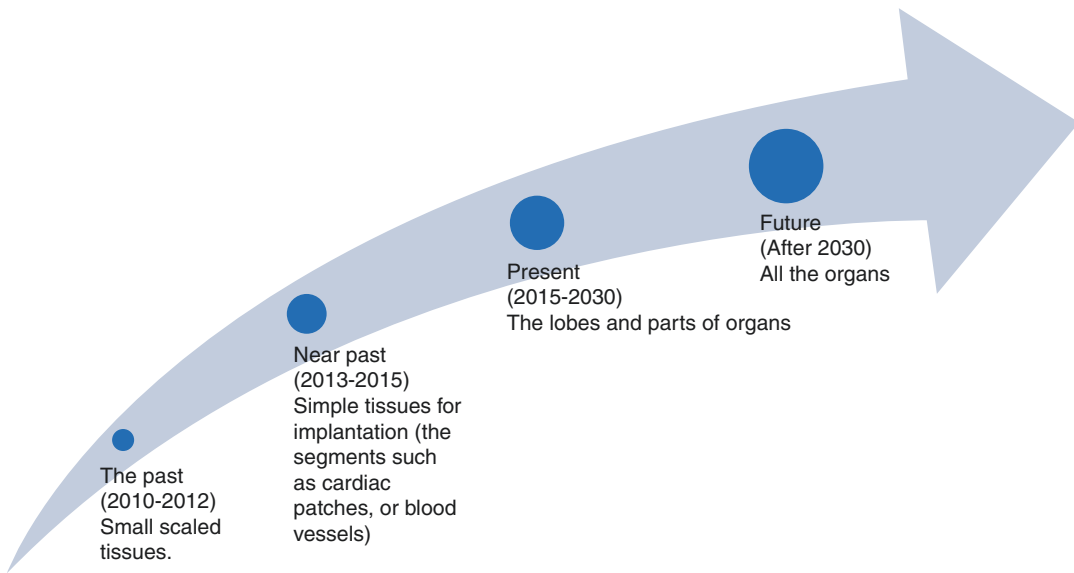


Fig. 9.11 Medical innovative development of 3D printing technology

skeleton models, disease models, and bone and organ for educational purposes in medical faculties or in the departments of life sciences. Another area of practice is the three-dimensional printing of the body part of the surgery region after modelling before surgical operations; owing to that the duration of surgery is shortened, and more productive results may be obtained for the patient and the surgeon.

Tissue and organs can be produced in 3D bioprinters, and studies have been conducted demonstrating that these tissues preserved their viability. These produced tissues and miniaturize organs are planned to be used in the studies of drug experiments, tissue engineering, and innovative medical studies related to treatment in the short term.

The practice of 3D printing technology in medical area provides very important contributions for the studies of tissue engineering where the cellular biology and material science are jointly used. Various tissues are produced including the layered skin, bone, vascular grafts, tracheal splints, heart tissue, and cartilage structures. Cardiac patches, small- and medium-length blood vessels, skin tissue, and soft tissues (adipose, muscle) for reconstructive surgery have recently

been produced in the past. In addition, successful studies have been continued on the vascularized microorganisms which may be grown in the bioreactor for completing the function of a diseased organ such as the liver (Fig. 9.11).

References

1. Panchbhai SA. Wilhelm conrad röntgen and the discovery of X-rays: revisited after centennial. *J Indian Acad Oral Med Radiol.* 2015;27(1):90–5.
2. Plessis A, Broeckhoven C, Guelpa A, Gerhard le Roux S. Laboratory x-ray micro-computed tomography: a user guideline for biological samples. *GigaScience.* 2017;6(6):1–11.
3. Bhattacharyya KB. Godfrey Newbold Hounsfield (1919–2004): the man who revolutionized neuroimaging. *Ann Indian Acad Neurol.* 2016;19(4):448–50. <http://www.mayo.edu/research/labs/physiological-imaging/images>
4. Keleş A, Alçın H, Kamalak A, Versiani MA. Micro-CT evaluation of root filling quality in oval-shaped canals. *Int Endod J.* 2014;47(12):1177–84.
5. Khalil S, Sun W. Bioprinting endothelial cells with alginate for 3D tissue constructs. *J Biomech Eng.* 2009;131:111002–8.
6. Yao R, Zhang R, Luan J, Lin F. Alginate and alginate/gelatin microspheres for human adipose derived stem cell encapsulation and differentiation. *Biofabrication.* 2012;4(2):025007.

7. Zhang Y, Chen H, Ozbolat IT. Characterization of printable micro-fluidic channels for organ printing. Texas: International Mechanical Engineering Congress & Exposition Houston; 2012.
8. Langer R, Vacanti JP. Tissue engineering. *Science*. 1993;60:920–6.
9. Hollister SJ. Porous scaffold design for tissue engineering. *Nat Mater*. 2005;4(7):518–24.
10. Kim BS, Park IK, Hoshiba T, Jiang HL, Choi YJ, Akaike T, Cho CS. Design of artificial extracellular matrices for tissue engineering. *Prog Polym Sci*. 2011;36:238–68.
11. Ma Z, Kotaki M, Yong T, He W, Ramakrishna S. Surface engineering of electrospun polyethylene terephthalate (PET) nanofibers towards development of a new material for blood vessel engineering. *Biomaterials*. 2005;26(15):2527–36.
12. Mann BK, West JL. Cell adhesion peptides alter smooth muscle cell adhesion, proliferation, migration, and matrix protein synthesis on modified surfaces and in polymer scaffolds. *J Biomed Mater Res*. 2002;60(1):86–93.
13. Berry CC, Campbell G, Spadaccino A, Robertson M, Curtis AS. The influence of microscale topography on fibroblast attachment and motility. *Biomaterials*. 2004;25(26):5781–8.
14. Wan Y, Wang Y, Liu Z, Qu X, Han B, Bei J, Wang S. Adhesion and proliferation of OCT-1 osteoblast-like cells on micro- and nano-scale topography structured poly (L-lactide). *Biomaterials*. 2005;26(21):4453.
15. Lam CXF, Mo XM, Teoh SH, Hutmacher DW. Scaffold development using 3D printing with a starch-based polymer. *Mater Sci Eng C*. 2002;20(1/2):49–56.
16. An J, Ee Mei Teoh J, Suntornnond R, Kai Chua C. Design and 3D printing of scaffolds and tissues. *Engineering*. 2015;1(2):261–8.
17. Ma Z, Kotaki M, Inai R, Ramakrishna S. Potential of nanofiber matrix as tissue-engineering scaffolds. *Tissue Eng*. 2005;11(1–2):101–9.
18. He P, Zhao J, Zhang J, Li B, Gou Z, Gou M, Xi L. Bioprinting of skin constructs for wound healing. *Burns Trauma*. 2018;6:5.
19. Lanza R, Langer R, Vacanti J. Principles of tissue engineering. 3rd ed. Cambridge: Academic Press; 1997. eBook ISBN: 9780123983701
20. Singh D, Singh D, Han SS. 3D printing of scaffold for cells delivery: advances in skin tissue engineering. *Polymers*. 2016;8(1):19.



Application of Micro-CT in Soft Tissue Specimen Imaging

10

Gina Delia Roque-Torres

10.1 Introduction

The novella *Flatland: A Romance of Many Dimensions* describes a two-dimensional world occupied by geometric figures, wherein women are simple line segments, while men are polygons with various numbers of sides. This two-dimensional world is insufficient to describe the actual universe. Science popularizers were Carl Sagan who recreates this thought experiment as a setup to possibilities of higher dimensions of the physical universe and Stephen Hawking who highlights the impossibility of life in two-dimensional space. From the literary world to the scientific, two dimensions lack the necessary depth to provide a complete picture; for this reason three-dimensional (3D) imaging is necessary to be studied. Notwithstanding several adopted techniques for characterizing the 3D structure of non-calcified tissues and biomaterials which are well-established, in practice, they can be technically challenging, time-consuming, limited to spatial resolution and small volumes, and, in some cases, prone to inducing artifacts. As an alternative to these techniques, X-ray computed microtomography can image the internal 3D structure of an opaque sample at

submicron resolutions (*ex vivo*) and visualize dynamic changes in living tissues at a microsecond scale (*in vivo*).

Soft tissues surround other structures and organs of the body, which include tendons, ligaments, fascia, skin, fibrous tissues, fat, synovial membranes, muscles, nerves, and blood vessels, constituted by cells and extracellular matrix responsible for biological functions [1]. A wide range of imaging methods have been developed to analyze biological tissues at microscale in *ex vivo* and *in vivo* samples, which provide information on the morphological, chemical, and physical properties.

The low contrasting properties of soft tissue create significant challenges for preparations and imaging of samples; in this case imaging needs to be aided by using stains and contrast agents to label specific components. The primary methods for visualizing 3D structures of soft tissue are often dictated by the needs of the users as well as the abilities and limitations of each modality [2]. Those methods include optical microscopy, electron microscopy, confocal microscopy, magnetic resonance imaging, ultrasound, absorption and phase-contrast synchrotron X-ray imaging, light sheet (based) fluorescence microscopy, and X-ray micro-computed tomography (micro-CT) (Table 10.1) [2, 4, 5].

The history of imaging tools begins with the discovery of X-ray radiographs in 1895, up to the

G. D. Roque-Torres (✉)
Center for Dental Research, Loma Linda University,
Loma Linda, CA, USA
e-mail: gdrtorres@llu.edu

Table 10.1 Basic overview for visualizing the three-dimensional structures of biological samples

Specimen	Optical microscopy	Electron microscopy	Confocal microscopy	Magnetic resonance imaging	Ultrasound	Absorption and phase-contrast synchrotron X-ray imaging	Light sheet (based) fluorescence microscopy
Resolution	Physical sections or block face 1 μm	Physical sections or block face SEM-nm TEM-50 pm	Intact (thin or small) 1 μm	Intact 30 μm^3	Intact 25 μm^3	Intact Better than 1 μm	Physical sections 1–2 μm
Speed	Weeks or months	Days or weeks	Seconds or minutes	Minutes or hours	Minutes	Seconds or minutes	Seconds or minutes
Used in vivo	$\times\checkmark$	\times	$\times\checkmark$	\checkmark	\checkmark	\times	\times
Advantages	Reveals tissue architecture. Biological components can be stained. Birefringence of collagen	High-resolution images can be produced. Elemental mapping	Histological stains, immunological techniques with higher resolutions but at limited depths and coverage	Noninvasive and nondestructive. Good depth penetration. 3D reconstructions	Noninvasive and nondestructive. Good depth penetration. Mechanical information	Anatomical and biological specimens with very high contrast for lower dose, high lateral resolution	Used in developmental biology
Disadvantages	Tissue must be fixed prior to processing (histology). Limited depth penetration	Fixation and processing of tissue is laborious. Destructive. Identification of specific matrix compositions difficult	Fixation and embedding are required	Low contrast between interface components. Identification of specific matrix compositions difficult	Identification of specific matrix compositions difficult	Nonconventional image features, require special interpretation techniques	Fixation, embedding, and staining of tissue are laborious and required
Cost	Moderate	Moderate to high	Moderate to high	Moderate	Moderate	High	Moderate

Bannerman et al. [2]; Weon et al. [3]

introduction of hospital-based computed tomography scanners in the 1970s, which are into clinical use. Laboratory-based micro-CT instruments followed up in the 1980s, which were typically used to image calcified tissues [4]. Recently, X-ray absorption by heavy-element dyes allows the 3D visualization of microstructures of soft tissue.

To date, we have several types of contrasting agents (high atomic number elements) that bind to components of the soft tissue. The principal contrast agents that have been used on biological specimens include barium sulfate suspension, gallocyanin-chromalum, gold, iodine potassium iodide, iodine, iron oxide, lead, mercuric chloride, osmium, phosphomolybdic acid, phosphotungstic acid, platinum, potassium iodide, silver, uranyl acetate, potassium dichromate, and silver nitrate, among others. Each of these agents allows the visualization of particular tissues or cells, which have been proven by subjecting them to tests due to their ability to improve tissue discrimination and the limits of the organs.

Some issues described in several works are related to the capability of the diffusion of the staining agent into the samples, long staining times, the highly concentration of certain staining solutions which may cause sample shrinkage, or even just achieve limited epidermal layers. Thus, it is important to consider the sample preparation, mounting, data collection, and reconstruction to overcome the current limitations in order to have the best high-contrast visualization of 3D tissue samples [6].

Many current clinical applications which utilize 3D visualization of microstructures of soft tissue include lung, heart, brain, kidney, liver, testicle, musculoskeletal, and microvascular imaging, as well as providing information on tumors, the anatomy of different animals, and food or tissue engineering.

In this chapter, we discuss the current capabilities of micro-CT with regard to soft tissue. To that end, we present fundamentals of X-ray microtomography, how to process data, and the various biological applications.

10.2 Fundamentals of X-Ray Microtomography

X-rays are a form of electromagnetic radiation, generated by a vacuum tube using high voltage to accelerate electrons from a cathode to a (usually) tungsten alloy anode. In the process, the accelerated electrons release electromagnetic radiation in the form of X-rays, and the maximum energy of the radiation is limited by the energy of the incident electron [7].

10.2.1 X-Ray Interaction of Biological Tissue

Biological soft tissue is composed of low-atomic number (low- Z) elements, which produce little contrast in a hard X-ray image. Therefore, most of them show uniform density, in which only the outline but no internal structure is visualized, leading to a lack of understanding of the whole tissue [1].

Historically, materials with high atomic number (high- Z) tend to better absorb X-rays, expressed by the formula for X-ray absorption. The atomic number (Z) allows the contrast level of the different tissues making it of significant importance in clinical applications. To increase the absorption coefficient, X-ray attenuation contrast media containing atoms of high atomic number (agents contrast) must be frequently used to obtain images of soft tissue [7]. The elements used as contrasting agents are mostly in the fifth or sixth row of the period table.

10.2.2 Contrast Agents

Several staining methods have been proposed to increase soft tissue contrast in *ex vivo* and *in vivo* specimens scanned with micro-CT. Elements with atomic numbers of 67–83, which have their absorption edges between 8 and 14 keV, can give sufficient contrast and are included successfully in an *ex vivo* micro-CT imaging. These elements as nanoparticle contrast agents also show great

potential for functional and molecular for in vivo micro-CT imaging application following the categories of low molecular weight and blood pool. However, radiation dose is a concern and limitation for in vivo imaging [1, 8].

The attenuate X-rays are measured in Hounsfield units (HU), where water is assigned 0 HU as a density value and air -1000 HU and most soft tissue falls within 30–100 HU. It is challenging to produce 3D images of two adjacent tissues (e.g., tongue/tumor) or tissues in con-

tact with blood or other physical fluids (e.g., brain aneurysm). Therefore, contrast agents are used to improve the visualization, enhance differentiation among different tissues, and provide biomechanical information as well as evaluation of tissue/organ function or performance. These requirements are of significant interest and highly assessed, especially those who have a long retention time and are nontoxic [7].

To carry out the above requirements, various contrast agents are currently in use (Table 10.2).

Table 10.2 Basic overview of the contrast agents

Contrast agent	Binding preference	Visualized soft tissue structures	Advantages	Limitation
Osmium [5, 9]	Phosphate Lipids, proteins, and nucleic acids	Vertebrates Insects	Natural contrast Wide availability High contrast Can be used on resin blocks	Toxic Expensive disposal Limited penetration Not useful for alcohol-stored tissues
Gold [7]	Peptides and antibodies antigen-specific RNA aptamer High-density lipoproteins	Cardiovascular system in rodents Thrombotic disease Hepatocellular carcinoma Tumors in vivo Vasculature, kidneys, and tumors in mice Cell therapy Pancreatic islet of Langerhans cells Atherosclerotic plaques in mice	Higher contrast per unit weight No appreciable cytotoxicity Prolonged blood circulation times Increased chemical stability, long circulation times Largely nontoxic and biocompatible	Potential toxicity issues in high doses Instability in buffered May exhibit toxicity in certain high particle-size in vivo
Iodine [5, 7, 9, 10]	Glycogen and lipids Potassium	Cardiovascular system in rodents Bovine bone ex vivo Breast tumor lesions Insects	Rapidly filtration by the kidney Safety Low risk to nephropathic patients	Lower X-ray attenuation Non-specific biodistribution High “per dose” concentrations are required Using ionic iodinated: high intrinsic osmolality, toxicity, and physiological problems Low bone tissue differentiation when used as aqueous solution
Platinum [7]	Iron/platinum (Fe/Pt)	Tumors	No notable cytotoxicity Good biocompatibility	Needs to be further tested
Phosphotungstic acid (PTA) [5, 9]	Proteins Connective tissue (collagen)	Vertebrates (musculature and nervous tissue) Insets (sensory organs, legs, and muscles) Neural tissues Collagenous tissue	Low toxicity Simpler to use Effectively stain in alcohol-stored sample Excellent contrast Stable stain Sharp tissue differentiation	Slow tissue penetration, limited to a few millimeters

Table 10.2 (continued)

Contrast agent	Binding preference	Visualized soft tissue structures	Advantages	Limitation
Barium sulfate suspension [7, 11]	Gold	Human gastrointestinal tract Microcracks in bovine tibiae ex vivo Dentinal cracks in ex vivo human and elephant teeth	Biologically inert Nontoxic	Oral ingestion for upper gastrointestinal imaging or rectal administration for lower gastrointestinal imaging
Uranyl acetate [7, 12]	Proteins and lipids with sialic acid carboxyl groups Nucleic acid phosphate groups of DNA and RNA	Microdamage in ex vivo human trabecular bone Collagen scaffolds porosity	Excellent X-ray attenuation properties	Toxicity in vivo
Iron oxide [13, 14]	Native CHO cells receptors	Stem cells	Good biocompatibility and biodegradability No disrupt stem cell viability	Possible cytotoxicity High X-ray attenuation/density only using high-resolution CT
Gallocyanin-chromalum [10]	Cell nuclei	Cell nuclei	Demonstrates cell densities and individual cells Possibly useful as counterstain	Low overall contrast
Iodine potassium iodine (IKI) Lugol's solution [5, 9, 10, 15–17]	Glycogen Lipids Potassium	Hard and soft tissues of the skull Muscle morphology Cardiovascular structures of mouse embryos Neural tissues Metazoan	Easy handling Low cost Different affinities for major types of soft tissues	Low solubility of elemental iodine (I ₂) in water Perceived nondestructiveness Low toxicity Rapid staining
Phosphomolybdic acid (PMA) [5, 9, 18]	Proteins Collagen	Insects Cartilage structures in mollusks Collagenous tissue in mouse embryos	Low toxicity	Spotting collagen in general rather than a specific type of collagen

In addition, some inconsistent results regarding the tissue discrimination may still remain, especially when applied to complete organisms. There are some alternatives to labelling of visualizing biological structures as the critical point drying and corrosion casting with resin. The critical point drying method showed structural distortion due to the sample shrinkage, and the corrosion casting method is mostly used in the vascular system [7].

10.3 Practical Aspects

Several methods for sample mounting have been developed. Some mounts used brass fitting with the smallest diameter, in which the sample can be adjusted. Nowadays, advancements in sample mounting systems made by the same companies of micro-CT have enabled the imaging of larger samples and decreased artifact movement as well as scanning time; this then provides better

images to analyze. Recalling that sample images must be taken at the resolution appropriate to analyze the sample structure, this depends on the fineness of the structure we are going to analyze; consequently it is also important to fit the sample in the best container to not increase the resolution.

Furthermore, the degree of staining with the high-Z element is important in the data collection. For example, in the probe element *gold*, if 0.1% of the voxel volume is occupied with metal gold, the voxel value falls to 3.5 cm^{-1} , which is three times the typical voxel value deviation showing clearly distinguished images, but if it is lower than 0.03% (v/v), the result would be an ambiguous image [1]. Hence, the selection, concentration, and procedure of the staining are crucial for the visualization and subsequent analysis of the sample.

The process that follows data collection, data reconstruction, may be accelerated by using a parallel computing environment, such as PCs, the CUDA, or OpenCL [1]. The data reconstruction is a critical process in which any errors introduced can seriously impact the reliability and interpretation of the data.

10.4 Biological Applications

10.4.1 Bone Imaging

Micro-CT has been used for mineralized tissues since its very inception. However, two soft tissues, bone marrow adipocytes and blood vessels, remain difficult to quantify because they are highly connected to bones. The detailed 3D visualization of these tissues can provide a better understanding of the vascular organization, blood flow, and the impact on bone homeostasis. Recent studies have revealed that the local mechanical environment of the fracture is influenced by the neovascularization showed by a quantitative 3D analysis [19]. Another study highlights the vasculature using micro-CT methods, opening broader possibilities in detection and characterization of the 3D vascular tree to assess vascular tissue engineering strategies [20].

Moreover, new novel contrast agents have been including a hafnium-based Wells-Dawson polyoxometalate, which allows clear differences in bone structure, vascular network organization, characteristics of the adipose tissue, and proximity of the different tissues to each other. It can help to improve the treatment in several bone pathologies, as well as performance of biomaterials for skeletal regeneration [21].

On the other hand, other bone pathologies involve the degradation of articular cartilage, which cannot be analyzed due to the low cartilage contrast limits by the use of classical X-ray imaging techniques. Delecourt et al. (2016) [22] demonstrated that volume and thickness of human cartilage can be measured using a conventional micro-CT system in patients that had osteoarthritis. Another study also showed a significant advance in the bone field with a quantitative analysis of articular cartilage thickness after contrast enhancement of the cartilage matrix [23].

10.4.2 Lung Imaging

The lung is the exception of the attenuation values for soft tissue, approaching -1000 HU due to high air content [7], and the use of the correct contrast agent is essential for the proper analysis [24] (Figs. 10.1 and 10.2). Micro-CT imaging in small animals like mice, crabs, and turtle also presents another challenge on account of their small size and rapid respiratory motion [8, 25, 26].

In order to further enable studies on lung disease, many investigators have established archival biobanks that contain tissue samples representative of multiple lungs diseases, which can be measured by micro-CT images [27]. Moreover, the feasibility of micro-CT for obtaining quantitative volumetric and morphologic information of changes in soft tissue, respiratory tracts, and vascularization is the main concern in the studies [28–31].

Understanding the three-dimensional (3D) micro-architecture of lung tissue can provide insights into the pathology of lung disease.

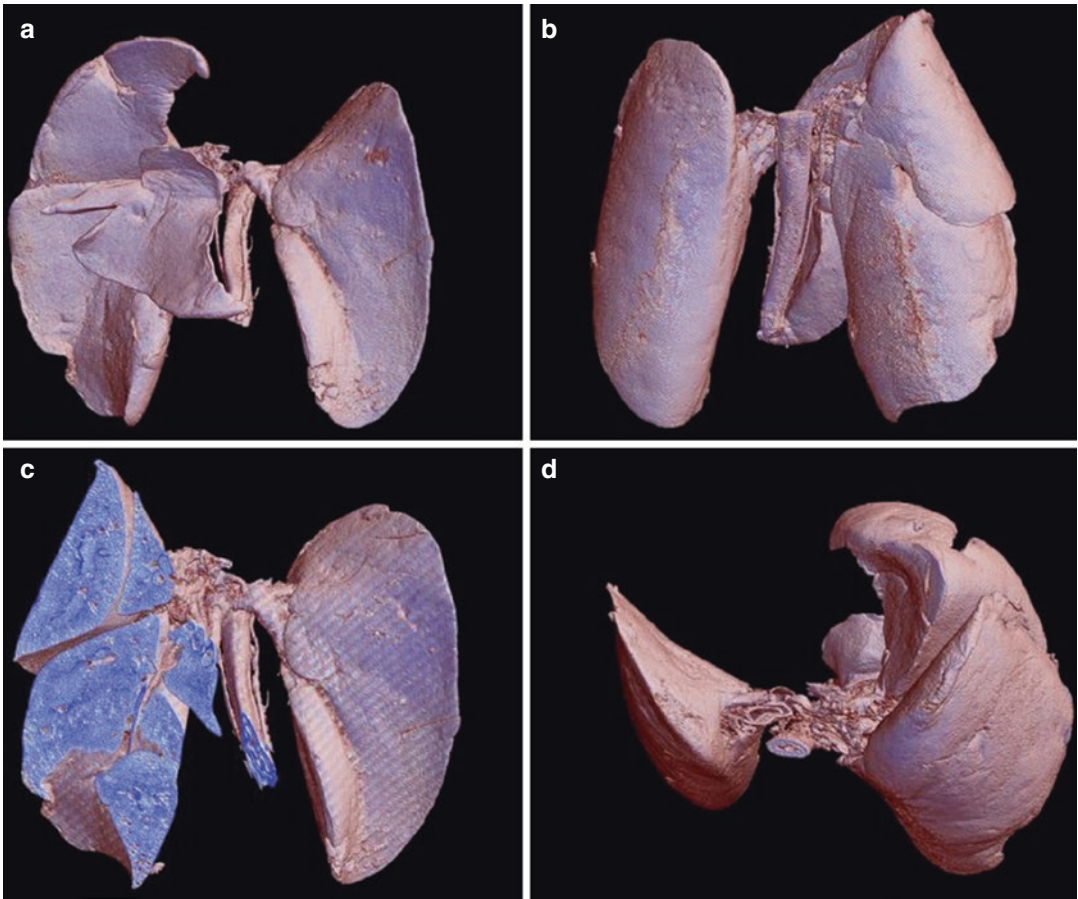


Fig. 10.1 3D volume rendering reconstruction of a mice lung. (a) Frontal view. (b) Back view. (c) Frontal view with section to show the interior of the right lung. (d) Top view

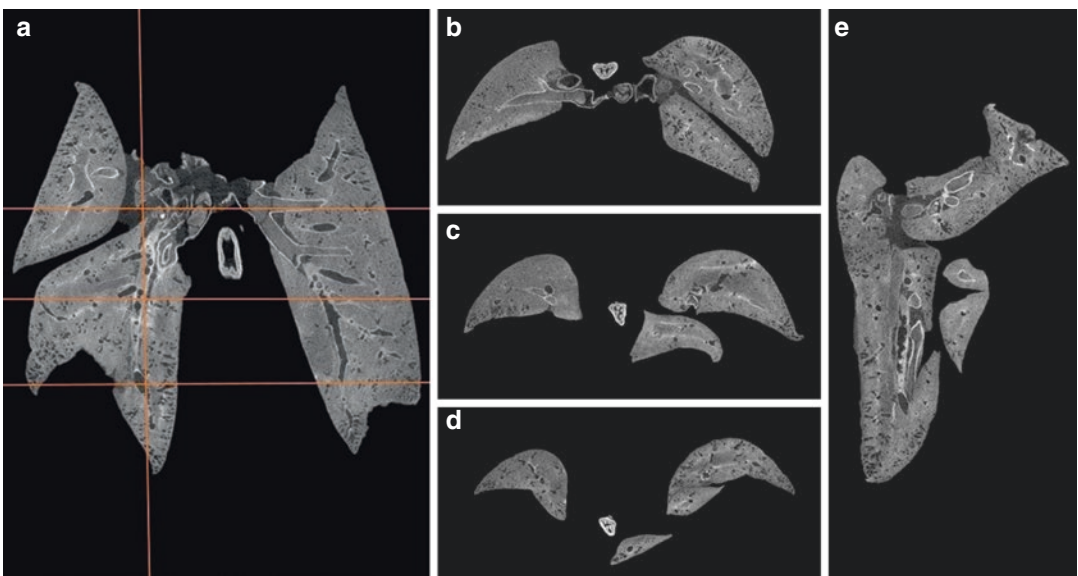


Fig. 10.2 Reconstructed data of the mice lung. (a) Coronal view. (b–d) Axial view of the regions (top, middle, and bottom). (e) Sagittal view of the right lung

The various studies of lung disease models, such as rheumatoid arthritis-associated interstitial lung disease [32], obstruction in chronic obstructive pulmonary disease [33], centrilobular and panlobular emphysema [34], and fibrosis, which is a late complication of radiotherapy [35–37], are some that have been studied.

Additional studies have monitored lung metastasis and host/lung response in preclinical studies, which will be valuable for translational applications [38]. Furthermore, micro-CT is used to optimize the monitoring of both progression and therapy of lung diseases, bleomycin-induced fibrosis, invasive pulmonary aspergillosis, pulmonary cryptococcosis, [39] sarcoma in an orthotopic lung cancer model [40], or even distinguishing between malignant and nonmalignant pulmonary nodules [41], which were developed in animal model lung tumors [42].

A further advantage related to 3D micropathology is that it allows a study of the three-dimensional lung structure preserved without the effects of fixatives while enabling subsequent studies of the cellular matrix composition and gene expression performed on frozen lung samples by the cryostage on the micro-CT. The same workflow and methods can be applied to other frozen tissue samples, which opens up new investigative possibilities for integrating morphometrical and biological studies [43].

10.4.3 Cardiac Imaging

While magnetic resonance (MR) has been considered the “gold standard” for cardiac imaging, the micro-CT may offer alternatives and even some advantages but does have a limitation such as the use of ionizing radiation in the case of *in vivo* imaging [44]. The micro-CT has the ability to visualize the 3D coronary circulation and internal pressure, as well as to evaluate cardiac morphology and function [8, 44–46] (Figs. 10.3 and 10.4).

This is a powerful tool for the 3D depiction of morphological alterations of hearts in high

resolution and can be combined with classical histological analysis, which as a preclinical research method can unravel structural alterations of various heart diseases [47] and also assess the best anatomic approach such as the ascending aorta [48].

The cardiac function metrics such as wall motion, wall thickening, regional ejection fraction, ejection fraction, end-diastolic volume, end-systolic volume, stroke volume, myocardial mass, and cardiac output can be assessed via cardiac micro-CT [8, 44]. Micro-CT has played an important role in the assessment of mouse models of cardiovascular diseases and the determination of functional parameters such as the left ventricular volume [49].

The use of contrast agents is fundamental in the cardiac-micro-CT in order to be able to discriminate between the myocardium and blood. In majority of studies, blood pool contrast agents have been used [8]. For example, Chang-Lung Lee et al. (2014) showed DE-micro-CT and 4D-micro-CT are effective preclinical imaging approaches that provide not only anatomic but also functional information to noninvasively measure radiation-induced cardiac injury in mice with two nanoparticle-based contrast agents—a blood-pool liposomal iodine (Lip-I) [31] and a PEGylated gold nanoparticle (AuNp) [50]—and the iodine staining-enhanced micro-CT with computational anatomical analysis also represents a valid addition to classical histology for the delineation of compact myocardial wall thickness in the mouse embryo [51]. More recently, a contrast called eXIA 160—an aqueous colloidal polydisperse contrast agent—allows sufficient enhancement between blood and tissue with very low injection volumes [45].

Moreover, the cardiac micro-CT has been used to detect the presence of thrombi, induced by stenosis of the inferior vena cava in experimental models, giving a reliable and reproducible method for the longitudinal assessment of venous thrombus [52]. It has also been used to detect myocarditis caused by exposure to external pathogens such as the coxsackie B virus (CVB) [53] and for evaluating myocardial infarction and potential therapies [45]. In the most common

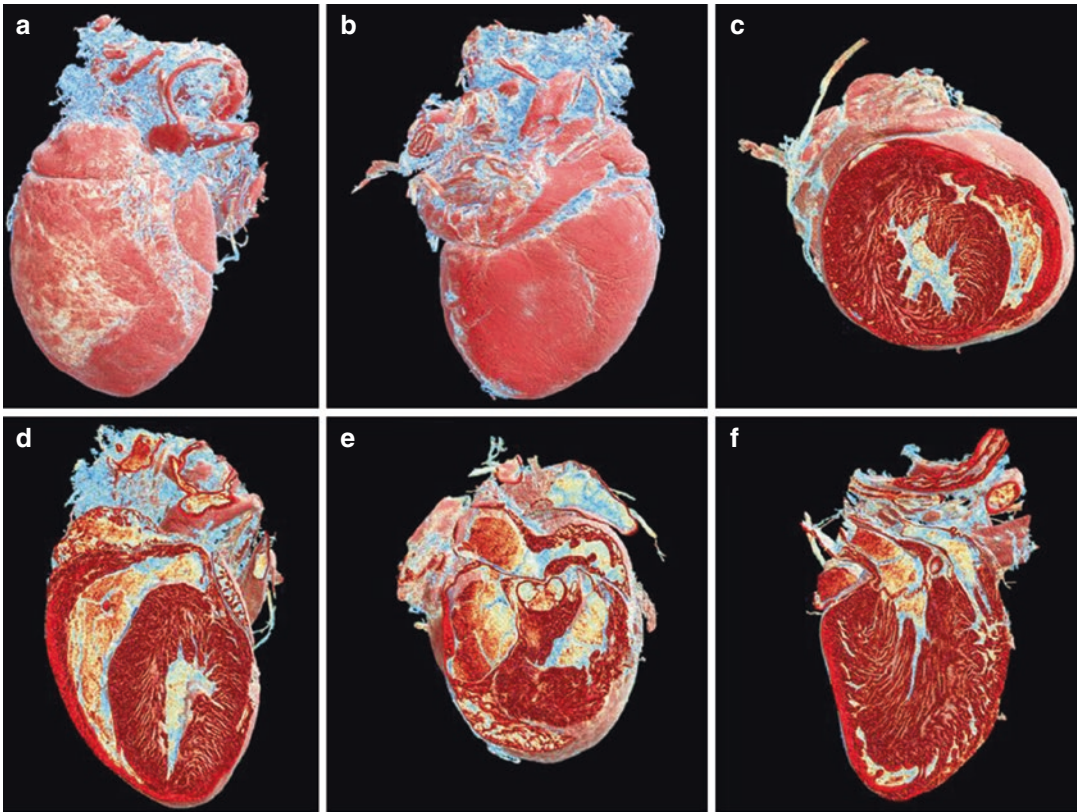


Fig. 10.3 3D volume rendering reconstruction of a mice heart. (a) Frontal view. (b) Back view. (c) Axial view of the middle. (d) Coronal view of the middle front. (e) Axial view of the top. (f) Coronal view of the middle back

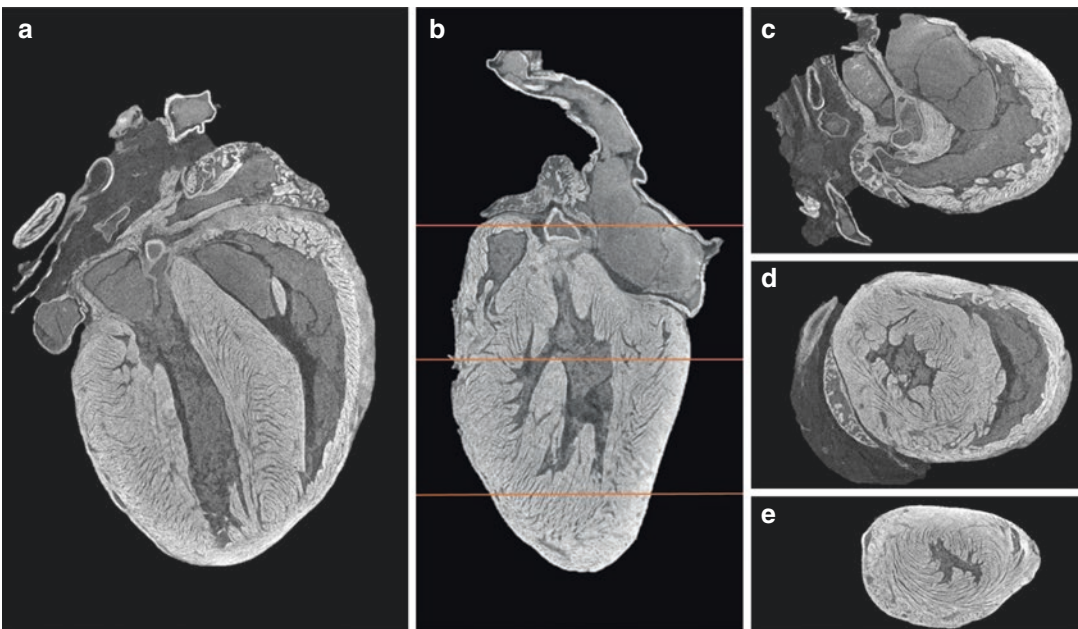


Fig. 10.4 Reconstructed data of the mice heart. (a) Coronal view. (b) Sagittal view. (c–e) Axial view of the regions (top, middle, and bottom)

arrhythmia such as the atrial fibrillation, it has been used to investigate the structural basis for conduction during sinus rhythm, atrial pacing, and sustained atrial flutter [54].

Numerous efforts are ongoing to improve material and kinematic characterizations of soft tissues and engineered biomaterials, and these pursuits are facilitated by the increased availability of micro-CT [55]. One specific instance relates to quantifying between long-term in vitro dynamic calcification and abnormal flow patterns associated with three porcine bioprosthetic heart valves [56] or to visualizing the conformation of an implantable device or soft robots to the heart, which can mimic or assist in complex biological functions such as the contraction of heart muscle [57].

Extending their observations to three dimensions using X-ray microtomography shows a vastly different picture to what they had been accustomed to; scientists have been intrigued by the intricate structures formed by different animals, for example, marine organisms such as the heart of an urchin [58] and zebrafish [59], among others [9].

10.4.4 Brain Imaging

The 3D whole brain shape is best suited for rapid phenotyping applications due to experimental treatment [60]. The micro-CT is suitable for defining tumor boundaries by providing contrast between tumor and normal brain tissue and for also allowing the tumor volume estimate, making it well suited in accessing tumor burden. It may provide a rapid characterization of morphological changes resulting from genetic manipulation of animals and thus find application in a wide range of studies involving genetics with histopathological correlation [61] (Figs. 10.5 and 10.6).

The cerebrovasculature is a network of blood vessels (arteries, veins, sinuses, arterioles, venules, and capillary beds) which supply blood to the brain. Study of cerebral vascular structure, such as pathologies that can lead to cerebrovascular disorders, can be understood by utilizing high-resolution 3D imaging modalities, using some automatic segmentation and recognition methods to facilitate the comparison of blood vessels [62]. Imaging is also useful

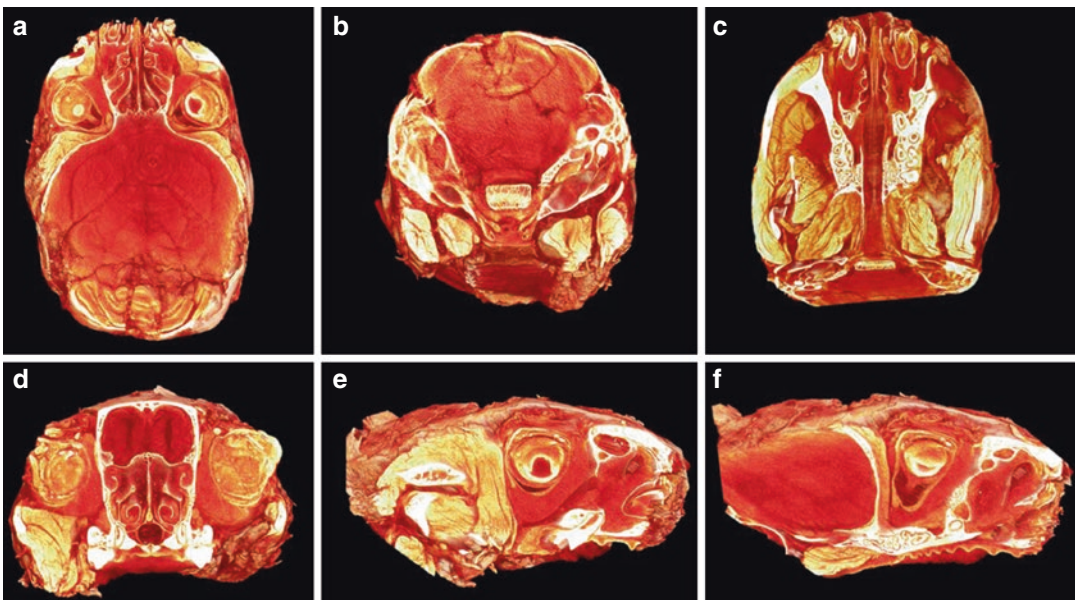


Fig. 10.5 3D volume rendering of a mice head. (a) Axial view of the middle. (b) Coronal view of the posterior region. (c) Axial view of the inferior region. (d) Coronal view of the anterior region. (e, f) Sagittal view

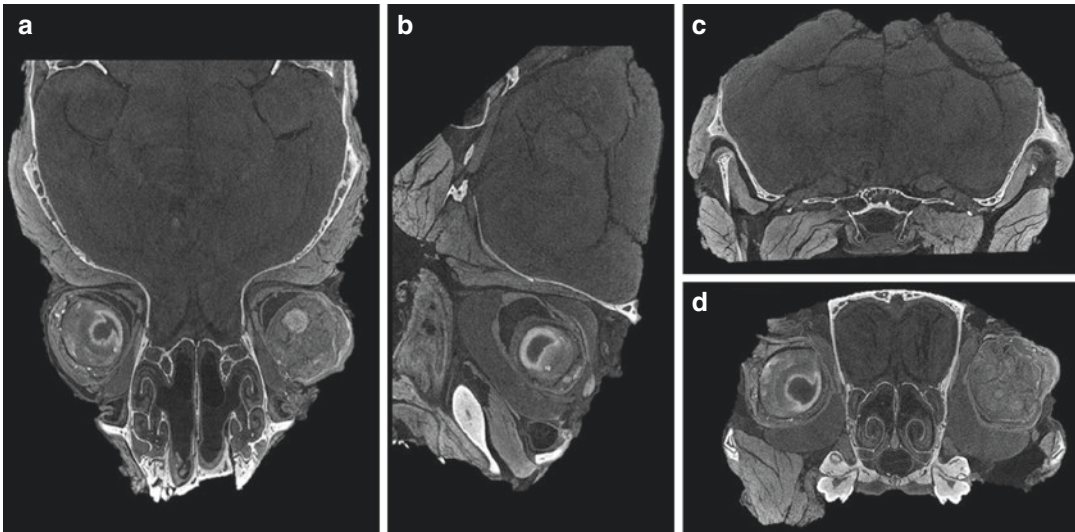


Fig. 10.6 Reconstructed data of the mice head. (a) Axial view. (b) Sagittal view. (c, d) Coronal view of the posterior and anterior region respectively

for detecting the axonal networks of the murine brain [63] or even detecting the mouse brain myelin structure [64] and the cranial venous outflow [65].

Abnormalities in the cerebrovascular system play a central role in many neurologic diseases. The micro-CT allows the visualization of large cerebrovascular networks, including the circle of Willis, as well as morphometric changes that are practically impossible to identify using current histological methods [66]. Cerebral cavernous malformations are hemorrhagic brain lesions, where the micro-CT allows high-throughput assessment of lesion count and volume [67]. Another frequent type of hemorrhagic stroke such as the subarachnoid hemorrhage is a further demonstration of the type of analysis possible by the quantification of vasospasm from micro-CT data [68, 69].

Other utilities of the micro-CT using fibrin-targeted gold nanoparticles as a contrast agent include the detection of thrombotic disease, quantifying the thrombus burden, and guiding thrombolytic therapy [70]. Also, the micro-CT can be combined with positron emission tomography (PET) to assess the carotid atherosclerosis after ischemic attack or minor ischemic stroke

[71]. The ischemic lesion from the non-infarcted tissue [72] or ischemia with stroke [73, 74] may also be evaluated.

For instance, a three-dimensional finite element model of the rat brain and braincase obtained from micro-CT images was also studied to expand on the knowledge concerning mild traumatic brain injuries [75].

During early stages of postnatal development, pressure from the growing brain and cerebrospinal fluid, i.e., intracranial pressure, load the calvarial bones. This loading contributes to the peripheral bone formation at the sutural edges of calvarial bones. Scanning with micro-CT may estimate the cranial growth by intracranial volume and skull length [76, 77]. Such modeling can be a contributing factor to bone formation at the sutures during early stages of development, which has the potential to be translated to human skull growth in order to enhance our understanding of the different reconstruction methods used to manage the craniosynostosis, for example. Data collected can then be used for development and validation of computational models of skull growth and may reduce the number of reoperations in children displaying this condition and thereby enhance their quality of life [77, 78].

Finally, some authors conclude that micro-CT is highly suitable for targeting neuroanatomy, as it reduces the risk of artifacts and is faster than classical techniques in the analysis of the brains of selected arthropods [79]. Other studies also found the first anatomical evidence of this structure in early thalattosuchians [80]; explored and described the anatomy of the brain in the jumping spider *Marpissa muscosa* [81]; quantified and described the internal anatomy of the skull in primate species [82–84], the tammar wallaby [85], squirrels [86], crocodylians [87], and insects [88]; and even observed the vascular patterns in iguanas and other squamates [89], among others [5, 9, 90].

10.4.5 Kidney Imaging

Most of the articles evaluated anatomy ex vivo to compare 3D anatomy to histological slices particularly in human specimens, whereas few publications describe renal structures in animals [91, 92]. Conversely, other studies describe in vivo imaging procedures for mouse kidney anatomy evaluation using contrast-enhanced high-resolution measurement of kidney volume, length, and thickness, providing a useful follow-up research tool for renal disease studies [93]. This may also open up broader possibilities in the detection and characterization of the 3D vascular tree of the kidney to assess vascular tissue engineering strategies [20] (Figs. 10.7 and 10.8).

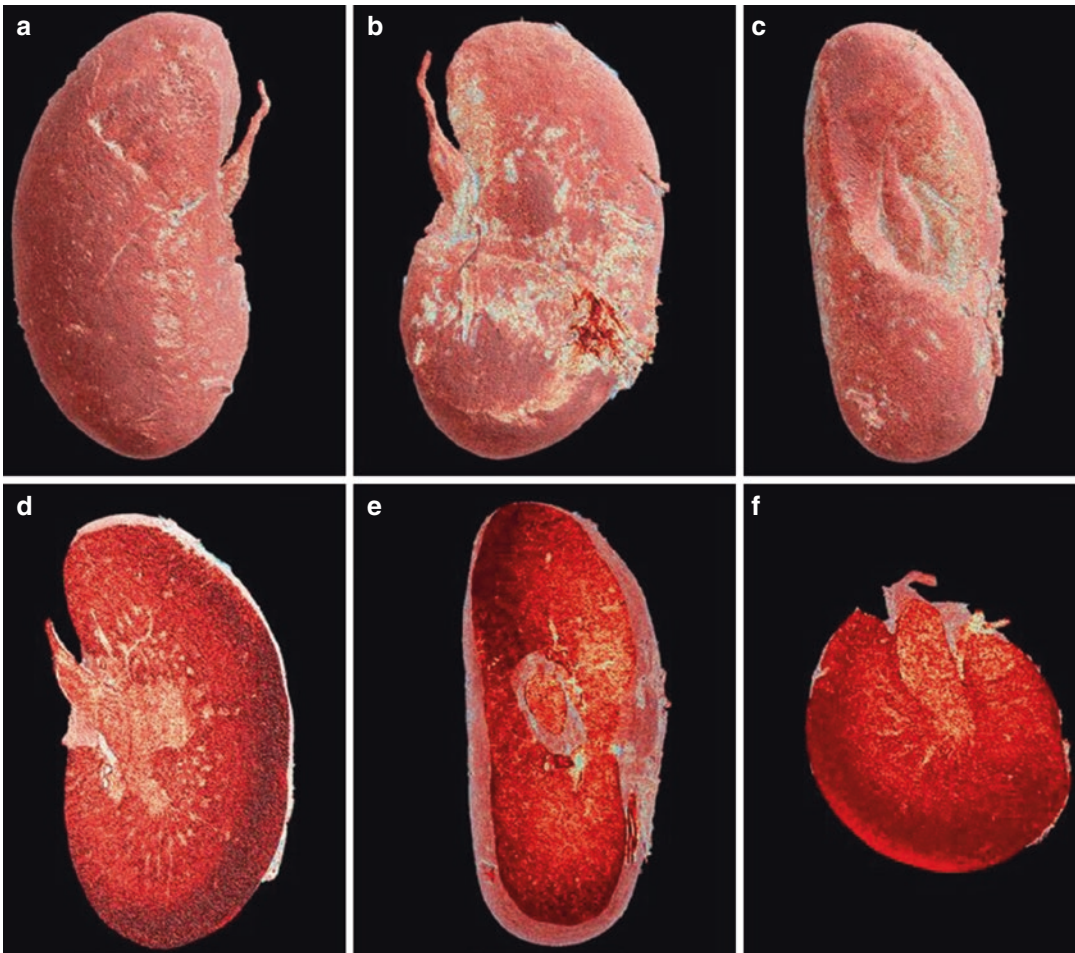


Fig. 10.7 3D volume rendering of a mice kidney. (a) Frontal view. (b) Back view. (c) Medial view. (d) Coronal view. (e) Sagittal view. (f) Axial view

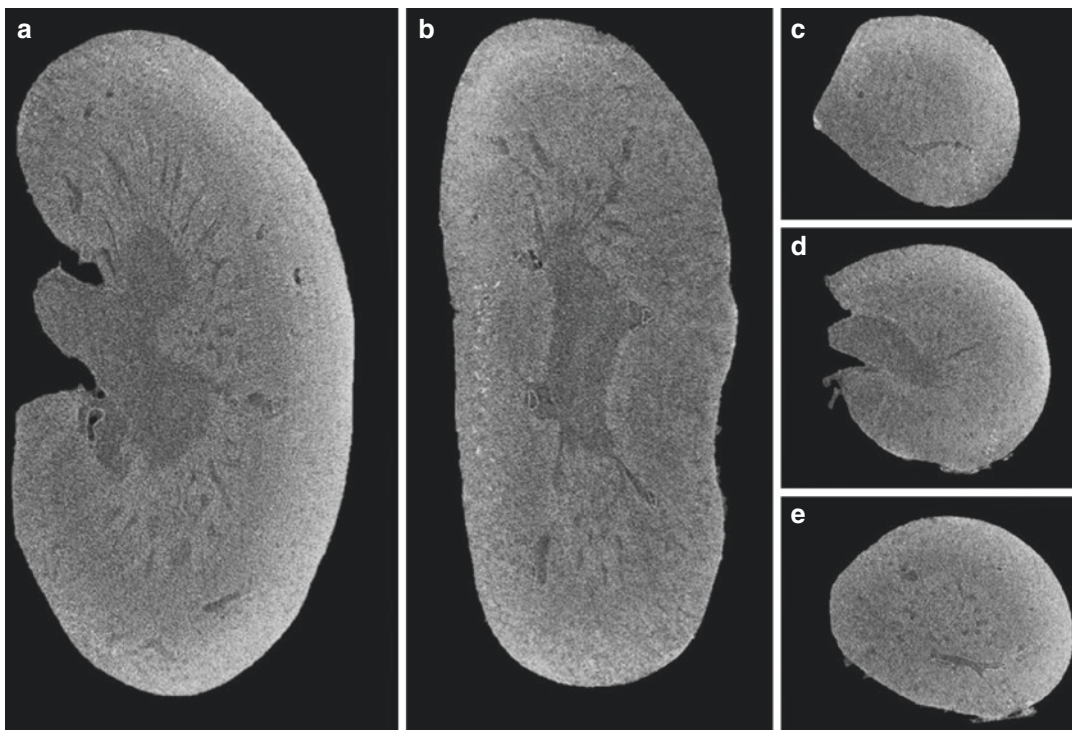


Fig. 10.8 Reconstructed data of the mice kidney. (a) Coronal view. (b) Sagittal view. (c–e) Axial view of the regions (top, middle, and bottom)

In the surgical setting, horseshoe kidneys (HKs) cause certain confusion because of their complicated morphology. A study observed the vascular and collecting system of the HK using anatomical and contrast imaging techniques from a voluntarily donated postmortem cadaver. These observations can contribute to a better understanding of fundamental knowledge and progress in the surgery of HKs [94].

Another possible application and advantage of the micro-CT is the evaluation of congenital abnormalities of the renal tract, performed on three human fetal kidneys: one structurally normal kidney, one with autosomal recessive polycystic kidney disease, and one with multicystic dysplastic kidney disease. It could be utilized to augment conventional autopsy practice and be used for noninvasive examination [95]. Furthermore, evaluation of an animal model highlighted a decline in renal function and blood flow associated with a decrease in the number of intrarenal vessels during aging [96]. Other stud-

ies focus on kidney disease and the investigations of the kidney function, which may lead to pioneering research and novel therapeutics using preclinical disease models and innovative analytical techniques.

Proper renal perfusion is critical for kidney function and the cause of many renal diseases. Analysis of total and cortical renal vasculature volume (vascular number (V.N), vascular thickness (V.Th), and vascular separation (V.Sp)) combined with a method to isolate and quantify the number of perfused glomeruli (glomerular number (Glom.N) and glomerular density (Glom.Dn)) to assess vascular changes can be done by micro-CT, which may improve understanding of numerous disease models, biological mechanisms, and treatments [97]. Another study showed the quantitative analyses of three-dimensional vascular networks in three models (ischemia-reperfusion, unilateral ureteral obstruction, and Alport syndrome mice). These analyses revealed significant and

previously unrecognized alterations of preglomerular arteries [98].

These results have obvious important implications for human medicine, showing effective improvement of an important clinical problem, even for wealthier nations in the clinical setting of kidney diseases. However, some of the therapeutic approaches are not entirely well-established, as in the study of a progression of renal diseases delayed by angiotensin II blockers, in which it was demonstrated that these blockers can improve blood tissue perfusion and filtration capacity and lead to regression of the kidney fibrosis [99]. Another study in animal model showed that vitamin D supplementation accompanied by calcium administration to avoid bone demineralization would promote kidney stone formation. Hence, one should be cautious about the cumulative risk of kidney stone formation in humans when exposed to both vitamin D supplementation and high calcium intake [100]. The chemical composition of the stone, which is difficult to determine using standard imaging techniques, was also evaluated by micro-CT and proved clinical feasibility by accurately classification [101].

10.4.6 Liver Imaging

The liver differs from other organs in that two vascular systems deliver its blood (hepatic artery and the portal vein) [102], which are the keys to successfully perform liver surgery and to elucidate liver pathology; however, it has not yet been fully unravelled. The human hepatic vasculature was evaluated at different scales, and performing a morphological analysis by combining vascular corrosion casting with novel micro-CT provided unique data on the human hepatic vasculature from the macrocirculation down to the microcirculation [103]. Other assessments included a 3D reconstruction and quantification of the hepatic circulation, ranging from the major blood vessels down to the intertwined and interconnected sinusoids [104] and two biliary trees. The vascular system may play a major role in various diseases (e.g., cirrhosis, heart disease, tumors, peripheral

vascular disease, diabetes) (Sinnatamby 2006; Standing and Gray 2008). Therefore, the ability to characterize geometrical differences in vascular structures will also be useful for outlining differences within the same vascular structures in, for example, different states of disease [105].

Moreover, the micro-CT offers the opportunity to capture images of liver structures and lesions in mice with a high spatial resolution, calculation of vessel tortuosity and density, as well as liver lesion volume and distribution. Longitudinal monitoring of liver lesions is also made possible. This modality has been combining anatomical and functional imaging and, specifically, improved visualization and characterization of tumors in animal models [106].

Other diseases assessed by micro-CT are polycystic liver disease [107] and liver cirrhosis, which is characterized by diffuse fibrosis. To date, the vascular remodeling and altered hemodynamics due to cirrhosis are still poorly understood, even though they seem to play a pivotal role in cirrhogenesis. The micro-CT imaging of a single human cirrhotic liver generated detailed datasets of the hepatic circulation, including typical pathological characteristics of cirrhosis such as shunt vessels and dilated sinusoids. Future research will focus on the development of models to study time-dependent degenerative adaptation of the cirrhotic macro- and microcirculation [108]. Furthermore, the cholangiopathies, a diverse group of biliary tract disorders, were evaluated by the micro-CT and nuclear magnetic resonance (MR) in a model for primary sclerosing cholangitis (PSC) and bile duct ligated (BDL) [109].

The distribution of radiopaque beads (ROBs) after hepatic embolization was also evaluated; the authors concluded that the quantitative measures of embolic distribution demonstrated significantly better visualizations in micro-CT images with decreasing kVp [110]. Also, the partial hepatectomy (PH) model has been used in the field of liver regeneration. Currently, the extent of regeneration is analyzed by measuring the weight of the liver postmortem or by magnetic resonance imaging. In one study, the PH model utilized micro-CT to accurately measure liver volume

gain. In addition, this technique demonstrated that volume gain over multiple time points can be measured with the same animal sample, reducing the number of animals sacrificed [111].

The combination of micro-CT and fluorescence-mediated tomography enables improved reconstruction and analysis for preclinical research applications, as in a study to determine elimination and retention of typical model drugs and drug delivery systems. It allows the differentiation of hepatobiliary and renal elimination routes and allows for the noninvasive assessment of retention sites in relevant organs including the liver, kidney, bone, and spleen [112]. Moreover, the analysis by finite element model built from the micro-CT has been studied to simulate the mechanical testing conditions, allowing the determination of elastic modulus of normal and fibrotic murine livers compared to independent mechanical testing method. More specifically, the results demonstrated that normal and advanced fibrotic livers can be statistically identified with these techniques [113].

The high resolution and good contrast of μ CT allow for all the assessment aforementioned as well as the volumetric quantification of adipose tissue. Preliminary data in a longitudinal study of adipose development in mice indicate that a relative increase in either subcutaneous, visceral, or total fat negatively influences skeletal quantity and that fat infiltration in the liver is greatly increased by a high-fat diet [114].

Micro-CT imaging of liver diseases relies on high soft tissue contrast to detect small lesions such as liver metastases. One of the most commonly used contrast agents are the nanoparticulate contrast agents ExiTron nano 6000 and 12,000, which provide strong contrast of the liver, spleen, lymph nodes, and adrenal glands up to weeks, thereby allowing longitudinal monitoring of pathological processes of these organs in small animals [115, 116]. ExiTron nano 12,000 is particularly optimized for angiography due to its very high initial vessel contrast [116]. Another useful hepatobiliary contrast agent for micro-CT is 1,3-Bis-[7-(3-amino-2,4,6-triodophenyl)-heptanoyl]-2-oleoyl glycerol (DHOG, Fenestra LC) [117, 118].

The potential of the protocol in imaging animal organs is also illustrated in the 3D rendering of a mouse liver by modulating the image transparency, through which liver lobes profile along with details in the vascular structure can be seen [6]. This may be applied to other animals like the turtle too [26]. Finally, in the context of ecotoxicological research, micro-CT has the potential to greatly increase the information value of experiments conducted with fish. There is significant potential for the noninvasive longitudinal assessment of environmental pollution and its impacts on different species [119].

10.4.7 Musculoskeletal Imaging (Ligament and Tendon)

In a musculoskeletal system (Fig. 10.9), skeletal muscle models are used to investigate motion and force generation. However, they often lack a realistic representation of the muscle's internal architecture which is primarily composed of muscle fiber bundles, known as fascicles. Micro-CT allows for the identification the inner and external tongue muscles [120], the fibrous structure of skeletal muscle [121], the fascicular spatial arrangement and geometry of the superficial masseter muscle [122], feasible imaging of the human peripheral nerve fascicles [123], the analysis of an entire regenerated nerve [124], as well of microstructural deformation of soft tissue, including the tendon, intervertebral disc, and artery [46] (Figs. 10.10 and 10.11). Additionally, 3D microstructure data can be used as a biofabrication model, which can contribute to tissue engineering designs for a personalized, biological microenvironment digitized model [123].

Musculoskeletal modeling is a valuable tool to understand how neural, muscular, skeletal, and other tissues are integrated to produce movement. For instance, some authors developed a model of a mouse hind limb and pelvis, to better understand this complex task [125]. Likewise, muscular contraction plays a pivotal role in the mechanical environment of bones. These contractions have been evaluated via the

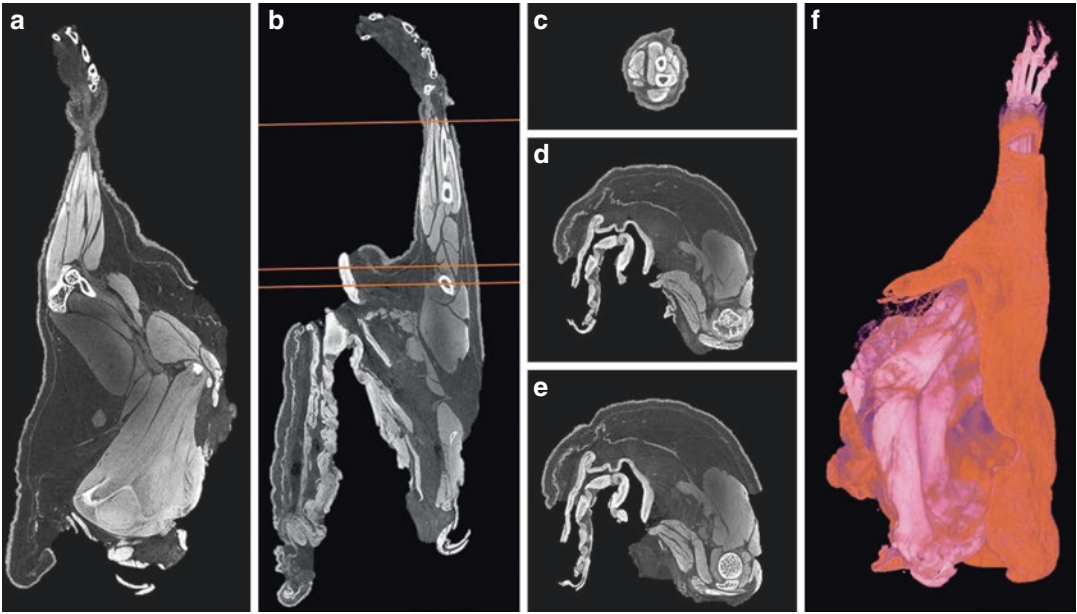


Fig. 10.9 Reconstructed data of a mice arm. (a) Coronal view. (b) Sagittal view. (c–e) Axial view of the regions (top, middle, and bottom). (f) 3D volume rendering

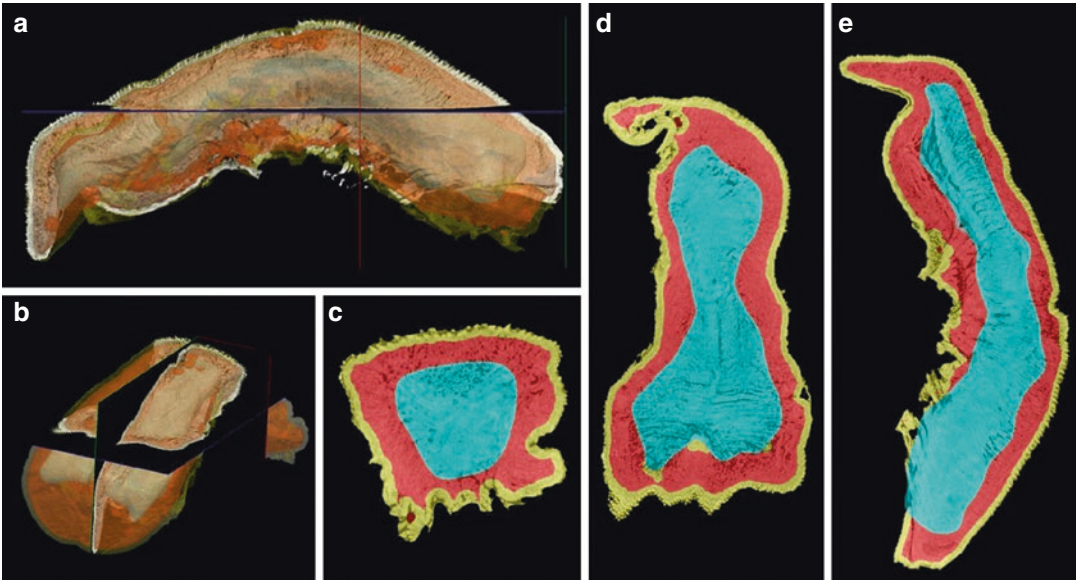


Fig. 10.10 (a, b) 3D volume rendering of a mice tongue. (c–e) Reconstructed data of a mice tongue (coronal, axial, and sagittal view) with the segmentation of the different anatomic structures

use of implantable stimulators to elicit programmed contractions, and whose findings suggest that a carefully designed muscle stimulation protocol could offer targeted bone

growth to at risk regions of bone [126]. On the other hand, loss of bone secondary to muscle wastage induced by Botulinum toxin and recovery showed a parallel evolution for bone

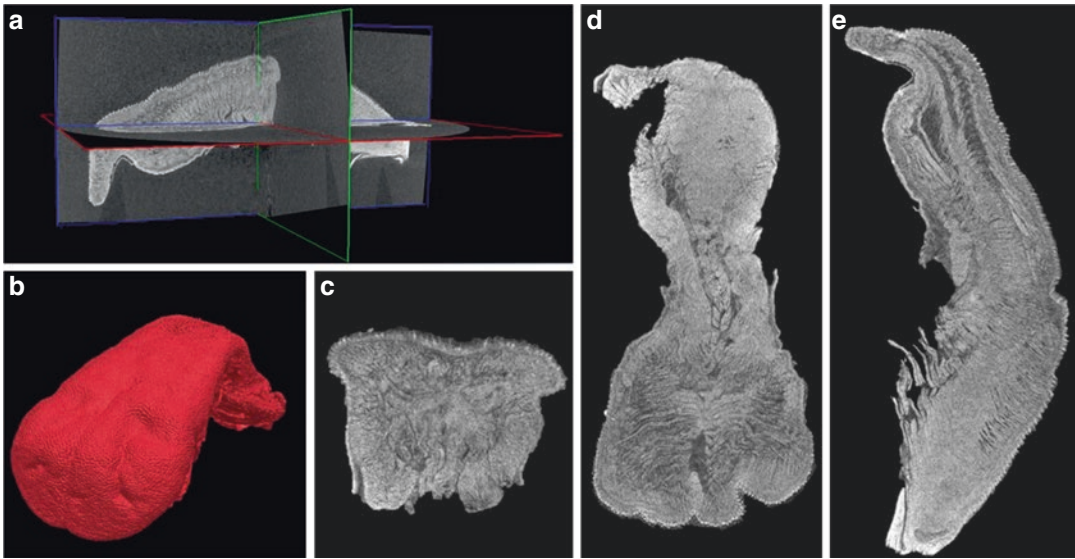


Fig. 10.11 (a) Reconstructed data showing the three planes. (b) 3D volume rendering of a mice tongue. (c–e) Reconstructed data of a mice tongue (coronal, axial, and sagittal view)

and muscles [127]. These are significant findings in the light of the burden of bone disease for healthcare providers.

The anatomical structures of the orbicularis oris and nasalis, which are closely associated with the appearance of the upper lip and lower part of the nose, have also been assessed by micro-CT. The relationship of this complicated 3D anatomical structure with the outline shape was determined in a scan of nasolabial tissues of aborted fetuses [128]. Plastic surgeons performing cleft lip correction surgery can also understand the anatomic structure of nasolabial region in fetuses with cleft lip and perform the study of three-dimensional finite element analysis for surgical simulation [129]. Moreover, the specific shape and aesthetics of the lip and nose are improved by repairing the muscle tension in the nasolabial complex shown in a micro-CT study [130].

The 3D and digital nature of micro-CT data allows assessment of the following: the myocardium [51, 131], inside the infarcted rat heart, the 3D spatial distribution of rat cardiac progenitor cells via labelling with iron oxide nanoparticles, [132], the mitral valve system [133], and finally through invasive assessment of conductance catheters insertion. Such data collection offers

the potential to measure cardiac dysfunction in mice in a way not possible with other imaging methodologies [134]. This new imaging approach appears to be an important way to investigate the cellular events involved in cardiac regeneration and represents a promising tool for future clinical applications.

Accurately calibrated 3D images of musculo-skeletal systems can also be used to quantify muscle fiber numbers and cross-sectional areas, muscle attachment areas, and bone or cartilage sizes and shapes and facilitate functional modeling in different animals [9] like insects [135, 136], alligator and crocodilian [137], seahorse [138], primates [139], squirrel, guinea pig, and rats [140]. Images can also be used to analyze the morphology of the jaw-closing musculature of the naked mole-rat [15].

10.4.8 Vascular Imaging

Three-dimensional data of vascular systems is of major importance to a number of research areas in medicine and biology [141]. Micro-CT imaging techniques permit the visualization and quantification of vasculature and organ structure in

disease models *in vivo* or *ex vivo* like in tumor vasculature, the modeling of blood flow, analysis of the genetic effects of vascular development; metastasis or neovascularization; analysis of vessels of the head or hind limbs and of organs like the heart, liver, kidneys, spleen, etc. [142, 143]; or even the vascular network in a rodent model [144]. Moreover, these techniques represent reliable and reproducible methods for the longitudinal assessment of venous thrombus [52], the visualization of the neovascularization of the arterial wall which is an important process associated with atherosclerosis [145], and the three-dimensional architecture of collagen fibers inside vessel walls to observe the collagenous network, [146] in addition to measuring the fetoplacental vascular system [147].

In the bone, the pattern of vascularity during the process of bone healing and the effect of stable fixation on neovascularization was studied by three-dimensional reconstruction images of neovascularization of the soft tissues surrounding the fracture with vascular perfusion and micro-CT imaging [19]. Also, a 3D representation of the bone marrow vasculature and adipose tissue was performed [21]. In the case of treating adult nerve injuries, an analysis of reconstructed peripheral nerves enabled the quantitative assessment, i.e., surface morphology, nerve fascicles, nerve tissue volume, geometry, and vascular regrowth [124].

In the visualization of thoracic structures such as tumors, vascular structures, and thoracic air space, the micro-CT images enabled identification of tumor margins, pulmonary airways, vascular remodeling, etc. [24, 28]. Micro-CT images also led to analysis of the diameters, lengths, and branching angles of the airway, arterial, and venous trees in the lungs [28], as well as the lung's acinar morphometry in a quantitative fashion [148]. The diseases studied to assess the respiratory tracts and vascularization were fibrotic and emphysematous in human lung specimens [31], or the pulmonary arterial hypertension, which is a rare disease characterized by significant vascular remodeling within the lung [29, 149].

The structure and function of the heart have been of great interest to anatomists, physicians, surgeons, scientists, and engineers. Yet, a complete understanding of its complex function remains elusive. Micro-CT imaging has led to a better understanding of some of the structures that help this functioning, such as the mitral valves [55], the coronary artery wall, [150], and the pericardium, in particular to clarify the relevance of the vascular calcification and the scattered calcium deposits in the fiber bundles [151], as well as the aortae to quantify calcification [152]. Moreover, these imaging protocols are promising approaches to assess changes in vascular permeability and cardiac function in the preclinical setting, which may be useful to identify patients treated with radiation therapy who have developed vascular injury in the heart that may lead to radiation-related heart disease [50]. They may also lead to potential therapeutic approaches for clinical intervention [152].

The need for reproducible noninvasive imaging methods for high-resolution visualization of the complete cerebral vasculature is also important, as shown in a study that presented the anatomical structure of the cranial venous by micro-CT [65] as well as the abnormalities in the cerebrovascular system, which plays a central role in many neurologic diseases. This technique enabled 3D visualization of large cerebrovascular networks, including the circle of Willis [66]. However, the high complexity and 3D nature of the cerebral vasculature make comparison and analysis of the vessels difficult, time-consuming, and laborious, which has led some authors to develop an automatic segmentation allowing us to study cerebrovascular variations [62]. Some of the cerebrovascular variations that can be assessed via micro-CT are large cerebral vessels in ischemic stroke [153], the quantification of cerebral vasospasm after subarachnoid hemorrhage [68], or a direct visualization of cerebrovascular thrombi which can then guide thrombolytic therapy [70]. In addition to the potential clinical implications, this finding indicates the potential of this treatment strategy for

future clinical use with patients, and the advanced imaging will likely have multiple uses in current basic/translational vascular research and theranostic nanomedicine research, for which there is currently no direct therapy.

Although a full understanding of the hepatic circulation is one of the keys to successfully perform liver surgery and to elucidate liver pathology, relatively little is known about the functional organization of the liver vasculature. Currently 3D reconstruction and quantification of the hepatic circulation, ranging from the major blood vessels down to the intertwined and interconnected sinusoids [104], and anatomic evidence for hepatic arteriolo-portal venular shunts occurring between hepatic artery and portal vein branches have been found [102]. It could also contribute to understanding perfusion CT imaging [154]. All this may lead to novel insights into liver circulation, such as internal blood flow distributions and anatomical consequences of pathologies [103], for example, in cirrhosis, in which vascular remodeling and altered hemodynamics have been observed, implying a locally decreased intrahepatic vascular resistance probably due to local compensation mechanisms (dilated sinusoids and shunt vessels) [108], and in the hepatic transarterial embolization by studying bioeffects of different bead sizes, relative efficacy of embolization procedures, and drug distribution following embolization with drug-eluting beads [110].

The kidney's vascular network has also been studied, with one experiment applying a method for assessing the total and cortical renal vasculature as well as isolating and quantifying the number of perfused glomeruli to assess vascular changes [97]. Such assessment can also be done for microvascular kidney disease [92] in a pre-clinical renal transplantation model [155], in a congenital abnormality such as the horseshoe kidney [94], or even in an aging kidney, in which a significant decrease in renal cortical microvascular density and increased interstitial fibrosis was observed [96]. Furthermore, progressive kidney diseases and renal fibrosis revealed significant and previously unrecognized alterations of

preglomerular arteries like a reduction in vessel diameter, a prominent reduction in vessel branching, and increased vessel tortuosity using micro-CT methodology [98]. Images are also useful in the analysis for detecting chronic renal failure and follow-up vascular calcifications [156, 157] and for comparing treatment of this disease [99]. This body of work provides new evidence concerning the renal vascular diseases and could potentially guide future therapy.

Finally, analysis of organ microvasculature carries special importance for toxicological sciences, in particular the evaluation of drug-induced vascular toxicity. Vascular toxicity studies through 3D analysis allow for very high resolution and characterization of drug effects on the microvasculature and can be used as a valuable tool in drug safety assessments. It can also be applied to examine drug-induced vascular toxicities in different organs, such as the kidney, heart, the central nervous system, or the liver [158].

The vascular pathway was also studied in some animals: in iguanas to determine sites of thermal exchange by the cephalic vascular anatomy [89], in *Euarchonta* (mammal species) to assess the internal carotid arterial canal size and scaling [82], and even in soft-bodied marine invertebrates to study the anatomy of nervous or vascular systems [159] (Figs. 10.12, 10.13, 10.14, and 10.15).

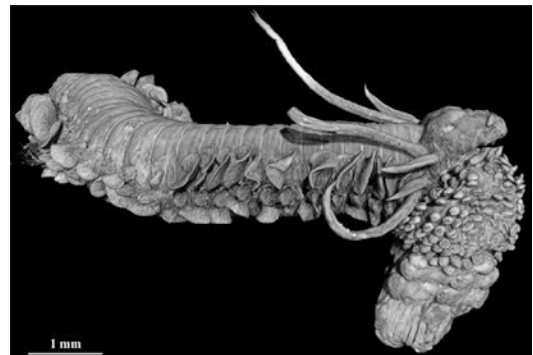


Fig. 10.12 3D volume rendering reconstruction of *Phyllodoce lineata* (Claparède, 1870) (unstained). Courtesy of M. Candás, X. Cunha, J. Moreira and J. Parapar. Estación de Biología Mariña da Graña, Universidade de Santiago de Compostela



Fig. 10.13 2D sagittal section of *Doto pinnatifida* Montagu, 1804. Courtesy of M. Candás, G. Díaz-Agras and V. Urgorri. Estación de Biología Mariña da Graña, Universidade de Santiago de Compostela



Fig. 10.14 3D volume rendering reconstruction (frontal section) of *Limapontia* sp. Courtesy of M. Candás, Á. Montero and V. Urgorri. Estación de Biología Mariña da Graña, Universidade de Santiago de Compostela

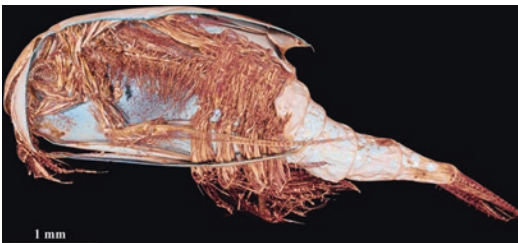


Fig. 10.15 3D volume rendering reconstruction (sagittal section) of *Sarsinebalia cristoboi* Moreira, Gestoso & Troncoso, 2003. Courtesy of M. Candás and J. Moreira. Estación de Biología Mariña da Graña, Universidade de Santiago de Compostela

10.4.9 Cancer Imaging

The early detection of tumors and the prompt initiation of active therapy are related with the successful outcomes for patients with cancer. Early-stage lesions undetected due to the low

resolution of current anatomical and functional imaging modalities are one of the major challenges in the treatment of cancers in several organs.

A major limitation in using murine liver tumor models in cancer research is the inability to accurately detect and monitor tumor volume. Micro-CT is an excellent means to monitor tumor diameter in murine hepatic and spleen tumor models [160, 161]. One of the most common cancer-related deaths worldwide is the hepatocellular carcinoma (HCC), in which the tumor evolution was tracked by micro-CT imaging [162, 163] as well as in the mouse model of metastatic pheochromocytoma that reproducibly generated multiple liver tumors in the animals. These models may be useful for studies of tumor biology and for development of new strategies to treat cancer [164].

The tumor margins and accurate quantification in the thoracic region were measured by the micro-CT [24]. The detection of the development of lung tumors like lung adenocarcinoma is described with a monthly follow-up with micro-CT, identifying dynamic changes in the lung tumor, such as the appearance of additional nodules, increase in the size of previously detected nodules, and decrease in the size or complete resolution of nodules in response to treatment [42]. Additionally, monitoring lung metastasis was an efficient and cross-validated means to noninvasively and repeatedly monitor analysis over the course of the experiment [38]. This operation has also been performed in a metastasis of a lung carcinoma that spread to the liver [165]. Analyzing tumor vascular networks in a rigorous and quantitative manner can enhance our understanding of the impact of tumor angiogenesis [166]. These findings are important to better assess the possibility for future monitoring of lung cancer progression and treatment, which will be beneficial for translational applications.

Tissue invasion and infiltration for brain tumors pose a clinical challenge. However, micro-CT has been used to map tumor invasion, delineate, and view the intrinsic components from surrounding tissues [167]. These methods

for longitudinal monitoring of treatment effects in live animals were rated in a glioblastoma multiforme by the presence of tumors, tumor diameter, and tumor volume [168, 169]. Another tumor model analyzed was the medulloblastoma, which is one of the most aggressive malignant brain tumors of childhood, a disease for which new molecular-targeted strategies are needed [170].

Micro-CT is also a promising modality applicable to breast tumor, which could potentially be used for rapid assessment of breast cancer dimensions in an intact lumpectomy specimen in order to guide surgical excision [171], thus allowing for the precise evaluation of the dynamics of the primary tumor by their volume [172] or even to assess a model of highly metastasizing orthotopic allogeneic breast carcinoma [172].

Radiotherapy is a key component of cancer treatment, and one study has demonstrated how an affordable industrial micro-CT can be converted into a small animal image-guided radiotherapy device at very low costs, even of critical target volumes such as the brain [173]. However, more studies are needed to be extrapolated to pre-clinical radiotherapy or tumor development studies [174].

10.4.10 Histology Imaging

As demonstrated, micro-CT is a promising and widely used technique in various scientific fields and has also demonstrated a great potential for histological purposes [175] (Fig. 10.16).

The micro-CT approach complements histology with improved accuracy and efficiency and can be applied to lesion burden assessment or targeting neuroanatomy in brain diseases [61, 67, 79, 176] and small airway pathology as seen in chronic obstructive pulmonary disease [33]. The examination of the success of biomaterial implants used for tissue engineering repairs [177] minimally invasive autopsy of fetal organs, [95] thoracic vascular structures enabled identification of tumor margins and accurate quantification, [24] chronic renal failure, [157] or even in cellular therapy approaches to generate new myocardium, involving transcortical and intra-

myocardial injection of progenitor cells [132]. Overall, therefore, these combinations can substantially expand the study of the success and effectiveness of this new 3D imaging approach and represent a promising tool for future clinical applications since it provides additional data to standard histomorphometry, with more spatial information [21].

Micro-CT is a novel method for investigating lung tumor angiogenesis, and this might be considered as an additional complementary tool for precise quantification of angiogenesis because a quantitative evaluation has been limited by difficulties in generating reproducible data [166]. Thus, further translational studies on pathological models using the micro-CT technique would also provide knowledge for preemptive medicine by not only comparing with histology but also with immunohistochemical techniques as in the previously cited study [73].

Micro-CT bases images were assessed as an alternative to MRI imaging in genetically engineered mouse models of cancer, which proved to be a more cost-effective technique and less labor-intensive. A study further determined that micro-CT-based virtual histology would significantly reduce the time spent on histopathology [170]. Another study reports on how and to what extent micro-CT of paraffin-embedded samples can provide a reliable three-dimensional approach for quantitative analysis of peripheral nerves [178]. Finally, a recent study concluded that a micro-CT-based virtual histology approach can be used as a supplement and guidance tool for traditional histology, providing 3D measurement capabilities and offering the ability to perform sectioning directly at a region of interest [179].

10.4.11 Food Imaging

Future trends for X-ray micro-CT that has been highlighted are food applications due to highly accurate analysis and characterization of internal structures, reproduction of high-resolution three-dimensional visualization and analysis of microstructures, and detection and characterization of

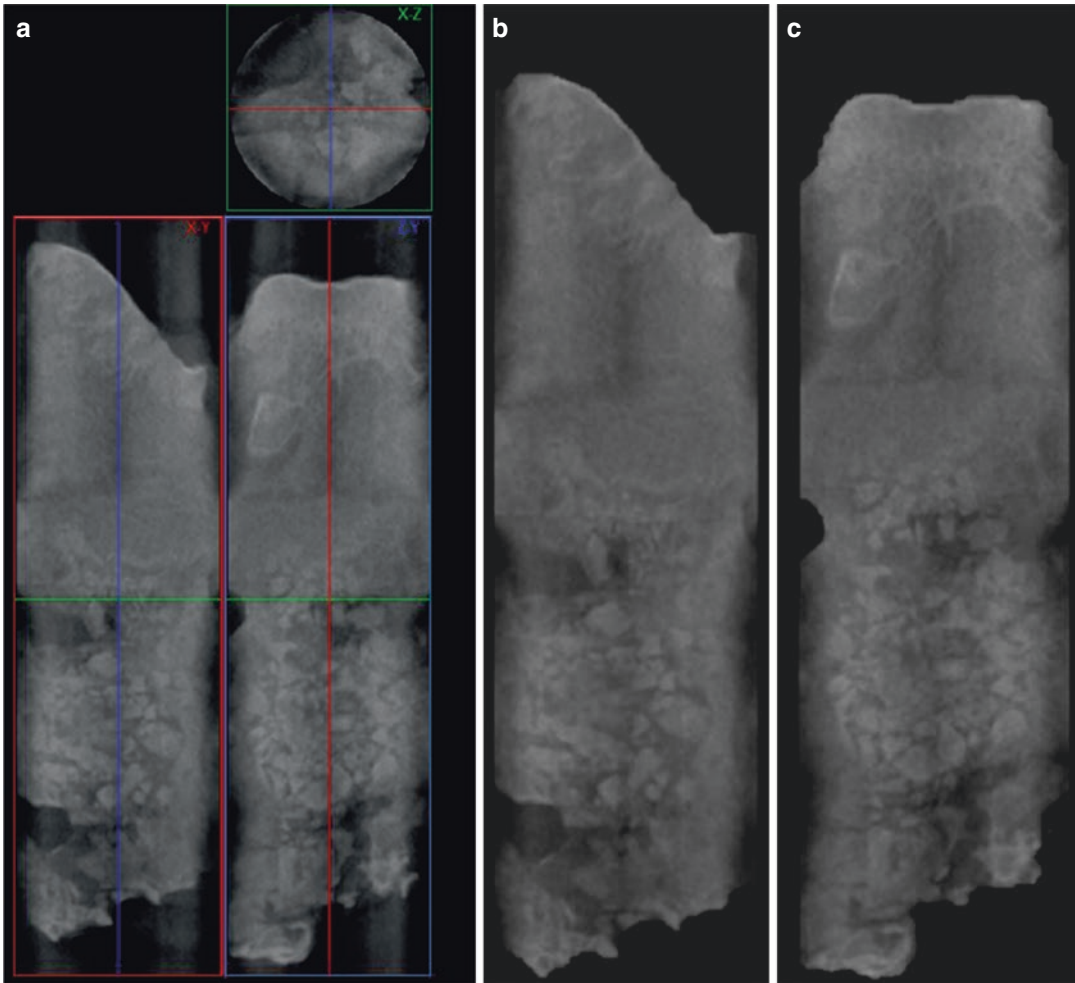


Fig. 10.16 Bone graft. (a) Reconstructed data in the three planes. (b, c) Sagittal and coronal view of a bone graft. Courtesy of Dr A. Herford, Oral and Maxillofacial Surgery Department, Loma Linda University School of Dentistry

internal defects without sample preparation [180]. Moreover, micro-CT is increasingly likely to be used to develop classification algorithms to sort food, especially fresh agricultural commodities, on the basis of their internal characteristics [181].

In this field, micro-CT has been used in the analysis of fat microstructure in different types of Italian salami [182] and quantifying intramuscular fat content and distribution in different breeds and commercial meat joints [183]. Furthermore, micro-CT allowed for 3D characterization of the cereal grains and revealed their air space distribution [184], determined volumes, and densities as a means to discriminate between good and poor

milling quality [185] as well as to establish the cooking behavior [186, 187]. Bread samples were also analyzed via micro-CT, providing important microstructural information of the product and classifying these products into specific group types based on the average or individual microstructural properties [188].

These imaging techniques have been used to investigate as a nondestructive characterization in order to quantify the internal structure of different kinds of fruits like apple, pomegranate, pear, mango, kiwi, etc. Analyzing has concerned the macro- and micro-architecture, pore network, plant breeding, and the detection of the presence

of unknown materials with different densities to fruit tissues such as insect larva and disease infection, or to determine the response to agronomic treatments, all without conducting lengthy storage trials [189–194].

Furthermore, micro-CT has been used to characterize the microstructure of beans at different roasting times: from green to very dark providing an accurate analysis of the pores and microstructure during the roasting process [195]. For instance, coffee beans porosity affected heat and moisture loss rate during roasting [196]. A series of new methods for estimating transport properties for foods has been presented, and with these additional methods available, researchers will be able to improve quantitative understanding of foods and develop more accurate transport models, which should lead to more efficient design and improved products and processes [197].

10.4.12 Tissue Engineering

Imaging is a key technique which allows for the visualization of the interface tissue engineering as well as for assessing its development and the composition and reaction of external factors of hard/soft tissue interfaces [2]. Recently, a new approach has emerged in regenerative medicine which is pushing the boundary of tissue engineering to create bioartificial organs such as eyes (Fig. 10.17). The biological scaffolds made of extracellular matrix preserve the 3D architecture of an entire organ. These bioartificial organs must characterize their mechanical properties and match them with those of the normal native organs [198]. 3D printing technology has been found to be practical and economical means for producing device and allows for customization for study-specific needs [199]; however there is a lack of studies regarding bioartificial organs.

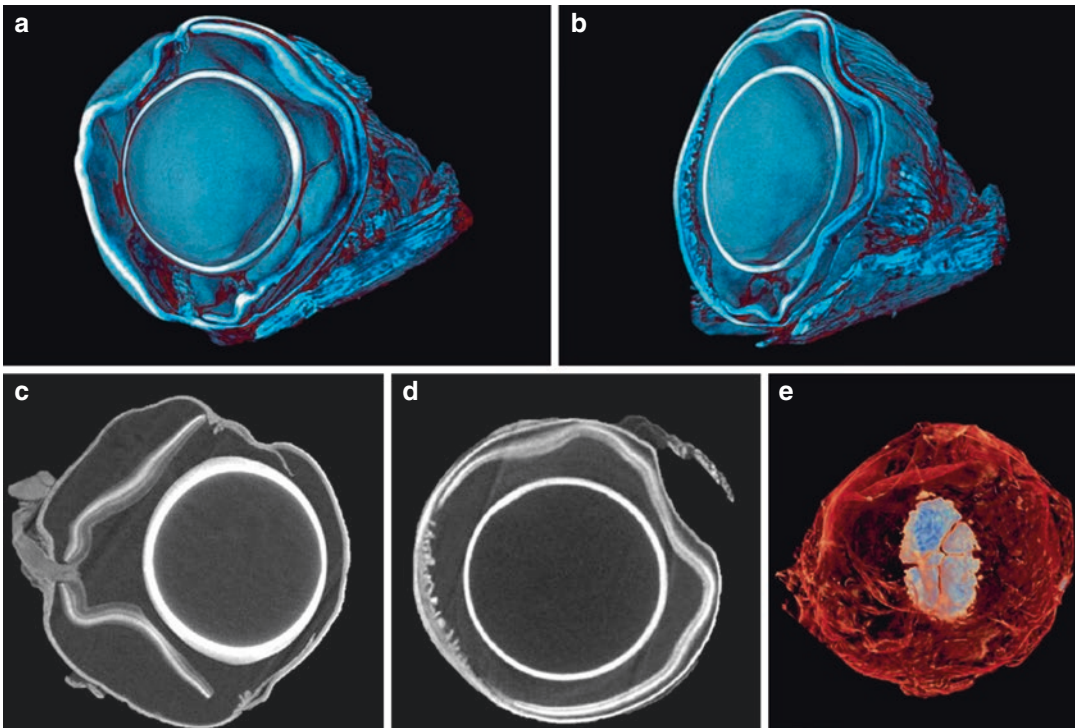


Fig. 10.17 (a, b) 3D volume rendering reconstruction of an eye mice. (c, d) Reconstructed data sagittal and coronal view. (e) 3D volume rendering reconstruction frontal

view. Courtesy of Dr Xiao Wen Mao. Division of Biomedical Engineering Sciences, Department of Basic Sciences, Loma Linda University

An example of model of bioartificial organ was produced in a study with highly accurate 3D models of the entire ear and particularly the cochlea scalae, including the auditory canal, tympanic membrane, malleus, incus, stapes, ligaments, oval and round window, scalae vestibule, and tympani [200]. Another presented an accurate and complete morphological 3D middle (and inner) ear model of gerbil [201]. These studies have led to the conclusion that 3D models are also useful in medical training as well as for the interpretation and presentation of experimental results.

10.5 Perspective

Anatomical, functional, genomic, and developmental studies continue to expand far beyond the few traditional methods of accurate three-dimensional imaging. Most of these studies are looking for a representation of anatomical structures with their natural shapes, orientations, and spatial relationships in as close to their natural state as specimen preparation can allow; currently published studies as cited in this chapter show how the micro-CT is providing a better understanding. Future developments in detector design and the use of micro-CT may lead to the growth of tasks possible with micro-CT, such as real-time 3D imaging of dynamically biological samples.

Exciting new approaches have emerged for the use of micro-CT, for example, in regenerative medicine which is advancing the possibilities of tissue engineering to create bioartificial whole organs. This approach has been applied to create bioartificial hearts, kidneys, and lungs with the goal of using them in the future as organ transplants. Moreover, accurate histopathological analysis of potentially affected tissue is crucial for the investigation and treatments of diseases, making this one of the best promising utilities for this technology.

In addition to the potential clinical implications, the advanced imaging will likely have multiple uses in current basic/translational research and nanomedicine research. Finally, the different models indicate that the microtomographic struc-

ture of soft tissues can be used to fabricate biometric structures via bioprinting techniques.

10.6 Conclusion

In summary, we believe that the potential of micro-CT has not yet been fully realized in many science applications and its potential is only starting to be explored for the scientific community. Even as this technology is widely used by numerous investigators and has become very popular for imaging of high-contrast structures such as bones, with the use of micro contrasting methods, micro-CT may also be used for different soft tissues as evidenced throughout this chapter. Finally, with all this technology, it has become possible to monitor changes in the 3D architecture of organs, tumors, and their microvasculature which may have an immediate impact on the global understanding in the evaluation of experimental therapies. Development of multimodality systems that combine anatomical and functional imaging should expand the applications of micro-CT and, more specifically, improve the visualization and characterization of different diseases in animal models. It is hoped that this overview will be an inspiration for new investigations who may benefit from further use of this breakthrough technology.

Acknowledgments Author is greatly indebted to Loma Linda University School of Dentistry, Center for Dental Research, Micro Imaging Research Facility for facilitating the use of the micro-CT instrument and to Luis E. Salazar for his help with the skillful assistance in the English revision and to Danieli Moura PhD, Brasil for the summary of the different contrast agents.

References

1. Mizutani R, Suzuki Y. X-ray microtomography in biology. *Micron*. 2012;43(2–3):104–15.
2. Bannerman A, Paxton JZ, Grover LM. Imaging the hard/soft tissue interface. *Biotechnol Lett*. 2014;36(3):403–15.
3. Weon B, Je J, Hwu Y, Margaritondo G. Phase contrast x-ray imaging. *Int J Nanotechnol*. 2006;3:280–97.

4. Shearer T, Bradley RS, Hidalgo-Bastida LA, Sherratt MJ, Cartmell SH. Three-dimensional visualisation of soft biological structures by X-ray computed micro-tomography. *J Cell Sci.* 2016;129(13):2483–92.
5. Descamps E, Sochacka A, de Kegel B, Van Loo D, Hoorebeke L, Adriaens D. Soft tissue discrimination with contrast agents using micro-ct scanning. *Belgian J Zool.* 2014;144(1):20–40.
6. de S. e Silva JM, Zanette I, Noël PB, Cardoso MB, Kimm MA, Pfeiffer F. Three-dimensional non-destructive soft-tissue visualization with X-ray staining micro-tomography. *Sci Rep.* 2015;5:14088.
7. Hrvoje L, Greenstaff MW. X-ray computed tomography contrast agents. *Chem Rev.* 2014;113:1641–66. <https://doi.org/10.1021/cr200358s>.X-Ray.
8. Clark DP, Badea CT. Micro-CT of rodents: state-of-the-art and future perspectives. *Phys Med.* 2014;30(6):619–34.
9. Metscher BD. Micro CT for comparative morphology: simple staining methods allow high-contrast 3D imaging of diverse non-mineralized animal tissues. *BMC Physiol.* 2009;9(1) <https://doi.org/10.1186/1472-6793-9-11>.
10. Metscher BD. Mi for developmental biology: a versatile tool for high-contrast 3D imaging at histological resolutions. *Dev Dyn.* 2009;238:632–40. <https://doi.org/10.1002/dvdy.21857>.
11. Wathen CA, Foje N, van Avermaete T, Miramontes B, Chapaman SE, Sasser TA, et al. In vivo X-ray computed tomographic imaging of soft tissue with native, intravenous, or oral contrast. *Sensors (Basel).* 2013;13:6957–80. <https://doi.org/10.3390/s130606957>.
12. Faraj KA, Cuijpers VMJI, Wismans RG, Walboomers XF, Jansen JA, van Kuppevelt TH, et al. Micro-computed tomographical imaging of soft biological materials using contrast techniques. *Tissue Eng Part C Methods.* 2009;15:493–9. <https://doi.org/10.1089/ten.tec.2008.0436>.
13. Kim J, Chhour P, Hsu J, Litt HI, Ferrari VA, Popovtzer R, et al. Use of nanoparticle contrast agents for cell tracking with computed tomography. *Bioconjug Chem.* 2017;28:1581–97. <https://doi.org/10.1021/acs.bioconjchem.7b00194>.
14. von zur Muhlen C, von Elverfeldt D, Bassler N, Neudorfer I, Steitz B, Petri-Fink A, et al. Superparamagnetic iron oxide binding and uptake as imaged by magnetic resonance is mediated by the integrin receptor Mac-1 (CD11b/CD18): Implications on imaging of atherosclerotic plaques. *Atherosclerosis.* 2007;193:102–11. <https://doi.org/10.1016/j.atherosclerosis.2006.08.048>.
15. Cox PG, Faulkes CG. Digital dissection of the masticatory muscles of the naked mole-rat, *Heterocephalus glaber* (Mammalia, Rodentia). *PeerJ.* 2014;2:e4448.
16. Degenhardt K, Wright AC, Horng D, Padmanabhan A, Epstein JA. Rapid 3D phenotyping of cardiovascular development in mouse embryos by micro-CT with iodine staining. *Circ Cardiovasc Imaging.* 2010;3:314–22. <https://doi.org/10.1161/CIRCIMAGING.109.918482>.
17. Gignac PM, Kley NJ, Clarke JA, Colbert MW, Morhardt AC, Cerio D, et al. Diffusible iodine-based contrast-enhanced computed tomography (diceCT): an emerging tool for rapid, high-resolution, 3-D imaging of metazoan soft tissues. *J Anat.* 2016;228:889–909. <https://doi.org/10.1111/joa.12449>.
18. Nieminen HJ, Ylitalo T, Karhula S, Suuronen J-P, Kauppinen S, Serimaa R, et al. Determining collagen distribution in articular cartilage using contrast-enhanced micro-computed tomography. *Osteoarthr Cartil.* 2015;23:1613–21. <https://doi.org/10.1016/j.joca.2015.05.004>.
19. Zhao F, Zhou Z, Yan Y, Yuan Z, Yang G, Yu H, et al. Effect of fixation on neovascularization during bone healing. *Med Eng Phys.* 2014;36(11):1436–42.
20. Blery P, Pilet P, Vanden-Bossche A, Thery A, Guicheux J, Amouriq Y, et al. Vascular imaging with contrast agent in hard and soft tissues using microcomputed-tomography. *J Microsc.* 2016;262(1):40–9.
21. Kerckhofs G, Stegen S, van Gestel N, Sap A, Falgayrac G, Penel G, et al. Simultaneous three-dimensional visualization of mineralized and soft skeletal tissues by a novel microCT contrast agent with polyoxometalate structure. *Biomaterials.* 2018;159:1–12.
22. Delecourt C, Relier M, Touraine S, Bouhadoun H, Engelke K, Laredo JD, et al. Cartilage morphology assessed by high resolution micro-computed tomography in non OA knees. *Osteoarthr Cartil.* 2016;24(3):567–71.
23. Kün-Darbois JD, Manero F, Rony L, Chappard D. Contrast enhancement with uranyl acetate allows quantitative analysis of the articular cartilage by microCT: Application to mandibular condyles in the BTX rat model of disuse. *Micron.* 2017;97:35–40.
24. Lalwani K, Giddabasappa A, Li D, Olson P, Simmons B, Shojaei F, et al. Contrast agents for quantitative MicroCT of lung tumors in mice. *Comp Med.* 2013;63(6):482–90.
25. Paoli F, Wirkner CS, Cannicci S. The branchiostegal lung of *Uca vocans* (Decapoda: Ocypodidae): Unreported complexity revealed by corrosion casting and MicroCT techniques. *Arthropod Struct Dev.* 2015;44(6):622–9.
26. Schachner ER, Sedlmayr JC, Schott R, Lyson TR, Sanders RK, Lambert M. Pulmonary anatomy and a case of unilateral aplasia in a common snapping turtle (*Chelydra serpentina*): developmental perspectives on cryptodiran lungs. *J Anat.* 2017;231(6):835–48.
27. Scott AE, Vasilescu DM, Seal KAD, Keyes SD, Mavrogordato MN, Hogg JC, et al. Three dimensional imaging of paraffin embedded human lung tissue samples by micro-computed tomography. *PLoS One.* 2015;10(6):e0126230.
28. Counter WB, Wang IQ, Farncombe TH, Labiris NR. Airway and pulmonary vascular measurements

- using contrast-enhanced micro-CT in rodents. *AJP Lung Cell Mol Physiol*. 2013;304(12):L831–43.
29. Faight EM, Verdelis K, Zourelis L, Chong R, Benza RL, Shields KJ. MicroCT analysis of vascular morphology: a comparison of right lung lobes in the SUGEN/hypoxic rat model of pulmonary arterial hypertension. *Pulm Circ*. 2017;7(2):522–30.
 30. Phillips MR, Moore SM, Shah M, Lee C, Lee YZ, Faber JE, et al. A method for evaluating the murine pulmonary vasculature using micro-computed tomography. *J Surg Res*. 2017;207:115–22.
 31. Kampschulte M, Schneider CR, Litzlbauer HD, Tscholl D, Schneider C, Zeiner C, et al. Quantitative 3D micro-CT imaging of human lung tissue quantitative 3-D-mikro-CT-Bildgebung von humanem Lungengewebe. *Fortschr Röntgenstr*. 2013;185(9):869–76.
 32. Bell RD, Rudmann C, Wood RW, Schwarz EM, Rahimi H. Longitudinal micro-CT as an outcome measure of interstitial lung disease in TNF-transgenic mice. *PLoS One*. 2018;13(1):1–13.
 33. Tanabe N, Vasilescu DM, Kirby M, Coxson HO, Verleden SE, Vanaudenaerde BM, et al. Analysis of airway pathology in COPD using a combination of computed tomography, micro-computed tomography and histology. *Eur Respir J*. 2018;51(2):1701245.
 34. Tanabe N, Vasilescu DM, McDonough JE, Kinose D, Suzuki M, Cooper JD, et al. Micro-computed tomography comparison of preterminal bronchioles in centrilobular and panlobular emphysema. *Am J Respir Crit Care Med*. 2017;195(5):630–8.
 35. Zhou Y, Chen H, Ambalavanan N, Liu G, Antony VB, Ding Q, et al. Noninvasive imaging of experimental lung fibrosis. *Am J Respir Cell Mol Biol*. 2015;53(1):8–13.
 36. Lee J-G, Shim S, Kim M-J, Myung JK, Jang W-S, Bae C-H, et al. Pentoxifylline regulates plasminogen activator inhibitor-1 expression and protein kinase A phosphorylation in radiation-induced lung fibrosis. *Biomed Res Int*. 2017;2017:1–10.
 37. Ackermann M, Kim YO, Wagner WL, Schuppan D, Valenzuela CD, Mentzer SJ, et al. Effects of nintedanib on the microvascular architecture in a lung fibrosis model. *Angiogenesis*. 2017;20(3):359–72.
 38. Marien E, Hillen A, Vanderhoydonc F, Swinnen JV, Vande Velde G. Longitudinal microcomputed tomography-derived biomarkers for lung metastasis detection in a syngeneic mouse model: added value to bioluminescence imaging. *Lab Invest*. 2017;97(1):24–33.
 39. Vande Velde G, Poelmans J, De Langhe E, Hillen A, Vanoirbeek J, Himmelreich U, et al. Longitudinal micro-CT provides biomarkers of lung disease that can be used to assess the effect of therapy in preclinical mouse models, and reveal compensatory changes in lung volume. *Dis Model Mech*. 2016;9(1):91–8.
 40. Gu L, Deng ZJ, Roy S, Hammond PT. A combination RNAi-chemotherapy layer-by-layer nanoparticle for systemic targeting of KRAS/P53 with cisplatin to treat non-small cell lung cancer. *Clin Cancer Res*. 2017;23(23):7312–23.
 41. Lartey FM, Rafat M, Negahdar M, Malkovskiy AV, Dong X, Sun X, et al. Dynamic CT imaging of volumetric changes in pulmonary nodules correlates with physical measurements of stiffness. *Radiother Oncol*. 2017;122(2):313–8.
 42. Hegab A, Kameyama N, Kuroda A, Kagawa S, Yin Y, Ornitz D, et al. Using micro-computed tomography for the assessment of tumor development and follow-up of response to treatment in a mouse model of lung cancer. *J Vis Exp*. 2016;111:1–8.
 43. Vasilescu DM, Phillion AB, Tanabe N, Kinose D, Paige DF, Kantrowitz JJ, et al. Nondestructive cryo-micro-CT imaging enables structural and molecular analysis of human lung tissue. *J Appl Physiol*. 2017;122(1):161–9.
 44. Befera NT, Badea CT, Johnson GA. Comparison of 4D-microSPECT and microCT for murine cardiac function. *Mol Imaging Biol*. 2014;16(2):235–45.
 45. Ashton JR, Befera N, Clark D, Qi Y, Mao L, Rockman HA, et al. Anatomical and functional imaging of myocardial infarction in mice using micro-CT and eXIA 160 contrast agent. *Contrast Media Mol Imaging*. 2014;9(2):161–8.
 46. Disney CM, Lee PD, Hoyland JA, Sherratt MJ, Bay BK. A review of techniques for visualising soft tissue microstructure deformation and quantifying strain Ex Vivo. *J Microsc*. 2018;272(3):165–79.
 47. Dullin C, Ufartes R, Larsson E, Martin S, Lazzarini M, Tromba G, et al. μ CT of ex-vivo stained mouse hearts and embryos enables a precise match between 3D virtual histology, classical histology and immunohistochemistry. *PLoS One*. 2017;12(2):1–15.
 48. Domínguez E, Ruberte J, Ríos J, Novellas R, del Alamo MMR, Navarro M, et al. Non-invasive in vivo measurement of cardiac output in C57BL/6 mice using high frequency transthoracic ultrasound: evaluation of gender and body weight effects. *Int J Card Imaging*. 2014;30(7):1237–44.
 49. Maier J, Sawall S, Kachelrieß M. Assessment of dedicated low-dose cardiac micro-CT reconstruction algorithms using the left ventricular volume of small rodents as a performance measure. *Med Phys*. 2014;41(5):051908.
 50. Lee C-L, Min H, Befera N, Clark D, Qi Y, Das S, et al. Assessing cardiac injury in mice with dual energy-microCT, 4D-microCT and microSPECT imaging following partial-heart irradiation. *Int J Radiat Oncol Biol Phys*. 2014;88(3):686–93.
 51. Merchant SS, Kosaka Y, Yost HJ, Hsu EW, Brunelli L. Micro-computed tomography for the quantitative 3-dimensional assessment of the compact myocardium in the mouse embryo. *Circ J*. 2016;80(8):1795–803.
 52. Grover SP, Saha P, Jenkins J, Mukkavilli A, Lyons OT, Patel AS, et al. Quantification of experimental venous thrombus resolution by longitudinal nanogold-enhanced micro-computed tomography. *Thromb Res*. 2015;136(6):1285–90.

53. Peter AK, Bradford WH, Dalton ND, Gu Y, Chao CJ, Peterson KL, et al. Increased echogenicity and radiodense foci on echocardiogram and microCT in murine myocarditis. *PLoS One*. 2016;11(8):1–13.
54. Zhao J, Hansen BJ, Csepe TA, Lim P, Wang Y, Williams M, et al. Integration of high-resolution optical mapping and 3-dimensional micro-computed tomographic imaging to resolve the structural basis of atrial conduction in the human heart. *Circ Arrhythm Electrophysiol*. 2015;8(6):1514–7.
55. Pierce EL, Bloodworth CH, Naran A, Easley TF, Jensen MO, Yoganathan AP. Novel method to track soft tissue deformation by micro-computed tomography: application to the mitral valve. *Ann Biomed Eng*. 2016;44(7):2273–81.
56. Barannyk O, Fraser R, Oshkai P. A correlation between long-term in vitro dynamic calcification and abnormal flow patterns past bioprosthetic heart valves. *J Biol Phys*. 2017;43(2):279–96.
57. Roche ET, Horvath MA, Wamala I, Song SE, Whyte W, Machaidze Z, et al. Soft robotic sleeve restores heart function. *Sci Transl Med*. 2017;9(373):eaaf3925.
58. Müter D, Sørensen HO, Oddershede J, Dalby KN, Stipp SLS. Microstructure and micromechanics of the heart urchin test from X-ray tomography. *Acta Biomater*. 2015;23:21–6.
59. Babaei F, Hong TLC, Yeung K, Cheng SH, Lam YW. Contrast-enhanced x-ray micro-computed tomography as a versatile method for anatomical studies of adult zebrafish. *Zebrafish*. 2016;13(4):310–6.
60. Anderson R, Maga AM. A novel procedure for rapid imaging of adult mouse brains with MicroCT using iodine-based contrast. *PLoS One*. 2015;10(11):1–7.
61. De Crespigny A, Bou-reslan H, Nishimura MC, Phillips H, Richard A, Carano D, et al. 3D microCT of the postmortem brain. *J Neurosci Methods*. 2009;171(2):207–13.
62. Ghanavati S, Lerch JP, Sled JG. Automatic anatomical labeling of the complete cerebral vasculature in mouse models. *NeuroImage*. 2014;95:117–28.
63. Mizutani R, Saiga R, Ohtsuka M, Miura H, Hoshino M, Takeuchi A, et al. Three-dimensional x-ray visualization of axonal tracts in mouse brain hemisphere. *Sci Rep*. 2016;6:1–11.
64. Saito S, Murase K. Ex vivo imaging of mouse brain using micro-CT with non-ionic iodinated contrast agent: a comparison with myelin staining. *Br J Radiol*. 2012;85(1019):973–8.
65. Mancini M, Greco A, Tedeschi E, Palma G, Ragucci M, Bruzzone MG, et al. Head and neck veins of the mouse. A magnetic resonance, micro computed tomography and high frequency color doppler ultrasound study. *PLoS One*. 2015;10(6):1–15.
66. Starosolski Z, Villamizar CA, Rendon D, Paldino MJ, Milewicz DM, Ghaghada KB, et al. Ultra high-resolution in vivo computed tomography imaging of mouse cerebrovasculature using a long circulating blood pool contrast agent. *Sci Rep*. 2015;5:1–11.
67. Girard R, Zeineddine HA, Orsbon C, Tan H, Moore T, Hobson N, et al. Micro-computed tomography in murine models of cerebral cavernous malformations as a paradigm for brain disease. *J Neurosci Methods*. 2016;271:14–24.
68. Neulen A, Pantel T, Kosterhon M, Kirschner S, Brockmann MA, Kantelhardt SR, et al. A segmentation-based volumetric approach to localize and quantify cerebral vasospasm based on tomographic imaging data. *PLoS One*. 2017;12(2):1–14.
69. Choi JP, Yang X, Foley M, Wang X, Zheng X. Induction and micro-CT imaging of cerebral cavernous malformations in mouse model. *J Vis Exp*. 2017;127:1–5.
70. Kim J-Y, Ryu JH, Schellingerhout D, Sun I-C, Lee S-K, Jeon S, et al. Direct imaging of cerebral thromboemboli using computed tomography and fibrin-targeted gold nanoparticles. *Theranostics*. 2015;5(10):1098–114.
71. Vesey AT, WSA J, Irkle A, Moss A, Sng G, Forsythe RO, et al. ¹⁸F-fluoride and ¹⁸F-fluorodeoxyglucose positron emission tomography after transient ischemic attack or minor ischemic stroke clinical perspective. *Circ Cardiovasc Imaging*. 2017;10(3):e004976.
72. Dobrivojević M, Bohaček I, Erjavec I, Gorup D, Gajović S. Computed microtomography visualization and quantification of mouse ischemic brain lesion by nonionic radio contrast agents. *Croat Med J*. 2013;54:3–11.
73. Hayasaka N, Nagai N, Kawao N, Niwa A, Yoshioka Y, Mori Y, et al. In vivo diagnostic imaging using micro-CT: Sequential and comparative evaluation of rodent models for hepatic/brain ischemia and stroke. *PLoS One*. 2012;7(2):e32342.
74. Park JY, Lee SK, Kim JY, Je KH, Schellingerhout D, Kim DE. A new micro-computed tomography-based high-resolution blood-brain barrier imaging technique to study ischemic stroke. *Stroke*. 2014;45(8):2480–4.
75. Lamy M, Baumgartner D, Yoganandan N, Stemper BD, Willinger R. Experimentally validated three-dimensional finite element model of the rat for mild traumatic brain injury. *Med Biol Eng Comput*. 2013;51(3):353–65.
76. Moazen M, Alazmani A, Rafferty K, Liu ZJ, Gustafson J, Cunningham ML, et al. Intracranial pressure changes during mouse development. *J Biomech*. 2016;49(1):123–6.
77. Marghoub A, Libby J, Babbs C, Pauws E, Fagan MJ, Moazen M. Predicting calvarial growth in normal and craniostotic mice using a computational approach. *J Anat*. 2018;232(3):440–8.
78. Goldie SJ, Arhatari BD, Anderson P, Auden A, Partridge DD, Jane SM, et al. Mice lacking the conserved transcription factor Grainyhead-like 3 (Grhl3) display increased apposition of the frontal and parietal bones during embryonic development. *BMC Dev Biol*. 2016;16(1):1–12.

79. Sombke A, Lipke E, Michalik P, Uhl G, Harzsch S. Potential and limitations of x-ray micro-computed tomography in arthropod neuroanatomy: a methodological and comparative survey. *J Comp Neurol*. 2015;523(8):1281–95.
80. Pierce SE, Williams M, Benson RBJ. Virtual reconstruction of the endocranial anatomy of the early Jurassic marine crocodylomorph *Pelagosaurus typus* (Thalattosuchia). *PeerJ*. 2017;5:e3225.
81. Steinhoff POM, Sombke A, Liedtke J, Schneider JM, Harzsch S, Uhl G. The synganglion of the jumping spider *Marpissa muscosa* (Arachnida: Salticidae): Insights from histology, immunohistochemistry and microCT analysis. *Arthropod Struct Dev*. 2017;46(2):156–70.
82. Boyer DM, Kirk EC, Silcox MT, Gunnell GF, Gilbert CC, Yapuncich GS, et al. Internal carotid arterial canal size and scaling in Euarchonta: re-assessing implications for arterial patency and phylogenetic relationships in early fossil primates. *J Hum Evol*. 2016;97:123–44.
83. Kirk EC, Daghighi P, Macrini TE, Bhullar BAS, Rowe TB. Cranial anatomy of the duchesnean primate *Rooneyia viejaensis*: new insights from high resolution computed tomography. *J Hum Evol*. 2014;74:82–95.
84. Orliac MJ, Ladeveze S, Gingerich PD, Lebrun R, Smith T. Endocranial morphology of palaeocene plesiadapis tricuspidens and evolution of the early primate brain. *Proc R Soc B Biol Sci*. 2014;281(1781):20132792.
85. Nasrullah Q, Renfree MB, Evans AR. Three-dimensional mammalian tooth development using diceCT. *Arch Oral Biol*. 2018;85(March 2017):183–91.
86. Bertrand OC, Amador-Mughal F, Silcox MT. Virtual endocast of the early oligocene *Cedromus wilsoni* (Cedromurinae) and brain evolution in squirrels. *J Anat*. 2017;230(1):128–51.
87. Brusatte SL, Muir A, Young MT, Walsh S, Steel L, Witmer LM. The braincase and neurosensory anatomy of an early jurassic marine crocodylomorph: implications for crocodylian sinus evolution and sensory transitions. *Anat Rec*. 2016;299(11):1511–30.
88. Smith DB, Bernhardt G, Raine NE, Abel RL, Sykes D, Ahmed F, et al. Exploring miniature insect brains using micro-CT scanning techniques. *Sci Rep*. 2016;6(1):21768.
89. Porter WR, Witmer LM. Vascular patterns in iguanas and other squamates: blood vessels and sites of thermal exchange. Sugihara I, editor. *PLoS One*. 2015;10(10):e0139215.
90. Gignac PM, Kley NJ. Iodine-enhanced micro-CT imaging: Methodological refinements for the study of the soft-tissue anatomy of post-embryonic vertebrates. *J Exp Zool Part B Mol Dev Evol*. 2014;322(3):166–76.
91. Schambach SJ, Bag S, Schilling L, Groden C, Brockmann MA. Application of micro-CT in small animal imaging. *Methods*. 2010;50(1):2–13.
92. Missbach-Guentner J, Pinkert-Leetsch D, Dullin C, Ufartes R, Hornung D, Tampe B, et al. 3D virtual histology of murine kidneys –high resolution visualization of pathological alterations by micro computed tomography. *Sci Rep*. 2018;8(1):1–14.
93. Almajdub M, Magnier L, Juillard L, Janier M. Kidney volume quantification using contrast-enhanced in vivo X-ray micro-CT in mice. *Contrast Media Mol Imaging*. 2008;3(3):120–6.
94. Iwanaga J, Saga T, Tabira Y, Watanabe K, Yamaki K. Contrast imaging study of the horseshoe kidney for transplantation. *Surg Radiol Anat*. 2015;37(10):1267–71.
95. Hutchinson JC, Barrett H, Ramsey AT, Haig IG, Guy A, Sebire NJ, et al. Virtual pathological examination of the human fetal kidney using micro-CT. *Ultrasound Obstet Gynecol*. 2016;48(5):663–5.
96. Urbieto-Caceres VH, Syed FA, Lin J, Zhu X-Y, Jordan KL, Bell CC, et al. Age-dependent renal cortical microvascular loss in female mice. *Am J Physiol Metab*. 2012;302(8):E979–86.
97. Perrien DS, Saleh MA, Takahashi K, Madhur MS, Harrison DG, Harris RC, et al. Novel methods for microCT-based analyses of vasculature in the renal cortex reveal a loss of perfusable arterioles and glomeruli in eNOS^{-/-} mice. *BMC Nephrol*. 2016;17(1):1–10.
98. Ehling J, Babikova J, Gremse F, Klinkhammer BM, Baetke S, Knuechel R, et al. Quantitative micro-computed tomography imaging of vascular dysfunction in progressive kidney diseases. *J Am Soc Nephrol*. 2016;27(2):520–32.
99. Remuzzi A, Sangalli F, Macconi D, Tomasoni S, Cattaneo I, Rizzo P, et al. Regression of renal disease by angiotensin II antagonism is caused by regeneration of kidney vasculature. *J Am Soc Nephrol*. 2016;27(3):699–705.
100. Letavernier E, Verrier C, Goussard F, Perez J, Huguet L, Haymann JP, et al. Calcium and vitamin D have a synergistic role in a rat model of kidney stone disease. *Kidney Int*. 2016;90(4):809–17.
101. Scherer K, Braig E, Willer K, Willner M, Fingerle AA, Chabior M, et al. Non-invasive differentiation of kidney stone types using x-ray dark-field radiography. *Sci Rep*. 2015;5:1–7.
102. Kline TL, Knudsen BE, Anderson JL, Vercnocke AJ, Jorgensen SM, Ritman EL. Anatomy of hepatic arteriolo-portal venular shunts evaluated by 3D micro-CT imaging. *J Anat*. 2014;224(6):724–31.
103. Debbaut C, Segers P, Cornillie P, Casteleyn C, Dierick M, Laleman W, et al. Analyzing the human liver vascular architecture by combining vascular corrosion casting and micro-CT scanning: a feasibility study. *J Anat*. 2014;224(4):509–17.
104. Peeters G, Debbaut C, Laleman W, Monbaliu D, Vander Elst I, Detrez JR, et al. A multilevel framework to reconstruct anatomical 3D models of the hepatic vasculature in rat livers. *J Anat*. 2017;230(3):471–83.

105. Kline TL, Zamir M, Ritman EL. Relating function to branching geometry: A micro-CT study of the hepatic artery, portal vein, and biliary tree. *Cells Tissues Organs*. 2011;194(5):431–42.
106. Martiniova L, Schimel D, Lai EW, Limpuangthip A, Kvetnansky R, Pacak K. In vivo micro-CT imaging of liver lesions in small animal models. *Methods*. 2010;50(1):20–5.
107. Stroope A, Radtke B, Huang B, Masyuk T, Torres V, Ritman E, et al. Hepato-renal pathology in *Pkd2ws25/–* mice, an animal model of autosomal dominant polycystic kidney disease. *Am J Pathol*. 2010;176(3):1282–91.
108. Peeters G, Debbaut C, Cornillie P, De Schryver T, Monbaliu D, Laleman W, et al. A multilevel modeling framework to study hepatic perfusion characteristics in case of liver cirrhosis. *J Biomech Eng*. 2015;137(5):051007.
109. Tabibian JH, Macura SI, O'Hara SP, Fidler JL, Glockner JF, Takahashi N, et al. Micro-computed tomography and nuclear magnetic resonance imaging for noninvasive, live-mouse cholangiography. *Lab Invest*. 2013;93(6):733–43.
110. Thompson JG, van der Sterren W, Bakhutashvili I, van der Bom IM, Radaelli AG, Karanian JW, et al. Distribution and detection of radiopaque beads after hepatic transarterial embolization in swine: cone-beam CT versus MicroCT. *J Vasc Interv Radiol*. 2018;29(4):568–74.
111. Will OM, Damm T, Campbell GM, von Schönfels W, Açil Y, Will M, et al. Longitudinal micro-computed tomography monitoring of progressive liver regeneration in a mouse model of partial hepatectomy. *Lab Anim*. 2017;51(4):422–6.
112. Al Rawashdeh W, Zuo S, Melle A, Appold L, Koletnik S, Tsvetkova Y, et al. Noninvasive assessment of elimination and retention using CT-FMT and kinetic whole-body modeling. *Theranostics*. 2017;7(6):1499–510.
113. Barnes SL, Lyschchik A, Washington MK, Gore JC, Miga MI. Development of a mechanical testing assay for fibrotic murine liver. *Med Phys*. 2007;34(11):4439–50.
114. Lublinsky S, Luu YK, Rubin CT, Judex S. Automated separation of visceral and subcutaneous adiposity in in vivo microcomputed tomographies of mice. *J Digit Imaging*. 2009;22(3):222–31.
115. Hua XW, Lu TF, Li DW, Wang WG, Li J, Liu ZZ, et al. Contrast-enhanced micro-computed tomography using ExiTron nano6000 for assessment of liver injury. *World J Gastroenterol*. 2015;21(26):8043–51.
116. Boll H, Nittka S, Doyon F, Neumaier M, Marx A, Kramer M, et al. Micro-CT based experimental liver imaging using a nanoparticulate contrast agent: a longitudinal study in mice. *PLoS One*. 2011;6(9):1–6.
117. Stout DB, Suckow CE. MicroCT liver contrast agent enhancement over time, dose, and mouse strain. *Mol Imaging Biol*. 2008;10(2):114–20.
118. Henning T, Weber AW, Bauer JS, Meier R, Carlsen JM, Sutton EJ, et al. Imaging characteristics of DHOG, a hepatobiliary contrast agent for preclinical microCT in mice. *Acad Radiol*. 2008;15(3):342–9.
119. Brinkmann M, Rizzo LY, Lammers T, Gremse F, Schiwy S, Kiessling F, et al. Micro-computed tomography (μ CT) as a novel method in ecotoxicology—determination of morphometric and somatic data in rainbow trout (*Oncorhynchus mykiss*). *Sci Total Environ*. 2016;543:135–9.
120. Aoyagi H, ichi IS, Yoshizawa H, Tsuchikawa K. Three-dimensional observation of the mouse embryo by micro-computed tomography: Meckel's cartilage, otocyst, and/or muscle of tongue. *Odontology*. 2012;100(2):137–43.
121. Jeffery NS, Stephenson RS, Gallagher JA, Jarvis JC, Cox PG. Micro-computed tomography with iodine staining resolves the arrangement of muscle fibres. *J Biomech*. 2011;44(1):189–92.
122. Kupczik K, Stark H, Mundry R, Neininger FT, Heidlauf T, Röhrle O. Reconstruction of muscle fascicle architecture from iodine-enhanced microCT images: a combined texture mapping and streamline approach. *J Theor Biol*. 2015;382:34–43.
123. Yan L, Guo Y, Qi J, Zhu Q, Gu L, Zheng C, et al. Iodine and freeze-drying enhanced high-resolution MicroCT imaging for reconstructing 3D intraneural topography of human peripheral nerve fascicles. *J Neurosci Methods*. 2017;287:58–67.
124. Bikis C, Degrugillier L, Thalmann P, Schulz G, Müller B, Hieber SE, et al. Three-dimensional imaging and analysis of entire peripheral nerves after repair and reconstruction. *J Neurosci Methods*. 2018;295:37–44.
125. Charles JP, Cappellari O, Spence AJ, Wells DJ, Hutchinson JR. Muscle moment arms and sensitivity analysis of a mouse hindlimb musculoskeletal model. *J Anat*. 2016;229(4):514–35.
126. Vickerton P, Jarvis JC, Gallagher JA, Akhtar R, Sutherland H, Jeffery N. Morphological and histological adaptation of muscle and bone to loading induced by repetitive activation of muscle. *Proc R Soc B Biol Sci*. 2014;281(1788):1–9.
127. Libouban H, Guintard C, Minier N, Aguado E, Chappard D. Long-term quantitative evaluation of muscle and bone wasting induced by botulinum toxin in mice using microcomputed tomography. *Calcif Tissue Int*. 2018;102(6):695–704.
128. Wu J, Yin N. Detailed Anatomy of the Nasolabial Muscle in Human Fetuses as Determined by Micro-CT Combined with Iodine Staining. *Ann Plast Surg*. 2016;76(1):111–6.
129. Wu J, Yin N. Anatomy research of nasolabial muscle structure in fetus with cleft lip: An iodine staining technique based on microcomputed tomography. *J Craniofac Surg*. 2014;25(3):1056–61.
130. Yin N, Wu J, Chen B, Song T, Ma H, Zhao Z, et al. Muscle tension line concept in nasolabial muscle complex—based on 3-dimensional reconstruction of nasolabial muscle fibers. *J Craniofac Surg*. 2015;26(2):469–72.

131. Goethals LR, de Geeter F, Vanhove C, Roosens B, Devos H, Lahoutte T. Improved quantification in pinhole gated myocardial perfusion SPECT using micro-CT and ultrasound information. *Contrast Media Mol Imaging*. 2012;7(2):167–74.
132. Hendriks J, Riesle J, van Blitterswijk CA. Co-culture in cartilage tissue engineering. *J Tissue Eng Regen Med*. 2010;4(7):524–31.
133. Toma M, Jensen MØ, Einstein DR, Yoganathan AP, Cochran RP, Kunzelman KS. Fluid–structure interaction analysis of papillary muscle forces using a comprehensive mitral valve model with 3D chordal structure. *Ann Biomed Eng*. 2016;44(4):942–53.
134. Detombe SA, Xiang F-L, Dunmore-Buyze J, White JA, Feng Q, Drangova M. Rapid microcomputed tomography suggests cardiac enlargement occurs during conductance catheter measurements in mice. *J Appl Physiol*. 2012;113(1):142–8.
135. Garcia FH, Fischer G, Liu C, Audisio TL, Economo EP. Next-generation morphological character discovery and evaluation: An X-ray micro-CT enhanced revision of the ant genus *zaspinctus wheeler* (hymenoptera, formicidae, dorylinae) in the afrotropics. *Zookeys*. 2017;2017(693):33–93.
136. Li D, Zhang K, Zhu P, Wu Z, Zhou H. 3D configuration of mandibles and controlling muscles in rove beetles based on micro-CT technique. *Anal Bioanal Chem*. 2011;401(3):817–25.
137. Holliday CM, Tsai HP, Skiljan RJ, George ID, Pathan S. A 3D interactive model and atlas of the jaw musculature of *alligator mississippiensis*. *PLoS One*. 2013;8(6):e62806.
138. Praet T, Adriaens D, Van Cauter S, Masschaele B, De Beule M, Verheghe B. Inspiration from nature: dynamic modelling of the musculoskeletal structure of the seahorse tail. *Int J Numer Method Biomed Eng*. 2012;28(10):1028–42.
139. Dickinson E, Stark H, Kupeczik K. Non-destructive determination of muscle architectural variables through the use of DiceCT. *Anat Rec*. 2018;301(2):363–77.
140. Cox PG, Jeffery N. Reviewing the morphology of the jaw-closing musculature in squirrels, rats, and guinea pigs with contrast-enhanced microCt. *Anat Rec Adv Integr Anat Evol Biol*. 2011;294(6):915–28.
141. Marxen M, Thornton MM, Chiarot CB, Klement G, Koprivnikar J, Sled JG, et al. MicroCT scanner performance and considerations for vascular specimen imaging. *Med Phys*. 2004;31(2):305–13.
142. Das NM, Hatsell S, Nannuru K, Huang L, Wen X, Wang L, et al. In vivo quantitative microcomputed tomographic analysis of vasculature and organs in a normal and diseased mouse model. *PLoS One*. 2016;11(2):1–18.
143. Vasquez SX, Gao F, Su F, Grijalva V, Pope J, Martin B, et al. Optimization of microCT imaging and blood vessel diameter quantitation of preclinical specimen vasculature with radiopaque polymer injection medium. *PLoS One*. 2011;6(4):2–7.
144. Prajapati SI, Keller C. Contrast enhanced vessel imaging using microCT. *J Vis Exp*. 2011;47:4–6.
145. Aoki T, Rodriguez-Porcel M, Matsuo Y, Cassar A, Kwon T-G, Franchi F, et al. Evaluation of coronary adventitial vasa vasorum using 3D optical coherence tomography—animal and human studies. *Atherosclerosis*. 2015;239(1):203–8.
146. Nierenberger M, Rémond Y, Ahzi S, Choquet P. Assessing the three-dimensional collagen network in soft tissues using contrast agents and high resolution micro-CT: application to porcine iliac veins. *Comptes Rendus - Biol*. 2015;338(7):425–33.
147. Rahman A, Cahill LS, Zhou YQ, Hoggarth J, Rennie MY, Seed M, et al. A mouse model of antepartum stillbirth. *Am J Obstet Gynecol*. 2017;217(4):443.e1–443.e11.
148. Kizhakke Puliyakote AS, Vasilescu DM, Sen-Sharma K, Wang G, Hoffman EA. A skeleton-tree based approach to acinar morphometric analysis using micro computed tomography with comparison of acini in young and old C57Bl/6 mice. *J Appl Physiol*. 2016;120(12):1402–9.
149. Shields KJ, Verdellis K, Passineau MJ, Faight EM, Zourelis L, Wu C, et al. Three-dimensional micro computed tomography analysis of the lung vasculature and differential adipose proteomics in the Sugen/hypoxia rat model of pulmonary arterial hypertension. *Pulm Circ*. 2016;6(4):586–96.
150. Pai VM, Kozlowski M, Donahue D, Miller E, Xiao X, Chen MY, et al. Coronary artery wall imaging in mice using osmium tetroxide and micro-computed tomography (micro-CT). *J Anat*. 2012;220(5):514–24.
151. Liu J, Zhong S, Lan H, Meng X, Zhang H, Fan Y, et al. Mapping the calcification of bovine pericardium in rat model by enhanced micro-computed tomography. *Biomaterials*. 2014;35(29):8305–11.
152. Huesa C, Millán JL, Van't Hof RJ, MacRae VE. A new method for the quantification of aortic calcification by three-dimensional micro-computed tomography. *Int J Mol Med*. 2013;32(5):1047–50.
153. Schleicher N, Tomkins AJ, Kampschulte M, Hyvelin JM, Botteron C, Juenemann M, et al. Sonothrombolysis with BR38 microbubbles improves microvascular patency in a rat model of stroke. *PLoS One*. 2016;11(4):1–12.
154. Jiřík M, Tonar Z, Králíčková A, Eberlová L, Mírka H, Kochová P, et al. Stereological quantification of microvessels using semiautomated evaluation of X-ray microtomography of hepatic vascular corrosion casts. *Int J Comput Assist Radiol Surg*. 2016;11(10):1803–19.
155. Maíga S, Allain G, Hauet T, Roumy J, Baulier E, Scepi M, et al. Renal auto-transplantation promotes cortical microvascular network remodeling in a preclinical porcine model. *PLoS One*. 2017;12(7):1–16.
156. Persy V, Postnov A, Neven E, Dams G, De Broe M, D'Haese P, et al. High-resolution X-ray microtomography is a sensitive method to detect vascular calcification in living rats with chronic renal failure. *Arterioscler Thromb Vasc Biol*. 2006;26(9):2110–6.

157. Postnov AA, D'Haese PC, Neven E, De Clerck NM, Persy VP. Possibilities and limits of X-ray microtomography for in vivo and ex vivo detection of vascular calcifications. *Int J Card Imaging*. 2009;25(6):615–24.
158. Ramot Y, Brauner R, Kang K, Heymach JV, Furtado S, Nyska A. Quantitative evaluation of drug-induced microvascular constriction in mice kidney using a novel tool for 3D geometrical analysis of ex vivo organ vasculature. *Toxicol Pathol*. 2014;42(4):774–83.
159. Dinley J, Hawkins L, Paterson G, Ball AD, Sinclair I, Sinnett-Jones P, et al. Micro-computed X-ray tomography: A new non-destructive method of assessing sectional, fly-through and 3D imaging of a soft-bodied marine worm. *J Microsc*. 2010;238(2):123–33.
160. Weber SM, Peterson KA, Durkee B, Qi C, Longino M, Warner T, et al. Imaging of murine liver tumor using microCT with a hepatocyte-selective contrast agent: accuracy is dependent on adequate contrast enhancement. *J Surg Res*. 2004;119(1):41–5.
161. Almajdub M, Nejari M, Poncet G, Magnier L, Chereul E, Roche C, et al. In-vivo high-resolution X-ray microtomography for liver and spleen tumor assessment in mice. *Contrast Media Mol Imaging*. 2007 Mar;2(2):88–93.
162. Bour G, Martel F, Goffin L, Bayle B, Gangloff J, Aprahamian M, et al. Design and development of a robotized system coupled to mCT imaging for intratumoral drug evaluation in a HCC mouse model. *PLoS One*. 2014;9(9):e106675.
163. Takakura K, Koido S, Fujii M, Hashiguchi T, Shibazaki Y, Yoneyama H, et al. Characterization of non-alcoholic steatohepatitis-derived hepatocellular carcinoma as a human stratification model in mice. *Anticancer Res*. 2014;34(9):4849–55.
164. Ohta S, Lai EW, Morris JC, Bakan DA, Klaunberg B, Cleary S, et al. MicroCT for high-resolution imaging of ectopic pheochromocytoma tumors in the liver of nude mice. *Int J Cancer*. 2006;119(9):2236–41.
165. Chang CH, Jan ML, Fan KH, Wang HE, Tsai TH, Chen CF, et al. Longitudinal evaluation of tumor metastasis by an FDG-microPET/microCT dual-imaging modality in a lung carcinoma-bearing mouse model. *Anticancer Res*. 2006;26(1A):159–66.
166. Savai R, Langheinrich AC, Schermuly RT, Pullamsetti SS, Dumitrascu R, Traupe H, et al. Evaluation of angiogenesis using micro-computed tomography in a xenograft mouse model of lung cancer. *Neoplasia*. 2009;11(1):48–56.
167. Apps JR, Hutchinson JC, Arthurs OJ, Virasami A, Joshi A, Zeller-Plumhoff B, et al. Imaging Invasion: Micro-CT imaging of adamantinomatous craniopharyngioma highlights cell type specific spatial relationships of tissue invasion. *Acta Neuropathol Commun*. 2016;4(1):57.
168. Kirschner S, Felix MC, Hartmann L, Bierbaum M, Maros ME, Kerl HU, et al. In vivo micro-CT imaging of untreated and irradiated orthotopic glioblastoma xenografts in mice: capabilities, limitations and a comparison with bioluminescence imaging. *J Neuro-Oncol*. 2015;122(2):245–54.
169. Yahyanejad S, Granton PV, Lieuwens NG, Gilmour L, Dubois L, Theys J, et al. Complementary use of bioluminescence imaging and contrast-enhanced micro-computed tomography in an orthotopic brain tumor model. *Mol Imaging*. 2014;13(4) <https://doi.org/10.2310/7290.2014.00038>.
170. Prajapati SI, Kilcoyne A, Samano AK, Green DP, McCarthy SD, Blackman BA, et al. MicroCT-based virtual histology evaluation of pre-clinical medulloblastoma. *Mol Imaging Biol*. 2011;13(3):493–9.
171. Tang R, Saksena M, Coopey SB, Fernandez L, Buckley JM, Lei L, et al. Intraoperative micro-computed tomography (micro-CT): a novel method for determination of primary tumour dimensions in breast cancer specimens. *Br J Radiol*. 2016;89(1058):20150581.
172. Baklaushev VP, Grinenko NF, Yusubaliev GM, Abakumov MA, Gubskii IL, Cherepanov SA, et al. Modeling and integral x-ray, optical, and mri visualization of multiorgan metastases of orthotopic 4T1 breast carcinoma in BALB/c mice. *Bull Exp Biol Med*. 2015;158(4):581–8.
173. Felix MC, Fleckenstein J, Kirschner S, Hartmann L, Wenz F, Brockmann MA, et al. Image-guided radiotherapy using a modified industrial micro-CT for pre-clinical applications. *PLoS One*. 2015;10(5):1–11.
174. Kersemans V, Thompson J, Cornelissen B, Woodcock M, Allen PD, Buls N, et al. Micro-CT for anatomic referencing in PET and SPECT: radiation dose, biologic damage, and image quality. *J Nucl Med*. 2011;52(11):1827–33.
175. Pauwels E, Van Loo D, Cornillie P, Brabant L, Van Hoorebeke L. An exploratory study of contrast agents for soft tissue visualization by means of high resolution X-ray computed tomography imaging. *J Microsc*. 2013;250(1):21–31.
176. Kirschner S, Mürle B, Felix M, Arns A, Groden C, Wenz F, et al. Imaging of orthotopic glioblastoma xenografts in mice using a clinical CT scanner: comparison with micro-CT and histology. *PLoS One*. 2016;11(11):1–13.
177. Hopkins TM, Heilman AM, Liggett JA, LaSance K, Little KJ, Hom DB, et al. Combining micro-computed tomography with histology to analyze biomedical implants for peripheral nerve repair. *J Neurosci Methods*. 2015 Nov;255:122–30.
178. Bikis C, Thalmann P, Degrugillier L, Schulz G, Müller B, Kalbermatten DF, et al. Three-dimensional and non-destructive characterization of nerves inside conduits using laboratory-based micro computed tomography. *J Neurosci Methods*. 2018;294:59–66.
179. Albers J, Markus MA, Alves F, Dullin C. X-ray based virtual histology allows guided sectioning of heavy ion stained murine lungs for histological analysis. *Sci Rep*. 2018;8(1):1–10.

180. Arendse E, Fawole OA, Magwaza LS, Opara UL. Non-destructive prediction of internal and external quality attributes of fruit with thick rind: a review. *J Food Eng.* 2018;217:11–23.
181. Schoeman L, Williams P, du Plessis A, Manley M. X-ray micro-computed tomography (μ CT) for non-destructive characterisation of food microstructure. *Trends Food Sci Technol.* 2016;47:10–24.
182. Frisullo P, Laverse J, Marino R, Del Nobile MA. X-ray computed tomography to study processed meat microstructure. *J Food Eng.* 2009;94(3–4):283–9.
183. Frisullo P, Marino R, Laverse J, Albenzio M, Del Nobile MA. Assessment of intramuscular fat level and distribution in beef muscles using X-ray microcomputed tomography. *Meat Sci.* 2010;85(2):250–5.
184. Zhu LJ, Dogan H, Gajula H, Gu MH, Liu QQ, Shi YC. Study of kernel structure of high-amylose and wild-type rice by X-ray microtomography and SEM. *J Cereal Sci.* 2012;55(1):1–5.
185. Guelpa A, du Plessis A, Manley M. A high-throughput X-ray micro-computed tomography (μ CT) approach for measuring single kernel maize (*Zea mays* L.) volumes and densities. *J Cereal Sci.* 2016;69:321–8.
186. Mohorič A, Vergeldt F, Gerkema E, van Dalen G, van den Doel LR, van Vliet LJ, et al. The effect of rice kernel microstructure on cooking behaviour: a combined μ -CT and MRI study. *Food Chem.* 2009;115(4):1491–9.
187. Schoeman L, Du Plessis A, Manley M. Non-destructive characterisation and quantification of the effect of conventional oven and forced convection continuous tumble (FCCT) roasting on the three-dimensional microstructure of whole wheat kernels using X-ray micro-computed tomography (μ CT). *J Food Eng.* 2016;187:1–13.
188. Cafarelli B, Spada A, Laverse J, Lampignano V, Del Nobile MA. X-ray microtomography and statistical analysis: tools to quantitatively classify bread microstructure. *J Food Eng.* 2014;124:64–71.
189. Magwaza LS, Opara UL. Investigating non-destructive quantification and characterization of pomegranate fruit internal structure using X-ray computed tomography. *Postharvest Biol Technol.* 2014;95:1–6.
190. Herremans E, Verboven P, Defraeye T, Rogge S, Ho QT, Hertog MLATM, et al. X-ray CT for quantitative food microstructure engineering: the apple case. *Nucl Instruments Methods Phys Res Sect B.* 2014;324:88–94.
191. Diels E, van Dael M, Keresztes J, Vanmaercke S, Verboven P, Nicolai B, et al. Assessment of bruise volumes in apples using X-ray computed tomography. *Postharvest Biol Technol.* 2017;128:24–32.
192. Muziri T, Theron KI, Cantre D, Wang Z, Verboven P, Nicolai BM, et al. Microstructure analysis and detection of mealiness in 'Forelle' pear (*Pyrus communis* L.) by means of X-ray computed tomography. *Postharvest Biol Technol.* 2016;120:145–56.
193. Cantre D, Herremans E, Verboven P, Ampofo-Asiama J, Nicolai B. Characterization of the 3-D microstructure of mango (*Mangifera indica* L. cv. Carabao) during ripening using X-ray computed microtomography. *Innov Food Sci Emerg Technol.* 2014;24:28–39.
194. Cantre D, East A, Verboven P, Trejo Araya X, Herremans E, Nicolai BM, et al. Microstructural characterisation of commercial kiwifruit cultivars using X-ray micro computed tomography. *Postharvest Biol Technol.* 2014;92:79–86.
195. Frisullo P, Barnabà M, Navarini L, Del Nobile MA. *Coffea arabica* beans microstructural changes induced by roasting: An X-ray microtomographic investigation. *J Food Eng.* 2012;108(1):232–7.
196. Oliveros NO, Hernández JA, Sierra-Espinosa FZ, Guardián-Tapia R, Pliego-Solórzano R. Experimental study of dynamic porosity and its effects on simulation of the coffee beans roasting. *J Food Eng.* 2017;199:100–12.
197. Warning A, Verboven P, Nicolai B, Van Dalen G, Datta AK. Computation of mass transport properties of apple and rice from X-ray microtomography images. *Innov Food Sci Emerg Technol.* 2014;24:14–27.
198. Suki B. Assessing the functional mechanical properties of bioengineered organs with emphasis on the lung. *J Cell Physiol.* 2014;229(9):1134–40.
199. Zarghami N, Jensen MD, Talluri S, Foster PJ, Chambers AF, Dick FA, et al. Technical note: immunohistochemical evaluation of mouse brain irradiation targeting accuracy with 3D-printed immobilization device. *Med Phys.* 2015;42(11):6507–13.
200. De Paolis A, Watanabe H, Nelson JT, Bikson M, Packer M, Cardoso L. Human cochlear hydrodynamics: a high-resolution μ CT-based finite element study. *J Biomech.* 2017 Jan;50(32):209–16.
201. Buytaert JAN, Salih WHM, Dierick M, Jacobs P, Dirckx JJJ. Realistic 3D computer model of the gerbil middle ear, featuring accurate morphology of bone and soft tissue structures. *J Assoc Res Otolaryngol.* 2011;12(6):681–96.

Applications of Micro-CT in Cardiovascular Engineering and Bio-inspired Design

11

Bilgesu Çakmak, Erhan Ermek, Muhammad Jamil,
Asım Horasan, and Kerem Pekkan

11.1 Introduction

Micro-computed tomography (micro-CT) is a nondestructive imaging tool that facilitates the construction of very high-resolution three-dimensional (3D) images which are made up of two-dimensional (2D) trans-axial projections of a sample.

The main principle of micro-CT is the interaction of X-ray with the sample. As an X-ray beam propagates through the sample, the intensity of the beam is reduced [1]. This attenuation depends on the sample and the source energy. By utilizing the differences in X-ray attenuation properties of the sample, reconstruction of 3D structure becomes possible.

The main steps of micro-CT are image acquisition, reconstruction, processing, and visualization using image analysis. There are several segmentation methods for reconstruction. The simplest and the most commonly used one for the micro-CT applications is the thresholding method. In this method, after obtaining the scans, an intensity threshold is set to extract the region of interest. Image processing and visualization tools like Slicer software let you apply a manual

thresholding which facilitates choosing the optimal threshold. Another method which is widely used for reconstruction is region growing. In this method, firstly some seed points are selected according to some given criteria (e.g., color). Then, the regions are grown from these seed points to the neighboring points that fit to the criteria. Again, Slicer software has the option to segment by region growing. After importing the scans, the user chooses a set of seed points, the number of iterations, and the neighborhood radius.

The use of micro-CT has been linked to imaging of the bone since X-rays are attenuated more by the calcified tissue. However, recently, with the use of contrast agents, it became possible to image the soft tissues such as lung, cardiovascular, and cancer tissues with the micro-CT. Thus, progression of a disease or structural information of a tissue or a device can be monitored with micro-CT. D'Onofrio et al. analyzed the flow field dynamics inside two hollow fiber membrane (HFM) oxygenators based on micro-CT scans [2]. After scanning the oxygenator by using Nikon XT H 225 with a source voltage of 55 kV and a source current of 174 μ A, they built a 3D geometry with a CAD software and set up a computational fluid dynamics (CFD) model to investigate the design properties of oxygenators. In [3], authors developed a novel method to track mitral valve tissue deformation by using micro-CT. They first applied fiducial markers and then tracked them with multiple loading conditions. Furthermore, Kim et al.

B. Çakmak · E. Ermek · M. Jamil · K. Pekkan (✉)
Department of Mechanical Engineering, Koç
University, Sarıyer, Istanbul, Turkey
e-mail: kpekk@ku.edu.tr

A. Horasan
Teknogem, Istanbul, Turkey

[4] analyzed the embryonic chick morphogenesis by using micro-CT. They labeled the embryos between 4 and 12 days with osmium tetroxide and scanned them with a resolution of 25 μm . They established mathematical relations for the growth of the heart, limb, eye, and brain. They demonstrated that some organs such as the eye and the heart grew exponentially. Besides, they showed that cardiac myocardial volumetric growth varies according to time and specific chamber. Likewise, in our earlier study [5], we have investigated the flow model by using CFD, changes in aortic arch geometry, and wall shear stress (WSS) distribution in the chick embryo. To obtain the 3D morphology of the developing great vessels, we used polymeric casting followed by micro-CT scan. 3D geometries of the aortic arch were detected by injecting a rapidly polymerizing resin (diluted MICROFIL[®] Silicone Rubber Injection Compounds MV-blue, Flow Tech Inc., Carver, MA) into the dorsal aorta. Then micro-CT scanning was performed (Scanco Inc.) with a resolution of $\sim 10 \mu\text{m}$. 2D dicom data were preprocessed to optimize image contrast using DicomWorks, and the 3D reconstruction was completed by using the software Simpleware ScanIP (Simpleware Ltd. Innovation Centre, UK). Then, these 3D models were imported into Geomagic (Geomagic Inc., Durham, NC) for CFD analysis. Moreover, Ritman et al. [6] scanned the lungs and pulmonary vascular system via micro-CT. They chose micro-CT over CT due to its higher resolution so that the basic microstructures such as alveoli can be visualized and determined individually. Moreover, Kriete et al. imaged the lung tissue by confocal microscopy and micro-CT [7]. They pointed out that using confocal microscopy was a time-consuming approach and it also required a precise alignment and correction of the dissected tissue. However, with micro-CT, these preparations are not required, and imaging of the lung tissue which contains volumes of 5–15 mm in diameter with 10–50 μm resolution can be easily achieved. As stated earlier, first applications of micro-CT involved examining the bone architecture since the density difference leads to high contrast. Yet by adding a heavy metal stain, it becomes also possible to image the tissues where

there is no much density difference such as the lungs. The main limitation of confocal microscopy is that since its working principle involves scattering and absorption, it does not work in tissues having more than 100 μm thickness. Yet since X-rays can penetrate thick tissues, micro-CT works in this situation and successfully displays the complete volume. With the aid of micro-CT, Lin et al. quantified the microarchitectural parameters as a function of porogen concentration in biodegradable porous polymer scaffolds and demonstrated the relation with compressive mechanical properties [8]. Furthermore, to evaluate the cardiac function and functional reserve in rats, Badea et al. imaged dobutamine (DOB) stress using micro-CT [9]. In their earlier study, they have developed a dual micro-CT system for small animal imaging [10], and they used this system in this study as well. They concluded that micro-CT was able to provide isotropic data on the cardiac function. Some of their important findings are that compared with MR, micro-CT is faster and less costly and compared with echocardiography, it provides higher accuracy. In another study, Kim et al. used contrast-enhanced micro-CT to detect congenital heart disease in mice, and they discovered that the overall accuracy was greater than 85% for all of the anomalies analyzed (including aortic arch anomalies, outflow tract anomalies, etc.), except for coronary artery fistulas which was 50.0% [11]. In [12], authors have utilized micro-CT to demonstrate the age-related alterations in the coronary vasculature. They compared the volume of the aged hearts and the young hearts and noted that the aged hearts were significantly larger in total as well as epicardial vessel volumes compared with the young heart, and the intramyocardial vessel size was same for both. Table 11.1 shows a summary of the studies involving micro-CT.

Table 11.2 shows a comparison of micro-CT with other imaging modalities. As the field of view and the resolution are inversely proportional, in this table, we listed the optimum resolution that can be obtained with the corresponding modality. Likewise, scan time is dependent on the sample. Yet here, we give an approximate duration so that the user has a brief idea.

Table 11.1 Summary of studies involving biomedical applications of micro-CT

Micro-CT scanner	Device/model scanned	Source voltage	Source current	Resolution	Exposure time	Authors
Nikon XT H 225	Two hollow fiber membrane (HFM) oxygenators	55 kV	174 μ A	NM	2 s	D'Onofrio et al. (2017) [2]
Siemens Inveon	Mitral valve	80 kV	500 μ A	9–17 μ m	650 ms	Pierce et al. (2016) [3]
GE eXplore CT120	Chick embryo	70–120 kV	0–50 mA	25 μ m	NM	Kim et al. (2011) [4]
Scanco Inc.	Chick embryo aortic arch	80 kV	150 μ A	10 μ m	2.35 ms	Wang et al. (2009) [5]
NM	Lungs and pulmonary vascular system	60 kV	NM	5 μ m	NM	Ritman (2005) [6]
Skyscan 1072	Lung tissue	130 kV	NM	Up to 5 μ m	NM	Kriete et al. (2001) [7]
Scanco Inc.	Porous polymer scaffolds	50–70 kV	150 μ A	20 μ m	120 ms	Lin et al. (2003) [8]
Self-developed dual-tube/detector micro-CT system ^a	Rat heart	80 kV	160 mA	Isotropic resolution of 88 μ m (voxel volume = 0.6 μ L)	10 ms	Badea et al. (2011) [9]
Siemens Inveon multimodality	Mice heart	80 kV	100 μ A	45 μ m (neonates) & 15 μ m (fetuses)	500–800 ms	Kim et al. (2013) [11]

NM Not mentioned

^aConsists of Varian Medical Systems X-ray tubes, EMD technologies X-ray generators, photonic science X-ray detectors

Table 11.2 Comparison of micro-CT with other imaging modalities

Property	Micro-CT	Micro-ultrasound	MRI	OCT	Confocal microscopy
Requires sectioning and alignment	No	Yes	Yes	No	Yes
Penetration depth	Entire body	Limited—3 cm	Limited—10 cm	Limited—3 mm	Limited—300 μ m
Scan time	Milliseconds	Milliseconds	Hours	Minutes	Minutes
Resolution	<20 μ m	30 μ m	1 mm	<10 μ m	1 μ m

11.2 Example Applications

11.2.1 Selected Cardiovascular Device Scans

We have scanned several devices and studied the flow inside them. To obtain a decent quality 3D image of the sample, we must generate images with a high signal to noise ratio and a good contrast ratio. Therefore, we should adjust the scanning parameters. The micro-CT device that we

use for scanning is NewTom 5G scanner (QR Verona, Verona, Italy). The energy of the X-ray source is fixed, and it is 110 kV. The rotation step is 1°, with a total rotation of 360°. We do not apply frame averaging; thus, we obtain high resolution. The device employs a total filtration with 1.4 mm Al (inherent filtration) + 9.5 mm Al (supplementary filtration). The maximum conical beam dimension is 265 mm \times 287 mm (detector area). The device makes use of CBCT technology with a focal spot of 0.3 mm.

Table 11.3 Detector properties

Pixels	1920 × 1536
Pixel size	127 × 127 μm
Pixel depth	14 bit
S/N	90 dB
Max frame rate	30 F/s

Table 11.3 shows the detector properties.

11.2.1.1 Cannulae Scans

Extracorporeal membrane oxygenation (ECMO) is a method of cardiopulmonary life support, in which the drained blood from the venous system is circulated outside the body by a mechanical pump. During this circulation, it is saturated with oxygen, carbon dioxide is removed, and then the blood is returned back to the body [13]. Over the years, ECMO became a pivot tool in severe cardiac and pulmonary dysfunctions. Double lumen cannula (DLC) is a critical component of the venovenous (VV) ECMO circuit which has partitioned lumens for deoxygenated blood drainage and infusion. Therefore, success of VV ECMO is related with the cannula design and its orientation in the heart. The positions of the infusion and drainage ports are of vital importance for the device hemodynamics. In addition, correct positioning of the cannula is also very important since malposition may result in hypoxemia and recirculation. To analyze the effect of malposition and the hemodynamics performance of the cannulae, we scanned several of them and carried out a computational fluid dynamics (CFD) analysis. In this chapter, you will find some of the selected ones.

Reconstruction of 13Fr Origen Biomedical Double Lumen Cannula

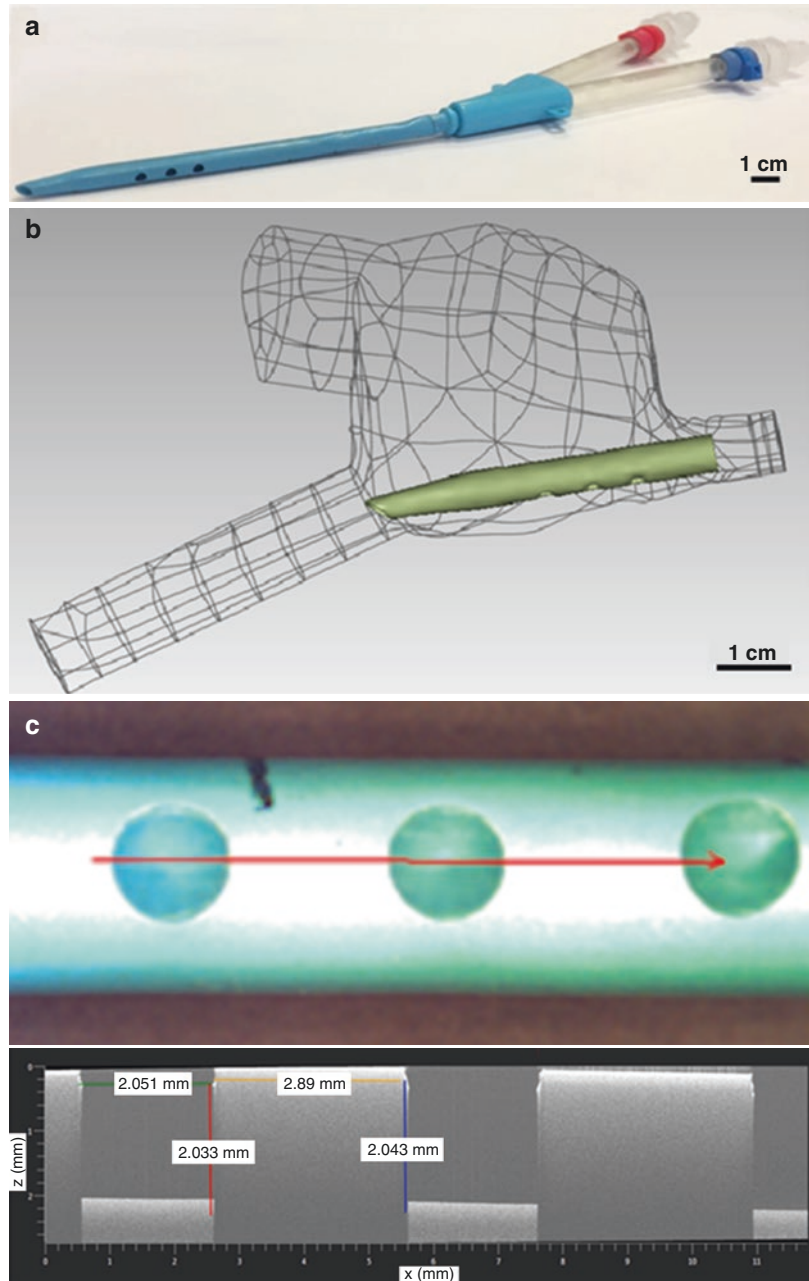
A clinically approved 3D model of the standard double lumen cannula (13Fr Origen Biomedical, Austin, Texas, USA) was scanned using micro-CT with a resolution of 75 μm. Since micro-CT can resolve structural features as small as a few micrometers in size, it is more advantageous than the conventional CT. 3D reconstruction of

the cannula was obtained from these scans using 3D Slicer software. Figure 11.1a, b shows the double lumen cannula and the reconstruction result, respectively. The scanning parameters were 110 kV and 1.56 mA with an exposure time of 4.8 s. To validate our scan results, we imaged the cannula under optical coherence tomography (OCT) (Thorlabs Telesto 2). A realistic reconstructed 3D model is the basis for detailed CFD analysis of DLC. For accurate performance evaluation, the imaging method should be able to capture the critical features of DLC such as expiration holes, infusion port, and diameter. 3D model can be influenced by the parameters used during reconstruction such as thresholding. In order to validate and compare our 3D model, we made some measurements of critical DLC structures using OCT. We made some measurements such as the diameter of the expiration holes on the cannula, and we proved that the reconstruction of micro-CT scans was consistent with the OCT result (see Fig. 11.1c).

Reconstruction of 13Fr Avalon Elite Bi-caval Dual Lumen Cannula

Another cannula that we scanned was 13Fr Avalon Elite bi-caval dual lumen cannula (Rastatt, Germany) (see Fig. 11.2a) with a resolution of 125 μm. Avalon cannula is the most frequently used cannula in clinical practice. The design consists of proximal and distal aspiration holes that are strategically placed to drain the deoxygenated blood from inferior and superior venae cavae, while infusion hole directs the oxygenated blood to tricuspid valve. This specific cannula has metal parts inside. Therefore, before scanning we applied a 1-mm-thick bronze filter to the metal part so that the reflections of the metal are prevented. The scanning parameters for the part with bronze filter were 110 kV and 16.43 mA with an exposure time of 7.3 s. For the part without the bronze filter, we applied 110 kV and 8.88 mA with an exposure time of 7.3 s. 3D reconstruction of the cannula was obtained from these scans using 3D Slicer

Fig. 11.1 (a) 13Fr Origen Biomedical double lumen cannula, (b) reconstructed double lumen cannula placed in the atrium, (c) measurements of the expiration holes under optical coherence tomography (OCT)



software (see Fig. 11.2b). For accurate CFD analysis, we needed to scan the tip at a higher resolution to capture critical components such as infusion hole and aspiration holes. Therefore,

we scanned only the lower part once again and obtained the below reconstruction with a resolution of $75\ \mu\text{m}$ in which drainage and infusion ports are more visible (see Fig. 11.2c).

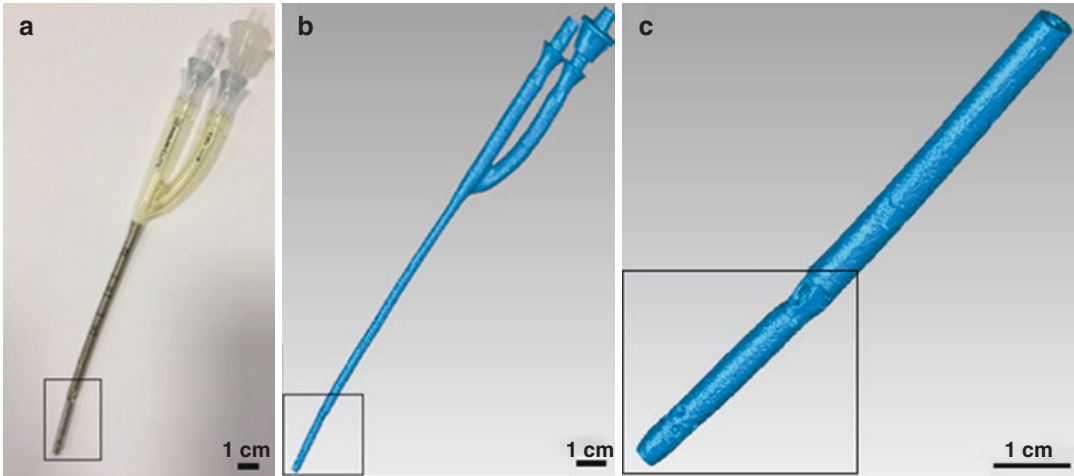


Fig. 11.2 (a) Avalon Elite bi-caval dual lumen cannula, (b) reconstructed dual lumen cannula, (c) reconstructed lower part with a higher resolution

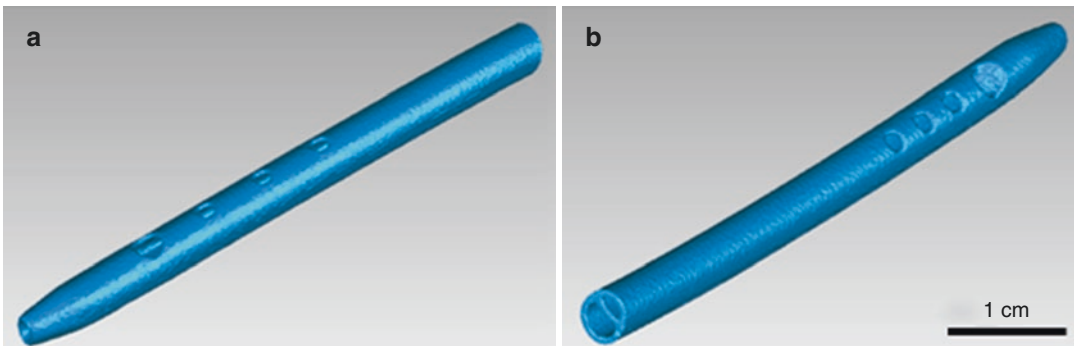


Fig. 11.3 (a) Reconstructed front view, (b) reconstructed back view of Maquet double lumen cannula

Reconstruction of 13Fr Maquet Double Lumen Cannula

Lastly, we scanned 13Fr Maquet double lumen cannula (Rastatt, Germany) with a resolution of $75\ \mu\text{m}$. This design represents a different design paradigm and consists of multiple infusion and aspiration holes. The scanning parameters were 110 kV and 1.56 mA with an exposure time of 4.8 s. Figure 11.3 shows the front view and the back view of the cannula. When we view it from the back, we see that the single tube separates into two so that the oxygenated blood and the deoxygenated blood are not mixed.

11.2.1.2 Adult Membrane Oxygenator (Sorin Compactflo Evo Oxygenator)

A membrane oxygenator is a device which removes carbon dioxide from and adds oxygen to the blood (see Fig. 11.4a). The working principle of the oxygenators has been tested; however the complex flow field inside them is still unknown. Therefore, we scanned an adult membrane oxygenator with a resolution of $100\ \mu\text{m}$ to perform a CFD analysis. The scanning parameters were 110 kV and 7.56 mA with an exposure time of 6.2 s. The raw data of the oxygenator can be seen in Fig. 11.4b. The outer body and

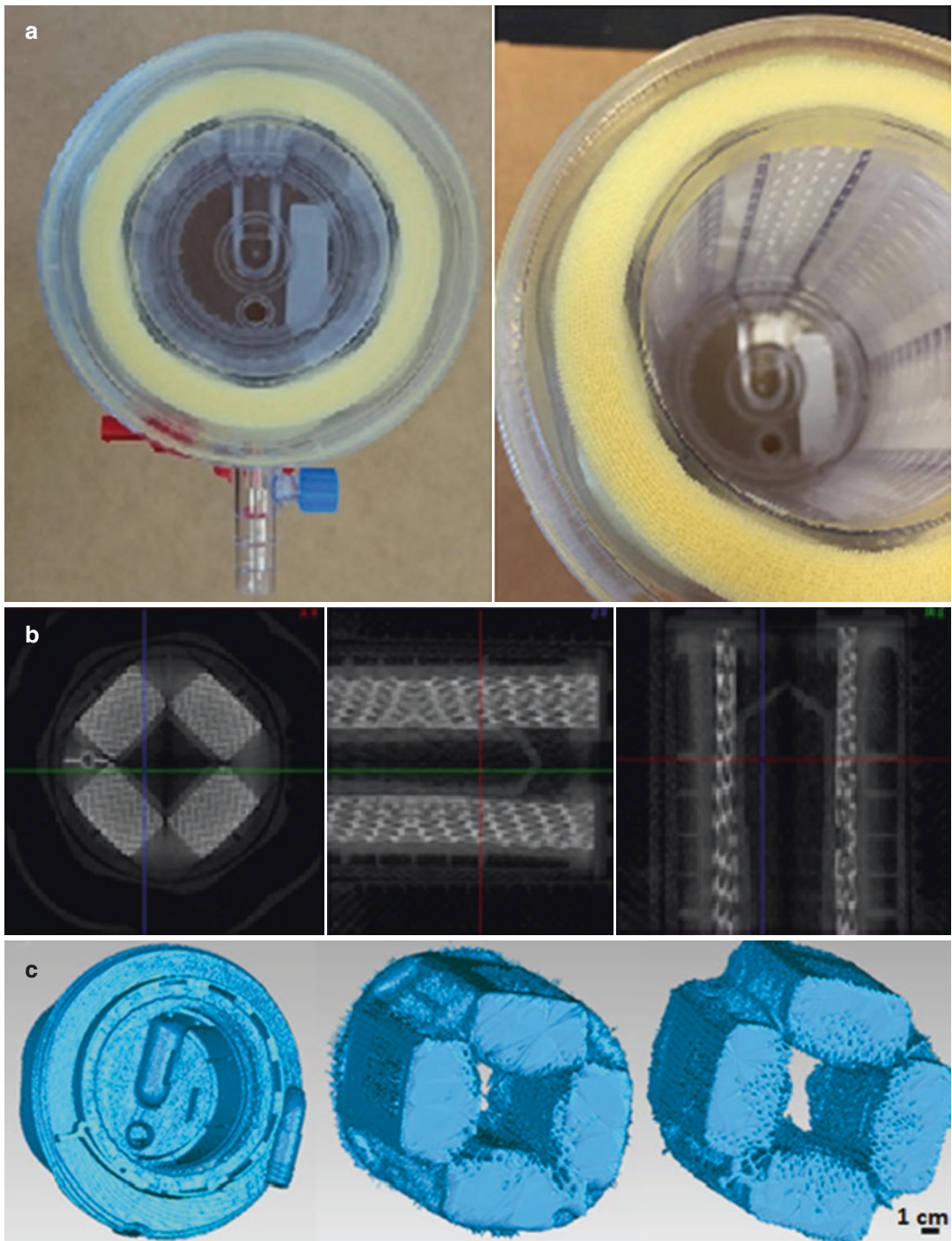


Fig. 11.4 (a) Sorin compactflo evo oxygenator, (b) raw data of the oxygenator, axial, sagittal, and coronal view; (c) reconstructed oxygenator in three parts—lid with water connections, heat exchanger aluminum plates

the heat exchanger aluminum plate were correctly reconstructed and displayed (see Fig. 11.4c). Yet, we were not able to differentiate the fibers through which blood flows with this system. A more precise system such as Bruker Skyscan micro-CT will serve better for rendering the internal volume of a sample up to resolution of 10 μm .

11.2.1.3 Aortic-Turbine Venous-Assist Device

In our earlier study [14], we have developed a prototype of an implantable integrated aortic-turbine venous-assist (iATVA) system that can be used for Fontan patients, and we have evaluated the hemodynamic performance of the device. This device does not require an external drive power, and it maintains low venous pressure. In our future studies, we will plan a CFD analysis for the device. Therefore, we first disassembled the device (see Fig. 11.5a), and then we scanned the device with a resolution of 75 μm and reconstructed the device accordingly (see Fig. 11.5b). The scanning parameters were 110 kV and 3.2 mA with an exposure time of 5.3 s.

11.2.2 Selected Applications of Micro-CT in Animal Models

11.2.2.1 Reconstruction of the Rabbit Carotid Artery

In rabbit model carotid artery imaging, our group was able to examine the effect of physiological changes on lumen due to flow. In our study, in vivo lumen imaging with a resolution of 75 μm was performed by using contrast agent with micro-CT. Studies performed on rabbit and mouse models usually involve injecting contrast agent into the aortic outlet by entering the femoral artery with a cannula and imaging performed simultaneously [15]. This method requires specialized personnel and equipment.

There are many other studies performed by contrast agent injection from ear vein to monitor the carotid artery [16]; however we were not able to monitor the carotid artery with this methodology as the contrast agent spreads all over the body. Another method is using the main artery of the ear in rabbits [17]. Therefore, we used the ear main artery to inject the contrast agent, and with this method we were able to view the carotid artery successfully (see

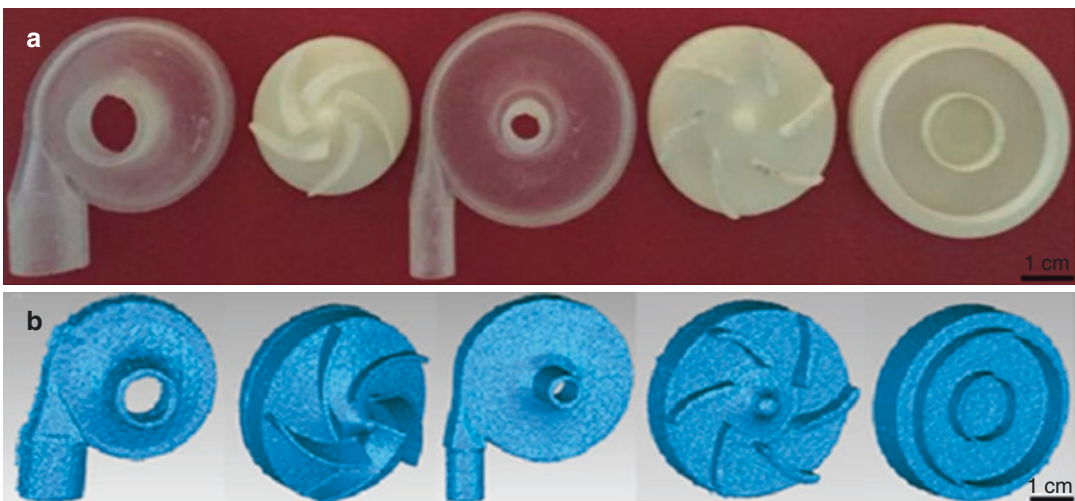


Fig. 11.5 (a) Disassembled aortic-turbine venous-assist device in five parts, (b) reconstruction of the device after disassembly

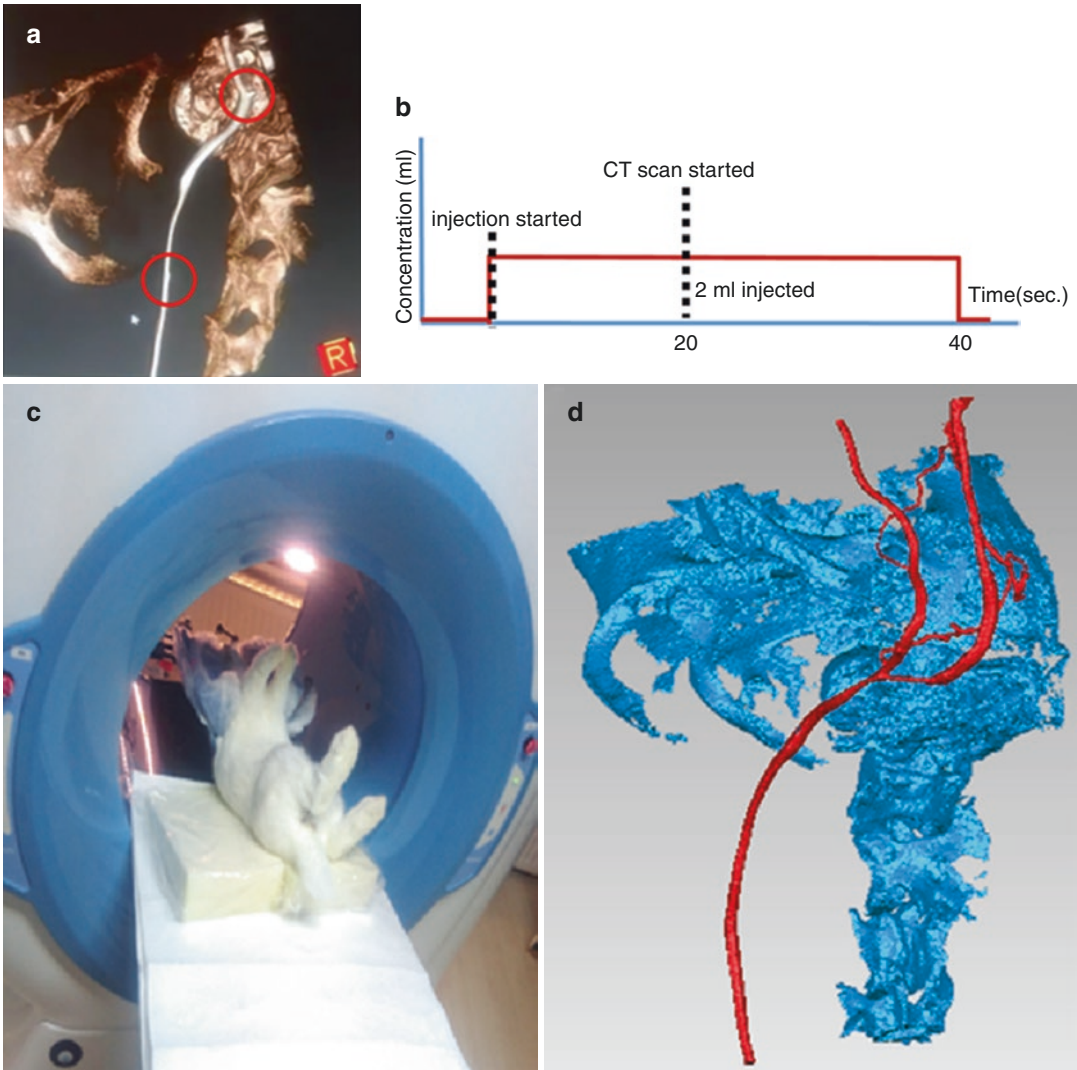


Fig. 11.6 (a) Vein imaging: branch connections shown with red markers, (b) contrast agent injection rates and timing, (c) rabbit positioned on the micro-CT table, (d) reconstructed rabbit model. Carotid artery shown with red color

Fig. 11.6a). Desired arterial images were taken from the main ear artery, and the arterial line can be seen by diffusing the contrast material. Syringe pump is used for contrast agent injection, and optimized injection rates are shown in Fig. 11.6b. Kopaq 300 mg/mL contrast agent was injected at a rate of 3 mL/min for 35 s from

the left ear main artery [18]. Scanning started at 20th s. Total injection volume was 2 mL and the duration was 35 s. The scanning parameters were 110 kV and 2.08 mA with an exposure time of 7.3 s. Rabbit positioned on the micro-CT table and the reconstruction result can be seen in Fig. 11.6c, d.

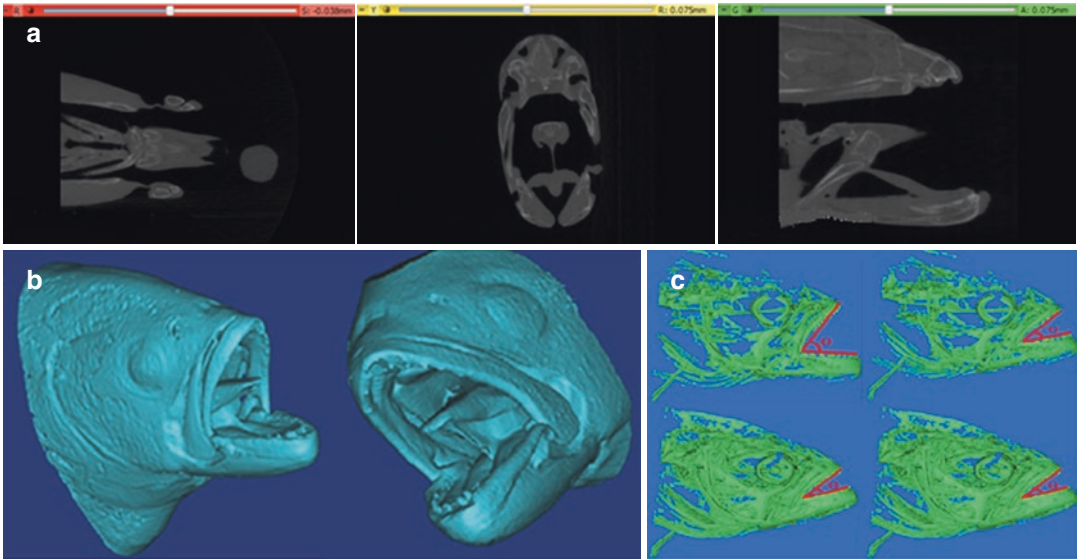


Fig. 11.7 (a) Raw data of the blue fish, axial, sagittal, and coronal view; (b) reconstruction result of the blue fish; (c) bluefish mouth opening in different angles and diameters—top left $\theta = 53.03$ -degree, $D = 22$ mm; top

right $\theta = 38.5$ -degree, $D = 13$ mm; bottom left $\theta = 24.5$ -degree, $D = 9.7$ mm; bottom right $\theta = 19.4$ -degree, $D = 5.8$ mm

11.2.2.2 Fish Feeding

To investigate the feeding of bluefish (*Pomatomus saltatrix*) and obtain the mouth morphology, we scanned it with a resolution of $75\ \mu\text{m}$. The scanning parameters were 110 kV and 3.46 mA with an exposure time of 6.3 s. Detailed analysis can be conducted by running CFD on the 3D models obtained from reconstructions. Figure 11.7a, b shows the raw data and the reconstruction results, respectively. Moreover, we measured different angles of opening and the diameters of the mouth which can be seen in Fig. 11.7c.

11.3 Discussion and Conclusion

In the previous chapters, we have briefly mentioned some of the fundamental medical usages of micro-CT and applications that we have utilized. Yet, the use of micro-CT can be extended to other applications. For instance, in [19], authors developed a technique to evaluate the size of stent cells with high accuracy using micro-CT. They investigated five different stents and concluded that the sizes differ significantly. Therefore, an appropriate stent should be selected when applying a

particular bifurcation stenting technique. Jamil et al. used micro-CT reconstructed model of DLC and identified several design limitations of the DLC [20]. It was identified that there was imbalanced flow among the drainage holes and very little flow passed through the tip of the cannula. Furthermore, in [21], authors have evaluated post-bifurcation coronary stent morphology in vitro using dual-source CT, and they validated the results with micro-CT. In addition, Vanommeslaeghe et al. [22] utilized micro-CT to quantify coagulation in fibers of hemodialyzers to accurately determine the thrombogenicity of dialyzers used during hemodialysis. They obtained the images at a resolution of $25\ \mu\text{m}$ and counted the open, non-coagulated fibers.

Due to its ability to visualize noninvasively with high spatial resolution, micro-CT imaging provides internal analysis of samples which have non-accessible internal components (e.g., blood oxygenator) or multi-material components (e.g., metal cannula). Thus, micro-CT allows quality control of devices, and functional mechanisms can be further investigated. As a result, defects can be reduced, and manufacturing process can be improved.

References

1. Boerckel JD, Mason DE, McDermott AM, Alsberg E. Microcomputed tomography: approaches and applications in bioengineering. *Stem Cell Res Therapy*. 2014;5(6):144.
2. D'Onofrio C, et al. Three dimensional computational model of a blood oxygenator reconstructed from micro-CT scans. *Med Eng Phys*. 2017;47:190–7.
3. Pierce EL, Bloodworth CH, Naran A, Easley TF, Jensen MO, Yoganathan AP. Novel method to track soft tissue deformation by micro-computed tomography: application to the mitral valve. *Ann Biomed Eng*. 2016;44(7):2273–81.
4. Kim JS, Min J, Recknagel AK, Riccio M, Butcher J. Quantitative three-dimensional analysis of embryonic chick morphogenesis via microcomputed tomography. *Anat Rec (Hoboken)*. 2011;294(1):1–10.
5. Wang Y, et al. Aortic arch morphogenesis and flow modeling in the chick embryo. *Ann Biomed Eng*. 2009;37(6):1069–81.
6. Ritman EL. Micro-computed tomography of the lungs and pulmonary-vascular system. *Proc Am Thorac Soc*. 2005;2(6):477–80.
7. Kriete A, Breithecker A, Rau WD. 3D imaging of lung tissue by confocal microscopy and micro-CT. *Proc SPIE*. 2001;4257:8.
8. Lin ASP, Barrows TH, Cartmell SH, Guldborg RE. Microarchitectural and mechanical characterization of oriented porous polymer scaffolds. *Biomaterials*. 2003;24(3):481–9.
9. Badea CT, Hedlund LW, Cook J, Berridge BR, Johnson GA. Micro-CT imaging assessment of dobutamine-induced cardiac stress in rats. *J Pharmacol Toxicol Methods*. 2011;63(1):24–9.
10. Badea CT, Johnston S, Johnson B, Lin M, Hedlund LW, Johnson GA. A dual micro-CT system for small animal imaging. *Proc SPIE*. 2008;6913:691342.
11. Kim AJ, et al. Micro-computed tomography provides high accuracy congenital heart disease diagnosis in neonatal and fetal mice. *Circ Cardiovasc Imaging*. 2013;6(4):551–9.
12. Sangaralingham SJ, et al. Cardiac micro-computed tomography imaging of the aging coronary vasculature. *Circ Cardiovasc Imaging*. 2012;5(4):518–24.
13. Makdisi G, Wang IW. Extra corporeal membrane oxygenation (ECMO) review of a lifesaving technology. *J Thoracic Dis*. 2015;7(7):E166–76.
14. Pekkan K, et al. In vitro validation of a self-driving aortic-turbine venous-assist device for Fontan patients. *J Thoracic Cardiovas Surg*. 2018;156(1):292–301.e7.
15. Thiex R, et al. Haemorrhagic tracheal necrosis as a lethal complication of an aneurysm model in rabbits via endoluminal incubation with elastase. *Acta Neurochir*. 2004;146(3):285–9.
16. Kim M-S, et al. Intravenous contrast media application using cone-beam computed tomography in a rabbit model. *Imaging Sci Dent*. 2015;45(1):31–9.
17. Miskolczi L, Nemes B, Cesar L, Masanari O, Gounis MJ. Contrast Injection via the central artery of the left ear in rabbits: a new technique to simplify follow-up studies. *Am J Neuroradiol*. 2005;26(8):1964.
18. Pannu HK, Thompson RE, Phelps J, Magee CA, Fishman EK. Optimal contrast agents for vascular imaging on computed tomography: iodixanol versus iohexol. *Acad Radiol*. 2005;12(5):576–84.
19. Mortier P, et al. Comparison of drug-eluting stent cell size using micro-CT: Important data for bifurcation stent selection. *EuroIntervention*. 2008;4:391–6.
20. Muhammad J, et al. Patient-specific atrial hemodynamics of a double lumen neonatal cannula in correct caval position. *Artif Organs*. 2018;42(4):401–9.
21. Eom H-J, et al. Coronary bifurcation stent morphology in dual-source CT: validation with micro-CT. *Int J Card Imaging*. 2016;32(11):1659–65.
22. Vanommeslaeghe F, Van Biesen W, Dierick M, Boone M, Dhondt A, Eloot S. Micro-computed tomography for the quantification of blocked fibers in hemodialyzers. *Sci Rep*. 2018;8(1):2677.



Applications of Micro-CT Technology in Endodontics

12

Marco A. Versiani and Ali Keleş

12.1 Introduction

In dentistry, a specialty is an area that has been formally recognized by an official dental association as meeting specified requirements aiming to protect the public and improve the quality of care. There are essential dental specialist types, including oral and maxillofacial radiology, dental public health, oral and maxillofacial pathology, oral and maxillofacial surgery, orthodontics, pediatric dentistry, periodontics, prosthodontics, and endodontics. However, depending on the country, there may be different types of specialties available for those seeking a career in dentistry.

From the Greek words “endo” (inside) and “odont” (tooth), endodontics is a specialty of dentistry concerned with the morphology, physiology, and pathology of the human dental pulp and periradicular tissues. Its study and practice encompass the basic and clinical sciences, including the biology of the normal pulp and the etiology, diagnosis, prevention, and treatment of diseases and injuries of the pulp and associated periradicular conditions [1]. However, to understand how to improve knowledge regarding the

endodontic treatment procedures, it is important to know basic concepts about the anatomy of teeth.

A tooth is made of up of a number of highly specialized tissues. The enamel is the hard outer covering visible in the mouth. Below the enamel there is a less hard and porous material named dentin that makes up the majority of the tooth (Fig. 12.1a). The root of the tooth is often twice the length of the crown and is supported inside the jaw bone by a ligament. Inside the body of the tooth is the pulp space (Fig. 12.1b), which contains a connective tissue, called dental pulp. The pulp is an important tissue for tooth growth and development. It contains blood vessels, nerves, and cells, providing sensory and protective functions for the tooth during its lifetime. The pulp extends from an area within the crown of the tooth called the pulp chamber to the tip of the roots (Fig. 12.1b), where it connects to the surrounding tissues [2].

Teeth can be damaged by dental decay, fractures, or other reasons which may expose the pulp to bacteria from saliva. Unless treated, the problem may increase, and symptoms such as pain and swelling can occur as the nerves and blood vessels become progressively more damaged, and eventually the pulp space becomes completely infected with bacteria. An inflammatory response to the bacteria occurs, resulting in damage to the bone around the root, often appearing as a dark shadow at the tip of the root on a dental radiograph (Fig. 12.2a).

M. A. Versiani (✉)
Department of Oral Health, Brazilian Military Police,
Minas Gerais, Brazil

A. Keleş
Faculty of Dentistry, Department of Endodontics,
Ondokuz Mayıs University, Samsun, Turkey

Fig. 12.1 External and internal tooth components. (a) A tooth is basically made up of two parts: the crown and the root. Different tissues make up each tooth: the enamel, the dentin that supports the enamel, and the pulp that is a soft tissue located within a tooth, in a place called pulp cavity (b) that is divided into root canal and pulp chamber

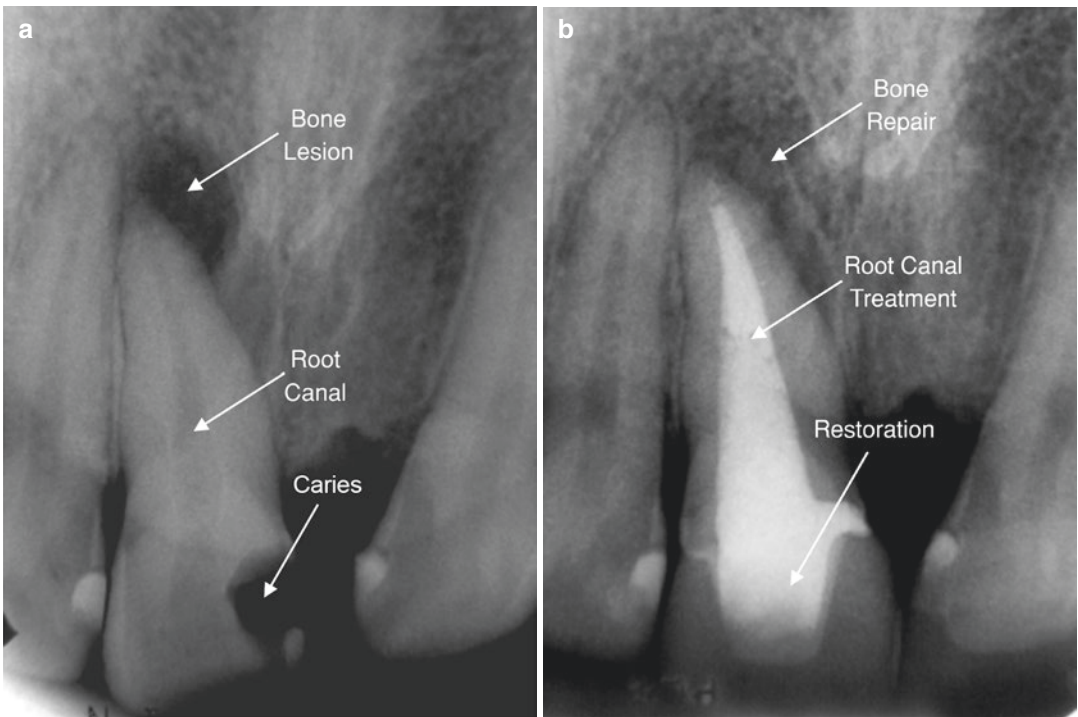
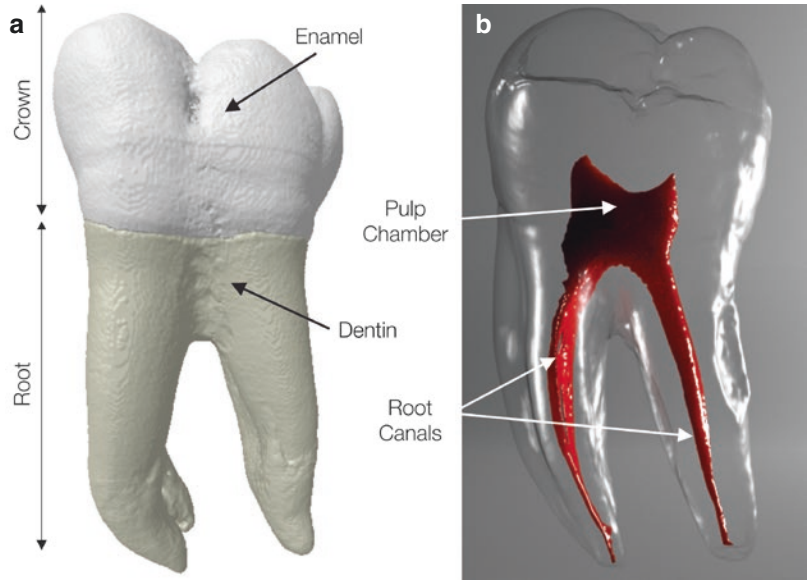


Fig. 12.2 Root canal treatment of a maxillary right central incisor presenting chronic apical periodontitis (bone lesion). (a) Microorganisms gained entry into root canal space via the caries process. The infection was not arrested, and pulp tissue necrosis led to the infection of

the entire root canal space, resulting in damage to the bone around the root which appeared as a dark shadow on the radiograph; (b) after root canal treatment and proper restoration of the tooth's crown, an evidence bone repair can be seen after a 6-month follow-up

Once it happens, there are only two ways to resolve it: either extract the tooth or carry out a procedure called a root canal or endodontic treatment.

Endodontic treatment can often be performed in one, two, or more visits and involves the following steps:

1. An access cavity is made on the occlusal surface of posterior teeth or on the lingual/palatal surface of anterior teeth to reach the pulp space and allow the location of the root canals. There may be a number of these canals in a tooth, depending on what type of tooth is being treated. The root canals can vary in size but are generally small.
2. Once access has been gained to the pulp space and root canals have been located, they are enlarged using a variety of instruments followed by the delivery of irrigant solutions to clean the pulp space. It is currently thought that preparing and irrigating the canals to its end give the best chance to the treatment be successful.
3. The canals are irrigated with a variety of solutions aiming to thoroughly clean the root canal space. Generally, irrigation is performed with a needle attached to syringe, although a variety of techniques are currently available. The irrigation process removes residual infected tissues, debris created during the preparation of the canals, and also bacteria.
4. Once the entire canal space has been enlarged and cleaned, it can be filled with a suitable filling material. The most common filling material is called gutta-percha. The basic technique consists in inserting a number of gutta-percha cones together with a proper sealer into the root canals until the prepared space is completely filled. It is currently thought that a well-filled canal can prevent bacteria from infecting the tooth again.
5. Following the filling of the root canals, the tooth can be properly restored with a suitable restoration to seal the root canals, restore the

tooth to its function, and further protect it from bacteria.

In summary, root canal treatment aims to remove the inflamed or infected pulp, followed by carefully cleaning and shaping the inside of the root canal and then filling the space. Afterward, a restoration is placed on the tooth in order to protect and restore it to its function. Once the treatment has been completed, and following a period of healing, the tissues around the root return to normal, and radiographs will show the resolution of any “shadow” (bone lesion) caused by bacterial contamination (Fig. 12.2b). Thus, endodontic treatment saves teeth that would otherwise need to be extracted. Although the pulp is removed, the treated tooth remains in function, nourished by the surrounding tissues. In the future, however, a new trauma, deep decay, or a loose, cracked, or broken filling may allow a new infection. In some cases, the clinician may also discover additional canals that were not be treated during the first treatment. In these situations, a new endodontic treatment (a procedure called retreatment) or surgery may be carried out. The purpose of this chapter is to discuss advancements in endodontic research using micro-CT technology in order to improve the root canal treatment in clinics.

12.2 Micro-CT Technology in Endodontics

In the twentieth century, technological advancements allowed for a considerable range of techniques to be successfully employed to visualize the anatomy of the human teeth, including three-dimensional wax models, digital radiography, resin injection, radiographic methods with radiopaque contrast media, and scanning electron microscopy, among others [3]. Undoubtedly, these techniques have shown great potential in endodontic research, and their findings have had a noteworthy influence on clinical practice as well as on dental education. However, while most

of these methods require the partial or even full destruction of the studied samples, resulting in irreversible changes in the specimens and many artifacts, others provide only a two-dimensional image of a three-dimensional structure [4]. These inherent limitations have been repeatedly discussed, encouraging the search for new methods with improved possibilities.

In 1986, Mayo and colleagues [5] introduced computer-assisted imaging in the field of endodontic research by injecting contrast medium into the root canal of extracted teeth and taking six radiographs of each tooth from defined angles. By combining all six views, a mathematically determined 3D representation of the canals was obtained. From this data, the volume and diameters of the root canals were determined using a computerized video image processing program.

From the early to mid-1990s, the first application of a computerized and digital approach based on micrographs of grinding sections was proposed. Using diamond and silicon carbide disks, Blašković-Šubat et al. [6] cross-sectioned extracted teeth and photographed these sections using a camera attached to a stereomicroscope. Each photograph was then digitized, the shape manually outlined, and the resulting stacks of labeled shapes were rendered in 3D using dedicated software. Although partly digital, this approach still required the destruction of the samples under study [7].

The invention of X-ray computed tomography (CT) provided a significant step forward in diagnostic medicine. CT produces a two-dimensional map of X-ray absorption into a two-dimensional slice of the subject. This is achieved by taking a series of X-ray projections through the slice at various angles around an axis perpendicular to the slice. From this set of projections, the X-ray absorption map is computed. By taking a number of slices, a three-dimensional map is produced. In 1990, Tachibana and Matsumoto [8] were the first authors to suggest and evaluate the feasibility of CT imaging in endodontics. However, because of high costs, inadequate software, and low spatial resolution, they concluded that CT had only limited usefulness in endodontics as the produced images were not accurate. Further

improvements in digital nondestructive image systems have also been used to evaluate root canal anatomy, including magnetic resonance microscopy, tuned-aperture computed tomography, optical coherence tomography, and volumetric or cone beam CT [3]. These methods, however, are hampered by insufficient spatial resolution for the study of root canal anatomy [9].

A decade after the CT scanner was developed, Elliott and Dover [10] built the first high-resolution X-ray micro-computed tomographic device. The term “micro” in this new device was used to indicate that the pixel sizes of the cross sections were in the micrometer range, the machine was smaller in design compared to the human version, and it was indicated to model smaller objects. Applications of micro-CT technology to endodontic research were recognized 13 years after its development and described in a paper entitled *Microcomputed Tomography: An Advanced System for Detailed Endodontic Research* [11]. In this article, the authors evaluated the reliability of using micro-CT in the reconstruction of the external and internal anatomy of four maxillary first molars, assessing the morphological changes in the root canal after instrumentation and obturation, using an isotropic resolution of 127 μm . The authors concluded that micro-CT had potential as an advanced system for research and also provided a foundation for micro-CT as an exciting, interactive educational tool.

With further developments in micro-CT scanners, improvements in the speed of data collection, resolution, and image quality yielded greater accuracy compared with the first studies using computational methods, with voxel sizes decreasing to less than 40 μm [9, 12]. Dowker et al. [9] demonstrated the feasibility of this technology for endodontic research using a resolution of 38.7 μm to evaluate the morphological changes of the root canal after different steps of endodontic treatment. The authors concluded that micro-CT could offer the possibility of learning tooth morphology by an interactive study of surface-rendered images and slices and contribute to the development of virtual reality techniques for endodontic teaching.

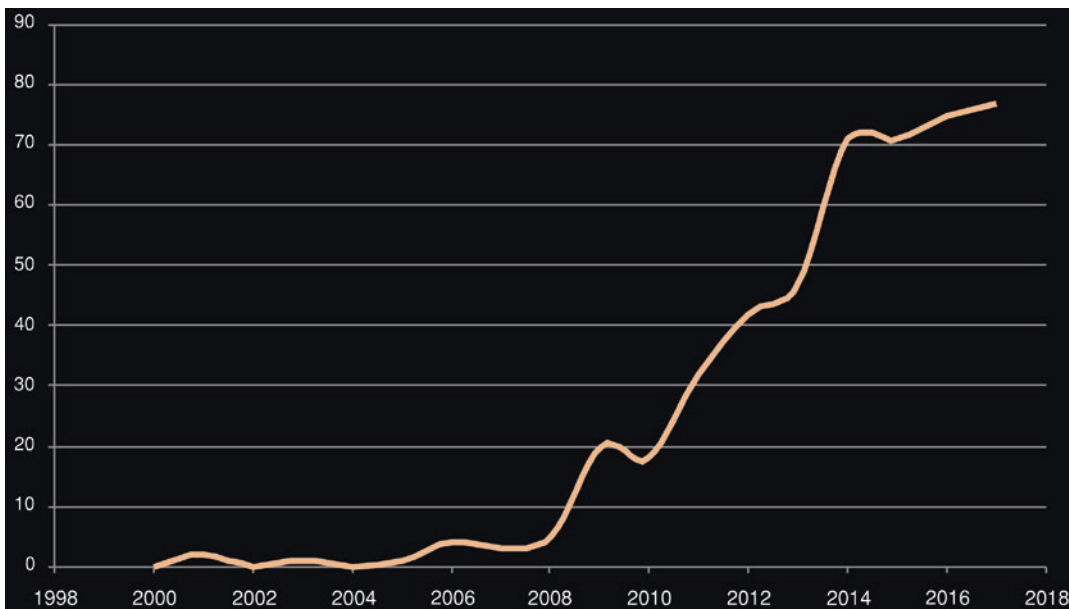


Fig. 12.3 Graphic showing the increasing number of publications using micro-CT in endodontics in the last decade

The first attempt to use micro-CT for a quantitative analysis of root canal anatomy was done by Bjørndal et al. [13]. The authors correlated the shape of the root canals to the corresponding roots of five maxillary molars scanned at a pixel size of 33 μm . In the following year, Peters et al. [14] studied the potential of micro-CT for detailing the root canal geometry of 12 maxillary molars regarding some morphological parameters including volume, surface area, diameter, and structured model index.

In the last decade, micro-CT has gained increasing popularity in endodontics (Fig. 12.3). This noninvasive, nondestructive, high-resolution technology allows the three-dimensional study of the root canal system and can be used to understand its influence on the different treatment/retreatment procedures, by reconstructing digital cross sections of the teeth, which can be stacked to create 3D volumes. These volumes can be used to generate computerized images of specimens that can be manipulated, or measured, to reveal both internal and external morphologies. Nowadays, micro-CT technology is considered the most important and accurate research tool to the study of root canal anatomy [4, 14, 15]. Therefore, a specific chapter regarding the applications of micro-CT in endodontics is justified in this book.

Conversely, given that scanning and reconstruction procedures take considerable time, the technique generates excessive radiation and is not suitable for clinical use. Moreover, the equipment is expensive, and the complexity of the technical procedures requires a steep learning curve and an in-depth knowledge of dedicated software. It is important to point out that the technical procedures related to the micro-CT methodology with the aim of evaluating aspects related to the morphological analysis of root canal anatomy are complex, and a thorough discussion is beyond the scope of this chapter. However, understanding some parameters is desirable to ensure better comprehension of the possibilities of using micro-CT as a tool for endodontic teaching and researching.

12.3 Anatomy of the Root Canal System

From the Latin *anatomia* for dissection and from the Greek *anatome*, where *ana* means “up” and *temnein* means “to cut,” this word represents the study of the body and the determination of the regions in an organism that are to be considered its parts [3]. As Hippocrates postulated that anat-

omy is the foundation of medicine, the anatomy of the root canal is also the fundamental basis of the endodontic specialty [3]. Consequently, a thorough understanding of the canal morphology and its variations in all groups of teeth is a basic requirement for successful endodontic treatment.

The main role of laboratory-based studies is to develop well-controlled conditions that are able to reliably compare certain factors. The main confounding factor of *ex vivo* studies is the anatomy of the root canal system under investigation. Consequently, the results might demonstrate the effect of canal anatomy rather than the variable of interest. In endodontics, a variety of extracted human and animal teeth have been used in laboratory-based experiments. The reproduction of the clinical situation, however, might be regarded as the major advantage of using extracted human teeth. On the other hand, the wide range of variations in three-dimensional root canal morphology makes standardization difficult. Thus, if selection bias is not taken into account when the sample is selected, then certain conclusions drawn might be incorrect. On the basis of micro-CT data, it is possible to further improve sample selection using established morphological parameters to provide a consistent baseline. As the state of current knowledge on root canal anatomy advances rapidly, the clarification of the purposes of sample selection protocols may assist investigators to arrive at meaningful conclusions [4].

12.3.1 Qualitative Evaluation

The anatomy of the root canal system is often complex [16], and because of the large amount of dissimilarities in the canal configuration among the teeth, different classification systems have been proposed [17, 18]. Traditionally, the configuration of the root canal system has been based on the number of root canals that begin at the pulp chamber floor, extend through the length of the root, and open through the apical foramen [16]. Weine et al. [17] were the first to categorize

the root canal configurations within a single root into four types, depending on the division pattern of the main root canal along its course from the pulp chamber into the root apex. Later, Vertucci et al. [18] developed a classification system based on the evaluation of 200 cleared maxillary second premolars in which the pulp cavities were stained with dye; they found eight canal configuration types, which were more complex than those described by Weine and co-workers. Despite these efforts, additional canal configurations have been continuously reported by several authors within different populations. According to a comprehensive review carried out by Versiani and Ordinola-Zapata [19] on root canal morphology using micro-CT, a total of 37 root canal configuration types have been described, which probably include the most common anatomical configurations that can be observed in a single root. From a clinical point of view, it is important for the clinician to be aware of the variability in the root canal configuration in order to implement an appropriate treatment plan and increase the success rate of endodontic procedures [16]. Qualitative 3D analysis can also be applied to evaluate the presence and location of other anatomical landmarks such as isthmuses, accessory canals, and apical ramifications. Therefore, because of the nondestructive nature of micro-CT technology, it can be used for a precise and accurate qualitative characterization of the root and root canal anatomy in different groups of teeth [20].

Most of the micro-CT studies on root canal anatomy evaluated anatomical variations present in specific groups of teeth, such as the second canal in the mesiobuccal root of maxillary first molars [21], three-rooted mandibular premolars [22] and molars [23], four-rooted maxillary second molars [15], two-rooted mandibular canines [24] and premolars [25], C-shaped canals in mandibular premolars [26] and molars [27], radicular grooves [28], and isthmuses [29, 30]. Other authors have evaluated the anatomical configuration of mandibular incisors [31], mandibular canines [4], mandibular first premolars [32], and maxillary molars [33].

12.3.2 Quantitative Evaluation

The digital images acquired by micro-CT are a geometric representation of the internal and external microstructure (morphology) of teeth. Therefore, a morphometric characterization of the root canal system can be performed through geometric concepts and morphological operations applied to the binarized (segmented) images. Root canal morphometry has been typically described using two- and three-dimensional quantitative parameters, as described in Table 12.1.

12.3.2.1 2D Parameters

In the first research studies on root canal anatomy, quantitative morphological data were obtained from measuring parameters such as area, diameter, and perimeter, acquired from a few cross sections of the roots. Images were recorded together with a scale that allowed for further calibration of a dedicated software. Then, the operator was responsible for carefully tracing the contour of the structure to be measured by clicking and releasing the computer mouse button until the results were displayed. Thus, the outcome of studies on root canal anatomy using

Table 12.1 2D and 3D morphometric parameters used to evaluate root canal geometry

<i>2D parameters</i>	<i>Definition</i>	<i>Measurement</i>
Area	The extent of a two-dimensional root canal shape in the plane	Pratt algorithm [34]
Perimeter	Path that surrounds the two-dimensional shape of the root canal	Pratt algorithm [34]
Diameter	The largest distance formed between two opposite parallel lines tangent to root canal boundary	Major diameter: distance between the two most distant pixels in the binarized canal Minor diameter: the longest chord through the root canal that can be drawn in the direction orthogonal to that of the major diameter
Aspect ratio	Ratio of the geometric shape sizes in different canal dimensions	Ratio of the major and minor diameters of the root canal
Roundness	Cross-sectional appearances of the root canal	$4A/(\pi \cdot [d_{\max}]^2)$, where A is the area and d_{\max} is the major diameter. The value of roundness ranges from 0 to 1, with 1 signifying a circle
Form factor		$(4 \cdot \pi \cdot A)/P^2$, where A and P are object area and perimeter, respectively. Elongation of individual objects results in smaller values of form factor
<i>3D parameters</i>	<i>Definition</i>	<i>Measurement</i>
Volume	Quantity of 3D space enclosed by a closed surface, i.e., the volume of binarized root canal within the volume of interest (VOI)	Marching cubes method [35]
Surface area	Measure of the total area that the surface of the object occupies, i.e., the surface area of binarized root canal within the volume of interest (VOI)	Marching cubes method [35]
Structure model index (SMI)	3D geometry of an object by an infinitesimal enlargement of its surface	$6 \cdot [(S' \cdot V)/S^2]$, where S is the object surface area before dilation and S' is the change in surface area caused by dilation. V is the initial, non-dilated object volume. An ideal plate, cylinder, and sphere have SMI values of 0, 3, and 4, respectively [36]

sectioning roots was highly influenced by the operator’s experience. Conversely, using micro-CT technology, quantitative parameters of root canals can be accurately measured and plotted on graphs in hundreds of slices at once (Fig. 12.4). Another advantage of this method is the possibility of describing the cross-sectional appearance of the root canal mathematically by

means of two morphometric parameters: form factor and roundness (Fig. 12.5). The evaluation of root canal shape using these parameters in single-rooted canines has demonstrated different cross-sectional forms throughout the root canal [4]. In the past, the canal shape was qualitatively classified in sectioned roots as round-, flat-, oval-, or irregular-shaped [37]. Despite its appli-

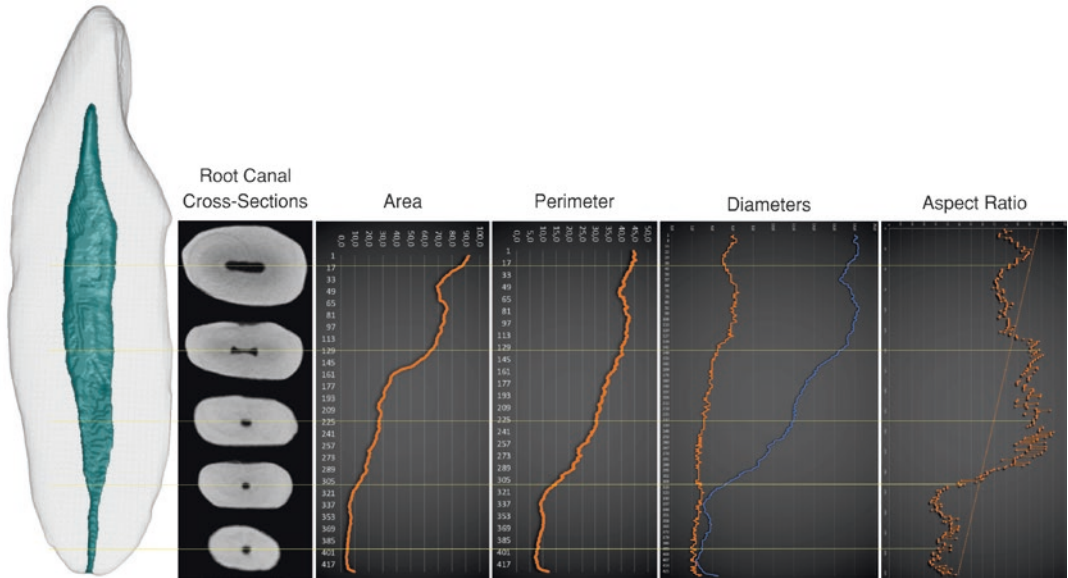
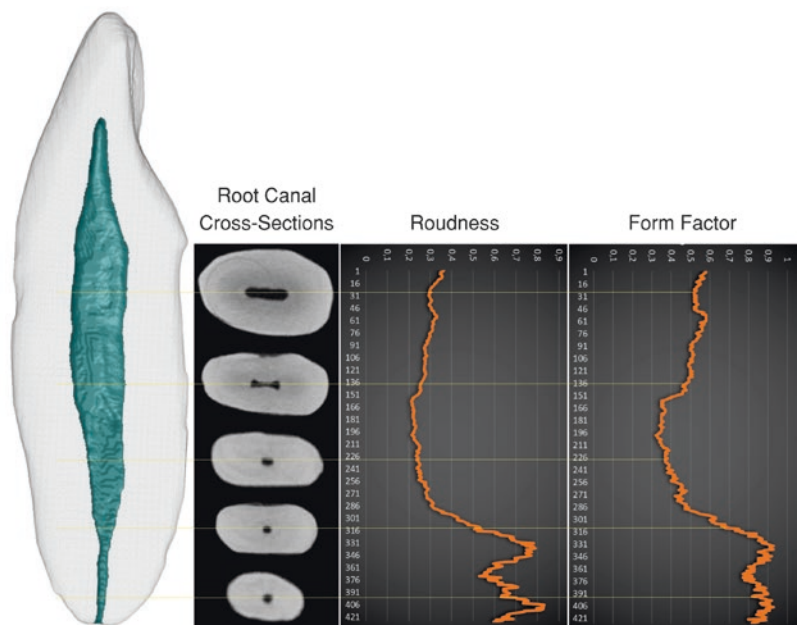


Fig. 12.4 Using micro-CT imaging system, 2D quantitative parameters (area, perimeter, aspect ratio, major and minor diameters) of the root canal of a mandibular incisor were measured in 421 slices and plotted on graphs

Fig. 12.5 Using micro-CT technology, cross-sectional appearance of the root canal (form factor and roundness) of a mandibular incisor was measured in 421 slices and plotted on graphs



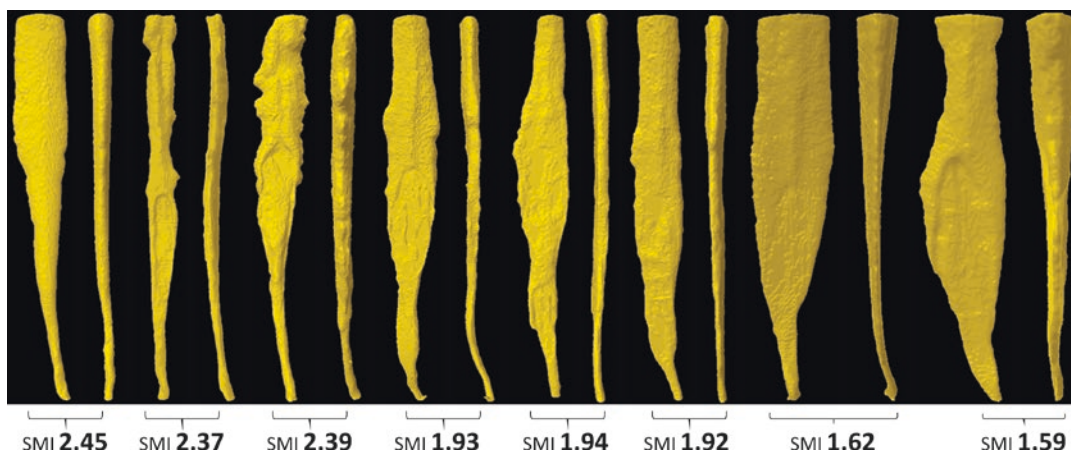


Fig. 12.6 Lateral and frontal view of the root canals of eight mandibular canines showing differences in the geometric 3D shape of the root canal (Structure Model Index—SMI)

capability, a qualitative evaluation is always subjective and may lead to inaccurate results.

12.3.2.2 3D Parameters

Among other parameters, 3D analysis of the root canal using micro-CT algorithms allows for the calculation of volume and surface area [14]. The clinical significance of such parameters has been emphasized by studies demonstrating that variations in canal geometry before preparation procedures had a greater effect on the changes that occurred during preparation than that of the instrumentation techniques [38]. Another important 3D parameter of root canals that can be measured using micro-CT is the structure model index (SMI) (Fig. 12.6). SMI is unfeasible to achieve using conventional methods such as radiographs or root sectioning. This parameter reflects the geometric 3D shape of the root canal and has been used in comparative studies of different groups of teeth [4, 14, 15, 24]. Dissimilarities in SMI values amongst teeth must be taken into consideration during sample selection in studies on root canal preparation as it might compromise the outcome.

12.4 Access Preparation

The endodontic access cavity is considered the foremost step in root canal treatment and can be defined as the opening prepared in a tooth to gain

entrance to the root canal system for the purpose of cleaning, shaping, and obturating [1]. In root canal treatment, an adequately prepared access cavity is crucial for effective locating, negotiating, debriding, disinfecting, and filling of the root canal system. Consequently, it is deemed that all subsequent steps that follow endodontic cavity preparation may be compromised if adequate access is lacking [39].

Traditional access preparations are geometrically predesigned shapes that are defined primarily by the morphology of the individual pulp chamber of the tooth to be treated. The roof of the pulp chamber must be completely removed in order to locate all orifices of the root canals and provide direct access to the apical foramen or to the initial curvature of the canal by removing cervical dentin protrusions and enlarging the canal orifice. However, according to some authors, conventional access preparation removes a large amount of dentin structure, which may weaken the dental structure and reduce its resistance to fracture [40]. It has been hypothesized that modification of the original access geometry plays a crucial role in the biomechanical response of the tooth structures to functional forces [39], since the remaining dentin can serve as a foundation for the restorative procedures that follow endodontic treatment. Thus, it would be desirable to preserve the dentin structure and maintain the geometry of the

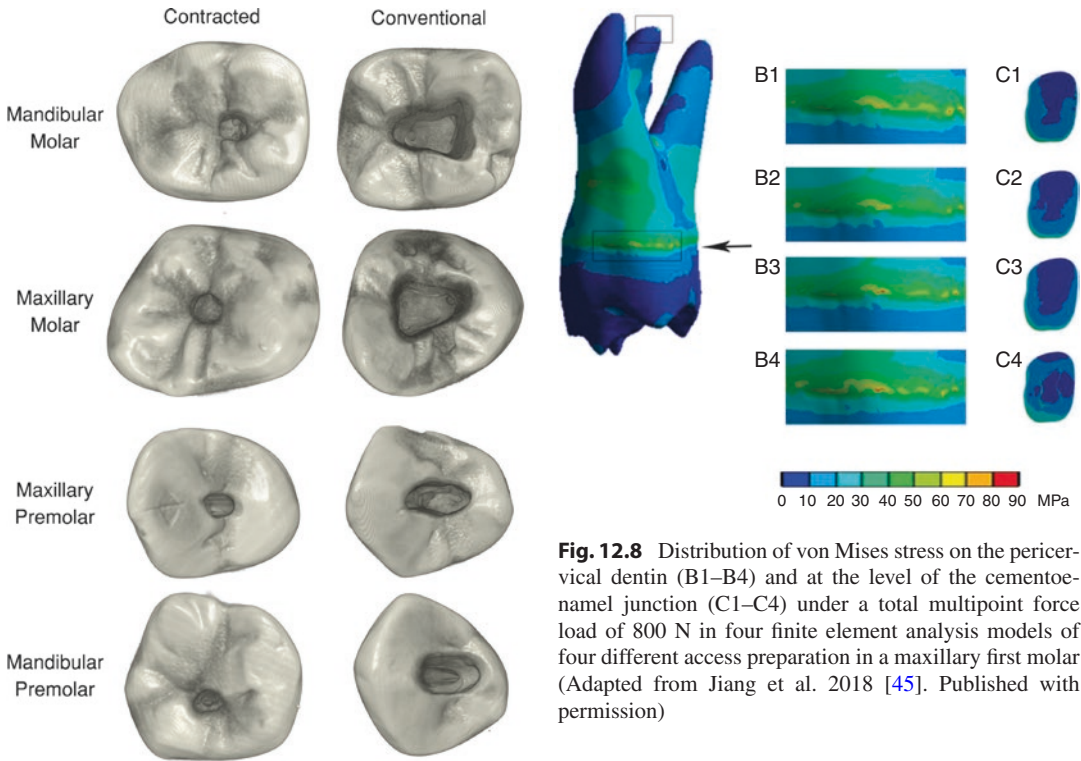


Fig. 12.7 3D models of the crowns (occlusal view) of four groups of posterior teeth showing differences in size and shape according to the type of access preparation: contracted or conventional

root canal anatomy so as to conserve the mechanical integrity of the teeth [41]. In this way, new designs for endodontic access cavities called conservative or contracted cavities have been advocated in order to minimize tooth structure removal [39] (Fig. 12.7). Contracted endodontic cavities are considered to be an alternative to traditional endodontic cavities in maintaining the mechanical stability and subsequently the long-term survival and function of endodontically treated teeth.

Within this background, the micro-CT imaging system has been used to measure the volume of the enamel and the coronal dentin removed by different access cavity preparations in an attempt to correlate those values with results acquired from fracture testings [42–44]. One study showed that the stress distribution on the occlusal surface of teeth was similar when comparing conservative, traditional, and extended access cavities;

Fig. 12.8 Distribution of von Mises stress on the pericervical dentin (B1–B4) and at the level of the cementoenamel junction (C1–C4) under a total multipoint force load of 800 N in four finite element analysis models of four different access preparation in a maxillary first molar (Adapted from Jiang et al. 2018 [45]. Published with permission)

however, with the enlargement of the access preparation, the stress on the pericervical dentin increased dramatically [45] (Fig. 12.8). Thus, although the influence of contracted endodontic cavity on fracture resistance outcomes still remains controversial, a recent systematic review of studies using micro-CT technology demonstrated that there is no scientific evidence that supports the use of conservative over traditional access preparation aiming to increase the fracture resistance of human teeth [40].

Eaton et al. [46] also used micro-CT to evaluate the interrelationship between some anatomical landmarks of the root canal system and apply them in the design of different access cavity outlines in mandibular molars. It was performed linear measurements of dentin removal required to relocate the orifice and changes on canal primary angle of curvature for each access design (Fig. 12.9). Authors concluded that tested outline designs had varying impacts on canal preparation, dictated by the degree of pulp chamber calcification, and that anatomically based access forms and orifice relocation should be reserved for teeth with reduced pulp chambers.

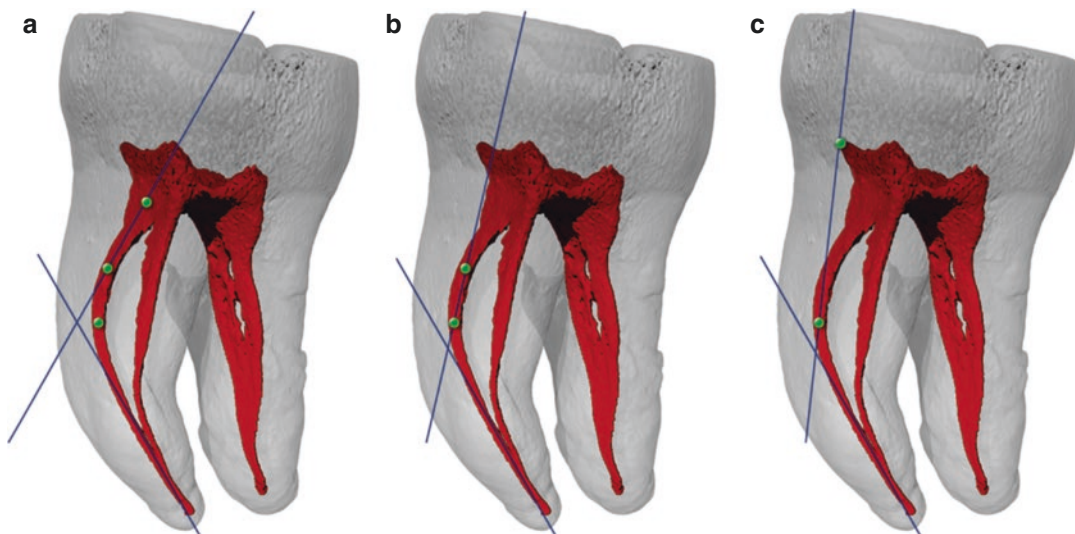


Fig. 12.9 Three-dimensional volumetric representation of micro-CT data showing the determination of the maximum angle of curvature in the maximum curvature view for the mesiobuccal canals for the different access designs:

(a) minimally invasive, (b) straight-line furcation, and (c) straight-line radicular (Adapted from Eaton et al. 2015 [46]. Published with permission)

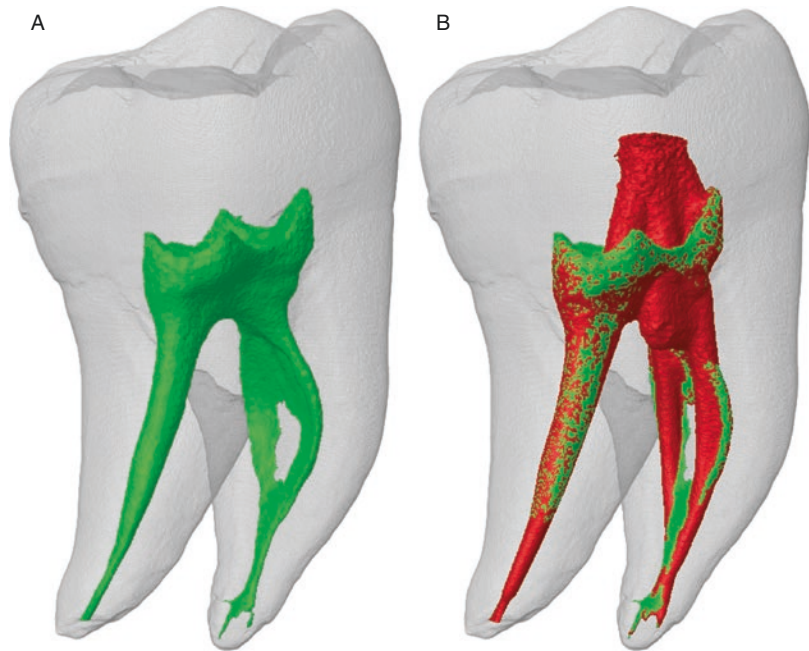
12.5 Chemomechanical Procedures

Root canal preparation is intended to clean, disinfect, and shape the root canal. These objectives are distinct but achieved simultaneously by means of the mechanical effects of instrumentation and the mechanical and chemical effects of irrigation. Consequently, these are commonly referred to as chemomechanical procedures and are regarded as the most important phase of the root canal treatment [47]. Recent advances in endodontic instrument design have made proper canal shaping more efficient and predictable. The most noteworthy advance was the development of mechanical preparation using nickel-titanium (NiTi) instruments. Since NiTi instruments were introduced, they have evolved through a market-driven, largely empirical process. Manufacturers have experimented with alloy-type, tip, taper, and cross-sectional configurations, rotation modes, and heat treatment during manufacturing in order to optimize instrument properties. Indeed, it appears that at least 200 brands of NiTi instruments, with greatly varying market shares, are

currently used in different countries. With many new systems available on the market, clinicians require an impartial evaluation of these instruments in order to select the most appropriate for clinical use. Therefore, several methodologies have been used to evaluate the shaping abilities of these instruments. However, some inherent limitations have encouraged the search for new methods able to produce accurate and reproducible results.

In the last decade, noninvasive micro-CT technology has gained increasing significance for the assessment of root canal system. This method allows for creating color-coded 3D models of the root canals, using pre- and post-preparation co-registered datasets and automated image registration software with high accuracy. Unprepared (green) and prepared (red) matched canals can be compared (Fig. 12.10) regarding the percentage frequency variation of the 2D and 3D parameters (Table 12.1) by subtracting values obtained for treated canals with those obtained from untreated counterparts. Then, unprepared surface areas are important to evaluate because they may harbor tissue and biofilm remnants and contribute to

Fig. 12.10 Co-registered 3D models of a mandibular first molar showing the root canal system before (in green) and after (in red) preparation procedures



persistent infection. Hence, measurement of the untouched root canal surface areas after root canal preparation can be obtained by calculating the number of static voxels, i.e., voxels present in the same position on the canal surface before and after instrumentation, expressed as a percentage of the total number of voxels present on the canal surface.

Canal transportation and dentin thickness are also important parameters to evaluate mostly if root canal enlargement is followed by unnecessary dentin removal, resulting in the weakness of the tooth structure. Using micro-CT, canal transportation can be achieved by connecting the center of gravity in each cross section of the canal with a fitted line (z-axis), through the length of the root, from the co-registered datasets before and after preparation. Then, mean transportation can be calculated by comparing the distance between the centers of gravity at each level of the root canal (Fig. 12.11). Dentin wall thickness can be acquired by the measurement of the width of dentin toward the external root surface, perpendicular to a line that connects the centers of gravity of the root canals, after superimposition of the datasets before and after canal preparation. Color-coded 3D models

of dentin thickness can also be created for qualitative evaluation (Fig. 12.12).

In recent years, the occurrence of root cracks resulting in the fracture of teeth has become a major concern in endodontics. Root fracture is currently considered as the third leading cause of tooth loss that can affect either sound or endodontically treated/restored teeth. In 2009, two studies using a conventional sectioning method associated root crack formation with canal preparation procedures [48, 49], calling the attention of the endodontic research community to this topic. Since then, the phenomenon of root cracks has gained importance in endodontic research, and the number of publications in high-impact peer-reviewed journals correlating root canal preparation to crack formation has increased [50]. Laboratory-based studies have reported that canal preparation using large-tapered NiTi instruments cut substantial amounts of dentin creating lateral forces that induce strain on the canal wall and cause root cracks, from which tooth fracture can develop [50]. In 2010, extracted non-restored or minimally restored necrotic teeth were evaluated using micro-CT [51] to demonstrate the presence of cracks extending from the coronal to the apical level of the root. Although it was not

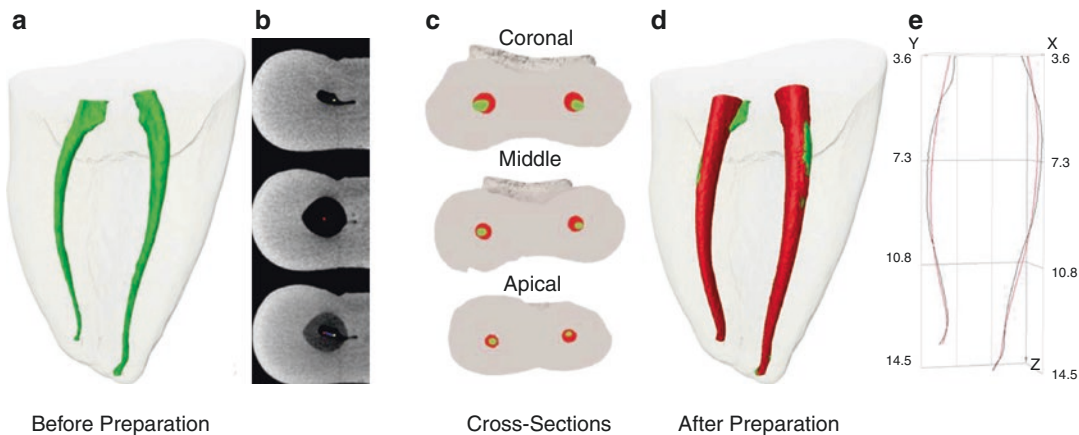


Fig. 12.11 Transportation of the (a) mesial root canal system of a mandibular first molar (in green) was achieved by comparing the (b) distance between the centers of gravity at each level of the root canal (c, d) after preparation

procedures (in red) calculated by (e) connecting the center of gravity of the root canal in each cross section through all length of the root with a fitted line (z-axis) from the co-registered datasets before and after preparation

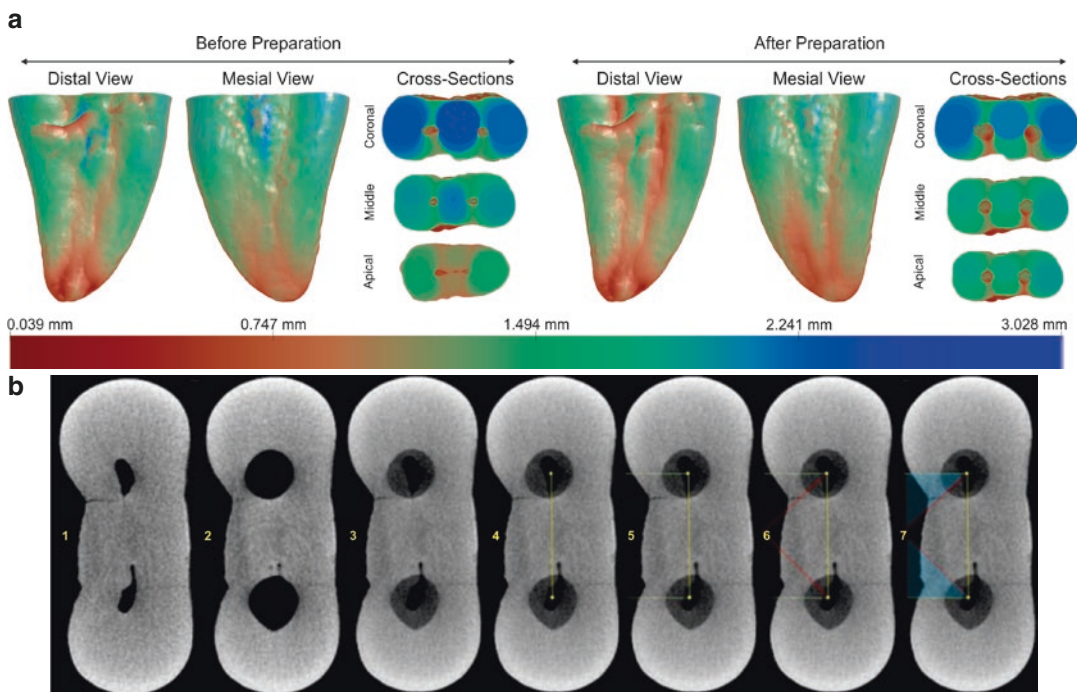


Fig. 12.12 Dentin thickness measurement by means of micro-CT technology. (a) Mesial, distal and axial cross section views of the color-coded 3D models of the mesial root of mandibular molars allow qualitative evaluation of dentin thickness before and after root canal preparation. Thick structures are indicated in blue and green, whereas red areas show thin dentin; (b) mean dentin thickness measurement in a cross-section slice at the coronal level of a mandibular molar mesial root. 1. Mesial root canals before preparation; 2. mesial root canals after preparation;

3. superimposed mesial root canal (before and after preparation); 4. centers of gravity of each canal connected by a yellow line; 5. a green line is traced perpendicularly to the yellow line from the centers of gravity toward the distal aspect of the mesial root; 6. red line is traced bisecting the 90-degree angle between yellow and green lines; 7. mean dentin thickness is calculated by measuring the thickness of dentin in each 1-degree interval of the highlighted blue area, in a total of 15 measurements

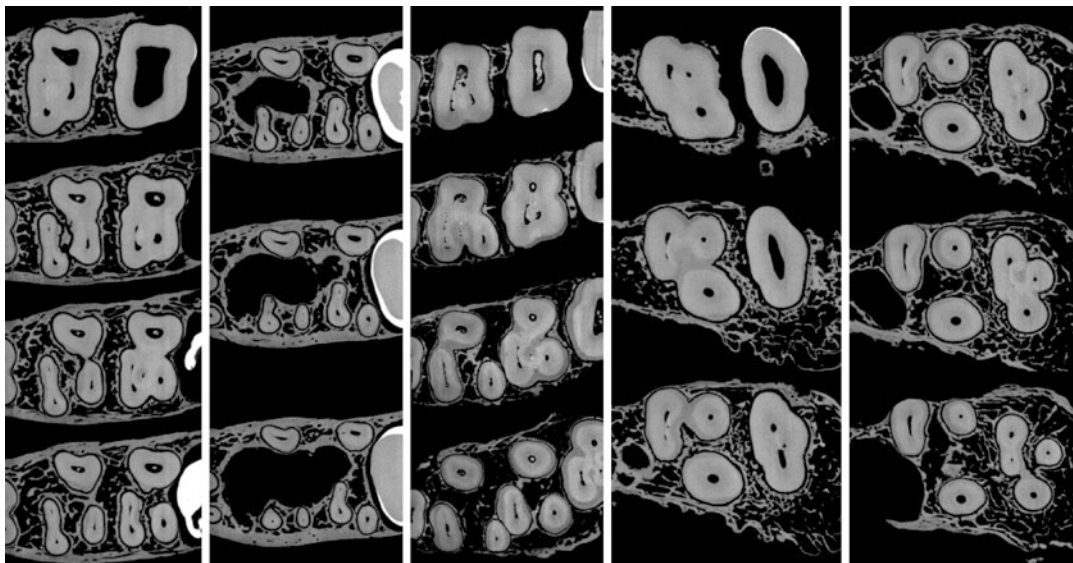


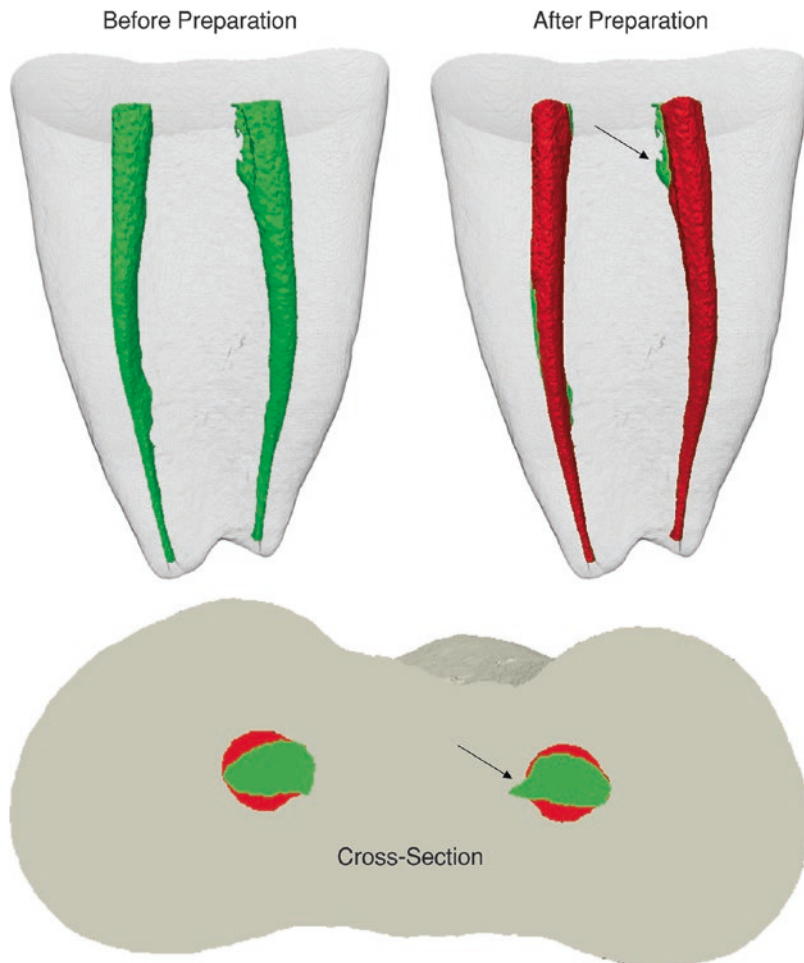
Fig. 12.13 Micro-CT images showing cross sections of maxillary posterior teeth in a cadaver study model

the main purpose of the study, the authors indirectly demonstrated the feasibility of using micro-CT to track dentinal defects, and, later, micro-CT was validated as a nondestructive method to evaluate cracked roots [52]. In disagreement with previous studies using sectioned roots, the micro-CT method was crucial to demonstrate the absence of a causal relationship between the development of root fractures and canal preparation using either extracted teeth or a cadaver model [53–55] (Fig. 12.13).

Advances in micro-CT analysis have brought new perspectives on the quality of mechanical preparation, confirming the inability of shaping tools to act within the anatomical complexity of the root canal [56–58]. Preparation of oval-, flattened-, or irregular-shaped cross-sectional root canals using different instruments has been shown to leave unprepared extensions or recesses (Fig. 12.14) that can harbor remnants of necrotic pulp tissue and biofilms [37, 58]. The disinfecting effects of instruments and irrigants may be additionally hampered in the presence of complex anatomy, such as accessory canals, ramifications, intercanal connections, fins, isthmuses, and apical deltas, which cannot be properly accessed and cleaned by conventional techniques [58–62]. These hard-to-reach areas may also be packed

with dentin debris generated and pushed therein by endodontic instruments, interfering with disinfection by both preventing irrigant to flow into them as well as by neutralizing its efficacy [63]. Accumulation of hard tissue debris is considered an undesirable side effect of mechanical procedures and is clinically relevant because it could easily harbor bacterial contents away from the disinfection procedures during root canal treatment [64–66]. Therefore, a comprehensive knowledge regarding different supplementary steps and the activation of irrigants using different protocols in order to remove hard tissue debris from the root canal space is of utmost importance. In 2011, Paqué et al. [67] were responsible to reopen the discussion about the debris packed into the root canal system after preparation using micro-CT. The authors demonstrated that this technology allowed for monitoring the accumulation and removal of radiopaque structures in the root canal space during and after preparation while preserving sample integrity. Quantification of hard debris can be performed by calculating the difference between the non-prepared and prepared root canal space using post-processing procedures. The sequence of acquired images can be further used to identify the debris by means of morphological operations.

Fig. 12.14 3D models of the mesial root canal system of a mandibular molar before (in green) and after (in red) preparation depicting that instruments has left unprepared extensions of the canal (arrows)

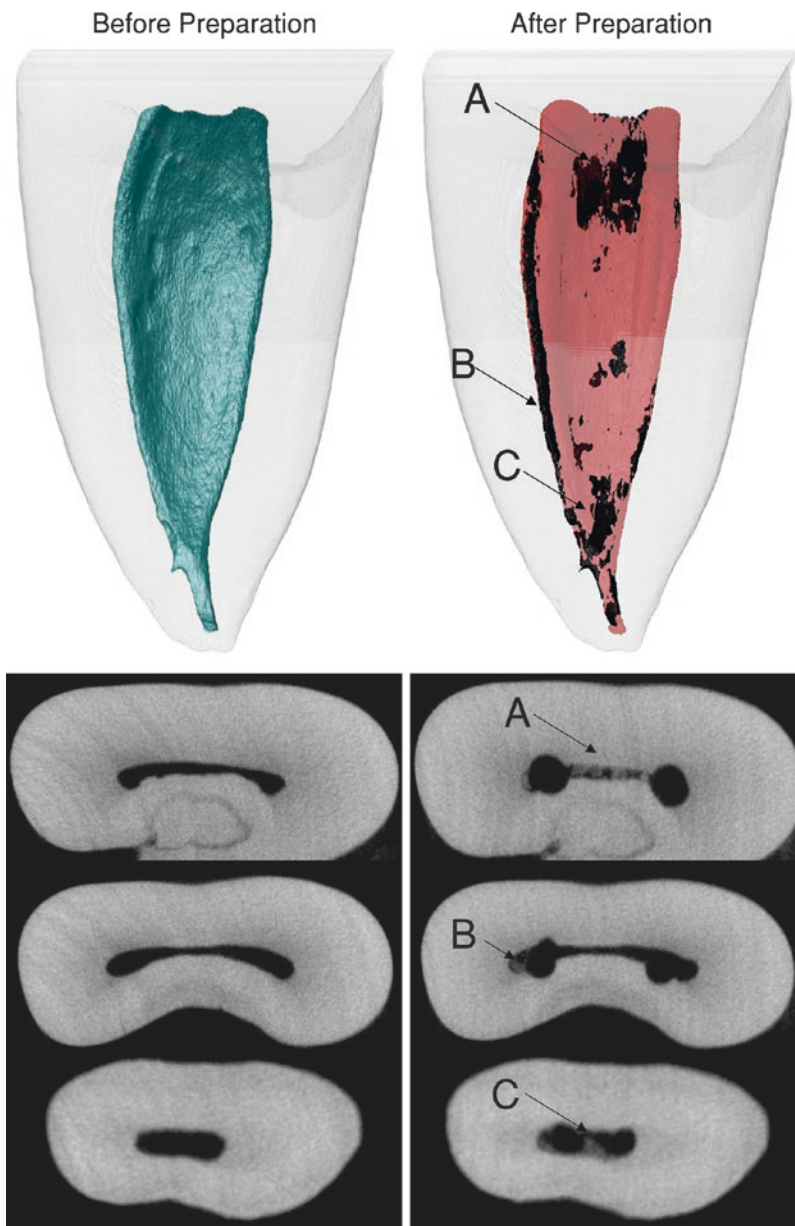


The presence of a material with a density similar to dentin in regions previously occupied by air in the non-prepared root canal space is considered debris and can be quantified by the intersection between images before and after canal instrumentation. The total volume of hard tissue debris can be calculated and expressed as the percentage of the total canal volume after preparation. Color-coded models of the root canal and debris can also be made to enable a qualitative comparison of the matched root canals before and after experimental procedures (Fig. 12.15).

Based on the aforementioned assumptions, spreading and flushing the irrigant throughout the canal space assume a pivotal role in treatment because it acts mechanically and chemically on debris and bacterial communities colonizing the root canal space [58]. In order to

circumvent limitations generated by the unpredictable anatomical configuration of the root canal, making cleaning and disinfection procedures more effective, several instruments and techniques have been proposed. Ideally, efficient irrigation solutions and protocols are required to provide fluid penetrability to such an extent as to accomplish microcirculation flow throughout the intricate root canal anatomy and to counterbalance the suboptimal debridement quality obtained by currently available technology in the mechanical enlargement of the root canal space [47]. In laboratory-based studies, several experimental models have been used to understand the intracanal effect of irrigants by different irrigation protocols. These include artificially created grooves, histological cross sections, computational fluid dynamics (CFD), and the *in vivo* use

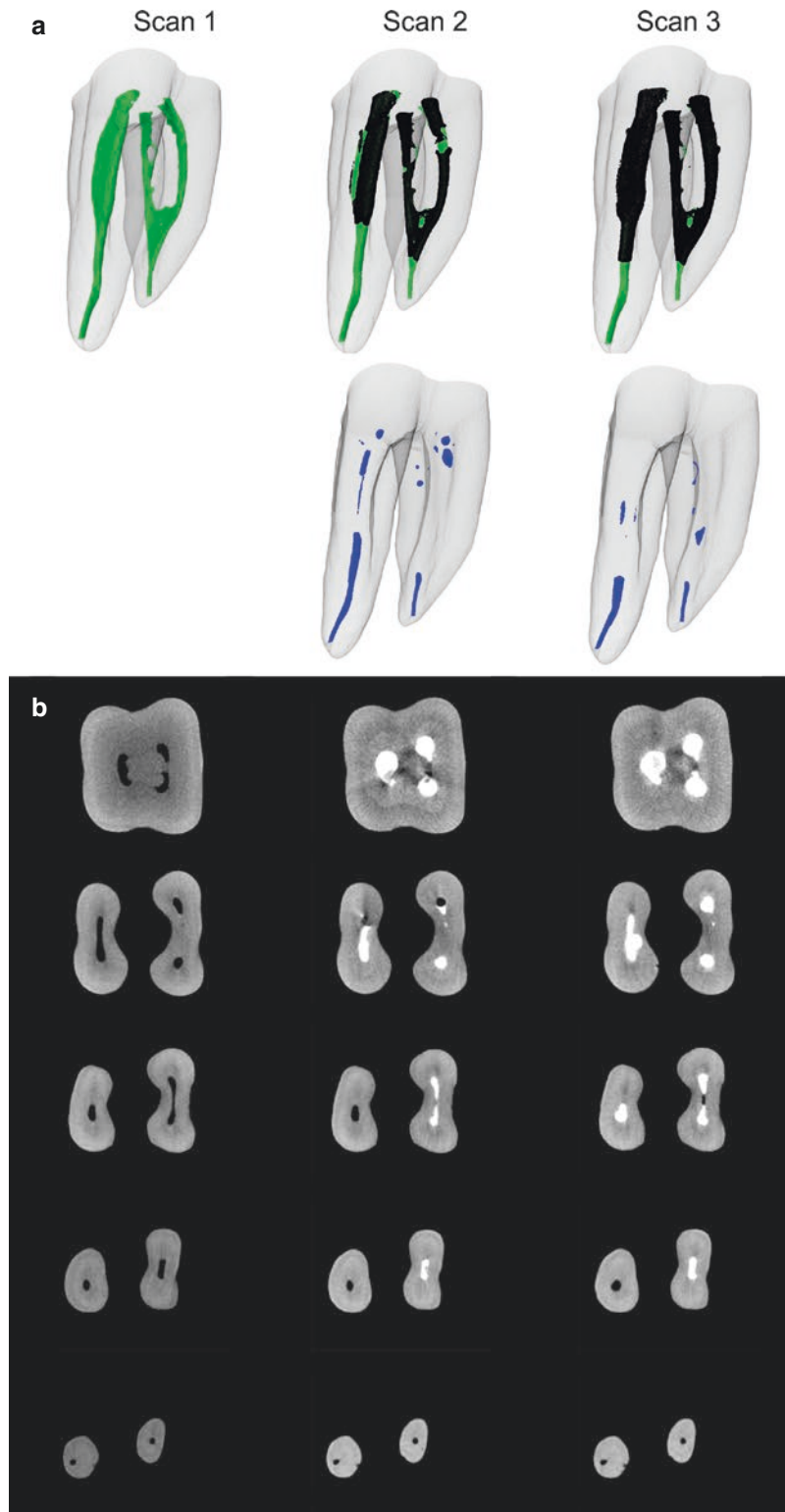
Fig. 12.15 3D models of the mesial root canal system of a mandibular molar before (in green) and after (in red) preparation depicting the presence of hard tissue debris (in black; arrows) at the (a) coronal, (b) middle, and (c) apical thirds



of radiopaque solutions. These methodological approaches provide valuable information about the quality of cleaning and shaping procedures that cannot otherwise be obtained, but they are unable to show some critical factors, such as the volume of the solution or the root canal areas effectively touched by the irrigant [68]. Additionally, the destructive approach of these methods is a major drawback, since the preoperative condition of the root canal is unknown.

An ideal experimental model should allow for a reliable in situ volumetric quantitative evaluation of the root canal space, offering a comprehensive understanding on the capabilities and limitations of different irrigation protocols. In this way, micro-CT technology may overcome several limitations displayed by conventional methods for the study of root canal irrigation, as it provides 3D quantitative volumetric and 2D mapping of the irrigant within the root canal space (Fig. 12.16).

Fig. 12.16 Micro-CT study on the irrigation of the root canal system of a mandibular first molar. **(a)** 3D models of the original root canal anatomy (in green) prior to treatment (Scan 1) and with the superimposition of an injected contrast solution (in black) after initial (Scan 2) and final (Scan 3) preparation procedures, as well as, 3D models of the same tooth showing the irrigant-free areas (in blue) after scans 2 and 3; **(b)** cross sections of the root in different levels showing the root canal space (in black) before preparation and the contrast solution (in white) and irrigant-free areas (in black) after initial (scan 2) and final (scan 3) canal preparations



Using micro-CT, the volume of the irrigant can be correlated to the full canal volume and the existence of anatomical irregularities or debris that may prevent its spreadability. The volume of the irrigant-free areas can also be calculated and correlated, for example, to the irrigant delivery method, fluid activation system, irrigation needle penetration and design, root canal configuration, amount of hard tissue debris, or shaping protocols. Additionally, three-dimensional visualization of these areas can provide useful information related to irrigation efficiency. Data can be further subjected to inferential statistical models to assess the relevance of different irrigation protocols following well-known parameters [68].

12.6 Obturation and Retreatment

Obturation has been defined as a procedure in which any material or combination of materials is placed inside the root canal after it has been completely cleaned, shaped, and disinfected, aiming to avoid any sort of communication or exchange between the root canal and surrounding tissues [1]. Conventional root fillings consist of a core material, usually gutta-percha, which should be closely adapted to the canal wall, and a cement that seals the interface between the core and the dentin, placed into the root canal space employing cold or warm techniques. Cold lateral compaction of gutta-percha is undoubtedly the most used and taught root canal filling technique worldwide. The basic protocol comprises the lateral compaction of accessory cones, undertaken by systematically penetrating spreaders sideways of the main gutta-percha cone. The core idea is to maximize the amount of gutta-percha inside the canal while reducing the sealer layer, since the latter is meant to display lower dimensional stability overtime [69]. Warm vertical compaction involves the use of successive heated pluggers and gradually pushing down compaction to form waves of softened gutta-percha aiming to obtain a homogeneous and dimensionally stable mass of filling material. As gutta-percha is heated, it becomes more plastic and therefore adapts to irregularities and recesses, especially in oval-

shaped root canals [70]. However, as gutta-percha is heated, it expands, and during cooling it contracts (1–2%), resulting in voids and gaps along the root filling [71]. Since the development of the warm compaction techniques, there has been debate regarding their superiority in comparison to cold lateral compaction. Although studies have demonstrated that no filling technique produces a void-free canal filling, warm vertical compaction is associated with a lower percentage volume of voids, while cold compaction techniques suffer from unpredictable distribution of the sealer and voids within the root canal space [72].

In the past, the quality of root canal obturation was investigated using laboratory-based techniques including microleakage tests, radiographic imaging, and root sections. In many studies, the percentage of gutta-percha-filled area was used as a surrogate measure of the quality of the root filling. However, most of these methods allow only a partial evaluation of the fillings, and some may create irreversible damages to the specimens. Unreliable results obtained from microleakage tests render the results obtained through this technique questionable. Evaluation of root sections is practical, but sectioning the root may cause irreversible damage to the specimens and only a limited number of sections can be obtained from each sample. Besides, this might lead to inaccuracies because some filling material might be lost during sample preparation. Although radiography does not cause any damage to the specimens and provides useful information, it has limited accuracy since it is based on two-dimensional visualization of a three-dimensional object. Therefore, an ideal experimental model should allow for the preservation of sample integrity avoiding irreversible structural damage [73].

In the last decade, nondestructive high-resolution micro-CT technology has emerged as an important 3D imaging tool to evaluate root filling procedures, overcoming most of the limitations of previous studies. Micro-CT enables visualization of the root canal filling as a 3D single object or evaluation of cross-sectional images of the root at each level; thus, the volume

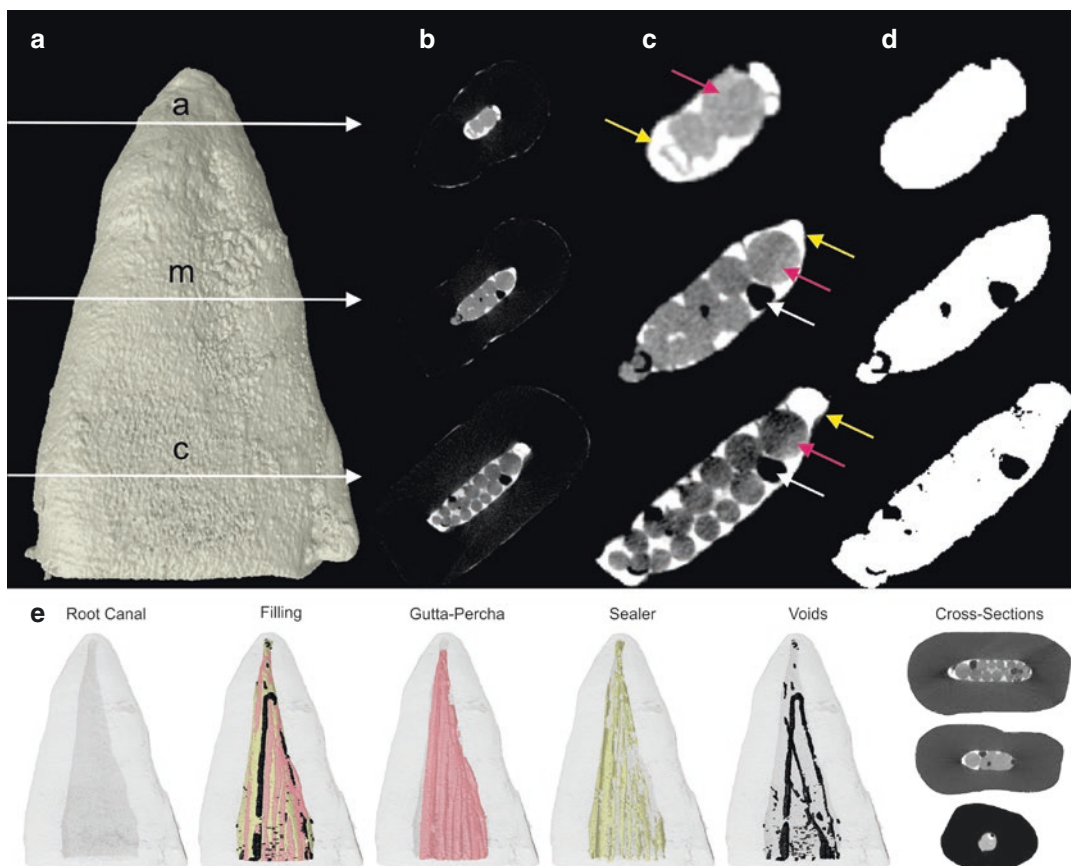


Fig. 12.17 (a) 3D model of a maxillary premolar root; (b) cross sections from apical (*a*), middle (*m*), and coronal (*c*) thirds showing an oval-shaped canal filled with cold lateral condensation where it is possible to observe the presence of (c) empty spaces (white arrows), sealer (yellow arrows), and gutta-percha (pink arrows). The gutta-percha is not mixed with the sealer which remains in direct contact with

the dentin; (d) root filling material after applying an automatic threshold. The high contrast of the filling to the dentin yielded excellent segmentation; (e) 3D reconstructions and cross sections of the internal view of the maxillary premolar in a, before and after root canal filling with cold lateral compaction technique, depicting gutta-percha (in pink), sealer (in yellow), and voids (in black)

of the root canal filling occupied by the gutta-percha, sealer, and voids can be calculated, determining whether the filling reaches the ramifications and isthmus area. Gutta-percha, sealer and voids can be also depicted individually by coloring or made transparent (Fig. 12.17). However, subtle complications can render micro-CT data problematic for quantitative use because of the high density of root canal filling materials. Scanning artifacts, such as beam hardening, can obscure details of interest or cause the CT value of a single material (or void) to change in different parts of the image. Similarly, partial-volume effects can lead to

erroneous determinations of feature dimensions and component volume fractions if not properly accounted for. These artifacts sometimes make it impossible to differentiate between different materials with similar radiographic densities. Although higher energy beams associated with the use of an attenuating filter can be beneficial, they are less sensitive to attenuation contrasts in materials and thus may not provide sufficient differentiation among the features of interest. For these reasons, it is important to perform different scans with alternative variables to determine the optimal parameters and material combinations before the experiment.

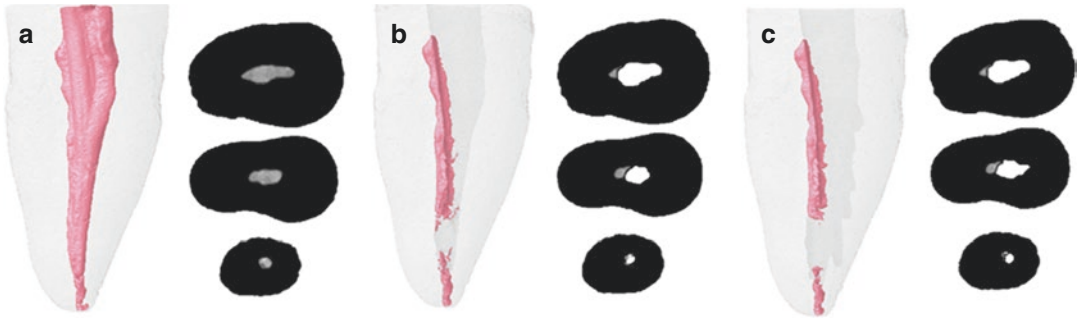


Fig. 12.18 3D models of a mandibular canine with an oval-shaped canal showing the filling material (pink) after (a) obturation with the warm compaction technique, (b) retreatment procedures, and (c) additional laser applica-

tion followed by the respective cross sections from the coronal, middle, and apical thirds (filling materials depicted in gray)

Although root canal treatment has been shown to be a predictable procedure with a high degree of success, failure can also occur. Impaired healing is attributed to persistent intraradicular infection originating from non-instrumented canals, dentinal tubules or in the complex irregularities of the root canal system [74]. Previously endodontically treated teeth with persistent infection might be preserved with nonsurgical retreatment, which attempts to re-establish healthy periapical tissues by regaining access to the root canal system through removal of the original obturation, further cleaning, and refilling. Therefore, the removal of as much filling material as possible from an inadequately prepared and/or filled root canal system is necessary to uncover remaining necrotic tissues or bacteria that might be responsible for persistent periapical inflammation and, thus, posttreatment disease [72].

Many techniques have been advocated for the removal of filling materials from the root canal system. Traditionally, retreatment has been accomplished using a solvent and hand files. Recently, the introduction of mechanical instruments specifically designed for retreatment has resulted in a more efficient way to remove the bulk of filling materials. In straight canals with a round cross section, the operator may simply use rotary files of greater dimensions in order to remove filling residues. On the other hand, the retreatment of oval-shaped canals requires additional procedures because further enlargement may create complications such as root perforation or canal transporta-

tion [75]. Although it has not been proven that the complete removal of filling materials can improve the outcome of the retreatment procedure, filling remnants can theoretically impair disinfection by preventing the irrigant from coming into contact with persistent microorganisms. In addition, filling residues can negatively affect the adhesion of the new filling material to the canal walls and may jeopardize its sealing properties. For these reasons, the removal of all root canal filling material must be the first step of the retreatment procedure. Nevertheless, despite the development of new instruments and devices, none of them can render a root canal system completely free of root filling residues [72] (Fig. 12.18).

Most early laboratory-based studies used destructive and two-dimensional methods to determine the amount of filling material remaining after retreatment procedures. However, it is not possible to precisely calculate the volume of filling material remaining after retreatment procedures using these methods. In contrast, the nondestructive micro-CT approach allows for a precise volumetric evaluation of filling materials remaining after different retreatment protocols, overcoming the limitations of previous methodologies. Using micro-CT, it has been demonstrated that the use of supplementary procedures such as ultrasonic tips [72] or laser irradiation [76] during retreatment improves the removal of filling remnants from the root canal space. The filling materials remaining after retreatment procedures can be expressed as a percentage of the

initial root filling volume using the formula $V_A * 100 / V_B$, where V_B and V_A mean the volume of the filling material before and after each retreatment stage, respectively. Polygonal surface representations of the teeth and the filling materials can also be constructed for a qualitative evaluation (Figs. 12.17 and 12.18). Finally, the possibility of calculating the volume of filling material remaining in the root canal after retreatment and the ability to examine the effectiveness of additional retreatment procedures using the same specimens repeatedly are some of the greatest advantages of using micro-CT technology.

12.7 Others

Other micro-CT applications in endodontics include:

1. Sealing ability, marginal adaptation (interface) of filling and retrofilling materials [77–82].
2. Physicochemical properties (dissolution, dislocation, solubility, and dimensional changes) of endodontic materials [83–85].
3. Porosity characterization of root canal sealers [86, 87].
4. Filling experimental internal resorptive cavities [88].
5. Stress distribution (deformation) of NiTi instruments [89].
6. Cutting efficiency of NiTi instruments [90].
7. Development of 3D models for mechanical testing simulations using finite element analysis [91–93].
8. Production of 3D printed replicas of teeth to standardize samples for laboratory studies [94, 95].
9. Calcium hydroxide removal from the root canal system [96, 97].
10. Dentin removal during post-space preparation [98, 99].
11. Adaptation of posts [100].
12. Gold standard reference to compare with other experimental methodologies [101].
13. Pulp pathosis in teeth of ancient populations [102].
14. In vivo healing of periapical lesions after nonsurgical or surgical root canal treatment in small animals. Periapical lesions are caused by bacterial invasion of the root canal system, which results in inflammation, leading to the destruction of surrounding tissues. Rats and mice have been widely used in studies assessing the pathogenesis and development of experimentally induced periapical lesions; these findings have been validated by histological evaluations, conventional and digital radiography and by means of micro-CT [103]. A histological evaluation is considered the gold standard for assessing periapical lesions. Nevertheless, this method is time-consuming and leads to sample destruction [104]. According to the literature, micro-CT is an important tool for research involving periapical bone lesions in small animals [103–108], providing results that are equivalent to those assessed by means of histology [103]. In addition, micro-CT allows for the assessment of microstructural features as well as subregional analysis of the developing lesion [104].

12.8 Educational Impact

The importance of preclinical training in endodontics has been well-established in the literature for endodontic education. The primary objective is to introduce students to cognitive and psychomotor skills related to the morphology and spatial and functional relationships of human dentition. For decades, endodontic teaching has relied almost exclusively on the use of natural human teeth. Practice on extracted teeth is a universal method of teaching preclinical endodontics and gives students the opportunity to gain expertise before moving on to patients. However, cross-infection control associated with the manipulation of extracted teeth, along with ethical factors, is threatening this practice in some teaching institutions. These drawbacks have stimulated the development of alternative simulation methods for endodontic teaching [109].

12.8.1 Applications of 3D Anatomy of the Teeth in Dental Education

Although endodontic teaching has been mostly based on the use of natural extracted human teeth, there are certain limitations for the use of human teeth in preclinical teaching as they may (a) be difficult to obtain; (b) become brittle and fracture easily; (c) be third molars that are not usually treated endodontically; (d) be extremely varied in internal anatomy; (e) break down because of caries or have large restorations, obliterating external anatomical landmarks; (f) have smaller pulp chambers because of the deposition of reparative dentin; or (g) present variations in internal anatomy that make the evaluation difficult for students and teachers. Consequently, several authors have proposed the replacement of natural teeth with artificial tooth models composed of resin [110].

A transparent model tooth offers a convenient and useful method that can be used for studying and teaching about the morphology of teeth, as it provides a three-dimensional view of the root canal system. Additionally, they are standardized and easy to obtain in quantity, do not pose any risk of infection, and can be a valuable aid for self-assessments. However, the hardness of the resin and the complex internal and external dental anatomy of the first transparent tooth models do not accurately reproduce natural teeth. Moreover, sometimes the characteristics of transparency and lack of radiopacity do not allow for the development of some technical skills related to radiographic interpretation, rendering their use limited in some phases of learning [109]. However, the development of micro-CT-based training replicas produced using 3D printing technology has improved the use of artificial teeth for teaching purposes (Fig. 12.19). Now, rather than every student having a different anatomic challenge hidden in the extracted teeth, all of them can work in the same anatomic form in the same class activity. Despite some inherent limitations regarding the development of motor skills using these resin replicas related to tactile perception during access preparation and canal instrumentation/

obturation, these printing prototypes can be extremely valuable for anatomical teaching purposes as they (a) allow for complete standardization of grading, (b) permit educators to lead a whole class through each of the classic endodontic challenges instead of teaching one student at a time, and (c) allow students to practice a given challenge as many times as they need to achieve competence in that root form, after which (d) they can be tested using a nontransparent replica with the same anatomy [111]. Furthermore, replicas with different root canal complexities can be printed as oversized models using a rapid prototyping 3D printer, allowing the students to hold them in their hands to observe details of the internal anatomy from different views. Additional applications of printed models in dental education also include the possibility of (a) scaling the teeth for didactic purposes, (b) building a collection of 3D tooth models showing atypical or only regionally prevalent anatomies, (c) producing a large number of teeth for destructive analysis, (d) presenting teeth in the form of individual substructures that need to be assembled correctly by the students, and (e) building an extensive collection of 3D models of healthy and diseased teeth using raw data made available online by researchers and dentists from all over the world [112].

12.8.2 Strategic Improvements for Web-Based Teaching of Root Canal Anatomy

As imaging has been adopted in the modern dental education, it has benefited from the concurrent development of technologies that allows materials to be presented electronically. One of the technologies with the greatest impact in this regard has been the Internet. The Internet has increasingly been utilized as an educational tool due to its ability to provide a large volume of educational material in a single, readily accessible location, as well as permitting flexibility in the format of the material. Images, text, interactive quizzes, and videos can be integrated seamlessly into a comprehensive educational resource.



Fig. 12.19 Replicas of various teeth manufactured from corresponding real-tooth micro-CT scans using 3D printing technology in assorted sizes for didactic or teaching purposes. (a) True Tooth® (images available at <https://den->

talengineeringlab.com/truetooth/); (b) RepliDens® (images available at <https://www.smartodont.ch/replidens/>)

Visualization technology has the potential to improve on traditional techniques for teaching visual discrimination and should provide students with (a) an extensive resource to learn dental terms related to tooth morphology, (b) interactive 3D tools to visualize and learn normal external tooth and pulp cavity morphologies, and (c) an extensive library of 3D images of tooth and pulp morphologies that deviate from normal and (d) progressive evaluation of knowledge in the form of quizzes that provide immediate feedback [109].

The field of endodontic education can also profit in several ways by the application of techniques and approaches that are already established in other scientific disciplines such as (a) the interactive exploration of tooth anatomy online, (b) expanded morphometric and volumetric analyses of internal tooth structures, and (c) large-scale correlations of external and internal tooth morphology using 3D virtual models [7]. This is possible because of recent advances in noninvasive imaging technologies that have opened up a new world in endodontic research

and teaching [112]. Recently, Kato and colleagues [7] made available freely accessible portable PDF-embedded 3D models of teeth based on micro-CT data in which the reader can freely manipulate the models and activate a series of preset views either by directly accessing a view in the drop-down menu of the main viewer window or by opening the “model tree” icon and switching from one view to the next. According to the authors, embedded 3D models of teeth in document format files are a valuable tool for dental students.

Since the data from micro-CT are digital, they can also be used to generate anatomical tooth data on a large scale and can be made publicly accessible through the Internet, thus circumventing the problems of individual researchers regarding access to high-cost scanning devices [7, 113]. This was the main motto for the creation of the web-based study guide called the “Root Canal Anatomy Project” (RCAP) (<http://rootcanalanatomy.blogspot.com.br/>). This website has received extensive traffic since its development in 2011, with visits by people from 192 different countries and more than 1,500,000-page views. The high-resolution images and videos available for download at the RCAP website can be freely used for attributed noncommercial educational purposes by educators, scholars, students, and clinicians, since proper attributions and citations are included. One of the most interesting resources available to download at the RCAP includes VXM files of all groups of teeth. A VXM file contains both the volume data and an associated transfer function. This format can be used in the free volume rendering app called CTvox (Brucker-MicroCT) that runs on either iOS or Android systems. CTvox displays a set of reconstructed slices as a realistic interactive 3D object with intuitive navigation and manipulation of both the object and the camera, a flexible clipping tool to produce cutaway views, background selection including custom scenery, and an interactive transfer function control to adjust colors and transparency. In other words, using a cell phone or tablet, it is possible to rotate, cut, color, create movies, highlight, shadow or magnify areas of interest, and more, from real 3D datasets

of different groups of teeth acquired by micro-CT technology. Considering that students nowadays are “digital natives” habituated to using web resources, digital and interactive 3D resources may increase the motivation of students to learn about the internal anatomy of the teeth.

12.9 Concluding Remarks

The intent of this chapter was to demonstrate that, although the micro-CT method is not suitable for clinical use, in the last decade, it has become a powerful tool for endodontic research as it offers a noninvasive reproducible and accurate technique for the qualitative and quantitative 3D assessment of the internal and external anatomy of teeth. Applications in experimental endodontology are now becoming extensive, as it can produce detailed informative images of root canal anatomy before, during, and after different endodontic procedures. A significant amount of information can be gleaned from the scans using dedicated software to extract morphological data from teeth, which would be otherwise impossible to acquire. Slices can also be recreated in any plane, while data can be presented in 2D or 3D images. Finally, micro-CT digital data can allow for preclinical training and education regarding the fundamental procedures of endodontic treatment. Even though increasingly less time is devoted to teaching the internal anatomy of teeth in conventional curricula compared to the development of technical skills, nowadays, students and clinicians may benefit from the sophistication of digital imaging technology. The rapid increase in noninvasive and 3D imaging techniques used for the study of internal tooth structures can largely be attributed to the improvement in the variety of CT scanners with several applications in endodontic research and teaching. Due to the digital nature of this technique, large amounts of data are likely to be made accessible online to researchers, practitioners, students, and faculty, providing a significant stimulus for the exploration of tooth anatomy. Furthermore, the data derived from noninvasive imaging techniques, when freely available on the Internet, can

be integrated into dental education and help students to acquire an improved understanding of the complex anatomy of human teeth. Given the constant progress in imaging technology, it is just a matter of time until the development of less costly high-resolution micro-CT systems that require only a short learning curve.

References

1. AAE. Glossary of endodontics terms. 8th ed. Chicago: American Association of Endodontists; 2015.
2. Tjäderhane L. Dentin basic structure, composition, and function. In: Versiani MA, Basrani B, Sousa Neto MD, editors. *The root canal anatomy in permanent dentition*. Switzerland: Springer International Publishing; 2018. p. 17–30.
3. Perrini N, Versiani MA. Historical overview of the studies on root canal anatomy. In: Versiani MA, Basrani B, Sousa Neto MD, editors. *The root canal anatomy in permanent dentition*. Switzerland: Springer International Publishing; 2018. p. 3–16.
4. Versiani MA, Pécora JD, Sousa-Neto MD. Microcomputed tomography analysis of the root canal morphology of single-rooted mandibular canines. *Int Endod J*. 2013;46:800–7.
5. Mayo CV, Montgomery S, de Rio C. A computerized method for evaluating root canal morphology. *J Endod*. 1986;12:2–7.
6. Blašković-Šubat V, Smojver B, Maričić B, Sutalo J. A computerized method for the evaluation of root canal morphology. *Int Endod J*. 1995;28:290–6.
7. Kato A, Ziegler A, Utsumi M, Ohno K, Takeichi T. Three-dimensional imaging of internal tooth structures: applications in dental education. *J Oral Biosc*. 2016;58:100–11.
8. Tachibana H, Matsumoto K. Applicability of X-ray computerized tomography in endodontics. *Endod Dental Traumatol*. 1990;6:16–20.
9. Dowker SE, Davis GR, Elliott JC. X-ray microtomography: nondestructive three-dimensional imaging for in vitro endodontic studies. *Oral Surg Oral Med Oral Pathol Oral Radiol Endod*. 1997;83:510–6.
10. Elliott JC, Dover SD. X-ray microtomography. *J Microsc*. 1982;126:211–3.
11. Nielsen RB, Alyassin AM, Peters DD, Carnes DL, Lancaster J. Microcomputed tomography: an advanced system for detailed endodontic research. *J Endod*. 1995;21:561–8.
12. Rhodes JS, Ford TR, Lynch JA, Liepins PJ, Curtis RV. Micro-computed tomography: a new tool for experimental endodontology. *Int Endod J*. 1999;32:165–70.
13. Bjørndal L, Carlsen O, Thuesen G, Darvann T, Kreiborg S. External and internal macromorphology in 3D-reconstructed maxillary molars using computerized X-ray microtomography. *Int Endod J*. 1999;32:3–9.
14. Peters OA, Laib A, Rueggsegger P, Barbakow F. Three-dimensional analysis of root canal geometry by high-resolution computed tomography. *J Dent Res*. 2000;79:1405–9.
15. Versiani MA, Pécora JD, Sousa-Neto MD. Root and root canal morphology of four-rooted maxillary second molars: a micro-computed tomography study. *J Endod*. 2012;38:977–82.
16. Vertucci FJ. Root canal morphology and its relationship to endodontic procedures. *Endod Topics*. 2005;10:3–29.
17. Weine FS, Healey HJ, Gerstein H, Evanson L. Canal configuration in the mesiobuccal root of the maxillary first molar and its endodontic significance. *Oral Surg Oral Med Oral Pathol*. 1969;28:419–25.
18. Vertucci F, Seelig A, Gillis R. Root canal morphology of the human maxillary second premolar. *Oral Surg Oral Med Oral Pathol*. 1974;38:456–64.
19. Versiani MA, Ordinola-Zapata R. Root canal anatomy: implications in biofilm disinfection. In: Chavez de Paz L, Sedgley C, Kishen A, editors. *Root canal biofilms*. Toronto: Springer International Publishing AG; 2015.
20. Versiani MA, Basrani B, Sousa Neto MD. *The root canal anatomy in permanent dentition*. 1st ed. Switzerland: Springer International Publishing; 2018.
21. Kim Y, Chang SW, Lee JK, Chen IP, Kaufman B, Jiang J, et al. A micro-computed tomography study of canal configuration of multiple-canal mesio-buccal root of maxillary first molar. *Clin Oral Investig*. 2013;17:1541–6.
22. Ordinola-Zapata R, Bramante CM, Villas-Boas MH, Cavenago BC, Duarte MH, Versiani MA. Morphologic micro-computed tomography analysis of mandibular premolars with three root canals. *J Endod*. 2013;39:1130–5.
23. Gu Y, Zhou P, Ding Y, Wang P, Ni L. Root canal morphology of permanent three-rooted mandibular first molars: Part III—An odontometric analysis. *J Endod*. 2011;37:485–90.
24. Versiani MA, Pécora JD, Sousa-Neto MD. The anatomy of two-rooted mandibular canines determined using micro-computed tomography. *Int Endod J*. 2011;44:682–7.
25. Li X, Liu N, Ye L, Nie X, Zhou X, Wen X, et al. A micro-computed tomography study of the location and curvature of the lingual canal in the mandibular first premolar with two canals originating from a single canal. *J Endod*. 2012;38:309–12.
26. Fan B, Yang J, Gutmann JL, Fan M. Root canal systems in mandibular first premolars with C-shaped root configurations. Part I: Microcomputed tomography mapping of the radicular groove and associated root canal cross-sections. *J Endod*. 2008;34:1337–41.
27. Fan B, Cheung GS, Fan M, Gutmann JL, Bian Z. C-shaped canal system in mandibular second

- molars: Part I--Anatomical features. *J Endod.* 2004;30:899–903.
28. Gu Y, Zhang Y, Liao Z. Root and canal morphology of mandibular first premolars with radicular grooves. *Arch Oral Biol.* 2013;58:1609–17.
 29. Keleş A, Keskin C. A micro-computed tomographic study of band-shaped root canal isthmuses, having their floor in the apical third of mesial roots of mandibular first molars. *Int Endod J.* 2018;51:240–6.
 30. Keleş A, Keskin C. Apical root canal morphology of mesial roots of mandibular first molar teeth with Vertucci Type II configuration by means of micro-computed tomography. *J Endod.* 2017;43:481–5.
 31. Leoni GB, Versiani MA, Pécora JD, Sousa-Neto MD. Micro-computed tomographic analysis of the root canal morphology of mandibular incisors. *J Endod.* 2014;40:710–6.
 32. Liu N, Li X, Ye L, An J, Nie X, Liu L, et al. A micro-computed tomography study of the root canal morphology of the mandibular first premolar in a population from southwestern China. *Clin Oral Investig.* 2013;17:999–1007.
 33. Meder-Cowherd L, Williamson AE, Johnson WT, Vasilescu D, Walton R, Qian F. Apical morphology of the palatal roots of maxillary molars by using micro-computed tomography. *J Endod.* 2011;37:1162–5.
 34. Pratt WK. *Digital image processing.* 2nd ed. New York: Wiley; 1991.
 35. Lorensen WE, Cline HE. Marching cubes: a high resolution 3D surface construction algorithm. *Comp Graph.* 1987;21:163–9.
 36. Hildebrand T, Rüegsegger P. Quantification of bone micro architecture with the structure model index. *Comput Methods Biomech Biomed Engin.* 1997;1:15–23.
 37. Wu MK, R'Oris A, Barkis D, Wesselink PR. Prevalence and extent of long oval canals in the apical third. *Oral Surg Oral Med Oral Pathol Oral Radiol Endod.* 2000;89:739–43.
 38. Peters OA, Laib A, Gohring TN, Barbakow F. Changes in root canal geometry after preparation assessed by high-resolution computed tomography. *J Endod.* 2001;27:1–6.
 39. Boveda C, Kishen A. Contracted endodontic cavities: the foundation for less invasive alternatives in the management of apical periodontitis. *Endod Topics.* 2015;33:169–86.
 40. Silva EJNL, Rover G, Belladonna FG, De-Deus G, Teixeira CS, Fidalgo TKS. Impact of contracted endodontic cavities on fracture resistance of endodontically treated teeth: a systematic review of in vitro studies. *Clin Oral Investig.* 2017;22:109–18.
 41. Ordinola-Zapata R, Versiani MA, Bramante CM. Root canal components. In: Versiani MA, Basrani B, Sousa Neto MD, editors. *The root canal anatomy in permanent dentition.* Switzerland: Springer International Publishing; 2018. p. 31–46.
 42. Krishan R, Paqué F, Ossareh A, Kishen A, Dao T, Friedman S. Impacts of conservative endodontic cavity on root canal instrumentation efficacy and resistance to fracture assessed in incisors, premolars, and molars. *J Endod.* 2014;40:1160–6.
 43. Moore B, Verdelis K, Kishen A, Dao T, Friedman S. Impacts of contracted endodontic cavities on instrumentation efficacy and biomechanical responses in maxillary molars. *J Endod.* 2016;42:1779–83.
 44. Plotino G, Grande N, Isufi A, Ioppolo P, Pedullà E, Bedini R, et al. Fracture strength of endodontically treated teeth with different access cavity designs. *J Endod.* 2017;43:995–1000.
 45. Jiang Q, Huang Y, Tu X, Li Z, He Y, Yang X. Biomechanical properties of first maxillary molars with different endodontic cavities: a finite element analysis. *J Endod.* 2018;44:1283–8.
 46. Eaton JA, Clement DJ, Lloyd A, Marchesan MA. Micro-computed tomographic evaluation of the influence of root canal system landmarks on access outline forms and canal curvatures in mandibular molars. *J Endod.* 2015;41:1888–91.
 47. Siqueira JF Jr, Roças IN, Ricucci D. Internal tooth anatomy and root canal instrumentation. In: Versiani MA, Basrani B, Sousa Neto MD, editors. *The root canal anatomy in permanent dentition.* Switzerland: Springer International Publishing; 2018. p. 277–302.
 48. Bier CA, Shemesh H, Tanomaru-Filho M, Wesselink PR, Wu MK. The ability of different nickel-titanium rotary instruments to induce dentinal damage during canal preparation. *J Endod.* 2009;35:236–8.
 49. Shemesh H, Bier CA, Wu MK, Tanomaru-Filho M, Wesselink PR. The effects of canal preparation and filling on the incidence of dentinal defects. *Int Endod J.* 2009;42:208–13.
 50. Versiani MA, Souza E, De-Deus G. Critical appraisal of studies on dentinal radicular microcracks in endodontics: methodological issues, contemporary concepts, and future perspectives. *Endod Topics.* 2015;33:87–156.
 51. Berman LH, Kuttler S. Fracture necrosis: diagnosis, prognosis assessment, and treatment recommendations. *J Endod.* 2010;36:442–6.
 52. De-Deus G, Belladonna FG, Marins JR, Silva EJ, Neves AA, Souza EM, et al. On the causality between dentinal defects and root canal preparation: a micro-CT assessment. *Braz Dent J.* 2016;27:664–9.
 53. De-Deus G, Belladonna FG, Souza EM, Silva EJ, Neves Ade A, Alves H, et al. Micro-computed tomographic assessment on the effect of protaper next and twisted file adaptive systems on dentinal cracks. *J Endod.* 2015;41:1116–9.
 54. De-Deus G, Cesar de Azevedo Carvalhal J, Belladonna FG, Silva E, Lopes RT, Moreira Filho RE, et al. Dentinal microcrack development after canal preparation: a longitudinal in situ micro-computed tomography study using a cadaver model. *J Endod.* 2017;43:1553–8.
 55. De-Deus G, Silva EJ, Marins J, Souza E, Neves Ade A, Goncalves Belladonna F, et al. Lack of causal relationship between dentinal microcracks and root

- canal preparation with reciprocation systems. *J Endod.* 2014;40:1447–50.
56. Gambill JM, Alder M, del Rio CE. Comparison of nickel-titanium and stainless steel hand-file instrumentation using computed tomography. *J Endod.* 1996;22:369–75.
 57. Versiani MA, Pécora JD, Sousa-Neto MD. Flat-oval root canal preparation with self-adjusting file instrument: a micro-computed tomography study. *J Endod.* 2011;37:1002–7.
 58. Siqueira JF Jr, Alves FRF, Versiani MA, Roças IN, Almeida BM, Neves MAS, et al. Correlative bacteriologic and micro-computed tomographic analysis of mandibular molar mesial canals prepared by Self-Adjusting File, Reciproc, and Twisted File systems. *J Endod.* 2013;39:1044–50.
 59. Fan B, Pan Y, Gao Y, Fang F, Wu Q, Gutmann JL. Three-dimensional morphologic analysis of isthmuses in the mesial roots of mandibular molars. *J Endod.* 2010;36:1866–9.
 60. Gu L, Wei X, Ling J, Huang X. A microcomputed tomographic study of canal isthmuses in the mesial root of mandibular first molars in a Chinese population. *J Endod.* 2009;35:353–6.
 61. Mannocci F, Peru M, Sherriff M, Cook R, Pitt Ford TR. The isthmuses of the mesial root of mandibular molars: a micro-computed tomographic study. *Int Endod J.* 2005;38:558–63.
 62. Somma F, Leoni D, Plotino G, Grande NM, Plasschaert A. Root canal morphology of the mesiobuccal root of maxillary first molars: a micro-computed tomographic analysis. *Int Endod J.* 2009;42:165–74.
 63. Paqué F, Laib A, Gautschi H, Zehnder M. Hard-tissue debris accumulation analysis by high-resolution computed tomography scans. *J Endod.* 2009;35:1044–7.
 64. De-Deus G, Marins J, Silva EJ, Souza E, Belladonna FG, Reis C, et al. Accumulated hard tissue debris produced during reciprocating and rotary nickel-titanium canal preparation. *J Endod.* 2015;41:676–81.
 65. Keleş A, Alcin H, Sousa-Neto MD, Versiani MA. Supplementary steps for removing hard tissue debris from isthmus-containing canal systems. *J Endod.* 2016;42:1677–82.
 66. Versiani MA, Alves FR, Andrade-Junior CV, Marceliano-Alves MF, Provenzano JC, Rocas IN, et al. Micro-CT evaluation of the efficacy of hard-tissue removal from the root canal and isthmus area by positive and negative pressure irrigation systems. *Int Endod J.* 2016;49:1079–87.
 67. Paqué F, Boessler C, Zehnder M. Accumulated hard tissue debris levels in mesial roots of mandibular molars after sequential irrigation steps. *Int Endod J.* 2011;44:148–53.
 68. Versiani MA, de Deus G, Vera J, Souza E, Steier L, Pécora JD, et al. 3D mapping of the irrigated areas of the root canal space using micro-computed tomography. *Clin Oral Investig.* 2015;19:859–66.
 69. Ørstavik D. Physical properties of root canal sealers: measurement of flow, working time, and compressive strength. *Int Endod J.* 1983;16:99–107.
 70. De-Deus G, Reis C, Beznos D, de Abranches AM, Coutinho-Filho T, Paciornik S. Limited ability of three commonly used thermoplasticized gutta-percha techniques in filling oval-shaped canals. *J Endod.* 2008;34:1401–5.
 71. Moeller L, Wenzel A, Wegge-Larsen AM, Ding M, Kirkevang LL. Quality of root fillings performed with two root filling techniques. An in vitro study using micro-CT. *Acta Odontol Scand.* 2013;71:689–96.
 72. Keleş A, Alcin H, Kamalak A, Versiani MA. Oval-shaped canal retreatment with self-adjusting file: a micro-computed tomography study. *Clin Oral Investig.* 2014;18:1147–53.
 73. Keleş A, Alcin H, Kamalak A, Versiani MA. Micro-CT evaluation of root filling quality in oval-shaped canals. *Int Endod J.* 2014;47:1177–84.
 74. Siqueira JF Jr. Reaction of periradicular tissues to root canal treatment: benefits and drawbacks. *Endod Topics.* 2005;10:123–47.
 75. Somma F, Cammarota G, Plotino G, Grande NM, Pameijer CH. The effectiveness of manual and mechanical instrumentation for the retreatment of three different root canal filling materials. *J Endod.* 2008;34:466–9.
 76. Keleş A, Arslan H, Kamalak A, Akcay M, Sousa-Neto MD, Versiani MA. Removal of filling materials from oval-shaped canals using laser irradiation: a micro-computed tomographic study. *J Endod.* 2015;41:219–24.
 77. Al-Fouzan K, Al-Garawi Z, Al-Hezaimi K, Javed F, Al-Shalan T, Rotstein I. Effect of acid etching on marginal adaptation of mineral trioxide aggregate to apical dentin: microcomputed tomography and scanning electron microscopy analysis. *Int J Oral Sci.* 2012;4:202–7.
 78. Celikten B, F Uzuntas C, I Orhan A, Tufenkci P, Misirli M, O Demiralp K, et al. Micro-CT assessment of the sealing ability of three root canal filling techniques. *J Oral Sci.* 2015;57:361–6.
 79. Huang Y, Orhan K, Celikten B, Orhan AI, Tufenkci P, Sevimey S. Evaluation of the sealing ability of different root canal sealers: a combined SEM and micro-CT study. *J Appl Oral Sci.* 2018;26:e20160584.
 80. Kim SY, Kim HC, Shin SJ, Kim E. Comparison of gap volume after retrofilling using 4 different filling materials: evaluation by micro-computed tomography. *J Endod.* 2018;44:635–8.
 81. Neves AA, Jaecques S, Van Ende A, Cardoso MV, Coutinho E, Luhrs AK, et al. 3D-microleakage assessment of adhesive interfaces: exploratory findings by μ CT. *Dent Mater.* 2014;30:799–807.
 82. Zaslansky P, Fratzl P, Rack A, Wu MK, Wesselink PR, Shemesh H. Identification of root filling interfaces by microscopy and tomography methods. *Int Endod J.* 2011;44:395–401.
 83. Cavenago BC, Pereira TC, Duarte MA, Ordinola-Zapata R, Marciano MA, Bramante CM, et al.

- Influence of powder-to-water ratio on radiopacity, setting time, pH, calcium ion release and a micro-CT volumetric solubility of white mineral trioxide aggregate. *Int Endod J.* 2014;47:120–6.
84. Silva EJ, Perez R, Valentim RM, Belladonna FG, De-Deus GA, Lima IC, et al. Dissolution, dislocation and dimensional changes of endodontic sealers after a solubility challenge: a micro-CT approach. *Int Endod J.* 2017;50:407–14.
 85. Torres FFE, Bosso-Martelo R, Espir CG, Cirelli JA, Guerreiro-Tanomaru JM, Tanomaru-Filho M. Evaluation of physicochemical properties of root-end filling materials using conventional and micro-CT tests. *J Appl Oral Sci.* 2017;25:374–80.
 86. De-Deus G, Scelza MZ, Neelakantan P, Sharma S, Neves Ade A, Silva EJ. Three-dimensional quantitative porosity characterization of syringe- versus hand-mixed set epoxy resin root canal sealer. *Braz Dent J.* 2015;26:607–11.
 87. Guerrero F, Berastegui E. Porosity analysis of MTA and Biodentine cements for use in endodontics by using micro-computed tomography. *J Clin Exp Dent.* 2018;10:e237–e40.
 88. Keleş A, Ahmetoglu F, Uzun I. Quality of different gutta-percha techniques when filling experimental internal resorptive cavities: a micro-computed tomography study. *Aust Endod J.* 2014;40:131–5.
 89. Kim TO, Cheung GS, Lee JM, Kim BM, Hur B, Kim HC. Stress distribution of three NiTi rotary files under bending and torsional conditions using a mathematic analysis. *Int Endod J.* 2009;42:14–21.
 90. Peters OA, Morgental RD, Schulze KA, Paqué F, Kopper PM, Vier-Pelisser FV. Determining cutting efficiency of nickel-titanium coronal flaring instruments used in lateral action. *Int Endod J.* 2014;47:505–13.
 91. Bonessio N, Pereira ES, Lomiento G, Arias A, Bahia MG, Buono VT, et al. Validated finite element analyses of WaveOne Endodontic Instruments: a comparison between M-Wire and NiTi alloys. *Int Endod J.* 2015;48:441–50.
 92. Kim HC, Sung SY, Ha JH, Solomonov M, Lee JM, Lee CJ, et al. Stress generation during self-adjusting file movement: minimally invasive instrumentation. *J Endod.* 2013;39:1572–5.
 93. Santos Lde A, Bahia MG, de Las Casas EB, Buono VT. Comparison of the mechanical behavior between controlled memory and superelastic nickel-titanium files via finite element analysis. *J Endod.* 2013;39:1444–7.
 94. Keleş A, Torabinejad M, Keskin C, Sah D, Uzun I, Alçin H. Micro-CT evaluation of voids using two root filling techniques in the placement of MTA in mesial root canals of Vertucci type II configuration. *Clin Oral Investig.* 2018;22:1907–13.
 95. Ordinola-Zapata R, Bramante CM, Duarte MA, Cavenago BC, Jaramillo D, Versiani MA. Shaping ability of reciproc and TF adaptive systems in severely curved canals of rapid microCT-based prototyping molar replicas. *J Appl Oral Sci.* 2014;22:509–15.
 96. Lloyd A, Navarrete G, Marchesan MA, Clement D. Removal of calcium hydroxide from Weine Type II systems using photon-induced photoacoustic streaming, passive ultrasonic, and needle irrigation: a microcomputed tomography study. *J Appl Oral Sci.* 2016;24:543–8.
 97. Ma J, Shen Y, Yang Y, Gao Y, Wan P, Gan Y, et al. In vitro study of calcium hydroxide removal from mandibular molar root canals. *J Endod.* 2015;41:553–8.
 98. Ikram OH, Patel S, Sauro S, Mannocci F. Micro-computed tomography of tooth tissue volume changes following endodontic procedures and post space preparation. *Int Endod J.* 2009;42:1071–6.
 99. Schroeder AA, Ford NL, Coil JM. Micro-computed tomography analysis of post space preparation in root canals filled with carrier-based thermoplasticized gutta-percha. *Int Endod J.* 2017;50:293–302.
 100. Uzun I, Keleş A, Arslan D, Güler B, Keskin C, Gündüz K. Influence of oval and circular post placement using different resin cements on push-out bond strength and void volume analysed by micro-CT. *Int Endod J.* 2016;49:1175–82.
 101. Ordinola-Zapata R, Bramante CM, Versiani MA, Moldauer BI, Topham G, Gutmann JL, et al. Comparative accuracy of the clearing technique, CBCT and Micro-CT methods in studying the mesial root canal configuration of mandibular first molars. *Int Endod J.* 2017;50:90–6.
 102. Versiani MA, Sousa-Neto MD, Pécora JD. Pulp pathosis in inlayed teeth of the ancient Mayas: a microcomputed tomography study. *Int Endod J.* 2011;44:1000–4.
 103. Kalatzis-Sousa NG, Spin-Neto R, Wenzel A, Tanomaru-Filho M, Faria G. Use of micro-computed tomography for the assessment of periapical lesions in small rodents: a systematic review. *Int Endod J.* 2017;50:352–66.
 104. Balto K, Muller R, Carrington DC, Dobeck J, Stashenko P. Quantification of periapical bone destruction in mice by micro-computed tomography. *J Dent Res.* 2000;79:35–40.
 105. Chen I, Karabucak B, Wang C, Wang HG, Koyama E, Kohli MR, et al. Healing after root-end microsurgery by using mineral trioxide aggregate and a new calcium silicate-based bioceramic material as root-end filling materials in dogs. *J Endod.* 2015;41:389–99.
 106. Martins CM, Sasaki H, Hirai K, Andrada AC, Gomes-Filho JE. Relationship between hypertension and periapical lesion: an in vitro and in vivo study. *Braz Oral Res.* 2016;30:e78.
 107. Oliveira KM, Nelson-Filho P, da Silva LA, Kuchler EC, Gatón-Hernandez P, da Silva RA. Three-dimensional micro-computed tomography analyses of induced periapical lesions in transgenic mice. *Ultrastruct Pathol.* 2015;39:402–7.
 108. von Stechow D, Balto K, Stashenko P, Muller R. Three-dimensional quantitation of periradicular

- bone destruction by micro-computed tomography. *J Endod.* 2003;29:252–6.
109. Basrani B, Versiani MA. Contemporary strategies for teaching internal anatomy of teeth. In: Versiani MA, Basrani B, Sousa Neto MD, editors. *The root canal anatomy in permanent dentition.* Switzerland: Springer International Publishing; 2018. p. 373–90.
110. Nassri MR, Carlik J, da Silva CR, Okagawa RE, Lin S. Critical analysis of artificial teeth for endodontic teaching. *J Appl Oral Sci.* 2008;16:43–9.
111. Buchanan LS. Everything's changed except the anatomy! *Dent Today.* 2012;31(100):2, 4–5.
112. Gutmann JL, Rigsby S. Meeting age old challenges in root canal procedures with contemporary technological assessments. *ENDO.* 2015;9:107–10.
113. Kato A, Ohno N. Construction of three-dimensional tooth model by micro-computed tomography and application for data sharing. *Clin Oral Investig.* 2009;13:43–6.



Micro-Computed Tomography (Micro-CT) Analysis as a New Approach for Characterization of Drug Delivery Systems

Müge Kılıçarslan, Miray İlhan, and Kaan Orhan

13.1 Introduction

In recent years, the design of new dosage forms that can provide treatment with the use of less drug and less dosing has been a prominent approach in medical treatment. With this approach, novel drugs are developed that can exhibit controlled release or sustained/extended release via new polymers and new drug delivery systems. The use of new techniques in *in vitro* and *in vivo* characterization studies in pre-formulation, formulation, and stability studies has become necessary as the preparation techniques of the drugs, the polymeric substances used, and the drug administration methods have changed. For example, organoleptic controls used to be performed visually in the preparation

Electronic supplementary material The online version of this chapter (https://doi.org/10.1007/978-3-030-16641-0_13) contains supplementary material, which is available to authorized users.

M. Kılıçarslan (✉) · M. İlhan
Faculty of Pharmacy, Department of Pharmaceutical
Technology, Ankara University, Ankara, Turkey

K. Orhan
Faculty of Dentistry, Department of Dentomaxillofacial
Radiology, Ankara University, Ankara, Turkey

Faculty of Medicine, OMFS IMPATH Research
Group, Department of Imaging and Pathology,
University of Leuven, Leuven, Belgium

Oral and Maxillofacial Surgery, University Hospitals
Leuven, University of Leuven, Leuven, Belgium

of drug formulations, but now detailed examination of much smaller dimensions has become possible by analysis methods such as optical microscope, scanning electron microscope (SEM), and transmission electron microscope (TEM). Through the elaboration of these and similar structural analyses, it will be possible to produce a drug in the desired critical quality attributes (CQA) more easily. In pre-formulation and formulation studies, critical process parameters (CPP) that may affect the CQA of the drug during the process need to be determined, at which point the use of accurate and detailed analysis methods plays a key role in achieving a more accurate result.

All the stages of release of the drug from the carrier system in the administered body part with the desired speed and mechanism and the ability to adjust the duration of drug activity in the application area, adjusting the mechanisms such as degradation/disintegration, absorption or resorption after the active agent exhibits the desired effect, and the elimination of the drug carrier system from the body, are guided by the elaboration of formulation characterization studies.

From the smallest drug to the largest, drug characteristics such as the size, shape, surface area of the drug, the volume, swelling or erosion characteristics, the presence or absence of porosity on the surface or inside, and whether these porosities structures are interconnected are important factors that may affect the CQA of the

dosage form. With the use of three-dimensional (3D) printers, a more detailed 3D examination of the produced dosage form has become possible today. Literature review revealed drug-related studies conducted with micro-computed tomography (micro-CT). In general, in the 2000s, this analysis method was first used in the production of biomaterials and then began to be used in the *in vivo* evaluation of some drug-loaded biomaterials, especially in the examination of bone and tissue regeneration studies, and more recently began to be used in the characterization studies in the production of tablet, granule, injectable preparations, implant, *in situ* implant, scaffold, film, and micro- and nanoparticles.

13.2 Micro-CT in Scaffold Characterization

Previously, micro-CT analysis was primarily used in *in vivo* evaluations in scaffold studies designed for tissue engineering and bone and tissue regeneration [1, 2]. Later, micro-CT began to be used for structural examinations in the production of drug-loaded scaffold for regeneration therapy. In this sense, the first and most widespread use of micro-CT in drug delivery systems is scaffold production. Effective scaffold assessment techniques were required for the selection of structures and architectures with proper characteristics during the preparation of scaffolds in tissue engineering, and it was found that evaluations could be made by micro-CT in addition to SEM analysis, mercury porosimetry, gas pycnometry, gas adsorption, and flow porosimetry [3]. It is important to determine characteristics such as porosity, pore size, surface area/volume ratio, interconnectivity, anisotropy, strut thickness, cross-sectional area, and permeability for the structural analysis of scaffolds and the selection and production of the appropriate structure [4–6]. Researchers have mostly examined porosity in the structural analysis of scaffolds, because porosity determines important characteristics such as cell seeding efficiency, diffusion, and mechanical strength. In addition to porosity, characteristics such as pore size and whether pores are interconnected in the matrix structure are effective factors in the diffusion of drug from

drug-loaded scaffold and its release in the administered tissue [3, 7].

Using micro-CT, Lin et al. [7] investigated the effect of 5% to 30% increased use of porogen substance (azodicarbonamide) in micro-CT studies and biodegradable porous poly(L-lactide-co-D,L-lactide) scaffold production, and they were able to examine 3D microstructural morphology and anisotropy of the samples with micro-CT. In the study, 3D scaffold images were converted to analyze pore interconnectivity by quantifying the number and size of connected pore space domains. With micro-CT, volume fraction, strut density, strut thickness, strut spacing, and anisotropy degree were determined, and volume fraction decreased with increasing amount of porosity as expected [7].

Surface area increases due to the increased microporosity, which leads to fast revascularization as the adhesion to the cell increases. Therefore, it is important to examine porosity in scaffold formulations. They determined that the calculation of the abovementioned characteristics from micro-CT measurements is important in terms of clarification such structures and formulation development. Wang et al. [8] also produced poly- ϵ -caprolactone (PCL) tissue scaffolds with precision extrusion deposition method and used micro-CT technique to examine microstructure and morphology. Thanks to micro-CT, 3D imaging became possible, and porosity and interconnectivity analysis could be performed [8].

In another study conducted with PCL, PCL matrix and superparamagnetic iron oxide or iron-doped hydroxyapatite nanoparticles were fabricated through a 3D fiber deposition technique. Micro-CT confirmed the possibility to design morphologically controlled structures with fully interconnected pore network. Pore size and shape and microstructure were analyzed by micro-CT. Mean fiber diameter of 500 μm and center-to-center fiber distance of about 1000 μm were calculated [6].

Another group of researchers prepared microporous biocomposite PCL matrices with the precipitation casting method and used micro-CT for structural investigations after release of lactose and gelatin which they loaded into the matrix. Micro-CT was used in the structural analysis performed on the samples after release of drug, and they found that protein

release from protein-loaded scaffold varied depending on the relationship between increase in pore diameter and particle specific area/dissolution rate. Micro-CT analysis of lactose-PCL and gelatin-PCL matrices was performed by taking internal microtomographs, before release and after release, and a detailed quantitative measurement of the equivalent pore diameters of the pores in the matrix could be made. Release studies have also demonstrated the importance of pore networks in the efficient diffusion of small molecule lactose and macromolecular gelatin. Areas smaller than 15 μm could not be determined due to the resolution capacity of the micro-CT used in this study, and this showed that the capacity of the device to be used and the dimensions to be examined in the study material should be compatible. In addition, it was found in this study that the diffusion and thus the release were reduced when interconnectivity between the intra-matrix pores was low, and owing to the detailed structure analyses conducted with micro-CT, it was determined that the scaffold planned to be applied to soft tissue could be prepared as storage systems in the controlled release of growth factors [9–11].

13.2.1 Micro-CT in Injectable In Situ Implant Scaffold Characterization

Porosity is an important design criterion for scaffolds used in tissue engineering applications, because porosity affects cell adhesion, migration, proliferation, and extracellular matrix production within the scaffold at a tissue defect site.

Scaffold applications may be in the form of hydrogel-based injectable preparations. In this type of scaffolds, it was determined that the porosity was nano-sized and not suitable for cell migration and proliferation. Micron-sized porosity can be provided on solid implants. Krebs et al. [12] prepared microporous injectable poly(lactico-glycolic acid) (PLGA) implants that could solidify in situ, and micro-CT method was used to examine the porosity in the structure. In this study, they used sodium chloride as a porogenic material and used micro-CT to determine porosity size, shape, and percentage and found that a

porosity of 31.19% in nonporous scaffolds could be increased to 72.24% in formulations prepared with porogenic materials [12].

13.3 Micro-CT in Microparticle Characterization

We have seen in recent years that different active substances and bioactive substances can be prepared as injectable systems of micro- and nanoparticles to be used in tissue engineering. In a study conducted on the preparation and characterization of microparticles with dexamethasone-loaded starch-polycaprolactone polymeric mixture, micro-CT method was used for morphological examination of porous surface microparticles. At the end of the analysis, %porosity could be calculated in addition to 3D imaging [13].

13.3.1 Micro-CT in Microparticle-Loaded Scaffold Characterization

Formulations capable of enhancing bone regeneration and increasing bone density could be prepared by attaching the microparticles to the inside or surface of scaffolds. In the case of high porosity and the interconnectivity of materials of different densities, it is observed that finding out the pore size and the degree of porosity in addition to 3D structural examination by micro-CT analysis is important for determining whether micro- or nanoparticles can be placed within this structure [13–16].

In bone regeneration studies, use of hydroxyapatite (HAp) due to its similarity to apatite, which already exists in the natural bone structure, stands out. Attaching therapeutic agents to the surface of this porous HAp scaffold and using drug release systems that enable long-term drug release have resulted in more successful outcomes in bone regeneration. In their study, Son et al. [15] produced dexamethasone-loaded PLGA microspheres, and these microspheres were also loaded into HAp scaffolds, and excellent bone formation was obtained in in vivo tests. The researchers used the micro-CT method in addition to SEM for the morphological

examination of the porous scaffold and detected the presence of open channels in the isotropic geometry by determining pore size and interconnectivity. In addition, formation of dense cortical bone was detected 10 weeks after implantation, and micro-CT analysis revealed that the application of dexamethasone-loaded microspheres in HAp porous scaffold yielded significantly higher bone mineral density [15].

Patel et al. [14] investigated bone morphogenetic protein-2 (BMP-2) release in BMP-2-loaded gelatin and PLGA microparticles from biodegradable composite and polypropylene fumarate scaffolds *in vitro* and *in vivo*, and they used micro-CT method to examine the 3D porosity and porous interconnectivity of scaffolds. With the 3D analysis made with micro-CT, both the porosity and pore size and the porosity percentage of the scaffold were determined prior to loading in order to better understand whether BMP-2-loaded microparticles could hold onto the pores in the scaffold structure. It was observed that sensitive determination of these properties provided a significant advantage in preparation of formulation [14].

13.4 Micro-CT in Granule Characterization

One of the most important properties of pharmaceutical granules is their porosity. Due to widespread use of micro-CT method in determination of pore size and porosity in regeneration studies, researchers have tried to use micro-CT analysis method to determine porosity in granules. Checking the pores in the granules is one of the important analyses that may affect the wet and dry strength of granules and their dispersion and dissolution properties in liquid medium and therefore the rate of release of the active substance they contain and dissolution and absorption in the affected area when administered as a drug. In order to optimize the abovementioned critical properties, the pore structure is characterized by various methods to keep the granules under control during their formulations and to produce granules with the desired porosity. Farber et al. [17] produced granules from man-

nitol, lactose, and lactose/Avicel (60%/40%) with different binders and methods and comparatively investigated porosity in granules by mercury porosimetry and SkyScan 1072 high-resolution X-ray microtomography. They were able to perform detailed morphological examinations on pore shape, spatial distribution, and connectivity characteristics. It was found that mercury intrusion measures the pore neck size distribution, while tomography measures the true size distribution of pores ca. 4 μm or larger [17]. The results of this study suggest that micro-CT analyses can be used more frequently in the future for especially drug production with quality by design (QbD) approach.

13.5 Micro-CT in Characterization of Tablets

There are some examples of the use of micro-CT for characterization of tablets. However, these published studies show that micro-CT analysis will gain more importance in characterization and formulation development in the following years. Density variations/distributions in tablets are examined in these studies. Density change in tablet compressing is a parameter that affects compact mechanical properties and should therefore be examined. Density changes affect the disintegration time and disintegration mechanism of the tablet after compressing, the dissolution rate and the mechanical properties of the tablet during the shipment (strength inside packaging), and storage and use of the tablets; for this reason, it is important to examine intra-tablet density variations and determine the most suitable process parameters for the production of tablets having the desired critical quality characteristics [18–21]. Two capsule-shaped tablets of identical size but different cup geometries were compressed using microcrystalline cellulose (Avicel PH 102) by Sinka et al. [19]. The researchers were able to prepare the density map of the tablets with the calibrated X-ray microtomography analysis method but concluded that the factors affecting the density distribution in tablets should be examined for each tablet formulation and compressing condition and generalizations cannot be made. However, by using the maps obtained by micro-

CT, they concluded that different cup geometries affected density distribution, density was less in the break-line region and on the upper surfaces of the tablet, density decreased on the convex side of uni-convex tablets, and although density increased in the two sides of the tablet and the middle and density distribution was more homogeneous in biconvex tablets, the density was lower compared to the other tablet. Porous material strength increases with density, which suggests that tablet performance may be adversely affected by low-density regions. Therefore, they concluded that a lower degree of density distribution in biconvex tablets was more likely to have a negative effect on post-compression properties such as coating, packaging, and dispersion. The study suggests that micro-CT analyses may be useful in the examination of the effects of shape, compression rate, and strength of the tablet punch on tablet hardness [19].

Another group of researchers compressed tablets with different porosities (from 7.7% to 33.5%) using microcrystalline cellulose (Vivapur 12[®]) and prepared density profiles by X-ray tomography. The researchers quantitatively evaluated heterogeneous density distribution within tablets compressed by direct compression method. As a result of the study, they found that Beer-Lambert low validation should be performed, and density variations could be measured with X-ray tomography which is a nondestructive inspection technique instead of a destructive technique like surface hardness. With this study, it is seen that the micro-CT method may be a solution for the elimination of undesirable fractures occurring independent of tablet hardness, depending on the force direction applied during the process and the shape of the tablet, which has been a topic of debate for years in methods of determining tablet hardness [20].

On the other hand, Losi et al. [21] used high-resolution X-ray CT to examine the swelling properties of Dome Matrix drug release modules. Drug delivery systems need to be able to release the drug at the required amount with the required kinetics in the desired region of the body. A significant proportion of oral drug delivery systems have a swelling matrix structure. Swelling matrices change their size and volume by taking the

liquid into their structures in the presence of water or body fluids and allow the drug to be released. In the systems prepared as Dome Matrix, it has been determined that the swelling property of the curved surface of the matrix significantly affects the release of drug and the release kinetics. However, the degree of dynamic swelling could not be determined by optical techniques. Thereon, the researchers thought of using the high-resolution X-ray tomography method to determine the swelling behavior of the Dome Matrix system, because this analysis method enabled examination of density distributions of the materials in previous studies, and the researchers decided that this analysis could be used because the visible density of the polymer changed when it was hydrated. With X-ray CT, it was possible to visualize the gel with a higher density than water. Thus, the image of solid particles, partially swollen particles, and the gel could be obtained. Dry glassy core volume and surface area were calculated during the swelling period using Blob 3D software. It was possible to obtain details such as how the gelling occurs and how the swelling changes depending on the polymer particle size. With this study, researchers proved that X-ray CT method can provide more detailed data in the examination of swelling and drug release mechanisms in drug delivery systems [21].

Doerr et al. [18] also declared in the Micro-CT User Meeting that X-ray nanotomography method was being used as a more detailed characterization method in the structural examination of 3D tablets prepared by 3D printing method, which has become more widespread in recent years and enables a more homogeneous final product, and quantitative results would be provided in future studies [18].

13.6 Micro-CT Analysis of Intraocular Drug Delivery Systems

One of the drug delivery systems characterized by micro-CT is the cross-linked poly(propylene fumarate) matrices, which provide intraocular extended release of fluocinolone acetonide (FA), an anti-inflammatory agent. It has been found that

the release from the FA-loaded rod matrices can be extended up to 400 days. With the structural analysis performed by micro-CT, the dimensional change of this drug delivery system and surface structures were examined, and they determined bulk erosion on the surface of drug delivery system. The data on the cross-sectional areas obtained by micro-CT were correlated with water content and mass loss analyses, which was presented as a proof that micro-CT is a reliable method [22].

13.7 Characterization Studies on Polyelectrolyte Complex Film and Nanoparticles by Micro-CT Analysis

13.7.1 Micro-CT in Characterization of Polyelectrolyte Complex Film

In our study, clindamycin phosphate (CDP) loaded alginate-chitosan mucoadhesive polyelectrolyte complex (PEC) films were prepared using solvent casting method in terms of periodontal applications in order to control the drug release and examine the effects of the concentration and molecular weight of polymers (low (LC) and medium (MC) molecular weight chitosan) and the volume of polymer solutions on the characteristics of the films. The thickness measurement, in vitro drug release studies, swelling studies, textural analysis, Fourier-transform infrared (FTIR) spectrum analysis, and morphological analysis were performed for characterization of the PEC films. Although structural analysis played an essential role in our study in order to observe the morphological features of the drug-loaded complex, sufficiently descriptive results could not be obtained by optical microscopy or SEM. Therefore, 3D microarchitecture of PEC films was analyzed by micro-CT [23].

Accordingly, high-resolution, desktop micro-CT systems (Bruker SkyScan 1275, Kontich, Belgium) were used to scan the PEC film formulations (scanning conditions: 100 kVp, 100 mA, 0.5 mm Al/Cu filter, 4.2 μm pixel size, rotation at 0.2 step). Air calibration of the detector was carried out prior to each scanning to minimize ring artifacts.

The NRecon software (ver. 1.6.10.4, SkyScan, Kontich, Belgium) and CTAn (ver. 1.16.1.0, SkyScan, Belgium) were used for the visualization and quantitative measurements of the sample, preferred in the modified algorithm described by Feldkamp et al. to obtain axial, two-dimensional (2D), 1000 \times 1000-pixel images [24]. For the reconstruction parameters, ring artifact correction and smoothing were fixed at zero, and the beam artifact correction was set at 40%. By using the NRecon software (SkyScan, Kontich, Belgium), the images obtained by the scanner were reconstructed in order to demonstrate 2D slices of the films. In total 1023 cross-sectional images were reconstructed from the entire volume in micro-CT. Moreover, the CTAn (SkyScan, Aartselaar, Belgium) software was used for the 3D volumetric visualization and analysis of the films. All reconstructions were performed on a 21.3-in. flat-panel color-active matrix TFT medical display (NEC MultiSync MD215MG, Munich, Germany) with a resolution of 2048–2560 at 75 Hz and 0.17-mm dot pitch operated at 11.9 bits.

After reconstruction, region of interests (ROI) were drawn to include entire specimen within the sample using CTAn software, where all specifications of the program were used in order to analyze the 3D microarchitecture of sample.

A suitable threshold was required in order to distinguish drug-loaded coacervate from the whole film specimen. Therefore, threshold was set as the lower limit was between 0 and 255 (in gray values) and the upper limit was at the top end of the brightness spectrum representing the highest-density value. For calculation of the coacervate volumes and radius in 3D volumes, the original grayscale images were processed with a Gaussian low-pass filter for noise reduction, and an automatic segmentation threshold was used. A thresholding (binarization) process which entails processing the range of gray levels to obtain an imposed image of black/white pixels was preferred. Then, a region of interest was selected to contain a single object entirely separately for each slice to allow calculation of volumes.

Four structural parameters in each sample were measured over the entire volume of the specimen as follows:

Table 13.1 Selected parameters from 3D micro-CT analysis of PEC films and nanoparticles

	TV (mm ³)	Obj. V (mm ³)	Obj. V/TV (%)	SMI		Radius of coacervates		
				Film	Coacervate	Min.	Max.	Average
F1	536	33.2	6.19	0.14	1.28	180 μm	389 μm	224 μm
F2	815	9.59	9.8	0.2	1.23	305 μm	1134 μm	682 μm
N1	1502	122.6	7.82	0.02	1.24	86 nm	148 nm	135 nm
N2	1062	138.4	11.76	0.014	1.82	66 nm	138 nm	104 nm

- Total volume (TV) refers to entire film specimen.
- Object volume (Obj.V) refers to the drug-loaded coacervate volume.
- Obj.V/TV (%) refers to the total amount of coacervates in relation to the analyzed film volume.
- Structural model index (SMI) determines the relative presence of either platelike or rodlike shape of the evaluated structure. It is defined in a range of 0–3, where closer to 0 corresponds to an ideal plate and 3 to an ideal cylinder. Moreover, the radius of the coacervates was measured.

The data obtained by micro-CT have demonstrated that coacervates formed in PEC films prepared with LC (F1) were smaller than coacervates in PEC films prepared with MC (F2). In addition, it was proved that it was possible to form more particles in F1 according to the data expressing the total volume of coacervates in the film (Obj. V) (Table 13.1). Furthermore, these findings were supported by 3D images obtained by micro-CT imaging (Fig. 13.1 and Movie Picture 13.1). In brief, both quantitative and visual comparison of the films were provided by means of this method. As a conclusion, it was revealed that this method could be very advantageous for further complexation studies than the other imaging methods in order to determine the complex film structure, the volume, and the size of the formed complexes within the structure at the same time [23].

13.7.2 Micro-CT in Characterization of CDP-Loaded Nanoparticles

In the other part of our study, imaging analysis was performed with CDP-loaded nanoparticles. Firstly, nanoparticles were prepared using a modified double-emulsion water-in-oil-in-water ($w_1/o/w_2$)

by solvent evaporation technique [25, 26] for loading on PEC film or graft. Briefly, 1 mL of internal aqueous solution containing 20 mg CDP was added dropwise to PLGA (ester terminated, 50:50, Mw: 24,000–38,000 (Sigma-Aldrich/Germany)) solution in dichloromethane (DCM) (100 mg/1 mL). The primary emulsion was prepared by using ultrasonic homogenizer (Bandelin Sonopuls, HD2070, Germany) in an ice bath for 1 min, at 38% power. Then primary emulsion was added to 20 mL of external aqueous solution containing 0.1% (N1) or 0.3% (N2) (w/v) of poly(vinyl alcohol) (PVA) (Mowiol 4–88, Mw: 31000 (Sigma-Aldrich, Germany)) and homogenized by Ultra-Turrax homogenizer (IKA, Labortechnik, T25 basic, Germany) for 10 min at 8000 rpm. The resulting $w/o/w$ emulsion was diluted with 10 mL of the same concentration of PVA solution and stirred for 3 h at 500 rpm with a magnetic stirrer under fume hood until DCM was completely evaporated. Nanoparticles were collected by centrifugation at 20,000 rpm for 30 min (Sigma 3–30 KS). The particles were washed with distilled water and centrifuged again at 20,000 rpm for 30 min. The resulting particles were frozen at -20 °C and lyophilized for 24 h (Christ Gamma 2–15 LSC). The nanoparticles were stored in glass vials at 4 °C.

Measurements for particle size and zeta potential were performed by Zetasizer Nano Series (Nano-ZS) (Malvern Inst., England), and encapsulation efficiency of N1 and N2 was calculated. According to the findings, increasing PVA concentration from 0.1% to 0.3% reduced the nanoparticle size (N1: 367.8 ± 73.00 nm; N2: 229.4 ± 6.00 nm). On the other hand, it increased encapsulation efficiency (%) (N1: 18.53 ± 0.80 ; N2: 44.89 ± 0.30). Following these analyses, micro-CT imaging was performed with nanoparticle formulations. Firstly, Bruker SkyScan 1275 micro-CT system (Kontich, Belgium) was used, but no clear image was obtained by means

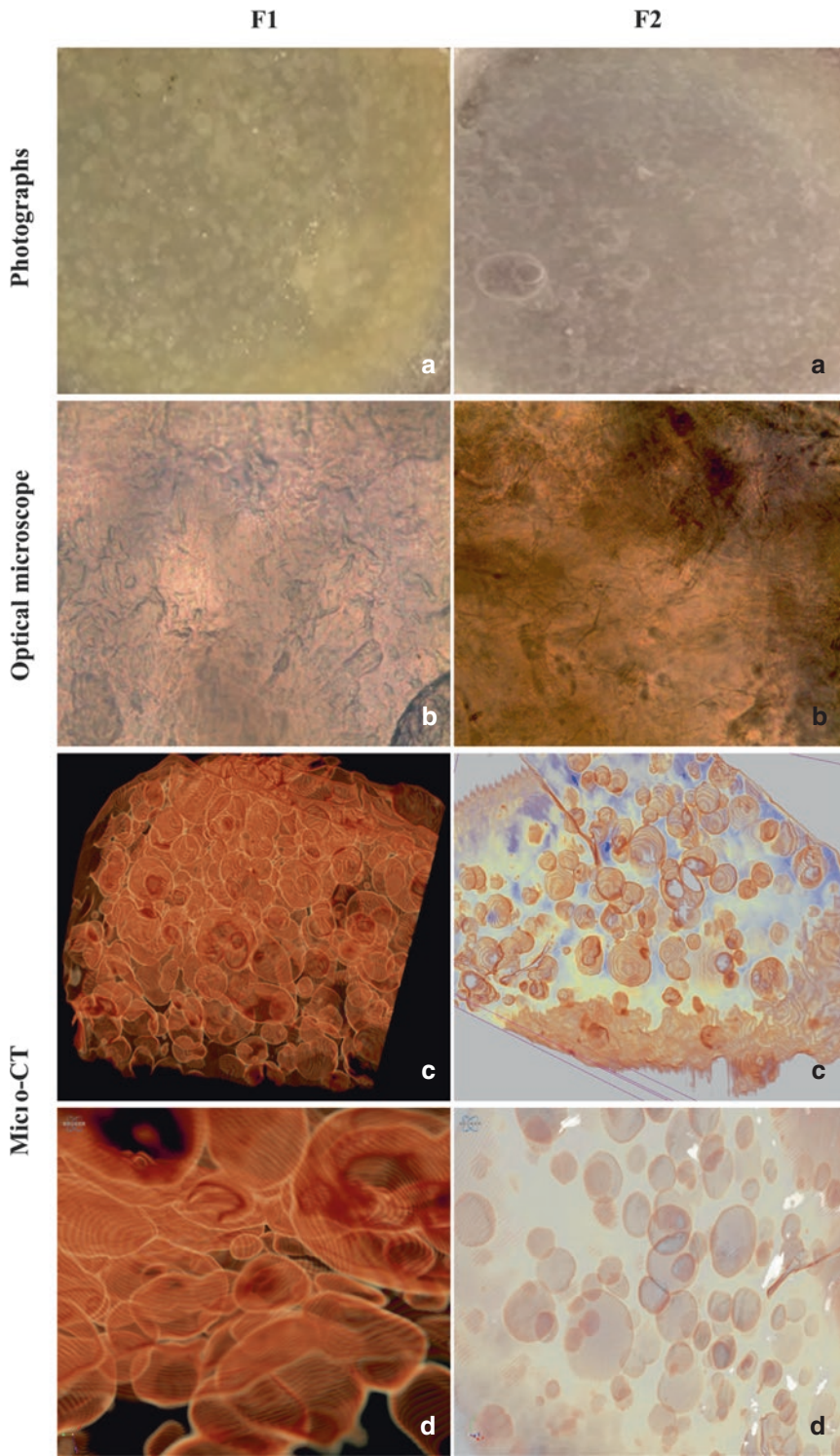


Fig. 13.1 Photographs (a), optical microscope images (10×) (b), and micro-CT images (c) of F1 and F2, and close-up images from inside the same films (d)

of desktop micro-CT systems. Therefore, different high-resolution, desktop micro-CT systems (Bruker SkyScan 1272, Kontich, Belgium) were used to scan the nanoparticle formulations (scanning conditions: 100 kVp, 100 mA, 0.5 mm Al/Cu filter, 600 nm pixel size, rotation at 0.2 step. Air calibration of the detector was carried out prior to each scanning to minimize ring artifacts). The program and software preferred in the previous micro-CT analysis were also used for the quantitative and visual analysis of nanoparticles (NRecon software (ver. 1.6.10.4, SkyScan, Kontich, Belgium) and CTAn (ver. 1.16.1.0, SkyScan, Belgium)).

According to the results, it could be determined by micro-CT analysis that the particle size was reduced by increasing PVA concentration (average particle size of N1, 135 nm, and N2, 104 nm)

(Table 13.1). Moreover, SMI values showed that the particle shape approached the rodlike structure by using 0.3% PVA (if SMI is closer to 0, it corresponds to an ideal plate, and if closer to 3, it corresponds to an ideal cylinder) (Table 13.1). When the pixel selected during the analysis was reduced from 4.2 μm to 600 nm, the nanoparticles were made visible by the micro-CT, but still could not be rendered in clear 3D image. The particle size measurements obtained by micro-CT were found to be different and smaller than the zeta sizer results (Table 13.1). Since both size and 3D images can be received at the same time with micro-CT, it can be determined that this difference in size is due to the fact that the particles are rodlike (Fig. 13.2). Moreover, developmental studies for the method have been continued.

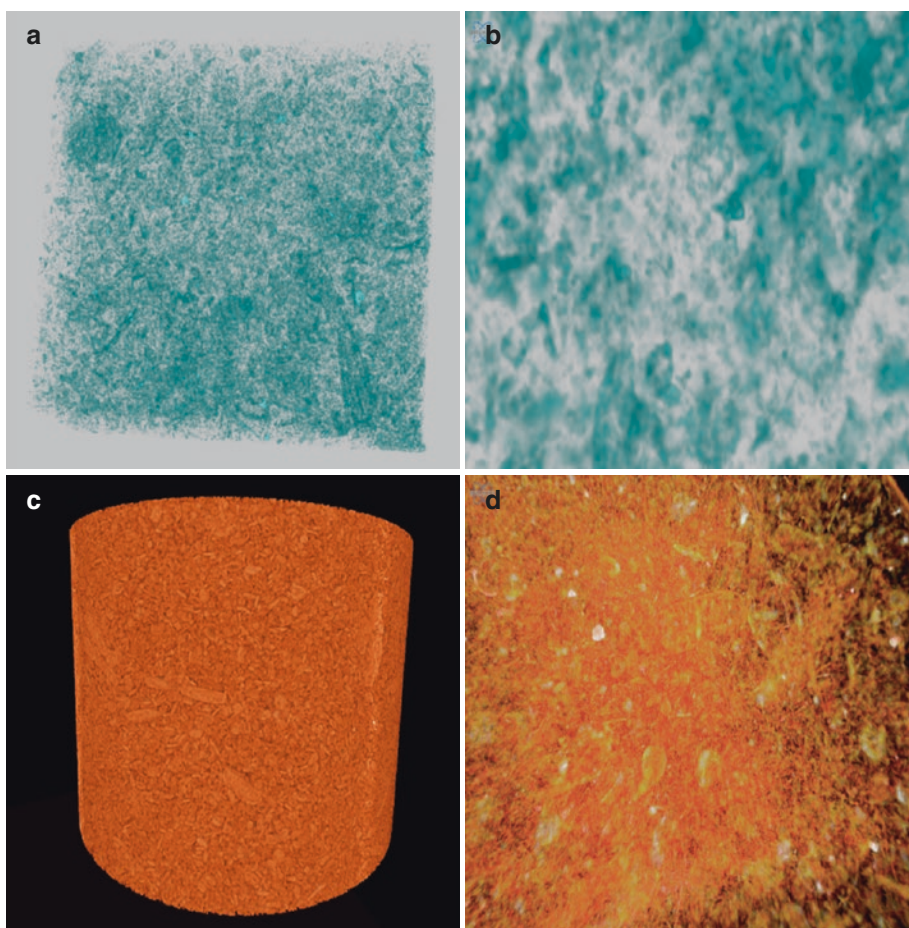


Fig. 13.2 3D micro-CT images of N1 (a) and N2 (c) and close-up images of them (b and d)

13.8 Conclusion

As a result of our review and formulation studies, the preparation and the *in vivo/in vitro* evaluation of various dosage forms by micro-CT analyses have been found to enable a more detailed examination of drug delivery systems than the other analysis methods used for formulation and quality control. Based on the results of our study, it is found that the ability to perform several quantitative analyses such as size and volume analysis of micro- and nanoparticles, density, porosity, pore size, and shape rather than just 3D imaging may provide ease of use by working with a simple method instead of multiple methods during the development phase of the formulation. However, this analysis method also has some disadvantages given as follows: what is the size of the sample to be analyzed, the resolution capacity of the device, the type of drug in the sample placement (powder or a compact structure or gel, etc.), duration of the analysis period, and high cost. As a conclusion, although micro-CT is a new method in the investigation of drug delivery systems, comparative studies have shown that this method can be used to make precise and more detailed structural analysis and be more preferred.

Acknowledgments This research has been supported by Ankara University Scientific Research Projects Coordination Unit (grant number, 17A0234001; continued; grant number, 17H0237006, 2017).

References

- Gauthier O, Muller R, von Stechow D, Lamy B, Weiss P, Bouler JM, et al. *In vivo* bone regeneration with injectable calcium phosphate biomaterial: a three-dimensional micro-computed tomographic, biomechanical and SEM study. *Biomaterials*. 2005;26:5444–53.
- Zhou H, Hernandez C, Goss M, Gawlik A, Exner AA. Biomedical imaging in implantable drug delivery systems. *Curr Drug Targets*. 2015;16:672–82.
- Ho ST, Huttmacher DW. A comparison of micro CT with other techniques used in the characterization of scaffolds. *Biomaterials*. 2006;27:1362–76.
- Williams JM, Adewunmi A, Schek RM, Flanagan CL, Krebsbach PH, Feinberg SE, et al. Bone tissue engineering using polycaprolactone scaffolds fabricated via selective laser sintering. *Biomaterials*. 2005;26:4817–27.
- Jones JR, Poologasundarampillai G, Atwood RC, Bernard D, Lee PD. Non-destructive quantitative 3D analysis for the optimisation of tissue scaffolds. *Biomaterials*. 2007;28:1404–13.
- De Santis R, Gloria A, Russo T, D'Amora U, Zeppetelli S, Tampieri A, et al. A route toward the development of 3D magnetic scaffolds with tailored mechanical and morphological properties for hard tissue regeneration: preliminary study. *Virtual Phys Prototyping*. 2011;6:189–95.
- Lin AS, Barrows TH, Cartmell SH, Guldberg RE. Microarchitectural and mechanical characterization of oriented porous polymer scaffolds. *Biomaterials*. 2003;24:481–9.
- Wang F, Shor L, Darling A, Khalil S, Sun W, Güçeri S, et al. Precision extruding deposition and characterization of cellular poly-ε-caprolactone tissue scaffolds. *Rapid Prototyp J*. 2004;10:42–9.
- Wang Y, Chang HI, Wertheim DF, Jones AS, Jackson C, Coombes AG. Characterisation of the macroporosity of polycaprolactone-based biocomposites and release kinetics for drug delivery. *Biomaterials*. 2007;28:4619–27.
- Wang Y, Wertheim DF, Jones AS, Chang HI, Coombes AG. Micro-CT analysis of matrix-type drug delivery devices and correlation with protein release behaviour. *J Pharm Sci*. 2010;99:2854–62.
- Wang Y, Wertheim DF, Jones AS, Coombes AG. Micro-CT in drug delivery. *Eur J Pharm Biopharm*. 2010;74:41–9.
- Krebs MD, Sutter KA, Lin AS, Guldberg RE, Alsberg E. Injectable poly(lactic-co-glycolic) acid scaffolds with *in situ* pore formation for tissue engineering. *Acta Biomater*. 2009;5:2847–59.
- Balmayor ER, Tuzlakoglu K, Azevedo HS, Reis RL. Preparation and characterization of starch-poly-ε-caprolactone microparticles incorporating bioactive agents for drug delivery and tissue engineering applications. *Acta Biomater*. 2009;5:1035–45.
- Patel ZS, Yamamoto M, Ueda H, Tabata Y, Mikos AG. Biodegradable gelatin microparticles as delivery systems for the controlled release of bone morphogenetic protein-2. *Acta Biomater*. 2008;4:1126–38.
- Son JS, Appleford M, Ong JL, Wenke JC, Kim JM, Choi SH, et al. Porous hydroxyapatite scaffold with three-dimensional localized drug delivery system using biodegradable microspheres. *J Control Release*. 2011;153:133–40.
- Lin L, Wang T, Zhou Q, Qian N. The effects of different amounts of drug microspheres on the *in vivo* and *in vitro* performance of the PLGA/β-TCP scaffold. *Des Monomers Polym*. 2017;20:351–62.
- Farber L, Tardos G, Michaels JN. Use of X-ray tomography to study the porosity and morphology of granules. *Powder Technol*. 2003;132:57–63.
- Doerr F, Brammer E, Wood S, Halbert G, Florence A. Morphological Characterisation of Solid

- Pharmaceutical Products using X-ray tomography. Bruker SkyScan Micro-CT User Meeting 2017; 2017.
19. Sinka IC, Burch SF, Tweed JH, Cunningham JC. Measurement of density variations in tablets using X-ray computed tomography. *Int J Pharm.* 2004;271:215–24.
 20. Busignies V, Leclerc B, Porion P, Evesque P, Couarraze G, Tchoreloff P. Quantitative measurements of localized density variations in cylindrical tablets using X-ray microtomography. *Eur J Pharm Biopharm.* 2006;64:38–50.
 21. Losi E, Peppas NA, Ketcham RA, Colombo G, Bettini R, Sonvico F, et al. Investigation of the swelling behavior of Dome Matrix drug delivery modules by high-resolution X-ray computed tomography. *J Drug Deliv Sci Technol.* 2013;23:165–70.
 22. Haesslein A, Ueda H, Hacker MC, Jo S, Ammon DM, Borazjani RN, et al. Long-term release of fluocinolone acetonide using biodegradable fumarate-based polymers. *J Control Release.* 2006;114:251–60.
 23. Kilicarslan M, Ilhan M, Inal O, Orhan K. Preparation and evaluation of clindamycin phosphate loaded chitosan/alginate polyelectrolyte complex film as muco-adhesive drug delivery system for periodontal therapy. *Eur J Pharm Sci.* 2018;123:441–51.
 24. Feldkamp LA, Goldstein SA, Parfitt AM, Jesion G, Kleerekoper M. The direct examination of three-dimensional bone architecture in vitro by computed tomography. *J Bone Miner Res.* 1989;4:3–11.
 25. Abdelkader DH, El-Gizawy SA, Faheem AM, McCarron PA, Osman MA. Effect of process variables on formulation, in-vitro characterisation and subcutaneous delivery of insulin PLGA nanoparticles: an optimisation study. *J Drug Deliv Sci Technol.* 2018;43:160–71.
 26. Reix N, Parat A, Seyfritz E, Van der Werf R, Epure V, Ebel N, et al. In vitro uptake evaluation in Caco-2 cells and in vivo results in diabetic rats of insulin-loaded PLGA nanoparticles. *Int J Pharm.* 2012;437:213–20.



Challenges in Micro-CT Characterization of Composites

14

Güllü Kiziltaş, Melih Papila, Bengisu Yilmaz,
and Kaan Bilge

14.1 Introduction

Research on effective characterization strategies for composites has been an actively expanding area including their nondestructive evaluation (NDE) [1]. Nondestructive evaluation (NDE) stands for the evaluation of engineering materials to understand mechanical behavior and to determine defect existence or absence with size and location information, typically without altering the original features or instantaneous state and not harming the parts under investigation. Similarly, nondestructive testing (NDT) is known as the measurement of those specimens before

evaluation. One of the main advantages of NDT is that it is a cost-effective method for quality evaluation.

Currently, available and well-established NDTs to analyze mechanical behavior of composites can be categorized according to inspection types [2]. In past and current studies, suggested methodologies are listed as visual testing, thermographic testing, shearography testing, ultrasonic testing, electromagnetic testing, acoustic emission, radiographic (x-ray-based) testing, and the combination of these methods. The overall information along with advantages and disadvantages are given in Table 14.1.

Among all, radiographic testing appears a commonly used and preferred nondestructive testing method for composite materials [8–10]. This technique depends on the electromagnetic wave (usually x-rays and gamma rays) absorption level of the substrate and defects. It is very effective for inner defect detection. There are various radiographic testing methods used for understanding the mechanical behavior of composites: film radiography, computed radiography, computed tomography, and digital radiography. In particular, the x-ray computed tomography (XCT) is a nondestructive technique that visualizes interior features within specimens with 3D imaging. This effective characterization method can alter the focus size from micro to macro to obtain reliable image data [11]. Due to the radiation level of x-ray, the in situ experimentation

G. Kiziltaş (✉)
Faculty of Engineering and Natural Sciences,
Sabanci University, Tuzla, Istanbul, Turkey

Sabanci University Nanotechnology Research and
Application Center, Sabanci University, Tuzla,
İstanbul, Turkey
e-mail: gkiziltas@sabanciuniv.edu

M. Papila · K. Bilge
Faculty of Engineering and Natural Sciences,
Sabanci University, Tuzla, Istanbul, Turkey
e-mail: mpapila@sabanciuniv.edu;
kaanbilge@sabanciuniv.edu

B. Yilmaz
Faculty of Engineering and Natural Sciences,
Sabanci University, Tuzla, Istanbul, Turkey

Ultrasound Research Institute, Kaunas University of
Technology, Kaunas, Lithuania
e-mail: bengi@sabanciuniv.edu

Table 14.1 General information, advantages, and disadvantages of common NDT methods for composite materials

NDT Technique	Description	Advantages	Limitations
Visual inspection	Usually based on naked eye; could be improved with magnifying glasses, microscopes, cameras [3], and digital image correlation (DIC) [4]	Short-time response and analysis Low cost May eliminate the need of other NDTs	Only surface defects can be detected Not sensitive to small defects (as long as not improved by microscope, etc.)
Thermography	Based on thermal radiation arriving to surface. Can be stimulated by different sources such as IR lamps and eddy current induction [5]	Very responsive in time Sensitive considering defect size Easily applicable to large components	Surface and subsurface defects can be detected Time consuming post-processing User expertise required Expensive
Shearography	Laser light source with image acquisition system is used to measure the stress level to detect defects in composites [3]	Highly reliable due to high signal to noise ratio High resolution (up to nanometers) Responsive in time	Very expensive User expertise required Surface and subsurface defects Requires high stress solicitation
Ultrasonic inspection	Working principle is based on disruption in ultrasonic wave. Many options with variety of sensors, orientation, wave direction, wave type exist	Location and size of many possible defects such as cracks, flat-bottom holes, and delamination	Device mobility and construction of systems User expertise required
Electromagnetic inspection	Working principle based on magnetic and electrical fields response change. Involves many different techniques such as magnetic flux leakage and eddy current [6]	Reliable Mobility is possible Good resolution and response time	Surface and subsurface defects Very limited material application due to conductivity issues
Acoustic emission	Sensors collect acoustic data created on the surface [7]. No external stimulation necessary unlike in ultrasound imaging	Simple and reliable Easy to construct data for big structures on service, such as wind turbines	User expertise and experience required Large database for comparison in structural health monitoring applications
Radiography	Based on measuring electromagnetic wave (x-ray, gamma ray) absorption levels [8]. Involves film radiography, digital radiography, and computed tomography	Internal defect detection Full 3D internal structure construction possible	Very expensive Not time effective Most of the time, not possible mobile due to health hazard

with XCT may require substantially expensive and customized laboratory equipment.

Studies related to defect investigation of composite materials with x-ray-based computed tomography mostly focus on the void presence inside materials and its impact on the mechanical behavior of composites [12–17]. Additionally, the deformation of the reinforcement materials in mesoscale (such as fiber bundles and tow shapes) has been investigated by computed tomography in various studies [9, 18–21]. While most of the

previous work focused on the visualization and localization of defects inside composite materials, some followed simulations studies where the models are obtained directly from computed tomography imaging [22–26]. In particular, the deviation from the ideal characteristics of fiber/yarn architecture, in non-crimp fabric (NCF) composites, for instance, is an important research area among composite engineers [27–29]. The existing studies on the x-ray computed tomography of NCF composites focus on the influence of

microscale anomalies such as potential void formation and three-dimensional modeling of the reinforcement architecture.

Considering all x-ray-based nondestructive evaluation techniques, micro-computed tomography (micro-CT/ μ CT) stands out as a technique that allows creating three-dimensional images and deals with large amount of data with high resolution. Specifically, micro-CT allows focusing on small size components with high resolution in short time.

This chapter focuses on the localization and the quantitative investigation of processing related anomalies like the pore formation, sticking, and spreading of tows during a vacuum infusion process. A case study is presented in order to provide information on purchased tow and resin properties and the nature of the manufacturing process. Micro-CT analysis was employed to measure/evaluate this phenomenon nondestructively. Related post-processing parameters, namely, closed pore number, structure separation, structure thickness, and connectivity avail-

able in CT-An software, were used in order to analyze the microstructure of manufactured composite specimens. The limiting factors and challenges related to micro-CT scanning and 3D image analysis are also presented.

14.2 Case Study: Fiber Reinforced (UD Non-crimp Fabric) Composites

In a pre-designed experimentation scheme, glass fiber unidirectional non-crimp fabric (NCF) of four different yarn numbers (that is a measure of the fineness or size of a yarn expressed either as mass per unit length commonly expressed as TEX (g/km)) is industrially tailored and labeled as 300 TEX, 600 TEX, 1200 TEX, and 2400 TEX but with constant areal weight of 300 g/m² (Fig. 14.1, Table 14.2). The constant areal weight constraint forces an NCF to contain approximately same number of fibers. In a unidirectional

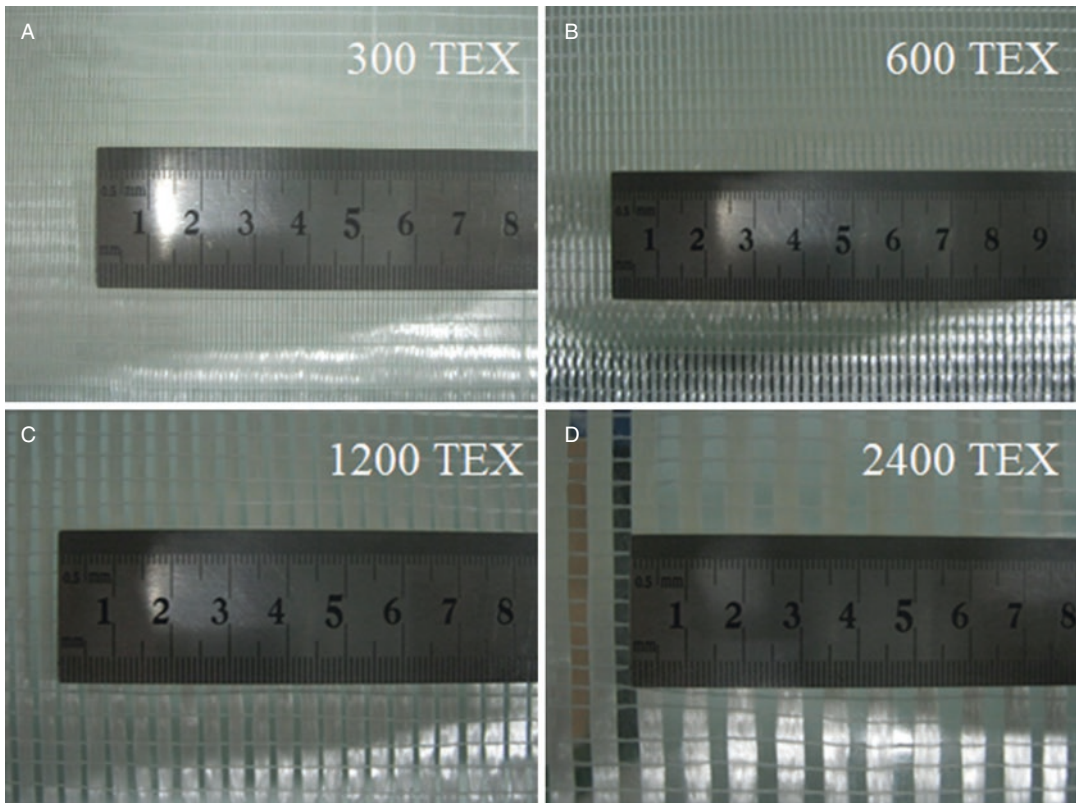


Fig. 14.1 Glass fiber UD NCF samples with different yarn numbers before impregnation

(UD) NCF, this suggests that fibers are stitched together as larger or smaller tows. These NCFs are stacked up to form a $(0)_8$ laminate followed by the impregnation and curing of a vinyl ester (VE) resin system under the same manufacturing conditions. Obtained glass fiber NCF panels are then cut into 25×25 mm micro-CT specimens.

A detailed micro-CT analysis is performed on each set of specimen in order to localize and relatively quantify (1) resin-based defects, namely, pores and (2) mesoscale internal structure relationship. The challenges associated with the scanning process and analysis studies are discussed. Several post-processing parameters and the relationship of those parameters to NCF composite material properties are analyzed. The relationship between micro-CT post-processing parameters and the anomalies due to manufacturing process with the sample's mesostructure is reported.

Table 14.2 Bundle width and interbundle distance of UD NCFs with different yarn numbers

Yarn number (prior to impregnation)	300 TEX	600 TEX	1200 TEX	2400 TEX
Fabric type	UD NCF	UD NCF	UD NCF	UD NCF
Fabric areal weight (g/m^2)	300	300	300	300
Bundle width (μm)	1000	2000	3000	4000
Interbundle width (μm)	500	800	1200	2000

14.2.1 Manufacturing of NCF Composite Laminates

All of the dry fabrics were impregnated with Crystic VE-676-03 unsaturated vinyl ester resin supplied by Scott Bader Co. Ltd by vacuum infusion. As shown in Fig. 14.2, pre-cut fabrics are placed layer by layer over a clean and nonsticking glass mold. Then the top surface of ply block is covered with peel ply in order to prevent any sticking of fabrics to the vacuum bag. Following, a distribution media is placed over the peel ply which is a highly permeable fabric that allows the resin flow to advance quickly from the top layer. The whole system is then covered with vacuum bag that is tightly sealed to the glass mold, and vacuum is applied so that the resin can be infused into the NCF stack. In this study, the vacuum level achieved was 0.9 bar. Since the liquid resin is mixed with its hardener during infusion, the infusion time is typically limited with resin gelation time. In other words, the flow front should reach to the end of the designated fabrics before the gelation kicks in. Once the flow front reaches the far end and infuses the whole fabric area, the resin flow line was cut. The lay-up system was kept under vacuum for 12 h first in order to allow enough time for the resin system to penetrate thoroughly into fiber bundles and interbundle regions, and then the effective compaction of the layers is secured during the curing reaction. In

Fig. 14.2 Vacuum infusion process

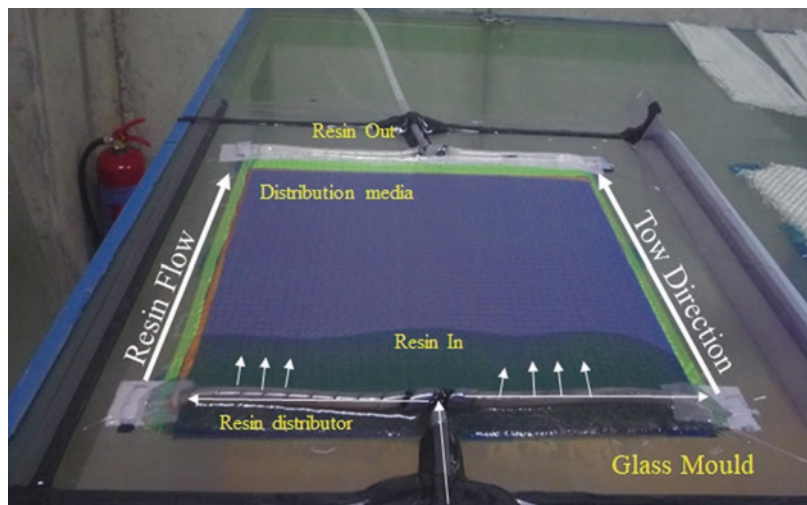


Table 14.3 Fiber volume fraction values of specimens according to loss-on-ignition test results

Yarn number (TEX)	V_f by Loss on ignition (%)
300	52
600	52.5
1200	50
2400	51

this study the resin was cured at room temperature, and a post-curing application aiming to achieve a fully cross-linked resin system at 80°C was employed.

In the presented case study due to difference in yarn numbers and corresponding bundle/interbundle sizes, the permeability of each fabric is different. For instance, an NCF with 300 TEX is formed of more close-packed fiber bundles, whereas for 2400 TEX both the bundle size and interbundle region are larger. Hence, under vacuum infusion processing conditions, the flow of resin in each fabric is expected to cause different types of effects, hereby named as anomalies. An inherent anomaly that is caused due to meso-architecture is the deformation of tows during resin flow. In other words the size/shape of bundles may vary differently with respect to their initial stage (prior to impregnation). Another cause of anomaly is the applied compaction pressure via vacuum bagging which leads to packing of the stacked fabrics as tight as possible. The associated anomaly is typically a result of the fiber bundles possibility of moving towards empty interbundle regions which depends on the yarn number in this case study.

Fiber volume fraction (V_f) is commonly considered as a measure of good wettability and compaction during manufacturing of composite materials. A major challenge in this case study was to fix the fiber volume fractions in each type of laminate so that manufacturing/mesostructure relation was isolated as the sole cause of variations. Since the areal weight of each fabric was kept constant at 300 g/m², we were able to approximate the number of fibers available in a

given fabric and tuned the amount of resin to be introduced by aiming a nominal volume fraction of 50% in each laminate. Table 14.3 summarizes the volume fraction values obtained for each laminate by loss-on-ignition method according to ISO 1887.

A second type of anomaly that is inherent in composite manufacturing is the amount of porosity inside the laminates. A dominant source for pore formation is the curing reaction where an exothermic cross-linking reaction occurs and depending on the nature of resin components (i.e., hardener-initiator system), gaseous volatiles are released. Although the vacuum application aims to remove these volatiles from the system, it may be insufficient, especially for thick laminates. Since it is impossible to reprocess a thermoset resin, these pores remain trapped inside the manufactured specimens. The presence of pores not only decreases the specimen quality but also causes other disadvantages as will be discussed.

After the panels were manufactured as described above, they were subject to micro-CT analysis in order to quantify and assess these anomalies. Towards that goal, micro-CT specimens were prepared with size 25mm x 25mm.

14.2.2 Micro-CT Analysis

Obtaining three-dimensional microstructure images of composite specimens, with satisfactory quality and the exact desired information, is a challenging task. X-ray computed tomography is a well-established radiographic nondestructive testing

methodology, the output of which is highly dependent on the parameters selected during scanning and analysis. In order to reduce and eliminate user-induced artifacts, the inspection should be performed with optimally selected parameters during pre-scan, scan, and post-processing processes.

14.2.3 Pre-imaging Considerations

Before every nondestructive measurement, one should consider the possible challenges and error sources related to the specimen, environment, limitations of equipment, and the capability of the user. Similarly, before the micro-CT evaluation, specific parameters of the sample such as geometry and material need to be considered as was done in the presented study.

The desired samples for 3D scanning with computed tomography usually have aspect ratios close to 1 within the cross section, such as spherical/cylindrical objects (e.g., for medical applications such as bones). On the other hand, composite samples are mostly considered as two dimensional, due to their high aspect ratio when compared to their thickness. In this case study, composite specimen dimensions were specified as ~25 mm (length) \times 25 mm (width) \times 2.5 mm (thickness). The “ideal” aspect ratio close to 1, could be achieved via placing the sample on the sample holder by inserting the sample with the surface dimensions 25 mm \times 25 mm being mounted onto the holder surface. While the relative absorption level during a full turn of sample, i.e., 360 degree of rotation, remains constant, due to anisotropic complexity of the internal structure of the composite, the scan results may vary greatly with the sample orientation, which is an undesired situation in micro-CT imaging. More specifically, the relatively small cross-sectional area of the specimen being exposed to the x-ray source causes even a small misalignment to result in large variations of the image quality. To optimize for these conditions, various orientations were investigated. When the samples were placed on the holder, such that the x-ray source was facing the thinner part of the sample, the aspect ratio

was close to 10, and the absorption levels changed drastically during a full turn of the scanning operation. A comparative analysis of the imaging results suggested that due to the dense fiber concentration in the composite sample, using the higher aspect ratio orientation with a compromise on the scanning voltage, results in an improved image contrast of the phase boundary between fiber and matrix.

The x-ray absorption level during scanning depends on several parameters, and it is possible to adjust the absorption level for “dense” or “less dense” specimens with, for instance, the voltage/current and/or power settings. However, to be able to identify a defect, or changes in the microstructure such as phase change of material, the absorption levels should display a satisfactory level of contrast. Just like the infrared cameras’ working principle is based on temperature changes, CCD camera inside the CT system records image pixels based on the photon sensitivity of the material, i.e. the absorption change of material phases when scanning each cross section of the specimen. Therefore, when scanning the composite specimens in the presented case study to clearly identify the phase boundary between bundles and matrix, the primary goal was to set the scanning such that x-ray absorption level of the fiber pockets of the bundle differed from the absorption level of the matrix. The composite samples in this study consist of vinyl ester and fiberglass for which the scanning parameters were optimized accordingly. It is noted that the settings for the samples containing other materials may differ due to varying x-ray absorption levels, for instance, for carbon-fiber epoxy-based composites.

As a final effect, the equipment limitations should also be considered before starting micro-CT measurements. The sample size of the equipment is one of the main limiting factors in a micro-CT scan. While industrial tomographic scanners are able to scan large-size samples (up to meters), micro-CT focuses on small volumetric areas with high-resolution and short-scanning time advantages. The resolution of the image also depends on the sample size due to limit on the distance of the sample from the camera and x-ray

source. The power of the x-ray source also may affect the quality of results for highly attenuated or absorptive material samples.

14.2.4 Scanning Settings and Parameters

The first step prior to composite characterization via micro-CT constitutes specimen preparation with specific dimensions that allows the analysis to focus on desired features. The next step is the actual scanning with micro-CT scanner. In this study, 25 mm × 25 mm × 2.5 mm large specimens of manufactured laminates were scanned with Skyscan1172 high-resolution micro-CT equipment located at Sabanci University Nanotechnology Research and Application Center. While using Skyscan1172, a user-friendly software is available to control the scanning parameters. The scanner is equipped with Hamamatsu C9300 11MP camera connected to the computer and allows for scanning at three scanning resolutions of 1K (1000 × 668 pixels), 2K (2000 × 1336 pixels), and 4K (4000 × 2672 pixels) to obtain the two-dimensional images. By changing the distance between the camera and the specimen, image pixel size can be adjusted. In addition, the x-ray source voltage, current, and power affect the image quality. The raw images are created by exposing the specimen to x-ray source with a particular exposure time and collecting the transferred signal (Fig. 14.3). Aluminum, copper, or combined filters are available for use in the system. The signal is saved in chosen image format by the connected computer system. Then the specimen is rotated by the selected step size, and another raw image is captured. The user should take the x-ray attenuation coefficient of the sample into consideration when choosing acquisition parameters. In this study, x-rays are generated with an electron-accelerating voltage of 81 kV with a tungsten reflection and a beam current of 124 mA. The camera is set to 1K, and the distance between the object to the source is specified as 256 mm to create images with 25.9 μm pixel size. The chosen exposure time is 480 ms,

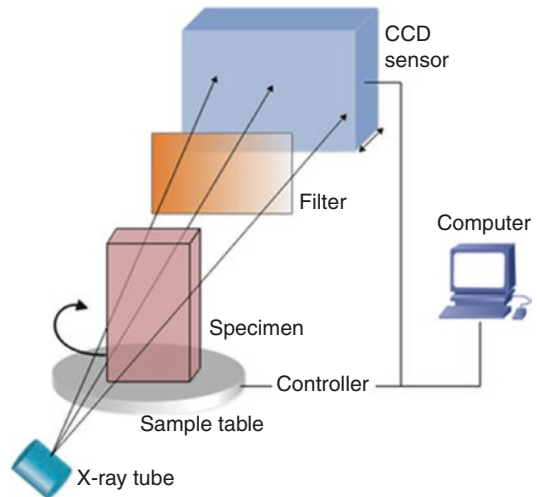


Fig. 14.3 Schematic explanation of the x-ray computed tomography working principle

and rotation step is 0.7°. Copper and aluminum combined filter was selected. The raw images are saved until the 360° full rotation is completed.

14.2.5 Analysis Steps

Main analysis procedure to calculate morphological properties of the scanned specimens after the scanning operation includes five major steps which are carried out with the help of suitable software as described below.

14.2.5.1 Reconstruction

After image acquisition is completed, two-dimensional projection images of the object that are captured and recorded by the micro-CT system should be reconstructed. The reconstruction process has to be optimized with parameters such as ring artifact correction, beam hardening, misalignment, and smoothing. The cross-sectional grayscale images are reconstructed with the selected parameters in order to prevent an undesired image deterioration. In this study, NRecon (version: 1.6.9.4) software which applies modified Feldkamp's back-projection algorithm [30] is used in reconstruction of the images that are collected by Radon transformation. The ring artifact correction is significant to

obtain better image quality. For the high values of correction factor, the image quality decreases, and this may result in information loss. For the lower values of this correction factor, the reconstructed images may contain ring-like artifacts possibly due to rotation of the specimen that may include voids. For composite specimens, voids are well-known manufacturing defects; therefore the ring artifact correction parameter is selected as 4. Beam hardening correction parameter helps to decrease the artifacts due to high attenuation of x-ray photons, usually when they interfere with specimens with high atomic number, such as bones, metals, and iodine. In our case, glass fiber and vinyl ester do not have high x-ray attenuation constants; therefore, the beam hardening correction value is selected as 33% of which is relatively lower than correction factors for metals [31]. Misalignment, or out of field artifact may occur during any rotational CT scan, due to the uncontrollable movement on specimen holder (in our case, where the x-ray source is moving, then due to the robotic control on the x-ray source). Since this is a mechanical effect on the images, it is easily aligned with selected parameter in NRecon. Misalignment parameter can be specific to any CT scan. In the beginning of the reconstruction, NRecon offers a value for misalignment correction. In the case of very high values offered, it may indicate that the specimen movement is significantly high and scan may need to be repeated with smaller rotation step. Moreover, smoothing parameter is selected as zero to preserve the information in each pixel for a more reliable analysis during post-processing. With the specified parameters, image reconstruction time in NRecon took 0.05 s to 0.06 s with a 24 GB Dell Precision T5500 workstation.

14.2.5.2 Coordinate System Alignment

DataViewer (version: 1.5.1) software is used to save rotated cross-sectional images in a cartesian coordinate system in line with the material coordinate system of composite samples. The cross-sectional images are saved from the sagittal view of reconstructed data, where X is the thickness and Y is the width of composite samples. The sig-

nificance of this alignment is to obtain reliable data during 2D analysis. The cross sections of bundles are corrupted if the laminate is disoriented from the material direction. In addition, the alignment in-between material coordinate system and 3D coordinate system of micro-CT images allows us to separate lay-up ROIs in a more reliable and easy way.

14.2.5.3 Segmentation (Binarization)

Segmentation is another important step to analyze three-dimensional images. Since reconstructed and rotated images contain grayscale color values, the analysis of objects is not directly applicable via use of software. There are several well-established statistical image segmentation methods for 3D images [32, 33]. However one of the most basic and commonly used methods is pixel value-based segmentation. In this case study, reconstructed three-dimensional objects, containing grayscale values for each voxel (3D pixel), have been segmented (binarized) by using peak-valley histogram thresholding method and were analyzed via CT-An (CT-Analyzer, version: 1.14.4.1) program. For consistency of data, the range of the threshold for specimens was kept constant for all three-dimensional images. As a result, matrix and fiber phase boundaries of all the composite samples were obtained with the same binarization threshold value.

14.2.5.4 ROI Selection

Prior to 3D analysis, region of interest (ROI) of the three-dimensional data needs to be selected, which is arguably one of the most challenging steps in carrying out micro-CT nondestructive evaluation of composites. This selection affects the evaluation results significantly. For the composite laminate containing eight layers of UD NCF fabric (0)8, nine different ROIs have been selected for analysis purposes (Figs. 14.4–14.7). The eight laminae, each presumably containing only one layer of NCF fabric, are investigated along with the rectangular prism covering the whole specimen. The total volume of ROI—for different yarn number specimens—is selected as close as possible to each other by limiting the number of cross sections in each specimen. The

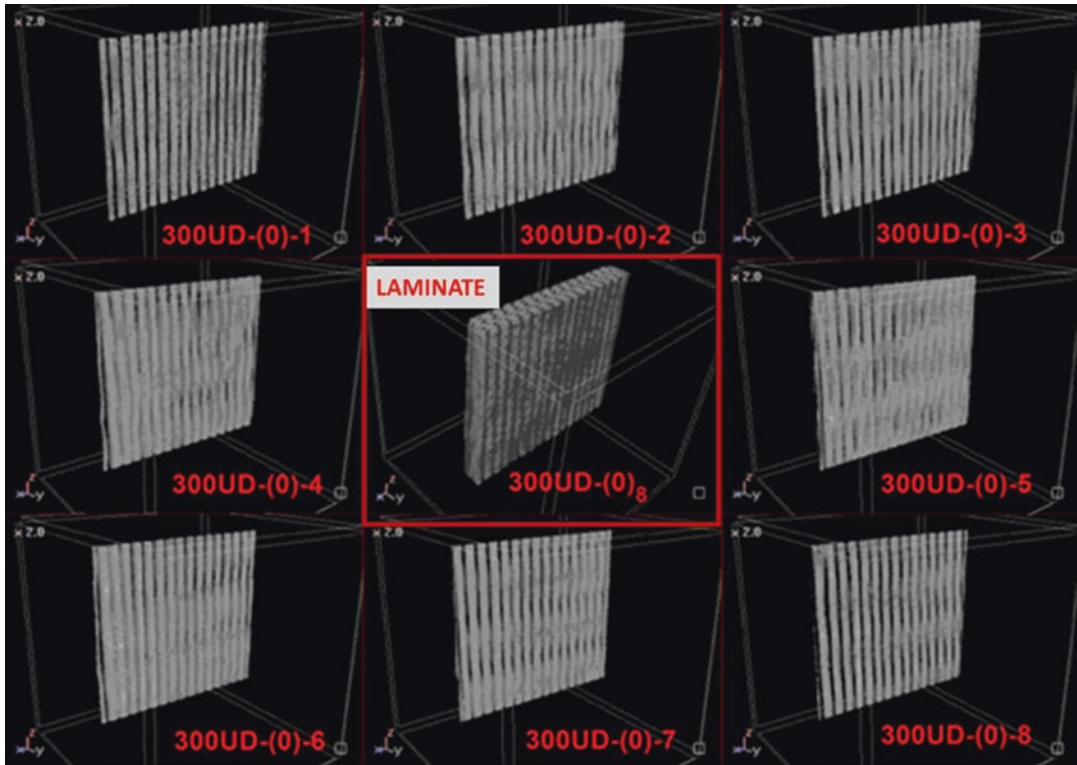


Fig. 14.4 Reconstructed 3D images of unidirectional 300 TEX specimen labeled as plies and $(0)_8$ laminate (at the center)

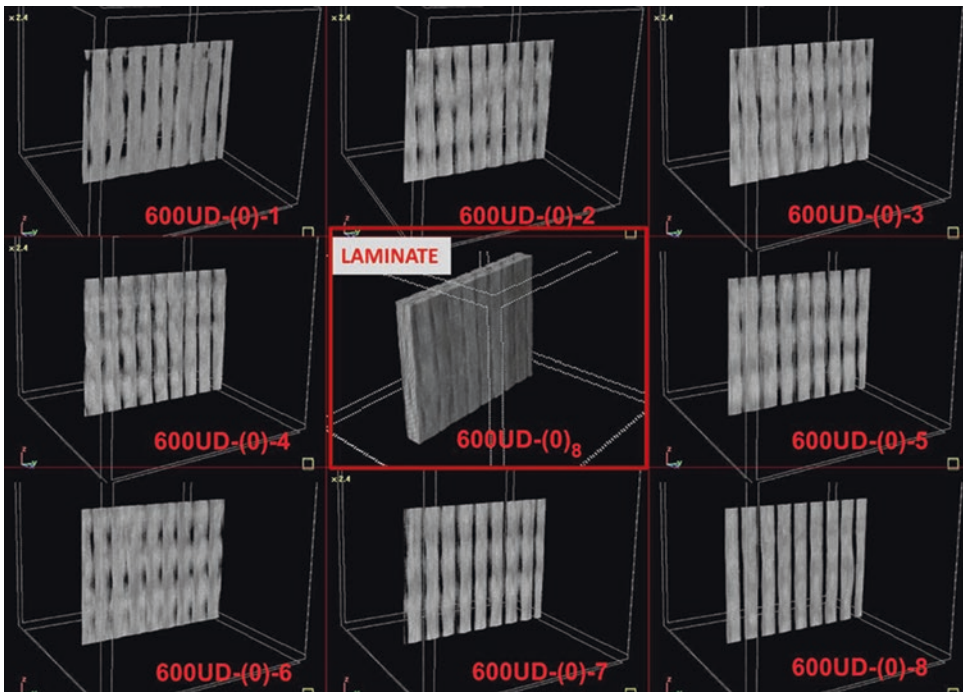


Fig. 14.5 Reconstructed 3D images of unidirectional 600 TEX specimen labeled as plies and $(0)_8$ laminate

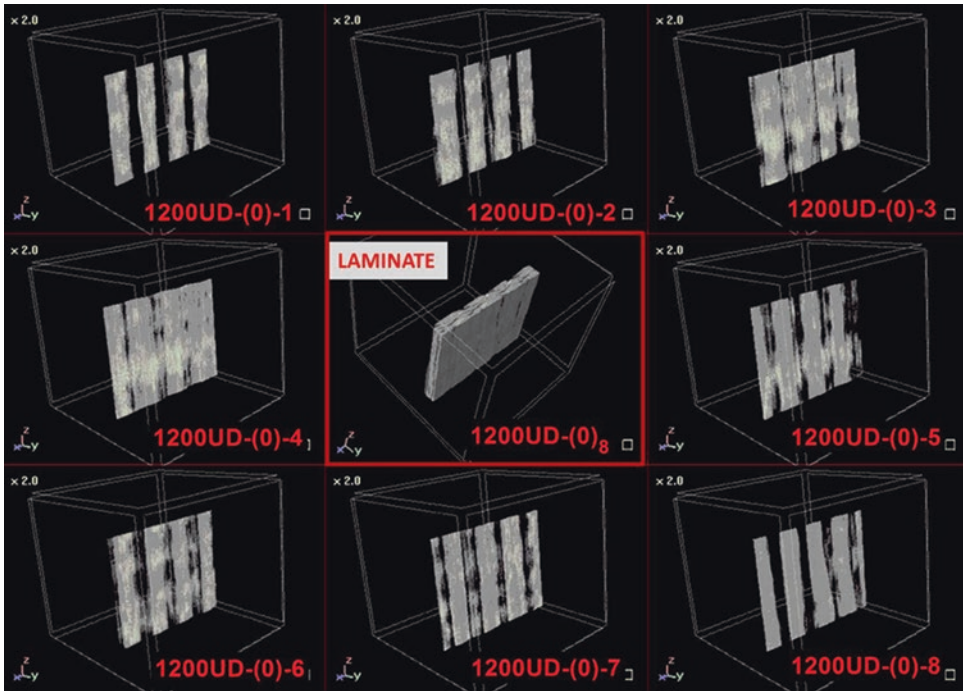


Fig. 14.6 Reconstructed 3D images of unidirectional 1200 TEX specimen labeled as plies and (0)₈ laminate

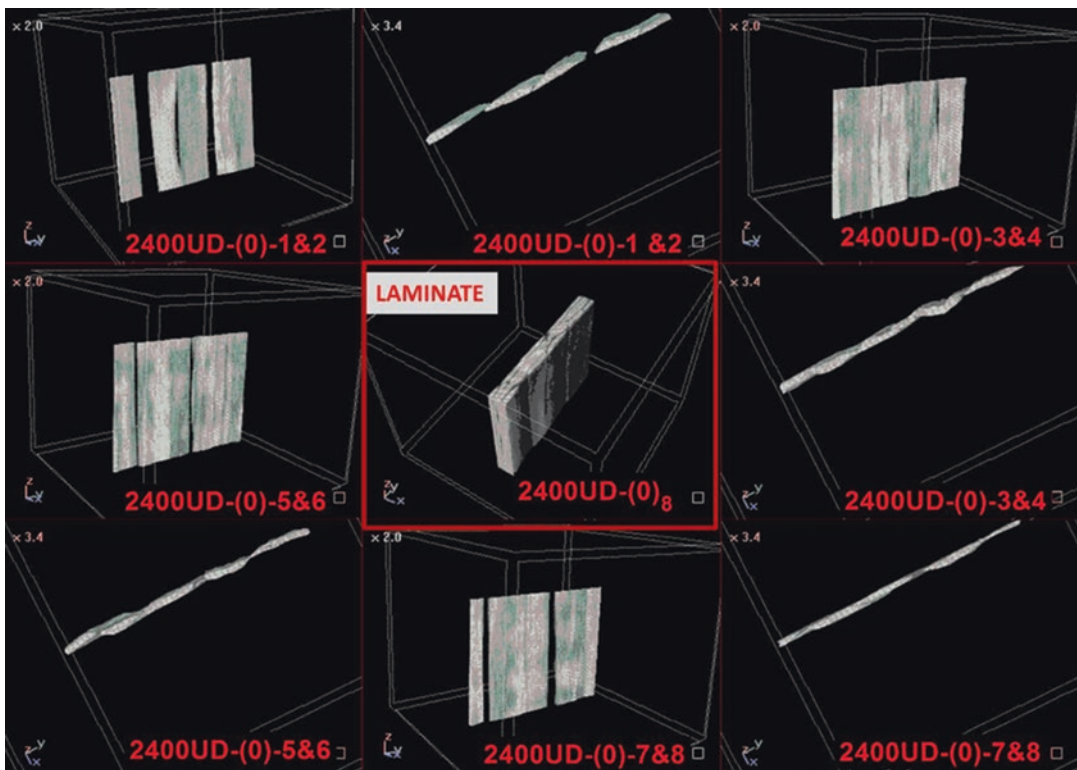


Fig. 14.7 Reconstructed 3D images of unidirectional 2400 TEX specimen labeled as plies and (0)₈ laminate

irregular shape of bundles, crimping, and complex internal through the composite length introduced extra challenges in the process. In particular, specimen 2400 TEX that had the largest spacing between bundles could not be separated into eight different layers. As seen in Fig. 14.8, the bundles on each consecutive ply are fused on one another, therefore the unified labeling of each consecutive pair. Hence, for ply analysis, there were only 4 ROIs constructed for the 2400 TEX sample, with each consecutive pair being labeled as such laminae (i.e., 1&2, 3&4, 5&6, and 7&8). Due to the limitation on fiber volume fraction and very long interbundle gap, manufacturing of the samples as desired by their ideal form as seen in the white and blue schematics in Figs. 14.8 and 14.9 was not possible.

However, this issue should be noted when considering the meso-architecture of laminates and interpreting their micro-CT analysis results.

14.2.5.5 Post-Processing Parameters

After obtaining three-dimensional binarized data representing fiber phase in the selected ROIs, the relationship between composite material parameters and the obtained data needs to be defined. In the data analysis software of SkyScan μ -CT scanner, namely, vCT-Analyzer (CT-An), standard available analysis parameters are mostly related to bone quality such as bone mineral density. The parameters that are selected for the investigation in this case study are porosity (cavity) number, structure separation, structure thickness, and connectivity which are discussed below.

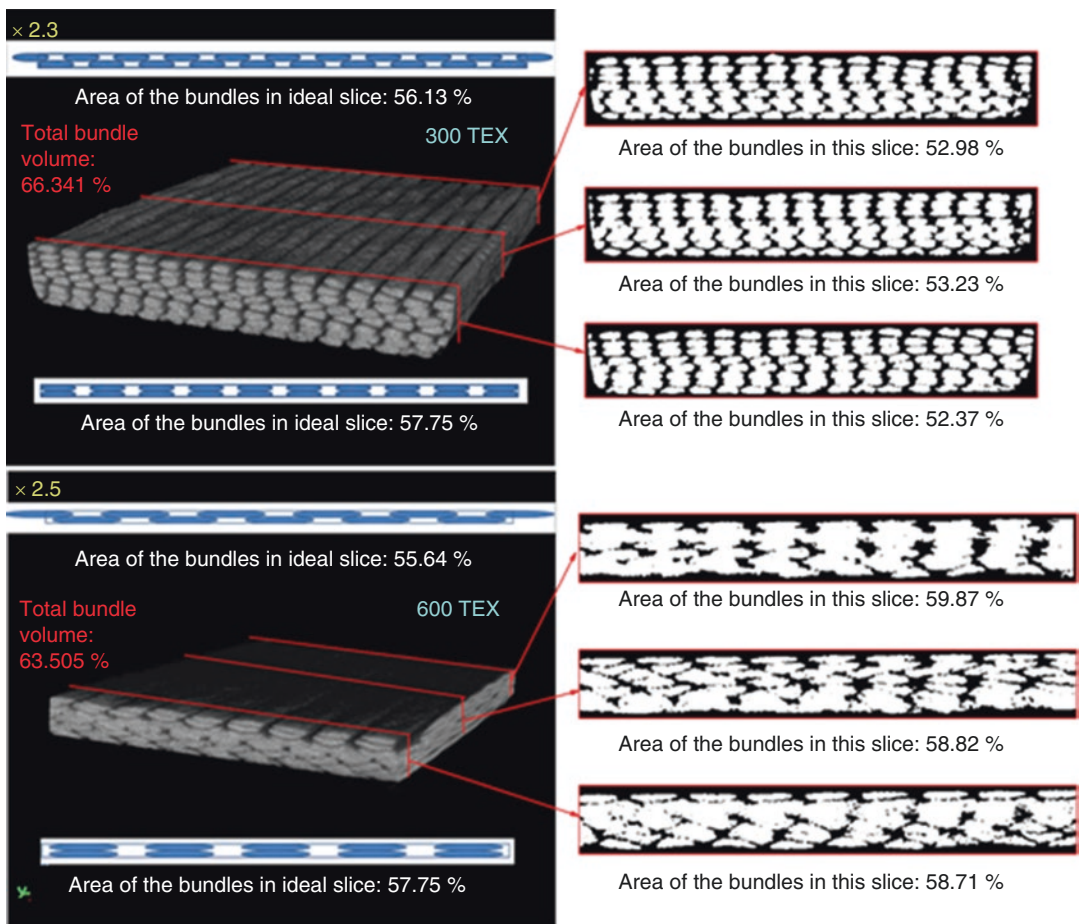


Fig. 14.8 Randomly chosen binarized cross-sectional images of 300 TEX and 600 TEX unidirectional samples and their ideal mesostructure are shown in the left in blue

and white. Area and volume of bundle percentages calculated from micro-CT images in 3D view on the left and their cross-sectional image on the right

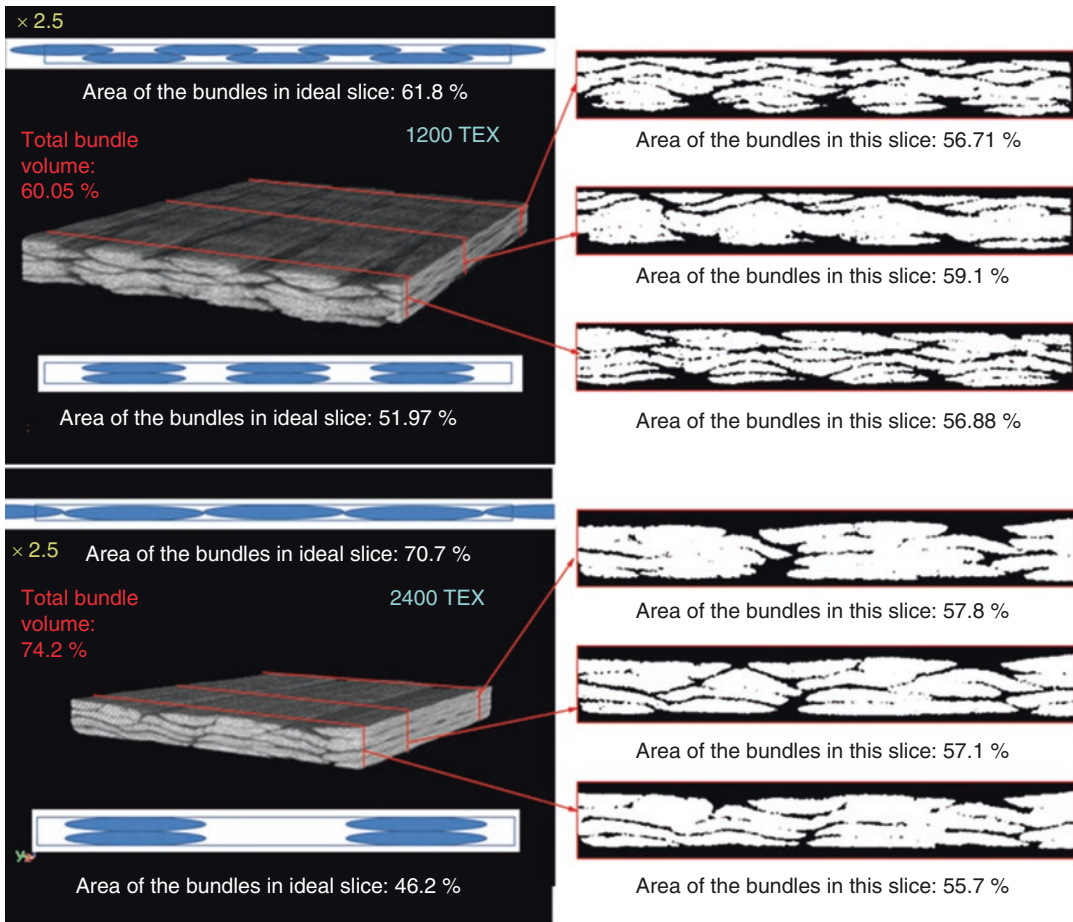


Fig. 14.9 Randomly chosen binarized cross-sectional images for 1200 TEX and 2400 TEX unidirectional samples and their ideal mesostructure are shown on the left in

blue and white. Area and volume of bundle percentages calculated from micro-CT images in 3D view on the left and their cross-sectional image on the right

Number of Closed Pores (Cavity Number)

As a part of the stereological analysis of the three-dimensional image, cavity number, in other words, the number of closed pores, has been calculated by the help of CT-An software. A closed pore is a connected assemblage of black voxels that is fully surrounded on all sides in 3D by white voxels, and the cavity number represents how many closed pores are present in the selected region of interest. Given that each laminate had the same areal weight, similar fiber volume fractions, and close fiber diameters, the experimental assumption was that each ply contained an equal number of fibers which have been arranged in different meso-architectures.

Hence, the counted number of closed pores inside each ROI was normalized by the corresponding object volume (object herein is referred as the total volume occupied by fiber pockets). This approach isolates the sole effect of yarn number on the presence of manufacturing related micro-voids.

Furthermore, the investigation regarding the pore size and location was done by treating closed pores as objects in 2D cross sections of each laminate. The grayscale images were binarized by selecting the threshold so that pores were identified as objects. The average diameter sizes of closed pores, along with the distances between pores, are reported.

Structure Separation

This parameter refers to the average diameter of existing spherical objects that can maximally fit into the empty spaces in-between each three-dimensional segmented object inside the selected region of interest [34]. The standard deviation of the diameters indicates the variability in the object separation. In the case study, structure separation represents the one-dimensional average distance of the segmented bundles from other bundles. Structure separation is calculated by CT-An software within specified ROIs. This parameter shows the splitting ratio of each bundle inside the selected ROI. During impregnation, flow of resin may change the distance between fiber bundles. Hence, the final laminate may have different bundle distances than the desired ones, i.e., different than the nominal dry form distance in Table 14.2. The calculation of the bundle distances is determined by analyzing the entire 3D data set, and the mean and standard deviation values for bundle distances are reported.

Structure Thickness

Similar to structure separation, structure thickness is the calculated average diameter of the various spheres that can fit into the objects inside selected ROI. The standard deviation of the diameters indicates the variability of the object thickness. In this study, structure thickness represents the dimensional average thickness of bundles viewed as three-dimensional objects. Structure thickness is also calculated statistically by CT-An within specified ROIs. Due to fiber orientation change during impregnation process, ideal connection of the fibers may be disrupted inside the laminate. This parameter shows the sticking ratio of each bundle inside the selected ROI. How much the bundle sticks together is calculated by considering the entire 3D data set inside ROI and is reported with corresponding mean and standard deviation.

Connectivity

As part of three-dimensional image analysis, connectivity which is calculated by the help of CT-An software indicates the redundancy of connections inside ROI. Redundant connectivity is derived from Euler number [35]. Euler number is

calculated in terms of the numbers of voxel volumes (a_3), faces (a_2), edges (a_1), and corners (a_0) of white parts which have a neighbor with white voxel region. In order to eliminate the position of a ROI surface, Euler number of the 3D structure is calculated as follows:

$$EN = \sum (-1)^i a_{i=0} - a_1 + a_2 - a_3$$

Euler number is a primary topologic measure for bone strength [34] which is calculated as the number of objects plus the cavity number inside bone minus the number of connections that must be broken to split the bone into two parts.

$$EN = \text{Number of Objects} - \text{Connectivity} + \text{Cavity Number}$$

As explained in Odgaard's study [40], these two equations lead to connectivity measurement on 3D structures as follows:

$$\text{Connectivity} = \text{Number of Objects} - \text{Euler Number} + \text{Cavity Number}$$

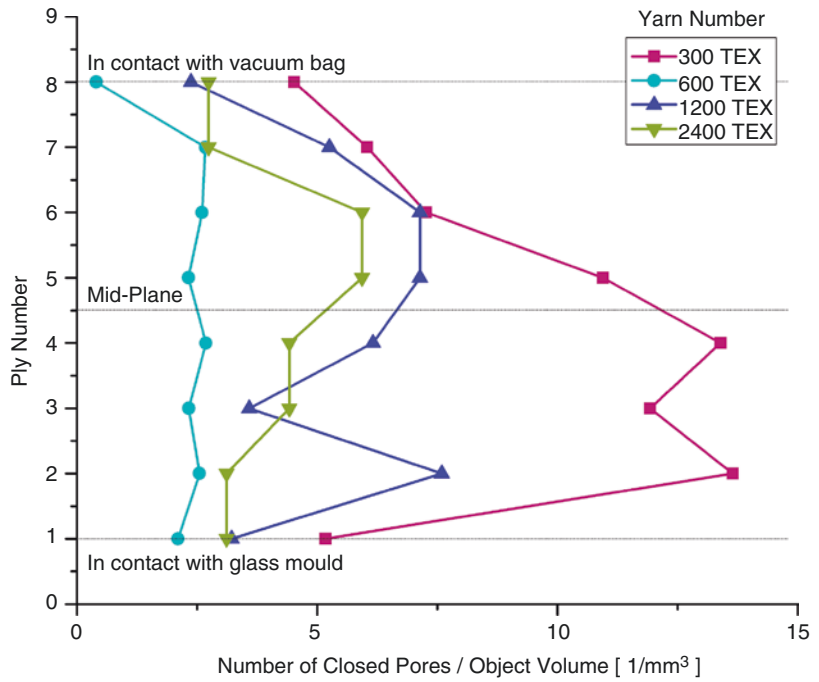
The connectivity of three-dimensional structures is usually indicated as connectivity density (connectivity value per volume) since the connectivity value is dependent on the object volume and ROI volume [34].

In the case of textile composites, this value represents the meso-architecture effect on the composite since the binarized structure shows only bundles inside ROI. In other words, in this study the meso-structure connectivity of composite samples is calculated with the use of the standard connectivity parameter. The mesostructure connectivity depends on the sticking and splitting of fiber bundles since CT images were binarized to differentiate bundle boundaries. Due to change in the viscosity and permeability of the resin flow during impregnation process, the size of the connectivity values varies in each sample with different yarn number.

14.3 Results and Discussions

In this study, several post-processed built-in parameters available in the CT-An image analysis software were calculated to understand the abnor-

Fig. 14.10 Ply number vs. number of closed pores per object volume for specimens with different TEX numbers



malities inside non-crimp composite samples. Each of the parameters is shown in divided color-coded bar-plot graphs to compare their effect on the yarn property of the samples. Unless otherwise stated, in the bar plots, the horizontal axis of the chart represents the ROI, and the longitudinal axis indicates the post-processed property with given units. Post-processed 3D image parameters that were analyzed are structure separation, structure thickness, cavity number, and connectivity.

Since fiber-matrix volume fraction (V_f) was close for all specimens and the fabrics forming the laminates had equal ply areal weights, the effect of yarn number can be considered as a sole mesostructure related yarn property. This constraint also allows for a reliable micro-CT analysis and 3D image processing.

14.3.1 Closed Pore Analysis

As a post-processing property so as to explain the manufacturing anomalies and the mesostructure of unidirectional NCF composites, the cavity numbers were calculated with earlier specified ROI selections. Figures 14.10 and

14.11 show the cavity number per object volume inside bundles for samples with four different yarn numbers. The correlation between 3D image analysis and the composite laminate performances was identified in [15] as the number of closed pores inside the laminates rather than the void percentage of specimens. Therefore, the porosity analysis only focuses on the number of closed pores inside bundles, their size, and their distribution.

The significant decrease in cavity number for all yarn properties is observed in the top (number 8) and bottom (number 1) laminae. Porosity numbers are lower due to the manufacturing technique of composites: the bottom ply is sharing a surface with glass mold, while top ply is covered with vacuum bag. The impregnation of NCF fabrics is done by the resin flow from top to the bottom of laminate under vacuum pressure due to the presence of highly permeable distribution media at the top of plies [36].

The most critical change while moving inside the laminate is seen in 300 TEX laminae. The number of closed pores is more than twice as the top or bottom ply in the mid laminae, namely,

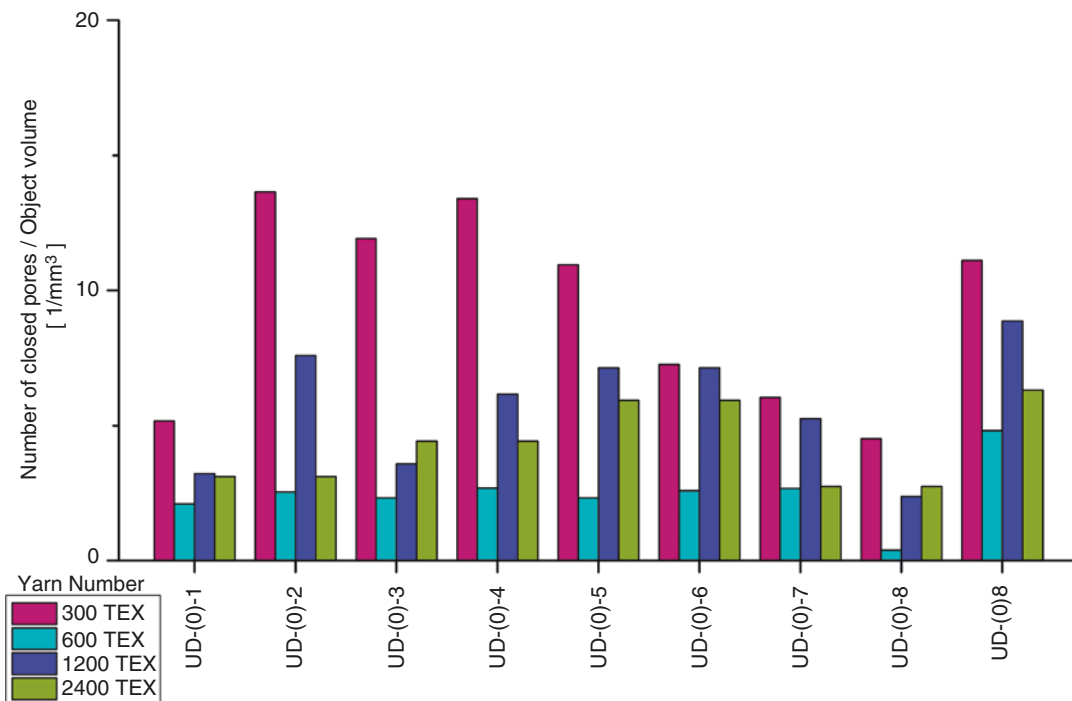


Fig. 14.11 Number of closed pores per object volume for specimens with different TEX numbers

lamina 4, 5, 6, and 7. On the other hand, it is almost stable throughout the laminate when we focus on 600 TEX plies. Similar to 300 TEX case, 1200 TEX also has relatively high number of closed pores in the middle plies compare to bottom and top ply. Due to plies being not separable as discussed in the section of the ROI selection, for the 2400 TEX specimen, a ply-by-ply discussion was not possible. Despite the overlapping problems, leading to identification of consecutive ply couples in the case of 2400 TEX specimen, the center ply couples, namely, laminae couple 3&4 and 5&6, show lower number of closed pores than 1&2 and 7&8 (Fig. 14.5).

During impregnation of the composites, it is possible that 300 TEX specimen's relatively low permeability resulted in locally unwetted regions that are reflected as increased number of closed pores especially located in middle plies. Also, the pore diameter size graph indicates that most of the pores in 300 TEX sample are smaller than $130\ \mu\text{m}$ (Fig. 14.12). For pores with larger diameter, almost each specimen has the same amount

of pores. On the other hand, when the average distance between the pores is investigated, as shown in Fig. 14.13, it can be seen that for the 300 TEX sample, this distance is very small, on the order of 30 pixels.

Overall, porosity analysis shows that 300 TEX has much more number of closed pores than other yarn numbers with smaller size and small distances between them. The vacuum-assisted manufacturing effect is visible in almost all yarn numbers, by a smaller number of porosity calculated on the top and bottom ply as apparent in Fig. 14.10.

14.3.2 Structure Separation and Thickness

In selected region of interests, the bundle and interbundle dimensions were statistically measured as the post-processed built-in properties of structural separation and structural thickness, respectively. Among calculated properties, the average structural separation and thickness of

Fig. 14.12 Number of closed pores vs. pore diameter inside specimens with different TEX numbers (p value represents the pixel size)

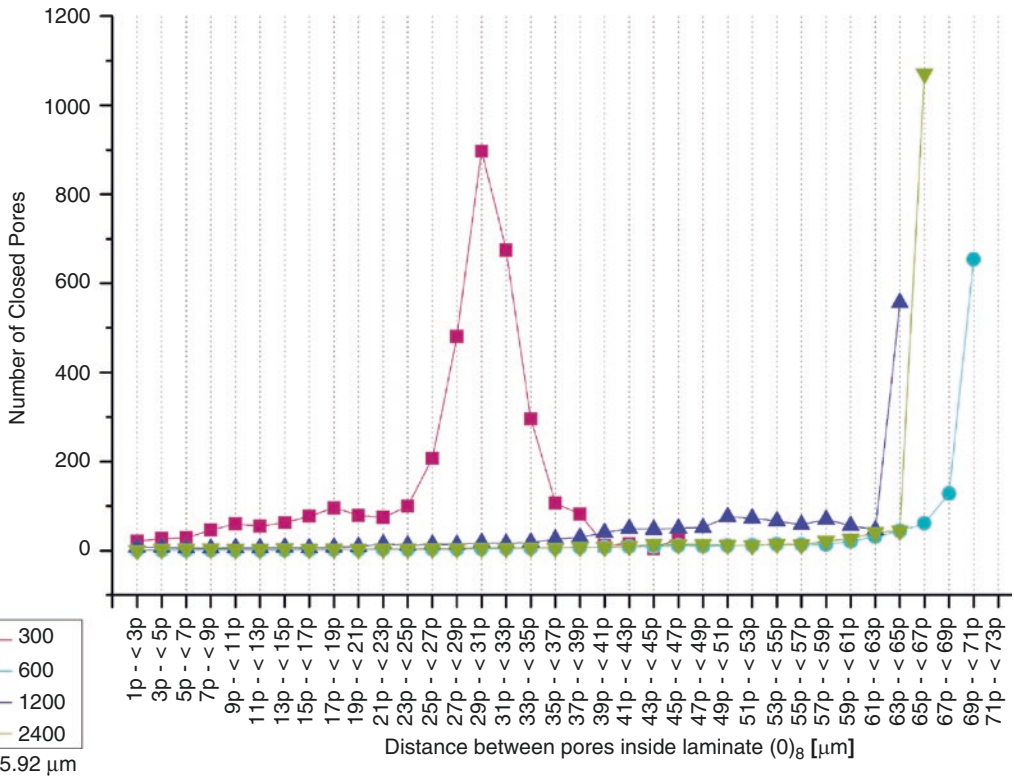
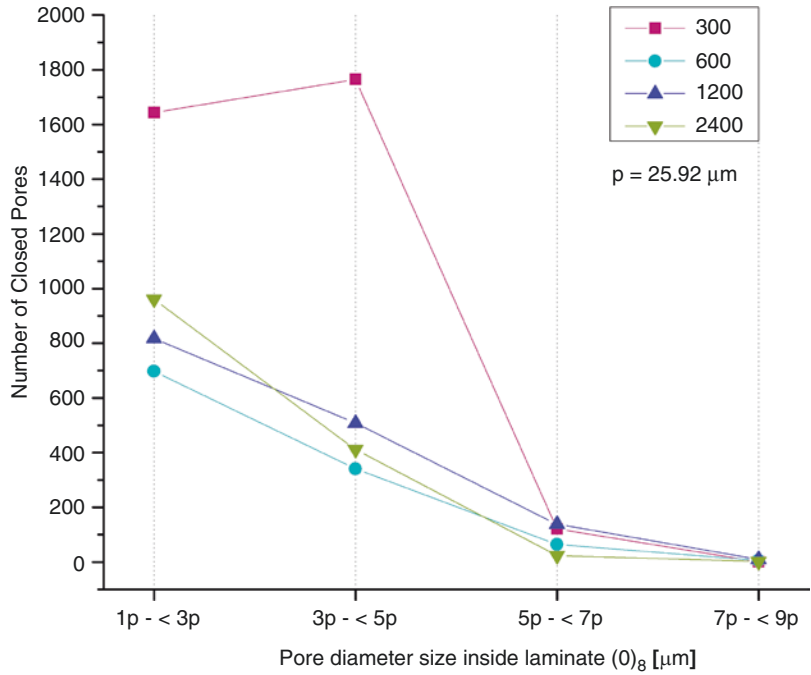


Fig. 14.13 Number of closed pores vs. distance between pores inside specimens with different TEX numbers (p value represents the pixel size)

Fig. 14.14 Ply number vs. structural separation for each specimen with different TEX number

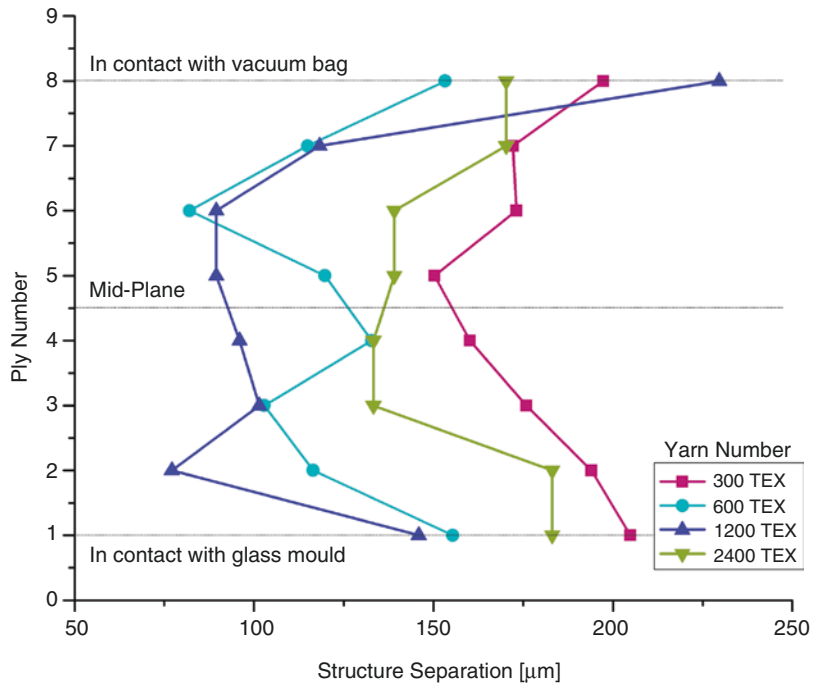
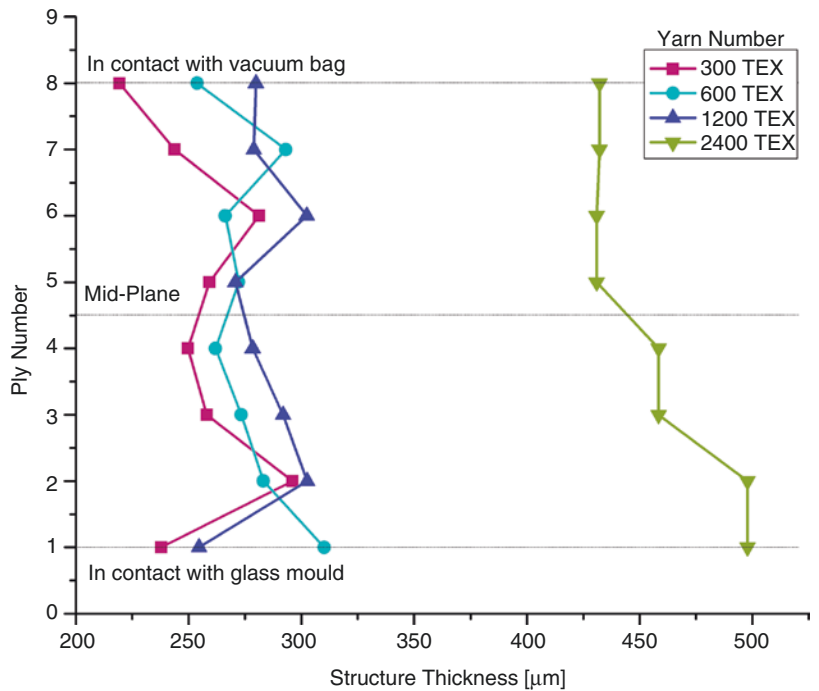


Fig. 14.15 Ply number vs. structural thickness for each specimen with different TEX number



separate ply-by-ply and laminated unidirectional composites are displayed with error bars in Figs. 14.14 and 14.15. To magnify the manufacturing effect on the ply-by-ply level, average values for structural separation and thickness are

shown as seen in Figs. 14.16 and 14.17. The interbundle distance values given in Table 14.2 are also considered for image correlation.

Due to permeability of the resin through laminate, the structural separation and thickness val-

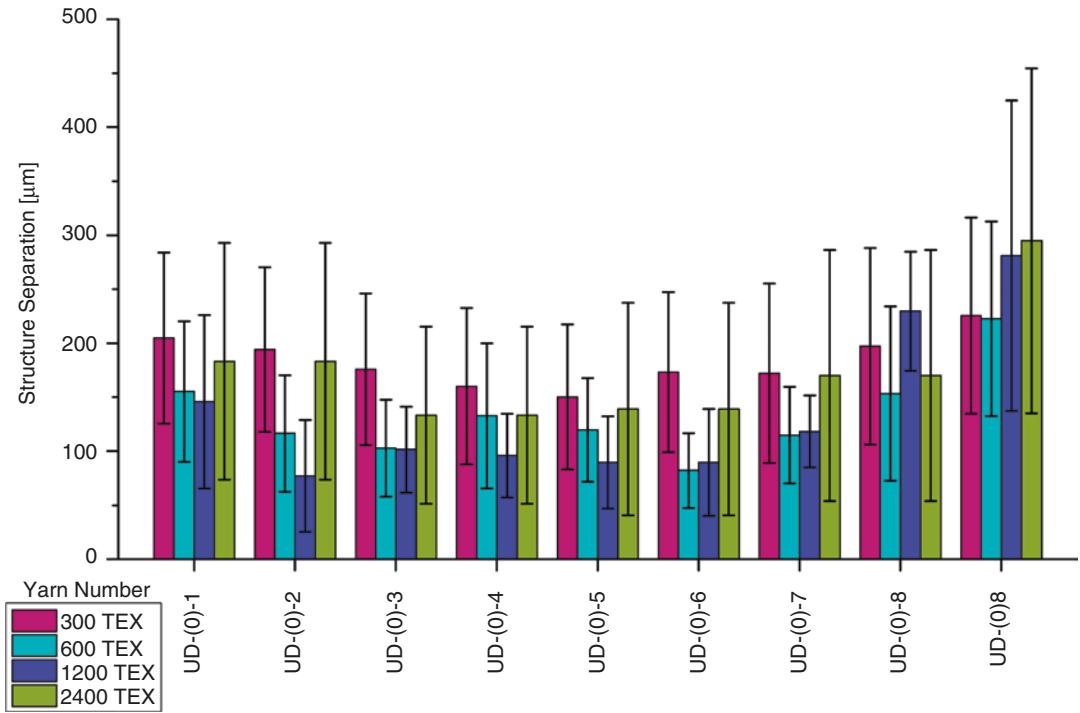


Fig. 14.16 Structure separation for each specimen with different TEX number on ply-by-ply basis

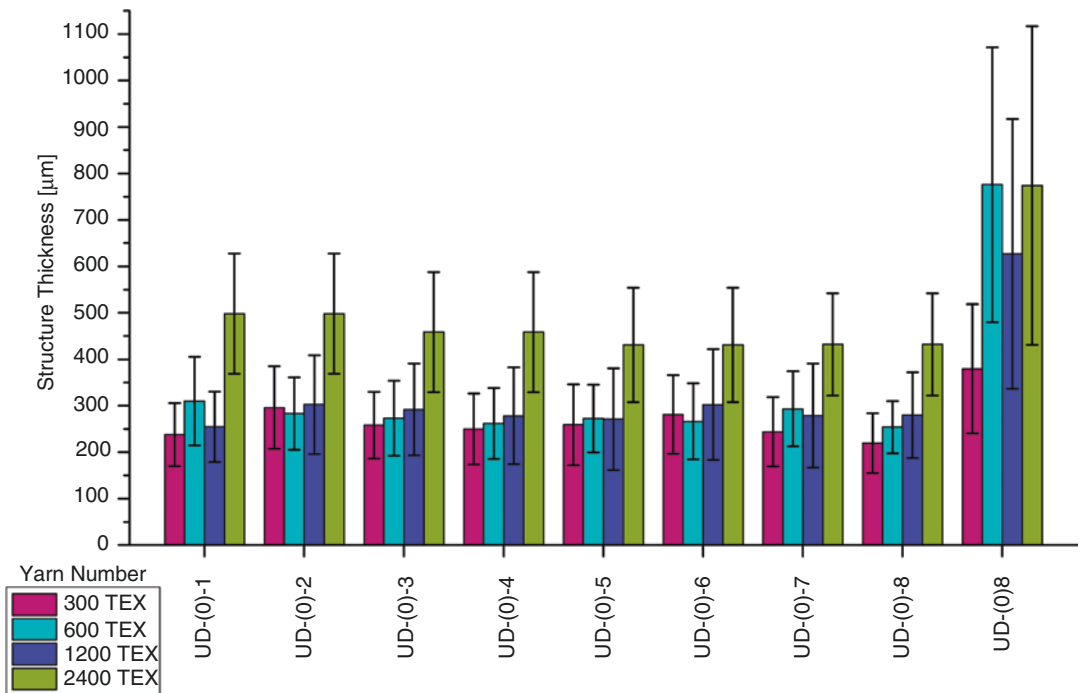


Fig. 14.17 Structure thickness for each specimen with different TEX number on ply-by-ply basis

ues differ in inner and outer plies significantly. Structural separation results suggest that the inner layers have higher values than outer plies (top and bottom) for all yarn number specimens, while the highest change is seen in inner and outer plies of the 1200 TEX plies. Even though ROIs were only separable as consecutive couples, 2400 TEX specimen still shows the same behavior as the other TEX specimens. Furthermore, the structural thickness values for inner and outer plies follow a similar trend to the structural separation results except for 2400 TEX specimen. The outlier effect of 2400 TEX is attributed to the problem of separating each laminae due to their merging and internal structure with a large bundle-to-bundle distance as seen in Fig. 14.5. Other three specimens with yarn numbers 300 TEX, 600 TEX, and 1200 TEX have lower structural thickness in the mid lay-ups.

Structural separation and thickness results suggest that for 300 TEX, 600 TEX, and 1200 TEX on the outer layers, the bundles have lower separation between them with higher structure thickness than inner plies. This meso-architecture can be attributed to the relative ease of resin flow at the top surface, facilitated by the flow media and solid boundary at the bottom glass mold during impregnation.

Overall, structural separation and structural thickness analysis suggest that the in situ meso-structure of fiber bundles was preserved after impregnation of 300 TEX, 600 TEX, and 1200 TEX. The sticking and splitting of the bundles compared to preferred bundle distance and thickness (Table 14.2) are quantifiable in inner and outer layers of the stack.

14.3.3 Connectivity

The specimens having small yarn numbers (e.g., 300 TEX), despite finer meso-architecture, may cause inadvertently manufacturing defects due to the resin flow anomalies during manufacturing process as some fibers inside the closed-packed bundle may not get impregnated enough. Since fiber bundles have been aligned in one direction in the unidirectional composites, con-

nectivity density values can be viewed as inversely correlated to the overall interbundle distances.

To analyze these effects in a comparative fashion, the connectivity values for each yarn number should be evaluated within themselves. The specimens of 300 TEX call for the most closed-packed configuration among other yarn numbered samples as seen in Fig. 14.14. Also, their connectivity density is demonstrating the highest values in Fig. 14.18. On the other hand, 1200 TEX has very similar connectivity values and follows a similar trend over laminae; however the meso-structure of 1200 TEX is different than 300 TEX as proposed and can be seen in the respective 3D images (Figs. 14.6 and 14.4). 1200 TEX specimen has a higher bundle size (also measured as structure thickness) and lower bundle distance (also measured as structure separation) than the 300 TEX specimen. This finding indicates that the connectivity value by itself is not enough to understand meso-architecture of UD NCF laminates. However, it can be complementary to distinguish differences between 600 TEX and 1200 TEX. While they both show similar values in structure thickness and separation analysis, the connectivity of 600 TEX is dramatically lower than 1200 TEX almost in all lay-ups except lamina 7 and in the overall laminate (Fig. 14.18).

14.4 Conclusions

The challenges and limiting factors regarding micro-CT characterization of composites have been reported in this chapter. Pre-imaging considerations such as sample size, sample geometry, x-ray absorption level of constituent materials of the composite specimens, and equipment capability were discussed. The ideal placement strategy of the presented samples and the scanning parameters were proposed and should be applicable for other NCF glass fiber composites and their investigations with micro-CT characterization. Post-processing analysis and ROI selection criterion are given in detail that should form a good analysis basis for composite materials. The meso-architecture and processing-related anomalies such as

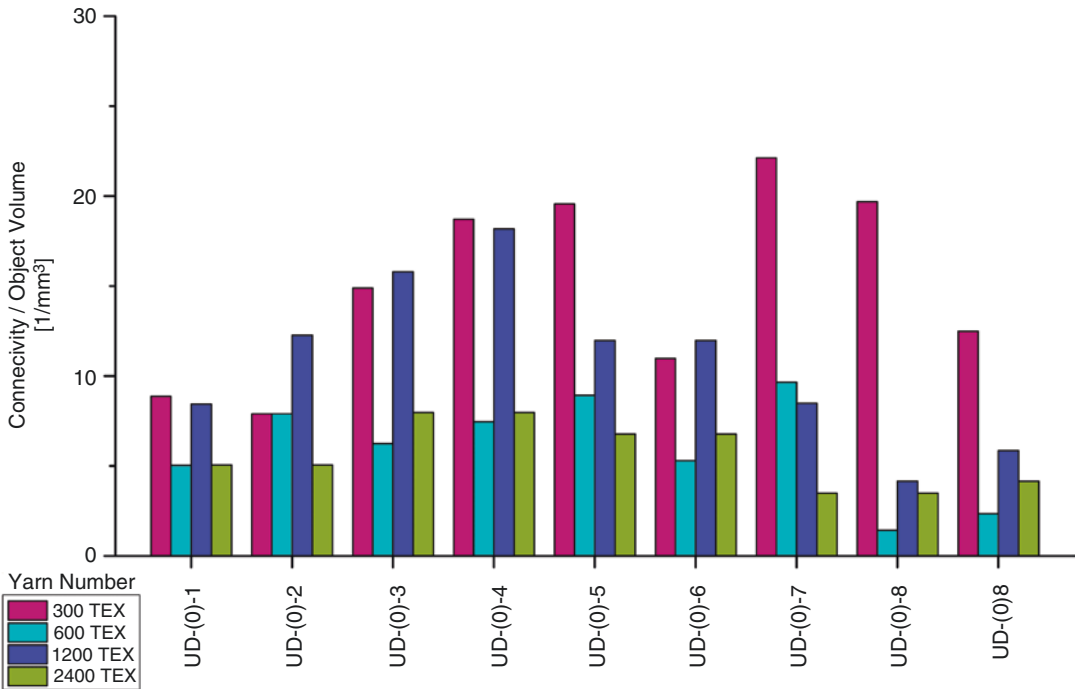


Fig. 14.18 Connectivity density (calculated as connectivity per object volume) for each specimen with different TEX number on ply-by-ply basis

porosity, sticking, and spreading of tows during vacuum infusion process have been investigated by using post-processing parameters in CT-An software. In order to build knowledge on tow and resin properties and the nature of the manufacturing process, nondestructive evaluation was shown to be useful with micro-computed tomography and post-processing. Analysis parameters such as number of closed pores, structure separation, structure thickness, and connectivity were used for the assessment of the specimens within the analysis and were related to their glass fiber NCF composite characteristics.

Micro-CT analysis results demonstrate that the anomalies regarding resin infusion manufacturing process can be quantitatively evaluated with this NDE technique. The internal microstructure of composites can be quantified with post-processing parameters such as structure separation, structure thickness, and connectivity. The ply-by-ply analysis reveals information about the movements of plies during resin flow-based impregnation. These results may lead to

further studies where the relationship between stiffness and strength of composite materials and micro-CT analysis outputs could be interrelated.

14.5 Future Work

Micro-CT analysis of composite materials can be regarded as a relatively new but rapidly advancing approach offering new means to analyze the internal microstructure of these complex materials. Bottlenecks of this specific research area are both related to scientific demand and instrumental capabilities.

In the field of composites science, the ability to analyze and digitize the infrastructure directs the research effort toward two main aims. First is related to the ability to characterize the damage formation during and after loading. With in situ integrated testing devices, micro-CT is able to monitor crack formations and propagation appearing inside of the composite laminates. In parallel, increasing efforts toward other NDT

methods like acoustic emission and thermography, more empirical approaches to characterize composite fracture are emerging. Secondly, since micro-CT is able to create a 3D image of the internal structure of a given specimen, it provides a solid background on computational studies aiming to predict the composite properties by creating idealized representative volume elements (RVE). The empirical approach provided by CT helps scientists to create more efficient RVEs and to come up with better property predictions. However, specimen size herein is the main limiting factor since for a higher resolution, smaller samples are required. Also signal acquisition capability (i.e., temporal resolution) may be stated as a bottleneck in order to capture associated failure modes in composites which may happen rather fast. Since the temporal resolution is directly associated with the type and power of the energy source, the use of electron-based laser technologies may improve the acquisition time.

The quality of a micro-CT scan also depends on optimizing the scanner parameters and the applicability of signal/image processing. As per the subject of this chapter, pre-scanning conditions and parameters are of crucial importance for a qualitative micro-CT analysis and are usually developed in-house. In order to provide more reliable data, the standardization of pre-scanning conditions is required for each set of specimen to be investigated via micro-CT characterization. In terms of composite materials, available studies are only limited to composites with conventional reinforcement materials such as glass and carbon. More sophisticated analysis and choice of parameters may be required for composites with more complex material compositions.

References

1. Kiefel D, Stoessel R, Grosse C. Quantitative impact characterization of aeronautical CFRP materials with non-destructive testing methods. *AIP Conference Proceedings*. 2015;1650(1):591–8.
2. Gholizadeh S. A review of non-destructive testing of composite materials. *Procedia Struct Integr*. 2016;1:50–7.
3. Ehrhart B, Valeske B, Bockenheimer C. Non-destructive evaluation (NDE) of aerospace composites: methods for testing adhesively bonded composites. *Non-Destructive Eval Polym Matrix Compos*. 2013:220–37.
4. Andrew JJ, Arumugam V, Bull DJ, Dhakal HN. Residual strength and damage characterization of repaired glass/epoxy composite laminates using AE and DIC. *Compos Struct*. 2016;152:124–39.
5. Cheng L, Tian GY. Comparison of nondestructive testing methods on detection of delaminations in composites. *J Sensors*. 2012;2012
6. Heuer H, Schulze MH. Eddy current testing of carbon fiber materials by high resolution directional sensors. *Proc NDT Canada*. 2011:1–13.
7. Surgeon M, Wevers M. Modal analysis of acoustic emission signals from CFRP laminates. *NDT E Int*. 1999;32(6):311–22.
8. Tan KT, Watanabe N, Iwahori Y. X-ray radiography and micro-computed tomography examination of damage characteristics in stitched composites subjected to impact loading. *Compos Part B Eng*. 2011;42(4):874–84.
9. Topal S, et al. Late-stage fatigue damage in a 3D orthogonal non-crimp woven composite: an experimental and numerical study. *Compos Part A Appl Sci Manuf*. 2015;79:155–63.
10. Vallons K, Lomov SV, Verpoest I. Fatigue and post-fatigue behaviour of carbon/epoxy non-crimp fabric composites. *Compos Part A Appl Sci Manuf*. 2009;40(3):251–9.
11. Bayraktar E, Antolovich SD, Bathias C. New developments in non-destructive controls of the composite materials and applications in manufacturing engineering. *J Mater Process Technol*. 2008;206(1–3):30–44.
12. Feng Y, et al. Micro-CT characterization on porosity structure of 3D Cf/ SiCm composite. *Compos Part A Appl Sci Manuf*. 2011;42(11):1645–50.
13. Stamopoulos AG, Tserpes KI, Prucha P, Vavrik D. Evaluation of porosity effects on the mechanical properties of carbon fiber-reinforced plastic unidirectional laminates by X-ray computed tomography and mechanical testing. *J Compos Mater*. 2016;50(16):2087–98.
14. Ponikiewski T, Katzer J, Bugdol M, Rudzki M. Determination of 3D porosity in steel fibre reinforced SCC beams using X-ray computed tomography. *Construct Build Mater*. 2014;68:333–40.
15. Scott AE, Sinclair I, Spearing SM, Mavrogordato MN, Hepples W. Influence of voids on damage mechanisms in carbon/epoxy composites determined via high resolution computed tomography. *Compos Sci Technol*. 2014;90:147–53.
16. Sisodia SM, Garcea SC, George AR, Fullwood DT, Spearing SM, Gamstedt EK. High-resolution computed tomography in resin infused woven carbon fibre composites with voids. *Compos Sci Technol*. 2016;131:12–21.
17. Lambert J, Chambers AR, Sinclair I, Spearing SM. 3D damage characterisation and the role of voids in the fatigue of wind turbine blade materials. *Compos Sci Technol*. 2012;72(2):337–43.

18. Pazmino J, Carvelli V, Lomov SV. Micro-CT analysis of the internal deformed geometry of a non-crimp 3D orthogonal weave E-glass composite reinforcement. *Compos Part B Eng.* 2014;65:147–57.
19. Yoshimura A, Hosoya R, Koyanagi J. X-ray computed tomography used to measure fiber orientation in CFRP laminates. *Adv Compos Mater.* 2016;25(1):19–30.
20. Djukic LP, Herszberg I, Walsh WR, Schoeppner GA, Gangadhara Prusty B, Kelly DW. Contrast enhancement in visualisation of woven composite tow architecture using a MicroCT Scanner. Part 1: Fabric coating and resin additives. *Compos Part A Appl Sci Manuf.* 2009;40(5):553–65.
21. Schell JSU, Renggli M, van Lenthe GH, Müller R, Ermanni P. Micro-computed tomography determination of glass fibre reinforced polymer meso-structure. *Compos Sci Technol.* 2006;66(13):2016–22.
22. Badel P, Sallé EV, Maire E, Boisse P. Simulation and tomography analysis of textile composite reinforcement deformation at the mesoscopic scale. *Int J Mater Form.* 2009;2(Suppl. 1):189–92.
23. Djukic LP, Pearce GM, Herszberg I, Bannister MK, Mollenhauer DH. Contrast enhancement of microCT scans to aid 3D modelling of carbon fibre fabric composites. *Appl Compos Mater.* 2013;20(6):1215–30.
24. S. Kalafat, A.-M. Zelenyak, and Sause MG. In-situ monitoring of composite failure by computing tomography and acoustic emission. In: 20th International Conference on Composite Materials, pp. 1–8; 2015.
25. Naouar N, Vidal-Salle E, Schneider J, Maire E, Boisse P. 3D composite reinforcement meso F.E. analyses based on X-ray computed tomography. *Compos Struct.* 2015;132:1094–104.
26. Li Y, Sun B, Gu B. Impact shear damage characterizations of 3D braided composite with X-ray micro-computed tomography and numerical methodologies. *Compos Struct.* 2017;176:43–54.
27. Edgren F, Mattsson D, Asp LE, Varna J. Formation of damage and its effects on non-crimp fabric reinforced composites loaded in tension. *Compos Sci Technol.* 2004;64(5):675–92.
28. Mattsson D, Joffe R, Varna J. Methodology for characterization of internal structure parameters governing performance in NCF composites. *Compos Part B Eng.* 2007;38(1):44–57.
29. Mattsson D, Joffe R, Varna J. Damage in NCF composites under tension: Effect of layer stacking sequence. *Eng Fract Mech.* 2008;75(9):2666–82.
30. Feldkamp L a, Davis LC, Kress JW. Practical cone-beam algorithm. *J Opt Soc Am A.* 1984;1(6):612.
31. Boas FE, Fleischmann D. CT artifacts: Causes and reduction techniques. *Imaging Med.* 2012;4(2):229–40.
32. Kandwal R, Kumar A, Bhargava S. Review : Existing Image Segmentation Techniques. *Int J Adv Res Comput Sci Softw Eng.* 2014;4(4):153–6.
33. Straumit I, Hahn C, Winterstein E, Plank B, Lomov SV, Wevers M. Computation of permeability of a non-crimp carbon textile reinforcement based on X-ray computed tomography images. *Compos Part A Appl Sci Manuf.* 2016;81:289–95.
34. Bouxsein ML, Boyd SK, Christiansen BA, Guldberg RE, Jepsen KJ, Müller R. Guidelines for assessment of bone microstructure in rodents using micro-computed tomography. *J Bone Miner Res.* 2010;25(7):1468–86.
35. Odgaard A. Three-dimensional methods for quantification of cancellous bone architecture. *Bone.* 1997;20(4):315–28.
36. Bender D, Schuster J, Heider D. Flow rate control during vacuum-assisted resin transfer molding (VARTM) processing. *Compos Sci Technol.* 2006;66(13):2265–71.



Modeling and Mechanical Analysis Considerations of Structures Based on Micro-CT

15

Gökhan Altıntaş

15.1 Overview of Micro-CT in Terms of Visual and Physical Modeling

It is very difficult to refer to all of the examples in this context, and it is highly probable that the scientists and the practitioners interested in the subject have different conclusions in the forthcoming parts of the chapter. Micro-CT is a gold standard, especially for volumetric modeling and sensitivities, although some of the applications listed below, especially some of the superficial shell models, can be done with other different undamaged inspection applications.

Micro-CT data can be used for many different purposes:

- Performing various investigations using raw or processed states as appropriate for the images in the ordered sections
- Creation of point clouds and making related analyses
- Analysis and reconstruction of surface geometries
- Creation of volumetric solid models constituting the basis for many geometric and physical analyses

- Reconstruction of many biological, human-made, fixed, or mobile structures based on the original, for the creation of examination and production models on different scales

It is always possible to enlarge and diversify the list above. In this study, the use of models created by the creation of geometric and physical models in mechanical analysis has been considered, and the literature review was shaped in this regard. It is useful to refer to a brief literature review before proceeding to working examples and method descriptions.

Primary analyses using micro-CT scan data are related to the determination of geometric properties, which are frequently found in literature related to biomaterials and porous materials. Among the many properties that can be defined as geometric properties, features such as surface area, volume, porosity, wall thickness, and space orientation can be obtained by many other methods. However, their accuracy rates vary greatly and may need to be supported by empirical methods.

In another study, an explanatory comparative table was compared with in their comparison of micro-CT with other methods in the determination of geometric characteristics of structures [1]. Only micro-CT can be used to obtain all these properties from the investigated methods depending on the porosity, surface area, volume, cavity dimensions, wall thicknesses, and permeability.

G. Altıntaş (✉)
Engineering Mechanics Division, Department of
Civil Engineering, Manisa Celal Bayar University,
Manisa, Turkey
e-mail: gokhan.altintas@cbu.edu.tr

A preliminary study on modeling and examination of bone tissue using a combination of micro-CT data and CAD/CAM techniques was performed [2]. The authors compared the applicability of the Skyscan® Ctan®, and Materialize Mimics® software. It is important to note that with this work being a premise study, used software may have undergone very different developments from the publication date of the article until today.

Since porous structures can be obtained in the most obvious way by examining mono- and multiphase structures, studies using micro-CT image data are increasing day by day. In this context, related references in literature are comparatively presented [3]. Particularly, the study considering bone tissue has also taken place in the development of micro-CT technology.

The use of micro-CT does not only consider the micro-architecture of organic tissues but also enables working in many areas where micro-architecture is important. In another study, two-dimensional CT data were examined for the void spaces of the soil sample [4]. The technology used and the method of operation are simpler than the ones mentioned above, but it is a worthwhile work in terms of putting the importance of the CT data in the identification studies.

Micro-CT is also one of the nondestructive imaging methods, which can be used not only in their location but also in the follow-up of displacements and deformations when they are subjected to different effects and in the creation of associated models.

Although porous bone density has a significant effect on bone strength, it is not sufficient by itself, and properties about the microstructure of the bone shall particularly be taken into consideration on bone strength [5]. It was examined that voxel-based FE models of trabecular bone combined with mechanical properties of the volume fractions, micro-CT reconstructions, mechanical tests, and model-specific nano-indentation experiments for the validation method [6].

Noninvasive imaging methods were compared between each other by using trabecular bone tissue [7]. The results are quite informative in terms of resolution values, which are used during the

study of trabecular bone tissue. The relationship between CT slice thickness and mechanical properties of porcine vertebral cancellous bone has been studied [8]. Firstly, the effect of micro-CT slice thickness on natural vibration properties of porous bone models was studied according to the voxel-based FEM [9]. Change of slice thickness also changes the cubic structure of voxels in the classic voxel-based FEM and causes an occurrence of rectangular voxels that are unsuitable in terms of FEs. Three-dimensional analysis of soil samples exposed to mechanical and hydraulic stresses were evaluated by performing various analyses using three-dimensional models generated from micro-CT data [10].

In recent years, integrated applications in which models of micro-CT data can be processed, as well as analysis and simulation, have become very important. The main reason for the need for integrated software is that analysis can only be done with a multidisciplinary group work. In other words, knowledge and technical competence to make all modeling and analysis phases are not usually found in one person. However, even today's most integrated applications have not succeeded in overcoming this problem. Numerous programs such as Simpleware ScanIp®, Materialize Mimics®, Amira®, and Avizo® can directly process micro-CT data, creating surface and volume structures but making the mechanical and geometric analysis feasible, and creating the most accurate models is a matter of considerable experience. The basis of this work is the processing of data, the creation of models that can be analyzed, and the mechanical analyses. It is aimed to gain familiarity with geometrical modeling and mechanical analysis which can be based not only on visualization but also on academic studies in accordance with the aims of people who come from different branches.

15.2 Usage Fields of Micro-CT Data

Although micro-CT data can be used for many different purposes, they can be grouped into four main categories.

- Imaging
- Modeling
- Production/reproduction
- Analysis

Each goal above has different requirements, and the awareness of the small differences between very similar procedures to know these requirements is thought to facilitate the work of scientists and practitioners.

15.2.1 Micro-CT-Based Visual Presentation Form Usage for Inspection

The micro-CT data is delivered to the end user in general as rotational or sequential image data. There are a large number of software for transforming ordered image data into a structure that can be examined in a three-dimensional environment, and these softwares can be easily converted into 3D visual models such as isosurfaces and point clouds, etc. Generated 3D visual models and even sequenced image data are already widely used for various measurements and determinations for instance geometric form or shape matching. The geometrical properties that can be obtained from these data are very limited. However, artificial intelligence-assisted applications are increasingly being used in objective determinations, such as tumor formation, or in the detection of various forms. Although applications of visual models are easy, their performance at geometric sizes such as volume and surface area is not as effective as those obtained from volumetric models.

15.2.2 Use of Micro-CT-Based Reverse Engineering Techniques in Production or Reproduction

One of the main purposes of reverse engineering is the creation of models that enable the production or reproduction of the inspected structure. This method can be applied with the highest precision, especially when the internal structure is

difficult or impossible to determine precisely by other methods in geometric and topological manners. In this way, a modeling need can be used in modeling trabecular bone tissue, a very complex geometric carrier system, and at the same time, and even increasingly, in the larger manufacturing industry, it can be used to replicate the internal structure and reproduce it on the desired scale without breaking up a product. This technique has unfortunately opened the way for unpleasant purposes such as copying products in industrial espionage. But on the other hand, in areas such as the study of historical mechanisms or fossilized structures, it has provided great advantages and ease at a time when it has never been before.

However, there are big differences between the aim of production and the creation of three-dimensional models and the creation of models for imaging. Whether you want to produce on CNC machines or on 3D printers, there are absolutely necessary conditions for 3D model files. These requirements are quite different from the known production techniques, such as the so-called ground handling, which can later be separated into structures in the form of reverse droplets of the model to be produced on the 3D printer. If the model to be produced is designed and prepared on a computer, these conditions are always provided automatically. However, the same situation may not be available for geometries obtained by reverse engineering methods. For example, in the case of an STL-type file consisting of triangles, the surface geometry that is carried must form a closed volume. It is also necessary that models have continuity characteristics so that they can form a whole. Some programs provide these requirements automatically, while some programs allow users to make selections and allow local surface operations. But if the models emerged as a result of choices of inexperienced users, they would not topologically produce errors in production; the resulting model might have formed quite differently from the actual object. In order to avoid all these undesirable situations, algorithms which are useful for implementation are mentioned later in the chapter.

15.2.3 Micro-CT-Based Models to Be Used in Analyses

A complete reverse engineering exercise involves the steps that are taken in mechanical analysis. There are some vital differences even if the approaches used to create the models to be used in production and analysis are very close to each other. In this case, models to be used in mechanical analysis need to be created, and in these models, there are additional requirements that must be satisfied.

A brief explanation on these obligatory requirements will be helpful in understanding the matter; further information will be provided in the following sections of the work.

Volumetric models are usually used directly in geometric and mechanical analyses after a few routine fixes. For the surface models to be used for analysis, the surfaces must be completely enclosed, which is a must in geometric and topological analyses. Namely, the smallest gap in the surface mesh that must form a closed volume makes it impossible to determine precisely which area of the surface of the program is inside or outside. However, this is in the foreseeable software, but in the case of sensitive work, the operator will be able to decide how reliable it is for the job. It is necessary to include enclosed volumes of superficial models carried by file types like STL (STereo Lithography) and OBJ (Object Files). Some special algorithms have to be used in order to achieve this.

In order to be able to perform in mechanical analysis, the models need to satisfy some conditions. Particularly, problems such as buckling, natural frequency, and eigenvalue-eigenvector analysis should not have disconnected regions in the models. In order to ensure that the whole structure is in one piece, it is imperative that some algorithms such as “Region Growing” or “Flood Fill” algorithms are applied during the creation phase of the models. However, depending on the type of problem, it may be necessary to use it in additional algorithms, and the structure of the model to be examined sometimes may be decisive. Multiphase composite structures,

porous, or composite porous materials sometimes require different modeling steps. It is expected that the definitions referred to in this section will become more understandable after the applications presented in this section.

15.3 Preparation of Samples for Micro-CT and Sizes to Be Decided

The quantities to be mentioned in this section are dealt with in order to create solid models based on the necessity of creating models that can be analyzed. The principle of operation of CT with an X-ray source and detector unit rotating synchronously around the sample is given in Fig. 15.1a. Rotational images are acquired continuously during rotation in Fig. 15.1b. The resulting rotated images are transformed by software into sequential images that can be expressed as slices at certain intervals (see Fig. 15.1c). There are φ angle difference between rotated image samples and β distance between sequential image slices. Researchers interested in mechanical analysis often work with sequential image segments if they are not directly involved in the underlying structure of the micro-CT device.

It is a method that allows relatively small details to be observed, as can be understood from the name of micro-CT. In order to be able to apply this method properly, there are quantities that the scientist who decided to use micro-CT.

The basic steps to be taken in this context are as follows:

1. Determining the minimum detail size, in other words the edge length of an image pixel, depending on the type of problem to be worked on.
2. Determine the resolution based on the actual edge length of the pixel.
3. Determine the external environmental size of the structure to be scanned.
4. Selection of a scanner suitable for the needs determined in items 1, 2, and 3 or revising such sizes if necessary.

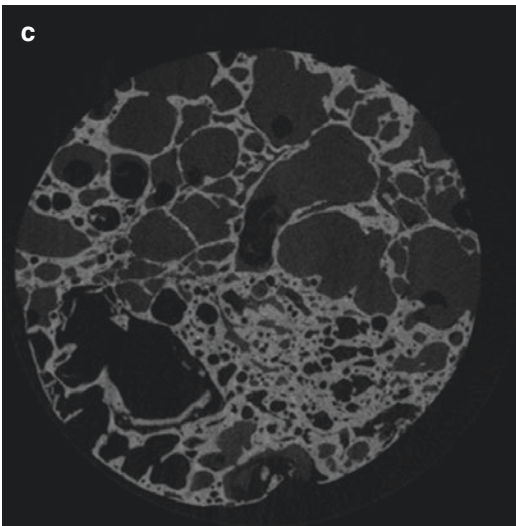
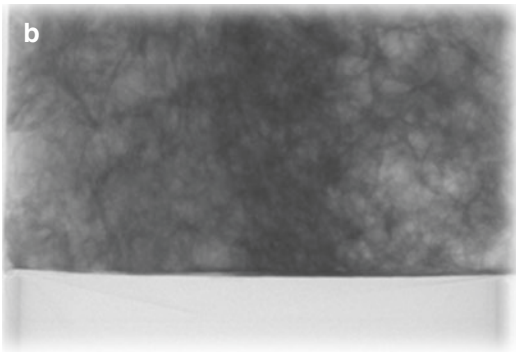
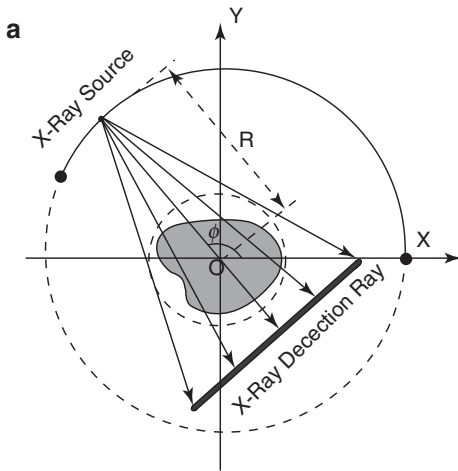


Fig. 15.1 CT imaging: (a) rotational imaging with an X-ray source and detector unit (b) rotational images (c) sequential images

As a different way, micro-CT scans of sample different resolutions can be taken and compared. However, this does not appear to be a method that can be recommended in terms of time and cost.

15.3.1 Sample Resolution Detection Study

The coral sample to be used as an implant and having a diameter of 0.32 cm and a thickness of 0.08 cm will be obtained from the coral structure, and an approximate resolution will be determined in order to model structural system.

- For this purpose, in order to determine the minimum detail size, it is first scaled under the microscope, as can be seen in Fig. 15.2, in a region that will be considered as the smallest important detail of sample in slice. In this section, it is planned to use the part in the middle region of the coral skeleton examined. It is obvious that the thickness determination of the thin-walled structures seen as the structure in this region cannot be done with the image presented in Fig. 15.2 and a scaling study will be done on a closer image in Fig. 15.3.
- After reviewing the various resolution images, it was found that the thinnest wall thickness, which is believed to have load-carrying capac-



Fig. 15.2 *Acropora cervicornis* skeleton

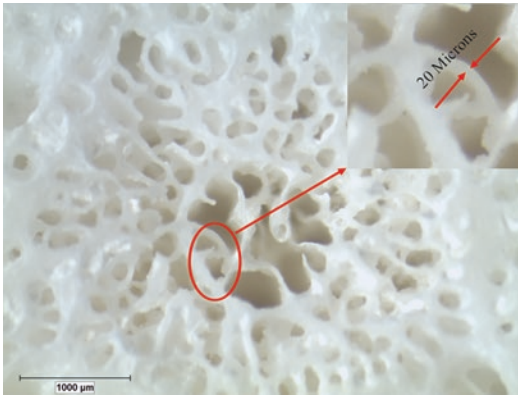


Fig. 15.3 Visual inspection of thickness detection

ity in the middle region of the sample, is on the order of $20\ \mu\text{m}$. Note that the dimensions of the edge lengths of the pixels depend on the scanner used, so long as their resolution is the same. If small lengths are required to be visible in detail, small samples need to be scanned in the relevant scanners.

- It has been decided that the edge lengths of the pixels should be no more than $4\ \mu\text{m}$, considering that the thickness is about $20\ \mu\text{m}$ and the wall may not be parallel to the pixel edges. The experience gained from work done on previous models played an important role in making this decision. Any scan to be performed at a value below $4\ \mu\text{m}$ is acceptable here, and a very crude version of the actual image of the scans to be made at values greater than $4\ \mu\text{m}$ is expected to emerge. The comparison with the image of the model created with the selected $4\ \mu\text{m}$ pixel edge length value and the possibility of viewing in the microscope will help to make the most accurate decision.
- The diameter of the sample was $0.32\ \text{cm}$. For a square area that will contain this diameter, it should not be forgotten that the edge length of each pixel is at least $4\ \mu\text{m}$ in the resolution calculation. If there are 800 pixels with $4\ \mu\text{m}$ edge lengths on each side of the square cross section, the intended image resolution of $0.32\ \text{cm}$ ($3.2\ \text{mm}$ or $3200\ \mu\text{m}$) will be obtained. As a result, images with a minimum resolution of 800×800 will be needed and should be taken from a scanner that can scan a sample with a diameter of $0.32\ \text{cm}$.

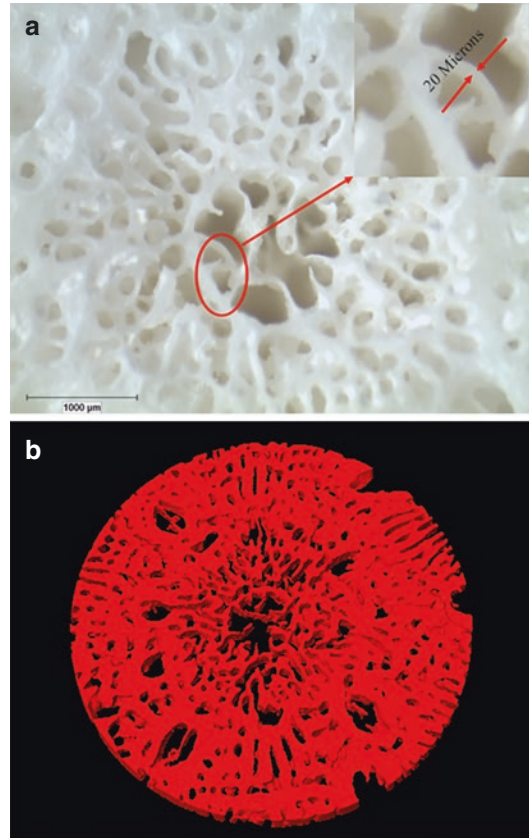


Fig. 15.4 Detail comparison: (a) close view images of coral sample (b) solid 3D model of coral sample

In the final case, when 3D model raw view is obtained, it is absolutely necessary to check whether the images taken with microscope are transferred to the model (see Fig. 15.4). This is not always possible, but the experience of the experienced practitioners working with the same materials and models can be relied upon. Transferring the resulting high-resolution images and models based on them directly to the finite element models with the same precision and resolution is limited by the boundaries of the environment in which the finite element solver is located.

15.4 Basic Operations of Sequential Images Before Creating Solid Models

Although micro-CT data were first used to examine biological structures, they are now widely used in studies in many different areas. There are

many options and methods for processing images, and this section will focus on the most basic processes used by people working on the subject. Whichever method is applied to the processing of images, it is necessary to apply the same operations to an entire series of images, except exceptional cases rarely encountered. This also means that a large number of images must be handled quickly and batch processing programs must be selected. The most common way of doing things is to classify them as follows.

15.4.1 Basic Filters and Applications

Filtering methods basically require that images be improved for the certain aim, or the undesirable noises, shadows, etc. that occur during the imaging process should be corrected as much as possible. Filtering methods can be used to improve the quality of images or removing unwanted visual objects or effects. For instance, unwanted effects and noises occur during imaging process, such as unwanted shadows caused by sharp edges of sample should be corrected as much as possible. While the process being performed provides an intended feature, it must not inflict any other property or visual quality loss that is already provided. After each step it is necessary to carry out these inspections and to back up. Filters can be used to improve images, or they can be used to make certain features or shapes more distinguishable on images. There may not be a need for many of them in the production of standard solid models together with a large number of filters. Especially if proper purpose scans, suitable devices, and faultless models without sharper sample angles to create shadows are prepared, filtration needs the least. In some cases, segmentation methods and filters can be found in close results.

15.4.2 Segmentation Methods

Image segmentation is the process of separating an image into numerous parts. This is classically used to recognize objects or other significant information in images. Threshold, Flood Fill, and

Region Growing segmentation methods are among the most important segmentation methods that can be used frequently and vitally for micro-CT studies. Threshold and Flood Fill are vital algorithms that can be used in almost all micro-CT-based modeling applications.

15.4.2.1 Threshold Algorithm

The Threshold algorithm can be roughly considered as a decomposition based on the color values of the pixels of the images. When any image is handled in the gray scale, a pixel takes values between 0 and 255. Zero black, 255 white indicates different shades of gray for values in between. This scale can be changed according to the purpose. It is available with free programs such as CTan[®], Osirix[®], Bio Image Suite[®], and ITK[®], which can apply the Threshold algorithm collectively to image series, or commercial programs like Materialize Mimics[®], Avizo[®], and Amira[®].

The implementation of an image series threshold algorithm is to specify a range for the threshold. In Fig. 15.5, a threshold application was made on the image taken from a series of micro-CT scan of porous stone sample [11].

In most micro-CT scans, the space appears black, but there may be changes in the images after the various filters are applied. This may need to be taken into account and may require visual comparison with raw images. In Fig. 15.5, it is known that the images on the gray scale are negative for the original images and the black regions express the void. In this context, it is necessary to determine the threshold value of the stone sample of the user and the threshold value at which the threshold value is based on an image as shown in Fig. 15.5b. In Fig. 15.5b, the pixel in the gray scale that is focused is very close to black and has a gray-scale value of 25. As a result of such an examination, the user can decide that the material is within a certain threshold range and continue the process.

However, it should be noted that different users can classify different values as material or space, and there is always no possibility of visual confirmation under the microscope. This is one of the most important problems encountered in studies and can often overshadow the reliability

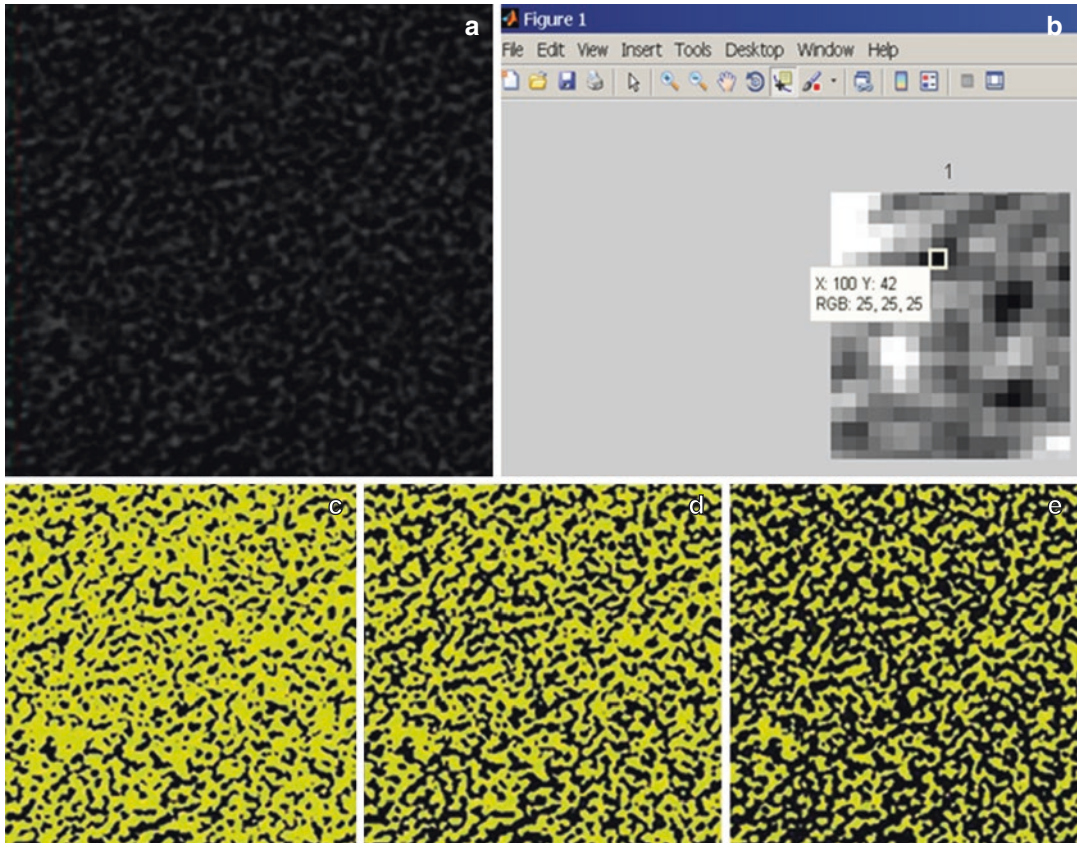


Fig. 15.5 Threshold segmentation of (a) porous stone X-ray image (in here reversed gray scale). (b) CUBOID-SI2FE Matlab®. (c) Threshold 5–255 (range size 250). (d)

Threshold 10–255 (range size 245). (e) Threshold 15–255 (range size 240) [11]

of the results. In this regard, this part of this study particularly important and is a separate matter of debate in literature [11–14].

Outputs after threshold operations separated by small value differences are presented in Fig. 15.5c, d, and e. In Fig. 15.5, the space is left black again, and it should be remembered that the stone material is masked with yellow color. Here, only about 2% of the visual difference results are presented. Even with an instantaneous view of the pictures, it is clear that the difference in the amount of threshold 2% caused this difference to be far beyond. Models obtained for the different threshold ranges of the sample with the region of interest (ROI) dimensions of 2275 mm × 2275 mm × 0.091 mm are presented in Fig. 15.6.

It is obvious that the values used in the implementation of the thresholding algorithm

have a large effect on the geometry of the three-dimensional models. However, with the use of three-dimensional models in analysis, these volumetric differences in simulation of various mechanical events and experiments are much more important than visual differences [11].

The mass and stiffness changes are directly related to the volumetric changes. In other words, the different selections in the threshold values to which the model volume depends are not the same on mass and stiffness. As a result of setting the wrong threshold range, the strength, natural frequencies of a structure, or all the mechanical properties to be homogenized can be calculated incorrectly. This should be known to have serious consequences both in academic and practical applications. Not all researchers can come to a

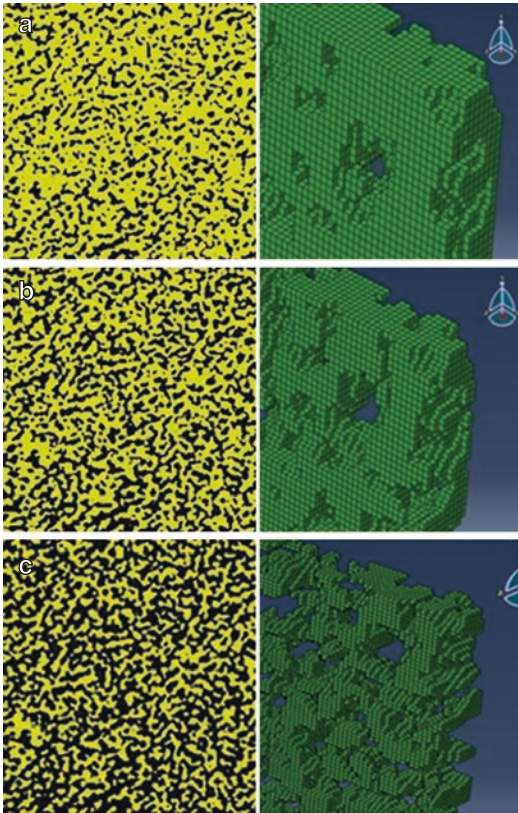


Fig. 15.6 The 3D models obtained according to the threshold value selection: (a) segmented image for threshold 5–255 and produced solid model with 0.337 mm^3 volume, (b) segmented image for threshold 10–255 and produced solid model with 0.271 mm^3 volume, (c) segmented image for threshold 15–255 and produced solid model with 0.199 mm^3 volume [11]

concrete agreement in selection of ranges of values in thresholding, although the differences in selection of ranges are small, awareness of the possible influence of range selection on outcomes is of vital importance. Natural frequency analysis of the model presented in this subject is presented in Fig. 15.7. The first nine natural vibration modes were obtained where the material properties were presented as density, $2.71\text{E}-10 \text{ (t/mm}^3\text{)}$; elasticity, $5986 \text{ (N/mm}^2\text{)}$; and Poisson's ratio, 0.23.

As the mode number increases, the selection of the threshold values is clearly visible in Fig. 15.7. A brief description of this section is provided to illustrate the importance of threshold segmentation. You can find further information in the following sections.

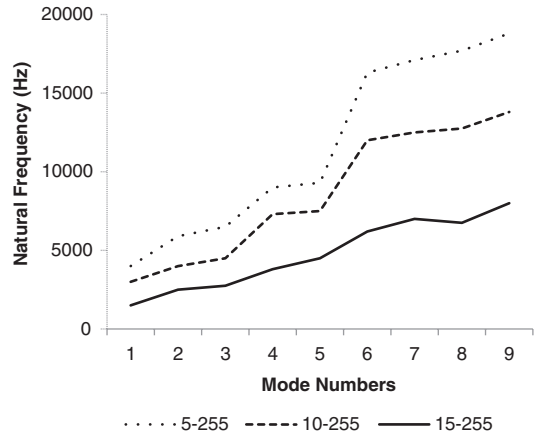


Fig. 15.7 Effects of threshold values on natural frequencies [11]

15.4.2.2 Flood Fill Algorithm

The Flood Fill algorithm is a process in which similar pixels are separated from others by certain conditions. The key point in this separation process is the neighborhood relationship of the pixels. The Flood Fill algorithm starts with a certain pixel and creates a region expanding by adding neighboring pixels like itself. This region covers an area created by pixels adjacent to each other in a manner such as expanding within boundaries defined by the fluids the name of the algorithm implies in Fig. 15.8.

In this study, a three-dimensional version of the two-dimensional Flood Fill algorithm is necessary since three-dimensional solid models are used. Some definitions should be made for a better introduction of the three-dimensional Flood Fill algorithm. The three-dimensional Flood Fill algorithm is applied to the voxels, which can be defined as three-dimensional states of the pixels, not the pixels. In this context, after making a detailed explanation of the voxel concept for a better understanding of the subject, the three-dimensional application of the Flood Fill algorithm will be referred to again.

Voxelization

The process of creating 3D models using pixels in images can be called voxelization in Fig. 15.9. A pixel with a distance in a two-dimensional plane of an image can be expressed as a voxel

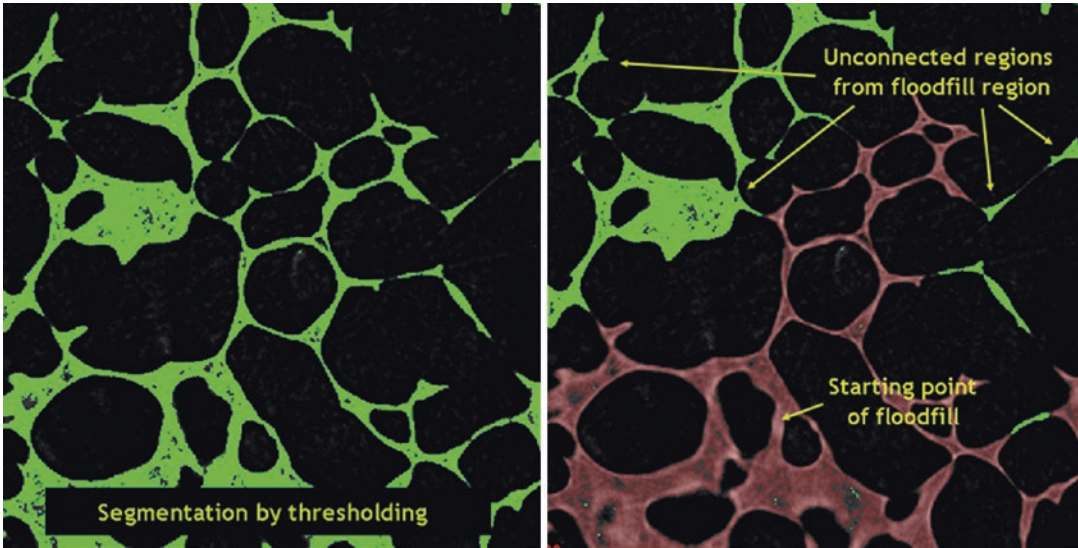


Fig. 15.8 Visualization of Flood Fill algorithm usage

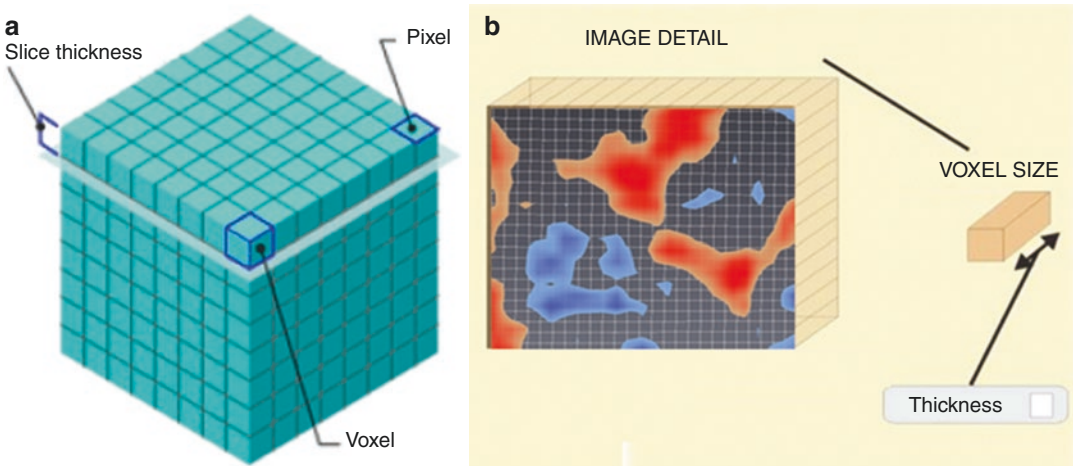


Fig. 15.9 Voxelization concept images: (a) definitions (b) voxel and X-ray image connection

with a given thickness converted into volumetric elements. If there is no exception, one pixel is moved to the third dimension with the thickness of the distance between the two consecutive views. If there is no exception, one pixel is transformed into a three-dimensional voxel by adding the third dimension that having distance value between two slices. Name for this distance is slice thickness.

Once the pixel has been converted to voxels with a thickness, it becomes possible to con-

vert these volumetric elements into finite elements that can be used in the calculation. The finite element models with different mechanical definitions are positionally addressable so that analyses used in the simulations can be performed.

3D Flood Fill Algorithm

Voxelization and solidification methods are not adequate for rebuilding of the models in mechanics. It is voxelized in a volumetric environment, and the Flood

Fill algorithm is quite different from the algorithms used in the 2D solutions. Flood Fill algorithms are used in single-phase and multi-phase structures to distinguish voids and materials. By selecting a starting point within the region of interest, it is possible to start a flow in the virtual environment starting at the point of entry, spreading to all connected regions. Flood Fill algorithms eliminate parts such as unwanted unconnected components, islands, etc. from the model. The use of the three-dimensional Flood Fill algorithm is a necessity when it comes to mechanical analysis. Because the rigidity matrices of systems where there are disjoint parts exist zero-valued elements on the diagonal. 3D Flood Fill algorithms must be used for mechanical calculations especially including eigenvalue analyses.

In other words, the determination of the natural frequency and buckling load, especially in terms of eigenvalue and eigenvector, cannot be achieved by standard procedures. Other problems arise in other static, dynamic, and fluid mechanics problems.

Figure 15.10 shows the state of the 3D geometry before and after the implementation of the 3D Flood Fill algorithm. The unconnected pieces in the images are given the name “islet.” These may be due to unconnected particles of material or because the images cannot pass through filters or due to visual noises. In other words, the Flood Fill algorithm also serves as a segmentation task. It should be considered that the Flood Fill algorithm is compulsory where necessary for analysis, while other geometric calculations may be necessary. As an example, it may not be necessary to analyze aggregates for concrete with Flood Fill, but this creates a problem in volumetric calculations. On the other hand, if analysis with a trabecular bone texture is not carried out, it should be considered that the parts in the cavity should be treated by considering the noise source of the whole part. This also ensures a conservative analysis. These procedures are quite complex and require versatile experience and knowledge.

Three-dimensional Flood Fill algorithms can be formed in many different ways, but they need to be highly optimized in terms of software and that the prices of many commercial software are high. If a Flood Fill algorithm involves too many repetitive structures such as recursive calling, it

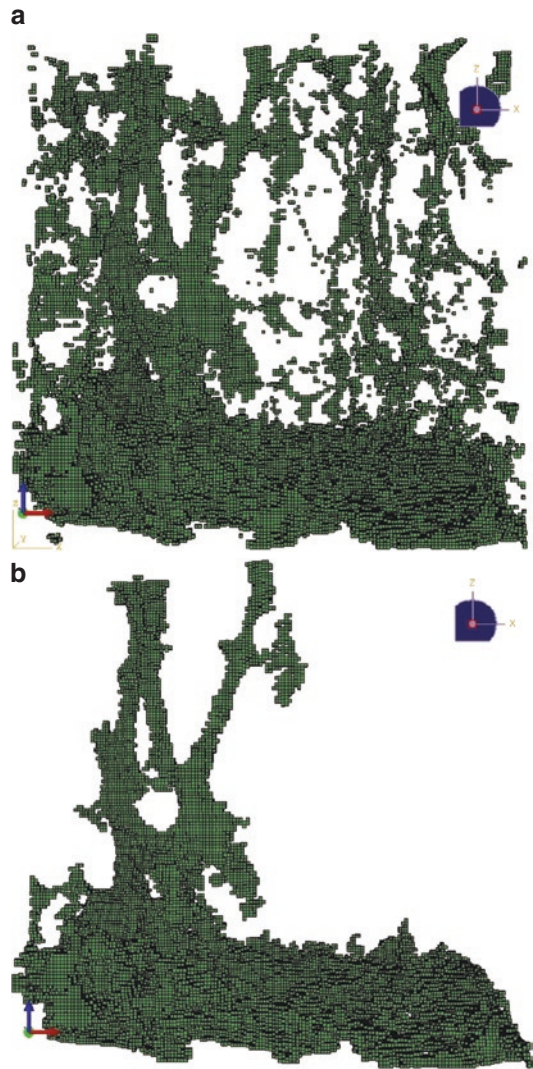


Fig. 15.10 3D Flood Fill algorithm application for cancellous bone: (a) noisy solid model with unwanted islets, (b) cancellous bone structure model after application of 3D Flood Fill algorithm [15]

can make it harder to deal with large problem types or it can result in long processing times at a time that cannot be used in practice.

The application of two-dimensional Flood Fill algorithms to flat images does not make any sense in terms of the success of three-dimensional analysis. Perhaps the two-dimensional and three-dimensional Flood Fill algorithms of very simple geometric shapes can give the same results. But the smallest complexity in the topology makes the Flood-Fill algorithms on separate planes useless.

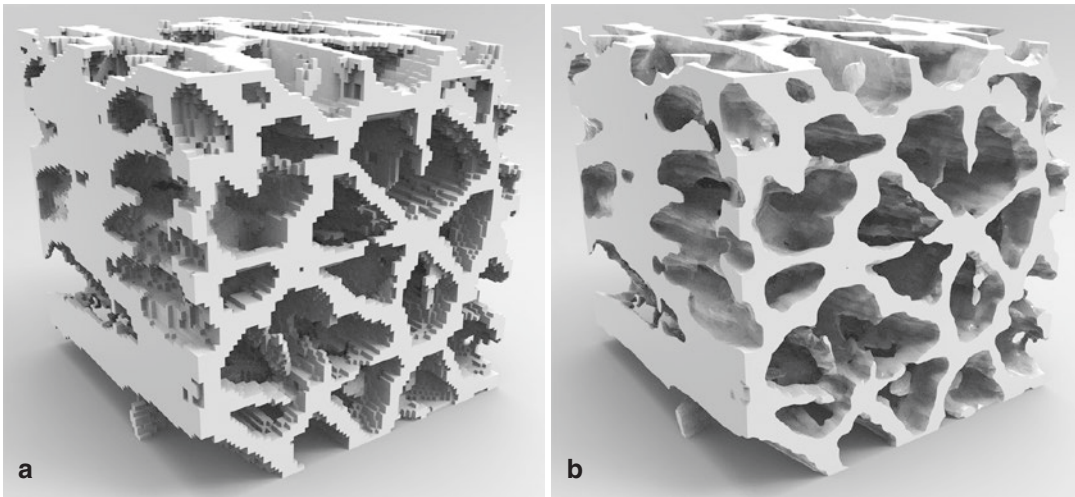


Fig. 15.11 Micro-CT-based model surfaces: (a) pure voxel-based surface, (b) smoothing algorithm applied surface

Literature contains numerous studies telling use of various algorithms for Flood Fill applications [16–21].

As a result, it should underline that the use of the 3D Flood Fill algorithm is inevitably necessary for mechanical analysis.

15.4.3 Surface Geometry

Almost all of the solid models obtained from the micro-CT data are composed of combined cubic forms because they are composed of voxels (see Fig. 15.11a). However, particularly surface details of real-life objects are not in the cubic structure of the voxels, and this can be considered as one of the convergences of the micro-CT-based models. On the other hand, it is very useful to use surface smoothing algorithms when constructing surfaces (see Fig. 15.11b).

Surface geometry has a great deal of prominence in all of the problems involving fluid mechanics and interaction. Because in fluid mechanics models where surface friction plays an important role, direct voxel-based surfaces create extreme surface friction. A similar situation exists where solid objects interact with each other. To prevent this, the parameters of surface smoothing algorithms can be adjusted by analyzing the real surface. Another important issue is the risk that

the surface smoothing algorithm can change the geometry provided by the use of the Flood Fill algorithm and should be used with caution.

15.5 Investigations and Mechanical Analyses Made with Micro-CT-Based Solid Models

15.5.1 Effects of Three-Dimensional Isotropic Resolution on Model Geometry of Trabecular Bone Tissue

As a result of the micro-CT scan performed to examine the trabecular bone tissue, a region of interest (ROI) was selected in the dimensions presented in Fig. 15.12. The selected volumetric region is sliced with 388 images with a slice thickness of 36 μm , each of which has 188×188 pixels with a 36 μm pixel edge size. In other words, in the present case, volumetric structures can be formed with voxels with dimensions 36 $\mu\text{m} \times 36 \mu\text{m} \times 36 \mu\text{m}$.

The basis of the scenario to be addressed in this section is that it is sometimes thought that users may need to artificially reduce the resolution of images due to technical inefficiencies. The main reason for this is the desire to have

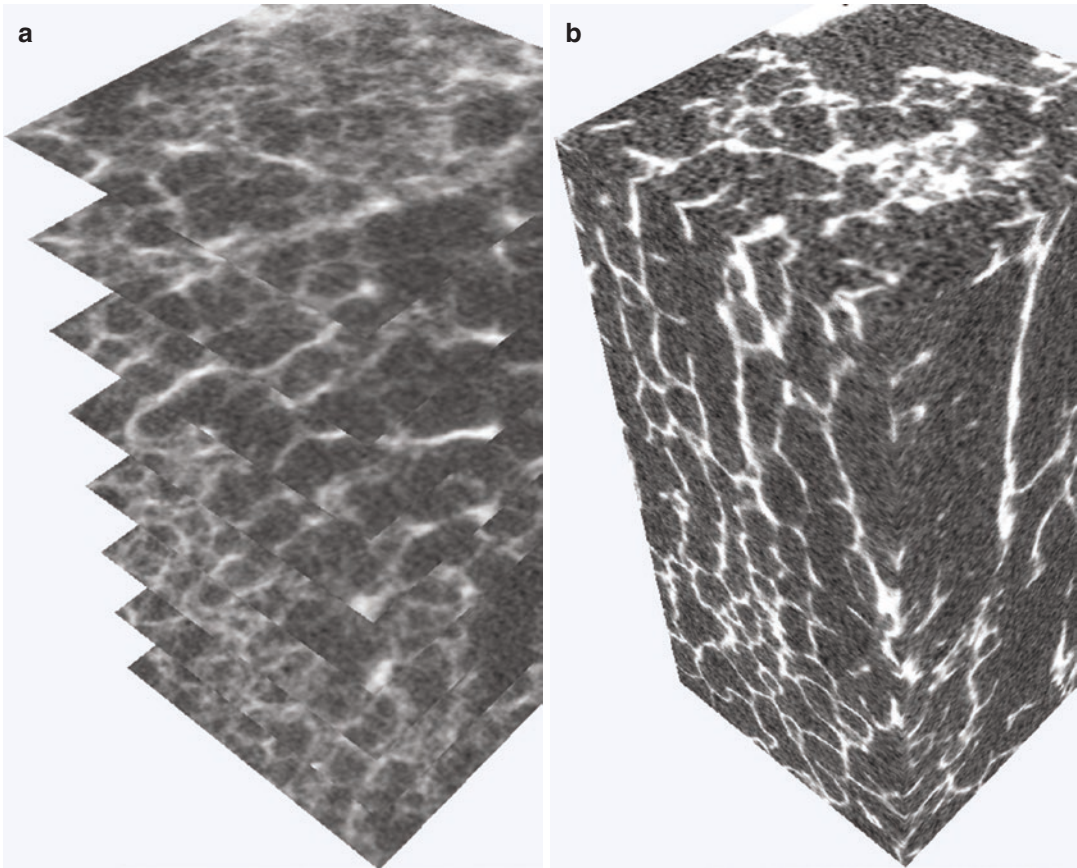


Fig. 15.12 Outputs from rotational X-ray data: (a) sequential slice, (b) voxelized model based on sequential slices

image processing and mechanical analysis time intervals at reasonable levels. However, when optimizing the timing of operations, it may be the case that model geometries and solutions go beyond acceptable levels. In order to prevent this, convergence checks should be done absolutely in modeling and analysis studies. In many software related to the subject, resolution can be done in three separate directions by means of a tool called “resample.” However, this process is simple and can be done with any image processing program. In Table 15.1, the first-line micro-CT image set was set with original slice count and resolution, and the other sets were obtained using this set. All sets were constructed so that cubic voxels could be obtained and the resolution and number of slices were reduced as presented.

Table 15.1 Micro-CT data sets [22]

	Slice thickness (μm)	Resolution	Number of slices
Micro-CT set 1	36	188×188	388
Micro-CT set 2	72	94×94	194
Micro-CT set 3	144	47×47	97

The 3D model images based on micro-CT datasets are presented in Fig. 15.13.

It is extremely difficult to predict the geometric and mechanical behavior of models with different resolutions, and it is often the case that anticipated predictions do not occur. The complexity and topological properties of the studied structure can change the expected effect

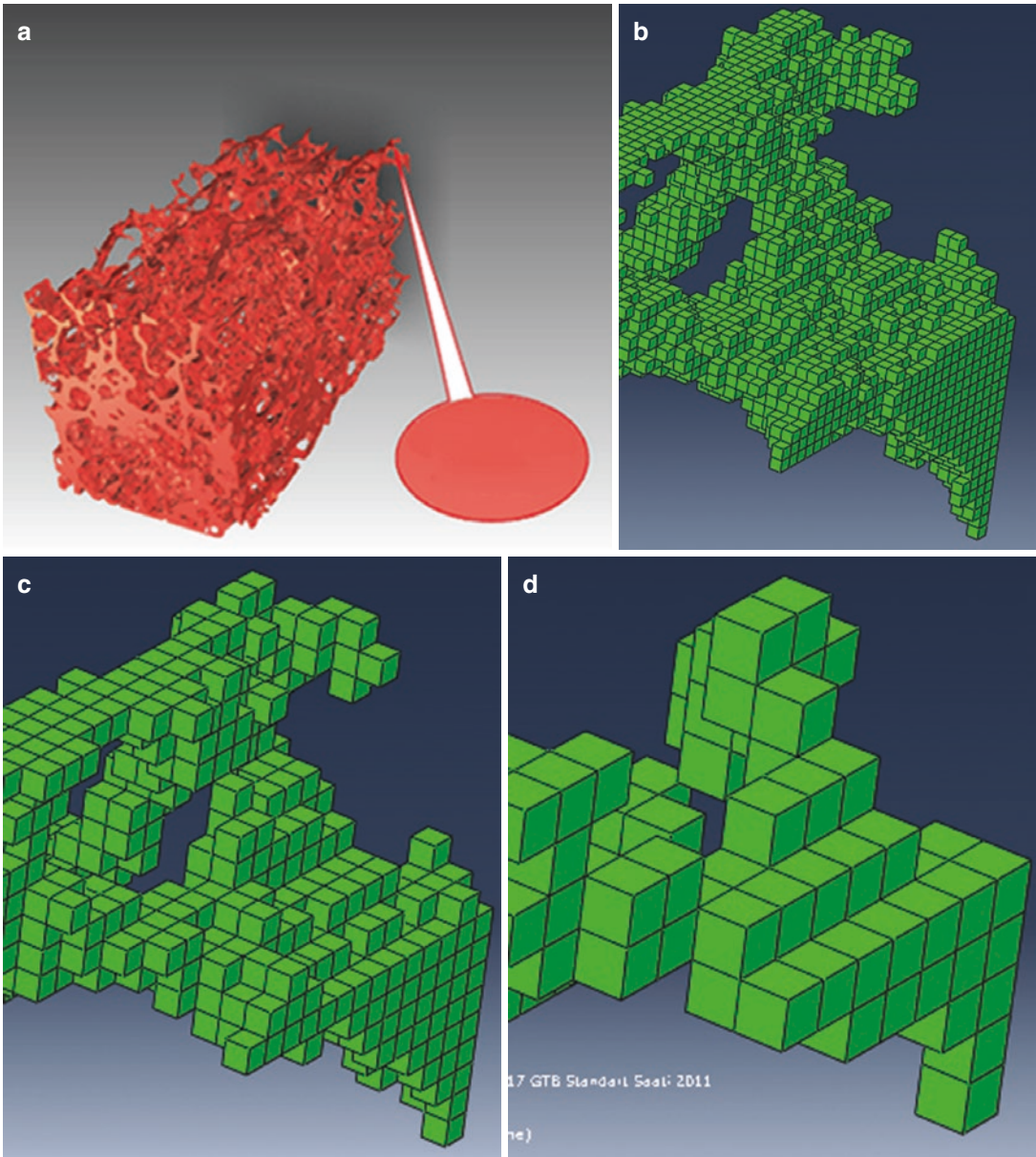


Fig. 15.13 Micro-CT-based models with different isotropic resolutions: (a) model and close view region, (b) micro-CT set 1 voxel view (36 μm), (c) micro-CT set 2 voxel view (72 μm), (d) micro-CT set 3 voxel view (144 μm) [22]

of resolution. High-resolution images, for example, reveal more detail, and it is expected that the surface area will be larger as compared to low-resolution images. It is extremely difficult to predict the geometric and mechanical behavior of models with different resolutions, and it is often the case that anticipated predictions do not occur. The complexity and topological properties of the studied structure can change the expected effect of resolution. High-resolution images, for exam-

ple, reveal more detail, and it is expected that the surface area will be larger as compared to low-resolution approaches. Due to low resolution, actual parts may not be transferred to the model. Or, conversely, regions that are never actually present can be present in the model.

Table 15.2 presents the geometric properties of the samples based on cubic voxels of different edge sizes. When the table is investigated, volumes of the models are not remarkably different from

Table 15.2 Characteristics of models for different resolutions [22]

Property name	Models for pixel edge size		
	(36 μm)	(72 μm)	(144 μm)
Volume mm^3	88.6166801	87.5669668	86.6741576
Surface area mm^2	2552.20158	2181.75903	1574.00374
Number of nodes	2,930,333	459,500	72,033
Number of elements	1,899,363	234,608	29,027

each other, but the differences between the surface areas are quite large. This can be particularly important if the modules are subjected to fluid mechanics analyses or other interaction-related mechanical analysis. Since voxels can directly be converted to finite elements, the sensitivity and solution times of the finite element analysis are highly dependent on the voxelization parameters. For this reason, the resolution of the scanned images has a direct effect on the solution time of the finite element model and the accuracy of the results. Since the number of elements in the model directly determines the dimensions of the stiffness matrices, the computer capacity required for the finite element analysis and the estimated solution time may be predicted.

15.5.2 Determination of the Relationship Between the Homogeneous and Porous Elasticity Modules of the Kula Volcanic Basalt Numbers

The study presented in this section is a part of Altıntaş's project funded by Celal Bayar University entitled "Examination of the Differences Between the Tissue Module and the Elasticity Module of Materials with High Porosity Rates" [23]. The purpose of this application is to examine the Young's modulus and strength behavior of the Kula relatively homogeneous volcanic basalts on orthogonal directions. The solution was made in the virtual environment. In simulations, the modulus of elasticity that the porosity model and accompanying homogeneous model must have for obtaining the same mechanical performance is demonstrated.

As the actual counterpart of this scenario is realized in practice, the sample is subjected to compression, and the modulus of elasticity is determined without consideration of internal

Table 15.3 Properties of finite element model [23]

Number of nodes	Number of elements	Volume (mm^3)	Surface area (mm^2)	Porosity
274,043	1,121,070	15.730	31.486	60%

architecture and void ratio. In this case, the modulus of elasticity obtained is obtained by direct homogenized modulus of elasticity. By trial-and-error method, instructing various elasticity moduli in the model obtained by micro-CT, it is expected to obtain the same displacements for a constant load in the virtual environment. The virtual experiment is terminated when the load and displacement pair valid for the homogeneous model is obtained in virtual tests of the porous sample for a certain elasticity modulus. The elastic modulus is generally referred to as the tissue module of the porous specimen. It should be noted, however, that the pressure test may cause damage in a sample such as basalt and may only be applied once, in which case real experimentation may not be possible for behavior in other directions. In this work, it is aimed that the elastic modulus of the model formed by equivalent homogeneous material is aimed to be accepted by considering that the tissue modulus of the porous material is known for better understanding of the subject. Of course, depending on the problem type, an opposite approach can be possible.

It is known that porous material has a mass density of $2.71\text{E}-11 \text{ t/mm}^3$, an elasticity modulus of 6000 N/mm^2 , and a Poisson's ratio of 0.29. The geometry is obtained from the micro-CT scan, and the mesh properties of the finite elements are as presented in Table 15.3.

In Fig. 15.14, the displacements of the micro-CT model of the sample in three individual directions in the Abaqus® environment for a 1-Newton loading are shown.

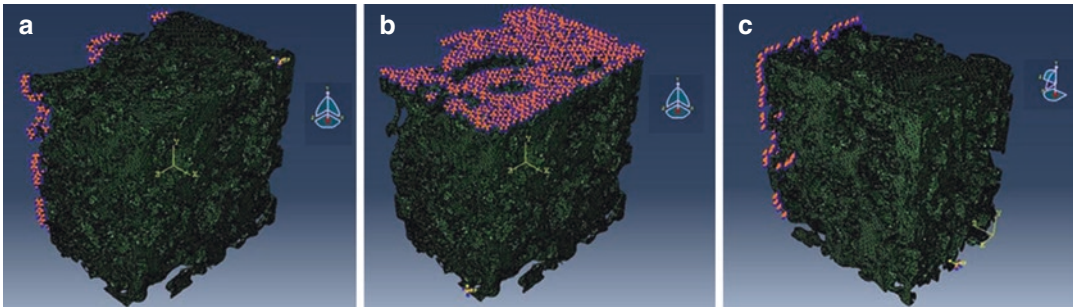


Fig. 15.14 Loading directions of porous sample in Abaqus®: (a) X direction, (b) Y direction, (c) Z direction [23]

Table 15.4 Displacement for different directions [23]

Loading direction	Displacement (mm)	Tissue modulus (N/mm ²)
X	-0.000264234	6000
Y	-0.000382555	6000
Z	-0.000384816	6000

Results were obtained for loading levels affecting within the elastic limit of material in Table 15.4. The results show that an object with a heterogeneous structure exhibited anisotropic behavior at the same time. The sample showed different displacements in all three directions for the same loading value. Based on these displacements, the modulus of elasticity to be attained has revealed the possibility of using three different elasticity moduli for the same object depending on the directions.

In this next step, the elastic modulus that the homogeneous model with the same loading, external geometric lengths, and mass has to have in order to give the same response as the porous model will be calculated.

As a result of the calculations made, the modulus of elasticity in the x direction was found to be 1295 N/mm², the modulus of elasticity in the y direction was 865 N/mm², and the modulus of elasticity in the z direction was 480 N/mm² in Table 15.5. If the results are presented in a tabular form as seen in Table 15.6, they will be clearly demonstrated in the differences between the Homogeneous Elasticity (HE) and Porous Elasticity (PE) modules.

As a result of the analyses, the values of the elasticity modules show that micro-CT-based models are anisotropic. If the compression of a very fragile material such as volcanic basalt is considered to be possible only once, then the

elasticity moduli of the studies performed using the micro-CT data can be compensated according to only one direction in which the experiment is performed.

15.5.3 Investigation of the Effect of Slice Thickness in Micro-CT Scans on Natural Frequency Values of Porous Rock Sample

The study presented in this section is a result of the Celal Bayar University Project Grant No.2011-042 [11]. The external dimensions of the sample used in this analysis are a rectangular piece with 0.4368 mm × 0.4368 mm × 2.2568 m. The material properties of this part are mass density = 2.71E-10 (t/mm³), elasticity modulus = 5988 (N/mm²), and Poisson's ratio = 0.23. Models were created for slice thicknesses of 0.0364 mm and 0.0182 mm. Where the slice thickness is the distance between the two slices mentioned, in this case slice thickness is equal to the pixel edge size. In other words, cubic voxels are used in the models. A detailed view of the created models is presented in Fig. 15.15. It should be emphasized that the effect of slice thickness at the same time is the same as the effect of volumetric resolution, since voxels are cubic.

Before mechanical analysis, it is useful to be informed of the effect of image resolutions on the volumes of the models and mesh properties of finite element models. In order to demonstrate the effect of resolutions only in the analyses, all other variables are kept constant, and the “surface smoothing” algorithm is not applied to the models.

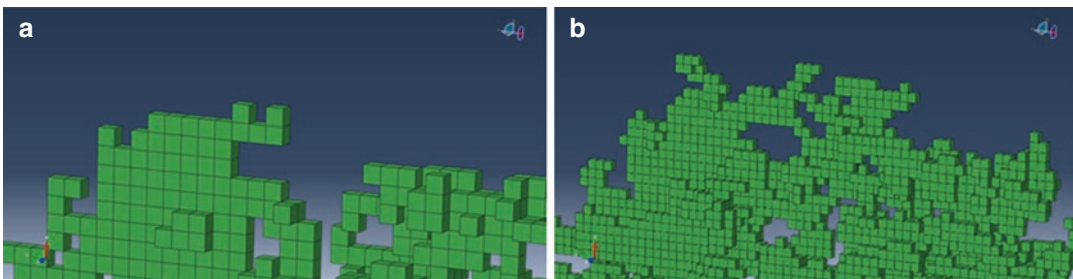
When we observe the values obtained for two different slice thicknesses in Table 15.7, it is

Table 15.5 Evaluation of bulk elasticity modulus of Kula volcanic basalt for different displacement ranges [23]

	X direction		Y direction		Z direction	
	Elasticity modulus (N/mm ²)	Displacement (mm)	Elasticity modulus (N/mm ²)	Displacement (mm)	Elasticity modulus (N/mm ²)	Displacement (mm)
Porous model	6000	0.000264234	6000	0.000382555	6000	0.000384816
Homogenized model	1500	0.000228224	1500	0.000219841	1500	0.000123502
	1250	0.000273869	1295	0.000254642	750	0.000247004
	1400	0.000244526	800	0.000412201	550	0.000336824
	1300	0.000263336	950	0.000347117	450	0.000411674
	1310	0.000261325	920	0.000359827	505	0.000366838
	1290	0.000265377	890	0.000371956	495	0.000374249
	1295	0.000264231	880	0.000376183	485	0.000381965
			870	0.000380507	480	0.000384844
		865	0.000382606			

Table 15.6 Homogenized bulk elasticity modulus for directions [23]

Loading direction	Young modulus of porous models (PE) (N/mm ²)	Young modulus of homogenized models (HE) (N/mm ²)	HE/PE
X	6000	1295	0.22
Y	6000	865	0.14
Z	6000	480	0.08

**Fig. 15.15** Close view of the same region for different voxel sizes: (a) Voxel edge length 0.0364. (b) Voxel edge length 0.0182 [11]**Table 15.7** Model properties for slice thickness [11]

Slice thickness	0.0364 mm	0.0182 mm
Number of nodes	10,216	65,690
Number of elements	5,536	40,805
Volume	0.2670 mm ³	0.2460 mm ³

understood that when the slice thickness decreases, the number of points increased about 6 times, the number of elements increased about 8 times, but the volume decreased by 0.08 times. Hence, it is apparent that the various properties are not directly proportional to the resolution. Similar results can be found in literature [9, 15, 23–26].

The voxel structures in the created models were transferred to the Abaqus® finite element

program using the “hexahedral C3D8” element type without changing the geometry and adhering to the above mechanical properties. The results of the natural frequency analysis using the finite element method are presented in Table 15.8 depending on the slice thicknesses.

Table 15.8 shows that as the slice thickness values decrease, the natural frequency values also decrease. However, as seen in Table 15.8, it is expected that natural vibration modes will appear in smaller values because the sample with large slice thickness has a large mass due to the volume. First three natural vibration mode shapes of micro-CT-based models for

Table 15.8 Natural frequency values for the first nine natural vibration modes [11]

Mode number	Slice thickness	
	0.0364 mm	0.0182 mm
1	287125 Hz	254551 Hz
2	302754 Hz	267642 Hz
3	466700 Hz	418077 Hz
4	703781 Hz	562181 Hz
5	739080 Hz	635232 Hz
6	852685 Hz	656760 Hz
7	965771 Hz	777976 Hz
8	1191280 Hz	827250 Hz
9	1194170 Hz	897004 Hz

two different slice thickness are shown in Fig. 15.16.

In such a case, it should be remembered that the volume increase may require mass increase, but it may strengthen the connections, and the stiffness enhancement may become more dominant. This is true for the example studied, and image processing parameters and modeling operations have very different effects on mechanical analysis. These effects are not only qualitative but quantitative at the same time.

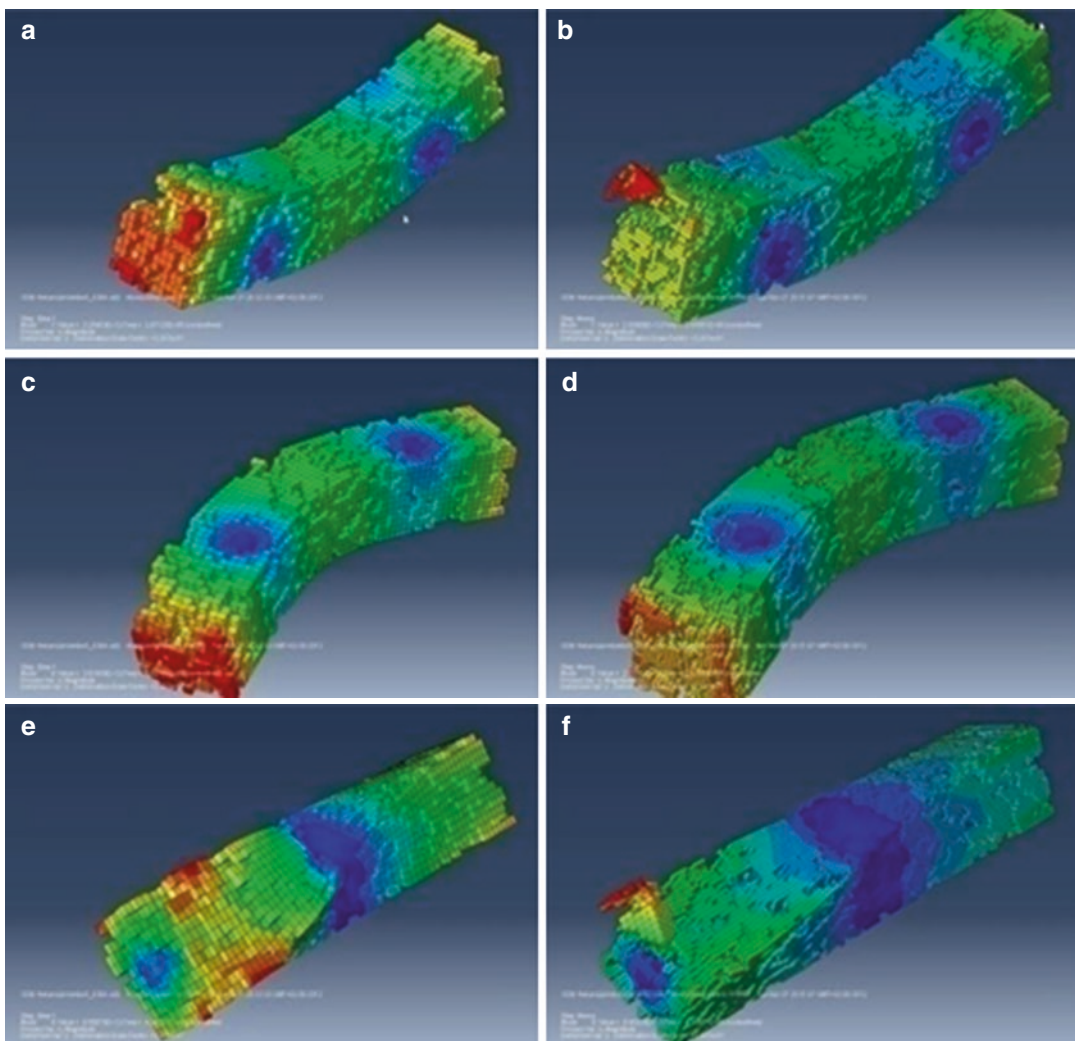


Fig. 15.16 First three natural vibration mode shapes of beam models derived for different slice thickness: (a) first mode, slice thickness is 0,0364 mm; (b) first mode, slice thickness is 0.0182 mm; (c) second mode, slice thickness

is 0.0364 mm; (d) second mode, slice thickness is 0.0182 mm; (e) third mode, slice thickness is 0.0364 mm; (f) third mode, slice thickness is 0.0182 mm [11]

15.6 Conclusion

In this chapter, production of visual and physical models by micro-CT-based models is used, for use in different research areas. Since the subject is new and can be utilized by the interacting individuals in multidisciplinary workgroups, the common language used by the people considering to work on this subject and the transfer of experience during analysis stage is of main importance.

This chapter aims to provide a complementary approach on the use of micro-BT data in visual modeling, derivation of geometric attributes and analyses to be performed. The study is considered to contribute to the perspective of the practitioner and academic staff of the concept of working with micro-CT.

Acknowledgment Projects with Grant Numbers 2011-041 and 2011-042 cited in this chapter were supported by Scientific Research Project Office of Celal Bayar University.

References

1. Tuan HS, Hutmacher DW. A comparison of micro ct with other techniques used in the characterization of scaffolds. *Biomaterials*. 2006;27:1362–76.
2. Tuan HS, Hutmacher DW. Application of micro ct and computation modeling in bone tissue engineering. *Comput Aided Des*. 2005;37:1151–61.
3. Linden JC, Waarsing JH, Weinans H. The use of micro-ct to study bone architecture dynamics noninvasively. *Drug Discov Today Technol*. 2006;3:213–9.
4. Martínez FSJ, Martín MA, Caniego FJ, Tuller M, Guber A, Pachepsky Y, Gutiérrez CG. Multifractal analysis of discretized X-ray CT images for the characterization of soil macropore structures. *Geoderma*. 2010;156:32–42.
5. Griffith JF, Genant HK. Bone mass and architecture determination: state of the art. *J Clin Endocrinol Metab*. 2008;22(5):737–64.
6. Chevalier Y, Pahr D, Allmer H, Charlebois M, Zysset P. Validation of a voxel-based FE method for prediction of the uniaxial apparent modulus of human trabecular bone using macroscopic mechanical tests and nanoindentation. *J Biomech*. 2007;40(1):3333–40.
7. Genant HK, Jiang Y. Advanced imaging assessment of bone quality. *Ann N Y Acad Sci*. 2006;1068(1):410–28.
8. Teo JCM, Si-Hoe KM, Keh JEL, Teoh SH. Relationship between CT intensity, micro-architecture and mechanical properties of porcine vertebral cancellous bone. *Clin Biomech*. 2006;21:235–44.
9. Altintas G. Effect of slice step size on prediction of natural vibration properties of bone tissue. *Math Comput Appl*. 2012;17(3):235–43.
10. Peth S, Nellesen J, Fischer G, Horn R. Non-invasive 3d analysis of local soil deformation under mechanical and hydraulic stresses by μ ct and digital image correlation. *Soil Tillage Res*. 2010;111:3–18.
11. Altintas G, Güner OB, Arslan B. Modeling of microstructures by use of reverse engineering and finite element methods for evaluation of model geometries. Project final report. Manisa Celal Bayar University Research funds grant no. 2011–042. Manisa: Celal Bayar University; 2012.
12. Freeman TA, Patel P, Parvizi J, Antoci V, Shapiro IM. Micro-CT analysis with multiple thresholds allows detection of bone formation and resorption during ultrasound-treated fracture healing. *J Orthop Res*. 2009;27(5):673–9.
13. Hara T, Tanck E, Homminga J, Huiskes R. The influence of microcomputed tomography threshold variations on the assessment of structural and mechanical trabecular bone properties. *Bone*. 2002;31:107–9.
14. Yan YB, Wei Q, Tian-Xia Q, Ee-Chon T, Wei L. The effect of threshold value on the architectural parameters and stiffness of human cancellous bone in micro CT analysis. *J Mech Med Biol*. 2012;12:1–16.
15. Altintas G. Node-id based non-recursive flood Fill algorithm for nonuniform discrete solid domains. In: Karahoca A, editor. 2nd World Conference on Information Technology; 2011 November 23–27. Antalya, Turkey: Academic World Education & Research Center. p. 46.
16. Guoying Z, Hong Z, Ning X. Flotation bubble image segmentation based on seed region boundary growing. *J Min Sci Technol*. 2011;21(2):239–42.
17. Lu Y, Miao J, Duan L, Qiao Y, Jia R. A new approach to image segmentation based on simplified region growing PCNN. *Appl Math Comput*. 2008;205:807–14.
18. Malek AA, Rahman WEZWA, Ibrahim A, Mahmud R, Yasiran SS, Jumaat A. K. region and boundary segmentation of microcalcifications using seed-based region growing and mathematical morphology. *Procedia Soc Behav Sci*. 2010;8:634–9.
19. Shih FY, Cheng S. Automatic seeded region growing for color image segmentation. *Image Vis Comput*. 2005;23(10):877–86.
20. Wu Y, Li M, Zhang P, Zong H, Xiao P, Liu C. Unsupervised multi-class segmentation of SAR images using triplet Markov fields models based on edge penalty. *Pattern Recogn Lett*. 2011;32(11):1532–40.
21. Žalik B, Kolingerova I. A cell-based point-in-polygon algorithm suitable for large sets of points. *Comput Geosci*. 2001;27:1135–45.
22. Altintas G, Ergut A, Goktepe AB. Effect of 3d isotropic resolutions of sequenced images on natural vibration properties of trabecular bone. *Sci Iran B*. 2013;20:492–9.
23. Altintas G, Gücüyün E, Arslan B. Investigation of differences among modulus of bulk elasticity and tissue

- modulus of highly porous materials. Project final report. Manisa Celal Bayar University Research funds grant no. 2011-041. Manisa: Celal Bayar University; 2013.
24. Altıntaş G. Natural vibration behaviors of heterogeneous porous materials in micro scale. *J Vib Control*. 2014;20(13):1-7.
 25. Altıntaş G. Effect of slice thickness variation on free vibration properties of micro-CT based trabecular bone models. In: 2nd International Symposium on Computing in Science & Engineering, Kuşadası, 2011, June 1-4.
 26. Altıntaş G, Erdem RT. Effect of micro-ct slice intensity on natural vibration behavior of cancellous bone models based on reverse engineering techniques. *Procedia Tech*. 2012;1:318-22.



The use of Micro-CT in Materials Science and Aerospace Engineering

16

Sinan Fidan

16.1 Introduction

In materials science, understanding the key factors affecting material micro- and macrostructure during production or service conditions is vital. In order to evaluate the structure of the material and flaws generated during production or service life, the nondestructive testing (NDT) methods such as ultrasound, radiographic, or eddy current play an important role. Especially in aviation and aerospace industry, inspection of the high-risk parts has a crucial role. Using these conventional NDT, techniques give valuable information about the material. However, using those methods on a regular basis calls for a qualitative characterization of the efficiency and an assessment of the suitability of those systems with regard to the respective application [1]. X-ray tomography method has been used as an alternative [2]. Laboratory-based micro-computed tomography (micro-CT) machines using X-rays are readily available and provide resolutions in the order of a micrometer or less [2].

Manufacturing critical items in mechanical engineering (car and aircraft engines, cooled turbine buckets, rocket engines, etc.) is virtually impossible without highly informative technical diagnostics and nondestructive quality testing tools. X-ray com-

putational tomography (XCT) systems have been developed and are fabricated for these purposes. These systems can qualitatively study the internal spatial structure of items of any complexity [3].

Micro-CT is also an attractive tool for bulk material microstructure characterization. When sample mounted on a rotating stage between X-ray beam source and the detector is rotated through 180° (for synchrotron tomography) or 360° (for laboratory tomography), a set of radiographies are recorded and are then used to reconstruct the 3D image, in which the gray levels reflect the microstructure constituents in the bulk of sample [4]. X-ray computed tomography has already been used in the field of experimental mechanics for the in situ characterizations of damage evolutions in the bulk of specimen [4].

16.2 Basic Components of Micro-Computed Tomography

Tomography started with the theoretical justification of the possibility of reconstructing the distribution of a certain parameter across a planar section of an object from its projections [3]. This method was first put into practice in the 1970s [3]. In 1979, the Nobel Prize in medicine was awarded to Godfrey Newbold Hounsfield and Allan McLeod Cormack for the development of computational tomography [3]. Originally, XCT found applications in medicine, and later, in various other domains of science and technology [3].

S. Fidan (✉)

Faculty of Aeronautics and Astronautics, Airframe and Powerplant Maintenance Department, Kocaeli University, İzmit, Kocaeli, Turkey
e-mail: sfidan@kocaeli.edu.tr

A generalized structure of any X-ray computational tomography consists of the following elements [3]:

- An X-ray source(s)
- A radiometric sensor or a one- or two-dimensional array of radiometric sensors
- A scanning system for varying the mutual spatial configuration of the radiation source, radiometric sensors, and an object that is tested
- Software for controlling the tomography; gathering raw radiometric information (the projections) and transforming it into tomographic images, viz., two- or three-dimensional distributions of the parameter in question (density, effective atomic number, and so on) across a certain section or over the entire volume of an object that is tested; and visualizing tomographic images

In CT scanning, X- or γ -rays are emitted from a source and pass through the sample to a detector. The intensity of the radiation signal on the detector is dependent on the linear attenuation

characteristics of the sample material and the distance from the source to the detector. This variation in attenuation through a sample is defined as its profile, and this can be reconstructed to form a single “slice” through the sample material. In CT many such slices are taken at different orientations around the subject [5].

Although various experimental setups can be used to perform X-ray tomography, the basic principles of the technique remain the same (see Fig. 16.1): an X-ray beam is sent on a sample mounted on a rotator; a series of N radiographs (the series is called a scan) corresponding to N angular positions of the sample in the beam is recorded on a detector which is generally a CCD in modern tomographs [6].

In some cases, a three-dimensional numerical image processing and analysis is performed by researchers in order to obtain a more detailed reconstructed 3D model of the sample. The common main steps of 3D digital image processing and analysis can be seen in Fig. 16.2 [4].

Fig. 16.1 Schematic illustration of the principle of X-ray attenuation tomography: an X-ray beam coming from a laboratory or synchrotron source impinges on a sample set on a rotation motor. For a given angular position of the sample, a radiograph of the sample is recorded. A series of N radiographs (called a scan) is recorded and used by a reconstruction software to produce a 3D map of the linear X-ray attenuation coefficient μ within the studied sample [6]

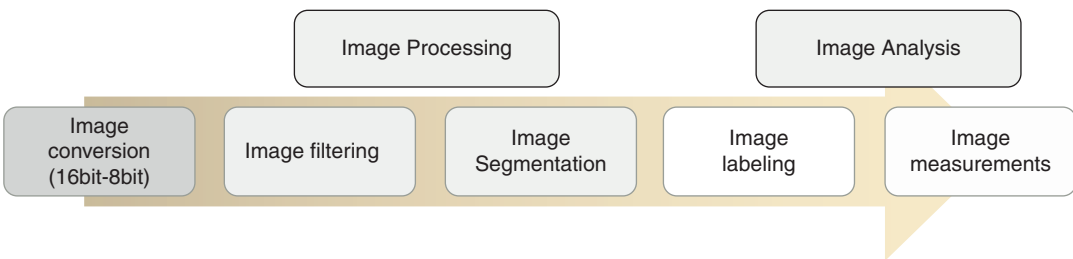
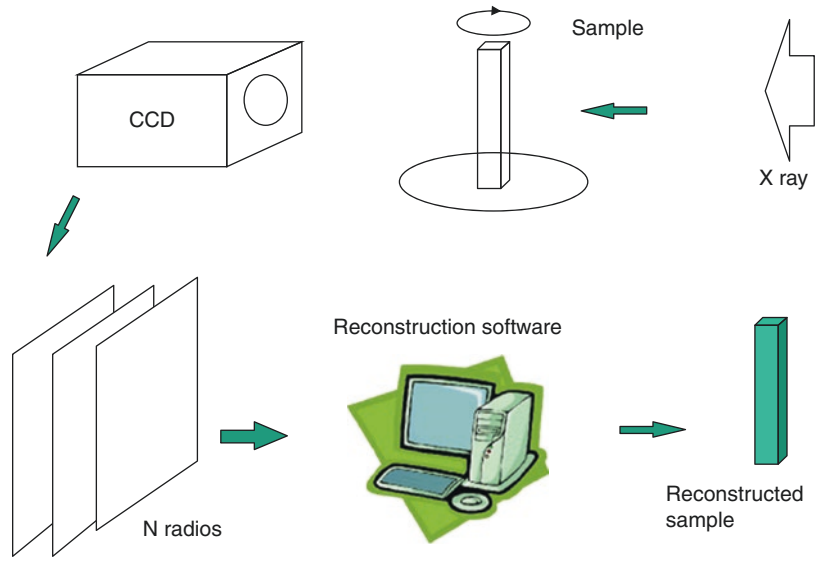


Fig. 16.2 The main steps of 3D digital image processing and analysis [4]

16.3 Materials Science Damage Evaluation with Micro-CT

Obtaining high-resolution images of internal and external structures of materials is possible by using micro-CT, and 3D models can be created nondestructively. The flexible scanning methodology of micro-CT is an advantage when characterizing the target samples' density, thickness, internal microscale construction, surface, or material type. The scanning time varies depending on the density, X-ray transmittance, resolution, and size of the materials. After micro-CT scanning process, the reconstructed 3D models can be obtained by using special software codes. 3D models obtained from reconstructed 2D micro-CT images of samples make it possible to visualize real structure of the materials. Moreover, slicing 3D model from any point for analyzing and characterization can be achieved with ease. By this way, accurate measurements of internal defects such as voids, cracks, delaminations, and laminar defects can be done. In this section, various literature works in the field of materials science which uses micro-CT as an analyzing and characterization tool will be given.

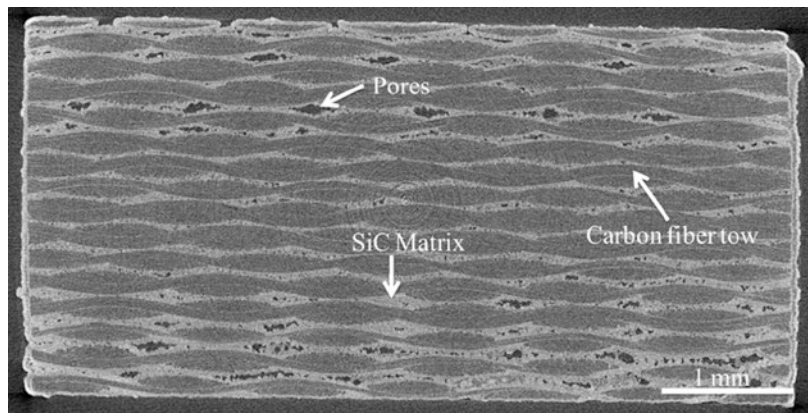
Wang and others [4] study the influence of pores on damage mechanisms in C/SiC composites by using in situ observations with X-ray computed tomography and the three-dimensional characterizations of pores and damages by using X-ray computed tomography. They scanned undamaged samples by using a Phoenix x|Nanotom m X-ray nano CT system in Key Laboratory for Advanced Materials Processing

Technology, Ministry of Education (Tsinghua University, Beijing, China) with a voxel size of $2.5\ \mu\text{m}$ for the purpose of characterizations of pores as well as the microstructures in the bulk of material [4]. A length of 5.8 mm in the beam specimen was scanned with the current resolution, and a cube volume of $3\ \text{mm} \times 6\ \text{mm} \times 5.8\ \text{mm}$ was obtained for material characterizations [4] (Fig. 16.3).

They used an YXLON microfocus computed tomography in State Key Laboratory of Nonlinear Mechanics (Institute of Mechanics, Chinese Academy of Sciences, Beijing, China) with a voxel size of $5.0\ \mu\text{m}$ in order to characterize the damages in the bulk of specimen [4]. A length of 10.72 mm in the damaged beam specimen was scanned with the current resolution, and it allows the final fracture area and its neighborhood areas being characterized [4].

For damaged specimens, the morphologies of fiber tow, SiC matrix, and pore in different orthogonal directions are shown in Fig. 16.4a [4]. Fiber tows present totally different morphologies in the laminate plain and in the plains perpendicular to the laminate as a result of material design and fabrication process. In order to visualize the 3D morphology of pores and their relations with fiber tow and SiC matrix, the pores and SiC matrix in a cube with a side length of 0.75 mm inside the specimen are extracted and are shown in 3D rendering in Fig. 16.4b–d. Even in a small cube, the pores presenting individual morphology in the 2D plain (Fig. 16.3) present a connected morphology in Fig. 16.4b: the pores located in the different laminates can

Fig. 16.3 Tomography slice in two-dimensional plain woven C/SiC composite fabricated by CVI process (undamaged specimen). The slice is perpendicular to the laminate plain [4]



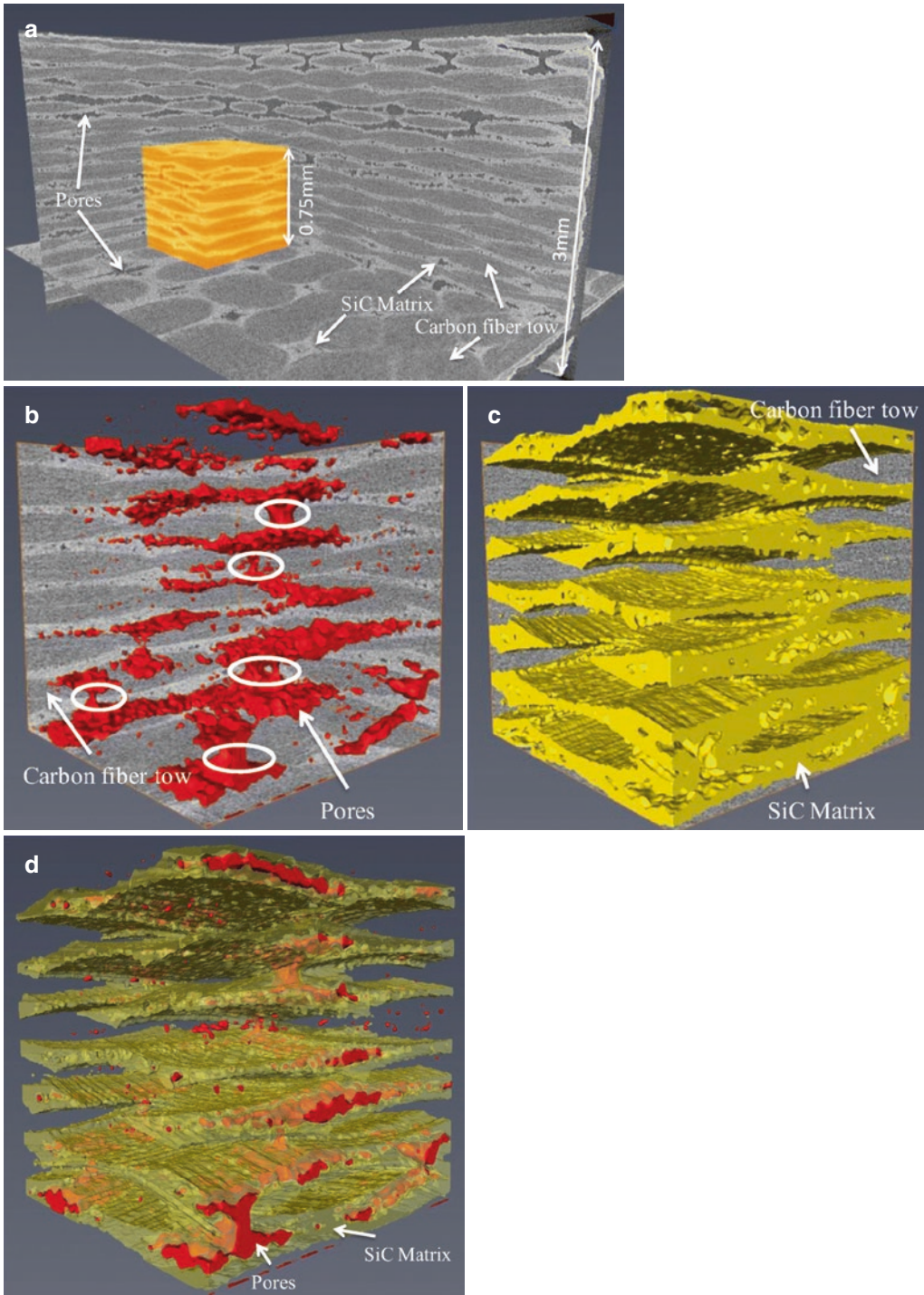


Fig. 16.4 (a) Orthogonal slice view inside the undamaged C/SiC specimen shows the morphologies of fiber tow, SiC matrix, and pores in different orthogonal directions. A cube with a side length of 0.75 mm inside the specimen is shown in 3D volume rendering. Pores and SiC matrix in this cube are segmented separately and are

shown in 3D rendering: (b) pores are shown in red solid with orthogonal slices; (c) SiC matrices are shown in yellow solid with orthogonal slices; (d) pores are shown in red solid with SiC matrix shown in yellow translucence, while fiber tows are concealed [4]

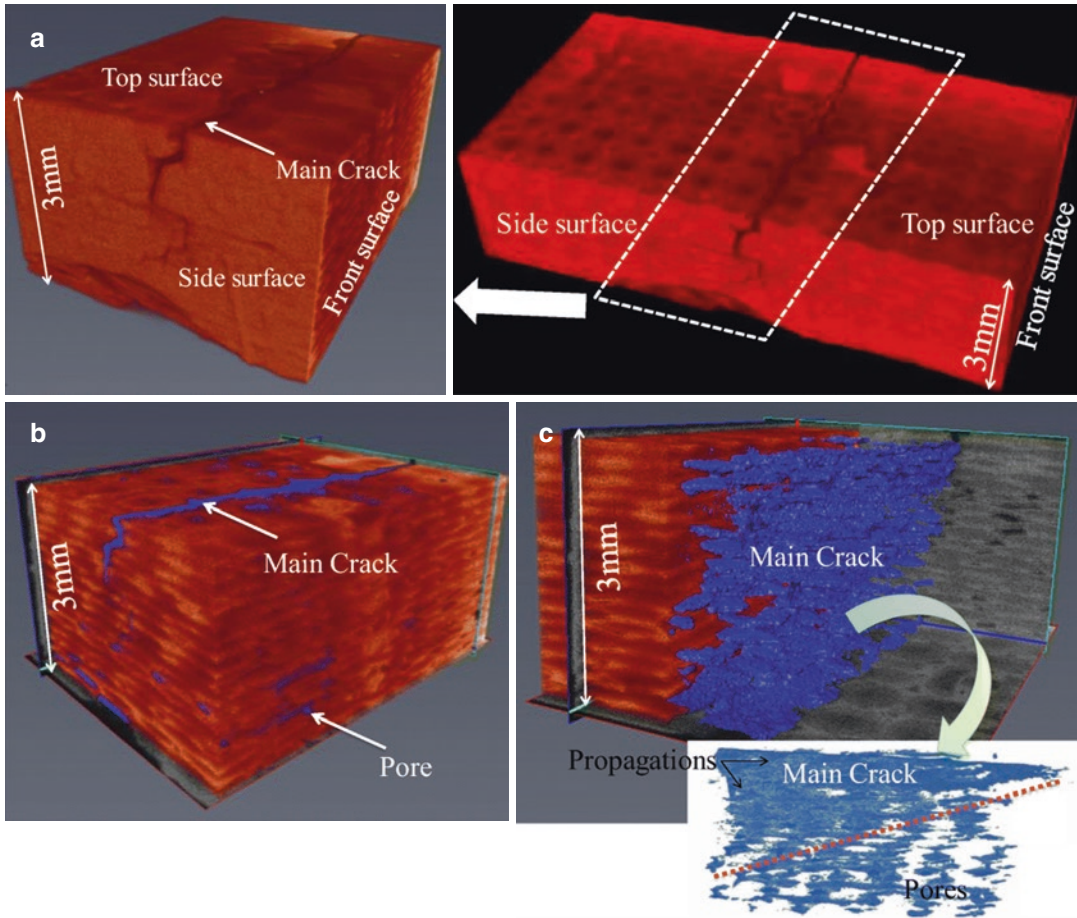


Fig. 16.5 (a) 3D volume rendering of the damaged specimen in the final fracture area (left) and in the whole scanned volume (right); (b) 3D rendering of main crack and pores in blue solid with 3D volume rendering of the damaged specimen; (c) half of the 3D volume rendering

of the damaged specimen in (b) is concealed in order to show the 3D morphology of main crack, while the main crack and its neighbor pores in the fracture plain are shown in 3D rendering in the right bottom [4]

also connect with each other, and some examples are marked with circles. The SiC matrices present plain-like morphology, and they connect a lot between different laminates as shown in Fig. 16.4c. If the 3D renderings of pores and SiC matrix are shown in the same time in Fig. 16.4d, it is found that almost all pores are surrounded by SiC matrix except to some dispersed quite small pores which may be real small pores located inside the fiber tows or be due to image noises.

The damaged specimen fractured after high-temperature three-point bending fatigue test was used for the characterization of pores in the material [4]. The 3D volume rendering of the dam-

aged specimen and the 3D rendering of segmented cracks and pores are shown in Fig. 16.5. The main crack is perpendicular to the top surface and passes through many laminates. They concluded that X-ray computed tomography is found to be very effective to characterize the pores and damages in the studied material [4].

Matsuda and others [7] used X-ray computed tomography (CT) for nondestructive observation of machined surface and subsurface structure of hinoki (*Chamaecyparis obtusa*) produced in slow-speed orthogonal cutting. The cutting experiments were conducted under several cutting conditions, and the chip formations were observed with a high-

speed camera to be classified into four chip types [7]. After the cutting experiments, the machined surface and subsurface structure of all workpieces were scanned by a microfocus X-ray CT system (SMX-160CT-SV3S, SHIMADZU) [7]. Two scanning conditions (a) and (b) were applied for the scanning. For scanning condition (a), the size of the field of view was 6.2 mm in both R and T directions and 5.8 mm in L direction, and the voxel size of the tomogram was 12 μm . The width of the field of view in R direction was wider than the thickness of the workpiece, although the detailed appearance of cells could not be observed. On the other hand, for scanning condition (b), field of view was 1.4 mm in all three directions, and the voxel size was 2.7 μm . The lumens of the cells could be observed in this condition, although the field of view was limited. For both scanning conditions, the length of the field of view in L direction was not long enough to scan the entire machined surface, so that a part of the whole machined surface was scanned and investigated [7].

Figure 16.6 shows the CT images of one of the machined workpieces produced in type 0 chip formation [7]. The cutting angle employed was 30°, and the depth of cut employed was 0.1 mm for this workpiece. The intensity of a pixel in a CT image represents the density level of the pixel; the brighter the pixel is, the higher the density of the pixel is. Figure 16.6a shows a 3D rectangular prism image of a part of the workpiece. RL plane indicates the machined surface, while LT plane indicates the side surface of the workpiece. RT plane indicates a cross-sectional view, which is vertical to the cutting direction, of the workpiece. Figure 16.6b, c shows the cross-sectional views of the rectangular prism. Figure 16.6b was scanned by scanning condition (a), while Fig. 16.6c was scanned by scanning condition (b). The surfaces parallel to R direction in Fig. 16.6b, c are the machined surface. The two bright stripe-like zones running vertically from the machined surface in Fig. 16.6b are the latewood of the annual rings. The cells on the machined surface were cut

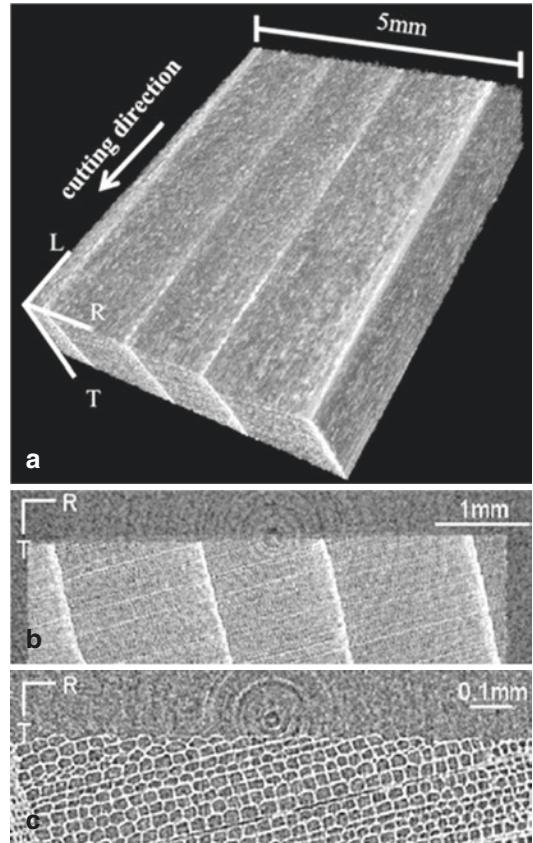


Fig. 16.6 CT images of the machined workpiece obtained by type 0 chip formation. Cutting angle was 30° and depth of cut was 0.1 mm. (a) 3D view of the workpiece. (b, c) cross-sectional view (RT plane) of the workpiece [7]

almost exactly at the path of the cutting edge, as shown in Fig. 16.6b. Most of the cells on and beneath the machined surface seemed to be neither compressed nor deformed, as shown in Fig. 16.6c. In addition, it was confirmed that the cut was mostly done along the intercellular layer. The characteristics of the surface and subsurface structure of type 0 observed with X-ray CT correspond to the fact that no deformation of the workpiece was observed in the video clip of type 0 [7]. They concluded that, using the X-ray CT system, it was possible to observe the quality of machined surface and the subsurface failures nondestructively [7]. The method used in this study may become a new method for evaluating the wood machinability [7].

16.4 The use of Micro-CT in Aerospace Engineering

In aerospace engineering, the use of micro-CT is mainly focused on special composites or structural materials manufactured for aero-vehicles. Hence, some examples related with aerospace materials will be given in this section.

Dietrich and others [8] introduced a new test and evaluation method for subsurface core damage in the indentation area of honeycomb sandwich structures using computed tomography. The combination of X-ray micro-computed tomography (X- μ CT) and an image analysis procedure adjusted to the detection of core deformation mechanisms allows the extraction and quantification of externally invisible, subsurface damage in the sandwich composite [8].

They at first cut the sandwich plates into circular samples using a diamond-tipped hole-cutting drill bit with a diameter of 100 mm [8]. Subsequently the samples are mounted into the in situ fixture to be fed into the measuring loop. A first X- μ CT measurement is carried out without loading the sample to capture the intact state of the sample. In the first loading step, the in situ device is placed on a Zwick universal testing machine with a 2.5 kN load cell and an inductive displacement transducer to apply the predefined indentation. During the indentation movement, the load and displacement history is recorded. As last step before the next X- μ CT measurement, the

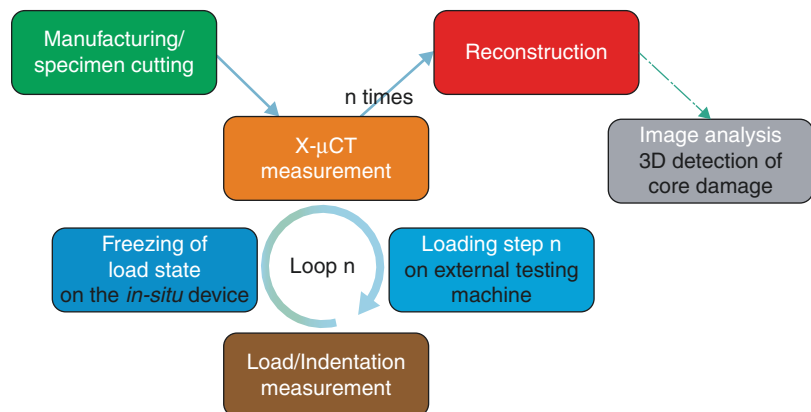
load state is frozen by a clamping fixture holding the indenter into position during X- μ CT data acquisition. For each X- μ CT measurement, a subsequent chain of reconstruction and image analysis is carried out in parallel and provides the final results for the failure behavior of the sandwich samples. The three main steps are depicted in Fig. 16.7 [8].

They obtained projections (see Fig. 16.8) have been reconstructed to generate the 3D volume data (voxel data) representing the linear attenuation coefficient of the samples microstructure.

They concluded that an innovative experimental and analysis procedure to investigate the compression collapse of honeycomb cores in sandwich structures under indentation loading was achieved [8]. This procedure is carried out during X- μ CT scanning, while the indentation load is applied to the sample [8].

Brault and others [9] carried out an experimental investigation technique to perform volume kinematic measurements in composite materials. The association of X-ray micro-computed tomography acquisitions and Digital Volume Correlation (DVC) technique allows the measurement of displacements and deformations in the whole volume of composite specimen [9]. To elaborate the latter, composite fibers and epoxy resin are associated with metallic particles to create contrast during X-ray acquisition [9]. A specific in situ loading device is presented for three-point bending tests, which enables the visu-

Fig. 16.7 Step sequence of indentation loading and X- μ CT measurements leading to a 3D evaluation of the core damage development in a block diagram [8]



alization of transverse shear effects in composite structures [9].

Two main experimental techniques are used in this study: X-ray micro-computed tomography (X- μ CT) and Digital Volume Correlation (DVC) [9]. The next paragraph details each technique and presents a review in the composite materials context, through the description of four steps of the experimental protocol, presented in Fig. 16.9 [9].

The first step concerns all the workout of the X- μ CT device, i.e., the composite specimen manufacturing, with the inclusion of particles and the mounting of the experimental loading device with the initialization of all sensors [9]. This step must be performed in accordance with needs of X- μ CT and DVC techniques [9].

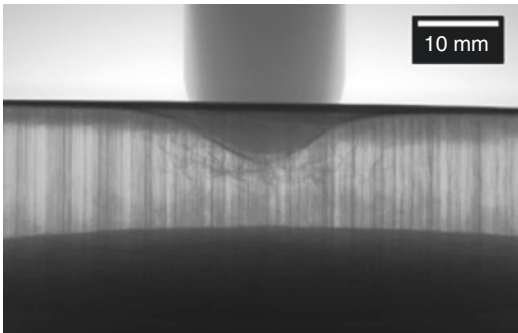


Fig. 16.8 Radiograph of a sandwich specimen in the in-situ apparatus with 6 mm penetration depth of the hemispherical PMMA indenter [8]

Second step concerns volume data acquisitions: several load states are imposed, and volume images must be recorded for each one [9]. In the present work, volume images are generated by a laboratory tomography device (Viscom X8050) [9]. Used acquisition parameters are a tension of 100 kV and an intensity of 833 μ A [9]. Specimen is positioned on a rotation stage, and 360 projections of transmitted X-ray intensity field are recorded at each angular step of 1° by a CCD camera through an X-ray detector (Fig. 16.10). Each projection is obtained by averaging four images recorded at the same angular position.

Third step is the tomographic volume reconstruction [9]. A volume image of the variations of the linear attenuation coefficient in the specimen is reconstructed [9]. The distribution of gray levels in 3D images is due to local differences of density and so corresponds to a 3D representation of the microstructure of the studied specimen (Fig. 16.11).

They concluded that obtained results allow validating the use of copper particles to achieve displacement and strain computation by X- μ CT and DVC techniques in composite materials, with a good uncertainty of 0.04 voxel [9]. DVC gives a good evaluation of the mechanical response of the composite specimen under the bending load, which is illustrated with consistency for longitudinal displacements, bending displacements, and shear strain [9].

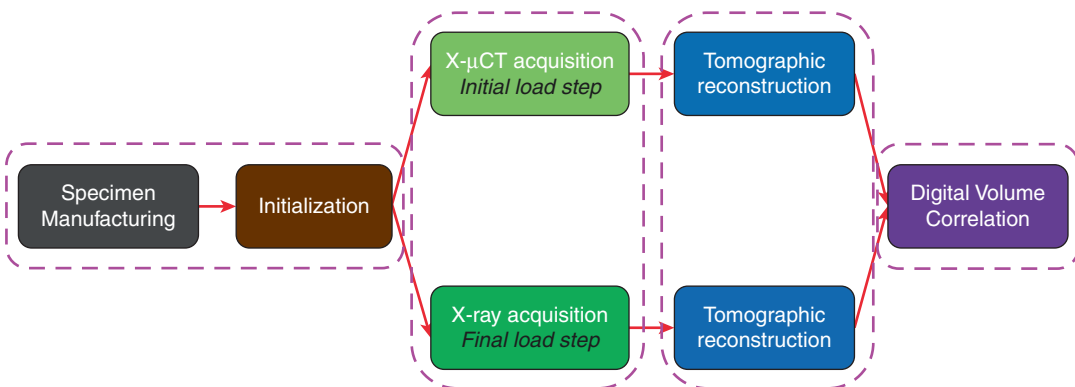


Fig. 16.9 Experimental procedure for composite materials volume measurements [9]

Fig. 16.10 X- μ CT in-situ loading device [9]

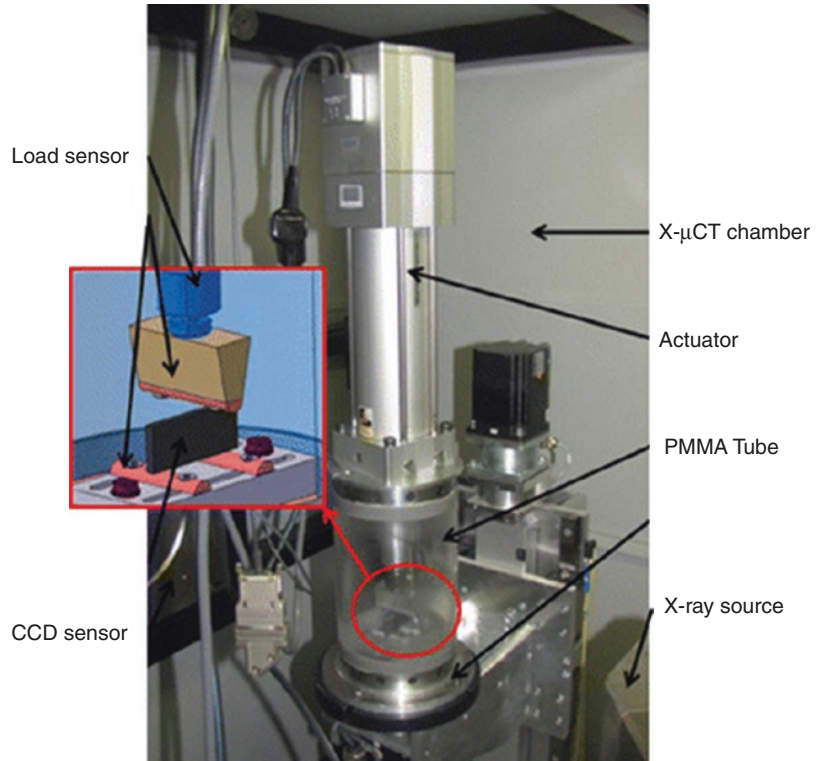
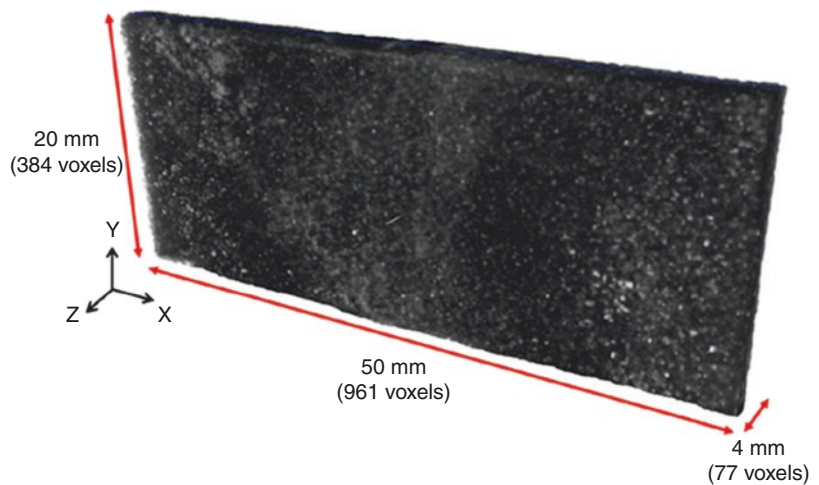


Fig. 16.11 Example of composite specimen tomographic volume [9]



16.5 Summary and Conclusions

Micro-CT is a nondestructive technique that can analyze the internal damages in materials and produce accurate 3D structure by reconstruction of sectional images. The 3D visualization of internal structures with a detailed damage model gives

valuable information. By using these 3D tomography images, the novel material investigations and manufacture processes can be achievable. Characterization of micro-architecture gives valuable information about materials strength, fatigue life, damage response, etc. The potential of the micro-CT technique is twofold [6]. First it is a

direct 3D imaging method, and second it is nondestructive which allows in situ experiments to be performed [6]. For a simple 3D characterization of the microstructure, laboratory tomography is likely to become *the* main technique as laboratory tomography can be found more and more frequently in laboratories as a standard equipment and also because long scanning times (if high resolution is required) are generally not an issue [6]. Synchrotron sources will remain necessary whenever phase contrast is required such as in the case of low-attenuating materials (polymers) or materials containing heterogeneities with similar attenuation coefficients (e.g., Al/Si alloys) or to improve the detection of cracks [6].

As a result, micro-CT will be one of the crucial methods in materials science investigations especially in aerospace and aviation industry materials.

Acknowledgments The author acknowledges Prof. Dr. Kaan Orhan for his valuable contribution and guidance. A special thanks also goes to Mr. Asım Horasan from Teknogem for his contribution in the creation of such a book.

References

1. Amrhein S, Rauer M, Kaloudis M. Characterization of computer tomography scanners using the probability of detection method. *J Nondestruct Eval.* 2014;33(4):643–50.
2. Penumadu D, Kim F, Bunn J. Damage of composite materials subjected to projectile penetration using high resolution X-ray micro computed tomography. *Exp Mech.* 2016;56(4):607–16.
3. Chakhlov SV, Osipov SP, Temnik AK, Udod VA. The current state and prospects of X-ray computational tomography. *Russ J Nondestruct Test.* 2016;52(4):235–44. <https://doi.org/10.1134/S1061830916040033>.
4. Wang L, Yuan K, Luan X, Li Z, Feng G, Wu J. 3D Characterizations of pores and damages in C/SiC composites by using X-ray computed tomography; 2018.
5. Lipscomb IP, Weaver PM, Swingler J, McBride JW. Micro-computer tomography-an aid in the investigation of structural changes in lead zirconate titanate ceramics after temperature-humidity bias testing. *J Electroceram.* 2009;23(1):72–5.
6. Buffiere JY, Maire E, Adrien J, Masse JP, Boller E. In situ experiments with X ray tomography: an attractive tool for experimental mechanics. *Proc Soc Exp Mech Inc.* 2010;67:289–305.
7. Matsuda Y, Fujiwara Y, Fujii Y. Observation of machined surface and subsurface structure of hinoki (*Chamaecyparis obtusa*) produced in slow-speed orthogonal cutting using X-ray computed tomography. *J Wood Sci.* 2015;61(2):128–35.
8. Dietrich S, Koch M, Elsner P, Weidenmann K. Measurement of sub-surface core damage in sandwich structures using in-situ hertzian indentation during X-ray computed tomography. *Exp Mech.* 2014;54(8):1385–93.
9. Brault R, Germaneau A, Dupré JC, Doumalin P, Mistou S, Fazzini M. In-situ analysis of laminated composite materials by X-ray micro-computed tomography and digital volume correlation. *Exp Mech.* 2013;53(7):1143–51.



X-Ray Computed Tomography Technique in Civil Engineering

17

Savaş Erdem and Serap Hanbay

17.1 Introduction to X-Ray Computed Technique

X-ray computed tomography technique is based on radiation released from a source to a material. The material rotates around an axis through 360° revolution, and 2D images are produced at this stage. The principal of the CT system used in one study was shown in Fig. 17.1 [1]. Also, 2D images can be used to create 3D images to make more detailed analysis. Microstructure of a material is analyzed to observe some mechanical parameters which affect the behavior of the materials like the volume of air voids or the distribution of additional materials in such materials. The main advantage of the method is being a nondestructive method and availability to apply the laboratorial experiments.

This method is widespread in several sectors and research fields such as health sector, industry, and engineering specifically mechanical and civil engineering. In this chapter of the book, the application of X-ray computed tomography (CT) in civil engineering will be scrutinized mainly,

and other parts of the use of CT will be excluded. In civil engineering, there is an increased interest to study the microstructure of concrete, asphalt and soil mixtures with and without fibers. Apart from this, that method is also useful for rail head checks and observing fatigue cracks by 3D visualization of defects [2, 3].

17.2 CT Technique in Concrete

Concrete is obviously one of the major construction materials in civil engineering today due to the ability of molding and having high compressive strength with relatively low cost. Concrete is composed of cement, water, and a mixture of fine and coarse aggregate including gravel, sand, crushed rock, etc. Moreover, many new materials such as fibers in macro, micro or nano-level have been included in the mixture to enhance the mechanical properties of concrete.

The components of concrete, especially the variety of aggregates and additional materials like fibers, entail the analysis of microstructure of concrete whether the level of porous structure of concrete exceeds the limits given in standards or not. Even though in the case of adding some external materials into concrete mixture porosity analysis is inevitable, in other cases determination of air voids is also significant.

Porosity analysis of concrete by the help of computed tomography technique is highly common

S. Erdem (✉)
Civil Engineering Department, Istanbul
University-Cerrahpasa, Istanbul, Turkey
e-mail: savas.erdem@istanbul.edu.tr

S. Hanbay
Civil Engineering Department, Alınbaşı University,
Istanbul, Turkey

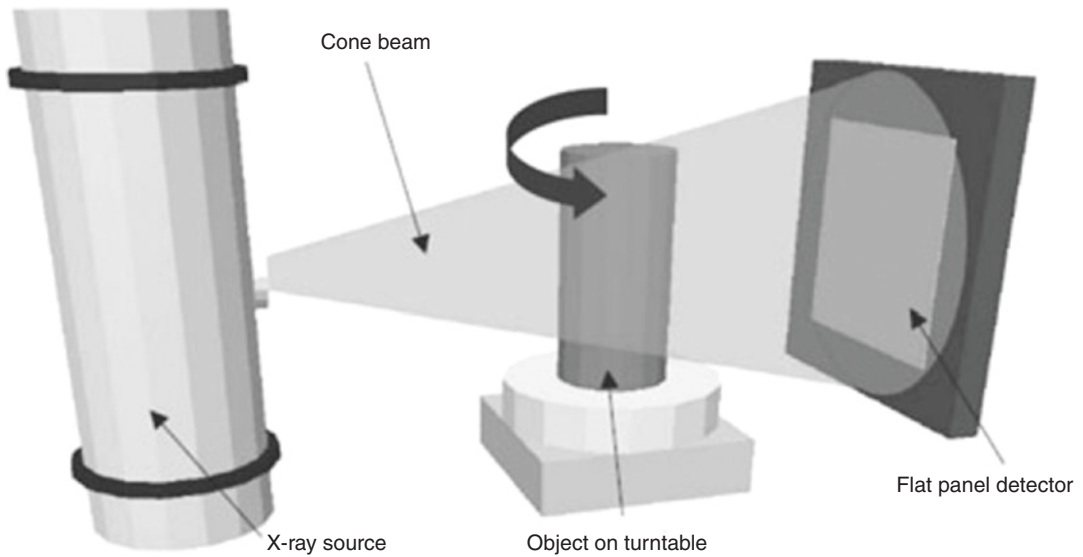
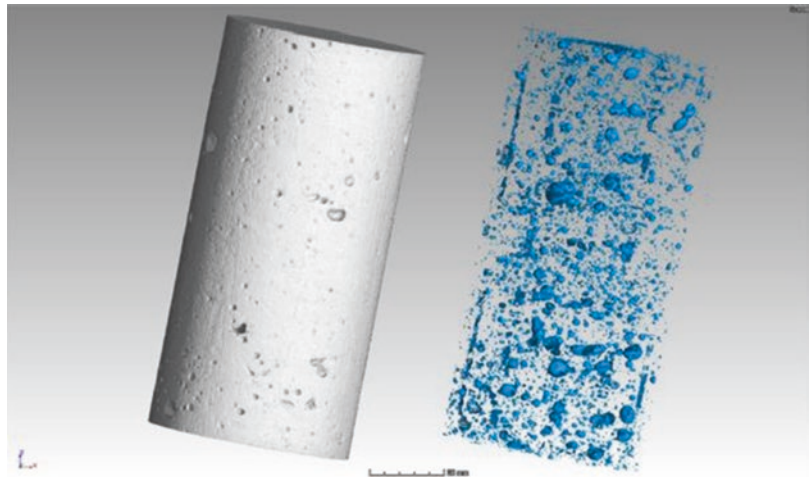


Fig. 17.1 The principal of computed tomography method [1]

Fig. 17.2 3D visualization of porosity in concrete in blue [4]



in literature due to the simplicity and cost-efficient nature of the technique [4–7]. A sort of multiple scales from 100 μm to 10 μm can be used in the analysis, and the size distribution histogram of voids presents similar results, and interpretation is satisfactory, thanks to reliable data although there are some special relations between the resolution and detected voids [4]. An instance of the 3D visualization of porosity in concrete in blue with a scale of 100 μm has been indicated in Fig. 17.2.

Air voids in concrete, which can be lightweight or not, can be measured in terms of distribution of

the voids. Furthermore, samples of a material can be analyzed under different loading conditions or only progressive compression loading to observe the changing of the internal structure of the material, which provide an insight of the fracture and failure mechanism of concrete [8, 9].

Carbonation of concrete is a crucial process due to giving the possibility of corrosion for reinforcement; however, this process takes long years to corrode these steel bars under good conditions related with enough cover and the quality of concrete.

Likely, carbonation process can be analyzed in terms of the changing of the structure of cement paste in micro level. Apart from micro-structure, meso-defect volume fractions can be also observed for different hardened cement pastes including a variety of water-to-cement ratios [1]. In one study considering this, it was concluded that 3D meso-defect volume fractions rise considerably after carbonation, micro cracks were appeared for the paste with higher w/c after carbonation, and gray values increased with an increase in w/c [1].

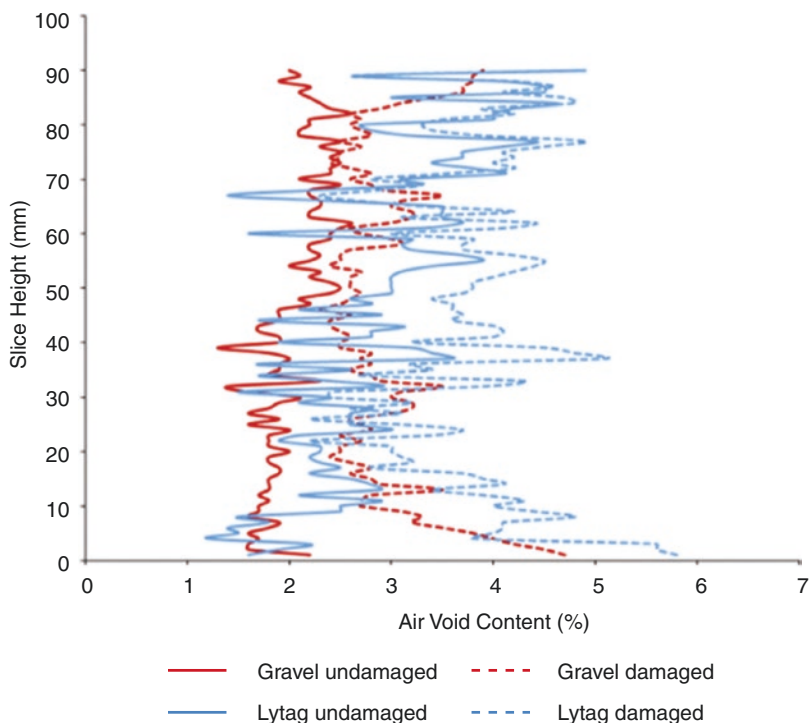
Sulfate attacks on cement pastes can be additionally observed by in situ X-ray CT method. Recently, a different sulfate solution has been applied to cement paste to monitor damage process and evaluate corrosion products' content and porosity of the sample in sulfate solutions comprising of sodium sulfate, magnesium sulfate, and a mixed of sodium sulfate and sodium chloride [10].

Several studies have also been conducted to quantify the damage within concrete mixtures using X-ray CT by characterizing the voids after applying damage. In a study, the damage evolu-

tion by measuring the increment in the voids content (cracks and air voids) from X-ray images in the concretes made with normal and lightweight aggregates before and after being subjected to impact loading has been monitored [11]. They observed a considerable crack growth at the middle regions compared to the top and bottom region of the specimen (Fig. 17.3) signifying that the damage is a localized phenomenon occurring in a critical location in heterogeneous materials.

Furthermore, concrete structures in marine environment are subjected to rebar corrosion which might cause appealing crack in the structure and decreasing in mechanical properties of concrete. Therefore, it is inevitable that the corrosion behavior of rebar has to be scrutinized and X-ray CT method can meet the demand in this point. Time-dependent corrosion of rebar has been visualized and evaluated in a study experimentally, and it is concluded that XCT is useful to visualize time-dependent corrosion of rebar and corrosion process includes three phases as in the case with frequently used corrosion technique [12]. Images of XCT measurements were exemplified in Fig. 17.4.

Fig. 17.3 The changes in air void distribution across the depth of the mixes [11]



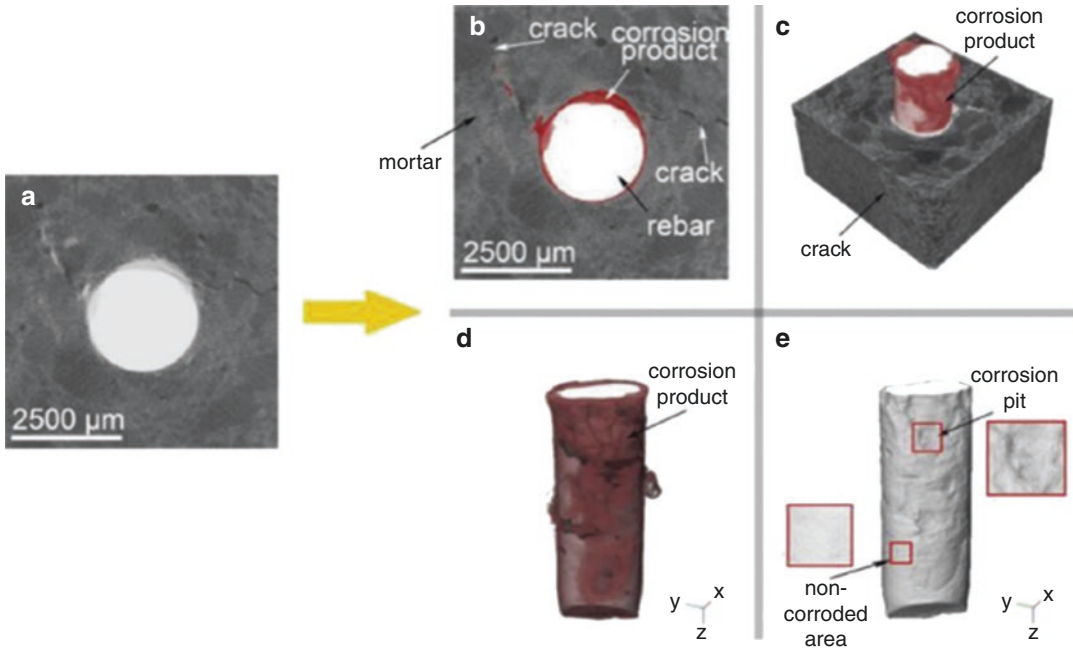


Fig. 17.4 The images of XCT measurement: (a) original sample; (b) labeled different substances; (c) 3D reconstructed image of specimen; (d) 3D reconstructed image

of corrosion products; (e) 3D reconstructed image for corrosion surface configuration of rebar [12]

The parameters of scanning have significant effect on reconstructed images to determine the structural properties of samples by X-ray CT. In this aspect, the parameters of scanning such as current, energy, exposure time, the type of filter, and so on were changed and created three different sets in a study which uses microcomputed tomography method [13]. It is concluded that while the quality of results depends on higher resolution, that is not always precise because the rotation step is also important [13].

What about the difference between medical scanner and microCT scanner? Defect analysis for concrete is attainable by using microCT, but is it also available using medical scanners? Medical scanners exaggerate the sizes of pores in the concrete due to poor resolution possibly according to a study [14]. The images obtained from that study and the histograms showing the size of pores have been given in Fig. 17.5.

17.3 CT Technique in Soil

Soil is a complex structure including the particles of sand, clay, and silt with groundwater together. The behavior of soil completely changes with water content and the amount of these different particles in soil. Especially water content is vital for geotechnical design due to effects on the strength of soil. Therefore, X-ray CT method is commonly used in the determination of the water content of soil. An old study has compared the X-ray CT method with nuclear magnetic resonance imaging (MRI) method to obtain water content value of soil, and it is concluded that X-ray CT was more an effective method and has the potential to apply to the laboratorial studies [15]. Likely, laboratorial studies have gained importance because doing an experiment, without giving harm to soil sample, is faster, cheaper, and easier method to obtain a parameter of soil than applying an in situ experiment.

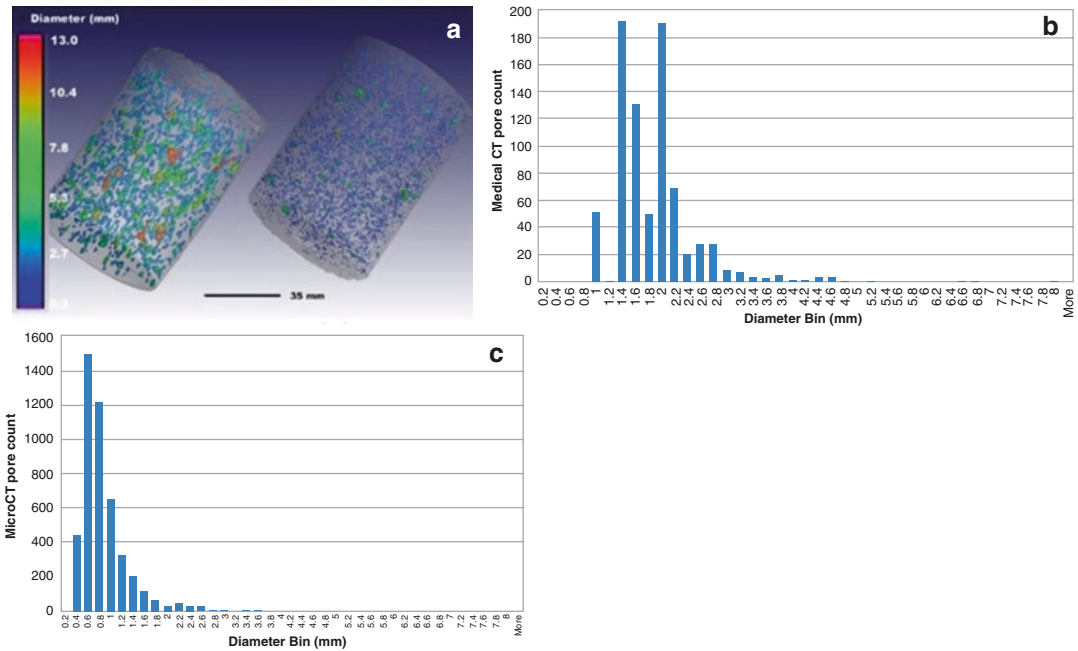


Fig. 17.5 The analysis of porosity of a concrete cylinder by medical CT and microCT (a) 3D color-coded pores (medical and microCT, respectively), (b) pore size distribution using medical CT, (c) pore size distribution using microCT [14]

tion using medical CT, (c) pore size distribution using microCT [14]

Pore structure analysis of soil is also vital to determine pore diameters which have an effect on flows and contaminant moving through the pores, and the analysis of images obtained from CT is useful for this aim [16]. The result of an image processing in 3D in a study related to determining the pore structure of soil is given in Fig. 17.6 [16]. Moreover, monitoring of the microstructure of the particles of sand by taking images at different stages of loading is also possible by X-ray CT technique. As confirmed in a recent study [17], one-dimensional compression at high level of loads leads to particle crushing that can be easily monitored using by X-ray CT technique in Fig. 17.7.

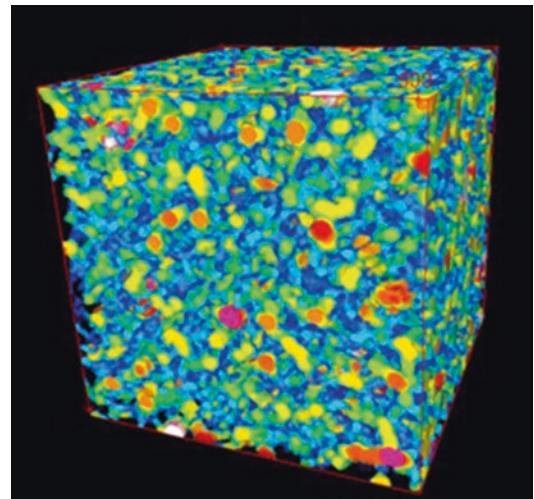


Fig. 17.6 3D perforated pore size distribution [16]

17.4 CT Technique in Asphalt

Asphalt is a mixture of bituminous substances and aggregates and has advanced mechanical properties such as high strength and durability; therefore, it is efficient to be used as road pave-

ment. Also, the mixture of asphalt cement and fine and coarse aggregates is called as asphalt concrete, and it serves a high binding quality which facilitates to be used in airport paving and highways.

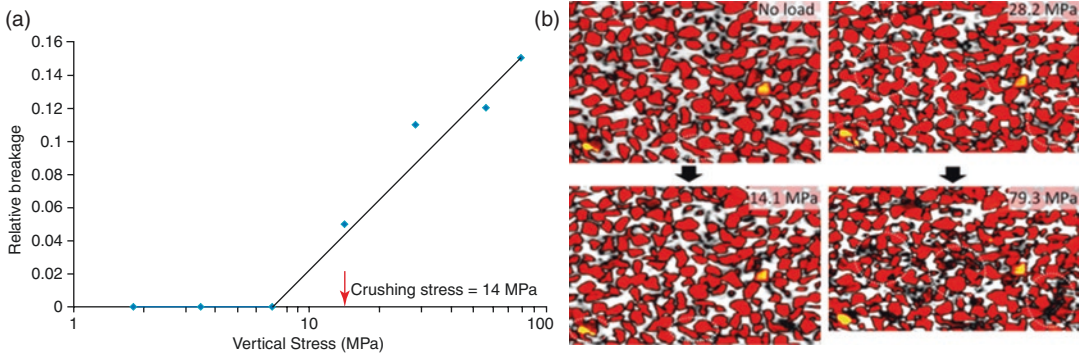


Fig. 17.7 Relative breakage and the images of breaking of particles [17]

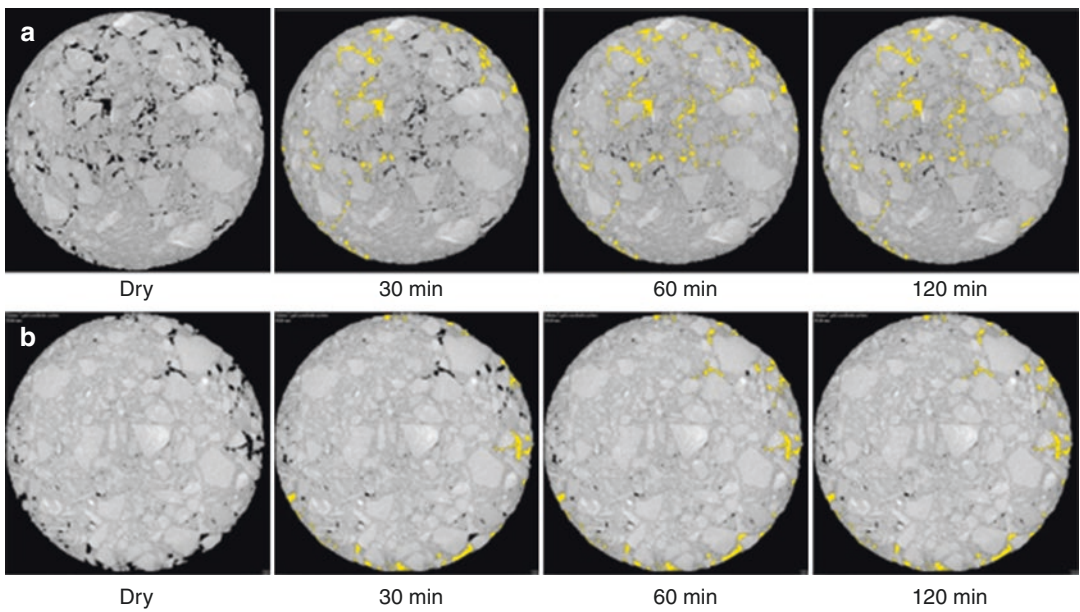


Fig. 17.8 Microscale moisture distribution in asphalt mixtures under different hydrodynamic loading times: (a) 14.5 mm depth; (b) 34.2 mm depth [21]

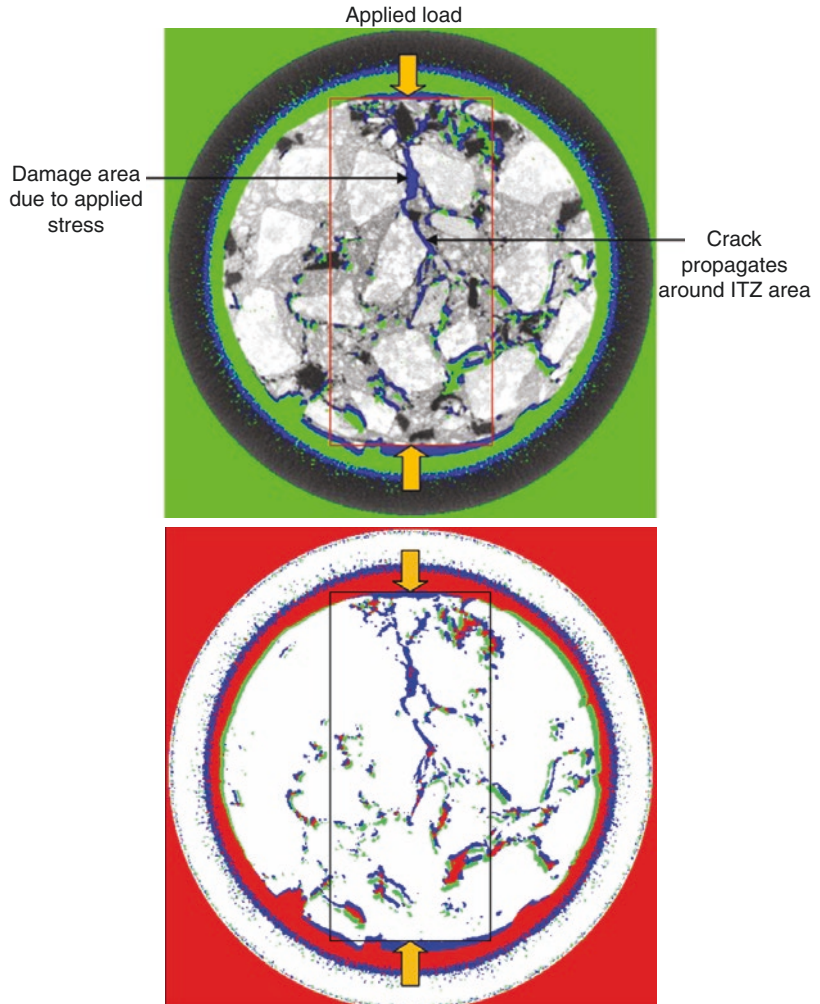
Asphalt, or asphalt concrete, has several morphological properties which should be evaluated such as texture, shape, and angularity. These properties can be captured easily by using X-ray CT technique in studies which used the technique for internal asphalt concrete characterization and quality evaluation of asphalt mixture [18–20].

Moisture distribution of asphalt mixture has to be searched inevitably because it might stir up deterioration in the mixture prematurely and influence hydraulic patterns and both velocity and loading of vehicles [21]. X-ray CT is there-

fore used to pick out the pore structure of such mixtures. Figure. 17.8 shows an example of moisture distribution in asphalt mixtures under different hydrodynamic loading time. The yellow colour in the figure indicates the moisture in the voids [21].

A similar concept of monitoring the damage in rubberized asphalt mixtures was adopted in another study [22], where the specimens were X-rayed at different stages of load cycles of fatigue testing. The damage was quantified in terms of the void growth within the specimen after completing each stage for a number of load

Fig. 17.9 X-ray CT image of the damaged area for rubberized asphalt mixture [22]



cycles. The results showed that the voids area increased with the increase in the number of load cycles. Moreover, it was observed that the damage area was concentrated in an area more or less corresponding to the positional configuration of the diametrical load applied to the specimen (Fig. 17.9). This observation confirmed that the crack formation was a function of the direction of an applied load. The figures showed that cracks were prone to initiate in the interfacial transition zone (ITZ) area between the aggregate and mastic and then propagate by taking the shortest way or the route with the fewest obstacles (such as aggregates and rubber particles) between the two points of the applied stress.

17.5 CT Technique in Metals

Metals are widespread materials in engineering because of its many properties such as being light, having conductivity and fracture strength, etc. Moreover, metal alloys have been manufactured by comprising of one or more metal or non-metal materials. By producing alloy metals, toughness and durability features are improved, and the resistance of metals against high temperature also becomes possible.

Material science is developing day by day to obtain materials having more strength and less density. This development creates a need to monitor the internal structure of such materials, and computed tomography serves this function for us.

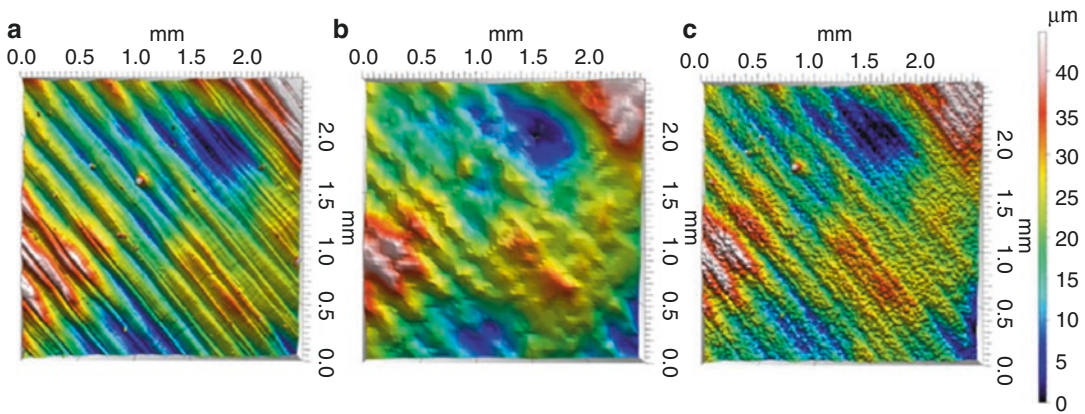


Fig. 17.10 Topographies from varying XCT setup: (a) CSI (reference); (b) XCT by 5 \times magnification; (c) XCT by 20 \times magnification [24]

In a study, internal structure of a porous metal has been observed and mesh data which needs a lot of work in traditional methods has been obtained easily [23].

Surface topography of additively manufactured metals can also be measured by X-ray CT (XCT); however, the measurements obtained from XCT are changing with respect to setup of the measurement parameters, which can be seen in Fig. 17.10 [24]. Therefore, optimum setting is necessary to obtain reliable results for XCT measurements, but it is still open to research. Layered defect which is likely about imperfect melting process can also be scrutinized with this nondestructive method, while other nondestructive methods cannot appropriate to reveal layered defect because of the presence of pores inside not on the surface [25].

17.6 CT Technique for Revealing the Distribution of Fibers

Both mechanical and electrical properties of cement-based materials like concrete can be improved by adding several engineering materials. In this point, mainly carbon and steel and glass, basalt, or PVA fibers in different sizes are commonly used to achieve high strength and toughness, more durability with less weight, and high workability. It is also advantageous to construction time because workload due to steel reinforcements is decreased.

Cement-based materials are commonly used with the aforementioned advanced macro, micro, or nano-materials; therefore, the mechanical properties of these composites have to be observed. X-ray CT is a useful technique for this observation, which can be used in obtaining air-voids volume or the distribution of additive materials, due to being one of the nondestructive methods [26–29]. Nondestructive X-ray CT method is applied before any destructive testing. Self-compacting concrete including especially steel fibers is one of the common research areas today [30, 31]. One study which investigated flexural behavior of self-compacting concrete beam-reinforced steel fiber stated that the results obtained from nondestructive method and mechanical behavior of samples are highly dependent to each other [32]. As seen in Fig. 17.11, a variety of numerical strategies can be generated for determination of porosity, fiber distribution and structure of such polymer composites [33].

Cracking phenomenon and its visualization together with air voids and fiber characterization in terms of distribution or fiber length-to-diameter ratio can be evaluated by X-ray microCT [34]. The evaluation of cracking mechanism of fiber-reinforced concrete is needed to perceive the role of cracking in the redistribution process of applied forces.

Visualizing fiber failure in such composites subjected to incremental loading is also possible

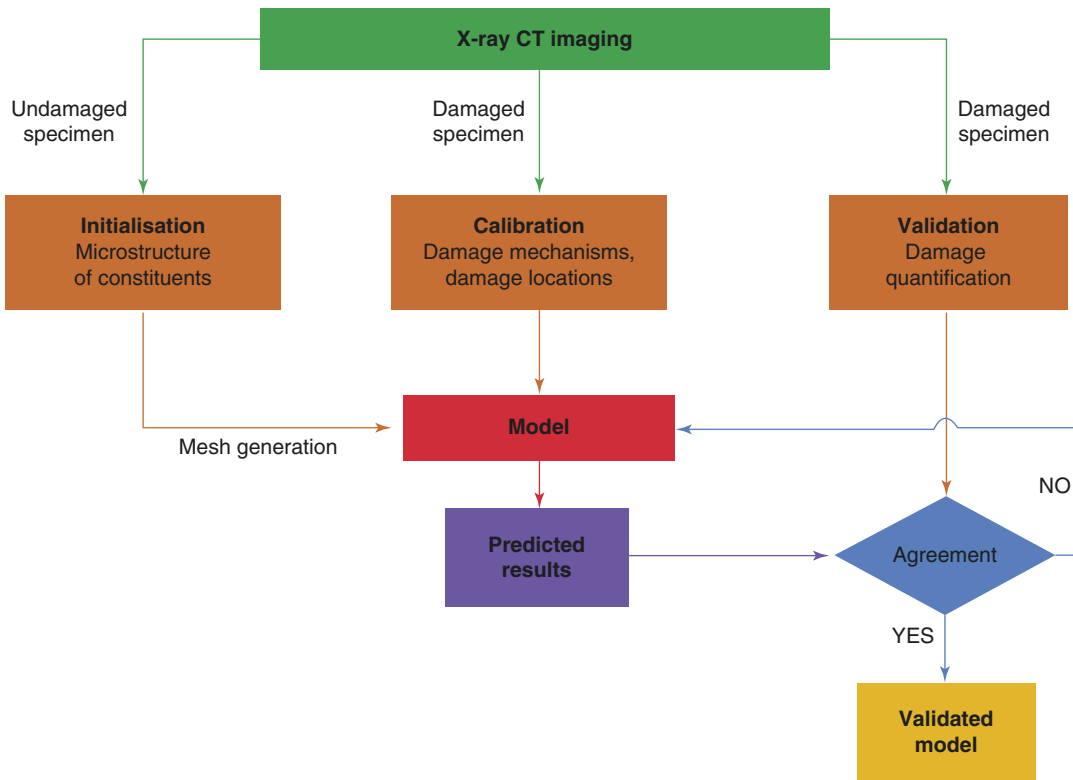


Fig. 17.11 CT in modelling [33]

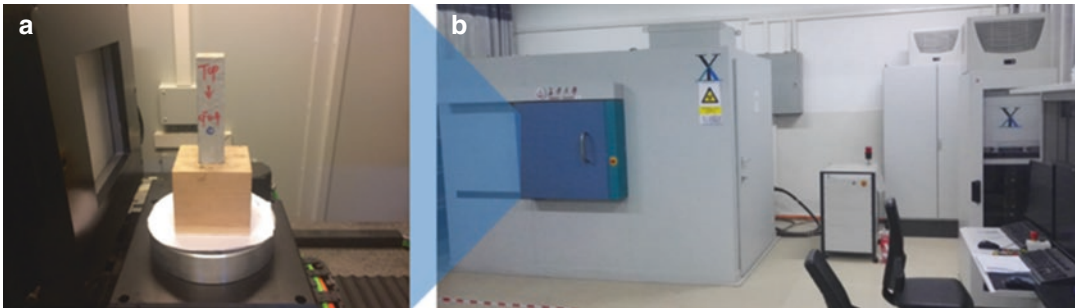


Fig. 17.12 A CT system setup: (a) scanning chamber inside; (b) overview for the system [35]

by in situ CT technology, and fast synchrotron radiation CT enables to capture damage just before final failure [35]. The CT technique would also successfully applied to carbon fiber composites for the microstructural evaluation [35]. The setup for a CT system used in this purpose is shown in Fig. 17.12.

The relation between fiber distribution and fiber-reinforced concrete or other composites

has been revealed in many other studies [36–41]. At this juncture, the use of computed tomography enables to recognize different areas in CT image including highly or not clustering and fiber space areas or pores by using the grayscale of it [42]. In a study, this observation obtained from CT image has been compared with the results of microscopic evaluation of samples, shown in Fig. 17.13 [42].

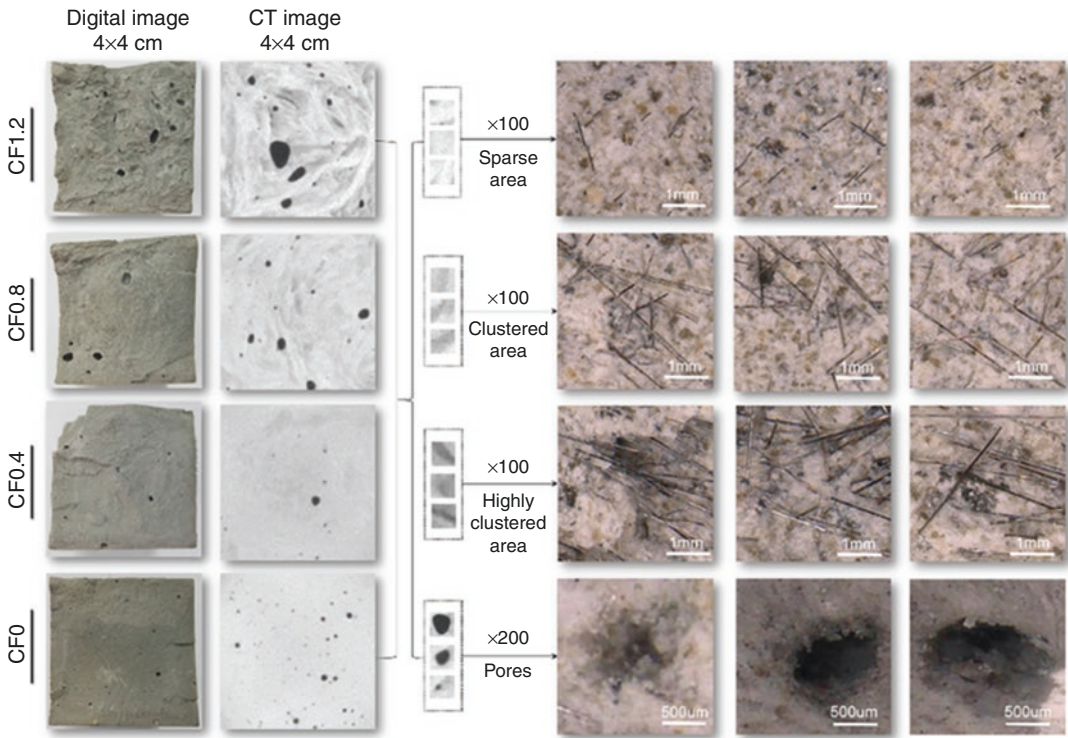


Fig. 17.13 The comparison of digital and CT images [42]

17.7 Conclusion

The use of X-ray computed tomography have been becoming a widespread technique in civil engineering due to being nondestructive and providing the analysis of pore structures of a number of materials. Concrete, soil, metals, asphalt, and some composite forms of them such as fiber-reinforced concrete or additively manufactured metal composites take an important place in the field of civil engineering. Observing microstructure of such materials and the changing in mechanical properties under loading by taking picture from CT scanner throughout loading contributes to enhance the properties of materials or mixtures.

References

- Han J, et al. Application of X-ray computed tomography in characterization microstructure changes of cement pastes in carbonation process. *J Wuhan Univ Technol-Mater Sci Ed.* 2012;27(2):358–63.
- Naeimi M, et al. Reconstruction of the rolling contact fatigue cracks in rails using X-ray computed tomography. *NDT and E Int.* 2017;92:199–212.
- Zhou Y, et al. Modeling of rail head checks by X-ray computed tomography scan technology. *Int J Fatigue.* 2017;100:21–31.
- Plessis A, et al. Simple and fast porosity analysis of concrete using X-ray computed tomography. *Mater Struct.* 2016;49:553–62. <https://doi.org/10.1617/s11527-014-0519-9>.
- Taud H, et al. Porosity estimation method by X-ray computed tomography. *J Petrol Sci Eng.* 2005;47(3):209–17.
- Diamond S. Aspects of concrete porosity revisited. *Cem Concr Res.* 1999;29(8):1181–8.
- Lu H, et al. Measurement of entrained air-void parameters in Portland cement concrete using micro X-ray computed tomography. *Int J Pavement Eng.* 2018;19(2):109–21. <https://doi.org/10.1080/10298436.2016.1172705>.
- Kim KY, et al. Evaluation of pore structures and cracking in cement paste exposed to elevated temperatures by X-ray computed tomography. *Cem Concr Res.* 2013;50:34–40.
- Yang Z et al. (2013) Characterisation of 3D fracture evolution in concrete using in-situ X-ray computed tomography testing and digital volume correlation. In: VIII International conference on fracture mechanics

- of concrete and concrete structures, FraMCoS 2013. pp. 236–42.
10. Yang Y, et al. In situ observing the erosion process of cement pastes exposed to different sulfate solutions with X-ray computed tomography. *Construct Build Mater.* 2018;176:556–65.
 11. Erdem S, et al. Impact load-induced micro-structural damage and micro-structure associated mechanical response of concrete made with different surface roughness and porosity aggregates. *Cem Concr Res.* 2012;42:291–305.
 12. Dong B, et al. Visualized tracing of rebar corrosion evolution in concrete with x-ray microcomputed tomography method. *Cement Concr Compos.* 2018;92:102–9.
 13. Latief FDE, et al. Digital 3D microstructure analysis of concrete using X-ray micro computed tomography SkyScan 1173: a preliminary study. *IOP Conf Ser: Mater Sci Eng.* 2017;267:012020. <https://doi.org/10.1088/1757-899X/267/1/012020>.
 14. Plessis A, et al. Comparison of medical and industrial X-ray computed tomography for non-destructive testing. *Case Stud Nondestruct Test Eval.* 2016;(6):17–25.
 15. Anderson SH, Gantzer CJ. Determination of soil water content by X-ray computed tomography and magnetic resonance imaging. *Irrig Sci.* 1989;10:63–71.
 16. Mukunoki T, et al. X-ray CT analysis of pore structure in sand. *Solid Earth.* 2016;7:929–42.
 17. Mahbub A, Haque A. X-ray computed tomography imaging of the microstructure of sand particles subjected to high pressure one-dimensional compression. *Dent Mater.* 2016;9:890. <https://doi.org/10.3390/ma9110890>.
 18. Onifade I, et al. Asphalt internal structure characterization with X-ray computed tomography and digital image processing. *Multi-Scale Model Charact Infrastruct Mater RILEM.* 2013;8:139–58.
 19. Coleri E, et al. A micromechanical approach to investigate asphalt concrete rutting mechanisms. *Construct Build Mater.* 2012;30:36–49.
 20. TANIGUCHI S, et al. A study on quality evaluation for bituminous mixture using X-ray CT. *Front Struct Civ Eng.* 2013;7(2):89–101. <https://doi.org/10.1007/s11709-013-0197-7>.
 21. Xu H, et al. Micro-scale moisture distribution and hydrologically active pores in partially saturated asphalt mixtures by X-ray computed tomography. *Construct Build Mater.* 2018;160:653–67.
 22. Norhidayah A. H. Microstructural characterisation of rubber modified asphalt mixtures, PhD Thesis. The University of Nottingham; 2012.
 23. Niu Z, et al. Mesh generation of porous metals from X-ray computed tomography volume data. *J Mech Sci Technol.* 2014;28(7):2445–51.
 24. Thompson A, et al. Effects of magnification and sampling resolution in X-ray computed tomography for the measurement of additively manufactured metal surfaces. *Precis Eng.* 2018;53:54–64.
 25. Plessis A, et al. Application of microCT to the non-destructive testing of an additive manufactured titanium component. *Case Stud Nondestruct Test Eval.* 2015:1–7.
 26. Kim KY, et al. Determination of air-void parameters of hardened cement based materials using X-ray computed tomography. *Construct Build Mater.* 2012;37:93–101.
 27. Manahiloh KN, et al. X-ray computed tomography and nondestructive evaluation of clogging in porous concrete field samples. *J Mater Civ Eng.* 2012;24(8):1103–9.
 28. Suuronen JP, et al. Analysis of short fibres orientation in steel fibre-reinforced concrete (SFRC) by X-ray tomography. *J Mater Sci.* 2013;48(3):1358–67.
 29. Zerbino R, et al. On the orientation of fibres in structural members fabricated with self compacting fibre reinforced concrete. *Cem Concr Compos.* 2012;34:191–200.
 30. Ponikiewski T, et al. Determination of 3D porosity in steel fibre reinforced SCC beams using X-ray computed tomography. *Construct Build Mater.* 2014;68:333–40.
 31. Ponikiewski T, et al. Determination of steel fibres distribution in self-compacting concrete beams using X-ray computed tomography. *Arch Civil Mech Eng.* 2015;15:558–68.
 32. Ponikiewski T, Katzer J. X-ray computed tomography of fibre reinforced selfcompacting concrete as a tool of assessing its flexural behavior. *Mater Struct.* 2016;49:2131–40. <https://doi.org/10.1617/s11527-015-0638-y>.
 33. Garcea SC, et al. X-ray computed tomography of polymer composites. *Compos Sci Technol.* 2018;156:305–19.
 34. Skarżyński Ł, Suchorzewski J. Mechanical and fracture properties of concrete reinforced with recycled and industrial steel fibers using Digital Image Correlation technique and X-ray micro computed tomography. *Construct Build Mater.* 2018;183:283–99.
 35. Garcea SC, et al. Mapping fibre failure in situ in carbon fibre reinforced polymers by fast synchrotron X-ray computed tomography. *Compos Sci Technol.* 2017;149:81–9.
 36. Pinter P, et al. Comparison and error estimation of 3D fibre orientation analysis of computed tomography image data for fibre reinforced composites. *NDT and E Int.* 2018;95:26–35.
 37. Mishurova T, et al. Evaluation of the probability density of inhomogeneous fiber orientations by computed tomography and its application to the calculation of the effective properties of a fiber-reinforced composite. *Int J Eng Sci.* 2018;122:14–29.
 38. Hassler U et al. (2007) Computed tomography for analysis of fiber distribution in carbon fiber preforms. In: *International Symposium on Digital industrial Radiology and Computed Tomography*, June 25-27, Lyon, France.
 39. Liao H et al. (2017) Evaluation of fiber distribution in steel fiber reinforced asphalt concrete based on CT

- image analysis. In: 1st International Conference on Transportation Infrastructure and Materials (ICTIM 2016), At Shaanxi, China.
40. Liu, et al. Study on 3D spatial distribution of steel fibers in fiber reinforced cementitious composites through micro-CT technique. *Construct Build Mater.* 2013;48:656–61.
 41. Sencu RM, et al. Generation of micro-scale finite element models from synchrotron X-ray CT images for multidirectional carbon fibre reinforced composites. *Compos A: Appl Sci Manuf.* 2016;91:85–95.
 42. Gao J, et al. Characterization of carbon fiber distribution in cement-based composites by computed tomography. *Construct Build Mater.* 2018;177:134–47.



Application of X-Ray Microtomography in Pyroclastic Rocks

H. Evren Çubukçu

18.1 Introduction

Geologists try to understand the processes that form and change the physical unity of earth by examining the rocks. Sometimes, a single piece of rock can reveal a plethora of geological information using various inspection techniques. Hence, an earth scientist should know more about the rock in order to know more about the earth.

A rock can be defined as a solid entity of one or more minerals with a definite strength. A mineral, on the other hand, is a natural solid with a homogeneous atomic structure (crystalline) and a definite chemical composition. However, natural rocks usually comprise various other components together with minerals. In simple terms, every natural feature in a rock separated by physical/chemical borders from another can be called as a component. Although they can be of different origins, the chief components of rocks are usually crystalline phases. Amorphous phases (i.e., volcanic glass), organic matter (i.e., fossils), cracks, and even voids/vesicles which are occasionally found in rocks are also regarded as the components of a rock.

X-ray microtomography represents a state-of-the-art nondestructive 3D data acquisition technique for rock componentry analyses. X-rays

passing through the rock sample, which is rotated in front of an X-ray source, are collected by a detector producing 2D shadow projections at each step. These images are then used by a computer algorithm in order to reconstruct virtual slices of the rock sample. Once the virtual sections are obtained, a solid rock model can be constructed.

Although the X-ray microtomography method is not that efficient to characterize/identify some compositionally similar rock components due to its operating principles, it precisely reveals their quantitative spatial distribution in the rock body. Since the usage of X-ray microtomography in earth materials yields high-resolution 3D quantitative data, earth scientists increasingly employ the technique for a broad range of purposes.

18.2 Petrographical Analyses

Petrography is the subdiscipline of geology, which obtains invaluable data by the inspection of rock components, texture, and chemistry. The entire measurable physical relationships between the rock components are termed as the texture of a rock. Rock texture is an important property which develops during/after rock formation and can reveal valuable information. Hence, the better the rock texture is investigated, the more geological data it yields. Textural componentry of rocks can be quantified in terms of size distribution, spatial distribution,

H. E. Çubukçu (✉)
Department of Geological Engineering, Hacettepe
University, Ankara, Turkey
e-mail: ecubukcu@hacettepe.edu.tr

and shape (Ref. [1] and references therein), all of which are satisfactorily realized using X-ray microtomography.

Petrographical studies require the determination of textural and mineralogical characteristics of a rock body. Microscopic techniques represent the conventional basis for such purposes. Especially, transmitted polarized light (optical) microscopy stands as the starting point of a petrographical analysis. The specimens (thin sections) examined under a polarizing light microscope (PLM) are prepared by cutting suitable slabs from rocks and by grinding down to a thickness of 30 μm . Occasionally, the thin sections are not covered by glass lamellae and polished to obtain a perfect flat surface in order to further analyze under scanning electron microscope (SEM) and integrated X-ray spectrometers (EDS, energy-dispersive spectrometer; WDS, wavelength-dispersive spectrometer). Although the preparation of even a single thin section is a tedious and a destructive process, the final outcome can be high-resolution visual and chemical data.

In its simplest form, a thin section can be regarded as a 2D plane cut from a rock. It usually does not fully represent the actual 3D structures since it depends on the location and the orientation of the cutting plane. Some rocks exhibit significantly discrete textural properties along different cutting planes due to orientation of rock components (Fig. 18.1). Hence, the orientation of the cutting plane should be carefully determined for reliable textural analyses. Recent advances in 3D imaging instrumentation and the increased availability of commercial systems facilitated the petrographical studies to be performed in 3D. Evidently, X-ray microtomography is progressively becoming a complementary method for 3D visualization of the spatial features of rock components. Various microscopic techniques can be employed on the same specimen in order to achieve a correlative microscopic approach. In geological samples, a prior petrographical information gathered by conventional methods will significantly improve the identification of the components by X-ray tomography.

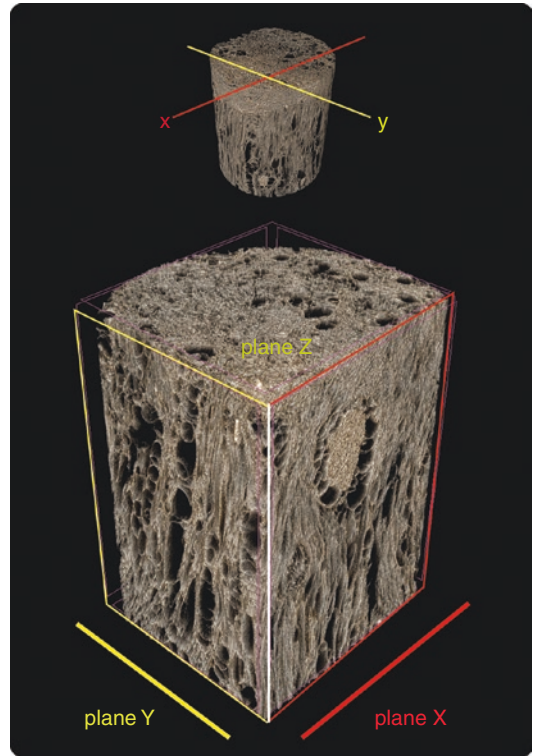


Fig. 18.1 Pumice sample displays different textures along different cutting planes

18.3 Pyroclastic Rocks

The rocks composed of magmatic material, fragmented during an explosive volcanic eruption, are called pyroclastic rocks (pyro, fire; clast, grain; derived from Greek). Although there are a number of processes that produce pyroclastic rocks, the main ingredient is commonly gas- and silica-rich magma. Silica-rich (>65% by vol.), viscous magmas contain dissolved gases. The sudden release of entrapped gases and the disintegration of the liquid magma body result in explosive volcanic activity. Such violent explosion of the highly fragmented gas-rich magma usually produces pyroclastic flows. Pyroclastic flow is a fast-moving (up to 700 km/h) current of hot (600–1000 °C) gas and dominantly fine-grained solidified magma fragments (tephra). This hot and fast-moving cloud, the pyroclastic flow, is denser than the ambient air and propa-

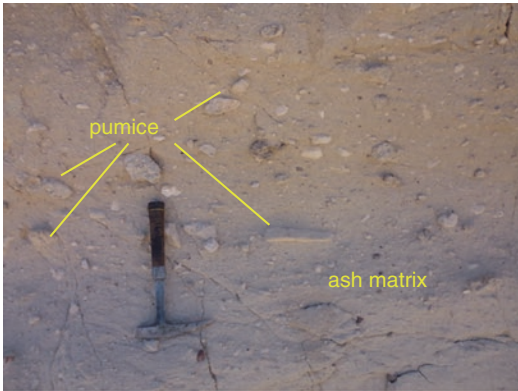


Fig. 18.2 A typical ignimbrite comprising pumice fragments dispersed in ash matrix

gates outward from the eruption center (or volcano). When the energy of the flow is diminished, it settles on the surface and begins to cool down. During cooling, it solidifies, becomes harder, and transforms into pyroclastic rock. These rocks, which contain crystals, fine-grained volcanic fragments (or volcanic ash), and pumice (juvenile magma droplet), are called “ignimbrites” (Fig. 18.2).

The samples used in this study are collected from the Cappadocian Volcanic Province. Cappadocia is a volcanic region in Central Anatolia, best known for its appealing landscapes formed by the erosion of existing pyroclastic rocks. In Cappadocian region, there have been ten significant pyroclastic eruptions producing extensive ignimbrite sheets between 10 and 5 millions of years ago. These pyroclastic units reflect variations of physical and chemical characteristics of erupting magmas as well as the dynamic controls during the eruptions throughout the time.

18.4 Principles of Image Formation in X-ray Microtomography

Minerals, the essential constituents of rocks, span a broad range of physical and chemical characteristics. 3D imaging of crystals using microtomography relies on the principle that passing X-rays

are attenuated inside the mineral depending on the physicochemical properties of the medium (c.f. absorption tomography). In order to distinguish the different minerals using this method, X-rays should be attenuated by measurable amounts [2]. The fraction of X-rays that is absorbed (or scattered) per unit volume of a material is expressed by attenuation coefficient (μ). The attenuation coefficient of a mineral is a function of its specific gravity, chemical composition, and the energy of X-rays being used. Usually, it is not possible to distinguish the minerals with similar attenuation coefficients [3]. Hence, a preliminary mineralogical/petrographical study should be conducted in order to specify suitable scanning parameters. Moreover, a prior knowledge on the rock componentry will also establish an efficient interpretation of tomographic datasets. A collection of attenuation coefficients of various elements and compounds (including minerals) can be obtained from NIST XCOM (Photon Cross Sections Database) (<http://www.nist.gov/pml/data/xcom/index.cfm>). In the following sections, the attenuation coefficients used in sample applications are calculated with MuCalcTool (<http://www.ctlab.geo.utexas.edu/software/mucalc-tool/>) and depicted in Fig. 18.3.

18.5 Essential Application Steps of X-Ray Microtomography in Earth Materials

As noted in the preceding sections, a prior geological information on the components of the analyte should be obtained by conventional petrographical analyses. The knowledge on the material will help to designate the appropriate scanning parameters, as well as to correlate the tomograms with the actual components present in the rock (modal composition). The essential steps of handling the X-ray microtomographic datasets are practically common for almost all types of samples. Once the dataset has been obtained, preprocessing, segmentation/separation, and analysis steps are performed. The generalized workflow is presented in Fig. 18.4.

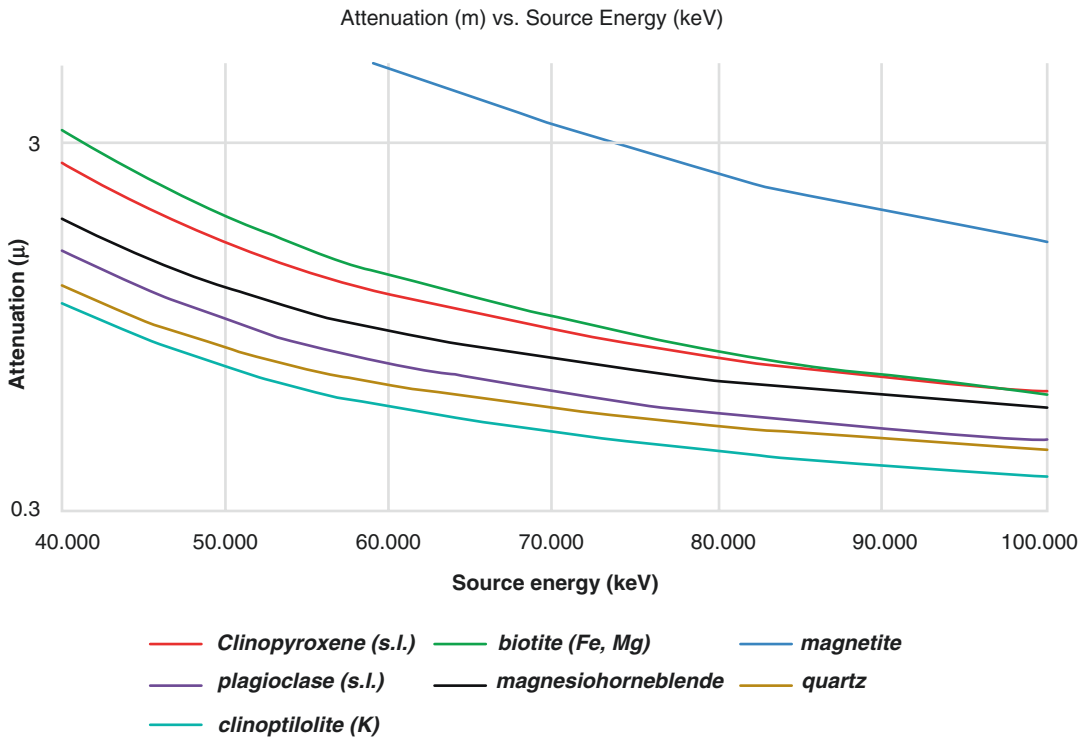


Fig. 18.3 Variation of attenuation coefficients of selected minerals versus X-ray energy of the source

18.5.1 Preprocessing

Microtomography datasets are comprised of a grayscale image stack which are simply the reconstructed virtual slices. Oftentimes, the images contain undesired visual artifacts, the errors formed during data acquisition. In order to prepare the dataset for reliable image analyses, visual artifacts should be minimized. Preprocessing step encompasses the definition of a study volume and the correction of the intrinsic image errors present in the dataset.

18.5.1.1 Defining a Volume of Interest (VOI)

In advance of all quantitative data handling, a representative volume should be designated. The selected portion of the scanned sample, on which further processing will be conducted, is called volume of interest (VOI). VOI can be any shape or volume specifically defined by the user according to the need (Fig. 18.4).

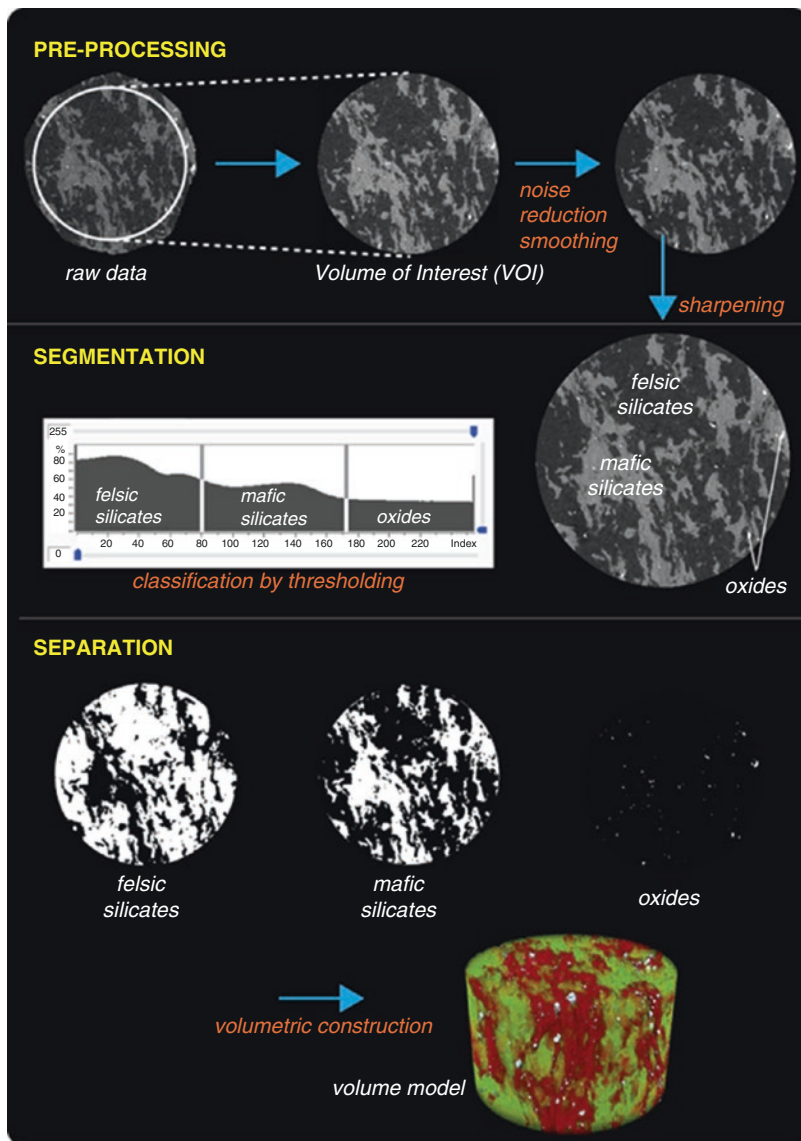
18.5.1.2 Artifact/Noise Reduction

X-ray datasets frequently contain visual artifacts (beam hardening, ring artifact, etc.) and digital noise due to the interactions between X-ray beam and the solid sample. In order to distinguish the components, to clarify the borders separating them, and to establish a representative analysis, visual defects should be minimized.

Most of the image processing platforms use similar nomenclature for basic digital image manipulation algorithms (filters). Hence, the filters mentioned here can be found in common image processing software. In order to reduce primary digital noise in datasets, “smoothing” filters such as *median*, *Gaussian blur*, *nonlocal means*, *average*, etc. can be employed. Noise reduction should be applied carefully, since it can lead to erroneous modification of data if used redundantly (Fig. 18.4).

Noise reduction usually results in the beclouding of the boundaries between components. Therefore, complementary “sharpening” filters

Fig. 18.4 Essential workflow for preprocessing and classification of a tomographic dataset, exemplified on a natural rock sample. Preprocessing encompasses the VOI (Volume of Interest) definition and noise reduction. Upon the representative sharpening of the component boundaries, felsic silicates (quartz and feldspars), mafic silicates (biotite, amphibole), and oxides (magnetite, ilmenite) can be classified according to the grayscale intensities (attenuation coefficients). Separation of each component into discrete subsets usually requires further noise reduction. Obtained subsets can be used to construct pseudocolored volume model of the sample



such as *sharpen*, *unsharpen mask*, etc. can be applied to clarify the borders (Fig. 18.4).

Once the undesired noise and artifacts are removed and component edges are clarified, data is ready for segmentation/separation.

18.5.2 Segmentation/Separation

Segmentation/separation is the overall image processing methods which aim to distribute the total volume data into grouped voxels representing the

components (Fig. 18.4). The criteria for grouping the voxels require similar spatial and chemical characteristics of data in a voxel. Basically, microtomography data is generated from 2D grayscale bitmaps where the spatial variation of the passing X-ray energies reveals the texture of the sample. The energy of the passing X-ray depends on the attenuation coefficient of the material. The denser the material, the less X-rays pass the sample, yielding a grayscale image set of “shadows” of each turn of the sample. These 2D shadow images are used to mathematically reconstruct the

sample in 3D where gray level (0–255) is a function of attenuation coefficient. Spatial information is crucial for the algorithms based on attenuation used for grouping voxels into “segments.” Since similar materials have similar attenuation coefficients, they produce similar data within a specific grayscale range. Thresholding is simply the binarization of 256 levels of grayscale images into black-and-white ones using explicit cutoff values (limits). By thresholding, or constraining the grayscale data, voxels with similar grayscale intensity can be classified into spatially substantive groups, which are represented by black-and-white, binary images. In such datasets, white pixels will state whether there is data or not, a straightforward expression of where the selected group is located inside the sample. For complex samples such as rocks, the components are represented by grayscale intervals, and significant overlapping is usual between structurally similar ones. In order to obtain a sound binary data with minimized data loss, a preliminary petrographic information is crucial. It is maybe the best practice to perform X-ray tomography not before than conventional petrographical analyses.

In geological samples, classification of tomographic datasets into geologically meaningful subsets is crucial. Thresholding usually discriminates various rock components such as voids, crystals, glass, etc. Once the similar rock components are grouped, it is possible to visualize and quantify the data they present. Segmentation algorithms are generally applied in concert with noise reduction, since processed data will produce negligible artifacts. Erasing omnipresent non-descriptive pixels facilitates further processing.

The digital separation of each subset data into corresponding components relies on complex image processing algorithms. Whichever the algorithm used for separation, the resulting datasets will reveal spatial distribution of rock components (Fig. 18.4).

The final datasets used in quantitative analyses should carry representative information. If the data obtained by segmentation/separation procedures do represent the actual rock, quantification of this data for rock components by further algorithms is possible.

18.5.3 Data Analysis

Following the separation of grouped voxels as individual objects representing the components of a sample, a plethora of quantitative measurements can be performed on datasets. These analyses are simply the numerical interpretation of relational information regarding the morphology and/or compositional data acquired. There are numerous software platforms where such analyses can be realized.

Upon the completion of the preprocessing steps, a binary dataset which is suitable for quantitative image processing techniques should be obtained. The dataset which will be used in image analysis should be representative, free of noise and image artifacts, and quantifiable. Quantification using image processing requires computer algorithms to detect desired features by automatic image evaluation without significant confusion. There are numerous software options where the user can directly control the filter parameters, yielding an interactive approach for image analysis. In this example, CTAn (from Bruker) has been used for VOI definition, thresholding, and further image analyses. Besides, open-source ImageJ, thanks to numerous available scientific plug-ins, is frequently used for noise reduction and morphological data evaluation.

18.6 Sample Applications

The X-ray scans used in the following examples are performed in the computerized microtomography facility at the Advanced Technologies Research and Application Center of Hacettepe University (HUNITEK) using Bruker SkyScan 1272 high-resolution scanner. 2D image sets acquired during scanning are reconstructed with InstaRecon algorithm producing 3D stacks of virtual slices. Data preprocessing including VOI definition and noise reduction followed by thresholding, segmentation, and final analyses is realized with bundled Bruker software such as CTAn, CTVol, CTVox, and ImageJ.

18.6.1 3D Quantitative Petrography of an Ignimbrite

An ignimbrite sample, belonging to Tahar unit erupted 6 million years ago, was collected from Cappadocian volcanic field and drilled in the laboratory to obtain cylindrical cores with 2 cm of diameter and 3 cm of height, suitable for X-ray scanning. Sample is then scanned using a source voltage of 70 keV filtered with 1 mm thick pure aluminum, with a rotation step of 0.3°. The final reconstructed dataset is with a 1 μm pixel size.

A preliminary polarized microscopy study reveals that the sample rock is comprised of free

crystals and pumice fragments which are surrounded by ash matrix. The crystalline phases are identified as plagioclase ($\text{NaAlSi}_3\text{O}_8\text{--CaAl}_2\text{Si}_2\text{O}_8$), clinopyroxene [$\text{Ca}(\text{Mg,Fe})\text{Si}_2\text{O}_6$], titanomagnetite [$\text{Fe}^{+2}(\text{Fe}^{+3}, \text{Ti})_2\text{O}_4$], and zircon (ZrSiO_4). Volcanic glass is represented by vesicular pumices and the ash matrix, composed of very fine-grained amorphous vitric (glassy) shards. Moreover, the rock contains abundant vesicles.

Following the reconstruction of the image dataset, image processing steps employed are shown in Fig. 18.5. First of all, a representative volume of interest (VOI) has been defined, and intrinsic noise was reduced using *median* and

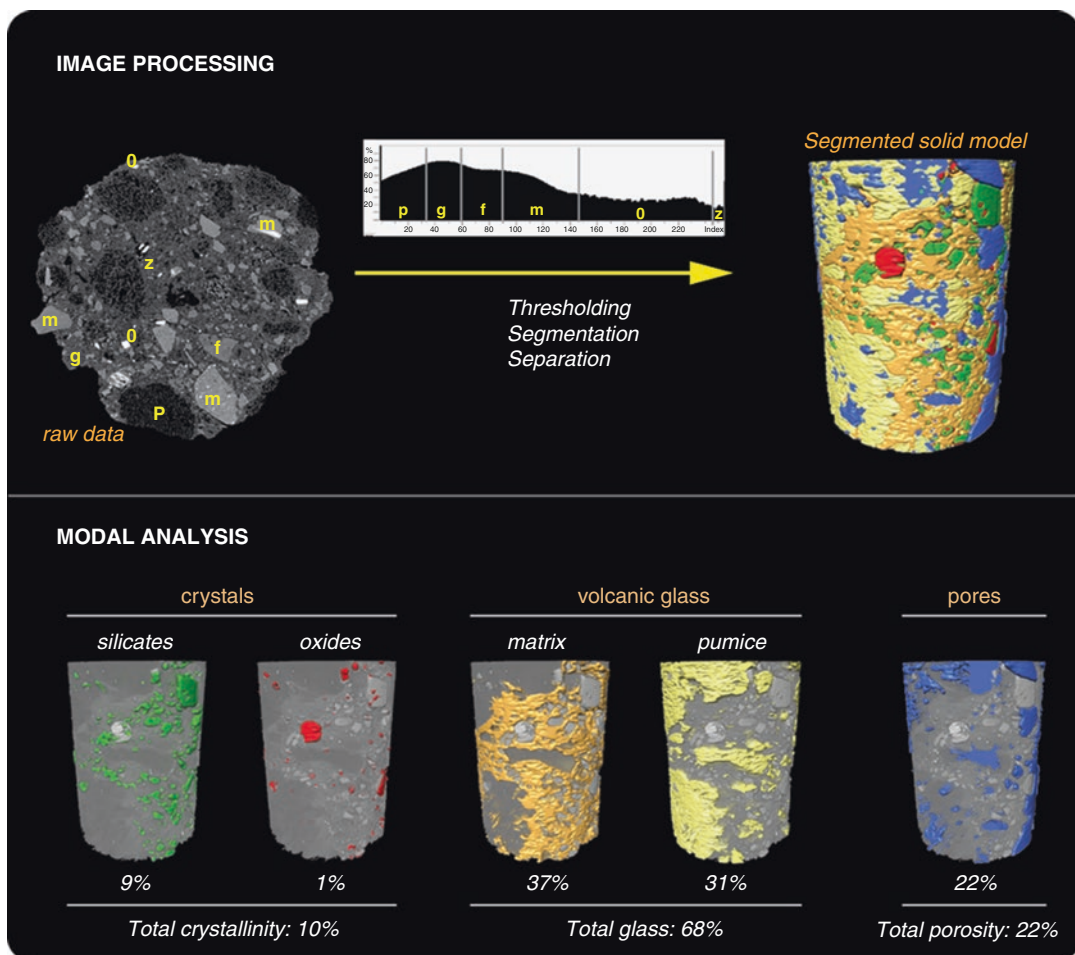


Fig. 18.5 Classification step and the results of modal analysis of the ignimbrite sample. Image stack has been classified by thresholding for the components: *p* pumice, *g* glass (in ash matrix), *f* felsic mineral (plagioclase),

m mafic mineral (clinopyroxene), *o* Fe-Ti oxide (magnetite), and *z* zircon. The calculated modal abundances of each component are visualized on volumetric models

Gaussian blur filters. Since noise reduction algorithms result in smoothed edges of visualized features, it is generally recommended to sharpen the image dataset, in order to define the boundaries of components, using image filters such as *sharpen*, *unsharpen mask*, etc. In this sample, each image in the set has been 2D sharpened using *unsharpen mask* filter with radius, 1, and amount, 50, at square kernel dimensions.

Segmentation step comprises of assigning the grayscale ranges by thresholding to specific components in order to classify the image data into meaningful groups. Since the rock componentry has been well-defined by earlier petrographical analyses, thresholding the dataset into discrete binary subsets of each phase is drastically facilitated. Upon the segmentation of rock components into pumice, ash matrix, vesicles, and free crystals, a further classification of crystals into each mineral revealed volumetric modal (actual) abundances. Quantitative measurements on the components show that the ignimbrite sample exhibits 10% crystallinity of which 9% is represented by silicates and the remaining 1% by zircon and Fe-Ti oxides. Volcanic glass is present both in pumice and in the ash matrix with a total abundance of 68% by volume. The separation of glass in pumice and in ash matrix required further spatial and morphological evaluation. The pumice is represented by closely packed vesicles rimmed by thin walls of volcanic glass yielding lower grayscale intensities. Hence, pumice subset is separated regarding the spatial distribution of vesicles. Once the pumice dataset is obtained, the total glass fraction in pumice is calculated to be 31%. Upon the separation of ash matrix, its glass fraction is also obtained as 37%. The amount of total volcanic glass of the sample is calculated by adding the glass contents in pumice and ash matrix. The overall porosity, the ratio of volume of pores to the total volume, is 22% (Fig. 18.5).

18.6.2 3D Porosity and Crystallinity in Pumice

Exsolution of dissolved volatiles in a rapidly ascending gas-rich magma in a volcanic conduit will lead to bubble coalescence and growth, turning

the rising magma into a frothy melt. If the volcanic eruption is intense enough, the magma droplets discharged from the neck will quench in the air retaining the initial pore structure formed during the magma ascension. The quenched magma droplet is called pumice, and it is represented by a porous, amorphous volcanic glass with/without magmatic crystals. Pumice is naturally a highly vesicular, friable, and delicate pyroclastic rock without significant mechanical strength.

Generally, it is quite difficult to prepare undamaged and representative petrographical thin sections from pumice samples for conventional 2D imaging using light and electron microscopy. Nonetheless, X-ray tomography provides excellent advantage since it is a nondestructive method to adequately quantify the macroporosity and crystal distribution in 3D. Pumice represents an ideal rock for X-ray tomography since textural properties can easily be distinguished due to the presence of isolated crystals in a porous glass [4].

During geological expeditions, different Cappadocian ignimbrite units are recognized in the field by the textural properties of contained pumice fragments, since they are the direct products of explosive volcanic eruptions they are formed. In order to quantify the textural componentry of pumice fragments and to provide a basis for characterization of Cappadocian ignimbrites, pumice fragments are collected from three ignimbrite units (Fig. 18.6). Pumice samples have been taken from Cemilköy, Tahar, and Göredeş ignimbrites, which have been formed by three consecutive explosive eruptions that occurred between 7.2 and 6.3 millions of years ago [5].

Coarse pumice samples are drilled to obtain cylindrical cores, the ideal shape for minimizing the X-ray scattering from the sharp edges of the specimen, with 2 cm of diameter and 3 cm of height. Samples are scanned using a source voltage of 60 keV filtered with 0.25 mm thick pure aluminum, with a rotation step of 0.3°. The final reconstructed dataset is with a 1 μm pixel size.

The acquired datasets are preprocessed and classified according to the procedures described earlier in the text. Generated volume models, pore networks, crystal distributions, and calculated total porosity and crystallinity are shown in



Fig. 18.6 Pumice hand specimens of Cemilköy, Tahar, and Göredeles ignimbrites

Fig. 18.7 The volume models, separated pore networks, and crystal contents of pumice samples collected from Cemilköy, Tahar, and Göredeles ignimbrites of Cappadocian Volcanic Province. Crystals are further classified by thresholding and pseudocolored. Representative modal assemblage consists of plagioclase (*p*), biotite (*b*), clinopyroxene (*c*), oxides + zircon (*o*)

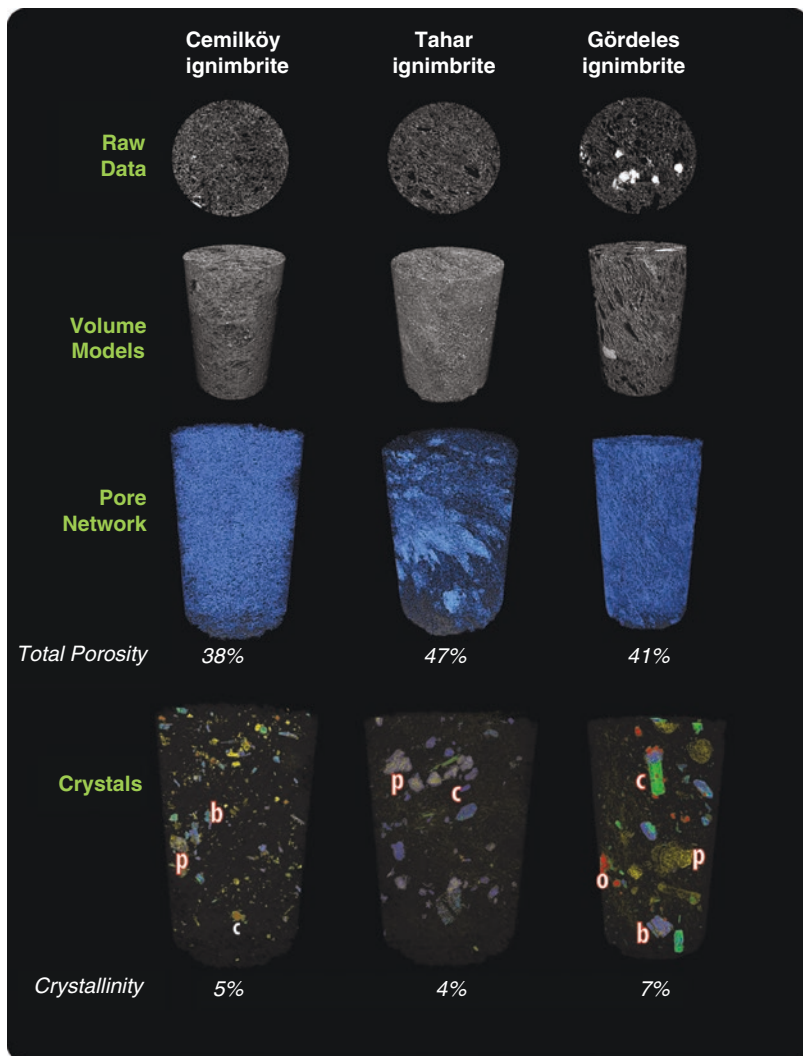
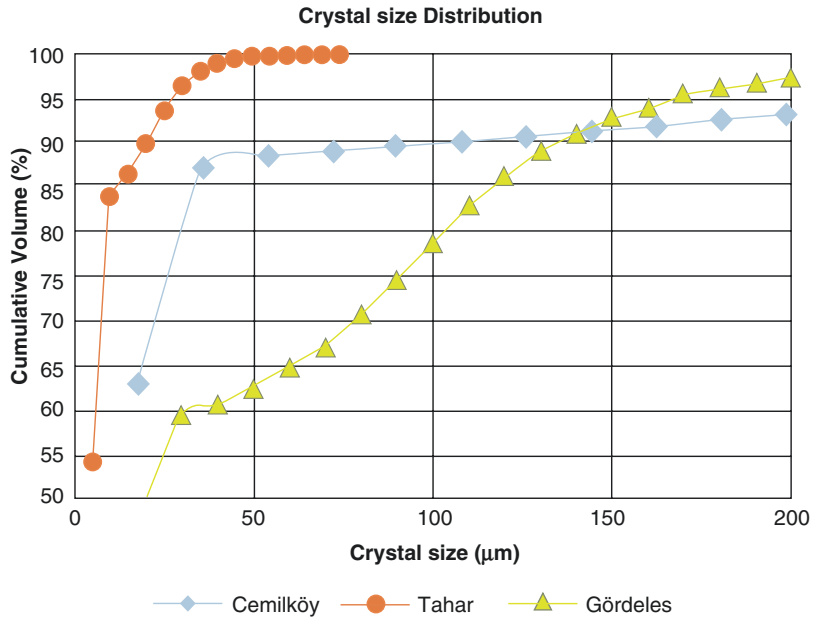


Fig. 18.7. Moreover, the crystals are depicted pseudocolored, by mapping the respective gray-scale intensity intervals of minerals to specific colors.

18.6.2.1 Crystal Size Distribution

The crystal size distribution (CSD) can be defined as the number (or the volume) of crystals of a mineral per unit volume within fixed size

Fig. 18.8 Cumulative volume of crystals versus crystal size diagram for pumice samples collected from three ignimbrites from Cappadocian Volcanic Province



intervals [6]. Crystal size is a commonly quantified textural property in igneous rocks, and CSD analysis can provide fundamental petrological information [7].

Crystal size distribution in volcanic rocks is a function of nucleation and crystal growth processes which occur in a cooling magma body, which reveals the preeruptive state of magmatic systems. 2D petrographical observations on rock thin sections yield potentially limited results due to either the insufficient amount of crystals or the inappropriate orientation of the thin section. On the contrary, X-ray microtomography can deliver reliable 3D data of crystalline phases in silica-rich pyroclastic rocks, thanks to the relatively higher attenuation coefficients of most minerals with respect to surrounding silicic glass.

Crystalline phases are classified and separated from tomographic datasets of Cemilköy, Tahar, and Gördeles pumices. Although the modal quantities are different in each unit, the common mineral assemblage consists of plagioclase, biotite, clinopyroxene, titanomagnetite, and zircon. Quartz is only observed in Gördeles ignimbrite. Since the attenuation coefficients of the minerals present in the pumice samples differ slightly under a given source energy (Fig. 18.3), minerals are separated by thresholding and pseudocolored

for visual representation (Fig. 18.7). All minerals are grouped under “crystalline phases” subdataset in order to demonstrate the applicability of CSD analyses in the given context. Quantitative CSD analyses have been realized in CTAn software (Fig. 18.8).

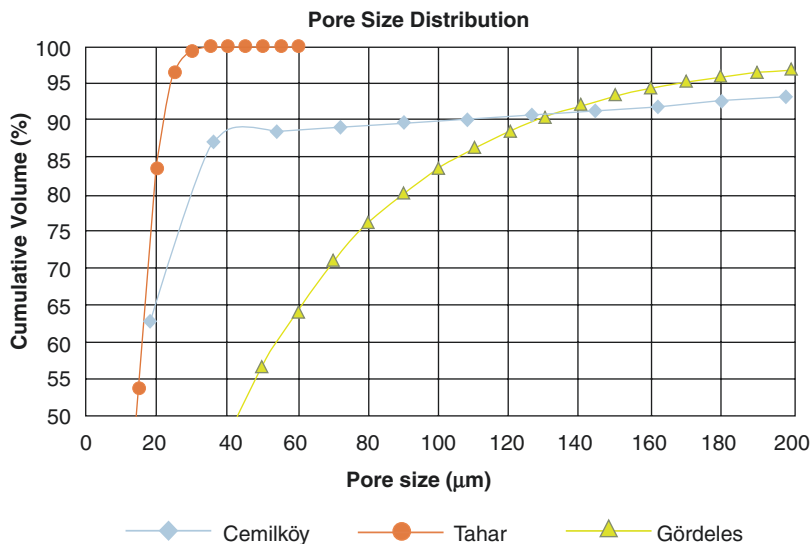
Cumulative volumetric CSD analyses revealed that more than 95% of crystals are smaller than 50 µm in Tahar pumice, whereas the quantities of coarser crystals in Cemilköy and Gördeles pumices are higher. In Cemilköy pumice 17% of the crystals, and in Gördeles sample 40% of the crystals are bigger than 50 µm. Gördeles crystals are significantly bigger than those in Cemilköy and Tahar samples; 10% of all crystals are bigger than 150 µm (Fig. 18.8).

These results indicate that the nucleation/crystal growth processes are significantly different in magmatic reservoirs of three consecutive eruptions occurred in ~1 million years of time.

18.6.2.2 Pore Size Distribution

Pores or vesicles represent the voids in the rock formed either during or after its formation. Porosity, the ratio of pore volume to total volume, has a vital role for interpretations concerning a geological sample. Since porosity is a multiscale property ranging from nanometer to decimeter in

Fig. 18.9 Cumulative volume of pores versus pore size diagram for pumice samples collected from three ignimbrites from Cappadocian Volcanic Province (pore sizes larger than 200 μm are not shown)



length, it is not easy to measure quantitatively. High-resolution X-ray microtomography can be used to reveal 3D structures of macropores ($0.1 > 100 \mu\text{m}$, IUPAC terminology) in rock samples. However, there are numerous analytical methods and approaches for representative quantification of porosity. For further information on various porosity determination methods, instrumentation, and analytical approaches in geological materials, the reader should refer to a very detailed review by Anovitz and Cole [8].

Detailed characterization of porosity is a useful approach for a better understanding of bubble nucleation in magmas. A pumice fragment is simply a magma droplet and by quenching the preexisting pore structure is almost retained. The structure of pore network in a pumice reflects the physicochemical properties of the erupting magma and the dynamics of eruption. Hence, the characterization of porosity of juvenile magma fragments such as pumices sheds light onto volcanic events occurred before/during an eruption. Pore size distribution (PSD) is an important parameter to determine physical conditions of explosive eruptions.

The void fractions are classified and separated from tomographic datasets of Cemilköy, Tahar, and Gördeles pumices. Upon the preparation of binarized pore datasets of each sample, volume models have been rendered to visualize the pore structure (Fig. 18.7). CTAn (Bruker) software

was used to quantify the cumulative volumetric size distribution of vesicles (Fig. 18.9).

According to the calculated data, more than 95% by volume of pores of Tahar pumice is smaller than 40 μm . Eighty-eight percent by volume of the total pore fraction in Cemilköy ignimbrite is smaller than 40 μm . However, PSD of Cemilköy ignimbrite displays a bimodal distribution where 8% of pore volume is represented by vesicles larger than 200 μm . PSD of Gördeles pumice exhibit a uniform distribution where more than 25% by volume of pore space is larger than 80 μm .

According to the porosity data, it can be inferred that the dynamic controls during these three consecutive eruptions vary significantly producing texturally different pumice fragments.

18.6.3 Quantification of Devitrification in a Hydrothermally Altered Ignimbrite

During an explosive volcanic activity, hot gas and volcanic material (pyroclasts) ejected from the eruption center may spread laterally as a gravity-assisted density current (or flow). Pyroclastic flows are chiefly comprised of ash-sized ($< 2 \text{ mm}$), amorphous juvenile magmatic glass fragments. In other words, pyroclastic

rocks – especially ignimbrites – contain high amounts of chemically metastable volcanic glass, present in the rock either as pumice or ash matrix. During or after the solidification of pyroclastic deposits, numerous agents from a broad range of natural processes can get into chemical reaction with the metastable volcanic glass. Hydrothermal alteration is a general term for the processes that change the overall mineralogical content in the rock body due to hot fluids. Meteoric or magmatic hot fluids with a variety of chemical compositions may percolate through the pyroclastic deposit and chemically interact with the glassy material. Devitrification is the crystallization of volcanic glass at temperatures below the glass transition temperature (T_g) [9]. Since volcanic glass in ignimbrites is metastable, it is prone to devitrification and secondary crystallization due to the chemical reaction with hot fluids. Following the devitrification, silicic volcanic glass usually transforms into fine-grained minerals such as feldspars, clays, and zeolites.

In order to quantify the extent of devitrification due to hydrothermal alteration in Tahar ignimbrite unit from Cappadocia, rock samples affected and not affected by the alteration are compared. The unaltered sample has been investigated earlier in Sect. 18.6.1. The altered sample belongs to the same ignimbrite unit and spatially very close to the unaltered counterpart; however, it has been observed to be chemically modified by preexisting lake waters in the vicinity throughout geological times.

It is essential to define the secondary crystals by microscopic methods in order to reveal the alteration characteristics. A detailed preliminary petrographical analysis revealed that the samples unaffected by hydrothermal alteration are moderately welded and glassy fragments are intact without devitrification. Under scanning electron microscope equipped with EDS, ash matrix is observed to be comprised of cusped glass shards with sporadic secondary clay (smectite) crystals. Moreover, primary magmatic crystal assemblage of plagioclase + clin-

pyroxene + biotite + Fe-Ti oxides is also unaltered. On the contrary, the hydrothermally altered samples are strongly welded with scarce remnants of zeolitized pumice. Ash matrix is thoroughly devitrified into secondary zeolites and sporadic clay. Furthermore, free crystals, especially Fe-Mg silicates, are usually rimmed by Fe oxides (Fig. 18.10).

The tomograms of two groups of rocks are acquired with the identical settings, 90 keV X-ray energy, filtered with 1-mm-thick pure aluminum, with a rotation step of 0.30° . The final reconstructed dataset is with a $1\ \mu\text{m}$ pixel size. The acquired tomograms are correlated with the actual rock componentry using petrographical data. Upon the definition of the volume of interest and preprocessing the image dataset, segmentation of rock components has been realized by thresholding the grayscale intensities regarding the morphological features (e.g., pumices have been classified by the spatial distribution of pores; refer to Sect. 18.6.1). Pore, pumice, ash matrix, and free crystals are segmented to obtain binary datasets of each component.

Data analysis on the binary subsets of components reveals that the unaltered ignimbrite is comprised of vesicles (22% by vol.), volcanic glass (68% by vol. including pumice and glassy ash matrix), and free magmatic crystals (10% by vol.). On the other hand, the altered ignimbrite is composed of vesicles (13% by vol.), non-devitrified volcanic glass (42% by vol.), and crystals (45% by vol.). The crystalline phase assemblage of altered sample is comprised of primary (pyrogenic, crystallized in magma) and secondary (due to devitrification of glass) minerals. Pyrogenic assemblage occupies 11% of the total volume, whereas secondary zeolites, which crystallize during alteration/devitrification of volcanic glass, represent 34% of the sample volume (Fig. 18.10).

The results show that the hydrothermal alteration has induced devitrification of ash matrix, where secondary zeolite crystallization in the pore space has reduced the total porosity.

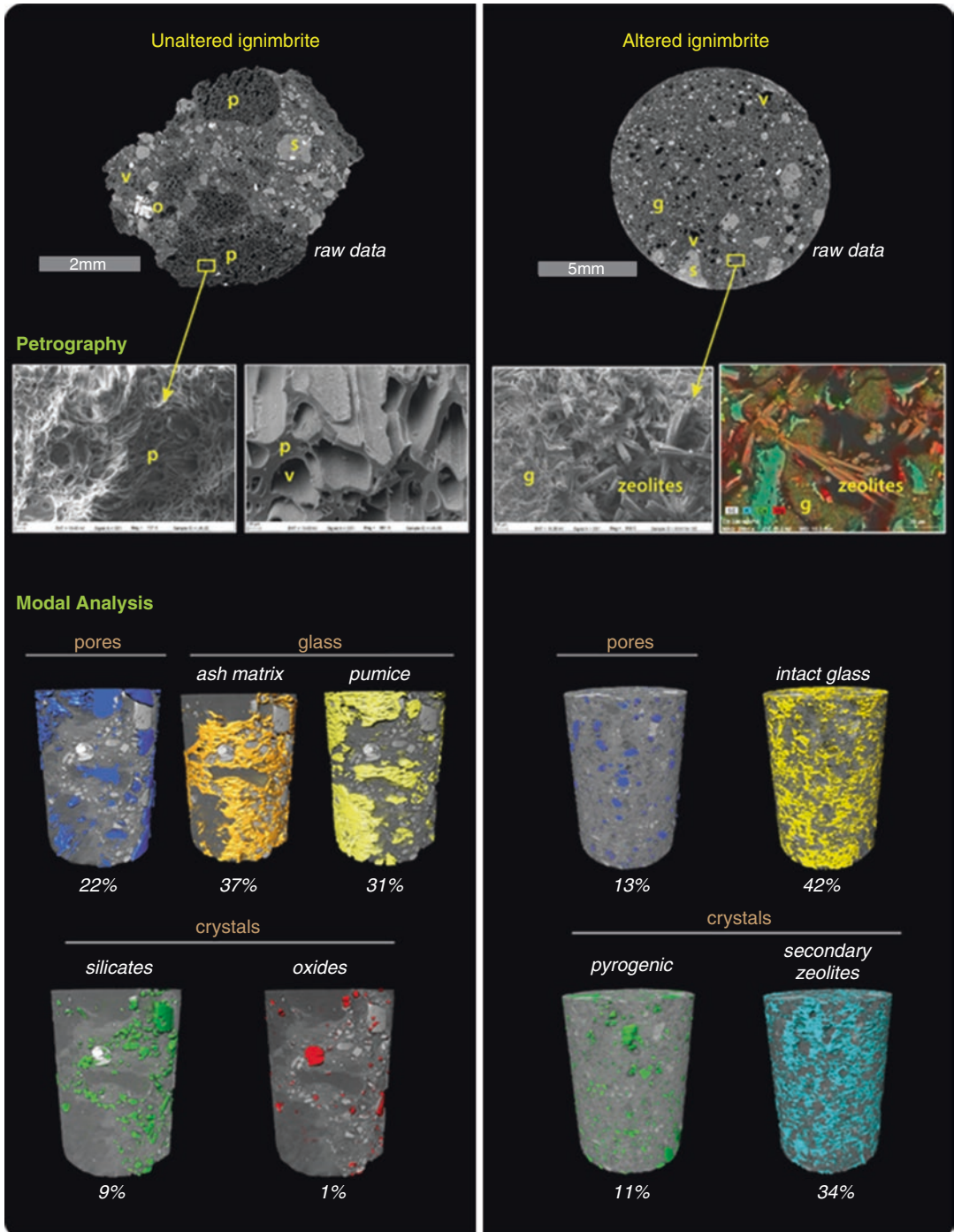


Fig. 18.10 Comparison of modal abundances of pores, volcanic glass, and crystals for unaltered and hydrothermally altered samples of Tahar ignimbrite. Petrographical

components in tomograms are correlated with SEM-EDS observations. In hydrothermally affected sample, ash matrix is devitrified and altered into secondary zeolites

18.7 Conclusions

X-ray tomography is a prominent and efficient method for high-resolution visualization and quantification of the microtextures and the componentry of geological materials. Due to its non-destructive nature, the method can be considered as an outstanding tool for the 3D observations of delicate specimens such as pyroclastic rocks. Although it is sometimes not possible to distinguish some compositionally similar componentry due to its operating principles, it precisely reveals their spatial distribution in the rock body. However, this drawback can be significantly compensated if the tomographic information is accompanied by prior petrographical/mineralogical observations. Once petrographical information is complemented with 3D tomographic data, it is possible to quantify the geological features of a rock using a broad range of image processing algorithms. The microtomographic analysis applications demonstrated above should be regarded as introductory since the usage of 3D data in volcanological context is merely limitless.

It is evident that 3D information on rock materials will be progressively used, thanks to the advancing technology and the increased availability of such acquisition systems. Moreover, the possibility of correlation and integration of analytical data obtained by different methods will eventually facilitate the usage of 3D quantitative tomographic information. The recent progress in analytical technology permits the application of more than one method simultaneously. For most of the multipurpose imaging instruments, the quantitative 3D visualization is becoming an essential element. It is clear that the

earth scientists will obviously benefit from technological progress that provides more precise 3D data on geological material.

Acknowledgments This study is funded by the Scientific and Technological Research Council of Turkey (TUBITAK Project No: 113Y439).

References

1. Gualda GAR. Crystal size distributions derived from 3D datasets: sample size versus uncertainties. *J Petrol.* 2006;47(6):1245–54.
2. Baker DR, Mancini L, Polacci M, Higgins MD, Gualda GAR, Hill RJ, Rivers ML. An introduction to the application of X-ray microtomography to the three-dimensional study of igneous rocks. *Lithos.* 2012;148:262–76.
3. Boone M, Dewanckele J, Boone M, Cnudde V, Silversmit G, Van Ranst E, Jacobs P, Vincze L, Van Hoorebeke L. Three-dimensional phase separation and identification in granite. *Geosphere.* 2011;7(1):79–86.
4. Gualda GAR, Pamukcu AS, Claiborne LL, Rivers ML. Quantitative 3D petrography using X-ray tomography 3: documenting accessory phases with differential absorption tomography. *Geosphere.* 2010;6(6):782–92.
5. Aydar E, Schmitt AK, Cubukcu HE, Akin L, Ersoy O, Sen E, Duncan RA, Atici G. Correlation of ignimbrites in the central Anatolian volcanic province using zircon and plagioclase ages and zircon compositions. *J Volcanol Geotherm Res.* 2012;213:83–97.
6. Chianese A. Characterization of crystal size distribution. In: Chianese A, Kramer HJ, editors. *Industrial crystallization process monitoring and control.* New York: Wiley; 2012. <https://doi.org/10.1002/9783527645206.ch1>.
7. Rannou E, Caroff M. Crystal size distribution in magmatic rocks: proposition of a synthetic theoretical model. *J Petrol.* 2010;51(5):1087–98.
8. Anovitz LM, Cole DR. Characterization and analysis of porosity and pore structures. *Pore-Scale Geochem Process.* 2015;80:61–164.
9. Lofgren G. Spherulitic textures in glassy and crystalline rocks. *J Geophys Res.* 1971;76(23):5635.



Detection of Dispersion and Venting Quality in Plastic Composite Granules Using Micro-CT

Orkun Ersoy

19.1 Introduction

Due to the increasing use of plastics in our daily lives, the production of plastic products is increasing day by day. Quality standards in the plastic manufacturing industry are constantly increasing in the meantime. Recently, companies that manufacture quality control devices in plastic production have begun to produce scanners for plastic processing. These devices include a combination of X-ray technology and an optical inspection. Both technologies have advantages and disadvantages. X-ray technology looks like a step ahead. A main advantage of X-ray technology is that it is color independent. Metallic contamination, air voids, and agglomeration of fillers can be detected online during plastic pellet production and processing (Fig. 19.1). But, the method, especially the limits of the equipment used, must be further developed. The contamination detection size is 50 μm on currently marketed systems, at a speed of 500 kg pellets per hour. Their targets in the next versions are to be able to detect finer-sized contamination. On desktop high-resolution micro-CT devices such as those used in this study, detail detectability is 0.35 μm . However, the use of these devices in online control systems does not seem appropriate

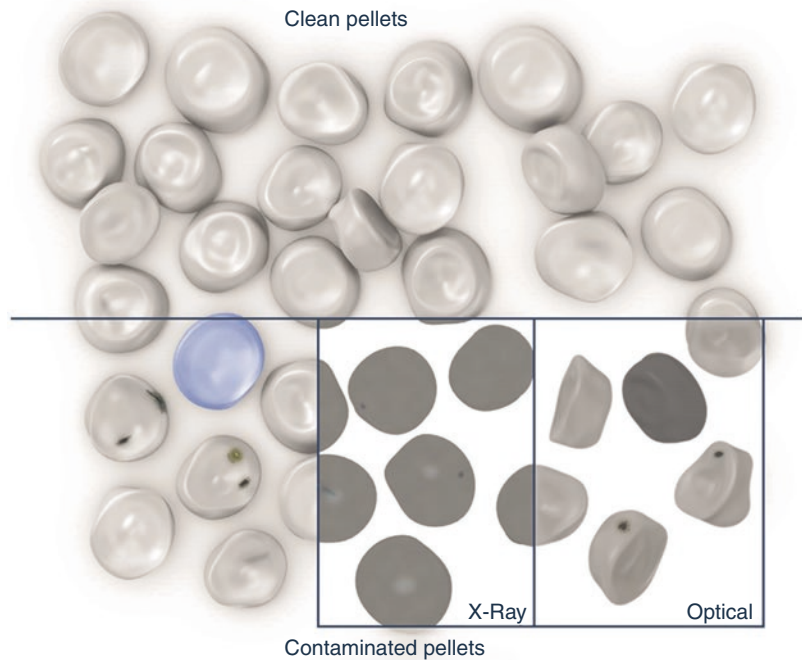
since the scanning times are long. For this reason, it is necessary to make a selection for the methods and devices to be used in the balance of sensitivity and scanning time. The method must be selected according to whether the inspection is done online or offline.

19.1.1 Dispersion

For the production of plastic composites which serve different purposes, composites with functional fillings in the polymer matrix are produced. Plastic (polymer) compounds are modified and improved by adding functional fillers to get more valuable end products. The reasons of adding fillers to plastics may be cost reduction, improved performance, or combination of both. The compounding quality depends on many reasons, but the dispersion status is one of the most important. A good dispersion of the filler is favorable to the material properties, whereas large aggregation with poor dispersion reduces or compromises the properties. Scientific studies on polymer nanocomposites are increasing every day, and these nanocomposites find their place in many areas of daily life. If one of the dispersed phases in composites is in nanoscale, due to their high surface-to-volume ratio, they tend to agglomerate and give deleterious effects on the properties of the resulting composite such as strength and stiffness, electrical and thermal conductivity, transparency,

O. Ersoy (✉)
Department of Geological Engineering, Hacettepe
University, Ankara, Turkey
e-mail: orsoy@ohu.edu.tr

Fig. 19.1 X-ray and optical online inspection of compound pellets for the detection of contamination (used with the permission of SIKORA AG)



and barrier properties [1, 2]. Several strategies have been used to improve dispersion quality, including either chemical or physical approaches. Surface modification of the filler particles to enhance the compatibility of the matrix and fillers is often used. Filler particle surfaces are coated with dispersing or coupling agents to reach a good dispersion state [3]. In terms of physical methods, dispersive mixing (intensive mixing) is required to overcome the cohesive resistance of agglomerates, and a certain minimum stress level is necessary to rupture the agglomerates [4]. High-speed mixers or extruders are widely used in polymer mixing. Application of ultrasonic vibrations has been reported to be effective in enhancing the dispersion state of nanoparticles both in solutions and melt polymers [3, 5].

Despite the used chemical surfactants, additives, and mixing processes for providing dispersion, there is currently no method available for plastic compounding producers which can give satisfactory results about the dispersion of fillers. Filter pressure value (FPV) was recently used by compound manufacturers to characterize the dispersion of fillings. The basic principle of the method is to determine how much pressure will

be produced when the melt material is passing through a screen mesh and to determine the amount of time that the melt material will block the mesh. Although the method is advantageous in that it can give the dispersion quality to a single value, the necessity of knowing the grain size of each single type or different type of fillings used and thus the necessity of selecting the size of the screen mesh is a weak direction of the method.

Several microscopy methods have been tried to examine filler dispersion within some composite systems: optical microscopy for microparticles while transmission electron microscopy (TEM), scanning electron microscopy (SEM), and atomic force microscopy (AFM) for nanoparticles [1]. There is a critical aspect for the obtained information from TEM, SEM, and AFM images. The analysis is restricted by some small area rejecting the rest of the specimen; this investigated area actually should be the representative of the whole specimen. The criterion of choosing the area for the image performing is subjective; therefore, visual analysis results may lead to errors. Usually when a small number of images are taken, their analysis is not sufficient for the

meaningful statistical evaluation of the overall system. It is believed that the micro-CT, which can nondestructively display the whole of the compound granules in three dimensions, and the analysis of the images obtained from micro-CT, is one of the most suitable methods to be used to characterize dispersion of fillers in compounds.

19.1.2 Venting

Ventilation is one of the processes required to mix polymers with additives and fillers to achieve the desired physical properties. The resulting pellet-form compound should be free from voids that may cause disturbances in the extruded or injection molded parts. If the venting section on the compounding extruder does not exist or is not working properly, any volatile in the compound can only be released in the final part of the extruder. Volatiles that cannot be exhausted lead to surface defects and voids in the compounds. Water-sensitive polymers are prone to hydrolysis or degradation of molecular weight due to the presence of moisture; efficient venting during compounding is critical to achieve acceptable physical properties. Due to the lower bulk densities of some type of fillers, the more air is introduced into the extruder barrel that must be vented [6]. Calcium carbonate (calcite) is one of the most widely used mineral fillers in the plastic industry and is used at high filler loadings (up to 80%) in compounds (masterbatches) for cost reasons. Surface defects and voids in compounds including high-loaded calcium carbonate are very common due to ventilation problems during extrusion.

19.2 Compound Extrusion

Compounds were produced using a laboratory-type twin-screw extruder with an L/D ratio of 44 and with a screw diameter of 18 mm. The polymer is fed from the gravimetric main feeder as granules, and the filling material is fed from the gravimetric side feeder as powder. The temperature settings of the extruder are adjusted accord-



Fig. 19.2 Compound granules including 50% calcium carbonate and 50% LDPE produced in this study. The diameter of the coin is 26.15 mm

ing to the type of polymer used. LDPE-type polymer is the carrier matrix of the produced compounds. Calcium carbonate (calcite) is used as filler material in compounds. Calcite is very common in compounding industry due to its advantages in terms of economy and its whiteness and non-abrasiveness. Calcite powders with stearic acid modified- and unmodified-surface were supplied from Niğ Taş Company (Nigde, Turkey). Compounds were taken as strands from the die head of the extruder, cooled in the water bath and cut in the pelletizer into granules (pellets) (Fig. 19.2). Polymer and fillers were fed into the extruder in equal amounts so that compound granules contain 50% filler and 50% polymer. This ratio was also tested with the ash content analysis according to ASTM D2584, D5630, ISO 3451.

19.3 Micro-CT Scanning

Compound granules were scanned with a high-resolution micro-tomography (Skyscan 1272, Bruker). Scanner was equipped with an automatic sample changer. Compound granules were placed on the stage using wax as an adhesive (Fig. 19.3). Since the micro-tomography device used generates polychromatic X-ray energy, it produces a broad spectrum of X-ray energies, and these rays behave differently when passing through the sample. Especially, those with low energies are

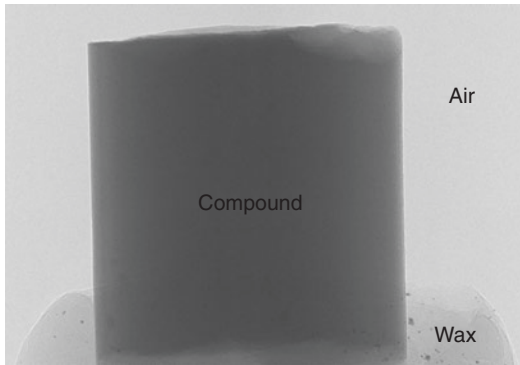


Fig. 19.3 Shadow image of a compound granule and the wax fixing the granule on the stage

damped in the edges of the sample and cause artifacts. Filters are used in micro-CT to adjust X-ray photon energy, to attain appropriate X-ray transmission through an object. A “filter” in X-ray imaging is a metal plate placed in the beam path between the X-ray source and camera, through which the X-ray passes either before or after passing through the sample. A filter removes the low energy part of the spectrum of X-ray energies in the X-ray sources in micro-CT scanners. In this study, aluminum filter with 0.5 mm thickness was placed in front of the X-ray source. Compound granule samples were rotated 360° at its own axis at an angle of 0.4°. Tomography scans of each granule sample took about 3 h and 40 min. Eighty granules were scanned for this study.

19.4 Image Processing

In micro-CT analysis, the scanned data must be processed by a user-friendly and comprehensive software. Software such as Mimics (Materialise NV, Belgium) used by CAD engineers includes additional software packages analyzing micro-CT data, and successful results can be obtained with such software [7]. Software written by companies that produce micro-CT devices also yield satisfactory results in converting image formats, opening and displaying raw data, reconstructing raw data, and processing reconstructed cross-section images. Such software have been developed to allow the necessary analysis to be done in almost

any work done with micro-tomography. In this study all of the preprocessing and image processing procedures were performed with software from Bruker company developed for Skyscan micro-CT scanners. From these software, NRecon is used to reconstruct the projection data sets obtained after tomography scans and to obtain the tomography sections. The raw images obtained within the scope of this study were transformed to images made of compound granule sections with the help of NRecon. A final alignment (post-alignment) is required to remove artifacts that occur when the sample is rotated and not precisely centered. The aligned samples were also subjected to beam hardening correction in the range of 25–30%. Beam hardening is the increase in the average energy of the polychromatic X-ray beam resulting from the higher attenuation during the passage of low-energy X-rays through the sample. Images were also subjected to ring artifact correction with a value of 5. Ring artifacts are changes in image illumination centered on the axis of rotation. Finally, the images were smoothed by Gaussian filtering. After reconstruction, the size of slice images was 2452 × 2452 pixels where the pixel size was 2 μm.

CTAn software is used to calculate quantitative parameters from 2D and 3D data sets obtained from micro-tomography scanning and to create visual models. It accepts images from a wide range of formats, including DICOM data sets, as input. In the CTAn software, 2D regions of interest can be selected on reconstructed sections, which are transformed into 3D areas by interpolation. The required parameters can be calculated on the areas of interest by selecting binary threshold levels on the histogram.

19.5 Results

19.5.1 Detection of Dispersion Quality in Compounding Process Using Micro-CT

Here, I will present a method of displaying a compound granule in three dimensions, and this method provides us how the filler particles are

dispersed in the polymer matrix at high resolutions. It is obvious that micro-computed tomography, which has been started to be used in many areas, can be successfully used in determining the quality of filler dispersion in polymer/filler composites.

Compound granule samples including 50% filler and 50% polymer were extruded using a twin-screw extruder. The fillers were coated (surface modified) and uncoated calcium carbonate. In order to see the venting effect on porosity of granules, compounding was also performed while the vacuum vent was on and off.

The dispersion quantity is related to the free-path spacing between the inclusion particle surfaces (rather than the particle center spacing), regardless of their shape or size. The more uniform the spacing between these inclusion surfaces, the higher the dispersion grade will be [8]. In order to quantify the dispersion quality, structural analysis was made on tomography images. Structural analysis is often used in trabecular bone studies in medical sciences. For this reason, bone and tissue terms in medical jargon are frequently confronted during tomography studies including structural analysis. For this reason, some software such as CTAn allows using both medical and scientific terms during analysis. Medical terms according to the American Society for Bone and Mineral Research or general scientific terms can be selected in preferences section of such software.

Structural model index (SMI) is an index that reveals the presence of structures such as rods or plates in a 3D structure. An ideal plate has a SMI value of “0,” a cylinder of “3,” and a sphere of “4.” The SMI values are important because if a spherical additive material is used, SMI can give information about the abundance of the spherical microparticles in the compound. Without aggregation, individual dispersions of the spherical microparticles within the compound will give SMI values close to “4.” Therefore, SMI can give information about the dispersion in the compound. The presence of wollastonite, glass fiber, or fibrous or rod-like fillers can also be demonstrated by the SMI value.

Structural thickness (ST) provides a value indicating 3D thickness. The method starts with a “skeletonization” identifying the medial axes of all structures. Then the “sphere-fitting” local thickness measurement is made for all the voxels lying along this axis [9]. This value, which is calculated as “trabecular thickness” in bone studies, is also calculated as “structural thickness” in general scientific nomenclature by CTAn software.

Structural separation (SP) is the thickness of the gaps (black) in the black/white images obtained after thresholding in volume of interest (VOI). The measurement by the software is computed the same as structural thickness, only the voids are measured instead of the solid voxel.

Structural linear density (SLD) corresponds to trabecular number, a very important term in bone studies. Structural linear density implies the number of traversals across a trabecular or solid structure made per unit length on a random linear path through the VOI [9]. Alternatively, this value can be expressed by the following formula:

$$SLD = 1 / (ST + SP).$$

Structural linear density gives information about the dispersion of the fillings in the compounds. To test this, artificial sections including beads with good dispersion and poor dispersion were created (Fig. 19.4). These sections were loaded into the CTAn software, and structural analyses were performed. It has been shown that SLD values can distinguish poorly dispersed beads from well-dispersed beads in the analyses performed. From tomography images, it is understood that in the samples including uncoated fillers, the filler dispersion is poor, there was no even spacing between particles, and there are agglomerates of filler particles. It has been observed that the individual filler particles are more dispersed in the composites prepared with coated fillers, in which the distribution is more homogeneous, the distances between the particles are almost equal, and there are no agglomerates. In order to quantitatively express this dispersion degree, the SLD values were calculated in these samples, and it was seen that the SLD values gave low values for bad dispersion and higher values for good dispersion. Aggregation of filler particles probably

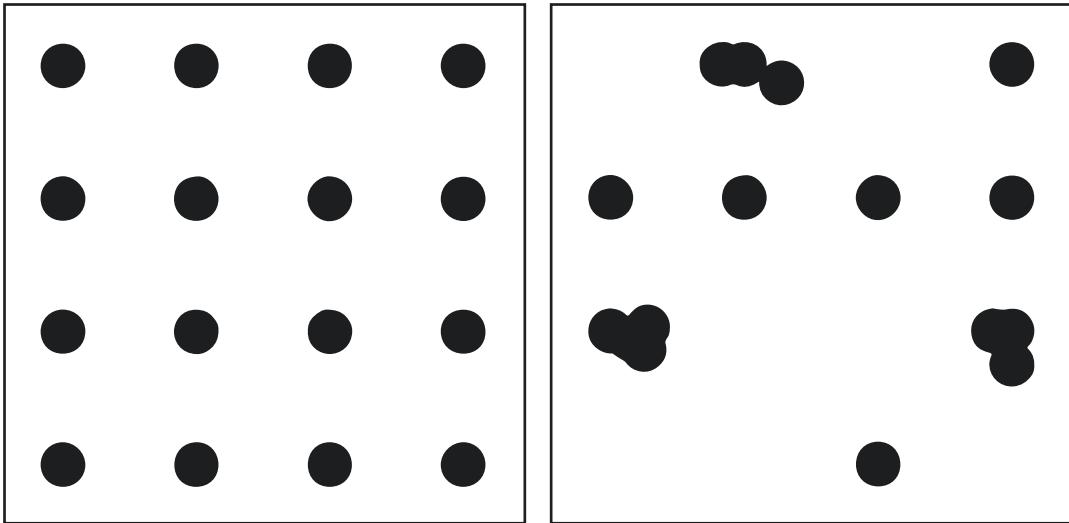
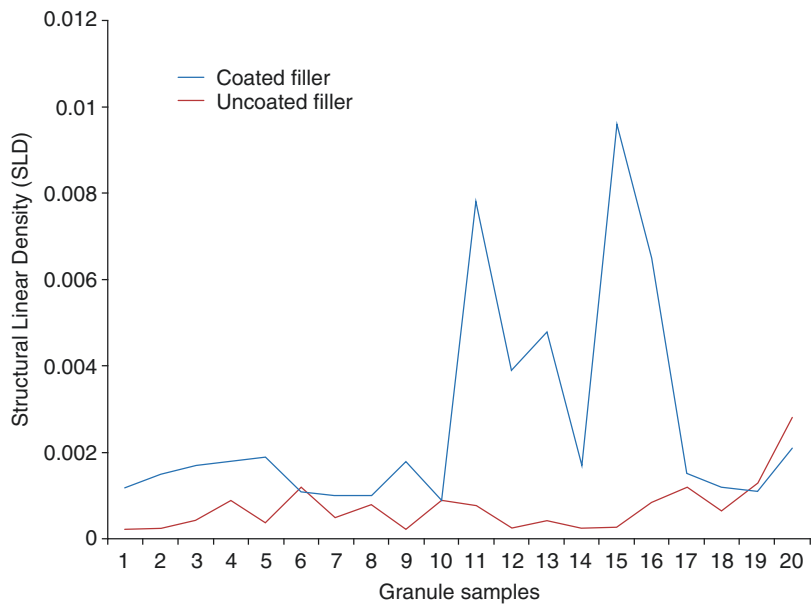


Fig. 19.4 Artificially created sections for good dispersion (left) and poor dispersion (right)

Fig. 19.5 Structural linear density values for granules including coated/uncoated calcium carbonate filler



increased the structural thickness (ST) values, resulting in a decrease in SLD values due to the inverse relationship in the above formula. In addition, the effect of agglomeration and poor dispersion has caused different spacing between the filler particles, and higher spacing values between the particles that accumulate in certain regions cause the structural separation (SP) value to rise. High SP values also caused low SLD values due to the inverse relationship in the equation.

In this study, for dispersion analysis 40 compound granules were analyzed. Half of these granules contained coated fillers, and the other half contained uncoated fillers. Granules including coated fillers with better dispersion quality have SLD values around 0.0027 ($\sigma = 0.0025$). Granules including uncoated fillers have SLD values around 0.0007 ($\sigma = 0.0006$) (Fig. 19.5). The dispersion of calcium carbonate particles in the polymer matrix can easily be seen on the 3D models of compound granules (Fig. 19.6). Stearic

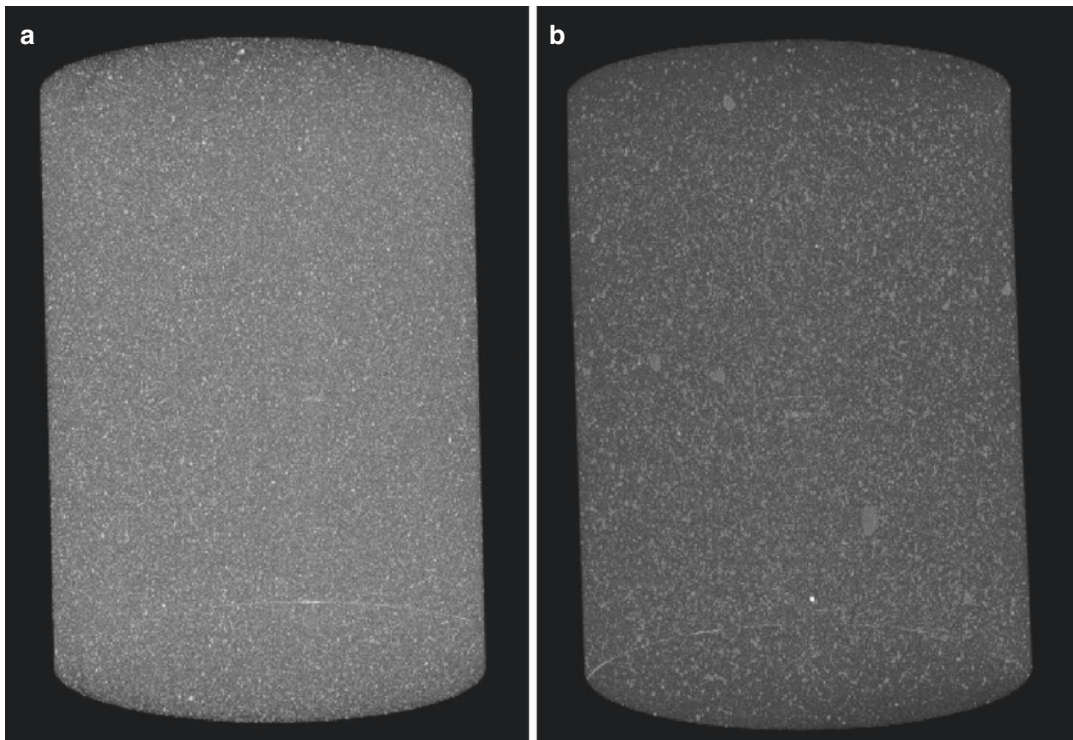


Fig. 19.6 Three-dimensional models of LDPE compound granules including (a) surface treated and (b) surface untreated calcium carbonate

acid coated calcium carbonate particles are more homogeneously distributed in the polymer matrix. Aggregates are observed in matrix including uncoated calcium carbonate grains.

19.5.2 Detection of Venting Quality in Compounding Process Using Micro-CT

Micro-tomography is a very effective method for diagnosing problems in compounding caused by ventilation problems due to its high resolution and its ability to perfectly distinguish components (polymer, filler, air, etc.) in the compound from their attenuation coefficients. In this study, compound granules including 50% LDPE and 50% calcium carbonate were extruded using twin-screw compounding extruder both when the vacuum vent was running and when it was not running. Granules obtained from two types of production were scanned with micro-CT.

In production with efficient venting, compounds are void-free, and their surfaces are smooth (Fig. 19.7). It was observed that the open

pores did not roughen the surface and no voids were formed in the inner parts of the compounds. Compound granules produced when the vacuum vent was not running have rough surfaces due to open pores on the surface (Fig. 19.8). These compounds also contain voids in their interior. The smoothness of the surface of compounds can be quantified with measuring some 3D parameters on tomography images. Surface-to-volume ratio or “specific surface” parameter is a useful parameter to characterize the complexity of surfaces.

Fractal dimension is another indicator of surface complexity. For the 3D calculation of fractal dimension, the volume is divided into an array of equal cubes, and the number of cubes containing part of the object surface is counted. This is repeated over a range of cube sizes such as 2–100 pixels. The number of cubes containing surface is plotted against cube length in a log-log plot, and the fractal dimension is obtained from the slope of the log-log regression [9].

The pores in and on the granules can be characterized in 3D by measuring some parameters. Closed or open porosity percentage in the gran-

Fig. 19.7 Transaxial, coronal, and sagittal views of a compound extruded while venting function of extruder was operating. 3D view of the compound is shown on the top right of the figure

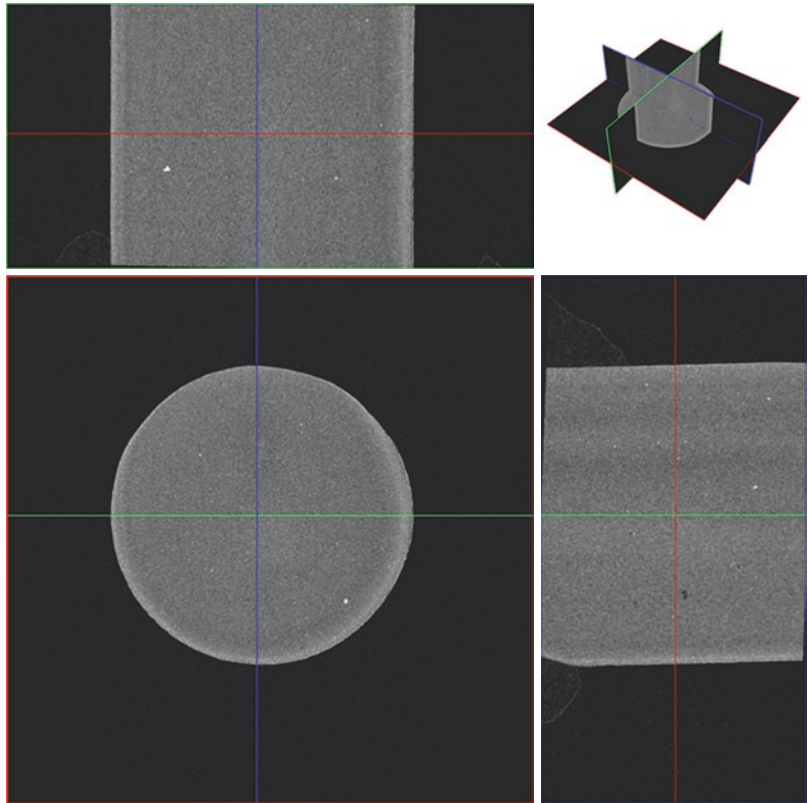


Fig. 19.8 Transaxial, coronal, and sagittal views of a compound extruded while venting function of extruder was disabled. Rough surface due to an open pore is marked with arrow. 3D view of the compound is shown on the top right of the figure

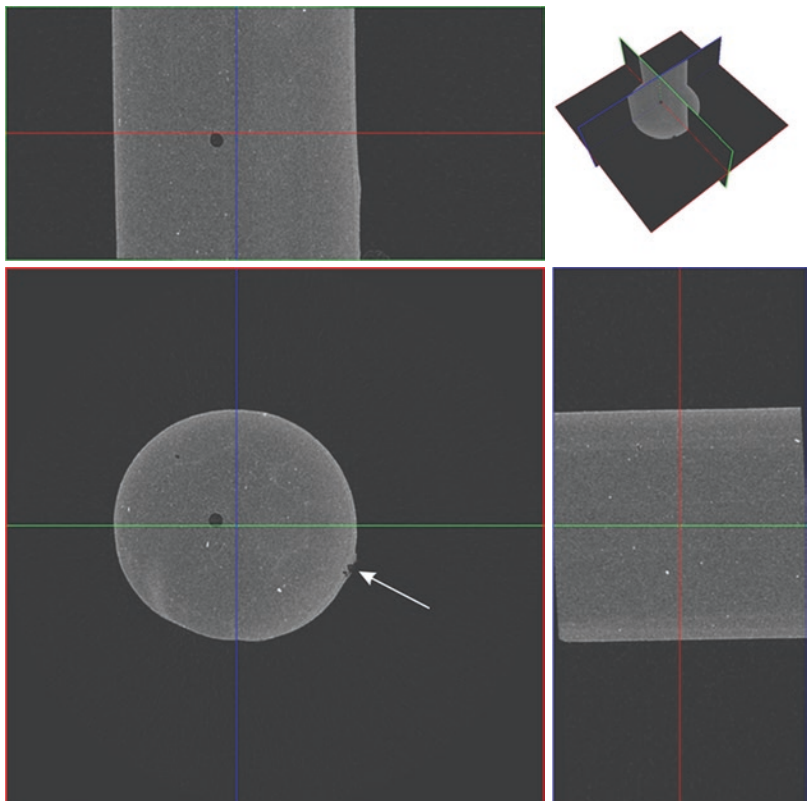
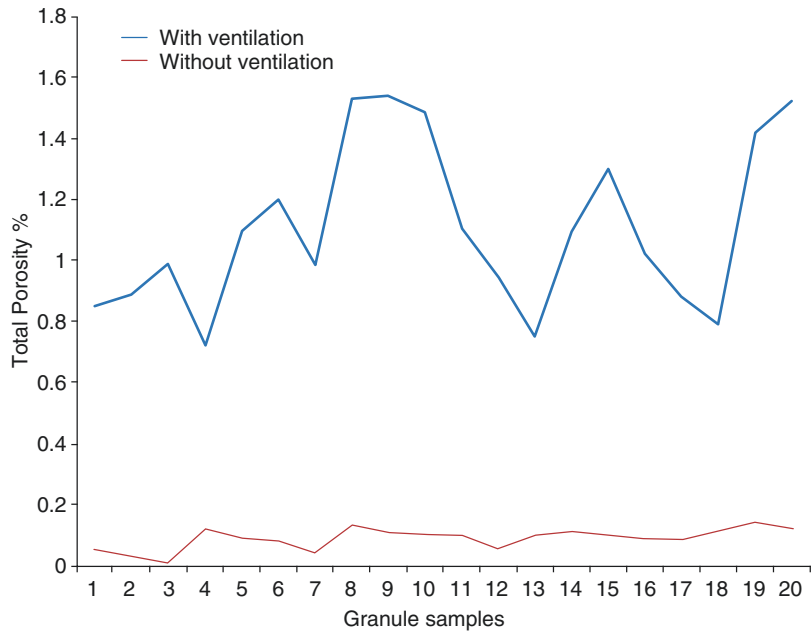


Fig. 19.9 Total porosity of granules produced with/without ventilation



ule allows us to comment on the success of the ventilation. The total porosity can also be calculated as the volume of all open plus closed pores as a percent of the total volume of interest (VOI).

Total porosity was calculated in 3D for 40 compounds. Half of these compounds were produced with ventilation during extrusion, and the other half were produced without venting. Total porosity values between 0.7% and 1.5% were calculated for granules produced without ventilation. According to venting of air and moisture, granules produced with venting have total porosity values between 0% and 0.1% (Fig. 19.9).

2D morphometric parameters can also be calculated on sections of granules. The smoothness of the outer wall of the granule can be characterized by parameters such as form factor, roundness, extent, and eccentricity.

19.6 Conclusion

The use of micro-tomography in science and the industry is increasing day by day because it is a nondestructive imaging method and gives high-resolution images of the sample. Tomography found areas of application itself in the plastic industry growing every day and took part in scien-

tific studies on plastics. In this study, the determination of venting and dispersion problems, which are frequently encountered in the production of plastic-based composites in industrial dimensions, has been tried by using micro-tomography. It can be seen that tomography, especially high-resolution devices, is able to distinguish the phases in the composite granules very successfully, depending on their attenuation coefficients.

In this study, dispersion quality of filler particles within compounds were determined using x-ray micro-tomography. While agglomeration was visualized, quantitative analysis of the dispersion quality was attempted with the help of quantitative analyses on these images. In addition to many approaches that can be applied, structural linear density calculations have been performed in this work to try to obtain a numerical value about the dispersion. Coated and uncoated fillers were used during granule extrusion. Dispersion in granules including coated filler was better with higher structural linear density values.

The porosity in the granules, which is a problem that can arise due to the moisture of the fillers and/or polymers used, has also been demonstrated in high resolution by tomography. To overcome this problem, the effectiveness of ven-

tilation, one of the measures that can be taken during granular extrusion, has also been proven by tomography images. The size and percentage of the pores in the granules produced by venting and without venting were visualized and measured by tomography. On tomography images total porosity values were calculated in 3D. Tomography proved that porosity increases in the absence of venting during extrusion.

References

1. Glaskova T, Zarrelli M, Borisova A, Timchenko K, Aniskevich A, Giordano M. Method of quantitative analysis of filler dispersion in composite systems with spherical inclusions. *Compos Sci Technol*. 2011;71:1543–9.
2. Hui, L., Smith, R.C., Wang, X., Nelson, J.K., Schadler, L.S.. Quantification of particulate mixing in nanocomposites. In: 2008 Annual report conference on electrical insulation dielectric phenomena. 2008, pp. 317–320.
3. Müller K, Bugnicourt E, Latorre M, Jorda M, Sanz YE, Lagaron JM, Miesbauer O, Bianchin A, Hankin S, Bözl U, Pérez G, Jesdinszki M, Lindner M, Scheuerer Z, Castello S, Schmid M. Review on the processing and properties of polymer nanocomposites and nanocoatings and their applications in the packaging, automotive and solar energy fields. *Nanomaterials (Basel)*. 2017;7(4):1–47.
4. Gramann, P., Rauvendaal, C., New dispersive and distributive mixers for extrusion and injection molding, w: 58 Annual Technical Conference ANTEC 2000, vol. 1, 2000, p. 111.
5. Xia HS, Wang Q. Preparation of conductive polyaniline/nanosilica particle composites through ultrasonic irradiation. *J Appl Polym Sci*. 2003;87:1811–7.
6. Dreiblatt A. Solve venting problems on twin-screw compounding extruders. *Plast Technol*. 2015;61(11):48–51.
7. Tuan HS, Hutmacher DW. *Comput Aided Des*. 2005;37(11):1151.
8. Luo ZP, Koo JH. Quantifying the dispersion of mixture microstructures. *J Microsc*. 2007;225:118–25.
9. Bruker. Morphometric parameters measured by Skyscan™ CTanalyser software. Kontich, Belgium: Bruker MicroCT; 2018. p. 1–49.